ÉCOLE DE TECHNOLOGIE SUPÉRIEURE
UNIVERSITÉ DU QUÉBEC

THESIS PRESENTED TO
ÉCOLE DE TECHNOLOGIE SUPÉRIEURE

IN PARTIAL FULFILLMENT OF THE REQUIREMENTS FOR
THE DEGREE OF DOCTOR OF PHILOSOPHY
Ph.D.

BY
Nicolas GASSET

REFINEMENT OF A MESOSCALE MODEL FOR LARGE EDDY SIMULATION

MONTREAL, JULY 25, 2014

BOARD OF EXAMINERS

THIS THESIS HAS BEEN EVALUATED

BY THE FOLLOWING BOARD OF EXAMINERS:

Mr. Christian Masson, Eng., Ph.D., Thesis Director
Département de génie mécanique, École de technologie supérieure

Mr. Robert Benoit, Ph.D., Thesis co-Director
Département de génie mécanique, École de technologie supérieure

Mr. François Brissette, Eng., Ph.D., Committee President
Département de génie de la production automatisée, École de technologie supérieure

Mr. Ayrton Zadra, Ph.D., External Examiner
Recherche en Prévision Numérique, Environnement Canada

Mr. Louis Dufresne, Eng., Ph.D., Examiner
Département de génie mécanique, École de technologie supérieure

THIS THESIS WAS PRESENTED AND DEFENDED

IN THE PRESENCE OF A BOARD OF EXAMINERS AND PUBLIC

ON OCTOBER 23, 2013

AT ÉCOLE DE TECHNOLOGIE SUPÉRIEURE

ACKNOWLEDGEMENTS

This doctorate was completed at the École de technologie supérieure (ÉTS) under the co-direction of Christian Masson and Robert Benoit. I would like to gratefully acknowledge them for their trust, support and patience throughout this long project. This has been greatly appreciated and has allowed me to successfully complete this doctorate.

I thank the Wind Energy Strategic Network (WESNet) of the Natural Sciences and Engineering Research Council of Canada (NSERC) and Environment Canada (EC) for their joint Ph.D. scholarships. I also thank the ÉTS for its grants and the facilities provided.

I also acknowledge the research group Recherche en Prévision Numérique (RPN) from EC for its support and for granting me access to advanced and not yet public versions of the Mesoscale Compressible Community Model (MC2) source code. Particularly, my sincere thanks to Dr. Claude Girard for his support and fruitful suggestions, and to Dr. Jocelyn Mailhot and Dr. Lubos Spacek for their guidance during the integration of the new physics library to the model.

I truly thank Dr. Ayrton Zadra, Prof. Louis Dufresne and Prof. François Brissette for agreeing to evaluate the work of this thesis.

I wish also to thank my colleagues at the Research Laboratory on the Nordic Environment Aerodynamics of Wind Turbines (NEAT), especially my friends Joël Bédard and Simon-Philippe Breton for their constant support, positive attitude and for helping me with the corrections of the literature review. I would also like to thank Jon Sumner for his inspiring ideas, comments and for reviewing the associated journal paper. And also my acknowledgement to Alex Flores Maradiaga for pursuing my work.

Finally, for their constant, active and unfailing support and clairvoyance at every moment during the many years of this project, a very special thanks to my parents and sister (despite the geographical distance, you were always nearby), my children, and above all, my wife.
Monelle: you have all been immensely wonderful and this thesis is dedicated to you.

REFINEMENT OF A MESOSCALE MODEL FOR LARGE EDDY SIMULATION

Nicolas GASSET

ABSTRACT

With the advent of wind energy technology, several methods have become mature and are seen today as standard for predicting and forecasting the wind. However, their results are still site dependent, and the increasing sizes of both modern wind turbines and wind farms tackle limits of existing methods. Some triggered processes extend to the junction between microscales and mesoscales.The main objectives of this thesis are thus to identify, implement and evaluate an approach allowing for microscale and mesoscale ABL flow modelling considering the various challenges of modern wind energy applications.

A literature review of ABL flow modelling from microscales to mesoscales first provides an overview of the specificities and abilities of existing methods. The combined mesoscale/large eddy simulation (LES) modelling appears to be the most promising approach, and the Compressible Community Mesoscale Model (MC2) is elected as the basis of the method in which the components required for LES are added and implemented. A detailed description of the mathematical model and the numerical aspects of the various components of the LES-capable MC2 are then presented so that a complete view of the proposed approach along with the specificities of its implementation are provided. This further allows to introduce the enhancements and new components of the method (separation of volumetric and deviatoric Reynolds tensor terms, vertical staggering, subgrid scale models, 3D turbulent diffusion, 3D turbulent kinetic energy equation), as well as the adaptation of its operating mode to allow for LES (initialization, large scale geostrophic forcing, surface and lateral boundaries). Finally, fundamental aspects and new components of the proposed approach are evaluated based on theoretical 1D Ekman boundary layer and 3D unsteady shear and buoyancy driven homogeneous surface full ABL cases. The model behaviour at high resolution as well as the components required for LES in MC2 are all finely evaluated, including: the dynamic kernel at high resolution; space and time discretization of the 3D turbulent diffusion; five subgrid scale models; and the sensitivity of the model to numerical parameters. Furthermore, LES test cases are thoroughly studied, showing that a longer time interval for post-processing than in the reference studies is needed due to a high but normal level of scatter in the results.

In the end, the obtained LES-capable mesoscale model is shown to perform on par with other similar reference LES models, albeit it is slightly more dissipative. It is thus demonstrated that the adapted MC2 is suitable for both micro- and mesoscales providing a strong foundation for more advanced studies.

Keywords: atmospheric boundary layer, large eddy simulation, column model, mesoscale, microscale, neutral, convective, compressible

REFINEMENT OF A MESOSCALE MODEL FOR LARGE EDDY SIMULATION

Nicolas GASSET

RÉSUMÉ

L'avènement de la technologie éolienne s'est accompagné de l'arrivé à maturité des méthodes pour prédire et prévoir le vent. Toutefois, leurs résultats dépendent encore des sites étudiés, et leurs limites commencent à être atteintes avec l'augmentation de la taille des parcs et des éoliennes modernes. Certains des processus en présence sont maintenant à la limite des microéchelles et des mésoéchelles. Les objectifs de la thèse sont donc d'identifier, d'implémenter et d'évaluer une approche capable de modéliser les écoulements dans la couche limite atmosphérique (CLA) à ces échelles en considérant les défis liés aux applications éoliennes.

Une revue de la modélisation des écoulements de la CLA allant des microéchelles aux mésoéchelles est tout d'abord réalisée. La combinaison des approches mésoéchelle/simulation aux grandes échelles (SGÉ) ressort comme étant la plus prometteuse, et le Modèle Mésoéchelle Compressible Communautaire (MC2) est choisi comme point de départ auquel sont ajoutés et implémentés les éléments requis pour la SGÉ. S'en suivent, la description détaillée du modèle mathématique et des aspects numériques de la version de MC2 adaptée pour la SGÉ. Ainsi, l'approche proposée est clairement illustrées tant dans son ensemble, qu'au niveau des spécificités de son implémentation. Cela inclus les améliorations et les nouvelles composantes de la méthode (séparation du traitement des parties volumétriques et déviatoriques du tenseur de Reynolds, discrétisation verticale, modèles de sous-mailles, diffusion turbulente 3D, équation prognostique 3D de l'énergie cinétique turbulente), ainsi que les adaptations de son mode opératoire permettant la SGÉ (initialisation, forçages géostrophiques grande échelle, condition limites de surface et latérales). Finalement, les aspects fondamentaux et les nouvelles composantes de l'approche proposée sont évalués basé sur des cas 1D de couche limite d'Ekman et des cas 3D et instationnaires de CLA complète neutre et convective au dessus d'une surface homogène. Cela permet de finement évaluer : le noyau dynamique à haute résolution ; la discrétisation spatiale et temporelle de la diffusion turbulente 3D ; cinq modèles de sous-maille ; et la sensibilité du modèle aux paramètres numériques principaux. De plus, létude détaillée des cas tests 3D démontre que des intervalles de temps plus long que dans l'étude de référence sont nécessaires à cause d'une dispersion importante mais normale dans les résultats.

En définitive, il est prouvé que le modèle mésoéchelle adapté pour la SGÉ est aussi performant que les modèles SGÉ équivalents, quoique sensiblement plus dissipatif. Il est donc démontré que les modifications apportées à MC2 lui permettent d'opérer tant aux microéchelle qu'aux mésoéchelles, ce qui représente une base solide pour des études plus avancées.

Mot-clés : couche limite atmosphérique, simulation aux grandes échelles, modèle colonne, mésoéchelle, microéchelle, neutre, convectif, compressible

CONTENTS

LIST OF TABLES

LIST OF FIGURES

LIST OF ABBREVIATIONS

agl	Above ground level
ABL	Atmospheric Boundary Layer
ADI	Alternative Direction Implicit preconditioner method
ADM	Approximate Deconvolution Model
AR-WRF	Advanced Research WRF model
ARM	Advanced Reconstruction Model
ARPS	Advanced Regional Prediction System
ASCII	American Standard Code for Information Interchange
CAPS	Center for Analysis and Prediction of Storms
CASES-99	Cooperative Atmosphere-Surface Exchange Study - 1999
CBL	Convective Boundary Layer
CFD	Computational Fluid Dynamics
CFL	Courant–Friedrichs–Lewy number
CLA	Couche Limite Atmosphérique
CLASS	Canadian LAnd Surface Scheme
CMC	Canadian Meteorological Centre
CNRM	Centre National de Recherche en Météorologie
COMPARE	Comparison of Mesoscale Prediction and Research Experiment
COSMO	COnsortium for Small-scale MOdelling

CPU	Computational Processor Unit
CWE	Computational Wind Engineering
CWEA	Canadian Wind Energy Atlas
DNS	Direct Numerical Simulation
DRM	Dynamic Reconstruction Model
DW	Deutscher Wetterdienst, German weather services
DWL	Dynamic Wong Lilly
EC	Environment Canada
EDQNM	Eddy-Damped Quasi-Normal Markovian theory
EPA	Environment Protection Agency
ERCOFTAC	European Research Community on Flow Turbulence and Combustion
ESL	Eddy Surface Layer
FE	Finite Element
FFT	Fast Fourier Transform
FORTRAN	FORmula TRANslator
FST	Fichier STandard from EC
FV	Finite Volume
GABLS	GEWEX Atmospheric Boundary Layer Study
GCM	General Circulation Models
GEM	Global Environment Multiscale unified model

GEWEX	Global Energy and Water Cycle Experiment
GFS	Global Forecast System
GMRES	Generalized Minimal Residual iterative solver
GPL	Global Public License
GRIB	GRIdded Binary or General Regularly-distributed Information in Binary form
HAZ	High Accuracy Zone
HIBU	Hydrometeorological Institute and Belgrade University
HIRLAM	High Resolution Limited Area Model
HPC	High Performance Computers
IOP	Intense Observation Period
ISBA	Interaction Soil-Biosphere-Atmosphere model
KAMM	Karlsruhe Atmospheric Mesoscale Model
LA	Laboratoire d'Aérologie
LAM	Limited Area Model
LEM	Large Eddy Model
LES	Large Eddy Simulation
LES-NWM	Near Wall Modelled LES
LES-NWR	Near Wall Resolved LES
LGPL	Lesser General Public Licence
LIDAR	LIght Detection And Ranging

LM	Lokal-Modell
LRR	Launder-Reece-Rodi second order Reynolds stress model
MAP	Mesoscale Alpine Programme
MATLAB	MAtrix LABoratory
MC2	Compressible Community Mesoscale Model
MERMOZ	Montreal-96 Experiment on Regional Mixing and Ozone
MIT	Massachusetts Institute of Technology
ML	Mixed Layer
MM5	Mesoscale Model version 5
MMK	Murakami, Mochida and Kondo k-e model
MMM	Mesoscale and Microscale Meteorology
MO	Monin-Obukhov
MOS	Model Output Statistics
MPG	Mesoscale Prediction Group
MRB	Meteorological Research Branch
MS94	Moeng and Sullivan (1994)
MSFD	Mixed Spectral Finite Difference
MY	Mellor and Yamada
NA	Not Accessible
NAM	North American Model

NBL	Nocturnal Boundary Layer
NCAR	National Center for Atmospheric Research
NCEP	National Centers for Environmental Prediction
NH	Non-Hydrostatic
NOAA	National Oceanic and Atmospheric Administration
NS	Navier-Stokes
NWP	Numerical Weather Prediction
PISO	Pressure Implicit with Split Operator method
PSU	Penn State University
PYREX	PYRenées EXperiment
RAMS	Regional Atmospheric Modeling System
RANS	Reynolds Averaged Navier-Stokes
RMS	Root Mean Square
RNG	ReNormalization Group
RPN	Recherche en Prvision Numrique
RSFS	Resolved SubFiltered Scale
RSM	Reynolds Stress Model
SA	StAndalone
SBL	Stable Boundary Layer
SD	Standard Deviation

SFS	SubFiltered Scale
SGE	Simulation aux Grandes Échelles
SGS	SubGrid Scale
SI	Semi-Implicit
SISL	Semi-Implicit Semi-Lagrangian
SL	Semi-Lagrangian
SODAR	Sonic Detection And Ranging
SSL	Shear Surface Layer
T-REX	Terrain-induced Rotor EXperiment
TKE	Turbulent Kinetic Energy
UDF	User Define Function
UK	United Kingdom
UKMO	United Kingdom Met Office
UM	Unified Model
URANS	Unsteady Reynolds Averaged Navier-Stokes Equations
US	United States
WAsP	Wind Atlas Analysis and Application Program
WEST	Wind Energy Simulation Toolkit
WMO	World Meteorology Organization
WRF	Weather Research and Forecast
WRF-NMM	WRF Non-hydrostatic Mesoscale Model

LIST OF SYMBOLS

Constants

c_p	Specific heat capacity of dry air at constant pressure: 1005.46 [$m^2/s^2/K$]
c_v	Specific heat capacity of dry air at constant volume: 717 [$m^2/s^2/K$]
e	Euler constant: 2.71828
κ	von Karman constant: 0.4
g	Gravitational acceleration: 9.80616 [m/s^2]
π	Pi number: 3.14159
R	Gas constant for dry air: 287.05 [$m^2/s^2/K$]
Ri_c	Critical Richardson number: 0.25

Operator and general mathematical notation (for any variable ψ)

i, j, k	Absolute and projected indices on the dynamics grid in the streamwise, spanwise and vertical directions
i, j, k	Projected indices on the physics grid in the streamwise, spanwise and vertical directions
$\boldsymbol{i}, \boldsymbol{j}, \boldsymbol{k}$	Unity vector in the streamwise, spanwise and vertical directions
$\psi_{i,j,k}$	Location of a variable on the dynamic grid in absolute index
$[\psi]_{i,j,k}$	Location of a variable on the dynamic grid in projected index
$\{\psi\}_{\mathrm{i,j,k}}$	Location of a variable on the physic grid in projected index
$\overline{\psi}^{\mathbf{X}}, \overline{\psi}^{\mathbf{Y}}\overline{\psi}^{\mathbf{Z}}$	Interpolation of a variable in the streamwise, spanwise and vertical directionss
$\delta_x\psi, \delta_y\psi, \delta_z\psi$	Finite difference of a variable in the streamwise, spanwise and vertical directions
δ_{ij}	Kronecker delta tensor
ε_{ijk}	Alternating tensor
$\boldsymbol{\psi}$	Vector of a variable
$\overline{\psi}$	Time (Reynolds) or space filtered variable
$\widetilde{\psi}$	Favre filtered variable
$\langle\psi\rangle$	Horizontally averaged variable
$\widehat{\psi}$	Variable transformed in the Fourier space
$\check{\psi}$	Variable transformed in sigma coordinate
$o(\psi)$	Scatter of result parameters; mean scatter of variables from 0 to $1.2z_i$ m
$\sigma(\psi)$	RMS of the scatter of variables from 0 to $1.2z_i$ m
$\boldsymbol{\nabla}$	Differential operator
$\lvert\psi\rvert$	Absolute value of a variable
$\lVert\boldsymbol{\psi}\rVert$	Modulus of a vector
f, g	Functions
f', g'	Derivative of functions
$d\psi/dt$	Material derivative of a variable
$\partial\psi/\partial t, \partial\psi/\partial x, \partial\psi/\partial y, \partial\psi/\partial z$	Partial derivative of a variable in time, and in streamwise, spanwise and vertical directions
ψ_1	Variable at the vertical mesh level z_1 (variable dependent) above the ground surface
ψ_a	Variable at a given height z_{a_M} or z_{a_H} above the ground surface in the surface layer

ψ_{diag}	Variable at a given diagnostic vertical level in the surface layer
ψ_{ls}	Variable representing the large scale reference state
$\psi_s, \psi\|_s$	Ground surface value of a variable
ψ'	Fluctuation from a Favre filtered variable ($= \psi - \widetilde{\psi}$)
ψ‘	Fluctuation from a time (Reynolds) or space filtered variable ($= \psi - \overline{\psi}$)
ψ''	Deviation from the hydrostatic isothermal stationary reference state ($= \psi - \psi_*$)
ψ'''	Deviation from the large scale stationary reference state ($= \psi - \psi_{ls}$)

Greek symbols

α	Coefficient
$\boldsymbol{\alpha}, \alpha, \beta, \gamma$	Half Lagrangian displacements vector at the centre of the trajectory and its streamwise, spanwise and vertical components
$\boldsymbol{\alpha'}$	Vector of the half Lagrangian displacement at the arrival of the trajectory
$\alpha_\psi, \alpha_M, \alpha_T$	Generic, momentum and temperature surface boundary condition inhomogeneous terms
α_u, α_v	Velocity component surface boundary condition inhomogeneous terms
β	Coefficient
$\beta_\psi, \beta_M, \beta_T$	Generic, momentum and temperature surface boundary condition homogeneous terms
β_u, β_v	Velocity component surface boundary condition homogeneous terms
γ	Coefficient; function; inverse of characteristic Ekman boundary layer height
$\gamma^{tot}_{\overline{uw}}, \gamma^{+}_{\overline{uw}}, \gamma^{-}_{\overline{uw}}$	Total, updrafts and downdrafts vertical momentum flux correlation coefficients
ϵ	Off-centring parameter
ε	Turbulent dissipation rate
θ	Potential temperature; wind velocity direction
$\theta_*, \theta_*^{SL}, \theta_*^{ML}$	General, surface layer and mixed layer temperature scale
θ_i	Initial profile of potential temperature profile of the sounding initialization
λ	Mixing length scale
λ_ε	Dissipation length scale
λ_0	Interior flow mixing length scale for neutral condition
λ_e	Asymptotic equilibrium mixing length scale for neutral condition
λ_H, λ_{3d}	Mixing length scale based on the horizontal resolution only, on the 3D resolution
λ_r	Characteristic mixing length scale of turbulence
μ	Molecular viscosity
μ_t	Turbulent eddy viscosity
ν	Kinematic molecular viscosity
ν_h	Kinematic turbulent thermal diffusivity
ν_t	Kinematic turbulent eddy viscosity; fluctuating eddy viscosity of Sullivan SGS model
ν_T	Ensemble averaged eddy viscosity of Sullivan SGS model
ν_{LES}	LES model viscosity
$\nu_{\textbf{sponge}}$	Numerical viscosity of the sponge layer
π	Exner function
$\boldsymbol{\varpi}, \varpi_u, \varpi_v, \varpi_w$	Random velocity perturbation vector, streamwise, spanwise and vertical components
ϖ_{max}	Maximum random velocity perturbation
ρ	Air density

σ	Parameter; sigma vertical coordinate
σ_B, σ_T	Bottom and top sigma levels
$\sigma_t, \sigma_m, \sigma_e$	Momentum, temperature and TKE sigma levels
τ_*	Eddy turnover time
τ_{ij}	Shear stress tensor (Reynolds tensor when an implicit filtering is used)
τ_w	Wall shear stress
ϕ_M, ϕ_H	Dimensionless velocity and temperature vertical gradients (*i.e.* stability functions, or flux-profile relationships)
Φ_M, Φ_H	Integrated dimensionless velocity and temperature stability functions (surface transfer coefficients)
ω	Specific dissipation rate
Ω_{ij}	Velocity rotation tensor
Δ	General LES filter width
Δ_{3d}	LES filter width based on the 3D resolution
Δ_H	LES filter width based on the horizontal resolution only
ΔS	Velocity speed-up
Δt	Time step
Δt_{out}	Output time step
$\Delta x, \Delta y, \Delta z$	Length increment in the streamwise, spanwise and vertical directions
$\Delta z_m, \Delta z_t, \Delta z_w$	Length increment on momentum, temperature and vertical velocity vertical levels
$\boldsymbol{\Psi}$	Model main variables in matrix form
$\boldsymbol{\Psi}_D^+$	$\boldsymbol{\Psi}$ at time t^+ after the Euler equation is solved
$\boldsymbol{\Psi}_{DE}^+$	$\boldsymbol{\Psi}$ at time t^+ after the nesting is achieved
$\boldsymbol{\Psi}_{DEF}^+$	$\boldsymbol{\Psi}$ at time t^+ after the physic is achieved
$\boldsymbol{\Psi}_{DEFH}^+$	$\boldsymbol{\Psi}$ at time t^+ after the horizontal diffusion is achieved
$\boldsymbol{\Psi}_T^0$	$\boldsymbol{\Psi}$ at time t^0 after the Robert/Asselin time filter is applied
$\boldsymbol{\Psi}_{\boldsymbol{x}}^+$	$\boldsymbol{\Psi}$ at time t^+ at the arrival of the Lagrangian trajectory
$\boldsymbol{\Psi}_{\boldsymbol{x}-2\boldsymbol{\alpha}}^-$	$\boldsymbol{\Psi}$ at time t^- at the upwind of the Lagrangian trajectory

Latin symbols

a, b, c	Coefficient; parameters
A, B, C, D	TKE prognostic equation terms
$A_{dyn}, B_{dyn}, C_{dyn}, D_{dyn}$	TKE prognostic equation terms computed in the dynamics
$A_{phy}, B_{phy}, C_{phy}, D_{phy}$	TKE prognostic equation terms computed in the physics
A, A_x, A_y, A_z	Intermediate isotropic turbulent diffusion terms (variances)
A_u, B_u	Intermediate streamwise velocity turbulent diffusion terms (fluxes)
A_v, B_v	Intermediate spanwise velocity turbulent diffusion terms (fluxes)
A_w, B_w	Intermediate vertical velocity turbulent diffusion terms (fluxes)
A_T, B_T, C_T	Intermediate temperature turbulent diffusion terms (fluxes)
A_k, A_ε	Closure constants of Redelsperger SGS model
b	Buoyancy (model main variable)
c_*	Sound speed
$\boldsymbol{c}_g$	Geostrophic wind forcing vector
CFL	Courant–Friedrichs–Lewy number

C_{CFL}	Free atmosphere CFL
$C_{\mathrm{CFL}}^{\max}$	Maximum local instantaneous CFL
$C_{\mathrm{CFL}}^{\langle\overline{u}\rangle}$	Time and horizontally averaged velocity CFL
C_d	Drag coefficient
C_{ij}	Cross terms stress tensor
C_M, C_H	Momentum and heat surface transfer coefficients
C_{Kol}	Kolmogorov constant generally taken equal to $1.5 - 1.6$
$C_S, C^{\mathbf{std}}$	Smagorinsky constant
$C_{S\,3d}$	Smagorinsky constant based on Δ_{3d} and effective value of $C_{S\,H}$
$C_{S_{eqv}}$	Equivalent Smagorinsky constant of non-Smagorinsky SGS models
$C_{S\,H}$	Smagorinsky constant based on Δ_H
$C^{\mathbf{dyn}}$	Dynamically found Smagorinsky constant
C_μ	TKE production closure constant of TKE based RANS models
C_k	TKE production closure constant of TKE based SGS models
C_ε	TKE dissipation closure constant of TKE based SGS models
C_{tke}	TKE diffusion closure constant of TKE based SGS and column models
C_k'	TKE production closure constant of the hybrid TKE SGS model and column model
C_ε'	TKE dissipation closure constant of the hybrid TKE SGS model and column model
C_Δ	Closure constant of the hybrid TKE SGS model related to the Smagorinsky constant
C_1, C_2	Coefficients; Closure constants for non-linear terms of Kosović SGS model
C_1'	Coefficient
C_b	Backscatter of TKE closure constant
C_t	Generic SGS model closure constant
C_u, C_v, C_g, C_{TKE}	Longitudinal, spanwise wind components, geostrophic drag and total TKE integrated coefficients
D_{nor}	Function used in the definition of new vertical mesh
$\mathcal{D}_k$	Diffusion term of the TKE equation
E	TKE (weather science); Energy spectra
$\boldsymbol{E}$	Nesting of the model variables with the driving data in matrix form
E_u, E_v, E_w	Longitudinal velocity spectra of streamwise, spanwise and vertical velocity components
$\mathbf{f}, \mathbf{f}_H, \mathrm{f}_w$	External forcing vector of Navier-Stokes equations and its horizontal and vertical components
f_m, f_h	Momentum and heat stability functions of UKMO Smagorinsky and hybrid TKE SGS models
$f_{m_{std}}, f_{h_{std}}$	Standard momentum and heat stability functions of UKMO Smagorinsky SGS model
F, G	Parameter
$\mathbf{F}$	External forcing of the filtered momentum conservation equations (includes $\mathbf{f}$ and turbulent diffusion terms)
$\boldsymbol{F}$	External forcing and heat sources of the filtered Euler equations in matrix form (includes $\mathbf{f}$, Q and turbulent terms)
$F^*_{\Psi\,\boldsymbol{x}}$	External forcing of the passive scalar conservation equation
$\boldsymbol{F}_{turb}$	Part of $\boldsymbol{F}$ including turbulent terms only
$F_{u\,turb}, F_{v\,turb}, F_{w\,turb}, F_{T\,turb}$	Streamwise, spanwise, vertical velocities, and temperature components of $\boldsymbol{F}_{turb}$

$\boldsymbol{F}^V_{turb}, \boldsymbol{F}^H_{turb}$	Vertical and horizontal part of $\boldsymbol{F}_{turb}$
$F^V_{u\,turb}, F^V_{v\,turb}, F^V_{T\,turb}$	Streamwise, spanwise velocities, and temperature components of $\boldsymbol{F}^V_{turb}$
$F^H_{u\,turb}, F^H_{v\,turb}, F^H_{w\,turb}, F^H_{T\,turb}$	Streamwise, spanwise, vertical velocities, and temperature components of $\boldsymbol{F}^H_{turb}$
h	Parameter; height of orography above sea level; height of the stable boundary layer
h_x, h_y	Streamwise and spanwise computational domain lateral halo sizes (in index)
$\boldsymbol{H}$	Numerical horizontal diffusion added to the Euler equations in matrix form
k	Turbulent kinetic energy (TKE)
k_{tot}	Total TKE (resolved and subgrid)
k_μ	Parameter of D_{nor} function
k_x	Longitudinal wave number
K_ψ, K_M, K_T, K_k	Generic, momentum, temperature and TKE turbulent mixing coefficients
l, l_t	Length; characteristic mixing length scale of turbulence
l_{RANS}, l_{LES}	RANS mixing length and LES filter width of Bechmann hybrid SGS model
L_{MO}	Monin-Obukhov length scale
L_{x_i}, L_x, L_y, L_z	Generic, streamwise, spanwise and vertical sizes of the computational domain
$\mathcal{L}_k, \mathcal{L}_\varepsilon$	Mixing and dissipation length scales of Redelsperger SGS model
$\mathcal{L}_N$	Mixing length based on N for stable stratification of Deardorff based SGS model
$\mathcal{L}_S$	Mixing length based on S for stable stratification of Kosovi SGS model
$\boldsymbol{L}$	Linear terms of the Euler equations of motion in matrix form
$\boldsymbol{L}^{tr}$	$\boldsymbol{L}$ averaged in time along the Lagrangian trajectory
L_{ij}	Léonard stress tensor
n	Integer parameter; iteration number
N	Brunt-Väisälä frequency
N_*	Reference isothermal state Brunt-Väisälä frequency
N_i, N_j, N_k	Number of points of the computational domain in the streamwise, spanwise and vertical directions
n_k	Numbers of vertical levels
$N_{\textbf{sponge}}$	Number of levels in the top sponge layer
p, p_t	Pressure on momentum and temperature levels
p_0	Constant; Pressure at the ground surface
p_h, p_{ht}	Hydrostatic pressure on momentum and temperature levels
p_{red}	Reduce pressure, *i.e.* including volumetric part of Reynolds tensor
p_*	Hydrostatic isothermal reference pressure
$\mathcal{P}_k$	Production term of the TKE equation
P	Generalized pressure (model main variable)
q	Normalized pressure ($= \ln(p/p_0)$)
q_*	Hydrostatic isothermal reference normalized pressure
$\mathcal{Q}$	Heat sources in the filtered internal energy conservation equation (Q and turbulent diffusion terms)
Q	Heat sources in the internal energy conservation equation
$\boldsymbol{Q}$	Linear and non-linear terms of the system of equation solve by the model
r	Parameter
R_{ij}	Reynolds stress tensor
$\boldsymbol{R}$	Non-linear terms of the Euler equations of motion in matrix form

$\boldsymbol{R}^{tr0}$	$\boldsymbol{R}$ spatially averaged along the Lagrangian trajectory at t^0
$\boldsymbol{R}_{turb}$	Part of $\boldsymbol{R}$ including only turbulent terms
$\boldsymbol{R}_{ls}$	Part of $\boldsymbol{R}$ including only large scale forcing terms
$R_{u\,ls}, R_{v\,ls}, R_{T\,ls}$	Streamwise, spanwise velocities and temperature components of $\boldsymbol{R}_{ls}$
$\mathfrak{R}$	Ratio of resolved over subgrid turbulent stress at the first grid level
S	Modulus of the strain rate tensor
S_{ij}	Strain rate tensor
$\mathcal{S}(k_c)$	Velocity derivative skewness function
t	Time
T	Absolute temperature
T_*	Hydrostatic isothermal reference temperature
$\boldsymbol{T}$	Robert/Asselin time filter in matrix form
T_{inert}	Inertial period
U	Wind velocity modulus
U_{MO}	Wind velocity modulus computed based on the similarity theory
u_t	Characteristic velocity scale of turbulence
u_*	Friction velocity
$\overline{u'v'}, \overline{u'w'}, \overline{v'w'}$	Turbulent momentum fluxes
$\overline{u'^2}, \overline{u'^2}, \overline{u'^2}$	Turbulent momentum variances
$\overline{u'\theta'}, \overline{v'\theta'}, \overline{w'\theta'}$	Turbulent heat fluxes
u^+w^-, u^-w^+	Sweeps process and ejection process
$\boldsymbol{v}, u, v, w$	Wind velocity vector and its streamwise, spanwise and vertical components (model main variables)
$\boldsymbol{v}_g, u_g, v_g$	Geostrophic wind vector, and its streamwise and spanwise components
w_*	Convective velocity scale
$\overline{w'u'^2}, \overline{w'v'^2}, \overline{w'^3}$	Vertical turbulent fluxes of velocity variances
$\overline{w'U'}\|_s$	Surface turbulent momentum fluxes in the wind direction
$\overline{w'\theta'}_i$	Turbulent heat flux at the inversion
W_{z_t}	Momentum to temperature levels vertical interpolation Coefficient
x, y, z	Streamwise, spanwise, and vertical Cartesian coordinates
$\boldsymbol{x}$	Arrival location of a Lagrangian trajectory (correspond to a grid point)
x, x_0, y, y_0	Intermediate variable of surface layer integrated stability functions
z^+	Dimensionless wall distance
z_0	Aerodynamic roughness length
z_{0_M}, z_{0_H}	Momentum and heat aerodynamic roughness length
z_1	Height above the surface of the first vertical level (variable dependent)
z_{a_M}, z_{a_H}	Height of the momentum and heat levels used to compute integrated surface transfer coefficients
z_c	Critical height
z_i	Height of the ABL (minimum heat flux at the inversion)
z_{i_e}	Stability dependent ABL height
z_m, z_w, z_t	Momentum, vertical velocity and temperature level heights
z_{ref}, z_{top}	Reference and top height defining the new vertical mesh
Z	New vertical coordinate
Z_{log}, Z_{nor}	Function used in the definition of new vertical mesh

INTRODUCTION

The last two decades have seen substantial growth of wind energy industry with northern Europe countries such as Denmark and Germany driving most of the early stage developments. Wind energy technology has become mature and versatile, and it is considered today as a realistic approach to produce mass electricity. The world cumulative installed wind capacity has grown exponentially as illustrated in Fig. 0.1. Canada and Québec are no exception with a total installed capacity that has been multiplied by 30 over the last decade going from a meagre 137 MW in 2000 mostly installed in Cap-Chat/Matane, Québec to 5511 MW in June of 2012 distributed across Canada with a fifth of that capacity installed in Québec.

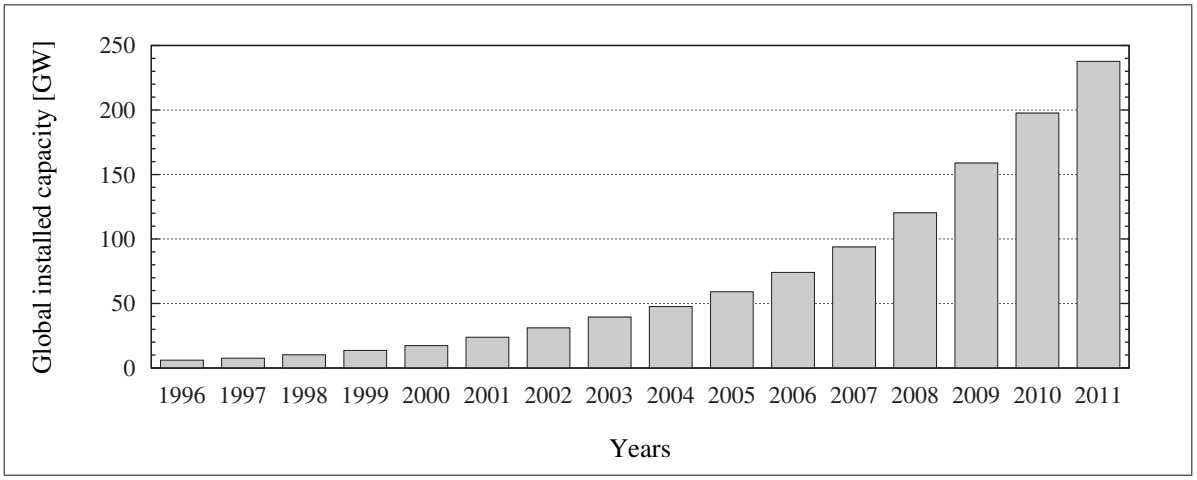

Figure 0.1 Global cumulative installed wind capacity from 1996 to 2011.
From Global Wind Energy Council (GWEC) (2011, p. 15)

Modern wind turbines usually produce up to a couple of megawatts (MW) in optimal conditions. Their hub is generally located at 100 m above the ground level (agl) with a rotor diameter of a similar size, and wind farms having up to a couple of hundred turbines are more and more common. They operate in the lowest part of the atmosphere, the so-called atmospheric boundary layer (ABL), or more precisely in the surface layer of the ABL, which is directly influenced by the earth surface. Considering that horizontal spacing between wind turbines is at least five times their diameter, wind farm usually spread across several kilometres.

In order to efficiently exploit the wind resource, a prediction of its geographical distribution is needed so that wind turbines can be installed in the best locations. Similarly, the optimal integration in the electricity network of the energy coming from wind requires wind production to be forecasted at least one day ahead. This, along with the forecast of electricity demand, allows grid operators to make the best use of wind energy by minimizing the required production from conventional power production facilities that are more polluting and more expensive to operate. As a result, wind resource prediction and forecasting are two crucial tasks for wind energy production to be economically appealing.

Problematic

Time and space variability of ABL flows highly depends on both local and large scale geophysical properties of the region of interest. Similarly, by going from blade airfoils to a region with large clusters of wind farms, wind energy production facilities impact (and are impacted by) ABL flows and wind resource at various scales as illustrated in Fig. 0.2 which is meant to be an analogy with Stull (1988, Fig. 1.15, p. 20)). Wind technology thus clearly presents a multiscale nature ranging from smallest microscales typical of engineering applications to mesoscales usually being the appanage of weather applications. Models and approaches used by the wind energy industry are thus borrowed from both the computational wind engineering (CWE) and meteorology domains, and there is a clear delimitation between these two domains in wind energy applications. Microscale and Computational Fluid Dynamics (CFD) approaches are commonly involved from the design of the blades to the design of a wind farm, while mesoscales approaches are mostly used as a basis for wind forecasting and large scale wind resource assessments.

With the advent of wind energy technology, several methods and tools have become mature and are seen today as standard for predicting and forecasting the wind by the wind energy industry and research community. These methods generally perform properly in optimal conditions featuring well know limitations. However, result quality is still a function of the properties of the sites studied. As a general rule, not considering the additional impact of wind turbine

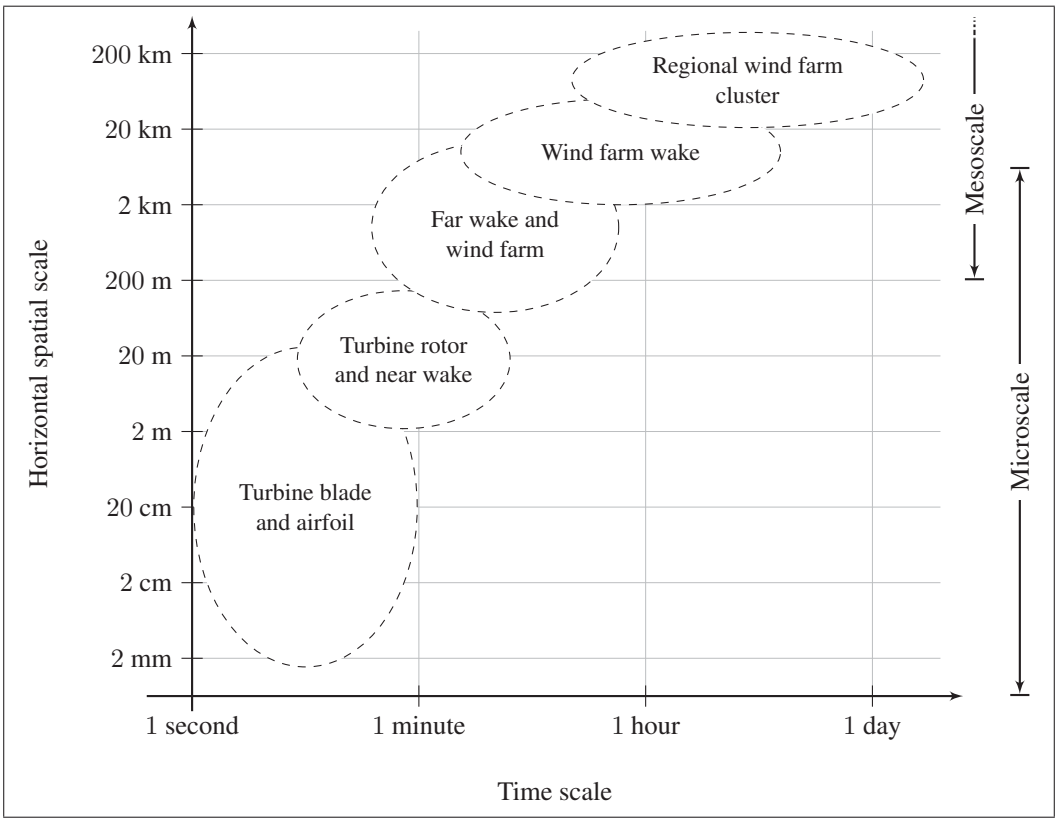

Figure 0.2 Typical time and space orders of magnitude for various aspects of wind energy production facilities in analogy with Stull (1988, Fig. 1.15, p. 20)

and wind farm, the more the site and its surrounding area are complex (orography and surface cover), the higher the errors are. As an example, there are often large differences between the predicted versus the effective annual energy production of wind farms. Similarly, 24 hours ahead production forecast commonly present an error of at least around ten percent. Thus, wind energy industry still faces numerous challenges in these area due to the complex nature of the environment in which wind turbines operate.

In addition, the large size of modern wind turbines as well as the increasing extent of wind farms tackle the limits of existing approaches. Indeed, some of the processes triggered, which are not yet fully understood (Wyngaard, 2004; Teixeira *et al.*, 2008), are at the limit between microscales and mesoscales. There is also the rise of new challenges in the regions with a high wind energy penetration (Shaw *et al.*, 2009). Indeed, on the one hand, most of the best

suited sites are taken requiring to install new wind turbines in more complex sites for which errors of standard approaches are higher. And on the other hand, wind farms start to have an impact on the regional wind climate which is not yet neither well understood nor considered by current mesoscale models. Finally, in the context of Quebec, and more generally of Canada, wind energy industry faces additional constraints, *i.e.* Nordic climate (very cold environment, freezing rain, frozen sea and lakes, large variation between summer and winter, boreal forest), for which methods for predicting and forecasting the wind were not designed.

As a consequence of the above, there is a need for more advanced approaches better taking into account the physical processes of ABL flows, such as distorted flow patterns induced by a complex surface and thermal stratification, and their multiscale nature. Furthermore, microscale approaches have to be able to deal with the largest microscales and the smallest mesoscales due to the increasing size of wind turbines and wind farms, while mesoscale approaches need to better take into account smallest mesoscale processes that are triggered by large wind energy production facilities. Thus, both the upper limit of microscale models and the lower limit of mesoscale models need to be pushed further. In that sense, ABL flow scales at the limit between microscales and mesoscales require a better understanding, which would allow to develop new approaches better addressing the various challenges of predicting and forecasting the wind for modern wind energy applications.

Objectives and methodology

The objective of the present study is thus to develop an approach or combination of approaches that would allow to predict and study ABL flows from microscales to mesoscales. For that sake, relevant components of both microscale and mesoscale methods need to be mixed together by adapting either an available microscale model to perform properly at mesoscale, or a mesoscale model to perform properly at microscale.

However, the best suited way as well as the most promising microscales and mesoscales approaches are at first unknown. As a result, the first associated objective is to review and evaluate the various possible approaches to model ABL flows. It will allow to clearly appreciate their

abilities and limitations with regards to the various processes of importance for wind energy applications, and thus permit to define what appears to be the best suited approach.

The combined mesoscale/large eddy simulation (LES) modelling turns out to be the most natural, promising and skilled approach. Furthermore, due to the environmental modelling abilities of mesoscale models, the latter appears to be the best suited starting point for the development of the new approach. As a result, the second associated objective of this study is to implement in the elected mesoscale model, *i.e.* the Compressible Community Mesoscale Model (MC2), the required components allowing for LES. A full overview of the required adaptations, such as the inclusion of the three dimensional turbulent diffusion and subgrid scale (SGS) models, is presented, and these new components are thoroughly described along the details and specificities of their implementation in the mesoscale model.

The third associated objective is to validate relevant aspects and new components of the introduced model, *i.e.* the LES-capable MC2, based on representative and challenging ABL flow cases. Considering that the elected mesoscale model has already been thoroughly evaluated for large scale flows, the validation of the new approach is mostly based on microscale typical cases (impossible to reproduce with the original MC2 model). To finely evaluate the fundamental aspects of the various new components, homogeneous surface stratified full ABL cases are elected. Note finally that this validation is achieved in comparison to existing solutions and other reference results from the literature.

Thesis structure

The first chapter of the thesis is dedicated to the review of the specificities and abilities of approaches used to model ABL flows at various scales. The three most common families of approaches are successively discussed, *i.e.* CWE models, environmental models, and finally LES models. The ultimate goal of the review is to identify an approach suitable to address the challenges faced by modern wind energy applications.

In a second chapter, the full mathematical model of the elected approach is thoroughly described. Fundamental equations are first introduced and filtered, followed by the various details of the turbulence modelling and other more specific aspects. Only momentum, internal energy and pressure are considered (as opposed to the traditional description of mesoscale models where others relevant processes for environmental modelling are also included).

The third chapter presents numerical method used to implement the mathematical model introduced in the previous chapter. Following the structure of the model, *i.e.* the dynamics, the physics, the initialization and the post-processing, all the details of the implementation are thoroughly presented focusing on the various new components introduced.

The last chapter focuses on the validation of the fundamental aspects and new components implemented in MC2 in the context of typical full ABL microscale flows. One dimensional Ekman theoretical cases (Berger and Grisogono, 1998) are first investigated to finely evaluate some aspect of the approach. Then, relying on the Moeng and Sullivan (1994) homogeneous surface stratified full ABL cases, the introduced model is thoroughly evaluated for the first time. In a third section, the sensitivity of the LES model to the principal numerical parameters is assessed and compared to other existing solutions. Finally, a last section is dedicated to the evaluation of the various refinement brought to the MC2 model.

Finally, the various contributions and achievements of the thesis are outlined in a conclusion along the recommendation for future work.

CHAPTER 1

LITERATURE REVIEW

Most of human activities are taking place in the lowest part of the atmosphere, commonly known as the Atmospheric Boundary Layer (ABL). Meteorological properties of this layer affect us directly. Temperature, precipitations and wind are certainly the most relevant. Thus, it is important to understand and predict the behaviour of such quantities. However, ABL is the cradle of several coupled non-linear multiscale phenomena. Both large scales and local phenomena interact as well as each quantities with each other. ABL can thus be regarded from a wide range of scales and with a degree of completeness being a function of the objectives of the studies. Only surface layer flows are considered by most civil engineering studies while the full ABL, *i.e.* from the earth surface to the free atmosphere, immersed in a large scale flow is modelled by Numerical Weather Prediction (NWP) approaches. As a result, Computational Fluid Dynamic (CFD) approaches used to model ABL flows vary a lot depending on the application and the information needed. Indeed, assumptions can be made in the Navier-Stokes (NS) equations that greatly simplify the problem at the price of representativeness. In a general sense, the time, horizontal and vertical scales of the problem as well as more practical considerations characterize the chosen ABL modelling approach.

In this chapter, the modelling of ABL flows in its broadest sense is addressed. A review of the main approaches used in various domains is intended, keeping in mind that wind energy applications are the ultimate goal of the present work. Thus, at first, the methods dedicated for modelling flows at the microscale level, *i.e.* CWE approaches, are presented. Afterwards, the modelling of ABL flows within large scales models, *i.e.* environmental modelling and NWP, is reviewed. Finally, LES approaches dedicated to the modelling of the ABL are investigated. In a conclusion, these approaches are further compared in order to clearly identify and justify the method chosen for the present work.

1.1 Computational Wind Engineering (CWE)

Computational Wind Engineering (CWE) consists in the numerical study of flows in the lower part of the ABL, *i.e.* the surface layer, in order to model, predict and understand wind flows and loads over various geometries and complex terrains (Stathopoulos, 2002). Microscale processes and small scale turbulence phenomena are dominant at these scales.

From an engineering perspective, only the most relevant ABL processes are considered, and the ABL is left to its most simplistic expression, *i.e.* retaining shear and surface roughness properties while considering only a perfectly neutrally stratified surface layer. Indeed, such a strategy is motivated either by the will to thoroughly study some aspects of the flow (without having the 'noise' from other processes) or to obtain a simple yet representative model dedicated to a practical use (*i.e.* wind resource assessment, study of wind loads, ...). In this section, after refining the ABL definition in view of engineering application, the approaches commonly used in computational wind engineering are reviewed, *i.e.* simple and highly dedicated approaches and CFD models. Focus is set on models promising for wind energy application.

1.1.1 ABL in view of engineering applications

The vast majority of CWE applications consider the ABL as being only the surface layer and they rely on the most common representation of the latter, namely the Monin-Obukhov (MO) similarity theory also known as the log-law velocity profile (Richards and Hoxey, 1993; Murakami, 1997; Stathopoulos, 2002). While this theory takes into account surface layer thermal stratification, non-neutral flows are rarely considered in CWE. This theory is also used to obtain other quantities such as the momentum flux or the TKE profile. It is however only valid for the surface layer of a statistically horizontally homogeneous ABL (Stull, 1988).

Instead, some applications use a very simplified ABL representation for which the velocity profile follows a power-law. This originated directly from classical fluid mechanics (Schlichting, 1979; Tritton, 1988). Indeed, the empirical formula of the classical velocity profile for turbulent boundary layer over a flat plane is given by $u(z) = u_a \left(z/z_a\right)^{\alpha}$ where u_a is the ref-

erence wind speed at the reference height z_a, u is the wind speed at the height z and α is the shear coefficient (an empirical exponent). For classical turbulent boundary layer over a flat plate, this exponent is usually taken to be $\alpha \approx 0.143 = 1/7$. Empirical in nature, this law can easily be used to provide an inlet boundary condition or for vertical interpolation. It has been used extensively for years in the wind energy domain (Spera, 1994; Manwell *et al.*, 2002), mainly thanks to its robustness and its ability to simply interpolate wind data. While the shear coefficient α has a highly non-linear behaviour, some researchers developed formulations of the power-law that take into account surface roughness or thermal stratification (Spera, 1994; Manwell *et al.*, 2002). Coming back to CWE, the classical log-law surface layer representation is also sometimes not used because model validations are based on wind tunnel experiment. Indeed, real ABL Reynolds number, roughness length parameter, z_0, and thus vertical profiles of velocity as well as turbulent quantities are not trivial to reproduce in a wind tunnel.

When only surface layer flows are considered in a restricted area, the Coriolis acceleration has no impact. As a result, Coriolis effect is generally not included in CWE. It is however sometimes present for practical reasons. Indeed, as discuss later, the top boundary definition and flow driving process appear somewhat more natural when using a geostrophic wind. In the wind energy sector, only the surface layer is most of the time considered for problems with total horizontal size smaller than 10 km. The Coriolis effect thus has negligible impacts (turning of the main flow is negligible). This approximation may be questionable when considering modern wind turbine, which top is often above surface layer (~ 10 % of ABL height), and large wind farms that span over more than 10 km.

Finally in CWE, ABL is mostly considered as being neutrally stratified, thus removing temperature from the problem. Such an assumption brings huge simplifications since all thermal effects are neglected and thus, only momentum and mass conservation need to be solved. This assumption is perfectly justified for comparison with laboratory flows. Full scale data have however to be used with caution when compared with numerical results based on this assumption. For the particular case of wind energy application, results based on this assumption are found to be representative enough to satisfy the industry requirements (at least for the moment).

Indeed, over flat terrain, the yearly averaged vertical velocity profile is often well approximated by the neutral profile.

To sum-up, the CWE approaches generally share the following representation of the ABL:

- 3D surface layer only;
- steady;
- neutrally stratified;
- no Coriolis effect;
- incompressible high Reynolds number flows.

As a result, unless specified, the term ABL will refer to the neutrally stratified surface layer only in this section.

1.1.2 Simple and highly dedicated approaches

Thanks to their inexpensive character, simple and highly dedicated approaches to model ABL flows over terrain are very popular, notably within the microscale wind resource assessment community. The two more popular approaches a presented in this section[1].

1.1.2.1 Mass conservation microscale model

One of the simplest approach to model the ABL over a terrain is to use interpolation based on the geophysical parameters of the surface and under the constraint of minimizing the momentum flux divergence. An example of such an approach is the MINERVE model (Finardi *et al.*, 1993). In this model, various weather data (generally surface wind from met towers) are first interpolated on the computational grid using the natural neutral log-law as well as a clever interpolation method taking into account topography and roughness. Afterwards, interpolated data are refined based on the mass continuity and ABL stratification. This approach thus contains no dynamics equation: it is purely kinematic.

[1] The approaches presented in this section are generally not included within CWE methods (even if they hold a computational character and were developed for engineering applications). They are part of this section because there are also part of the microscale approaches.

This type of model is less demanding than CFD approaches. However, as shown by Finardi *et al.* (1993), its results are heavily influenced by the interpolation methods used and also by the location and amount of input data. And since it is kinematic, every main dynamic flow feature has to be depicted by some input wind profile. In the comparison of Finardi *et al.* (1993), two mass conservation models were compared to a dynamic linearized Navier-Stokes equations based model. The author conclude that all models "show an ability to describe the flow with errors" lower than $20\ \%$.

1.1.2.2 Linearized Navier-Stokes equations approach

Linearized Navier-Stokes equations approach is still by far the most widely used for microscale surface wind studies (notably for wind resource assessment). The mathematical concepts and methods they invoke were introduced by Jackson and Hunt (1975) and are far from being trivial. In fact, this approach allows to quickly compute flows over hills with a gentle slope. This theory is based on the linearisation of the advection term in the conservation equations. This is done by directly computing the velocity speed-up and considering the background flow as constant in the terrain-following direction (horizontal). A vertical variation is allowed and the ABL is furthermore divided in several layers each based on a different equilibrium in the equation of motion. Due to the linearisation of the advection terms, this family of methods is sometimes called dynamic linearized models or simply linear models. In its original version, two layers were present:

The inner layer: closest of the surface. Viscous (molecular and turbulent) forces are dominants through the shear stress.

The outer layer: above the inner layer. In this region the flow can be considered as inviscid (rotational or irrotational).

Each of these layers is then matched asymptotically in the vertical direction to obtain the complete solution of the flow over orography. In general, the horizontal directions are processed based on Fourier transformation (implying periodical lateral boundary conditions) while in the

vertical direction, the layering approach used at first was replaced by finite differences that were found to be more convenient since they allow smoother transitions (Ayotte, 2008).

From the classical version described, many enhancements were tried, such as the implementation of a more complete turbulent closure in order to increase the model accuracy and further push its limits toward more complex terrain. It is also important to underline that the Jackson and Hunt (1975) approach considers only topography. As a result, it needs to be coupled with other models to be able to take into account all the earth surface properties which influence directly the wind profile, such as the roughness length. Ayotte (2008) achieved a comprehensive review of the evolution of these methods over the years.

Linear models are robust and require a very low computational cost. This mainly explains their success over the years. The most famous example of the application of this theory is the Wind Atlas Analysis and Application Program (WAsP) that was developed to create the European Wind Atlas by Troen and Petersen (1989). In fact, WAsP is the coupling of several dedicated sub-models such as the roughness changes model (non-linearly coupled with stratification) or the orography model (also called B-Z model) which is based on (Jackson and Hunt, 1975) model. Others implementations also exist such as MS-Micro of Taylor *et al.* (1983) (which is also known as the Mixed Spectral Finite Difference (MSFD) model).

This kind of approach leads to promising results when they are used within their working envelope *i.e.* neutrally stratified flow over low and smooth hills. Their theoretical limit is for small perturbation *i.e.* with a velocity speed-up, $\Delta S = u'/u$, lower than 0.2 (u being the unperturbed velocity and u' the velocity perturbation). In practice, they work well up to $u'/u \approx 0.5$ (Petersen *et al.*, 1998). However, they are not able to reproduce detached flow which may occur for a slope higher than 0.3 (the slope can be expressed as the height of the hill divided by its half width). As an example, the speed-up at the top of the hill is overestimated due to linearisation for flow over an isolated rough hill with a the slope value higher than 0.3. Non-linear models need to be used over such orography.

1.1.3 CFD modelling of ABL flows

CFD has experienced a tremendous amount of advances and refinement since its birth 40 years ago. A huge amount of studies were published, each time enhancing, applying, comparing and validating some of the possible approaches. The practical use of these methods has increased in the last 20 years and today they are about to become a standard for many applications. More than a decade ago, Stathopoulos (1997); Murakami (1997, 1998) presented comprehensive reviews of turbulence models applied to Computational Wind Engineering (CWE). After reviewing the various possible applications and associated challenges, some of the most common and most promising turbulence models were presented and discussed. While a wide range of results is introduced, the authors focus on bluff body flows to study in details various aspect of the closures. Such a flow presents several of the most challenging features, *i.e.* separation/recirculation, impinging area, vortex shedding, that are also relevant for flow over natural terrain. Murakami (1997, Tab. 6) presents a summary of particular interest: the various approaches discussed are organized as a function of their abilities. As a summary, concerning Reynolds Averaged Navier-Stokes (RANS) methods, the standard $k - \varepsilon$ model is the least dexterous due to inherent limitations of the underlying assumptions and the eddy viscosity hypothesis. Some modifications such as the use of a non-linear eddy viscosity are shown to correct its main drawback (such as the over-production of TKE in the impinging area causing a momentum deficit). Reynolds Stress Models (RSM), *i.e.* true second order models, lead to equivalent results with a more complete description of turbulence but enhancement of the result does not worth their higher complexity and computational cost. Finally, LES models are found by far more versatile, notably when using dynamic subgrid scale models. There are however very computationally demanding and less easily applicable. Stathopoulos (1997, 2002) concluded that CWE was still in its infancy and the numerical wind tunnel still needs development.

The ten last years have seen a large increase of the CWE use in environmental engineering applications such as microscale pollutant dispersion. For wind energy applications, even if historically simpler models were preferred, CFD is becoming a standard with the democratization of computational power. Ayotte (2008) depicted the computational methods used in wind engi-

neering attempting to clarify their abilities, limits and source of errors. Recently, Sumner *et al.* (2010) reviewed CFD in wind energy. The study is divided in two parts. First, small scale flows are treated *i.e.* aerodynamics of the wind turbine from the blade elements to the whole rotor. The second part, which is of concern to us, is dedicated to larger scale flows (aimed at wind turbine siting) *i.e.* simulation of the ABL flows from flat terrain to complex terrain and wind turbines and wind farm wake effects. The methods discussed in those two latter studies are of the same families as in Stathopoulos (1997, 2002), but they are refined to better address wind energy challenges. Furthermore, they are evaluated in the context of wind energy. The challenging problems (refinement of boundary conditions and turbulence models) are thoroughly discussed. Concerning the RANS methods, conclusions are also that the so-called standard $k-\varepsilon$ model is clearly put aside by the research community to the benefit of some variants such as the RNG $k-\varepsilon$ or non-linear viscosity models that are discussed later. RSM model popularity also suffer from its higher computational cost. The authors clearly state that RANS approaches are nevertheless not likely to overcome the difficulties related to terrain with a large slope where the modelled mean flow recovers too quickly (notably when the surface is rough). LES is found to be the best solution while still mostly used for research applications more than to solve practical problems.

In this section, CFD modelling of surface layer flows is presented in more details from the angle of wind energy applications. At first, the challenges and solutions to model the homogeneous surface layer are inspected. Then, ABL flows over heterogeneous terrain are considered, including flows over bluff bodies, ideal and real orographies. It is to note that, while the two former geometries serve us to study turbulence closure abilities, the latter allows to present the challenges faced in dealing with full scale real cases.

1.1.3.1 Modelling of the neutral homogeneous surface layer

An appropriate modelling of the neutral homogenous surface layer is the simplest yet critical requirement for successful CWE applications. The underlying challenge is a correct reproduction of the profile of the variable of interest as well as an ABL in equilibrium that is maintained

across the computational domain. In that sense, care has to be taken not only in the turbulence model but also in the boundary conditions. Challenges between the two main approaches, RANS and LES, differ. Indeed, RANS aim to reproduce a strictly horizontally homogeneous flow. In LES, eddies ranging from the problem size to the filter size have to be explicitly present with the right level of energy in order to statistically reproduce the same homogeneous state as RANS. In consideration of their properties, LES is thoroughtly reviewed in Sec. 1.3.

A true no-slip surface boundary condition with a mesh starting within the roughness sublayer, *i.e.* $z^+ = u_* z/\nu \leq 11$ (Schlichting, 1979), is non trivial for ABL flows due to their rough character. Indeed, ABL flows are high Reynolds number flows that are most of the time fully aerodynamically rough. It implies that the roughness sublayer is smaller than the roughness elements and that shear stresses are dominated by the Reynolds stresses at the height of rough elements. As a result, an explicit representation of the roughness element would be needed to solve the flow within and above roughness sublayer. This type of surface boundary condition is the most correct and it should be used whenever possible to strictly evaluate the turbulence model abilities while removing errors from the surface boundary condition. However, practical reasons sometimes prevent its use which is the case when modelling the surface layer with most of the RANS approaches. At that point, it is of interest to underline that $k-\omega$ models can overcome these shortcomings (Patel, 1998). By properly specifying the surface boundary condition using notably a roughness based Reynolds number to characterize the aerodynamic regime, Knopp *et al.* (2009) managed to obtain very promising solutions.

As a result of those difficulties close to the ground, from the simplest model to the most advanced once, the surface velocity boundary condition generally accepted is a wall function based on the log-law velocity profile. In that case, the first mesh point needs to be located in the logarithmic region of the boundary layer, *i.e.* $z^+ \geq 30$. The surface momentum flux, u_*, is computed from this law and imposed as a boundary condition for the turbulent diffusion; surface velocity is then updated. Another strategy is to add a drag form sink term in the momentum equations expressed as $-C_d \boldsymbol{v} |\boldsymbol{v}|$. C_d is a drag coefficient that is non-zero only within a layer close to the surface. This approach is often called the canopy stress model (Brown *et al.*,

2001) because it was first developed to better represent vegetative canopy. The integral of this force over the depth is equal to the surface stress. This allows to find correspondence between C_d profiles and the aerodynamic roughness, z_0. The canopy stress model is known to be better suited than the classical log-law approach over forest and complex land cover, such as patchy forest with well defined edges (Dalpé and Masson, 2008).

Other quantities at the surface and the inlet such as the turbulent properties are prescribed according to both experimental results and mathematical constraints of an homogeneous surface layer which follows the log-law velocity profile. Richards and Hoxey (1993) provided a simple set of boundary conditions and constants for the widely used $k-\varepsilon$ models to be able to reproduce correctly the ABL in homogeneous conditions. Thanks to the underlying strong arguments, these boundary conditions were generally adopted (Hargreaves and Wright, 2007). However, turbulence models closure constants are responsible of many debates. In fact, various experimental campaigns have led to different measurements. As an example the surface layer value of the TKE is found to vary from $3.75\,u_*^2$ (Wyngaard and Coté, 1974) to $5.47\,u_*^2$ (Garratt, 1992) which gives a value of the model constant C_μ ranging from 0.071 to 0.033 (based on TKE surface boundary condition from Richards and Hoxey (1993)) while the standard constant is 0.09. Thus, constants seem to be a function of the site. Currently, a stronger consensus however exists to adopt a modified set of constants more appropriate to the ABL (Sumner *et al.*, 2010) instead of the one originally proposed by Launder and Spalding (1974).

Concerning the commercial CFD softwares, it is to note that they are certainly the computer codes that are the most used, notably for practical applications. Generally, only research centres and large companies are able to have their own in-house codes specially dedicated to their needs. Even if commercial codes offer facilities to adapt the model (such as the User Define Function (UDF) in Fluent/CFX), they are often used with few or even no adaptations. Following this approach imposes to use the provided boundary conditions. However, Hargreaves and Wright (2007) recently demonstrated that the generally implemented rough wall condition in those codes (Nikuradse's sand grain equivalent roughness) was not suited for ABL modelling based on $k-\varepsilon$ approaches. They recommended and explained how to use the Richards and

Hoxey (1993) approach in such a case (notably for the surface and the top boundaries). While this set of conditions is largely used, a problem is often described: the development of a streamwise gradient in the TKE and ε in the near wall region. Sumner and Masson (2010) recently elucidated that it was caused by a numerical error related to the log profile curvature close to the ground and an insufficient grid refinement. The solution to correct such an error in the case of a mixing length model was introduced decades ago by Taylor and Delage (1971). However, the full correction for the $k - \varepsilon$ models further required correction of terms in the TKE and dissipation rate prognostic equations. After such a correction is applied, nearly perfect agreement is obtained between inlet and outlet for all variables (not only velocity as before). It can however be seen as an ad-hoc modification of the model since it is based on the log law profile only applicable for homogeneous flat terrain.

Concerning the lateral boundary conditions, the most common solutions are to use either symmetry or periodicity condition. And, for outlet condition, a velocity outflow or a pressure outflow is often chosen.

Finally, concerning the driving of the flow, several approaches are also possible. The most common and simple one is to use a symmetry at the top boundary and force the flow thanks to mass conservation and the inlet velocity profile (Gasset *et al.*, 2005). However, based on this approach, the shear in the vicinity of the top boundary is affected (Gasset *et al.*, 2005), and a lost of momentum can be observed when domains are very long in the streamwise direction. A more appropriate approach is to impose a shear stress at the top of the domain based on the log-law velocity profile in a same way it is done at the surface (Richards and Hoxey, 1993). This is considered as the optimum approach in CWE (Hargreaves and Wright, 2007). It is also possible to impose a pressure gradient between the inlet and the outlet of the domain such as in a channel flow (Bechmann, 2006). This gradient can be adjusted as a function of the divergence of the momentum fluxes in order to obtain the desired velocity at the top of the boundary layer. Note that this gradient should be negligible in comparison to shear stress effects close to the surface. The velocity profile is thus not affected by the former. Another approach is to use a pressure gradient, but in conjunction with the Coriolis effect such that a geostrophic wind drives

the flow. In that case, wind velocity components follow an Ekman spiral which are closer to a real ABL (without thermal effects). The two last approaches allow to use a stress free top boundary condition and are more generally used with LES and mesoscale models. Finally, the last approach for boundary conditions discussed here is nesting. Following this approach, all the boundary conditions (inlet, outlet, lateral and top) are coming from a computation on a larger domain and generally with a coarser resolution. This approach is very common for mesoscale model as opposed to CWE. It is more appropriate for LES or when dealing with full scale flows for which ideal homogeneous inflow conditions rarely exist.

1.1.3.2 Flow over topography

Once the homogeneous surface layer is correctly modelled, it is possible to think about introducing the desired heterogeneity within the computational domain. The meaning of topography here includes orography features as well as surface cover heterogeneity such as roughness changes. Full scale measurement campaigns are expensive, tricky and until recently it was not possible to have a knowledge of the complete velocity and turbulent fields in the ABL other than punctual. In addition, not being in a controlled environment also complicates the acquisition and the post processing of the data. As a result, a large part of the comparison and validation of the various CWE methods was undertaken based on more classical wind tunnel experiments. However, since the boundary layer obtained in wind tunnel differs from the ABL, CWE ABL models needs to be adapted through their constants to optimally reproduce wind tunnel flows. So the best practice appears to be the use of both wind tunnel and full scale experiments such as done by Kim and Patel (2000).

A distinction is also to acknowledge between bluff body flows and flows over natural, smoother topography. Indeed, vertical edges of bluff bodies encourage to use Cartesian grids while meshing based on curvilinear approaches is much straightforward for smooth and natural topography. Non-Orthogonal curvilinear meshes (also referred to as oblique coordinate) must be used with care since grid cells can get strongly deformated in the case of steep terrain. Mesh deformations can cause non-negligible numerical errors. A solution is to use the more advanced

orthogonal approaches for which vertical edges of the mesh are always perpendicular to the ground and mesh deformation is minimized (Kim and Patel, 2000). Another possibility is to use cell blocking approach (Murakami, 1997; Bonaventura, 2000; Gasset *et al.*, 2005).

As reviewed by Murakami (1997); Stathopoulos (1997, 2002); Sumner *et al.* (2010), a large amount of numerical studies exist that compare with both full scale and wind tunnel experiments. The aim of the present work is not to review all of them but to have a clearer image of the ongoing work and to illustrate the capacities of the various models.

1.1.3.2.1 Flow over bluff bodies and ideal topography

Concerning flows over bluff bodies and ideal topography, experimental cases generally found in the literature are: forward and backward facing step, cubes, buildings of all shapes, escarpments, triangular ridge, step mountains, bell shape hills and valleys. Among other things, we can cite Moss and Baker (1980) 2D forward and backward facing step with $\mathrm{Re} = 5 \times 10^4$ but a smooth surface, RUSHIL (2D hill) (Khurshudyan *et al.*, 1982) and RUSVAL (2D valley) (Khurshudyan *et al.*, 1990) EPA's experiments with a rough surface, Ishihara *et al.* (2001) smooth/rough 2D/3D hills and forward facing step and Ayotte (2008) changing steepness 2D smooth/rough hills. Several datasets are also available through the European Research Community on Flow Turbulence and Combustion (ERCOFTAC) (www.ercoftac.org). In their reviews, Stathopoulos (1997) and Murakami (1997) show numerous comparisons of numerical models with wind tunnel experiments (mainly for buildings and bluff bodies). In ours days, some research groups have further reproduced scaled city centres (Stathopoulos, 2002), as well as natural terrain topography such as the Bolund hill, 2008 (http://windenergyresearch.org/2010/09/the-bolund-project/). In that sense, the Wind Dome facility of the University of Western Ontario looks very promising (www.eng.uwo.ca/windeee/). However, besides bluff bodies, a large part of the wind tunnel test cases are 2D (Kim and Patel, 2000).

A turbulent closure model that is almost absent of the CWE literature is the $k - l$ approach. Indeed, this one to one-and-a-half order turbulence model is heavily used for the modelling of the stratified ABL but it is less popular for modelling the ABL over complex terrain because

the flow needs to be a priori known to best define the mixing length, which is impossible for complex terrain situation. Indeed, while for second order models the mixing length is computed based on the values of both k and ε, here it is directly set. The $k-l$ approach is however more natural in the case of a homogeneous stratified boundary layer since l is of the same order as the eddy characteristic scales. This approach is thus very common for meteorological application as discussed later (see Sec. 1.2). The microscale model Meteodyn WT (Delaunay *et al.*, 2004) is based on a $k-l$ closure derived from Mellor and Yamada (1982) which is further discuss in the next section. Meteodyn WT appears to be a promising tool for wind resource assessment, notably when considering its improvement over linear approaches, its computational efficiency and the fact that thermal stratification is taken into account.

Using RUSHIL and RUSVAL rough neutral test cases, Finardi *et al.* (1995) tried various mixing length based turbulent closures going from first order to one-and-a-half order. They tested three approaches for the computation of the velocity scale: mean velocity gradient ($\partial U/\partial z$), vertical velocity fluctuation ($\overline{w'^2}$) and the TKE. Concerning the mixing length, Blackadar (1962) and Hunt *et al.* (1989) approaches were tested. The inclusion in the definition of the mixing length of $\partial U/\partial z/\sqrt{\overline{w'^2}}$ (Hunt approach) was shown to give significant improvements over the standard Blackadar mixing length formulation. They also found that the velocity scale computed from TKE is not fully appropriate for the cases tested due to high vertical anisotropy of the turbulent field. In other words, the authors state that the additional complexity introduced by including the prognostic equation for TKE (or two equations for k and ε) may not produce a corresponding improvement in the results as opposed to using a full second order closure model such as the Reynolds Stress Model (RSM) that does not rely anymore on the eddy viscosity hypothesis.

Ross *et al.* (2004) present new wind tunnel results that are used to compare a range of one-and-a-half and full second order models (*i.e.* RSM). The experiments intend to reproduce scaled neutral and stably stratified atmospheric boundary layer flows over a 2D ridge of various slopes. The general conclusion is that while the RSM approach gives the best results (although it is less numerically stable), the various approaches tested perform adequately for neutral flow over a

2D hill, notably when the mixing length computation is tuned to take into account the local Reynolds stress. Indeed, the addition of the shear dependent term in the one-and-a-half order mixing length leads to significant improvements in predicting the development of the wake region downstream the hill in both neutral and stable cases. However, both one-and-a-half order schemes fail to provide a good prediction at the top of the hill, and only the full second order model is able to correctly model lee-side flow. None of the models are able to correctly reproduce $\overline{u'^2}$, $\overline{w'^2}$. Concerning the more classical RANS approaches, Zhang (1994) compared a standard $k-\varepsilon$ with the early results from Moss and Baker (1980), illustrating the difficulties of the $k-\varepsilon$ in recirculating areas. Later, Murakami (1997); Stathopoulos (1997) clearly documented those problems and illustrated the possible solution: alleviate the shortcoming of the isotropic eddy linear viscosity using a non-linear formulation. The Boussinesq eddy viscosity is said to be linear because it relates linearly strain rate and the stress (when not considering the expression of the eddy viscosity). In the non-linear viscosity model, this relation is based on a polynomial including both the deformation tensor, S_{ij}, and the rotation tensor, Ω_{ij}. In parallel and to address the same problems, approaches correcting terms in the dissipation prognostic equation were introduced such as the RNG $k-\varepsilon$. Both type of approaches are able to overcome the standard approach main limitations.

Easom (2000) and later Wright and Easom (2003) thoroughly reviewed the $k-\varepsilon$ family approaches as well as the RSM. Easom (2000) presents a large amount of results as well as comparisons with full scale measurements of flows over a building, a 6 m perfect cube and a fence. The conclusion of the study is that best suited $k-\varepsilon$ models are advanced non-linear eddy viscosity approaches such as the Craft non-linear model. The second best performing models are the RNG $k-\varepsilon$ and the RSM. However, the latter is less numerically stable. The author also claim that some non-linear models such as the MMK (Murakami, Mochida and Kondo) are based on ah-doc modifications. Both non-linear, RNG and RSM approaches correct the problem of over-production of TKE inherent to the standard $k-\varepsilon$. However, it is stated that none of the RANS models provide accurate results for the whole range of test cases. Interestingly,

Kim and Patel (2000) also found the RNG model to be performing well but they had troubles with the Craft non-linear model, which failed to work due to wall-functions problems.

Lun *et al.* (2003) tried classical and modified $k - \varepsilon$ approaches (Durbin realizable model and Shih non-linear eddy viscosity model) for flow over a hill and over a cliff for various surface roughness lengths. They also showed that non-linear and realizable models correct the over-prediction of TKE done by the classical approach in the impinging area. Furthermore, it was found that surface roughness has a significant impact on the length of the recirculation regions. The performance of several $k - \varepsilon$ models varied depending on the case reproduced notably concerning the Durbin $k - \varepsilon$ for the flow in the lee side of the hill. In fact, this latter model was not able to represent properly flows after an obstacle.

A year after, Bitsuamlak *et al.* (2004), achieved a review of the neutral surface layer flows modelling over complex terrain. The study shows a good amount of cases (wind tunnel and full scale data) and the models discussed go all the way from the National Building Code of Canada to advanced modified $k - \varepsilon$ closures. Both ideal and natural terrains are considered. The authors conclude that in general, numerical results are in agreement with field data in the upstream area of the complex terrain as opposed to the downstream region where larger differences are generally observed. The RNG $k - \varepsilon$ closure is often cited as giving the best results. Speaking of the influence of the roughness, Ayotte (2008) also evaluated RANS approaches with wind tunnel data of flows over a smooth ridge of various height and roughness, and found that roughness impacts the length of the recirculating zone, notably for moderately steep hill for which the recirculation area may or may not be present depending on the roughness. Ayotte (2008) shows that RANS models fail in the back face of the hill where the flow recovers too quickly. The maximum slope at which the RANS approach performs well is found to be 0.4 over a smooth surface and 0.3 over a rougher surface. He suggests that only the use of eddy resolving approaches can prevent those shortcoming. Furthermore, he states that wind tunnel data, while very helpful, are free of externally imposed length scales such as may be present in the atmospheric boundary layer (see Sec. 1.2). In addition, as clearly illustrated by Bitsuamlak *et al.* (2004) in its two last figures as well as during the Bolund intercomparison (Bechmann

et al., 2010), wind tunnel scaled models and full scale experiments lead to different results. None of the wind tunnel experiments were in the top ten best results of Bolund blind intercomparison. Several factors can explain this fact but one of the main causes is the differences in the boundary layer turbulent properties due to the wind tunnel characteristics and the scaling factors. These latter points, explains why models need to be adapted (through the constants) to perform better for full scale cases (Richards and Hoxey, 1993; Sumner and Masson, 2010).

1.1.3.2.2 Flow over real terrain

Several cases are presented in the literature that illustrate surface layer measurement campaigns over all sorts of terrain going from flat heterogeneous to very complex terrain and urban environment. The most well-known and used site is certainly the Askervein hill located in Scotland (Walmsley and Taylor, 1996). There are many other campaigns such as the Sirhowy valley or the Blashavar hill test case, less popular but as useful, as it is reviewed by Taylor *et al.* (1987). It is also important to cite some of the experiments based on full scale buildings. The most well known experiments may be those from the Silsoe research facilities including, buildings, a fence and a perfect cube (Hoxey *et al.*, 2002; Quinn and Richards, 2002) or the Texas Tech University building (Levitan *et al.*, 1990).Due to practical considerations, most of the well instrumented sites used for experiments are generally of limited size. Furthermore, as illustrated by Taylor *et al.* (1987), nearly perfect low hills are often elected. Historically, they were sought because being at the limit of suitability of linear approaches (*i.e.* the front side gives good results while on the lee side flow is too complex to be well reproduced by such simple methods). Recently, a full scale measurement campaign and blind test were led for a small hill called Bolund, close the Risø national laboratory in Denmark (Bechmann *et al.*, 2010). The hill was just ~ 12 m high, but the incoming boundary layer depth was small compared to the hill height (making the latter large in comparison). A LIDAR (Light Detection And Ranging) as well as sonic anemometers monitoring the three velocity components were used to measure wind properties along several sections of the hill.

At the opposite of the full scale heavily instrumented test cases, the huge part of full scale comparisons are based on another type of data, *i.e.* punctual measurements coming from met towers. Advanced 3D sonic anemometers are rarely used by the wind energy community. Cup anemometers are very often preferred instead for economical reasons. Thus, only horizontal wind modulus, direction and standard deviation (SD) of both are monitored (SD from the sub averaging frequency). In that case, the measures are generally more scattered, more prone to uncertainties of all kinds and less trivial to use. So post-processing and filtering are needed. Intercomparison of the results with other studies is furthermore less straightforward or impossible since each of those cases feature it own specificity. The studies from Gasset *et al.* (2005) to Brodeur and Masson (2008) illustrate the latter facts and the implicit limitations of working with punctual data. However, validation/comparison with measurement from cup anemometers is the closest from real life applications and it is heavily used in the wind energy sector. Such measurements are thus also useful even if less universal in terms of model validation.

Comparisons of RANS with full scale data generally lead to the same conclusion as for comparisons with wind tunnel data (Stathopoulos, 1997; Murakami, 1997; Easom, 2000; Stangroom, 2004; Bitsuamlak *et al.*, 2004). Indeed, the same limitations inherent to RANS models as illustrated in the above sections were observed here. As an example, Kim and Patel (2000) reproduce the flow over several natural topographies (Sirhowy valley and Askervein). As for the ideal cases, the best results were obtained with the RNG $k-\varepsilon$ approach. Stangroom (2004) concluded that advanced two equation closure models, such as the $k-\varepsilon$ RNG, are recommended, but that RSM models lead to better results.

Full-scale cases add also new important challenges: the heterogeneous character, even if small, of surface roughness, orography are important to consider as well as the impact on the flow of surrounding features and unsteady phenomena in the area of interest. A particular attention needs thus to be dedicated not only in the model, but also to the input data used in the boundary conditions of the model.

The Askervein hill dataset can be taken as an example to illustrate those facts. Generally, a constant roughness of 0.03 m was used. However, the top of the hill appeared to be slightly smoother. Castro *et al.* (2003) by modulating the value of the roughness with height on the hill, obtained better results: vertical profiles of TKE and speed-up were improved by lowering the roughness length on the hill. This explained a long standing problem of under-estimation of the velocity at the top of the hill by several models (Castro *et al.*, 2003). In the same way, Undheim *et al.* (2006) show that by using a finer description of the orography (2 m contours instead of the usual 10 m contours), the hill top speed-up was better predicted. Kim and Patel (2000) reported that the separation in the leeward side of the hill was not predicted by models if the surrounding hills were not included in the computational domain.

Concerning inlet, outlet and lateral boundary conditions, Brodeur and Masson (2008) precomputed the flow in two dimensions for each boundary in order to avoid using classical homogeneous boundaries. Then, in a nesting approach, those results were then used as inlet and lateral boundaries of a 3D domain. Eidsvik *et al.* (2004) present a nesting approach based on a three levels cascade using meteorological models. The first level uses an hydrostatic operational weather prediction model (HIRLAM). The outputs from HIRLAM are directly used for a second level of cascade that uses a non-hydrostatic mesoscale model (MC2, further described later). Finally, the last level is based on an anelastic model (SIMRA) at first dedicated to small scale engineering applications. SIMRA does not take into account the Coriolis effect and it is based on a $k-\varepsilon$ turbulence closure. The prediction system is used to study flows over an airport located in a complex terrain area. Flow features and turbulence level and pattern are found to be in agreement with experimental data from plane observations. Eidsvik (2005) further uses the same approach to successfully predict the flow over the Askervein hill. The anisotropy of the turbulence is further accounted thanks to a non-linear algebraic stress model. Interestingly the constant of the model were kept equal to the ones used for industrial flow.

Those few observations illustrate the importance and difficulties to properly take into account the natural parameters in order to conduct successful comparisons between numerical and real full scale experiments.

1.1.4 Summary of CWE

All along this section, CWE methods have been reviewed and a special attention was set on the need of and abilities for wind energy applications. A general conclusion is that while an appropriate turbulence closure associated to a correct modelling of the homogeneous surface layer is necessary condition, it is not sufficient, and a fine representation of the earth surface as well as local and surrounding environment properties are crucial notably for full scale studies.

Linearized NS equation models are inexpensive and lead to reasonable results over smooth topography and not too high roughness length, notably in the upstream region of hills. These approaches are not adapted for slope higher than $0.2-0.3$ and CFD approaches (solving the full non-linear NS equations) need then to be used. Concerning turbulence closure, $k-l$ models is rarely used but computation of l can be adapted to account of orography impact on the flow so that performances of the model can be enhanced also in the downstream part of the orography. Those approaches are however limited in complex terrain. The $k-\varepsilon$ family approach is the most appealing and used one. Some variants of the standard model are generally preferred, such as the RNG $k-\varepsilon$, due to the shortcomings of the former. RSM models give the same type of results as the latter with more information on the turbulent quantities but at a higher computational cost. They are found to be less interesting. Generally, all models tend to better predict flow upstream of the orography. Flows on the lee side are best predicted by advanced models. However, due to an over-prediction of turbulence associated with RANS limitations, flow generally recovers too quickly after obstacles. In addition, the use of RANS models is restricted by the highly unsteady and anisotropic character of flow above complex terrain where eddy resolving approaches, *i.e.* LES, appear to be best suited. As an example, a recirculating zone behind an obstacle is generally flapping and can even disappear intermittently. Such an information, of interest for locating a turbine, can not be captured by RANS approaches and measurements or LES are needed.

A fine representation of the earth surface includes both a representative and precise horizontal description of surface cover and orography, and also a surface boundary condition able to

properly take into account the type of surface cover. The use of the simple log-law profile only based on a roughness length for flow above complex land cover may result in erroneous results whatever the turbulent closure. Hence, the challenges are moved to the correct integration of a fine representation of the earth surface.

In summary, although model abilities are known and their results are promising, cases over heterogeneous natural terrain are still very challenging which is of concern for wind energy applications. Furthermore, by noting that ABL is effectively never neutral, that modern wind turbines are close to 150 m tall, which is roughly the height of surface layer top, and that wind farm horizontal extent can span more than $5 - 10$ km, which is in the mesoscale domain, it can be concluded that modern wind energy applications are beyond the limits of the hypothesis commonly used in CWE, *i.e.* only neutral surface layer without the Coriolis effect.

1.2 Environmental modelling of the ABL

Environmental models, such as large scale and mesoscale atmospheric circulation models (referred to as mesoscale model hereafter), face the challenge of accounting for the whole atmosphere's complexity by solving or modelling all relevant natural processes that interact, even indirectly, with it. Thus, in addition to simulate a flow over a rotating non-homogeneous sphere, they have to consider turbulent transfer of heat, humidity and momentum, phase changes, clouds, radiation, topography (orography and land cover), vegetation, soil, etc. Thus, as opposed to CWE, momentum turbulent mixing, albeit important, only represents a small part of the processes taken into account. Furthermore, horizontally, scales of interests range from few kilometres to the entire earth, and vertically, the soil, the earth surface and the whole atmosphere are considered. Here, the expression "environmental modelling of the ABL" refers to the modelling of the full ABL and earth surface processes by means of large scale and mesoscale models.

Some differences in terminology between CWE and meteorological applications are to underline: convection in environmental modelling is associated to buoyant processes. Thus, the transport due to the fluid motion, *i.e.* the convection of CWE, is called advection in the environ-

mental modelling literature. Terminology of model names also slightly differ. Historically, the TKE (resp. mixing length) have been referred to as k (resp. l) in CWE, while it is represented by E (resp. λ) in environmental modelling applications. Thus, $k-l$ is called $E-\lambda$ and $k-\varepsilon$ becomes $E-\varepsilon$. However, thermal stratification put aside, methods and approaches to model turbulence in environmental models are based on the same mathematical models and theories as for CWE as underlined by Pielke and Nicholls (1997). However, due to the model's aim and specificity of the processes of interest (notably because of the stratification and the large differences between horizontal and vertical scales interest), the "ecosystem" of models differs: $k-\varepsilon$ is not very popular and $k-l$ is the preferred approach.

In this section, the various possible approaches to model the ABL in environmental models are reviewed. Knowing that the ultimate concern of the study is ABL flows modelling for use in wind energy application, a special attention will be given to momentum treatment as well as the processes influencing directly the latter, such as thermal stratification of the ABL. At first, the ABL in view of environmental models is discussed. Then, mesoscale models are further described to better understand challenges associated to their use at high resolution for ABL flows. Finally, a review of most established models is done by first considering stratified ABL over flat homogeneous terrain and then over heterogeneous terrain.

1.2.1 ABL in view of environmental applications

While the ABL is not generally the primary objective of large scale and mesoscale models, it is of high concern since it drives a large part of energy exchanges of the atmosphere and it is where most of human activities are taking place. As further discussed in the next section, the time and space scales at which environmental models operate require the use of strongly deformated grid cells with generally $\Delta x/\Delta z \gtrsim 100$ in the ABL. Horizontal resolution go up to 1 km, which is roughly the height of the ABL, while the vertical resolution reaches generally a few tens of meters close to the surface (with at least one grid point located in the surface layer). Furthermore, since turbulent exchanges in the ABL are mostly vertical and horizontal gradients of the main variables (except pressure) are negligible compared to vertical gradients

in the ABL, large scale and mesoscale approaches generally consider the ABL as horizontally homogenous invoking the ergodic/Taylor hypothesis. Thus, horizontal components of the turbulence mixing are neglected by ABL models and it is also often assumed that there is no subsidence, *i.e.* $w = 0$ m/s (while fully 3D conservation equations of mass, energy and momentum are solved in the associated mesoscale model). These generally accepted simplifications are called boundary layer approximation (Stull, 1988; Holton, 2004), and ABL models relying on the latter are commonly known as ABL column models. Such a model is generally used within large scale and mesoscale model for the parametrization of turbulence mixing in the ABL and the whole atmosphere.

While the boundary layer approximation greatly simplifies the problem (only two out of nine Reynolds tensor terms need to be considered and the advection is neglected), environmental models still have to deal with unsteady stratified full (from the earth surface to the free atmosphere) non-dry ABL flows submitted to large scale forcing and diurnal and seasonal cycle sensitive to the free atmosphere, the earth surface and the soil state. Thus, numerous processes need to be parametrized in addition to turbulence closures that have to be able to seamlessly take into account the whole range of stratification from very stable to freely convective. The reader is referred to the scientific documentation of any of the mesoscale models introduced in the next section for a detailed description of all the features of such ABL models.

As a summary, mesoscale models generally share the following representation of the ABL:

- horizontally homogeneous full ABL (from the earth surface to the free atmosphere);
- unsteady (with the ability to reproduce the diurnal cycle);
- thermally stratified;
- Coriolis effect;
- incompressible high Reynolds number flows.

As a result in this section, unless specified, the term ABL will refer to the horizontally homogeneous stratified full ABL (from the earth surface to the free atmosphere).

1.2.2 Mesoscale models

Mesoscale models are currently the heart of Numerical Weather Prediction (NWP) models on which is based the everyday weather forecast. They are also used in a wide range of environmental applications going from wind energy forecast and resource evaluation to pollutant dispersion and flood studies. They can be seen as approaches being composed of many integrated sub-models: the dynamic model, *i.e.* the solving of the various conservation equations, may be the most important component, and all the physical parametrization form the other pillar of the model. Turbulence modelling is part of the latter sub-models, and while it is of prime importance to correctly reproduce ABL flows, the accuracy and efficiency to solve the conservation equations of mass, momentum and energy, as well as other quantities of interest, such as moisture, are a very critical aspect of the approaches. This latter fact is further enforced when flows at high resolution over a non-homogeneous surface ($\Delta x < 10$ km) are considered (Benoit *et al.*, 1997). Furthermore, while a coarse horizontal resolution tend to smooth surface properties, finer meshes leads to a finer surface representation and steeper orography which can introduce numerical complications. Considering that wind energy applications generally rely on high resolution mesoscale model outputs ($\Delta x < 10$ km or even $\Delta x < 1$ km), it is of prime interest to review high resolution mesoscale models.

In the next subsection, the main characteristics and abilities of mesoscale models will be reviewed. The aim is to introduce all key concepts notably for mesoscale models dealing with high resolution. As a result, mesoscale models are first introduced. Then, the main components in the structure of the models, grid properties and vertical coordinates are discussed. Finally, the use of mesoscale models in wind energy application is illustrated.

1.2.2.1 Introduction to mesoscale models

The simplest definition of mesoscale models would be that they are models dealing with mesoscale processes, namely topography forced flow regimes (*i.e.* orography and other surface properties) ranging between synoptic scales and microscales (2000 km to 1 km). They consider the full atmosphere from the surface to $\sim 20 - 30$ km and they generally retain the

abilities to deal with synoptic scale flows, and sometimes, to reproduce the general atmospheric circulation. Today, some mesoscale models also tackle microscale phenomena (after a proper adaptation of the various parametrization). As a result, they can be used for a very wide range of scales explaining their usefulness and wide spread application for environmental modelling.

Pressure, temperature, moisture and momentum conservation equations are generally considered by mesoscale models, but other passive or reactive quantities such as pollutant can further be included. The dynamic kernel, *i.e.* the solver of the various conservation equations, is of central importance and models are generally designed around the latter. Parametrization of unresolved processes, such as turbulence mixing, cloud microphysics and radiative exchanges are also fully taken into account through a so-called physical parametrization.

Due to their complexity, mesoscale models are traditionally developed and maintained through cooperative programs involving several universities, research groups and government agencies. Some of the operational global NWP models that are based on mesoscale models are:

GEM: the Global Environment Multiscale unified model from Recherche en Prévision Numérique (RPN), Meteorological Research Division (MRD), and the Canadian Meteorological Centre (CMC). GEM forecast ten days in advance at a horizontal resolution of 25 km. Open Source (LGPL). http://collaboration.cmc.ec.gc.ca/science/rpn.comm/.

GFS: the Global Forecast System (previously AVN) is run by the National Oceanic and Atmospheric Administration (NOAA) and the National Centers for Environmental Prediction (NCEP) to produce forecasts up to 16 days in advance at 35 km resolution. Open Source (MIT License) and all output are freely available. http://www.emc.ncep.noaa.gov/GFS.

UM: the Unified Model from the United Kingdom Met Office (UKMO). UM produce six days forecasts at 25 km resolution. License. http://www.metoffice.gov.uk/research/modelling-systems/unified-model

These models are also able to assimilate data from a wide variety of external sources, such as in-flight plane, radar, satellite, surface stations and also from other models. The assimilation of data is done in a four dimensional way, *i.e.* space (3D) and time. It allows for a more

realistic representation of surface and atmosphere at initial condition and during the spin-up period of the forecast. Based on permanent data assimilation, mesoscale models can also be run offline to produce analysis data, *i.e.* 4D seamless gridded databases of the surface and the atmospheric states. Analysis data (and re-analysis data which goes a step further) is the closest representation of the full atmosphere we can have.

Historically, an important aspect of mesoscale models has been the computational efficiency since their main goal is to operationally forecast the weather. Thus, in addition to the solvers, all components of the models have also to be efficient which adds restrictions on the approach that can be used. As an example, finite difference are most of the time preferred to the more flexible and advanced finite volumes and finite elements methods because of their efficiency (Steppeler *et al.*, 2003). Furthermore, all the main components of the models are generally optimized to run in parallel on multiprocessor architecture and High Performance Computers (HPC).

Hydrostatic hypothesis is well suited when modelling large scale flows (Holton, 2004), *i.e.* with $\Delta x > 10$ km. Indeed, at such scales, vertical velocity is negligible in comparison to horizontal velocity. As a result, $dw/dt = 0$ and w equation leads to the hydrostatic balance, *i.e.* $\partial p/\partial z = -\rho g$, and it is convenient to rely a pressure vertical coordinate as it brings numerous simplification in the system of equations to be solved. At the finest mesoscales (1 to 20 km), driven by processes including buoyancy and topographic effects, vertical velocity can locally become of the order or higher than the horizontal wind (Holton, 2004). In such a case, mesoscale flow is determined by non-hydrostatic processes. Surface heat, solar radiation, moisture fluxes, evaporation, condensation, convection and turbulence can also introduce non-hydrostatic effects. As a result, it is generally admitted that the hydrostatic approximation becomes inaccurate for a resolution finer than 10 km. Thus, high resolution mesoscale models have to be non-hydrostatic (NH), and wind energy applications should rely on NH models since they generally use high resolution model outputs ($\Delta x < 10$ km).

Based on the studies reviewed along the environmental modelling section, the following list introduces some of the mainstream operational or quasi-operational, compressible, NH mesoscale limited area models (LAM, see also Sec. 1.2.2.4):

ARPS: the Advanced Regional Prediction System developed at the Center for Analysis and Prediction of Storms (CAPS) at the University of Oklahoma. It integrates the LES capabilities. Open Source. http://www.caps.ou.edu/ARPS.

COSMO: formerly called Lokal-Modell (LM) and developed by the German weather services, Deutscher Wetterdienst (DW), it is now developed and maintained by the COnsortium for Small-scale MOdelling (COSMO). Open Source. www.cosmo-model.org.

Eta: the Eta model is named after its vertical coordinate. First, developed by Zaviša Janjić and Fedor Mesinger and named HIBU (Hydrometeorological Institute and Belgrade University), it was run operationally by the NCEP as the main regional North American Mesoscale (NAM) model before 2006. Open Source. http://etamodel.cptec.inpe.br.

GEM-LAM: the Global Environmental Multiscale model in non-hydrostatic LAM configuration. Open Source (LGPL). http://collaboration.cmc.ec.gc.ca/science/rpn.comm.

MC2: the Compressible Community Mesoscale Model from Recherche en Prévision Numérique (RPN), Meteorological Research Division (MRD), and the Canadian Meteorological Centre (CMC). Integration of LES capabilities is in progress. Open Source (LGPL). http://collaboration.cmc.ec.gc.ca/science/rpn.comm.

Meso-NH: the "modèle Méso-échelle Non-Hydrostatique" from the Centre National de Recherche en Météorologie (CNRM) and the Laboratoire d'Aérologie (LA) (Cuxart *et al.*, 2000). It integrates LES capabilities. Open Source. http://mesonh.aero.obs-mip.fr/mesonh.

MM5: the Fifth Generation Penn State University (PSU) and National Center for Atmospheric Research (NCAR) Mesoscale Model is freely provided and supported by the Mesoscale Prediction Group (MPG) at the Mesoscale and Microscale Meteorology (MMM) Division, NCAR. Open Source. http://www.mmm.ucar.edu/mm5.

RAMS: the Regional Atmospheric Modeling System developed at Colorado State University. It was the earliest mesoscale model to be applied to CWE problems (Pielke and Nicholls,

1997). It integrates LES capabilities. Open Source (GPL). http://bridge.atmet.org/users/software.php.

WRF: the Weather Research and Forecasting model is developed based on a cooperative partnership of NCEP, NCAR, and the meteorological research community of the US including universities and federal research laboratories. It is a fairly recent model. Open Source. http://www.wrf-model.org. WRF has two main configurations, namely:

WRF-NMM: the WRF Non-hydrostatic Mesoscale Model is currently the main regional weather forecast model ran operationally at the NCEP as the North American Mesoscale (NAM) model. http://www.dtcenter.org/wrf-nmm/users.

AR-WRF: the Advanced Research WRF is developed primarily at the NCAR with a strong support from the community. It integrates LES capabilities. http://www.mmm.ucar.edu/wrf/users (Skamarock *et al.*, 2008) (Klemp and Skamarock, 2004)

By not relying anymore on the hydrostatic balance, NH mesoscale models also have to deal with pressure and sound waves. While the latter do not have meteorological significance, they can pollute the solution if not properly treated. Indeed, due to their high speed, sound waves add severe restrictions on the time step. The anelastic approximation allows to filter sound waves without assuming hydrostatic balance[2]. However, while it permit to reproduce all kinds of stratified flows still considering an incompressible fluid, thermodynamic variables can only depart slightly from their reference state. This is not always satisfied in real cases which is one of the main weaknesses of anelastic approaches. In addition, the latter are known to "leak" energy since they are not strictly relying on the conservation of energy theorem (Randall, 2010). In the past, the anelastic approximation was often used, but current mainstream NH mesoscale models do not rely on it anymore, addressing sound wave through their time stepping schemes as discussed in the next section.

Finally, it is noteworthy that compressible NH mesoscale models solve the exact Euler equations of motion, *i.e.* the various conservation equations also known as the Navier-Stokes equa-

[2] The anelastic approximation is similar to the Boussinesq approximation where density equals a reference profile that varies vertically instead of being constant. Mass flux is non-divergent under the anelastic approximation.

tions without molecular and turbulent diffusion processes, without any approximation before discretization. Theoretically, they can be used at all scales without restrictions. Discretization, boundary conditions and physical parametrization however limit the range of applicability.

1.2.2.2 Time stepping and advection schemes

Modelling of the time evolution of atmospheric phenomena is one of the main purpose of mesoscale models. Numerical methods used to take into account time evolution and advection terms are thus of prime interest. This is further strengthen when further considering that they have to address sound waves in compressible mesoscale model.

Both explicit and implicit time discretization can be used. As a general remark, depending on the scheme, explicit approaches are inexpensive but time steps are restricted by the Courant-Friedrichs-Lewy condition ($\mathrm{CFL} = u\Delta t/\Delta x$) that generally have to be lower than 0.25. On the contrary, implicit scheme are costly and more complex but allow large time steps leading to $\mathrm{CFL} \gtrsim 1$ (Girard *et al.*, 2005). While implicit approaches are quite standard for hydrostatic models, explicit approaches are commonly used for NH models maybe due to their already higher complexity (Steppeler *et al.*, 2003).

Several compressible mesoscale models, such as ARPS, LM, MM5, RAMS and WRF are based on the Eulerian discretization of the advection. These models are considered as robust and as efficient as Eulerian hydrostatics models (Steppeler *et al.*, 2003). They are usually based on split-explicit schemes and on three time levels (leapfrog) time discretization (Holton, 2004). Slip-explicit (mode splitting) reduces restriction on time step by processing fast sound waves apart from slower advective tendencies. Furthermore, horizontal and vertical directions are treated differently. In the horizontal, the explicit treatment of sound wave is based on smaller, inner time steps that satisfy the sound speed CFL condition. These time steps are a fraction of the model time step used to compute the advection and all other terms. In the vertical, due to a higher resolution, an implicit discretization is generally used. Split-explicit approaches are well established because they do not require solving very large linear systems and they are easy to implement (also on HPC since only the information of surrounding meshes

is needed) (Steppeler *et al.*, 2003). They are however more restrictive on the time step in comparison with fully implicit approaches notably when considering large scale flows.

Implicit time discretization allows for a bigger time step, while each time step is more computationally expensive. Lagrangian advection schemes (discussed hereafter) are often used in combination with implicit approaches, which explains the Semi-Implicit Semi-Lagrangian (SISL) model denomination. These methods were adapted for an efficient modelling of large scale flows but they require more complex elliptic solvers (Thomas *et al.*, 1998). Indeed, implicit treatment leads to an Helmholtz equation for pressure. The latter is equivalent to Poisson equation for incompressible flows. It is only 2D in implicit hydrostatic models but it is 3D and asymmetric in compressible NH models Steppeler *et al.* (2003). Furthermore, the anisotropy of the system depends on the steepness of orography, and thus indirectly on the size of the mesh. A steeper orography may result in larger asymmetric terms and thus in a system harder to solve. However, with a cautious treatment, implicit approaches have the potential to be more efficient than explicit schemes. Tanguay *et al.* (1990) were the first to present a compressible SISL mesoscale model. Bergström and Juuso (2006), Benoit *et al.* (1997) and Laprise *et al.* (1997) further developed this approach by adding the topography based on Gal-Chen vertical coordinates (first test achieved by Pinty *et al.* (1995)). They also added all the features required by a fully operational mesoscale model: the MC2 model was born. The GEM unified global and regional operational model as well as the United Kingdom Meteorological Office unified forecast and climate model are also based on a SISL approach and can be used in both hydrostatic and non-hydrostatic configurations.

Advection is the main non-linearity in the equation of atmospheric motion. Thus, accurate and efficient treatment of this term is essential. The choice of advection scheme has generally a strong influence on the entire model architecture (Steppeler *et al.*, 2003). Historically, Eulerian schemes with centred finite difference coupled with a three time levels (leapfrog) discretization were widely used in both hydrostatic and NH mesoscale models. Schemes based on flux form of the advection terms allow the immediate conservation of advected quantities (Wilcox, 1994). Such an approach is used in the WRF model. Schemes based on the advective form of the

equations leads to equivalent results only if solutions are smooth (*i.e.* velocities are far from sound speed) which is the case for atmospheric motion (Steppeler *et al.*, 2003). As a result, Eulerian schemes based on the advective form of equation are also commonly used in NH mesoscale models. Models such as LM, MM5, ARPS and RAMS use variants of Eulerian scheme based on the advective form of equations. Finally, note that Eulerian leapfrog schemes are quite robust but they generally need an explicit filtering of the quantities (time and space) to avoid time step decoupling. This filtering increase effective numerical diffusion which can eventually reach a level equal to or higher than turbulent diffusion (Steppeler *et al.*, 2003).

Concerning the Lagrangian advection schemes, the advected quantities are updated at each grid point by interpolation of the trajectory's upstream values (previous time-step) reaching that mesh at the new time step. Thus, interpolation methods are critical, notably close to the surface. Semi-Lagrangian (SL) advection schemes are convenient for multidimensional advection discretization (Steppeler *et al.*, 2003). However, efficiency of SL schemes appears to decrease at high resolution, but no theoretical limitation support this remarks (Bartello and Thomas, 1996). As underlined by Thomas *et al.* (1998) and Randall (2011, Sec. 5.12), such a scheme can be interpreted as an Eulerian finite difference scheme which is shifted to the upwind grid cell (*i.e.* a generalized upstream scheme). It thus features the same properties, *i.e.* it is monotone but more diffusive than centred Eulerian scheme. Randall (2011) further adds that the intensity of this numerical diffusion can be lowered by using higher-order interpolations (to compute variable at the upwind location), but it cannot be avoided.

1.2.2.3 Discretization, vertical coordinate and topography

Structured grid allows for simple and light-weight data organization, implying a more efficient use and access to the memory. It thus allows for efficient model implementation which explains why they are adopted by most of mainstream NH models such as MM5, Meso-NH, LM, RAMS, ARPS, MC2 and GEM. In addition, seeing the properties of the computational domain, *i.e.* generally a square box, unstructured grid become less necessary than for engineering applications. They however present undoubtful advantages such as the ability to finely represent

complex surface features as estuaries at an equivalent resolution (Steppeler *et al.*, 2003). Structured grid discretization of mesoscale model based on finite difference is commonly based on horizontal Arakawa -B and -C staggering coupled to Charney-Phillips staggered vertical discretization (Holton, 2004; Steppeler *et al.*, 2003).

Vertical coordinates allow the representation of orography in mesoscale models. As opposed to hydrostatic models that largely rely on pressure based vertical coordinate, NH models commonly use fixed terrain following vertical coordinates (Holton, 2004; Steppeler *et al.*, 2003), such as Gal-Chen terrain following vertical coordinate. They were introduced by Gal-Chen and Somerville (1975) and Clark (1977). Such a curvilinear oblique coordinate consists in a normalization of the natural height coordinate z based on the height of orography above sea level h, and a height at which the mesh is not influenced by orography anymore Z_T, such that the new coordinate is defined as $(z-h)/(Z_T-h)$. The height Z_T equals the top boundary height in the original Gal-Chen vertical coordinate. In an hybrid coordinate system, Z_T is lower than the top boundary and a different vertical coordinate is used above Z_T. Instead of using the natural height, some NH mesoscale models such as MM5 or GEM also rely on pressure based vertical coordinate such as the sigma coordinate, σ. The latter is generally obtained by normalizing the pressure by a reference or a computed hydrostatic pressure. It also leads to a terrain following coordinate. This conveniently allows to directly reuse the same physical parametrization for the hydrostatic and NH configuration of the model (Steppeler *et al.*, 2003). However, σ coordinate is generally not fix in time.

Terrain following vertical coordinates allow a transformation to a rectangular computational domain which simplifies discretization of equations and model implementation. The ABL is furthermore treated uniformly, *i.e.* meshes are roughly at the same height above ground everywhere in the computational domain. However, traditional terrain following coordinate systems are based on perfectly vertical edges. The coordinate is non-orthogonal which imply a strong deformation of meshes over steep orography. With such coordinates, vertical walls cannot be reproduced, and the practical maximum slope that can be handled is reduced by numerical problems. Indeed, spurious flows can develop even in an atmosphere initially at rest

due to purely numerical discrepancies caused by a too steep orography (Girard *et al.*, 2005). This is particularly of concern at high resolution, since the finer representation of the surface implies a less smoothed orography and thus higher slopes.

To overcome this limitation, more advanced orthogonal terrain following coordinates can be used. It is also possible to rely on a coordinate based directly on the natural height with a cell blocking method such as for flow around buildings in CWE. The latter approach is however less straightforward to apply on natural terrain (Bonaventura, 2000). Furthermore, those approaches generally require the use of finite volume (FV) or finite element (FE) discretization. Nevertheless, FV methods are not sufficiently efficient to comply with the requirement of an operational model (Steppeler *et al.*, 2003). Bonaventura (2000) proposed an accurate and efficient approach equivalent to a FV method but dedicated to SISL. It is also possible to adopt an hybrid orography representation, such as the building block approach used by the Eta model. While this latter method appears promising at large scale, it has some difficulties at high resolution (Steppeler *et al.*, 2003).

1.2.2.4 Lateral boundaries and downscaling

Mesoscale models, notably at high resolution, have generally a finite domain (not global) which is called limited area model (LAM). As a result, they rely on larger scale data, commonly general circulation models (GCM) outputs, to provide them with initial and time evolving lateral (and top) boundary data. Various possible approaches can be used to achieve such a downscaling. Statistical downscaling exists but dynamical downscaling is the most common in NWP and consists in the four dimensional nesting (space and time) of a fully evolving flow. However, a higher resolution drastically increases the size of the problem: dividing by two the mesh size, the problem size is multiplied by 8, *i.e.* by two for each spatial direction and by two for the time step to comply with the CFL condition. Thus, it imposes the use of adaptative grid refinements to optimize computational power and memory usage.

The most common adaptative grid refinement method is to use several nested grids, all with a refined resolution in a defined sub region of a larger grid. Nesting is challenging since coarser

results need to be used to initiate and pilot a finer resolution problem. Processing of the initial and lateral boundary condition is thus a critical task. Mesoscale models generally include highly tuned self-nesting capabilities so that the downscaling results are optimized. For classical nesting, a ratio in the horizontal resolution around four is generally used between nesting levels, but it can vary depending of the model (Benoit *et al.*, 1997). Nesting based on data from another model is usually less trivial and requires a fine pre-processing of the data. In a one-way nesting, the finer scale model uses the results from the larger scale one as initial and boundary condition. A two-way nesting is when the larger scale computation further take into account the results of the finer scale one. With a two-way nesting, computations are coupled allowing for a representation of interactions between a broader range of scales. The smallest scales are able to influence the largest ones letting a chance the butterfly effect to occur.

Unconventional adaptative approaches have also been implemented in NH models based on both structured and unstructured meshes. Structured adaptative grids with variable resolution are interesting since they retain some of the structured grid advantages. They further allow the direct study of interaction between a wider range of scales without the need of a two-way nesting. In that sense, a downscaling is done directly with a unique grid. Following this approach the resolution is increased in a rectangular sub-region of the domain and it smoothly decreases outside this area. As a result, this grid type is also known as stretched or telescopic grid. It is to note however that the CFL constraints apply to the finest meshes, restricting the time step even in the coarse resolution areas.

1.2.2.5 Mesoscale models in wind energy applications

Mesoscale models play an important role in the wind energy domain. The most straightforward application is certainly to forecast wind power production, but they are also very commonly used for wind resource assessment.

In regions where wind power penetration is more than a few percent of the total energy production portfolio, a forecast of wind farms production is needed in order to optimize wind energy use and integration to the grid. The output of operational NWP system are most of

the time directly used by wind power production forecast models. Such models are generally based on purely statistical approaches similar to Model Output Statistics (MOS) modules (statistical downscaling), but simple physical model such as linear flow models (*e.g.* Sec. 1.1.2.2) can also be used (Landberg *et al.*, 2003a) (dynamical downscaling). Wind power forecasting community generally considers that up to 80 % of the production forecast error is coming from the input weather forecast data, thus from NWP models (Giebel *et al.*, 2003; Landberg *et al.*, 2003a; Kariniotakis *et al.*, 2004). In order to evaluate the probability of a forecast scenario, the output from several models or from the same model but with slightly different initial, boundary conditions and configuration, can be combined in order to obtain an ensemble prediction. This kind of forecast allows reducing the mean error while associating a fluctuating value to wind energy as a function forecast uncertainty (Pinson and Kariniotakis, 2004).

Modern wind resource assessment also heavily relies on mesoscale models. Landberg *et al.* (2003b) reviewed wind resource assessments methods and they clearly identified mesoscale models as part of the best suited approaches for the large scale seamless and contiguous wind resource assessment. In fact, instead of operational NWP model outputs, analysis and reanalysis data are used by large scale wind mapping applications which downscale this data up to the microscale level following statistical-dynamical downscaling approach. Commonly, the time evolving three dimensional representation of the atmosphere from the reanalysis data is first processed in order to obtain a representative large scale wind climate, *i.e.* a classification by speed bins and directions at several heights of geostrophic wind retaining also the information on thermodynamic variables (Frank and Landberg, 1997; Yu *et al.*, 2006). Instead of a classification, a statistical selection of representative event can also be used (Russo and Zack, 1997). Then, a mesoscale model is used to downscale each of the wind climate classes or events. A resolution of one to five kilometres is often used. Then, results can be recombined, based on the probability of occurrence of each class or event, in order to obtain the characteristics of the mean wind at the mesoscale level. This is however not sufficient and the geographical wind resource distribution need to be known at the microscale level, *i.e.* $\Delta x \sim 100$ m. This cascade thus allows going from few kilometres to a few tens of meters where the last level is generally

based on microscale models such as the one presented in the CWE section (simplest linear models are commonly used).

Such statistical-dynamical downscaling approaches have been used successfully starting with Frank and Landberg (1997) who introduced and validate the first mesoscale wind atlas approach based on the NH Karlsruhe Atmospheric Mesoscale Model (KAMM). Frank *et al.* (1999) further compared the latter approach and a linear microscale model (WAsP). KAMM was run with a resolution of 350 m. They clearly showed advantages and limitations of each approaches: while the microscale model was better skilled for fine topography due to the too low resolution of the mesoscale model, the latter, by taking into account stratification, was able to reproduce a decoupling phenomena related to a low level inversion, improving notably results over the microscale model in such situations. The KAMM model was later coupled to WAsP to obtain an efficient meso-micro wind mapping approach. The KAMM/WAsP approach have been heavily used all around the world (Landberg *et al.*, 2003b). Yu *et al.* (2006) introduced the Wind Energy Simulation Toolkit (WEST) which is an approach equivalent to KAMM/WAsP but based on the mesoscale model MC2 and the microscale model MS-Micro. It was used successfully to obtain the Canadian Wind Energy Atlas (CWEA), http://www.windatlas.ca (Environment Canada, 2004), and over a very complex terrain of Yukon, Canada (Pinard *et al.*, 2005), with however slightly less success. The three level nesting approach presented by Eidsvik *et al.* (2004) also follows an equivalent philosophy. The mesoscale models High Resolution Limited Area Model (HIRLAM) and MC2 are used in cascade followed by the microscale non-linear SIMRA model. The last level of nesting is based on an advance second order RANS model with the very same features as CWE models. (Eidsvik, 2005) further tested successfully the approach on the well-known Askervein smooth hill. In parallel, several private companies such as AWS TruePower (http://www.awstruepower.com) (Russo and Zack, 1997) and 3TIER (http://www.3tier.com/) have developed they own wind mapping system generally based on a mesoscale-microscale statistical-dynamical downscaling. Many countries such as the full US were completely mapped at the microscale level and free large scales wind resource maps of the whole earth surface exists.

1.2.3 Environmental modelling of ABL flows

ABL modelling in large scale and mesoscale approaches is generally based on the boundary layer approximation as discussed earlier. A so-called ABL column model is used, and most of the processes are parametrized. Turbulent diffusion is one the principal processes since it is the main driver for vertical transport in the ABL. Generally speaking, methods and approaches used to model turbulence in mesoscale models are the same as in CWE, *i.e.* RANS approaches, but in 1D as underlined by Pielke and Nicholls (1997). Their comprehensive classification can be found in Stull (1988, Chap. 6). However, thermal stratification, humidity as well as exchanges of all kinds with the earth surface and the free atmosphere play an important role that need to be considered by models, which clearly broadens the aspects to be investigated and increases the complexity of the approaches.

To add complexity, direct result comparisons with data coming from well controlled experiments are almost impossible due to the size of the problems. Indeed, when momentum only is considered, parameters such as the Reynolds number are well suited to scale the flow parameters. However, when adding temperature to the problem, other non-dimensional parameters such as Froude number become relevant, and scaling conditions are hardly satisfied all at once. As a result, models are generally compared to each others and to full scale experiments. Note also that they are indirectly evaluated through the everyday forecast. Mesoscale wind resource assessment are also interesting to evaluate surface wind modelling of mesoscale models.

Here, the most widely accepted ABL models (mostly column models) implemented in mesoscale approaches are reviewed and intercompared. Only momentum and heat turbulent mixing along with the inclusion of thermal stratification are considered. In a first section, the various similarity theories that apply to the ABL are presented. Then, the modelling of the stratified homogeneous ABL is considered. This section is thus purely devoted to ABL column models. Finally, based on common mesoscale flow types, we briefly review the mesoscale modelling of the ABL over heterogeneous surface. In this latter section, abilities of both ABL column models and mesoscale models are thus addressed.

1.2.3.1 Similarity theories in the ABL

Similarity theories can be seen as the simplest ABL models (zero order) (Stull, 1988). They allow a simple but precise representation of processes to which they apply. They play an important role in the prescription of surface boundary conditions of ABL models, as well as in the inclusion of thermal stratification (Stull, 1988). Depending on the scales considered by environmental models and their vertical resolution close to the surface, various representation of the ABL through similarity can be used.

In large scale models with very limited vertical resolution, *i.e.* ABL represented by one grid point, an estimation of the surface drag can be obtained based on the Rossby number similarity theory (Rossby, 1932). This theory allows to evaluate surface shear stress as a function of the surface Rossby number $\mathrm{Ro} = ||\boldsymbol{v_g}||/fz_0$ (where $||\boldsymbol{v_g}||$ is the geostrophic wind modulus, f is the Coriolis factor and z_0 is the roughness length). This zero-order model is the simplest representation of the full ABL (Stull, 1988). As confirmed by many experiments, it leads to representative results in regions with an homogeneous surface such as great plains or oceans. Thus, it often serve as a first evaluation of the full ABL (Blackadar, 1962; Detering and Etling, 1985; Garratt *et al.*, 1996). However, no general agreement exists concerning the universal function linking the surface drag to the surface Rossby number (Stull, 1988, Sec. 9.8).

After the mid 1980s, most mesoscale and general circulation models had a sufficiently high vertical resolution allowing the first grid point to be located in the surface layer. It thus permitted to use the surface-layer similarity theory, also known as the Monin-Obukhov (MO) similarity theory, as bottom boundary condition of ABL column models. The relevant surface related scales of this theory are z_0, L_{MO}, u_* as well as the temperature scale of the surface layer, θ_*^{SL}. Based on the latter scaling, the primitive of the dimensionless gradient functions (also know as universal gradient functions or flux-profile relationships) of temperature and momentum in the surface layer can be obtained. Integrating these functions allows the direct computation of velocity/temperature at a given height in the surface layer such as done by Benoit (1977). This is particularly convenient to prescribe surface boundary condition of ABL models . The Monin-

Obukhov similarity theory is largely accepted by the community and a large amount of studies tackled the problem of deriving and validating the associated flux-profile relationships (Stull, 1988; Foken, 2006). A general agreement exists today (Foken, 2006) on parameters such as the von Karman constant ($\kappa = 0.4$) and an adapted version of the widely used universal functions derived from Kansas data (Businger *et al.*, 1971) was proposed which are still in use today[3].

It is important to note that the Monin-Obukhov similarity theory is only valid for an homogenous surface layer when winds are not calm and u_* is not zero. However, as discussed by Delage and Girard (1992), the dependance of the universal gradient function on z/L_{MO} can be transformed to a dependance on a gradient Richardson number Ri, so that the same universal function linking turbulent mixing to stratification can be used everywhere in the ABL. Monin-Obukhov similarity theory is also invalid in the roughness sublayer (*i.e.* the lowest part of the ABL directly impacted by roughness elements as discussed in Sec. 1.1.3.1). This becomes notably critical for very rough terrain such as flow above a canopy (natural or urban) where the roughness sublayer can reach up to 2-3 times the canopy height (Garratt *et al.*, 1996). In such a case, the surface layer is clearly affected (being shallower or even absent), and universal gradient functions must be modified to take into account the height of the canopy and the effect of its roughness sublayer on the flow (Garratt, 1992).

Two main types of ABL exist with regards to thermal stratification: stable nocturnal boundary layers (NBL), and daytime convective boundary layers (CBL).

Nocturnal boundary layers (NBL) are still challenging to model (Cuxart *et al.*, 2006; Svensson and Holtslag, 2006; Bosveld *et al.*, 2010). As an example of their complexity, the turbulence can be intermittent, roughly half of the cooling is due to radiation (the other half comes from turbulent transport), and the height of the NBL is a function of its initial state (Garratt *et al.*, 1996). Furthermore, it is now recognized that there are several distinct types of stable boundary layer (Teixeira *et al.*, 2008). Nieuwstadt (1984) proposed a similarity theory for the local

[3] Historically, the surface layer community was divided on parameter values coming from two important experiments, the Wangara (1967), Australia, and the Kansas (1968), United States, experiments. In the end, it was proven that part of the Kansas experiment measurements were slightly biased (Foken, 2006).

scaling (*i.e.* $z - less$) of the turbulence in the NBL. This theory appears to be a generalization of the Monin-Obukhov theory using local scaling, *i.e.* that are the local values of L_{MO}, u_* and θ_*^{SL} respectively. This theory is very well suited for moderately stable NBL and generally accepted (Beare *et al.*, 2006).

Daytime convective boundary layers (CBL) also known as mixed layers were among the first ABL type to be numerically studied (Deardorff, 1972). They are indeed easier to model because of the large size of eddies generated by convection that confer them a well mixed character. Concerning the surface layer, either the Monin-Obukhov or the local free convection similarity theory can be used depending on the relative importance of surface heating with regards to surface stress (Wyngaard and Coté, 1974). These mixed-layer similarity theories rely on z_i, w_* and the mixed layer temperature θ_*^{ML}. It is generally accepted (Deardorff, 1972; Moeng and Sullivan, 1994) that the regime is convective and well represented by mixed-layer Monin-Obukhov similarity theory for $-z_i/L_{MO} > 4.5$.

A more extensive overview of the scaling applicability as a function of the ABL properties can be found in Holtslag and Nieuwstadt (1986). This latter literature review has been presented at the ABL Summer Course of Les Houches (van Dop *et al.*, 2008) by Dr. Holtslag himself with only few changes confirming that it is still up-to-date.

1.2.3.2 Stratified homogeneous ABL

The modelling of the stratified homogeneous ABL have drawn a large interest in the research community over the last 40 years. Here, the main ABL column models are illustrated. Their abilities are evaluated based on experimental data and intercomparison studies. Note that those discussion are devoted to ABL column models since mesoscale model abilities are not triggered in horizontal homogeneous cases.

1.2.3.2.1 ABL column models closures

Common closures The modelling of ABL effectively started in the 70's. Blackadar (1962) introduced and evaluated a first order model for neutral ABL, *i.e.* only based on a mixing length, that is still a reference today. Guided by observations, he specified that the mixing length increased approximately linearly near the surface, κz, and then asymptotically to reach a constant value at upper levels, λ_0. Two main definition of the asymptotic mixing length λ_0 are commonly accepted: $\lambda_0 = C||\boldsymbol{u_g}||/f$ or $\lambda_0 = Cu_*/f$ where C is a constant (0.00027 and 0.05 respectively), $||\boldsymbol{u_g}||$ is the geostrophic wind, u_* is the friction velocity and f is the Coriolis factor. This definition of the length scale is well suited for the neutral homogeneous ABL, but latter studies prove that thermal stratification effects can be further included by using stability functions to scale the mixing length or mixing coefficients (Stull, 1988).

Today, first order closures are still in use, mostly in operational forecast mesoscale models, however closures including a prognostic equation for TKE and a mixing length, *i.e.* $k-l$ one-and-a-half order models, are the most common (Cuxart *et al.*, 2006; Svensson and Holtslag, 2007; Bosveld *et al.*, 2010). This is explained by their good ratio between performances, simplicity and computational cost. Furthermore, the mixing length for stratified ABL has been historically simpler to parametrize: characteristic length scale of the eddy is easier to evaluate than temperature variance or TKE dissipation rate (Stull, 1988).

Mellor and Yamada (1974), in one of the first attempts to reproduce a diurnal cycle, compared and classified several closures going from the full second-order closures (model based on up to 13 partial equations for TKE and each turbulent momentum and heat fluxes and variances) to a first order. The models were classified into different levels according to their complexity, ranging from most sophisticated, full second-order closure (Level 4) to the simplest first order closure (Level 1). The intermediate model (Level 2.5) which drops the prognostic equation for temperature variance but retains the one of TKE and a mixing length, *i.e.* a $k-l$ model, appeared to be almost as skilled as the full second order models (Mellor and Yamada, 1982). This

one-and-a-half order model, which is referred to as the level 2.5 MY model in the literature, is still commonly used today to study the evolution of the ABL.

Nevertheless, approaches based on the eddy viscosity approximation, *i.e.* models with an order lower than two, can not reproduce the countergradient fluxes observed at the top of the CBL (André *et al.*, 1978). Indeed, the eddy mixing coefficient being by definition positively defined, countergradient can only be predicted with second or higher order closures. A parametrization is therefore needed for lower order models: a countergradient term can be explicitly included in the closure or a non-local scheme can be used (Stull, 1988).

As a example of a typical ABL model included in mesoscale model, the one-and-a-half order column model from EC mesoscale models (MC2 and GEM) can be cited. This $k - l$ column model that rely on Blackadar (1962) mixing length and stability functions was first introduced by Mailhot and Benoit (1982). Relevant physical processes (radiative effects and humidity) and exchange processes taking place at the surface and in the soil are addressed and it is capable of simulating diurnal cycle of the full ABL. Benoit *et al.* (1989) implemented Mailhot and Benoit (1982) model in the Canadian Regional Finite-Element Model. Later, Delage and Girard (1992) develop new surface layer stability functions for the neutral to convective ABL also valid at free convection limit ($U = 0$) from the surface layer to the Ekman layer. This allowed to use the same stability function from the surface to the ABL top. Delage (1997) further shown that the use of a critical Richardson number for SBL is not suited in large scale model claiming that it prevents to take into account the residual subgrid turbulence. They presented a modified simple parametrization that brought results similar to more complex approaches. Many other refinement were latter included in this approach, such as the Bougeault and Lacarrère (1989) non-local definition of the mixing length (Bélair *et al.*, 1999). Since Benoit *et al.* (1989) work, this one-and-a-half order column model have been used successfully in all the Canadian mesoscale model used for the operational weather forecast by CMC (Cuxart *et al.*, 2006; Svensson and Holtslag, 2007).

Higher order closures Very few mesoscale models rely on turbulent closure with an order higher than two. As for CWE, the enhancement of results is not significant in comparison to the increase in complexity and computational cost. However, they are useful and most of the time employed for research purposes. Some early studies can illustrate their abilities. Wyngaard and Coté (1974) presented a second order closure that they tested against the CBL of the day 33 of the Wangara experiment. Results were also compared with Deardorff's early LES results of the same test case and they compare well. Wyngaard (1975) extended the second order closure introduced above to be able to deal with stable stratification. Based on the Kansas and Minnesota datasets, the authors showed that the model predicts correctly the structure of the turbulence from neutral to moderately stable cases[4]. André *et al.* (1978) were the first to reproduce a full diurnal cycle (based on the Wangara experiment data) with a unique model: a third order RANS model. Results were in good agreement with both experimental data and other numerical studies. Only the stable boundary layer height was significantly underestimated. However, by pushing closure assumption to a higher order model, this work allowed to validate and refine the closures of the lower order models.

Finally, it is interesting to note that the $k - \varepsilon$ approach of Launder and Spalding (1972), while heavily used for engineering application to model the neutral ABL, is much less involved in meteorological applications where it historically drew less attention. With such an approach, while there is no need to compute a length scale (leading some researchers consider the $k - \varepsilon$ as a second order model), parametrization of the TKE dissipation rate with regards to stratification is more tricky than for others closure of the same order such as $k - \theta^2$ (André *et al.*, 1978). Furthermore as underlined by Weng and Taylor (2003), all the early applications of the classical ε equation (Launder and Spalding, 1972) to the fully neutral ABL led to too deep boundary layers. Several researchers however proposed modifications to the standard ε equation by adjusting production and destruction of TKE. Detering and Etling (1985) presented a modified version of the standard $k - \varepsilon$ that successfully addresses homogeneous neutral and

[4] As a side note, Wyngaard (1975) also found that ABL over a flat homogeneous surface with a constant surface cooling rate can reach a quasi-steady state where particular scaling can apply. This later proves to be of practical use to validate models (Cuxart *et al.*, 2006).

convective ABL. The authors claimed that the introduced $k-\varepsilon$ model is to be seen as a model that yields equivalent results of a $k-l$, concerning stratified ABL, but that is more skilled for complex flow configuration since the length scale does not have to be defined. For its part, Duynkerke (1988) presented a $k-\varepsilon$ model dedicated to the neutral and stable homogenous ABL which also proved to be appropriate. Duynkerke (1988) closure is today implemented in the mesoscale model Meso-NH. Recently, a modified version of the standard $k-\varepsilon$ model was also proposed by Alinot and Masson (2005) for stable, unstable and neutral ABL. This approach, which is not a column model but a 3D classical RANS approach, was found to greatly improve the results over previous studies, notably for the stable thermal stratification cases.

1.2.3.2.2 Recent column model intercomparisons

Now that the main ABL column models have been introduced, abilities are further studied though a review of recent intercomparisons.

Hurley (1997) intercompared 10 well established column model turbulent closures including three first order, three one-and-a-half order and four second order closures (several variants of Mellor and Yamada (1982), Duynkerke (1988) and Detering and Etling (1985) are used). All models are based on the so-called boundary layer approximation but Hurley (1997) underlines that horizontal turbulent diffusion effects can be added by means of new source terms. Closures are first evaluated for a one-dimensional convective boundary layer obtained after the mesoscale model is run for 48 hours (*i.e.* two full diurnal cycles). It is found that mean fields are satisfactorily reproduced even by simpler models. However, the more complex the model, the better the results, particularly for turbulence predictions, although, this cannot be generalized. Inclusion of countergradient was needed for some of the models to perform better in the convective regime, such as Duynkerke (1988). Nevertheless, all models under-estimate both the horizontal velocity variance and the TKE dissipation rate near the top of the mixed layer, and, discrepancies between the three most advanced models reach up to 20 % of the non-dimensional estimated variances values in the mixed layer.

Bélair *et al.* (1999) further evaluated various configuration of a $k-l$ model implemented in the MC2 mesoscale model for several CBL measured during the Montreal-96 Experiment on Regional Mixing and Ozone (MERMOZ). Some non-local aspects of the closures are regarded through the countergradient terms and length scale formulation. Two formulation of l are evaluated: the classical Blackadar formulation (Blackadar, 1962) (fully local) and the Bougeault-Lacarère approach (Bougeault and Lacarrère, 1989) (non-local). It is shown that the non-local approach better predict the CBL fast growth in comparison of the local approach. Concerning countergradient, Bélair *et al.* (1999) found that the explicit inclusion of this term in the vertical diffusion equation had a negligible impact on the modelled ABL, notably in comparison to enhancement obtained with the new non-local length scale formulation.

Weng and Taylor (2003) also tested several turbulent closures for an homogenous stratified ABL. Comparisons rely on neutral, stable ABL and full diurnal cycles. The closures evaluated are the standard $k-\varepsilon$, Detering and Etling (1985) $k-\varepsilon$, a $k-\varepsilon-l$ (where the length scale is used to parametrize the production in the dissipation equation), the level 2.5 from Mellor and Yamada (1982) noted $k-k^2l$ (with both the prognostic and diagnostic model of k^2l) and finally, two versions of the classical $k-l$ approach (based on André *et al.* (1978) or Delage (1974) for stable stratification). The study does not compare with experimental data, but models are compared with each others, to MO similarity and literature results. For the neutral case, the $k-l$ approach is taken as a reference. It is shown that $k-l$, $k-\varepsilon-l$, Detering and Etling (1985) $k-\varepsilon$ and diagnostic $k-k^2l$ are similarly satisfying. On the other hand, standard $k-\varepsilon$ and prognostic $k-k^2l$ largely over-estimate the turbulent mixing and ABL height. The picture is slightly changed for the stably stratified ABL. Indeed, all $k-\varepsilon$ and $k-k^2l$ produce a too deep stable ABL with, once more, too much mixing. The closures that compare best with similarity are Delage (1974) $k-l$ and $k-\varepsilon-l$ closures. Finally, the diurnal cycle is carried out by piloting the surface temperature (based on some Wangara data but not attempting to match results). A comparison of the results is done after 10 diurnal cycles. This latter intercomparison is based on four models and the general conclusions are the same as before: the $k-\varepsilon$, and the two $k-k^2l$ models over-estimate the mixing and ABL depth. The maximum value of the

TKE for models based on two equations is twice as large as the one based on one equation. In the end, the author states that the $k - l$ approaches are still quite good. Concerning higher order models, it is found that while they take into account more physical processes, they do not guaranty success (Weng and Taylor, 2003).

Finally, it is worth presenting the three recent and very extensive intercomparisons done under the aegis of the GEWEX Atmospheric Boundary Layer Study, GABLS project (http://www.met.wau.nl/projects/Gabls) (GEWEX stands for Global Energy and Water Cycle Experiment, http://www.gewex.org). In these intercomparisons, the abilities of various critical aspects of not only ABL column models implemented in mesoscale models, but also of LES models are evaluated. The latter also serve as a basis of comparison for the former.

GABLS 1 is based on the quasi-steady moderately stable Arctic boundary layer proposed by Kosović and Curry (2000), and that compare reasonably well with the Nieuwstadt similarity (Nieuwstadt, 1984). Twenty ABL column models implemented in sixteen research and operational mesoscale models are intercompared, see http://turbulencia.uib.es/gabls (Cuxart *et al.*, 2006). All evaluated models except one rely on the eddy viscosity assumption and compared closure include simple first order (8 models), most common one-and-a-half order (8 models) and more evolved second order (two $k - \varepsilon$ and a k_θ^2). The general conclusion for the single column models intercomparison is that, while vertical resolution is not a concern, first order closures have a tendency to increase the mixing in comparison to research dedicated models (generally based on higher order closures *i.e.* 1.5). The former over-estimates u_* and the upper stable boundary layer inversion does not develop. The latter are closer to LES results. Fine tuning the closure parameters (such as Prandtl number, stability function and mixing length) based on LES results proved to generally enhanced the results.

GABLS 2 is based on the Cooperative Atmosphere-Surface Exchange Study - 1999, CASES-99 (Poulos *et al.*, 2002) and its goals is to study and model the diurnal cycle over land (Svensson and Holtslag, 2006, 2007), see http://www.misu.su.se/~gsven/gabls/. Eighteen column models are compared. The first conclusions of the study are that all model results differ from each

others and do not fit observations. The most significant difference is the under-estimated diurnal cycle of wind speed at 10 m agl (too low during unsteady day and too high during the stable night). Furthermore, even though surface temperature was provided, the 2 m agl temperature differs between models (reaching 2 C differences). Discrepancies between models are generally most striking during morning hours.

GABLS 3 is based on one diurnal cycle of a moderately stratified, baroclinic, mid-latitude ABL (Bosveld *et al.*, 2010), see http://www.knmi.nl/samenw/gabls/. This last intercomparison relies on data coming from the 213 m high heavily instrumented Cabauw met mast and from other facilities in the Netherlands. As opposed to the previous two GABLS intercomparisons (where the surface temperature was prescribed), in GABLS 3, each participant had to use its own soil/vegetation, while radiation models, fine tuned geostrophic forcing and dynamic tendencies were prescribed broadening the investigated aspects. Nineteen models were compared ranging from first order to second order ABL column models. The emphasis was on the sunset and morning transition as well as nocturnal boundary layer. Preliminary results show that significant discrepancies between models are obtained for the 2 m agl temperature, the 200 m agl wind speed and boundary layer height. Thermal coupling between surface and stable boundary layer seems to be the principal factor explaining the differences between models and observations. Long wave radiation and turbulent mixing are found to be of secondary importance.

As a conclusion of all the intercomparisons presented above, it is clear that various components and parametrization of the ABL column models still need to be validated and enhanced notably in stable conditions and during the morning and evening transitions. Indeed, when comparing models to each other and to real cases, discrepancies are not negligible. However, some categories of turbulent closure seem to emerge (as for the $k-\varepsilon$ in CWE): namely the $k-l$ models. They appear to be the best compromise between computational cost, simplicity and result quality, at least for the stratified homogeneous cases. It is thus of interest to review the abilities of the same approaches but for cases where the surface in not homogeneous which is the topic of the next section.

1.2.3.3 Mesoscale modelling of ABL over an heterogeneous surface

The mesoscale modelling of ABL flows over an heterogeneous surface involves all the main components of environmental models, *i.e.* both the dynamic kernel and the ABL model are required to tackle mesoscale heterogeneous cases. Two main types of mesoscale surface heterogeneities can be considered, *i.e.* orography and land cover, and both subgrid and resolved heterogeneities are important. In the context of mesoscales phenomena, the characteristic size of resolved surface heterogeneities lies between one to hundreds of kilometres. They can be explicitly represented and resolved. Conversely, subgrid heterogeneities need to be implicitly taken into account through parametrization. The simplest and maybe most relevant example is the aerodynamic roughness length, z_0. As a side note, most of the problems considered in CWE have a characteristic size smaller than the grid size of environmental models.

Large scale and mesoscale approaches commonly rely on the boundary layer approximation, which is generally accepted for grids with $\Delta x > 1$ km (Stull, 1988). Hence, the vast majority of environmental modelling applications only consider the vertical turbulent mixing, and they fully rely on the mesoscale model dynamic kernel to reproduce 3D flow features. Furthermore, to overcome the lack of horizontal mixing, horizontal diffusion is often added numerically (Benoit *et al.*, 1997). However, this approach becomes clearly invalid if the horizontal resolution is refined, such as $\Delta x < 1$ km: horizontal turbulent mixing also need to be properly modelled (Teixeira *et al.*, 2008). Indeed, in the scales from 100 m to 1 km, 3D turbulent microscale phenomena become non-negligible, but mesoscale processes are still important. They merge and interact and it is very challenging for both experimental and numerical studies (Wyngaard, 2004). Wind turbines and wind farms interact with ABL flows at those scales; thus they deserve a special attention (Shaw *et al.*, 2009).

In this section, the common types of mesoscale flow over an heterogeneous surface are briefly introduced exploring the abilities and limitation of ABL column models through various examples. Small mesoscale heterogeneities are considered as they are more relevant with regards to the ABL model evaluation. Furthermore, some heterogeneities at the border between

mesoscales and microscales are also investigated to further evaluate the limits of the environmental models common hypothesis of validity.

1.2.3.3.1 Land cover discontinuities

Various type of mesoscale land cover heterogeneities exist, each impacting differently the main variables of the model. Natural discontinuities generally include a change of several surface parameters at the same time further complicating the problem.

Subgrid land cover heterogeneities have to be fully parametrized. Advanced models of the surface cover are generally used in mesoscale models to provide a surface boundary to the ABL model. The Interaction Soil-Biosphere-Atmosphere model (ISBA) or the Canadian LAnd Surface Scheme (CLASS) are two examples implemented in the GEM and MC2 models (Mailhot *et al.*, 1998). Those approaches generally consider that each mesh are composed by a few main land covers and the information on each land cover and their ratio in the mesh need to be provided as input to the model. Then, a budget is computed for each land cover and the aggregated result is used as boundary condition for atmospheric processes. Subgrid topography is also parametrized through those advanced surface models as discussed in the next section.

Concerning the resolved land cover heterogeneities, the ABL column models consider the surface changes but they are not able to predict the associated dynamics processes. Thus, the abilities of the approaches directly depends on the solver of the equations of motions.

Sea and inland breezes are mesoscale circulation of a characteristic size equal or greater than $50 - 100$ km that can be triggered by various type of surface discontinuities (allowing to evaluate various configuration of the model), and that requires energy, momentum and mass conservation equations to be properly solved. They have historically drawn a large interest from the environmental modelling community (Garratt *et al.*, 1996; Hurley, 1997; Crosman and Horel, 2010). Garratt *et al.* (1996) reviewed ABL importance in sea and inland breeze modelling. After summarizing the advances on this topic during the period from 70's to the mid 90's, they conclude that ABL column models based on a prognostic equation for TKE are quite suit-

able for predicting the turbulent structures of the sea-breeze system. Hurley (1997) compared 10 column models (zero, one and two equations - see the previous section) based on a 2D sea-breeze flow. All closures led to similar results and all models are found to produce a reasonable sea-breeze circulation pattern. TKE increases at the front, but, this is better defined for higher order models. Recently, Crosman and Horel (2010) achieved a thorough review of the sea and lakes breeze modelling considering the dependence of the modelled sea breezes on ten main geophysical variables. Concerning the ABL model, the authors underline the importance of using appropriate parametrization such as $k - l$, notably to properly consider the CBL. It is found that a poor turbulence modelling or an inadequate ABL model may not prevent to reproduce the sea/land breeze circulation, but some of its features may be impossible to reproduce. On the other hand, a higher level of sophistication as well as a slightly better resolution are not found to always improve results.

As a result of the above, it appears that, while important, the ABL column model closure have a limited impact on sea and land breeze results, and it can be concluded that $k-l$ column models are generally found to be sufficiently advanced to properly take into account key processes, while the added value of higher order closures does not appear clearly.

1.2.3.3.2 Flow over valley and hill

Flows over changing orography represent an important aspect of mesoscale models (Holton, 2004). However, as underlined by Teixeira *et al.* (2008), until recently most of the studies neglected or gave little attention to boundary layer effects. Instead, strong efforts were dedicated to the validation of the dynamics of the models by reproducing phenomena such as gravity waves (Clark and Peltier, 1977; Miranda and James, 1992; Pinty *et al.*, 1995; Bonaventura, 2000; Girard *et al.*, 2005). However, ABL interactions with mesoscale orographic flows are very complex and not yet fully understood (Teixeira *et al.*, 2008; Shaw *et al.*, 2009).

Commonly, both the mesoscale models and their associate ABL model are evaluated using full scale orographic flow cases. In fact, all the studies based on real cases evaluate the full mesoscale model and thus the ABL model indirectly. However, data coming from full scale

dedicated measurement campaigns, *i.e.* intense observation period (IOP), are the best suited for fine evaluation of the models. As an example of such experiments the Mesoscale Alpine Programme (MAP) (Benoit *et al.*, 2002), the PYRenées EXperiment (PYREX) (Georgelin *et al.*, 2000), or the very recent large deployment Terrain-induced Rotor EXperiment (T-REX) (Grubišić *et al.*, 2008) can be cited. Theoretical mesoscale orographic flow studies that consider ABL effects also exist but are more scarce. They allow to evaluate specific aspects of the model in a more generic and quantitative way by simplifying the problem and only triggering processes of interest. Finally, as opposed to CWE, wind tunnel experiments are of limited use for the evaluation of mesoscale models due to the large differences in scale and the broader range of processes to consider (not talking about the earth rotation or the diurnal cycle).

Subgrid topography play an important role: it increases the apparent roughness of the surface decelerating the whole flow and increasing the subgrid mixing in the ABL. It is thus generally taken into account through the ABL model. The simpler approach on which most of mesoscale rely is to directly increase the aerodynamic roughness length as a function of the subgrid topography. Direction dependent roughness is also sometimes used. However, during the Comparison of Mesoscale Prediction and Research Experiment (COMPARE) second exercise (Georgelin *et al.*, 2000) where fifteen mesoscale models were intercompared based on PYREX IOP 3, it was found that subgrid topography is a key element that models based on the above simple parametrizations fail to properly consider. More advanced surface boundary conditions are required, such as a vertically distributed drag (cf. canopy model). The large impact of the subgrid topography in Georgelin *et al.* (2000) study was partly caused by the coarse horizontal resolution (10 km - as operational model) voluntary used.

Resolved topography is fully taken into account by the dynamic kernel of the approach independently of the ABL column model (that most of the time does not see it). As an illustration of a typical study of a flow over orography that includes ABL impacts, Bergström and Juuso (2006) evaluated the channelling effect of a valley based on the MIUU hydrostatic mesoscale model and the level 2.5 MY ABL column model (Mellor and Yamada, 1982). Phenomena such as pressure-driven and forced channelling are studied based on ideal valleys of various

form factor (ranging from 4 km to 32 km width) considering several thermal stratification and surface properties. Most of the conclusions of this study regard the impact on the valley wind of the various geostrophic wind and the valley configuration. However, it is also found that ABL flow regime plays a key role: stable stratification increases valley wind, while convective situations decrease the valley wind because of downward momentum transport. The various features found numerically are qualitatively confirmed based on full scale data (Bergström and Juuso, 2006). Those finding are also corroborated by Pinard *et al.* (2005) who observed the exact same valley wind behaviour based on experimental data (but which, in their case, is not reproduced by the model due to a too coarse resolution).

In his intercomparison of 10 ABL column models, Hurley (1997) (see previous sections) also evaluated a diurnally cycling full ABL over a 2D Agnesi hill of 6 km half-width by 600 m high. The author concludes the following: (1) the general patterns of wind velocity are all similar and all models capture the temperature increase in the lee side of the hill due the mixing caused by the hill; (2) TKE level is quite different among models; (3) the ten ABL models are found to generally produce reasonable predictions of the mean variables, however, more complex turbulent closures such as the various $k-\varepsilon$ tested better predict turbulent fields.

At a finer scale, Castelli *et al.* (2001) evaluated turbulent closures from the RAMS mesoscale model against RUSVAL experimental wind tunnel data (*i.e.* neutral flow over a valley, see Sec. 1.1.3.2.1) for which a length scaling factor of 600 is used (valley depth and width become 70 m and 560 m which make the flow lying between microscales and mesoscales). Closures evaluated are the level 2.5 MY, the $k-\varepsilon$ and the $k-l$ model. It is noteworthy that the former is a column model while the two latter are 3D classical RANS approaches. MY closure is found to be clearly unsuited mostly because of the lack of horizontal turbulent diffusion. The other general conclusion is that the use of an additional ε equation does not clearly improves the results with respect to the $k-l$ model.

Castelli *et al.* (2005) achieved a similar comparison with wind tunnel data but for a 3D Gaussian hill of 100 m characteristic size (after scaling is applied). Deardorff (1980) SGS model

is evaluated (in addition to the models from Castelli *et al.* (2001)), and the MY model column model is enhanced thanks to an horizontal diffusion parametrization inspired from the Smagorinsky SGS model. Results confirm the findings of Castelli *et al.* (2001): Deardorff, $k-l$ model and $k-\varepsilon$ models lead to similar results while the MY model, even tweaked, is clearly not suited for such a problem. All closures give similar velocity maximum uphill, but the $k-l$ results are slightly better to those obtained with both $k-\varepsilon$ and Deardorff for the downhill region. The $k-\varepsilon$ tends to transport the TKE upward more than the other closures. Interestingly, those remarks are in good agreement with the findings of Sec. 1.1.3.2.

Today a growing number of mesoscale models consider the fully 3D turbulence (Pielke and Nicholls, 1997; Cuxart *et al.*, 2000; Klemp and Skamarock, 2004; Chow *et al.*, 2005; Castelli *et al.*, 2005). Furthermore, in the most advanced mesoscale models, *i.e.* ARPS, Meso-NH, RAMS or WRF, several turbulent closures are implemented to allow the use of the model from very large scales, where only vertical turbulent processes are considered and most of the heterogeneities are parametrized, to microscales, where both vertical and horizontal processes are taken into account (Klemp and Skamarock, 2004; Skamarock *et al.*, 2008). The ultimate goal is to seamlessly reproduce flow from mesoscales to microscales by tackling the so-called "Terra Incognita" (Wyngaard, 2004). In that sense, closures where mixing coefficients are not isotropic were recently implemented in WRF (Skamarock *et al.*, 2008) as suggested by Wyngaard (2004). Similarly, the three level nesting approach presented by Eidsvik *et al.* (2004) interestingly addressed the challenge of flow modelling from the large scales to the microscales (cf. Sec. 1.1.3.2.2 for more details). Those later approaches are very promising with regards to the needs of wind energy applications (Shaw *et al.*, 2009).

1.2.4 Summary of environmental modelling of ABL

This section illustrated various aspect of environmental modelling approaches with a special attention dedicated to the full ABL momentum and heat processes. Large scale and mesoscale model are the heart of environmental models which are capable to simulate atmospheric flows from the global to the local scales and predict weather up to a week ahead or more. Three

dimensional time evolving mass, energy and momentum conservation equations are solved in mesoscale model, *i.e.* the dynamic kernel, and the others relevant processes (that can not be simulated) such as turbulent diffusion and all ABL processes are modelled relying, most of the time, on the boundary layer approximation. However, a much broader range of processes have to be considered in comparison to CWE applications.

Concerning mesoscale models dynamic kernel, hydrostatic approaches are clearly unadapted to problems where $\Delta x < 10$ km, and most of the modern environmental models rely on the compressible non-hydrostatic Navier-Stokes equations. Such approaches however require an efficient treatment of the time variation and advection terms of the equations of motion which has repercussions on the whole model architecture (numerical methods and implementation). Terrain following non-orthogonal coordinates are generally used. However, they are known to cause numerical difficulties over steep terrain which situation is more likely to happen at high resolutions due to the less smoothed representation of the surface.

Concerning turbulence modelling in mesoscale models, given the typical horizontal resolution and grid anisotropy, most of the approaches only consider the vertical turbulent mixing. Thus, mesoscale model largely rely on ABL column models. Simple and first order closures are disappearing to the benefit of one-and-a-half order approaches, *i.e.* $k-l$ model. While simple and computationally efficient, the latter leads to promising prediction of both the mean variables and the turbulent quantities in most cases and for moderately stable to unstable homogeneous ABL. Higher order models, such as $k-\varepsilon$, $k-\theta^2$ or even full second and third order closures, also exist but there are generally used for research purposes only. Concerning $k-\varepsilon$ models, the parametrization of ABL thermal stratification is more tricky than in $k-l$ models. However, they are proven to slightly better predict orographic flows notably with regards to turbulent quantities. Models with an order higher than two are rarely used in modern mesoscale model. They were at first very useful to better understand phenomena and enhance parametrization of lower order closures. However, they are too computationally expensive in comparison to the enhancement they bring and LES models seems far more appealing.

The boundary layer approximation, *i.e.* ABL column model, is clearly proven to be invalid for $\Delta x < 1$ km. Indeed, within the mesoscale-microscale gap, *i.e.* scales from 100 m to 1 km, 3D turbulent phenomena become non-negligible (preventing the use of classical mesoscale model which rely in ABL column model), but mesoscale processes are still important (preventing the use of classical microscale model). This range of scales is also know as "Terra Incognita" (Wyngaard, 2004) as it has historically drawn less attention: some processes and interactions are not yet fully understood partly due to a lack of dedicated experimental and numerical studies (Teixeira *et al.*, 2008; Shaw *et al.*, 2009).

In conclusion, mesoscale approaches offer very promising features allowing to take into account the environment in which wind turbine operate. They are crucial tools for both forecasting and wind resource assessment. However, modern wind turbine have a diameter larger than 100 m and wind farm extent can reach 10 km or more. Thus, while large wind farms have an impact on the mesoscale flow, interactions of wind turbines with the large scale flow and with each other are in the mesoscale-microscale gap, slightly beyond classical mesoscale models abilities. Mesoscale models that can also operate correctly at microscale are thus of prime interest for wind energy applications.

1.3 Large eddy simulation of the ABL

Large Eddy Simulation (LES) is a modelling technique aiming to resolve the anisotropic and energy containing large turbulent structures, while modelling the dissipative isotropic homogeneous small eddies based on a Subgrid Scale (SGS) model. At some point, LES, which is part of CFD approaches, is closer to mesoscale modelling (than RANS) in the sense they both fully resolve part of the unsteady flow processes. Lilly (1962) and Smagorinsky (1963) were the first to propose and implement an approach based on a subgrid scale (SGS) model. At first, it was applied to large scale environmental flows[5], and while very limited by the computational power available at that time, they set the ground for more evolved LES studies. Currently, the Smagorinsky-Lilly SGS model is still considered and commonly used as reference. However,

[5] In fact, as underlined by Lesieur *et al.* (2005), it is hard to dissociate LES approaches and meteorology applications since the first LES were applied to atmospheric flow.

the last decade has seen considerable developments as well as an exponential growth in the use of LES models (Senocak *et al.*, 2007; Piomelli, 2008; Chow and Street, 2009; Bechmann and Sørensen, 2010), which is also correlated with the increase of computational power. The reader is referred to Pope (2000), Lesieur *et al.* (2005) and Sagaut (2006) books that present an up-to-date, thorough and comprehensive review of LES.

In the context of the full ABL, *i.e.* from the earth surface to the free atmosphere, LES models have to deal with a stratified high Reynolds number shear flow bounded by a no-slip rough surface and a flexible membrane (the inversion layer) separating two distinct regions of the flow, *i.e.* the ABL and the free atmosphere. The surface can present some complex cover and orographic features. In addition, others meteorological processes have to be taken into account when environmental problems are addressed as illustrated in the previous subsection. Considering the abilities of environmental models and the fact that they have the best possible features to take into account the environment in which wind turbines operate, LES-capable mesoscale models are of prime interest.

In this study, considering the needs of wind energy applications and the properties of the ABL, LES approaches that address the fully rough high Reynolds number flows are introduced and reviewed. Firstly, more details are given on the ABL from the LES point of view. Then, the LES of the ABL over an homogeneous surface is discussed by first reviewing the neutrally stratified and adiabatic ABL. The main classical and advanced SGS models are introduced in this section. Then, the inclusion of thermal effects is discussed. Finally, the LES modelling of the ABL over an heterogeneous surface is briefly introduced along with the associated challenges and abilities of LES models.

1.3.1 ABL in views of LES applications

LES aims to reproduce quantitatively and resolve the whole range of eddies smaller than the domain size and bigger than a spatial filter which is located in the inertial subrange scales (*i.e.* scales at which turbulence is considered homogeneous and isotropic and where the velocity power spectra follows a $-5/3$ slope, see Appendix II). Eddies smaller than the filter are

modelled while bigger ones are simulated. The filter often relies on the mesh explaining why subfilter scale (SFS) models are usually called subgrid scale (SGS) models. In such a case, the filtering is said to be implicit. However, some more advanced SFS models are based on an explicit filtering of NS equations. The latter approaches are more computationally expensive, since they must have several meshes within the filter, and more complex, as new terms appear in the expression of the SFS stresses (see Leonard decomposition Eq. (A II-17)). However, they are more flexible and powerful (Lesieur *et al.*, 2005). Both the solver of the spatially filtered unsteady NS equations and the SFS model are crucial for a successful LES of the ABL.

The ABL over an homogeneous surface modelled by means of LES is unsteady and no more horizontally homogeneous. This is thus clearly in opposition with RANS and ABL column models representation of ABL. Indeed, horizontal homogeneity as well as steady state are only reached statistically in LES. It is sometimes referred to a permanent state (statistically steady) or quasi-steady state. The unsteady nature of LES has great implication on how the models are operated and on the interpretation of the results. Inlet, outlet, lateral and top boundary conditions, while permitting to drive the flow, have to allow eddies to enter and escape the domain without spuriously impacting the solution. At the inlet, not only the first and the second order moments (resolved and subgrid), but also the spectral signature of the flow needs to be correctly reproduced. These latter facts further illustrate the increased complexity and the less straightforward application of LES in comparison to RANS.

Similarly concerning the model results, while RANS directly provides the averaged final solution, LES always requires a post-processing (based on time and space averages) to obtain statistically steady quantities. Furthermore, a sufficiently long time interval is required to obtain stable statistics. LES data is thus somewhat closer to real data and a complete spectral picture of resolved turbulence can be studied as opposed to previously presented approaches.

Depending on the LES model goals, the representation of the ABL may differ which influences the whole model configuration. LES dedicated to CWE generally only consider the neutral surface layer, and the Coriolis effect (and sometimes roughness) are neglected. Representation of

the ABL is thus partly the same as for the CWE RANS approaches and only the unsteady momentum and mass conservation are considered. At the opposite, LES applied to environmental modelling are naturally closer to mesoscale models and integrate several of the specifications of the latter with regards to the ABL and the earth surface, *i.e.* full ABL up to free atmosphere with the Coriolis effect, temperature, humidity, etc. Recently, SGS models have been implemented in mesoscale models which was shown to successfully reproduce ABL flows (Cuxart *et al.*, 2000; Chow *et al.*, 2005; Drobinski *et al.*, 2007).

LES applied to both CWE and environmental modelling have to face the challenge of reproducing turbulent atmospheric motion down to a spatial scale and bounded by a no-slip rigid and rough wall. Thus, while their background philosophy remains the same, LES can be used for a wide range of applications. However, LES of the ABL is still a research tool, computationally expensive, and not trivial to use, notably in real conditions as it is illustrated all along the following sections. Nonetheless, LES is becoming more and more popular due to its abilities.

As a summary, LES of the ABL generally share the following representation of the ABL:

- 3D surface layer or full ABL;
- unsteady;
- neutral or thermally stratified;
- with and without Coriolis effect.
- incompressible high Reynolds number flows.

Hence, unless specified, the term ABL will refer to the 3D time evolving ABL in this section.

1.3.2 LES of the homogeneous surface ABL

The simplest yet necessary step for a successful application of the LES of the ABL is to correctly reproduce the ABL over an homogeneous surface. It is thus somewhat similar to the philosophy of RANS and column models. This ideal representation of the ABL is relevant and useful for LES approaches going from the surface layer dedicated CWE studies to the stratified full ABL reproduced by environmental models. It is a practical way of evaluating the abili-

ties of both the solver of conservation equations and the SGS model (Porté-Agel *et al.*, 2000; Chow *et al.*, 2005). Indeed, for such a case the problem and model inputs are kept as simple as possible and cases are highly reproducible. In addition, it allows to study in detail the most fundamental ABL processes from the surface to the free atmosphere. Until recently, the use of LES by the meteorological modelling community was mainly focused on stratified full ABL for which surface is homogeneous and lateral boundary condition are periodic. Among other things, this allowed to better understand processes taking place in the middle and the top of the ABL (Deardorff, 1972; Moeng and Sullivan, 1994).

While adiabatic ABL, *i.e.* considering only momentum and mass conservation, appears to be simpler with regards to physical representation, they are more demanding than convective ABL notably close to the surface. The convective processes that drive the flow exhibit larger structures which allows resolving a bigger part of the flow with the same grid (Sullivan *et al.*, 1994). At the opposite, stable ABL show smaller structure than neutral ABL. There are thus more challenging than both unstable and neutral ABL (Beare *et al.*, 2006).

In the following section, the LES of the homogeneous surface ABL is reviewed. At first, aspects common to all homogeneous approaches are discussed such as boundary and initial conditions of the models. Then, LES modelling of neutral ABL is reviewed by considering approaches applied to both the surface layer only and to the full ABL. In parallel to the latter subsections, classical and advanced SGS models along with their various declinations and limitations are thoroughly reviewed. In a last part, the inclusion of thermal effects in the LES models is discussed by focusing on approaches dealing with the full ABL and that consider the internal energy conservation. It is noteworthy that all along this section a special attention will be given to the treatment of the near-surface region since it appears to be one of the most important limitations of LES applied to the ABL.

1.3.2.1 Common aspects

LES model applied to the homogeneous surface ABL have some specifications in common, whether the adiabatic surface layer or the stratified full ABL are considered. Methods for

driving the flow, surface, lateral and top boundary boundary conditions as well as initialization approaches roughly face the same challenges.

1.3.2.1.1 The challenge of the earth surface

The earth surface similarly as a wall restricts the size and behaviour of eddies and it affects small eddies isotropy. It can be said that it represents the Achilles' heel of LES of the ABL as discussed all along this section.

1.3.2.1.1.1 LES and no-slip rigid wall LES of a flow bounded by a no-slip rigid wall can be done following two main approaches as discussed by Pope (2000). Near wall resolved LES (LES-NWR) resolve at least 80 % of the turbulent energy everywhere, while near wall modelling LES (LES-NWM) resolve 80 % of turbulent energy only remote from the wall. In other words, the former resolve the flow down to the viscous sublayer based on the more universal true no-slip wall condition, while the latter take into account the surface through wall functions with a first cell being generally located in the log-law region of the boundary layer.

In addition, ABL is a high Reynolds number flow, and the higher the Reynolds number is, the thinner is the viscous sublayer. However, as opposed to RANS, highly stretched grid cells are not well suited for LES as they may cause numerical instabilities and spuriously affect the filter width (Andren *et al.*, 1994; Murakami, 1998). As a result, LES-NWR of the ABL requires very fine nearly isotropic meshes increasing the computational cost to an unrealistic level as illustrated by Piomelli (2008). On top of that, ABL surface is most of the time fully aerodynamically rough which further complicates the modelling within the roughness sublayer, as discussed in Sec. 1.1.3.1 (as opposed to the use of generally accepted and relatively simple wall function based on the similarity theory). As a result, LES based on a no-slip surface boundary conditions, *i.e.* LES-NWR, are far from being trivial to implement in the context of ABL flows. They are thus less appealing than the cheaper and simpler LES-NWM approaches for the reproduction of ABL flows. Those facts are enforced for methods addressing the full ABL due to mesh restrictions.

LES-NWR approaches are however commonly found in CWE where flow around non-rough bluff bodies is of concern. In those studies, the ABL is more often considered as a classical turbulent boundary layer (a turbulent boundary layer over a flat plate), as illustrated in the early review of Murakami (1998). In fact, the concept of LES slightly differs between CWE and environmental modelling community. Because of the size of the flow features to be resolved, the filter size differs. The grid cell size of LES based environmental modelling approaches is of the order of 20 m which is roughly the characteristic size of geometries studied in CWE. As a result, the latter LES approaches require a much finer grid but typical domain size is restrained compared to environmental models. No-slip surface boundary conditions are thus more realistic in CWE applications. Despite those differences and the fact that CWE generally only consider the neutral ABL, the results from those studies are of prime interests for environmental modelling applications, notably with regards to the SGS model abilities since the same or very similar approaches are used in every domain.

LES-NWM models rely on wall functions to provide wall boundary condition. However, while the eddy size decrease as the wall is approached, the LES-NWM resolution stays generally unchanged. As results, the flow is not sufficiently resolved in the layer close to the wall, and at least two assumptions, on which SGS models are generally based, are violated: the isotropy of the turbulence and the filter located in the inertial subrange (Mason and Thomson, 1992). Thus, even with correct wall functions, LES-NWM are biased close to the ground if no special care is taken to properly address those shortcomings and to adapt the SGS model formulation consistently. Such a limitation is easily diagnosed in ABL flows by comparing the profiles of non-dimensional velocity vertical shear close to the surface, Φ_M, from LES results and from the similarity theory. For neutral ABL, the latter should be constant and equals to one, while typical LES results exhibit a clear overshoot of Φ_M (Andren *et al.*, 1994). Independently of the SGS model, this error is a function of both the flow and surface properties (Stoll and Porté-Agel, 2006) and the numerical parameters such as the mesh resolution and cell aspect ratio close to the surface (Brasseur and Wei, 2010).

1.3.2.1.1.2 LES and surface layer similarity theory Wall functions used by LES-NWM of the ABL are commonly based on the Monin-Obukhov similarity theory, as illustrated in most of the paper introduced in this sections. Canopy model, which represent the surface by imposing volumetric forces on the few meshes close to the ground, are also sometime used (Brown *et al.*, 2001). They can be seen as an extension of the MO similarity for porous domains. This approach is known to properly take into account tall vegetation cover such as forest which is of interest for wind energy applications. In the LES context, it can also be used as a numerical technique to provide the model with a more advanced surface boundary condition (in three dimensions instead of two) (Chow *et al.*, 2005; Senocak *et al.*, 2007). However, the surface layer similarity theory (and canopy models) was developed based on ensemble averaged surface layer profiles: MO similarity describes the time or space averaged surface layer over an homogeneous surface. As a result, the use of such a theory with local instantaneous values of the velocity and temperature to provide the model with the surface boundary stress may be questionable, and as underlined by Porté-Agel *et al.* (2000); Stoll and Porté-Agel (2006), no universal agreement exist concerning wall-stress models.

The simplest and very common approach to provide LES-NWM of the ABL with a surface boundary condition is to apply the MO similarity theory locally (Mason and Thomson, 1987; Stoll and Porté-Agel, 2006; Sagaut, 2006; Drobinski *et al.*, 2007; Brasseur and Wei, 2010). In such a case, the wall shear stress is expressed as $\tau_{i3} = \tau_w \overline{u}_i / \|\overline{\boldsymbol{u}}\|$ where $\overline{u}_i$ is the horizontal component of the instantaneous velocity vector $\overline{\boldsymbol{u}}$, and the local total surface shear stress τ_w, *i.e.* the local friction velocity, is computed relying only on local instantaneous quantities.

This approach is popular due to it simplicity and because it can be used straightforwardly with an heterogeneous surface. However, it does not guarantee that the average surface stress equals the actual mean surface stress (Stoll and Porté-Agel, 2006). Indeed, it has the disadvantage of leading to a larger average stress for a given near-wall velocity (Silva Lopes *et al.*, 2007). Stoll and Porté-Agel (2006) further state that the underlying assumptions are only valid if meshes close to the surface are heavily deformed (*i.e.* grid cell aspect ratio $\Delta x / \Delta z \gg 1$).

To avoid such an inconsistency, a very popular approach is to compute total surface shear stress base on the ensemble averaged flow properties, and then used that value along the local flow properties to compute the local shear stress at the wall as proposed by Schumann (1975). In such a case, we have $\tau_{i3} = \langle \tau_w \rangle \overline{u}_i / U_{MO}$ where $\langle \tau_w \rangle = -u_*^2$ is the mean total surface shear stress obtained from similarity theory and U_{MO} is the velocity also computed based on the similarity theory. For an homogeneous surface case, the horizontally averaged velocity magnitude $\langle \| \overline{\boldsymbol{u}} \| \rangle$ is generally used to compute $\langle \tau_w \rangle$. Thus, only one value of the friction velocity u_* is computed, and U_{MO} is obtained based on the latter. Thus, this approach requires that the cases reproduced have at least one homogeneous direction (Schumann, 1975; Porté-Agel *et al.*, 2000) which is somewhat limiting. However, a time average can also be used so that this approach is valid for non-homogeneous cases. In that case, a relaxation can be used for the mean velocity and mean wall shear stress to be able to evolve (Silva Lopes *et al.*, 2007).

Other approaches, such as the one introduced by Moeng (1984), further considering the ensemble averaged surface shear stress and it local fluctuation also exist. They are however more complex and feature similar constraints as the Schumann (1975) approach. Furthermore, as stated by Sullivan *et al.* (1994), the various approaches to define the surface boundary condition have a very limited impact on the results.

In a recent study, Stoll and Porté-Agel (2006) evaluated various approaches to represent the stress at the surface boundary for LES models applied to the ABL. They compared four models of the surface shear stress. The first one is based on the horizontal averaged approach of Schumann (1975) introduced above (called SG). The second model features the same approach but uses a velocity of a fluid element displaced in the direction of the flow (by a given length which is a function of the flow structures orientation) when scaling the magnitude to get the stress components (called shifted SG). This approach intent to better take into account velocity fluctuations close to the ground, and thus fluctuation in the surface stress for low Reynolds number flow (Stoll and Porté-Agel, 2006). The third stress model is based on the local approach illustrated above (called local SG)[6]. Finally, the last approach is based on experimentally de-

[6] In Stoll and Porté-Agel (2006) paper this approach is wrongly refers to Moeng (1984) surface model.

veloped/validated model which relies on the streamwise velocity as presented by Marusic *et al.* (2001) (called MKP). This new surface stress model was designed so that, for any altitude in the logarithmic region, the modelled shear stress spectrum (obtained by applying the model on experimental data in the study) would properly reproduce the measured surface shear stress spectrum. Essentially, the model assumes that fluctuations of the wall shear stress are proportional to the near-wall tangential velocity fluctuations.

Stoll and Porté-Agel (2006) found that non-dimensional velocity gradient ϕ_M and variance $\overline{u'^2}$ at the first few meshes above the surface were influenced by roughness length when using the classic surface shear stress models, *i.e.* SG, shifted SG and local SG. A larger roughness length resulted in a stronger damping of velocity fluctuations near the surface. This had the consequence to lower the level of resolved velocity variances and energy spectra, and also to enlarge the values of the non-dimensional velocity gradient ϕ_M. The impact on the velocity spectra close to the surface is particularly notable with the local SG model using a large roughness length ($z_0 > 0.1$ m). All those problems were less significant for cases with a lower surface roughness. However, experimental results suggested that the roughness should not have any influence on those two quantities, *i.e.* ϕ_M and $\overline{u'^2}$. Only the MKP model was not influenced by roughness and managed to correctly perform, notably with regards to velocity spectra.

Stoll and Porté-Agel (2006) study is based on an advanced dynamical Smagorinsky SGS model presented in the next section. They found that the result enhancements in the surface region thanks to the use of this advanced SGS model were far more significant than only using a proper surface shear stress model in combination with a simple SGS model. However, the error introduced in velocity vertical gradient close to the surface propagates to the full velocity profile introducing a roughness dependent error(except with MKP) which would better be avoided. They concluded that, considering the differences of the results, surface stress model have a limited impact: neither the SG, the shifted SG nor the local SG are better, and only the MKP shown few enhancements.

1.3.2.1.2 Lateral and top boundary conditions

Lateral (*i.e.* inlet, outlet and lateral sides) and top boundary conditions have to be permeable to eddies of all size so that they can enter and exit the computational domain freely. Concerning lateral boundary conditions, several techniques are possible but in the context of a homogeneous ABL the most straightforward approach is to use periodical lateral boundary conditions, *i.e.* what is going out on one side of the domain comes in on the opposite side of the domain. Indeed, the periodic lateral boundary conditions heavily simplify the treatment since no special care has to be taken to reproduce all the range of eddies. The turbulence and thus the boundary layer are able to develop by themselves, mitigating initial condition importance. However, the flow need to be initially perturbed to trigger the various instabilities, and an appropriate spin-up period is require to reach a fully developed turbulent flow. Physically realistic initial conditions may only accelerate the development of the turbulent steady state, leaving the end result unchanged with respect to results based on more simplistic initialization approaches.

When only the surface layer is considered, Coriolis effect is negligible and the mean flow orientation is the same across the whole domain. As a result, inlet, outlet and sides boundary conditions can be clearly identified. This type of flow is sometimes referred to as channel flow. When simulating the full ABL, the Coriolis effect is included, and the mean flow is turning with height. Therefore, lateral boundary conditions, that see a flow parallel to them above ABL, are inlet and outlet boundary condition below the inversion. Periodic boundary conditions are thus even more convenient in such a case.

Periodic lateral boundary conditions also facilitate the use of Fourier transforms since the latter generally assume an infinite domain[7]. However, while the domain can be seen as infinitely periodic, its real elementary size needs to be sufficiently large in order to allow the excitation of energy producing eddies. Above a critical domain size, results should become independent of the horizontal domain size. However, using periodic boundary condition, the whole solution is prone to oscillate at the inertial frequency around an equilibrium profile since the flow velocity

[7] *c.f.* Sagaut (2006) for the development of NS equations in the Fourier space and a discussion on the Fourier transformation in finite domains.

is not prescribed at the lateral boundaries of the domain (as opposed to when inlet boundary condition is prescribed). Furthermore, cumulative errors such as a non-conservation of the mass can make the model diverge.

A Galilean transformation, *i.e.* a grid moving with the flow, is sometimes used in conjunction with the periodic boundary conditions in order to reduce discretization error and lower the stability limit for the time step (Andren *et al.*, 1994).

The nesting approach, as discussed in Sec. 1.2.2.4 can also be used for the lateral and sometimes the top boundary conditions (Sagaut, 2006). The same philosophy as for the mesoscale models can be followed but at finer scale (Drobinski *et al.*, 2007). Seeing the limitations of mesoscale models at fine scale, the use of a LES model as a last level of nesting is very promising. Nesting approach is useful to provide boundary condition for heterogeneous surface cases. In homogeneous surface cases, this approach is generally used to address meteorological problems where the large scale flow is evolving, *i.e.* advection of cold air, passing front, diurnal cycle influenced mesoscale phenomena (Drobinski *et al.*, 2007). The nesting approach can also be used in a two step approach. The mesh is unchanged but the first step is periodic while the second one is nested.

Finally, damping regions sometime called sponges (Benoit *et al.*, 1997; Ding *et al.*, 2001a; Lesieur *et al.*, 2005), are often implemented at the top and lateral boundaries of the domain when periodicity is not used. Such an approach is required for eddies (and gravity waves and sound waves, that can arise when the temperature is considered) not to be reflected in the computational domain when reaching the boundaries. Such phenomena have also to be properly addressed by the boundary conditions. These phenomena can pollute and thus bias the solution. Those damping regions are a transition between the domain boundary and the simulated flow inside the domain (Laprise *et al.*, 1997; Benoit *et al.*, 1997). Sometimes, the sponge region can be based on simple weighting functions (such as $\cos^2$ function). However, more evolved methods are often required, such as the addition of a numerical diffusion in order to smooth the flow fields when getting closer to the boundaries (Shuman, 1957). Several

advanced approaches also exist, such as the radiative boundary condition that trigger and damp explicitly only the waves and eddies that reaches the boundary of the domain (Gray *et al.*, 2001; Skamarock *et al.*, 2008).

1.3.2.1.3 Driving the flow

In LES, driving an ABL flow is most of the time achieved by means of a pressure gradient associated with a stress free top boundary condition (all LES studies discussed here). Two main reasons explain this choice for the top boundary. On the one hand, imposing a vertical shear requires the latter to be a priori known which is only the case in the surface layer (where the pressure gradient is negligible compared to the other terms in the equations) thanks to the MO similarity theory. At the opposite, the shear in the above part of the ABL (below the free atmosphere, and where the pressure gradient become non-negligible) is a priori unknown and the imposition of pressure gradient is more physically meaningful. [8]. On the other hand, imposing a vertical velocity shear or a moving layer at the top of the domain is less straightforward than when relying on CWE RANS approaches since eddies reaching the top boundary need to be either damped or able to exit smoothly without side effects.

When the Coriolis effect is neglected, *i.e.* channel flow, the pressure gradient is parallel to the velocity component. The mean flow has the same direction throughout the whole domain and across the vertical profile. LES models dedicated to the surface layer and CWE LES models often rely on this approach. They reproduce a relatively shallow partial ABL. The pressure gradient corresponding to a desired velocity can be computed such as presented by Porté-Agel *et al.* (2000). Similarity theory can be used to obtain an a priori estimate of the stress.

When the Coriolis effect is taken into account, the pressure gradient is roughly perpendicular to the wind above the ABL, *i.e.* in the free atmosphere. This is called the geostrophic balance and it is widely considered to be a good approximation of the free atmosphere horizontal

[8] Thus, this type of approach to drive the flow is very common for CWE RANS approaches as generally only the surface layer is considered (Richards and Hoxey, 1993; Hargreaves and Wright, 2007). However, while this is strictly valid only in the surface layer, computational domain of CWE RANS studies often extended well above its effective height for numerical reasons but the flow above the surface layer should not be considered as fully realistic.

equilibrium. This large scale pressure gradient in presence of the Coriolis effect is commonly referred to as the geostrophic wind. In such a configuration, the computational domain requires to be higher than the ABL and the top of the domain is thus at least a couple of thousands meters high. As the earth surface is approached, turbulent stresses increase, and momentum and thus the Coriolis effect decreases while the horizontal large scale pressure gradient stays unchanged. As a result, the wind turns with height as a function of the equilibrium between these three forces in the NS equation. This is the so-called Ekman spiral. Wind turns to the left (right) in the northern (southern) hemisphere. In that configuration, driving the flow by means of a pressure gradient is very practical.

In the case of fully periodic lateral boundary conditions, a proper treatment of the pressure variable is required since, at the same time, a mean gradient at the scale of the domain is needed, and the resolved pressure field also has to be periodic. The pressure gradient driving the flow is thus generally subtracted from the instantaneous pressure field, and imposed though new external forcing.

1.3.2.1.4 Initialization

An appropriate initialization is required to allow the "ignition" of turbulence in LES. Traditionally, perturbations are applied to the velocity components but temperature can also be targeted (Andren *et al.*, 1994; Moeng and Sullivan, 1994; Brown *et al.*, 2000). A wide range of methods can be used to generate perturbations going from totally random to spectrally organized and satisfying mass conservation. Some researcher also force an heterogeneous surface for a given number of iterations (Mason and Thomson, 1987). However, a spin-up period after the initialization is generally needed regardless of the initialization method used, so that organized turbulent eddies can develop with properties independent of the initial perturbations.

If initial fields do not satisfy mass conservation, incompressible/anelastic approaches generally require larger initial perturbations (Andren *et al.*, 1994). Too small perturbations can damp and the flow can revert to laminar. When compressible approaches are used, perturbations not satisfying the mass conservation have a direct impact on the temperature. The mean temperature

profile can then be affected depending of the set of random numbers used, notably close to the surface (see Sec. 3.4.2). If the approach takes into account internal energy, a heated surface in conjunction with small perturbations appears to be suited for both incompressible and compressible approaches since, on the one hand, it allows perturbations to propagate and organize due to the strong effect of convection, while on the other hand, the same phenomena evacuate spurious temperature perturbations (Moeng and Sullivan, 1994).

To increase the level of physical representativeness of initialization, velocity components perturbations can be scaled with a priori or experimental profile of velocity variances or TKE (Andren *et al.*, 1994). Mass conservation can also be a criterion of the initialization. This latter constraint, could be achieved by basing initialization on a kinematic decomposition of flow field in a rotational and potential part, such as presented in Panton (1996, Chap. 17).

1.3.2.2 SGS models for the adiabatic ABL

While being the simplest representation, surface homogeneous neutrally stratified/adiabatic ABL include challenging and fundamental features common to all ABL such as shear processes. The latter take more importance in neutral and stable ABL, where they are the unique source of mixing. As a result, modelling the neutral ABL allows validating some fundamental aspects of LES models of the thermally stratified ABL. It can be seen as a preliminary validation step of models that integrate a more complete representation of the ABL.

The simplest approach to reproduce neutral ABL flows based on LES is to consider an adiabatic ABL, or in other words, to only take into account momentum and mass conservation. In such a case the pure neutral ABL is modelled. As illustrated earlier, CWE approaches are generally based on such an assumption, and models are often dedicated only to the lower half of the ABL (Porté-Agel *et al.*, 2000). The channel flow approach is often followed. Some models also include the Coriolis effect intending to reproduce the idealized Ekman boundary layer (Andren *et al.*, 1994). Finally, models that also fully take into account internal energy or enthalpy conservation can also be used to reproduce neutral ABL. In that case, a neutral ABL capped by an inversion (Moeng and Sullivan, 1994) can be reproduced and temperature should not

have any effects in the neutral region. In any cases, the flow modelled presents similarity and non-dimensional quantities can be readily compared specially in the lower part of the ABL.

In this section, the neutral ABL serve to introduce the wide range of SGS models that have been applied to reproduce ABL flows based on LES. The abilities of those models to reproduce both quantities of interest and the ABL structure are discussed. All approaches discussed are based on periodic lateral boundary conditions, and the focus is on the LES-NWM approaches. A special attention is given to the flow processes close to the ground.

Classical SGS models are thus first reviewed along with their limitation and possible improvements. Then, advanced SGS models with and without explicit filtering are introduced in two separate sections and their abilities are discussed.

1.3.2.2.1 Classical SGS models

Classical SGS model refers to the several variants of the Smagorinsky-Lilly (Lilly, 1962; Smagorinsky, 1963) and TKE based (Lilly, 1966) SGS models. They are all based on the eddy viscosity hypothesis and subgrid mixing coefficients are assumed to be the product of a length scale l_t and a velocity scale u_t both representative of the turbulence, *i.e.* $\nu_t = l_t u_t$ as proposed by the Prandtl mixing length approximation. In the context of classical SGS models, the turbulent characteristic length scale is generally proportional to the 3D grid size, *i.e.* the implicit filter width Δ, such as $l_t = C_t \Delta$ where C_t is a closure constant (which is set once and for all but sometime a function of the height agl). The definition of the velocity scale differs depending of the approach. Based on these simple considerations, several SGS model were proposed that further take into account both the no-slip rough surface and the stratification to allow the reproduction of the full ABL with LES models. Classical SGS models are dissipative-only, meaning that the SGS mixing is considered to only dissipate energy of the resolved fields. They are simple and they have been heavily used to model a wide range of flow fields including the ABL (Murakami, 1998; Piomelli, 1999).

Here, the generic Smagorinsky SGS is first investigated. Then, the generic TKE based SGS models is discussed. Finally, limitations and possible enhancements of classical SGS models are reviewed. Note that, while this section is dedicated to the neutral homogeneous ABL, historically, most of the early LES studies that addressed the full ABL were focusing on the convective ABL as it is easier to reproduce based on LES and less computational demanding than neutral and stable ABL (discussed in further details in Sec. 1.3.2.3).

1.3.2.2.1.1 Smagorinsky SGS model The Smagorinsky-Lilly SGS model (Lilly, 1962; Smagorinsky, 1963) assume, as a first approximation, that production and dissipation of TKE are locally in equilibrium, *i.e.* equal at the subgrid level. The turbulent velocity scale is computed based on the product of filter width Δ and the modulus of the strain rate tensor $\|\boldsymbol{S}\| = (2S_{ij}S_{ij})^{1/2} = S$, such as $u_t = \Delta S$. This is thus a first order model and we have

$$\nu_t = (C_S\Delta)^2 S = \lambda^2 S, \tag{1.1}$$

$$\tau_{ij} - \frac{1}{3}\delta_{ij}\tau_{kk} = -2\nu_t S_{ij} = -2\lambda^2 S S_{ij}. \tag{1.2}$$

where traditionally, we have $C_t = C_S^2$ with C_S referred to as the Smagorinsky constant, the length scale $\lambda = C_S\Delta$, and the filter width $\Delta = (\Delta x \Delta y \Delta z)^{1/3}$.

Lilly (1966) obtained a theoretical value of the Smagorinsky constant C_S based on the Kolmogorov hypothesis (spectra model) for an isotropic homogeneous turbulence (see also Lesieur *et al.* (2005, p. 44)), giving

$$C_S \approx \frac{1}{\pi}\left(\frac{2}{3C_{Kol}}\right)^{3/4} \tag{1.3}$$

where C_{Kol} is the Kolmogorov constant found experimentally and generally taken equal to 1.5 in the ABL, thus giving $C_S = 0.17$. This value of the constant is theoretically well suited for the well resolved regions of the flow where the filter is properly located in the inertial subrange. It is the considered today as the traditional value of the Smagorinsky constant (Porté-Agel *et al.*, 2000; Lesieur *et al.*, 2005).

The first large eddy simulation of the ABL is certainly the one of Deardorff (1972) who, in a pioneering study based on Smagorinsky-Lilly SGS model with $C_S = 0.1$, reproduce a neutral and a convective ABL based on a 40^3 mesh. This computation took more than one year and a half which includes six month solely for the initialization. Deardorff (1972) noticed that the velocity profiles did not follow the similarity theory and he could not reproduce the logarithmic velocity profile. However, the full ABL (not the surface layer) was more of concern for this first promising study, that was focusing on the convective ABL.

The neutral static stability full ABL, *i.e.* the Ekman boundary layer, was for the first time thoroughly studied by Mason and Thomson (1987) using a Smagorinsky SGS model. The study was still exploratory and assessed the impact of resolution (a 40 by 40 horizontal domain was always used), the domain size (from 24 to 3 km) and the Smagorinsky constant (from 0.12 to 0.47). Mason and Thomson (1987) confirmed that the Ekman ABL height was roughly $0.35\, u_*/f$ and that for such a case, u_*/f is a proper scaling parameter for height. They also studied the ABL unsteady structure in order to better understand dynamic processes taking place at various heights. As for channel flow, elongated eddies in the direction of the wind were found close to the surface. In the middle of the ABL, *i.e.* far from the surface, correlations were more isotropic. First and second order moment profiles were satisfactorily compared with Deardorff (1972) and the Launder-Reece-Rodi (LRR) second order Reynolds stress model, but the limitations of the Deardorff (1972) approach were clearly underlined. Concerning the Smagorinsky constant, it was found that the larger the value of C_S is, the smoother are the flow fields. Furthermore, large values of C_S (higher than 0.2) led to a smooth well-resolved solution with small numerical errors (effective filter bigger than resolution and errors related to the discretization of the problem are small), while small values of C_S gave much choppy fields (*i.e.* with structures of the size of the mesh that can hardly be interpreted as physical as underlined by Mason (1994)) with larger numerical errors. This study allowed, in addition to the improvement brought to the Smagorinsky SGS model, to refine Ekman boundary layer understanding and requirements in terms of resolution, domain size and boundary conditions. It opened the path for more advanced approaches.

Later, in a thorough study, Mason and Brown (1999) discussed the behaviour of LES approaches based on the Smagorinsky SGS model with regards to some key parameters, such as the Smagorinsky constant C_S, the horizontal and vertical resolution, the model coefficient $C_S\Delta$, the size of the domain and the effects of the time period used to compute statistics. A convective ABL was used as test case (but similar conclusions are obtained for neutral ABL (Brown *et al.*, 2000)). Various aspects of the solution were regarded, and many velocity variance profiles and power spectra were presented by Mason and Brown (1999) for various configuration of the model, allowing for comparison. First, it is shown that for an equal value of the model coefficient, *i.e.* $(C_S\Delta)$, the model converge to similar results (turbulent quantities as well as velocity spectra) whatever the combination of C_S and Δ (in the limit of a sufficiently fine mesh and with an increasing numerical error when C_S is lower). As a consequence, it was considered by the authors that the SGS model as a whole determines the filter operation and not the numerical grid only. It follows that the Smagorinsky constant C_S is considered as a measure of the ratio of the filter scale to the numerical resolution. The authors further suggest that the SGS would better be called the subfilter scales, but as it is seen at the end of next subsection, subgrid and subfilter scales have a different meaning. However, as a recommendation, Mason and Brown (1999) show that a too small value of C_S (< 0.23 for Mason) lead to a build up of energy at the smallest scales, and the model could diverge. A large value of C_S is helpful (> 0.32 for Mason) to identify the role of numerical errors but the model efficiency is greatly affected since a higher resolution is needed to obtain the same results.

A year later, Brown *et al.* (2000) presented a continuation of Mason and Brown (1999) study, by further investigating the same parameters for a neutral boundary layer as well as studying the impact of using an advection scheme (monotone) known to be more diffusive. In neutral conditions, the same behaviour with regards to the numerical parameter earlier discussed was observed. Concerning advection scheme, the usual non-dissipative advection method was compared to a monotone advection scheme. This latter approach is generally used in cloud resolving LES models but conclusion can be further extended to numerical diffusion impact of all advection schemes. It was found that as long as the simulation is well resolved (either

numerically - high C_S - or with a filter being located well into the inertial subrange), LES results appear to be insensitive to the choice of advection scheme. In fact, SGS dissipation adapts to the numerical diffusion of the advection scheme and it gets lower in places where the flow is well resolved. Close to the surface however, some difficulties remained and the dissipative advection scheme had a non-negligible impact. And it was shown that it could affect the whole solution if both the mesh or C_S were not properly set.

While all the parameters discussed by Mason and Brown (1999) and Brown *et al.* (2000) had been already investigated in earlier studies, they clearly illustrate the behaviour of the model in the well resolved regions as a function of the main parameters of the SGS model.

The above discussion mostly regards the Smagorinsky SGS model parameters in the well resolved regions, *i.e.* the flow interior, and it was found that C_S values within 0.15 to 0.3 are commonly used for LES of ABL (Lilly, 1966; Mason, 1994; Mason and Brown, 1999; Porté-Agel *et al.*, 2000; Pope, 2000). Close to the surface where the shear dominates, *i.e.* in the surface layer, the value of C_S need to be adjusted to improve the results as discussed by Sagaut (2006, p. 124). Indeed, values around 0.1 are preferred for shear flows due to the fact that the field gradient is non-zero which contributes to the strain rate tensor modulus (Porté-Agel *et al.*, 2000). The constant thus has to be reduced in order to enforce the local equilibrium relation (Sagaut, 2006). As a result, for LES of the full ABL instead of a unique value, it would be better to use a vertical profile for the Smagorinsky constant. However, this profile is flow and case dependent and more advance approaches considering the local properties of the flow are needed to dynamically define this constant (*i.e.* dynamics Smagorinsky SGS models Sec. 1.3.2.2.3.2). However, Mason and Thomson (1987) proposed to defined the length scale λ of Smagorinsky SGS model as a function of the height agl (instead of being solely a function of the mesh) following an asymptotic behaviour such as

$$\lambda = \left[\frac{1}{(C_S \Delta)^n} + \frac{1}{(\kappa\,(z + z_0))^n} \right]^{-1/n} . \tag{1.4}$$

In the flow interior, *i.e.* in the mixed/Ekman layer far from the surface, the length scale λ equals $C_S\Delta$, and it is reduced as the surface approach in a Van Driest manner so that the effective Smagorinsky constant reach zero at the surface. The exponent n was set to 1 by Mason and Thomson (1987) but 2 was latter found to be better adapted (Mason and Thomson, 1992; Porté-Agel *et al.*, 2000). This approach prove to enhance near-surface results and it is still used today in the UKMO large eddy model (LEM) (Gray *et al.*, 2001), a descendant of Mason's model. However, as demonstrated by Mason and Thomson (1992), Porté-Agel *et al.* (2000) and Brasseur and Wei (2010), the sole adaptation of the length scale (which changes the effective constant of the model) is not sufficient to fully address the limitation of the classical SGS model in the near-surface region.

In this section, the Smagorinsky SGS model was illustrated through various studies (mostly from the UKMO LES research group). As it will be discussed all along the next sections, the Smagorinsky SGS model has been and is still heavily used today (Porté-Agel *et al.*, 2000; Chow *et al.*, 2005; Beare *et al.*, 2006; Piomelli, 2008; Churchfield *et al.*, 2010; Brasseur and Wei, 2010). It is very simple, yet well adapted as underlined by Murakami (1998). Therefore, it has been extensively studied and its limitations and behaviour are very well known. As a result, it commonly serves as a reference model in a huge amount of LES studies. It is also implemented in several Mesoscale models such as ARPS (Chow *et al.*, 2005), UM (Gray *et al.*, 2001), RAMS (Pielke and Nicholls, 1997). Thus, it represents an interesting first step in developing of a new LES model, allowing to evaluate the non-SGS parts of the model by comparison with the other studies using the Smagorinsky SGS model.

1.3.2.2.1.2 TKE based SGS model Instead of relying on the sole strain rate tensor, the eddy viscosity of the TKE based SGS model is expressed following the Prandtl-Kolmogorov proposal (Lilly, 1966), *i.e.* the turbulent velocity scale is set equal to the root of the TKE and

we have

$$\nu_t = C_k \lambda k^{1/2}, \tag{1.5}$$

$$\tau_{ij} - \frac{1}{3}\delta_{ij}\tau_{kk} = -2C_k \lambda k^{1/2}\, S_{ij}, \tag{1.6}$$

where the mixing length scale is equal to the filter width $\lambda = \Delta$ in neutral conditions and C_k is a closure constant. This SGS model was for the first time proposed by Lilly (1966) by simplifying a full second order model of the SGS stresses. Note that, a Van Driest damping of the mixing length scale λ is sometime used (similarly to the Smagorinsky SGS model). In that case, λ is reduced as a function of the height agl through a clipping with κz which is know to slightly enhance the near-surface results (Sullivan *et al.*, 1994; Ding *et al.*, 2001a).

Concerning the TKE, k, it is generally obtained thanks to its prognostic equation (also referred to as prognostic or conservation equation) that is to solve and which can be written

$$\left(\frac{\partial}{\partial t} + \overline{u}_j \frac{\partial}{\partial x_j}\right) k = \mathcal{P}_k - \varepsilon + \mathcal{D}_k \tag{1.7}$$

where the production $\mathcal{P}_k$, the dissipation ε, and the diffusion $\mathcal{D}_k$ terms can be expressed as (Deardorff, 1980; Moeng, 1984; Sullivan *et al.*, 1994; Kosović and Curry, 2000)

$$\mathcal{P}_k = -\tau_{ij} S_{ij}, \quad \varepsilon = \frac{C_\varepsilon}{\lambda_\varepsilon}\, k^{3/2}, \quad \mathcal{D}_k = \frac{\partial}{\partial x_i}\left(2\nu_t \frac{\partial k}{\partial x_i}\right), \tag{1.8}$$

where the dissipation length scale is generally taken equal to the filter width $\lambda_\varepsilon = \Delta$ in neutral conditions, and C_ε is a second closure constant. Note that the diffusion term include all the transport terms and the most generally accepted parametrization is presented here (Deardorff, 1980; Kosović and Curry, 2000).

This SGS model is relevant for relatively high Reynolds number flows where the TKE does not vanish. They are less suited to predict the laminar-turbulent transition. If TKE is initialized to zero, it may never change value and the model may stick to a laminar flow (Piomelli, 1999).

Considering turbulence in an equilibrium state, *i.e.* production and dissipation of TKE are equal, and using the Kolmogorov theory, Lilly (1966) obtained a value for the closure constants

$$C_\varepsilon = \pi \left(\frac{2}{3C_{Kol}} \right)^{3/2}, \tag{1.9}$$

and, based on the SGS TKE prognostic equation

$$C_k = C_\varepsilon^{1/3} C_S^{4/3} = \frac{1}{\pi} \left(\frac{2}{3C_{Kol}} \right)^{3/2} \tag{1.10}$$

giving $(C_k;\, C_\varepsilon) = (0.094;\, 0.93)$ with $C_{Kol} = 1.5$.

Based on Lilly (1966) derivation, Sommeria (1976) presented a SGS model with a diagnostic equation for all second order turbulent moments, and $(C_k;\, C_\varepsilon) = (0.0667;\, 0.7)$. The TKE was also diagnosed. The model was dedicated to the full ABL with the possible inclusion of boundary layer clouds. It was the first time a TKE based SGS model was applied to the ABL and the first time boundary layer clouds were modelled. While encouraging results were obtained, the author considered the study as preliminary since many aspects of the model were to clarify. Among other things, they suggested the need for a prognostic equation for TKE.

Deardorff (1980) presented a TKE based SGS model dedicated to the full ABL and similar to the one previously proposed by Lilly (1966) (with $(C_k;\, C_\varepsilon) = (0.1;\, 0.7)$ in neutral conditions) in which the prognostic equation of SGS TKE Eq. (1.7) was solved. One year later, Redelsperger and Sommeria (1981) enhanced the SGS model of Sommeria (1976) also adding such an equation. The inclusion of an prognostic equation for TKE, in addition to provide a value of the TKE itself, permitted to better take into account the history of the flow, and to include non-local aspects of turbulence while keeping the model relatively simple. By doing so, the TKE can be seen as one of the main variables of the model as proposed by Redelsperger and Sommeria (1981). With such a model, the SGS turbulence is not assumed in equilibrium (production and dissipation of TKE not equal anymore), and TKE can be transported thanks to its advection. As a result, this SGS model also appears to be more skilled than the Smagorinsky

SGS model for ABL over a complex surface but no significant improvement are to be expected for it in homogeneous cases (Andren *et al.*, 1994). It was found by Deardorff (1980) to be the optimum between first order Smagorinsky and full second order models. However, as opposed to RANS approaches where notable improvement are observed when going from a first order model (zero equation) to a one-and-a-half-order model (one equation) and to a second order (two equations), the enhancement is not that clear in LES. Indeed, on the one hand, since only a small part of the turbulence is modelled in LES compared to RANS (where everything is modelled), the impact of the details of the SGS model on the results is notably reduced (Andren *et al.*, 1994). On the other hand, the imbalance between production and dissipation of subgrid TKE is much smaller than in RANS. As a result, some authors considers that the increase in complexity and computational cost caused by the additional equation to be solved is worth only if the information on the TKE is required by some other parametrization schemes (apart from eddy viscosity) (Lesieur *et al.*, 2005).

Moeng (1984) later developed a LES model based on Deardorff (1980) SGS model and a mixed pseudo-spectral finite-difference solver. The latter requires the flow fields to be explicitly filtered which allows a better control on the LES filter. Furthermore, it avoids finite difference errors (in the horizontal directions) by processing horizontal components of the equations in the spectral space relying on Fast Fourier Transform (FFT). Moeng (1984) reproduced successfully day 33 of Wangara experiment with results in agreement with Deardorff's previous findings. By comparing with an advanced analytical spectra model (taking into account the filter and discretization effects) and observation, Moeng and Wyngaard (1988) further showed that the wave cut-off filter was more appropriate than the Gaussian filters. In addition, they calibrated the model constant with respect to the theoretical filtered spectra and found that $(C_k;\, C_\varepsilon) = (0.1;\, 0.93)$ performed best. These values are in good agreement with what obtained by Lilly (1966) based on Kolmogorov hypothesis. Today, they are still considered as appropriate for the flow interior (Redelsperger *et al.*, 2001).

Moeng and Sullivan (1994) also reproduced a neutral ABL based on the model just introduced (Deardorff, 1980; Moeng, 1984; Moeng and Wyngaard, 1988). This study is of particular

interest because the neutral case of Moeng and Sullivan (1994) is not strictly adiabatic since the internal energy conservation is considered and the ABL is capped by a strong inversion ($8°$K in 60 m). It allows to significantly reduce the height of the domain, to damp the inertial oscillation, and also to further validate the complete LES model by verifying that temperature, even if included, do not change the result in the neutral region. Despite the above considerations, the obtained profiles of the various turbulent quantities in the lower half of the ABL exhibit the very same characteristics as results from Moeng *et al.* model in Andren *et al.* (1994) study confirming the validity of the approach (albeit the solution consistently fail close to the surface)[9]. The main objective of Moeng and Sullivan (1994) was to further examine the flow properties and structure across the ABL, and the main features of the full ABL (latter observed experimentally) were recovered such as the near-surface streaks that occur in updraft/downdraft pairs elongated in the flow direction and that gradually disappear with increasing height (Moeng and Sullivan, 1994; Drobinski *et al.*, 2004).

The Deardorff-Moeng (Deardorff, 1980; Moeng and Wyngaard, 1988) SGS model was also implemented in WRF (Klemp and Skamarock, 2004). However, an adaptation of the constant was needed. Indeed, numerical schemes of this method are higher orders (third order Runge-Kutta time scheme and fifth order upwind advection scheme), reducing the numerical diffusion and thus increasing energy of small structures. By using the usual set of constant $(C_k; C_\varepsilon) = (0.1; 0.93)$, the obtained solutions were noisy with a build up of energy at the grid scale (*i.e.* many small structures of the size of the grid) (Klemp and Skamarock, 2004). Thus, C_k needed to be increased to smooth the results (due to the exact same reasoning as for the Smagorinsky constant). Those problems are also discussed by Takemi and Rotunno (2005) who first reviewed the set of constants that have been historically used with the TKE based SGS model. The latter authors suggested that $(C_k; C_\varepsilon) = (0.15; 0.93)$ were more appropriated for use in WRF, instead of the usual set of closure constants.

[9] For such a case, as opposed to the pure Ekman boundary layer, the ABL height z_i is define by the inversion, *i.e.* generally the height of the minimum heat flux. Thus, z_i is used instead of u_*/f as a height scaling parameter and to compare Moeng and Sullivan (1994) results with Andren *et al.* (1994) Ekman boundary layer results, height needs to be rescaled using the ratio $u_*/z_i f$

To close this section, concerning the inclusion of SGS models in mesoscale models, it is to note that Cuxart *et al.* (2000) added in the mesoscale model Meso-NH a SGS model similar to Sommeria (1976) and Redelsperger and Sommeria (1981). They validated the approach for several flow configurations, and the adiabatic ABL cases of Andren *et al.* (1994) (discussed in details in the next section), was also reproduced successfully by Cuxart *et al.* (2000). However, the model was not alleviating the near-surface departure from the similarity theory. The Smagorinsky and the TKE based SGS models have also been implemented in ARPS (Chow and Street, 2009) and a few other mesoscale models with the same general results.

1.3.2.2.1.3 Limitations of classical SGS models The main properties of the classical SGS models have been introduced in the previous section, and it has been seen that they were capable to reproduce full ABL flows. In this subsection, the main abilities of classical SGS models are further investigated notably discussing the Andren *et al.* (1994) mile-stone intercomparison. It is to underline that most of the attention is set on the near-surface region where LES-NWM suffer from under-resolution and SGS eddies tend to be anisotropic.

Andren *et al.* (1994) intercomparison Andren *et al.* (1994) intercompared four reference LES models of the full ABL, *i.e.* models of Mason, Moeng, Nieuwstadt and Schumann, based on an homogeneous surface fully adiabatic Ekman boundary layer similar to Mason and Thomson (1987). Thus, only momentum and mass conservation are considered[10]. The exact same numerical protocol is used in all the approaches, *i.e.* domain size, mesh, surface, lateral and top boundary conditions, initialization method, input data and post-processing. Only the Mason model had a stretched grid in the vertical direction along with a filter size Δ that only rely on Δx and Δy (Δz of the filter is thus implicitly set equal to horizontal resolution, and changed in the vertical resolution has no impact on the SGS model). In fact, these aspects (numerical protocol) along several aspects of the results are described in detail by Andren *et al.* (1994) and the study gives a good and thorough overview of the abilities of LES-NWM based on classical SGS model. As a result, Andren *et al.* (1994) intercomparison served as a reference along the

[10] Note however that each of the four models are also able to deal with temperature as they had been previously intercompared in a similar way but for a purely convective ABL (Nieuwstadt *et al.*, 1992), as discussed later.

years to evaluate LES models for the adiabatic full ABL over homogeneous surface (Kosović, 1997; Cuxart *et al.*, 2000; Chow *et al.*, 2005; Senocak *et al.*, 2007).

Mathematical model and numerical methods for both the solvers and the SGS models compared in Andren *et al.* (1994) differ from one model to the other. However, they all feature second order discretization schemes, and conservative approaches are used to compute advective terms. The only exception is Moeng's model for which the horizontal derivatives are computed based on a pseudo-spectral method. For their part, the SGS model compared are the standard Smagorinsky (Mason; introduced previously), the backscatter Smagorinsky (Mason; advanced SGS model presented in Sec. 1.3.2.2.2.2) and three variants of the TKE based SGS model (Moeng; introduced previously, Nieuwstadt and Schumann[11]) featuring different values for the TKE production and dissipation closure constants. To a priori compare all the SGS models, Andren *et al.* (1994) evaluated the associated Smagorinsky constant of each SGS model considering the dissipation and production of TKE in equilibrium. The constant value ranged from 0.13 for Schumann to 0.24 for Moeng.

Results of all models compared by Andren *et al.* (1994) are generally very similar despite the differences in mathematical models and numerical methods: they all reproduce the same inertial oscillation and are in good agreement above the first third of the ABL. The Smagorinsky and TKE based SGS models are found equally skilled for the neutral homogeneous Ekman boundary layer. In the lowest third of the ABL, however, some differences are observed. Models can be classified in two groups: Moeng, Nieuwstadt and the Mason's standard Smagorinsky, on one side, and Mason's backscatter and Schumann, on the other. In fact, the backscatter SGS model (and Schumann's model to a least extent) is notably less biased close to the surface clearly illustrating limitations of classical SGS models. Based on the backscatter SGS model, non-dimensional vertical gradient of horizontal velocity in the surface layer is in better agreement with MO similarity, *i.e.* without an overshoot, and friction velocity is increased in comparison to the others models. Longitudinal velocity variance profile does not exhibit a

[11] Note that, the Schumann SGS model used in Andren *et al.* (1994) study was relying on a classic TKE based SGS model and not on the two-part eddy viscosity approach introduced in Sec. 1.3.2.2.2.1 (Schumann, 1975).

"nose" close to the ground and vertical velocity variance profile becomes more linear (no more featuring an inflexion point in the middle of the surface layer). Furthermore, the backscatter and Schumann SGS models also feature a lower eddy mixing coefficient close to the surface resulting in lower SGS flux and variances close to the surface, and an increase of the resolved strain rates. Concerning velocity spectra, this decrease in SGS eddy diffusivity shift the spectral peak toward higher wave-numbers which is followed by a steeper drop-off, confirming the increase of small structures energy. Finally, the same eddy diffusivity was imposed by Andren *et al.* (1994) in all LES models (based on the Mason non-backscatter results) in order to evaluate the impact of the non SGS parts of the models Results of all the models converge to the same solution which proved that the differences previously observed were mainly due to the SGS model and not caused by the solver or numerical schemes.

Andren *et al.* (1994) clearly illustrated the abilities of classical SGS models for an adiabatic ABL and their limitations with regards to the surface layer. It was also demonstrated that the differences in the results were clearly related to SGS models. In fact, both Smagorinsky and TKE based classical SGS models are purely dissipative and deterministic as they assume that the subgrid motion is fully determined by the resolved motion. They were demonstrated to be over-dissipative (Mason and Thomson, 1992; Murakami, 1998; Piomelli, 1999; Porté-Agel *et al.*, 2000) which cause an over-reduction of the level of energy of the smallest resolved structures. This is illustrated in Andren *et al.* (1994) intercomparison by the higher SGS eddy diffusivity of classical SGS models. Furthermore, as discussed by Piomelli (1999), classical SGS models are unable to reproduce the details of the subgrid stresses accurately at a local level, notably with regards to the correlations and energy transfers to/from small scales from/to the energy producing large-scales. This is particularly critical where unresolved part of the flow is increased or in particular regions of flow over complex terrain (Piomelli, 1999).

In the near-surface region where the flow is already under-resolved, this tend to further damp the resolved vertical turbulent mixing, which allows a higher vertical shear of horizontal velocity, resulting in an overshoot of the non-dimensional wind shear and a too low friction velocity (Mason and Thomson, 1992; Porté-Agel *et al.*, 2000; Brasseur and Wei, 2010). The

nose shape in the non-dimensional wind shear, which was first described by Mason and Thomson (1992), is thus very typical of LES based on dissipative only SGS models (Andren *et al.*, 1994; Sullivan *et al.*, 1994; Porté-Agel *et al.*, 2000; Redelsperger *et al.*, 2001; Chow *et al.*, 2005; Piomelli, 2008). Many efforts were devoted by the research community to avoid this shortcoming by adapting the SGS model, and while some solution were proposed at an early stage (Schumann, 1975), it is still an open field of research (Piomelli, 2008) that receive a lot of attention (Andren *et al.*, 1994; Sullivan *et al.*, 1994; Porté-Agel *et al.*, 2000; Ding *et al.*, 2001a; Redelsperger *et al.*, 2001; Drobinski *et al.*, 2004; Chow *et al.*, 2005; Piomelli, 2008).

High Accuracy Zone (HAZ) It is only recently that Brasseur and Wei (2010) first proposed a solution to avoid the non-dimensional wind shear overshoot, only relying on a classical SGS model, but applicable to the other approaches. Brasseur and Wei (2010) first found the source of the overshoot problem inspired by an analogy with the physical behaviours of channel flow over a smooth wall (where an overshoot naturally exists and depends on the Reynolds number of the flow). Then, they demonstrated that the overshoot could be removed by properly adjusting some of the numerical parameters of the LES model, namely the vertical resolution in the surface layer, the grid aspect ratio close to the surface and the Smagorinsky constant. These findings largely contrast with the hitherto generally accepted fact that the overshoot could only be address by improving the SGS model, not by increasing the resolution (Mason and Thomson, 1992; Sullivan *et al.*, 1994).

Three theoretical criteria were developed to bring the LES in the so-call High Accuracy Zone (HAZ), *i.e.* the region in the $\mathfrak{R} - \mathrm{Re}_{LES}$ parameter space[12] where the overshoot is avoided and results are almost independent of the grid parameters.

The HAZ is defined by critical minimum value of $\mathfrak{R}$ and Re_{LES} that form the two first criteria of Brasseur's framework, see Brasseur and Wei (2010, Fig. 6) for a graphical illustration. In fact,

[12] $\mathfrak{R}$ is the ratio of resolved over subgrid turbulent stress at the first grid level, and $\mathrm{Re}_{LES} = z_i u_* / \nu_{LES}$ is a LES Reynolds number analogous to the Re of smooth wall channel flow but where z_i is the ABL height and ν_{LES} is the LES viscosity which is defined by the ratio of subgrid stress $\langle \tau_{13} \rangle$ over resolved strain rate $2 \langle S_{13} \rangle$ at the first grid level, see Brasseur and Wei (2010). In eddy viscosity closures, the LES viscosity is shown to be proportional to the product of the model constant by the grid aspect ratio each raised to a power (Brasseur and Wei, 2010).

increasing the horizontal resolution or lowering the model constant but keeping the vertical resolution unchanged tend to increase the resolved part of the flow close to the surface. As a result, both $\mathfrak{R}$ and Re_{LES} are increased. In such a case, $\mathfrak{R}$ is found to increase linearly with Re_{LES} in the $\mathfrak{R} - \mathrm{Re}_{LES}$ parameter space. At the opposite, only increasing the vertical resolution tend to lower the first level height and also indirectly lower the model constant which have a mixed effect on $\mathfrak{R}$ and Re_{LES}. In the $\mathfrak{R} - \mathrm{Re}_{LES}$ parameter space, this is found to change the proportionally between $\mathfrak{R}$ and Re_{LES}, *i.e.* the slope of the line obtained when only the horizontal resolution or the model constants were changed. As a result, a minimum vertical resolution is required to reach the HAZ, which is the third criteria of Brasseur's framework.

Brasseur and Wei (2010) further evaluated various reference results of the adiabatic ABL from the literature (Andren *et al.*, 1994; Sullivan *et al.*, 1994; Porté-Agel *et al.*, 2000; Chow *et al.*, 2005; Drobinski *et al.*, 2007) plotting them in the $\mathfrak{R}-\mathrm{Re}_{LES}$ parameter space, see Brasseur and Wei (2010, Fig. 7). While constraint imposed by the three criteria to move a LES in the HAZ are found relatively realistic in terms of grid requirements, only (Drobinski *et al.*, 2007) is located in the HAZ (which is also the only result not featuring an overshoot of the dimensionless wind shear). Brasseur and Wei (2010) proposed a practical methods to bring LES in the HAZ. The latter is successfully applied based Moeng and Sullivan (1994) shear case and using the Moeng/Deardorff pseudo-spectra model (Deardorff, 1980; Moeng and Wyngaard, 1988) along with a Smagorinsky SGS model. Note however that the three criteria are model and closure dependent and that an iterative procedure is needed to properly move the LES in the HAZ. In that sense, it is interesting to underline the differences between the various results from Andren *et al.* (1994) on Brasseur and Wei (2010, Fig. 7). Considering that numerical parameters of the models (except the constant) are identical in that study, it illustrates how model dependent are the three critical parameters. Finally, it is to underline that, while theoretically fully justified, the approach proposed by Brasseur and Wei (2010) has been found to lead to less satisfactory results with other codes (Churchfield *et al.*, 2010; Lapointe-Thériault, 2012).

Structure of the surface layer To end this section, a recent theory describing the structure of the neutral surface layer in introduced. In fact, this theory explains and unify a large number

of advanced observations and theoretical descriptions of the surface layer velocity component energy spectra (Drobinski *et al.*, 2004). It suggests the existence of two sublayers in the surface layer that arise from the eddies dynamical behaviour associated with surface proximity (Hunt and Carlotti, 2001). In a sublayer close to the ground, $z \lesssim 10$ m, the eddy surface layer (ESL), the dominant mechanism is the blocking of impinging eddies coming from above. The shear is also important. The other sublayer above, called the shear surface layer (SSL), is where only shear affects the isotropy of turbulence. It can be seen as an intermediate layer, a transition, between the ESL and the Ekman layer. The SSL exhibit the elongated rolls, also referred to as streaks, previously discussed.

Based on the latter theory and the velocity spectra it predicts as a function of the height agl, Redelsperger *et al.* (2001) developed a simple TKE based SGS model. In fact, in the latter approach only the mixing and dissipation lengths differ from Deardorff (1980) SGS model. They write $\lambda = (1-\gamma)A_k z + \gamma\Delta$ and $\lambda_\varepsilon = (1-\gamma)A_\varepsilon z + \gamma\Delta$, where A_k and A_ε are non-dimensional constants obtained by matching the new SGS model with similarity theory at the bottom boundary, and γ is a blending function going from 0 at the surface to 1 at a given height similar the one introduced by Sullivan *et al.* (1994). The proposed SGS model is thus simple to implement and valid in the whole ABL, complying with Kolmogorov theory in the flow interior, with the two-layer theory in the surface layer, and with MO similarity at the surface. Furthermore, the definition of the blending function given by Redelsperger *et al.* (2001) is more general than Sullivan *et al.* (1994) as it is also suitable for heterogeneous surface cases.

The approach proves to significantly enhance results close to the surface (Redelsperger *et al.*, 2001; Drobinski *et al.*, 2004). The overshoot of the non-dimensional wind shear was divided by two, allowing the velocity to better follow the log-law profile. Furthermore, the predicted dissipation rate was in very good agreement with the similarity theory. Considering its fundamentals, simplicity and abilities, this approach is clearly appealing. It was implemented successfully in the Meso-NH (Drobinski *et al.*, 2004, 2007).

1.3.2.2.2 Advanced SGS models

With the increasing computational power, the last fifteenth years have seen an exponential use of the LES tools. The LES technique evolved and in addition to reach a higher level of maturity, tremendous enhancements have been achieved. New SGS models have been proposed to address limitation of the existing approaches for both the flow interior and the region close to the surface. Furthermore, dedicated experimental campaigns have allowed to better understand ABL processes and validate some of the aspects of the LES models. As an example, the elongated rolls of the surface layer, *i.e.* the streaks, were effectively observed at full scale and quantitatively studied thanks to SODAR data acquired only recently (Poulos *et al.*, 2002; Drobinski *et al.*, 2004, 2007).

By advanced SGS model, we refer to the SGS that go beyond the classic Smagorinsky and TKE based SGS models and that were applied to the ABL or similar flows. The study of advanced SGS models allows to better appreciate and understand the limitation of the classical SGS models, further illustrating how they can be avoided.

In the the current section, an overview of the main advanced SGS models relevant for ABL flows is achieved, *i.e.* the two-part eddy viscosity SGS models, the backscatter SGS models and the hybrid RANS LES models.

1.3.2.2.2.1 Two-part eddy viscosity SGS models The two-part eddy viscosity SGS models is based on the legitimate assumption that in the region close to the surface, the flow fluctuates around an average profile which is well described by similarity theory. As a result, SGS stresses can be split in two parts as introduced by Schumann (1975): an isotropic or fluctuating part, which is computed based on the usual local isotropy assumption, and an inhomogeneous part that represent the averaged profile and that is modelled based on a simple RANS model (zero or first order). Schumann (1975) study, while not dedicated to the ABL, was a first promising attempt to address limitation of LES-NWM model close to the ground. It was also the first time a TKE based SGS model was used for a LES of a channel flow. The two-part

SGS model proved to be an important advance since the results close to the walls were found to be better reproduced independently of the mesh resolution.

Following Schumann (1975) concept, Sullivan *et al.* (1994) implemented a two-part eddy viscosity SGS model dedicate to the ABL and where thermal stratification is fully considered. Moeng's model (Moeng, 1984; Moeng and Wyngaard, 1988) was used as basis and the Deardorff/-Moeng TKE based SGS model was adapted. As in Schumann (1975) SGS model, SGS stresses are split into isotropic and inhomogeneous contributions, such as $\tau_{ij} = -2\nu_t\gamma S_{ij} - 2\nu_T \langle S_{ij} \rangle$ where γ is a so-called isotropic factor, *i.e.* a blending function. In the isotropic part (first term), the eddy viscosity ν_t is a function of the magnitude of a fluctuating strain rate, while in the inhomogeneous part (second term), the average eddy viscosity ν_T depends upon the magnitude of the strain rate computed from ensemble averaged flow quantities only. The isotropic part progressively reaches the total stress through the isotropic factor γ that is computed based on the ratio of fluctuating strain rate over total strain rate. The separation into mean and fluctuating parts allows a transition from LES to ensemble-average modelling as the wall is approached, which can be seen as a simple hybrid RANS-LES approach. Furthermore, unlike Schumann (1975), the mean eddy viscosity is computed so that the mean shear always matches similarity theory at the surface closest computational grid point.

Based on the shear and convective cases introduced by Moeng and Sullivan (1994) and focusing on the near-surface flow (an aspect that was left aside by Moeng and Sullivan (1994)), Sullivan *et al.* (1994) showed that the proposed approach notably improve the LES results close to the ground. With the new SGS model, profiles of velocity, temperature, as well as turbulent quantity are in agreement with the similarity theory; the friction velocity is also slightly increased compared to simpler SGS models as Deardorff (1980) due to the reduction of the near-surface shear (Mason and Thomson, 1992); the flow close to the surface is more resolved increasing notably the energy of small eddies; and results are further shown to be less sensitive to the resolution than the classical SGS models. Results enhancement brought by Sullivan SGS model are on par with the one obtained with the backscatter model (Mason and Thomson, 1992) (presented in the following section). However, the former might appear more appeal-

ing since it is deterministic and only based on simple physical consideration, it requires less computational time and it is simpler to implement.

Ding *et al.* (2001a) also introduced and validated two new SGS models dedicated to the ABL similar to Sullivan *et al.* (1994) SGS model but which are based on the Smagorinsky SGS model (not on a TKE based SGS model). This study is also solving Moeng and Sullivan (1994) cases. Results obtained are equivalent to the ones of Sullivan *et al.* (1994), albeit the two-part eddy viscosity model need to be further tweaked and some of the results present some suspicious discontinuities and shapes. In any case, this study confirms the abilities of the Schumann (1975); Sullivan *et al.* (1994) approach, in addition to, widening it applicability to the Smagorinsky SGS models.

The two-part eddy viscosity SGS model present some interesting abilities to notably lower the bias with respect to the similarity theory in the vicinity of the surface. However, some limitations have to be underlined. First, the flow properties close to the surface need to be a priori known in order to correctly express the anisotropic SGS model part. In the case of the ABL over an homogeneous surface, anisotropic part of the stress in the surface layer can be readily computed based the MO similarity theory, and the blending function between isotropic and anisotropic SGS part is generally computed based on the mean flow properties (horizontally averaged along the homogeneous direction), not locally. Over an heterogeneous surface, however, the application of such an approach is less trivial since MO similarity are valid only for statistically homogeneous flows (that satisfy ergodicity hypothesis). Finally, it is to note that some authors demonstrated (Piomelli, 2008) that even adapted to an heterogeneous surface, this approach may not be suitable when the surface flow is too complex, such as when there are recirculating regions, if the model of the anisotropic part is too simplistic (*i.e.* lower order).

1.3.2.2.2.2 Backscatter SGS model Both standard Smagorinsky as well as the TKE based SGS model are dissipative only. This is not always valid notably in flow close to a rigid no-slip wall. Indeed, it was shown experimentally and theoretically that while the averaged dissipation is positive, small eddies are able to transfer (give) energy to larger structures, resulting in

a locally negative instantaneous dissipation (Lesieur *et al.*, 2005). This process is called the backscatter of energy. It has to be modelled separately from eddy viscosity. The Eddy-Damped Quasi-Normal Markovian (EDQNM) theory allowed to estimate the theoretical backscatter rate. Based on those considerations, Mason and Thomson (1992) introduced a SGS model including the TKE backscatter effect. The main objective of this study was to address the short comings of standard Smagorinsky approach close to the ground notably for the neutral and stably stratified surface layer. It was the first times the systematical overshoot of the surface layer dimensionless wind shear was described.

Mason and Thomson (1992) backscatter SGS model is based on the introduction of additional stresses into the simulation providing backscatter of energy. These new stresses are generated based on random numbers that are properly scaled and processed (divergence free) to give the desired backscatter rate as predicted by the EDQNM theory. As discussed during the analysis of Andren *et al.* (1994) intercomparison, this stochastic backscatter SGS model is shown to bring notable improvements close to the surface. The velocity profile as well as turbulent quantities correctly follow the experimentally found profiles (Mason and Thomson, 1992; Andren *et al.*, 1994) and resolved part of the flow is increased notably close to the ground due to the stochastic backscatter. However, those structures have a more random character and are less organized than those predicted by the two-part eddy viscosity SGS model which is fully deterministic as shown by Sullivan *et al.* (1994). In comparison to the classical SGS models, the backscatter SGS models also show a shorter spin-up period and a fully developed ABL is reach earlier than with classical SGS models (Andren *et al.*, 1994; Mason, 1994). In addition, smaller fluctuations of the integrated TKE are observed which indicates that the backscatter models provide a more stable simulation (Mason, 1994). Hobson *et al.* (1999) based on an adiabatic ABL further compared Smagorinsky SGS model results with and without backscatter effect for several grid configurations using the Mason and Thomson (1992) model. Again, a clear enhancement is obtained thanks to the backscatter model, notably when a coarse resolution is used. It is also of interest that the authors find out that a simple mixing length RANS

model could be better performing than LES model close to the ground if no care was taken to properly address the near-surface region in LES.

The backscatter effect is the consequence of non-linear interaction while the redistribution of SGS TKE is the consequence of anisotropy induced by the shear. They can thus be viewed as deterministic. Based on these considerations and the non-linear constitutive theory, Kosović (1997) introduced a model based on a backscatter approach, but instead of relying on random number generated processes, a non-linear SGS model was used. It is thus solely based on a non-linear combination of the strain rate S_{ij} and rotation rate Ω_{ij} tensors (see Sec. 2.2.3.5). Kosović (1997) non-linear backscatter SGS model is evaluated based on Andren *et al.* (1994) Ekman case retaining the exact same the numerical parameter and protocol. In comparison to the linear models, *i.e.* classical SGS models, the non-linear backscatter SGS models show a shorter spin-up period which is in agreement with the findings of Mason and Thomson (1992). Concerning the first order moments, Kosovíc SGS model totally corrects the over-estimation of the shear close to the surface and the results clearly follow the similarity theory. This improvement exceeds the one of Mason and Thomson (1992), Sullivan *et al.* (1994) and Porté-Agel *et al.* (2000) and is similar to the one of Silva Lopes *et al.* (2007). Tangential stresses are slightly improved and their resolved part is increased close to the surface. TKE and streamwise velocity variance profiles are also notably improved in comparison the linear models. These turbulent quantities do not exhibit anymore a nose shape and the total TKE is nearly linear with height (as opposed to Mason and Thomson (1992)) with a maximum value $1/3$ smaller than the linear model which is in good agreement with other experimental and advanced LES studies (that address the limitation of classical SGS model close to the surface). However, in comparison to Mason and Thomson (1992), a lower value of the near-surface TKE is obtained with the non-linear model which also exhibits a significant reduction of TKE transport. These observed differences are said to be the consequence of the better reproduction of the normal components of the SGS stresses by the non-linear model (Kosović, 1997). Concerning velocity spectra, simulations with the non-linear SGS model do not show a fast drop-off as opposed to linear models. Indeed, even with a filter not well into the inertial subrange, *i.e.* close to the surface,

the slope of the spectra is in agreement with the generally accepted $-5/3$ slope of the inertial subrange. Furthermore, the spectra peak is shifted toward the larger wave number. These observation are in total agreement with previous studies.

To finish presenting Kosović (1997) non-linear backscatter SGS model abilities, it is to note that the structure of the flow is notably changed close to the surface in comparison to the linear and two-part eddy viscosity models. Indeed, the non-linear model tends to produce smaller and more isotropic structures close to the surface. As a result, the streak like structures, that were observed in previous experimental and numerical studied, are much weaker, poorly defined and not aligned with the flow. Unfortunately, no clear explanation is given by Kosović (1997) for such a phenomena, that appears to differ from reality (Drobinski *et al.*, 2004).

1.3.2.2.2.3 Hybrid RANS/LES models Hybrid RANS/LES methods intent to benefit from the best of each family of models depending of the local flow properties. In the case of high Reynolds number flows bounded by a rough wall, RANS approaches can lead to promising result in an inexpensive manner as illustrated in Sec. 1.1.3. For such flows, these methods do not alleviate the need of wall functions at the lower boundary, but they are able to reproduce correctly the near-wall region (if the RANS model is appropriate), even with grid cells that have a high aspect ratio (Δx large compared to Δz). At the opposite, a mesh aspect ratio close to one is required for LES. As a result, LES-NWM of high Reynolds number flows is unrealistically expensive if the inner layer is to be resolved (Piomelli, 2008). In hybrid models, RANS is used to model the flow in the inner and part of the outer layer and LES is used for the upper outer region where the filter is properly located in the inertial subrange. The RANS model can thus be viewed as acting as a wall model for the LES.

This family of models was, in fact, already introduced in this thesis. Indeed, SGS model such as the one of Sullivan *et al.* (1994) and Ding *et al.* (2001a), and to some extent, the approaches using a canopy model (Chow *et al.*, 2005; Silva Lopes *et al.*, 2007; Senocak *et al.*, 2007) can be considered as hybrid model since part of the SGS is directly related to the mean (in the Reynolds average sense) properties of the flow. However, in most of these approaches, a very

simple RANS model (zeroth or first order) was used generally requiring an a priori knowledge of the mean properties of the flow. As seen earlier, this was proven to give promising results for ABL over a homogeneous surface. For more complex flows, the underlying hypothesis of such simple RANS models are broken affecting their validity. A solution is to use more advanced RANS model, such as second order closures that are proven to perform correctly in such situations (Piomelli, 2008).

As an example of an advanced hybrid RANS/LES model applied to the ABL, Bechmann and Sørensen (2010) elegantly combined a $k-\varepsilon$ URANS and a $k-\varepsilon$ based SGS model. In their approach, the same filtered NS equations are contiguously solved for the whole computational domain, and the only difference between the URANS model and the LES model is hidden in the expression of turbulent stresses. Bechmann and Sørensen (2010) used the usual eddy viscosity definition of the $k-\varepsilon$ model everywhere, *i.e.* $\nu_t = C_\mu k^2/\varepsilon$. However the dissipation term in the TKE equation is expressed as in the $k-l$ model, *i.e.* $\varepsilon = k^{3/2}/l$ where l can whether take the value of the RANS mixing length, $l_{RANS} = k^{3/2}/\varepsilon$, or the LES length scale, $l_{LES} = C_\Delta \Delta$ where C_Δ is a closure constant related to the Smagorinsky constant. The criteria to switch between the two approaches is simply based on the hypothesis that, the flow is well resolved only in regions of the domain where the RANS mixing length is greater than the LES length scale, which can be expressed as $\bar{l} = \min(l_{RANS}, l_{LES})$. Following this approach, the classical $k-\varepsilon$ closure is fully recovered when l_{RANS} is used, while in the LES region, $k-\varepsilon$ equations adapt to the length scale so that $k^{3/2}/\varepsilon \propto l_{LES}$ (Bechmann, 2006). Thus, the introduced hybrid models appears as an extension of the popular TKE based SGS models featuring an advance surface boundary condition based on a $k-\varepsilon$ RANS model.

Bechmann (2006) hybrid RANS/LES approach as presented above is still relying on an uniquely dissipative SGS model. As a result, Bechmann and Sørensen (2010) also implemented a stochastic backscatter model following Mason and Thomson (1992). However, backscatter of energy is linked to the unsteady interaction between small and large structures not considered by RANS. As a result, backscatter effects are removed from the RANS region and a blending is used for them to rich their full value in the LES region.

Bechmann and Sørensen (2010) focused on the Askervein case, however, the abilities of the model were first evaluated for a flat homogeneous case similar to Andren *et al.* (1994) as illustrated in Bechmann (2006). The non-dimensional wind shear shows that the hybrid RANS/LES approach without backscatter feature a nose with a maximum error value similar to others classical SGS models (Andren *et al.*, 1994). However, its height is significantly lower and located at the transition between RANS and LES. The velocity profile is thus less affected than with classical SGS models. However, as it is usually the case for such hybrid approaches (Piomelli, 2008), part of the limitations of classical SGS model are addressed by the hybrid model, but the problems are transferred at the interface between the models. The addition of the backscatter of energy to the hybrid model clearly improve the results in the surface layer while they are mostly unchanged above (Bechmann and Sørensen, 2010). The various enhancement observed by Mason and Thomson (1992) (in variances, TKE and velocity spectra) are reproduce, and the maximum wind shear error at the transition between models is reduced by half. The backscatter model thus clearly improve the transition between RANS and LES.

The approach introduced by Bechmann (2006); Bechmann and Sørensen (2010), and more generally the hybrid RANS/LES approach shows some very interesting features. The combination of second orders RANS and SGS models is appealing notably for more complex cases. However, problems generally arise at the interface between the RANS and the LES regions (Piomelli, 2008), and it was shown by Bechmann and Sørensen (2010) that the addition of a simple stochastic backscatter model notably improved the results in this zone.

1.3.2.2.3 Advanced SGS models with explicit filtering

When a general convolution filter is used to filter the NS equations, *i.e.* explicit filtering, the subfilter stress tensor is the sum of three tensor which is called the Leonard decomposition (Leonard, 1974): $\tau_{ij} = L_{ij} + C_{ij} + R_{ij}$ where L_{ij} is the Leonard stress tensor, C_{ij} is the cross terms stress tensor and R_{ij} the Reynolds stress tensor. At the opposite, when an implicit filter is used, *i.e.* based on the mesh, subfilter stress tensor reduce to the Reynolds tensor.

The Leonard tensor is fully defined by resolved quantities while the other two tensors need to be modelled. The total subfilter scale (SFS) stress can thus be decomposed into a resolved part (*i.e.* Leonard tensor) sometimes called the resolved subfilter scale (RSFS) stress, and a subgrid part (*i.e.* the Reynolds tensor) generally called the subgrid scale (SGS) stress. The cross terms tensor is most of the time neglected. The total stress is thus the sum of the resolved, the RSFS and the SGS stresses, and it can be considered that the application of the filter (explicit) on top of the discretization operator (*i.e.* discretization of the equation on the grid) decomposes the energy spectrum of a turbulent flow in three parts (resolved, RSFS and SGS), that, once added, form the unfiltered energy spectrum, see Chow *et al.* (2005, Fig. 1). This decomposition allows to compute separately each stress and to evaluate their importance notably concerning the RSFS and SGS stresses. And while the use of an explicit filter add complexity to the SGS model, it add flexibility and allows to better take into account the subfilter physic.

1.3.2.2.3.1 Scale similarity SGS model The scale similarity SGS model of Bardina *et al.* (1980) was one of the first approaches to address the fundamental limitations of the classical SGS model by assuming that "the most active subgrid scales are those closer to the cutoff and that the scales with which they interact most are those right above the cutoff". In other words, properties and impacts of the largest subgrid eddies can be deducted from the properties of the smallest resolved eddies (rather than on the entire turbulent spectrum). To do so, largest subgrid eddies can be obtained by filtering the subgrid velocity such as $\overline{u}' = \overline{u} - \overline{\overline{u}}$ (in the context of a general convolution filter, *i.e.* using an explicit filter). The SGS stress tensor can then be parametrized as $\tau_{ij} = \overline{\overline{u}_i \overline{u}_j} - \overline{\overline{u}}_i \overline{\overline{u}}_j$ which is the "scale-similar" model also referred to as Bardina's model. It can be seen as the simplest reconstruction model (Chow *et al.*, 2005). Note, this model suffer from under-dissipation of turbulence, which is readily addressed by adding $-2\nu_t S_{ij}$ to the Bardina model to obtain the mixed Bardina model (Murakami, 1998) such as $\tau_{ij} = -2\nu_t S_{ij} + \overline{\overline{u}_i \overline{u}_j} - \overline{\overline{u}}_i \overline{\overline{u}}_j$. The scale similarity SGS model was the first to introduce the concept of double filtering. It was proven to allow for backscatter processes to be reproduced, and thus to allows a better reproduction of flows close to rigid walls. The Bardina model was

also coupled with a TKE based SGS model which was found to greatly enhance the results over classical SGS model in the context of complex terrain (Chow and Street, 2009).

1.3.2.2.3.2 Dynamic Smagorinsky SGS model In the mixed Bardina's model, as well as in all the approaches previously presented, the Smagorinsky constant need to be set in a somewhat arbitrary manner. However, this constant, and by extension the ones of TKE based SGS models, are found to be dependent of the flow fields (Germano *et al.*, 1991) and the distance to the wall. Germano *et al.* (1991) introduced a SGS model where the Smagorinsky constant is dynamically computed as a function of the local resolved flow properties. The so-called dynamic Smagorinsky SGS model was born.

The idea of Germano *et al.* (1991) was to use a test filter located in the simulate inertial subrange in addition to the usual implicit mesh filter. At this test level, local subgrid velocity fluctuations and thus subgrid fluxes can be directly computed which allows to determine the local Smagorinsky constant C^{dyn} (at the test filter level). Then, considering that the transfers of energy across the two filters is similar since they are both located in the inertial subrange, C^{dyn} is used as closure constant of the SGS model. This assumption is also referred to as the scale-invariance of C^{dyn} (Porté-Agel *et al.*, 2000). Note that there is no restriction on the sign on the dynamically computed model coefficient. As a result, negative values can be obtained allowing backscatter of energy (Germano *et al.*, 1991). Furthermore, the same dynamic procedure can also be applied to temperature and others scalars to obtain the dynamically turbulent Prandtl and Schmidt constants, respectively. However, the dynamic SGS models generally requires a notably higher computational time in comparison to the standard Smagorinsky approach (Murakami, 1998; Piomelli, 1999; Porté-Agel *et al.*, 2000).

Following the dynamics procedure proposed by Germano *et al.* (1991), C^{dyn} is over-defined and it can be computed as many Smagorinsky constants as the tensors has components, *i.e.* nine in total for shear stress tensor, and three for temperature and scalars. Germano *et al.* (1991) aggregated all the possible values based on the strain rate tensor S_{ij}. However, this approach can lead to values of C^{dyn} that are spurious or undefined or that present very sharp gradients. This

tends to generate numerical instabilities that destabilize numerical calculations (Murakami, 1998), and make the model inconsistent, affecting the whole approach. Lilly (1992) proposed a method to obtain an optimum value of C^{dyn} based on the minimization of the error on the latter (considering the square of the tensor representing the differences between the double filtered stress tensor and the Leonard tensor). Such an approach almost avoid the problems of division by zero faced by Germano *et al.* (1991). Furthermore, the local properties of the subgrid fluxes are better taken into account. However, sporadic undefined values can still arise requiring some extra processing and averaging.

The computational instability problems of the Germano-Lilly dynamic SGS model (generally referred to as the dynamic SGS model) can be addressed by averaging the various quantities necessary to compute the model coefficient over space (and/or time) prior to the computation of the latter. This have been very popular (Lesieur *et al.*, 2005). However, the flow need to have at least an homogeneous direction which limit the use of such an approach. Furthermore, the essence of the local dynamic computation of the Smagorinsky constant is lost by averaging. As a result of the limitation and instabilities discussed above and in order to further increase the applicability of dynamic approaches for more complex geometries, many methods have been proposed that address the dynamical computation of the model coefficient (Lesieur *et al.*, 2005). As an example, Meneveau *et al.* (1996) proposed a Lagrangian dynamic Smagorinsky SGS model based on the Germano-Lilly approach but for which the error on C^{dyn} is minimized along the fluid particle trajectory, and C^{dyn} is averaged along this trajectory allowing the use of the dynamic procedure without any homogenous directions (Murakami, 1998). However, this model prevents backscatter of TKE. The dynamic approaches can also be mixed with other complementary SGS models further improving both the physical representation of the flow and the numerical stability of the approach (Murakami, 1998; Piomelli, 1999; Ishihara *et al.*, 2001; Chow *et al.*, 2005). As an example, to take into account the backscatter effects of TKE, the scale similarity model of Bardina *et al.* (1980) (or Mason and Thomson (1992) approach) can be used in association to the dynamic Smagorinsky SGS model (Murakami, 1998; Porté-Agel *et al.*, 2000; Chow *et al.*, 2005; Senocak *et al.*, 2007). This so-called mixed dynamic SGS

models have been applied successfully further proving to be less affected by computational instability problems faced by the Germano-Lilly approach (Murakami, 1998; Chow and Street, 2009; Senocak *et al.*, 2007).

As a conclusion, Murakami (1997, 1998) thorough review clearly shown the abilities of the dynamical computation of the Smagorinsky constant for CWE (smooth wall). They compared LES-NWR approaches based on a large number of SGS models, *i.e.* the standard, the scale-similarity, the dynamic, the dynamic mixed, the Lagrangian dynamic and the Lagrangian dynamic mixed SGS models. Murakami (1997, Tabs. 5 and 6) summarize the abilities of these SGS model depending on the flow and flow feature to reproduce. The dynamic SGS model, *i.e.* the Germano-Lilly SGS model, is found to enhance significantly the results over the standard approach, but suffers of heavy numerical instabilities and presents a computational cost five times higher than the standard Smagorinsky model. The Lagrangian dynamic SGS model is found to be very stable but prevents backscatter of TKE. At the opposite, the dynamic mixed SGS models integrates backscatter of energy, and while it is more stable than the dynamic model, it is less stable than the Lagrangian approach. Both latter models have roughly twice the computational cost of the standard Smagorinsky. Finally, the Lagrangian dynamic mixed SGS model is found to perform best. It is as stable as the standard Smagorinsky SGS model while being only 50 % more computationally expensive. Furthermore, it retains the backscatter abilities of the scale similarity model. Conclusions of Piomelli (1999) review are similar concerning model abilities.

1.3.2.2.3.3 Dynamic SGS model and rigid no-slip wall Currently, dynamic Smagorinsky SGS models appear to be generally accepted. They have been applied successfully to a wide range of cases including channel flow and neutral ABL (Murakami, 1998; Piomelli, 1999, 2008), showing clear enhancement over the standard Smagorinsky approach. In fact, thanks to their self-adaptation abilities, the dynamic approaches are shown to be particularly skilled to account for the transition between laminar and turbulent regimes (Murakami, 1998; Piomelli, 1999). As a result, in the context of LES-NWR, the transition between the viscous sublayer, in which the flow is laminar, to the log region, where the flow is turbulent, is properly reproduced

by dynamic Smagorinsky SGS models and the computed Smagorinsky constant vanish as the surface is approached without any adaptation of the model (Murakami, 1998; Piomelli, 2008).

Situation isÂ however slightly changed for LES-NWM based on dynamic SGS models. Indeed, the viscous sublayer is not anymore resolved and the dynamics SGS models advantage of properly taking into account the laminar-turbulent transition close to the wall is lost. They have to rely on wall functions (Piomelli, 2008). As a result, the underlying problem of under-resolution close to the surface is common to both standard and dynamic Smagorinsky approaches. However, the nature of the biases differ. The over-dissipative standard Smagorinsky model damp the level of energy of the smallest resolved structures allowing a too high mean velocity shear close to the ground. At the opposite, velocity fluctuations are over-estimated by dynamics SGS models in the near-surface region because of an under-estimation of the SGS model coefficient. As a consequence, surface wind shear is under-estimated by dynamics SGS models as clearly illustrated by Porté-Agel *et al.* (2000). Thus, dynamic SGS models also require a fine tuning of the surface in the case of LES-NWM as opposed to LES-NWR.

However, as underlined by some authors, dynamic SGS models application to high Reynolds number flows such as the ABL, *i.e.* $\mathrm{Re} > 10^4$, received a keen interest only in the recent years Piomelli (2008). Indeed, considering their higher computational cost, their numerical stability shortcomings, and the fact that the laminar-turbulent transition is not a concern for LES-NWM applied to large Re flow such as the ABL, the dynamic SGS models have historically appeared less appealing for high Re flows than it was for low Re and transitional flows (Mason, 1994; Piomelli, 2008).

1.3.2.2.3.4 Hybrid RANS/standard/dynamics SGS model Seen the ambivalent properties of the standard and the dynamic SGS models close to the surface in LES-NWM, a simple and natural approach is to use an hybrid model based on both SGS models (Piomelli, 2008).

As an example, Iizuka and Kondo (2004) compared four SGS models with wind tunnel data of an aerodynamically rough flow over a ridge (at the 1/1000 scale) (Ishihara *et al.*, 2001). They found that a simple ad-hoc hybrid SGS model where a standard Smagorinsky SGS model

is used for three first levels and dynamics SGS model (either the Germano-Lilly or the Lagrangian dynamic SGS model) is used elsewhere, was better performing than the standard or the dynamic approaches alone, even if as a first approximation no particular care was taken at the interface between the models. However, some of the variables such as the eddy viscosity were presenting a notable discontinuity in this region.

Senocak *et al.* (2007) also compared various LES approaches for a neutral ABL over an homogeneous surface. They used the case from Andren *et al.* (1994) with some variant of the mesh. The study focuses on the evaluation of performance of different near-surface models at various grid resolutions which are the following: the backscatter SGS model of Mason and Thomson (1992); Brown *et al.* (1994), the canopy model from Brown *et al.* (2001)[13] and a proposed hybrid RANS/LES model. Both the canopy an the proposed model are based on a dynamic Smagorinsky SGS model, while the backscatter SGS model only rely on the standard Smagorinsky approach (with $C_S = 0.18$) (Senocak *et al.*, 2007). Note that the canopy model, while at first devoted to take into account the real plan/urban canopy, it used in this study as computational scheme to represent rough surface stresses for the dynamic SGS. The proposed hybrid RANS/LES model is a simple yet interesting approach that combines a "stratification conscious" Prandtl's mixing length model and the dynamic Smagorinsky model based on simple blending function. The height of the transition between models, h, need however to be provided. This length scale was set proportional to the filter width after a sensitivity study of the results showed its optimum value was evolving with resolutions.

Results from Senocak *et al.* (2007) clearly show that the proposed hybrid RANS/LES model is closer to MO similarity. However, with that model, resolved motion within surface layer is suppressed (as a function of h) and most turbulent quantities are modelled and not resolved. This latter point represents an important drawback of the hybrid approach notably for more complex case such as flow over an heterogeneous surface or if surface layer turbulence is to be studied. Finally, as underlined by the authors, only the backscatter backscatter and canopy approaches are able to reproduce the flow structure described by Drobinski *et al.* (2004),

[13] Note that the $\cos^2$ is used by Brown *et al.* (2001) while it is $\cos^3$ in Senocak *et al.* (2007) paper.

Finally, Silva Lopes *et al.* (2007) introduced a promising hybrid approach based on a mix of the standard and the Lagrangian dynamic Smagorinsky SGS model where a blending function is used to merge models, such as $C = \alpha C^{\text{std}} + (1-\alpha)\, C^{\text{dyn}}$. The blending coefficient α is similar to Brown *et al.* (2001) canopy model, *i.e.* $\alpha = \cos^2(\pi/2 \cdot z/z_{top})$ when $z < z_{top}$ and $\alpha = 0$ otherwise, with z_{top} being the maximum distance at which the merging is active (Silva Lopes *et al.*, 2007). It is thus claimed by the authors that this approach is similar to a hybrid RANS/LES model. Concerning the standard Smagorinsky SGS model, the damping function of Mason and Thomson (1987) is used to obtain the standard Smagorinsky model coefficient with $C_S = 0.16$ and $n = 2$, see Eq. (1.4). At the surface boundary, the wall stress model presented by Marusic *et al.* (2001) was used (*c.f.* Sec. 1.3.2.1.1.2). The study focuses on the flow over the Askervein hill that the authors previously studied based on a RANS approach (Castro *et al.*, 2003). However, in a first part, the flow over an homogeneous surface is studied in order to refine numerical parameters and find the best value of the parameter z_{top} allowing a smooth transition between surface and upper ABL SGS models.

Velocity profile as well as resolved turbulent quantities obtained by (Silva Lopes *et al.*, 2007) were in nearly perfect agreement with the similarity theory up to 1000 m and experimental results. Only a very slight deviation of the velocity profile is to note at the height where both models are merging, *i.e.* $150 - 180$ m. These results are one of the best discussed here illustrating the abilities of hybrid standard/dynamic standard SGS models.

1.3.2.2.3.5 Scale-dependent dynamic SGS model The source of the limitation inherent to the dynamics Smagorinsky SGS models in the near-surface region of LES-NWM was elucidated by Porté-Agel *et al.* (2000), who also proposed a solution, *i.e.* the scale-dependent dynamic Smagorinsky SGS model. In fact, classical dynamic SGS model assumes scale-invariance of the Smagorinsky constant C_S. In other words, the latter is considered not being a function of the filter size Δ, *i.e.* $C_S(\Delta) = C_S(2\Delta)$. However, by comparing vertical profiles of the dynamically found model coefficient for several mesh resolutions, Porté-Agel *et al.* (2000) showed that at a fixed height, C_S is a function of the filter size. This proved that the scale invariance assumption did not hold for high Reynolds number flows, notably close to a wall. In

the proposed scale-dependent dynamic SGS model, the Smagorinky constant is a function of the filter size, *i.e.* $C_S(\Delta) \neq C_S(2\Delta)$. However, subgrid stress model also become a function of the ratio of model coefficients, *i.e.* $\beta = C_S^2(2\Delta)/C_S^2(\Delta)$, which is unknown. By using a second explicit test filter (at 4Δ), and assuming that the dependance of β on Δ is approximated by a power law, Porté-Agel *et al.* (2000) managed to dynamically compute the model coefficient not relying on the scale invariance assumption.

Porté-Agel *et al.* (2000) based their analysis on an adiabatic homogeneous ABL not considering the Coriolis effect. They used a Lagrangian dynamics SGS model along with a pseudo-spectral approach with numeric and boundary conditions very similar to the model of Moeng (1984). However, the friction velocity is provided and the authors avoid deliberately the use of a wall model in order to prevent the latter to interfere with the proposed solution. The scale-dependent dynamic Smagorinsky SGS model led to clearly enhanced results compared to the standard Smagorinsky and the original dynamic SGS models. Most notably, the velocity spectra are very close to the experimental measurements and the profiles of first and second order moments are located between the standard Smagorinsky and the original dynamic SGS model results, and they are in better agreement with the similarity theory. Following the scale dependent approach, the value of model coefficient is only modified close to the surface, and $\beta = 1$ in the flow interior meaning that the scale invariance assumption is valid (in that region). The classical dynamic model coefficient is thus recovered in the flow interior ($C_S \sim 12.5$ here). Finally, as opposed to the various studies previously discussed in this section, Porté-Agel *et al.* (2000) enhancements were obtained without either changing the boundary condition or adding new near surface treatment to the model. Only the mathematical representation of the problem was more consistent with the physics of phenomena.

1.3.2.2.3.6 Dynamic reconstruction SGS model The last dynamic approach discussed here was introduced by Chow *et al.* (2005). It is an advanced model that combine some of the most promising enhancements reviewed above, in addition to include a reconstruction model for the resolved subfilter scale (RSFS) stresses. Chow *et al.* (2005) were the first to apply a re-

construction model to the ABL. Furthermore, the whole approach and the various comparisons are based on the ARPS mesoscale model.

As a reminder, when a general convolution filter is applied to NS equations, the turbulent stress tensor obtained features two new terms (the Leonard and the Cross terms tensors) in addition to the usual Reynolds tensor that is solely present when equations are implicitly filtered based on the grid. As opposed to SGS stress that need to be modelled, the RSFS stresses depend on the difference between the exact (discrete) and the filtered (by the explicit filter) velocity field (Chow *et al.*, 2005). Following Chow *et al.* (2005), RSFS stresses can be obtained, *i.e.* reconstructed, by first computing the unfiltered velocity based on an inverse filtering operation, known as a deconvolution of the filtered velocity. This operation can be achieved using Taylor series or the approximate deconvolution method (ADM)[14]. Including the RSFS stresses allows to take into account the backscatter of energy. Concerning the SGS stresses, Chow *et al.* (2005) elected a variant of the Germano-Lilly dynamics Smagorinsky SGS model, *i.e.* the dynamic Wong-Lilly SGS model (DWL), which is said to be simpler to implement and more stable than the classical Germano-Lilly while showing less difficulties close to the surface. However, to overcome under-dissipative nature of the dynamic procedure close to the surface, Chow *et al.* (2005) also used the Brown *et al.* (2001) canopy models as wall model.

Chow *et al.* (2005) evaluated the dynamic reconstruction model DRM-ARM based on Andren *et al.* (1994) case mostly focusing on the near-surface results. The standard Smagorinsky model is taken as a reference, and it is also evaluated and compared together with the dynamic Wong-Lilly (DWL) model. Concerning the results, first order moments from the DWL and the DRM-ARM SGS model are within 10 % of the similarity theory (with slight enhancement for the DRM-ARM) which is better than most of the approaches already discussed here. Differences between the DWL and the DRM-ARM models become clear in second order moments. DRM-ARM results show a smaller resolved vertical momentum flux, and a larger unresolved part. The SGS term is in fact, nearly equal between DWL and DRM-ARM, but the SFS is

[14] As a side note, when considering the simplest zeroth order series, the filtered and unfiltered velocity are equals and the scale similarity model of Bardina *et al.* (1980) is recovered.

increased due to the added effect of the RSFS stresses. By comparing with Direct Numerical Simulation (DNS) data and higher resolution results from the same case,Chow *et al.* (2005) shown that the SFS stresses from the DRM-ADM model are in much better agreement with the reference results than the DWL or the Smagorinsky models. The higher the order of the series to reconstruct the unfiltered velocity, the closer the results are from the reference data. However, even based on a low order series (≤ 2), results are clearly enhanced. Furthermore, with the DRM-ADM model results close to the surface are nearly unaffected by the grid, albeit the canopy model parameters require to be adapted as a function of the grid aspect ratio. Finally, in comparison to the Smagorinsky SGS model, the DWL model is roughly 20 % more computationally expensive and the DRM-ADM is at least 50 % more demanding (cost increase with the order of the series). Chow *et al.* (2005) found the DRM-ADM model with lower order series as been the optimum SGS model (enhancement/cost ratio).

As a result of the above, the DRM-ADM SGS model is very promising. Both first and second order moments are correctly reproduced and the approach is highly resilient to strongly deformated grid cell. The study also confirmed the relevance of accounting for the RSFS stresses (as previously proposed in a simplified manner by Bardina *et al.* (1980)) for the modelling of fully rough wall bounded high Reynolds number flows such as the neutral ABL.

1.3.2.3 Inclusion of thermal effects to SGS models

Thermal effects are coupled with shear processes and inhibit or enhance turbulent mixing in various manners. They affect production, dissipation of TKE in addition to the characteristic mixing length scale of the turbulence (Stull, 1988). The same general philosophy to include stratification effects with some exceptions is followed by LES as in mesoscale models, *i.e.* an additional conservation equation of the internal energy is solved (see Sec. 1.2.1), and surface boundary condition as well as momentum and heat SGS turbulent mixing are made dependent of the stratification (often through the use of Richardson number dependent functions). Classical and advanced SGS models dedicated to the neutral ABL can thus be generalized to include stratification effects, and as a side note, the same closure constant can be used since

the behaviour of the inertial subrange is not affected by stratification (but only its minimum wave number). However, as previously illustrated in Sec. 1.2.3.1 and 1.2.3, there are notable differences between unstable and stable regimes which affect SGS model abilities.

Convective ABL exhibit very large eddies of the size of the ABL and it is weakly influenced by the history of the flow (Stull, 1988; Moeng and Sullivan, 1994). Turbulence is produced by both shear and convective processes resulting in free or forced convection depending on the ratio of both processes (see Sec. 1.2.3.1). For $z_i/L_{MO} \leq -4.5$, convection processes become dominant and convective scaling, such as the convection velocity w_*, become fully valid (Deardorff, 1972; Moeng and Sullivan, 1994). Nieuwstadt *et al.* (1992) achieved the first LES intercomparison based on a freely convective ABL. They evaluated the same models as in Andren *et al.* (1994) intercomparison (except the backscatter SGS model). Very promising results were obtained and it was clearly demonstrated that SGS models have little influence on the results, albeit the impact of the Smagorinsky constant on quantities such as $\overline{w'^2}$ was illustrated. Differences between models were notably smaller than for the equivalent neutral intercomparison of Andren *et al.* (1994). In fact, most of the eddies of a convective ABL are resolved in LES which explains the small impact of the subgrid scale models (smaller than in neutral and stable conditions notably close to the surface) (Nieuwstadt *et al.*, 1992; Mason, 1994; Sullivan *et al.*, 1994; Mason and Brown, 1999; Ding *et al.*, 2001a). As a result, convective ABL are easier to reproduce than neutral or stable ABL since coarse meshes and simple SGS models can be used with a reasonable success (Sullivan *et al.*, 1994). This explains why early LES studies were mostly focusing on the convective ABL (Deardorff, 1972; Sommeria, 1976). However, it is noteworthy that SGS models applied to the convective ABL also need to be able to deal with stable stratification since the entrainment layer as well as the free atmosphere are stably stratified. Simple parametrizations were proven to lead to satisfying results (Mason, 1994; Sullivan *et al.*, 1994; Sorbjan, 2005a). As a result of the above, it is generally admitted that dry convective ABL over a flat homogeneous terrain are well understood and correctly reproduced by means of LES even using relatively simple SGS models (Nieuwstadt *et al.*, 1992; Sullivan *et al.*, 1994; Mason and Brown, 1999; Sorbjan, 2005a; Teixeira *et al.*, 2008).

On the other hand, stable ABL are shallow, tend to feature small eddies and they heavily rely on the history of the flow (Teixeira *et al.*, 2008). Depending on the strength of the stability, turbulence can be intermittent with turbulent patches travelling with the flow. Only shear processes produce turbulence while the stable stratification inhibit it (Stull, 1988). Backscatter of energy is also more significant in the stable surface layer (Brown *et al.*, 1994; Kosović and Curry, 2000). One of the first intercomparison of LES models for the stable ABL was achieved by Beare *et al.* (2006), *i.e.* GABLS 1 http://gabls.metoffice.com/. Eleven models were compared: two standard Smagorinsky, five TKE based, two dynamics Smagorinsky, two backscatter and one two-part eddy viscosity models. It was clearly demonstrated that SGS models play a larger role in stable than in neutral and convective conditions, and very fine grids are required for LES to properly simulate it. While classical SGS models have been heavily used, their simplistic representation of the subgrid scale turbulence is more problematic to properly reproduce stable ABL. Beare *et al.* (2006) further suggested that advanced SGS models are more efficient than classical ones by requiring a lower resolution to reach an equivalent quality. They were also more independent of the grid. As an example, they concluded that for a moderately stable ABL ($h/L_{MO} = 2$, h being the height of the stable boundary layer), a grid resolution of 6.25 m would produce a reasonable accuracy (of the order of 20 %) but a grid resolution of 3.125 m or lower would be ideal for a robust LES of such a case. As a consequence, the stable ABL is very challenging, computationally demanding and advanced SGS models are required if a realistic grid is to be used. The interest from the LES research community to better understand and model stable ABL has tremendously increased only very recently (Beare *et al.*, 2006; Teixeira *et al.*, 2008). This can be illustrated by the fourteen years that passed between the first intercomparison for convective and stable ABL.

In this section, the mainstream LES models dedicated to the stratified ABL are illustrated and discussed. Note that thermal effects are generally implemented by extending LES models of the neutral ABL. The latter were previously reviewed, and as a results, only the enhancements to take into account thermal processes are presented here. Both stable and convective ABL are considered and the section is organized following the great families of SGS models, as

previously done. Thus, the inclusion of the stratification is first presented for the Smagorinsky SGS model, and then for the TKE based SGS models.

1.3.2.3.1 Smagorinsky SGS model

Many adaptation of the Smagorinsky SGS model discussed in Sec. 1.3.2.2.1.1 were developed to be able to deal with the stratification and the full non-adiabatic ABL, see Deardorff (1972); Mason (1989); Brown *et al.* (1994); Ding *et al.* (2001a) for some examples. Every author introduces its own version, but the fundamental philosophy generally remains equivalent. The Large Eddy Model (LEM) from the UKMO Mason and Thomson (1987); Mason (1989); Mason and Thomson (1992); Brown *et al.* (1994); Mason and Brown (1999); Brown *et al.* (2000) is an established model and it can be taken as an example to illustrate the adaptations needed to take into account the stratification based on the Smagorinsky approach.

By extension to the standard Smagorinsky SGS model, Lilly (1962) and later Mason (1989) proposed the following expression of the eddy viscosity coefficient in stratified conditions

$$\nu_t = \lambda_r^2 S \left(1 - \mathrm{Ri}_f\right)^{1/2}, \tag{1.11}$$

where Ri_f is the local subfilter flux Richardson number, and λ_r is the characteristic length scale of turbulence. Most Smagorinsky SGS models dedicated to the non-adiabatic ABL rely on this definition of the eddy viscosity or a variant. In its simplest form, as used by Lilly (1962), λ_r is set equal to its neutral value, *i.e.* λ as defined in Eq. (1.4), which leads to consider only the direct influence of the buoyancy on the energy production (Mason and Thomson, 1992) and not on the turbulence length scale. As a result, λ_r has also to be a function of Ri_f and, notably, it must tend to zero as a critical Richardson number is reached, as underlined by Brown *et al.* (1994) and Delage (1997). This was later confirmed by Mason and Brown (1999), who shown that both the subgrid TKE and the length scale needed to be buoyancy dependent.

The heat mixing coefficient is commonly defined thanks to the turbulent Prandtl number such as $\nu_h = \nu_t / \mathrm{Pr}_t$. The latter was generally taken as constant in the early studies (before 1990),

which is suitable for convective ABL. However, it was found experimentally (such as in the Kansas measurement campaign) that Pr_t should also be a function of the stratification in stable condition (Brown *et al.*, 1994).

Following the above considerations, Brown *et al.* (1994) expressed the momentum and heat mixing coefficients as follow

$$\nu_t = \lambda^2 S f_m\left(\mathrm{Ri}\right), \tag{1.12}$$

$$\nu_h = \lambda^2 S f_h\left(\mathrm{Ri}\right), \tag{1.13}$$

where f_m and f_h are stability functions that depend on the local gradient Richardson number Ri (*i.e.* calculated based on the local surrounding cells) which can be conveniently expressed as follow $\mathrm{Ri} = N^2/S^2$ where S is the rate of strain modulus and N is the Brunt-Väisälä frequency. Concerning the Smagorinsky constant, Beare *et al.* (2006) found that a value lower than 0.2 is desirable for the Stable boundary layer modelling.

Stability functions f_m and f_h are derived from experimental observations of the ABL surface layer, as presented earlier in Sec. 1.2.3.1 for environmental model (Stull, 1988). Stability function from the UKMO Smagorinsky SGS model are further described in Sec. 2.2.3.1.2, see also Brown *et al.* (1994); Gray *et al.* (2001). Based on these function, the eddy viscosity expression shown in Eq. (1.11) is recovered in convective conditions. On the contrary and as suggested by experimental observations, in stable conditions, Pr_t is allowed to be stratification dependent going from 0.7 in convective and neutral conditions to 1 as the critical Richardson number Ri_c is reached. Above Ri_c, $f_m = f_h = 0$ and thus subgrid turbulence is avoided. As a side note, differences exist with mesoscale models notably in stable conditions due to the significantly higher resolution of LES (Brown *et al.*, 1994; Delage, 1997). Indeed, the local mesoscale Richardson number is at some point equivalent to the LES domain averaged Richardson number. As a result, in the mesoscale context, turbulence subsist (at least in patches) at the subgrid scale for Ri higher than its critical value, increasing the effective subgrid mixing (Beare *et al.*, 2006). At the opposite, a critical Richardson number is not well suited in the LES context (Ma-

son, 1994; Delage, 1997; Beare *et al.*, 2006). Note finally that, several forms for the stability functions have been proposed for use with the Smagorinsky SGS model (Brown *et al.*, 1994; Ding *et al.*, 2001a; Beare *et al.*, 2006).

Finally, concerning advanced models based on the Smagorinsky approach, Mason and Thomson (1992) stochastic backscatter SGS model was refined by Brown *et al.* (1994) and applied to the stables ABL. This approach is identical to the Smagorinsky SGS model described above, albeit it include the backscatter of energy as described in Sec. 1.3.2.2.2.2. Note that Brown *et al.* (1994) also added a new backscatter term for the potential temperature. This approach is found to notably improve the results in stable (and neutral) conditions (Brown *et al.*, 1994; Mason, 1994; Beare *et al.*, 2006), while it does not have a significant impact on the results in unstable conditions (Mason and Brown, 1999). The two-part eddy viscosity SGS model proposed by Ding *et al.* (2001a) and Ding *et al.* (2001b) introduced in Sec. 1.3.2.2.2.1 is also designed to deal with non-neutral full ABL. However, unlike Sullivan *et al.* (1994), this two-part eddy viscosity model (based on the Smagorinsky approach) is also applied to the temperature. MO similarity theory is used to compute the mean field eddy-viscosity, *i.e.* the inhomogeneous term of the two-part eddy viscosity SGS model. The model was found to properly perform from moderately stable to convective conditions clearly improving the results from the standard Smagorinsky model (Ding *et al.*, 2001a,b). However, this approach requires that similarity theory is valid. Finally, it is to underline that applications of dynamic Smagorinsky SGS models to the stratified ABL are more scarce due to their added complexity and requirement in computational time. However, Beare *et al.* (2006) clearly shown they are very appealing and at least as capable as the backscatter approaches.

1.3.2.3.2 TKE based SGS model

TKE based SGS models have received a large attention from the environmental modelling community as discussed previously and as an example, classical TKE based SGS models represent half of the schemes in the Beare *et al.* (2006) recent intercomparison. In fact, the extra information provided by the prognostic equation for TKE is useful or even required for the

parametrization of others processes such as cloud microphysics (Deardorff, 1980) which explain their success. The TKE based SGS model proposed by Deardorff (1980) is a simple yet complete SGS model that is fully able to deal with thermal stratification of the full ABL (Moeng and Sullivan, 1994). This model was introduced in Sec. 1.3.2.2.1.2 for neutral conditions. It is today considered by many authors as a reference TKE based SGS model dedicated to the full ABL (Moeng and Sullivan, 1994; Sullivan *et al.*, 1994; Cuxart *et al.*, 2000; Redelsperger *et al.*, 2001; Sorbjan, 2005a), and most of TKE based advanced approaches share a similar philosophy to take into account thermal stratification, *i.e.* inclusion of an additional production terms in the TKE equation and adaptation of the mixing and dissipation length scales as a function of the stratification. This model can thus serve as an example in the same way the UKMO Smagorinsky model served us in the previous section.

In the Deardorff (1980) SGS model, eddy viscosity and diffusivity are given by

$$\nu_t = C_k \lambda k^{1/2}, \tag{1.14}$$

$$\nu_h = \frac{\nu_t}{\mathrm{Pr}_t} \qquad \text{with} \qquad \mathrm{Pr}_t = \left(1 + \frac{2\lambda}{\Delta}\right)^{-1}, \tag{1.15}$$

where the various quantities are similar to Eq. (1.5). The mixing length is directly equal to the filter width, *i.e.* $\lambda = \Delta$, in neutral and convective conditions. As a result, the increase of subgrid mixing in buoyant conditions is solely taken into account thorough the subgrid TKE and resolved quantities. On the contrary, in stable conditions λ is a function of the stratification though a ratio equivalent to a Richardson number, *i.e.* $\lambda = \min\left(\Delta, 0.76k^{1/2}/N\right)$. This definition for stable conditions allows the mixing length to become much smaller than the grid resolution so that the subgrid mixing can be lower and even avoided in very stable regions. Furthermore, the Prandtl number Pr_t becomes a function of the stratification in stable conditions. This is on par with UKMO Smagorinsky SGS model (Brown *et al.*, 1994). While simple, such a parametrization of the length scale allows to properly reproduce the stable inversion at the top of the ABL (Sullivan *et al.*, 1994). It is generally accepted (Moeng, 1984; Moeng and Sullivan, 1994; Sullivan *et al.*, 1994; Kosović and Curry, 2000; Sorbjan, 2005a).

Additional terms appear in the subgrid scale TKE equation when considering internal energy. Under the Boussinesq shallow convection approximation (see Stull (1988)), the same TKE equation as presented in Eq. (1.8) is obtained with simply an additional buoyancy production term. The latter, which rely on the parametrization of the heat flux, can be either positive in convective conditions, or negative in stable conditions (as opposed to the shear production terms that is always positive). This approach is generally accepted to model the increase or decrease of subgrid TKE as a function of the stratification, which in turn affect turbulence mixing coefficients (Deardorff, 1980; Moeng and Sullivan, 1994; Sullivan *et al.*, 1994; Kosović and Curry, 2000; Sorbjan, 2005a).

As an example of a variant of the Deardorff TKE based SGS model, Sommeria (1976); Redelsperger and Sommeria (1981) also proposed a simple TKE based SGS model dedicated to the non-neutral full ABL. Cuxart *et al.* (2000) latter implemented this SGS model in the Meso-NH mesoscale model and Redelsperger *et al.* (2001) further enhanced this SGS model by better considering physical processes of the surface layer. Sommeria/Redelsperger SGS model share the same general philosophy as the one of Deardorff (1980). However, mixing length is always independent of the stratification (albeit Cuxart *et al.* (2000) underline that this would be required for stable stratification), and more importantly, complex stability function based on bulk Richardson numbers are used to scale the various turbulent flux, similarly as in the UKMO Smagorinsky SGS model. Several studies confirmed that Sommeria/Redelsperger approach is as suitable as the Deardorff (1980) SGS model for a wide range of stratification (Sommeria, 1976; Redelsperger and Sommeria, 1981, 1986; Cuxart *et al.*, 2000; Redelsperger *et al.*, 2001; Drobinski *et al.*, 2004; Beare *et al.*, 2006; Drobinski *et al.*, 2007).

However, as underlined by Beare *et al.* (2006), such classical SGS models are too simplistic to correctly reproduce the complex phenomena taking place in the stably stratified ABL with a realistic mesh. Advanced SGS model that better take into account the subgrid physical processes are far more appealing.

The two-part eddy viscosity SGS model of Sullivan *et al.* (1994) introduced in Sec. 1.3.2.2.2.1 was also designed to deal with non-neutral flows. The latter is mostly based on Deardorff (1980) SGS model in the flow interior. Thus, all the adaptation presented above are included in Sullivan *et al.* (1994) SGS model. Furthermore, the mean field eddy-viscosity, *i.e.* the inhomogeneous term of the two-part eddy viscosity, is computed relying on MO similarity theory. This approach was proven to enhance the results for neutral and slightly unstable case (Sullivan *et al.*, 1994), and this model was also used successfully during GABLS 1 stable ABL intercomparison (Beare *et al.*, 2006). Interestingly, Sullivan *et al.* (1994) found that applying the two-part eddy viscosity concept to the momentum only (and not to the temperature as opposed to Brown *et al.* (1994) and Ding *et al.* (2001a)), was sufficient to notably improve both velocity and temperature profiles close to the surface, albeit in unstable conditions.

Finally, Kosović and Curry (2000) introduced a SGS model able to deal with stable stratification that is based on the Kosović (1997) non-linear Backscatter SGS model previously introduced in Sec. 1.3.2.2.2.2. Kosović and Curry (2000) followed the ideas of Deardorff (1980) to include stratification, however mixing length scale is always set equal to the filter width, and only the dissipation length scale is explicitly a function of the stratification. Furthermore, the latter is also a function of the magnitude of the resolved shear in order to also take into account the shear production of TKE in stable regions. Kosović and Curry (2000) evaluated the model based on a quasi-steady stable ABL for which experimental measurement were available[15]. The approach was found promising, and results from GABLS 1 intercomparison (Beare *et al.*, 2006) shown that it was on par with the Mason and Thomson (1992) stochastic backscatter SGS models and dynamic SGS models.

1.3.3 LES of the heterogeneous surface ABL

Heterogeneous surface ABL further adds important challenges to the already non-trivial LES of the full ABL. It requires that not only the model perform properly in homogeneous conditions, but also that some of the aspects of the SGS model as well as the operating mode are

[15] As a side note, this cases was latter selected as the reference case of the GABLS 1 LES intercomparison (Beare *et al.*, 2006).

adapted. Indeed, because of the surface heterogeneities, the problem do not feature anymore homogeneous directions preventing a host of simplification in both the SGS models and the operating mode of the LES approach. As an example, periodicity of lateral boundaries of the domain, *i.e.* inlet, outlet and sides, which was largely simplifying their treatment, in addition to allow for ensemble averages and fast Fourier transform, is not well suited anymore for most heterogeneous cases. This also affect the post-processing in a similar manner.

Heterogeneous cases can be either theoretical or real. Real cases are however more challenging to deal with due to the non-controlled environment: several types of discontinuities have generally to be represented, and lateral boundary conditions are more complex to prescribe. Furthermore, there are a general lack of appropriate data to validated LES models in real conditions (Teixeira *et al.*, 2008; Shaw *et al.*, 2009). All these fact, explain why LES of real heterogeneous surface ABL is non-trivial and very scarce in the literature.

In this section, the various challenges of heterogeneous cases are briefly introduced and some possible approach to address them are discussed. First, the general consideration for the LES of heterogeneous cases are first presented. Then, the abilities of the various SGS models previously introduced in the context of an homogeneous surface ABL are quickly explored.

1.3.3.1 General considerations

The LES of ABL over heterogeneous surface present large differences in their common aspects compared to the LES over homogeneous surface. Because the surface is heterogeneous, the flow over it and its properties are also statistically heterogeneous. As a result, approaches and methods (SGS model, wall model and post-processing) relying on the ensemble averaged in space are invalid in the context of an heterogeneous surface, restraining their use to cases with at least one homogeneous direction. As an example, SGS models based on ensemble averages, such as Sullivan *et al.* (1994) or the Germano-Lilly dynamic SGS model (Germano *et al.*, 1991; Lilly, 1992) are not valid anymore. This represent one of the major complications faced by LES for heterogeneous and real cases.

Concerning the boundaries of the computational domain, the surface is generally processed as for homogeneous cases, *i.e.* the no-slip rough wall is modelled through wall functions, see Sec. 1.3.2.1.1.1. However, for all the cases not featuring an homogeneous direction, the models such as the one of Schumann (1975) is not anymore valid, and only wall models based on local quantities can be used. Furthermore, relying on the usual wall function based on the MO similarity is not always appropriate such as in recirculating zones as underlined by Piomelli (2008). Orography can be taken into account either using cell-blocking approach or using terrain following vertical coordinate (oblique and orthogonal) as discussed respectively in Sec. 1.1.3.2 and Sec. 1.2.2.3. The latter is generally preferred for real cases. The surface boundary condition is further discussed in the next section.

Concerning the inlet, outlet and lateral boundary conditions, unless an infinite repetition of the same surface feature is considered such as in Hobson *et al.* (1999) study, periodical lateral boundary condition are not suitable for the LES of surface heterogeneous cases. Thus, other inlet, outlet and lateral boundary conditions need to be prescribed while being able to freely let eddy in and out of the computational domain.

At the inlet, fully developed ABL need thus to be explicitly prescribed. This can be achieved based on an analytical/statistical mathematical representation of the ABL (Iizuka and Kondo, 2004), which can go from averaged profiles simply perturbed with scaled random numbers to a more advanced and faithful representation of the turbulence. Instead of fully manually prescribes the inlet, one can also let the turbulence develop by itself following a wind tunnel like approach (Uchida and Ohya, 2003), *i.e.* using explicit obstacles to generate turbulent structures. However, these approaches are far from being trivial, and generally, a long enough upstream domain is needed to let the turbulence properly develop which is computationally expensive

An other way to prescribe the inlet, which is the most common, is to use a precursor simulation based on an homogeneous surface and fully periodic boundary conditions (Bechmann, 2006; Bechmann and Sørensen, 2010; Silva Lopes *et al.*, 2007; Chow and Street, 2009). Such a simulation allow to obtain a fully developed ABL flow as discussed in the previous section,

that is stored in a wind database. Then, the result from this simulation is used as inlet and sometimes lateral boundary conditions of an heterogeneous problem not anymore periodical. Note that Chow and Street (2009) however reported some numerical instabilities and had to use a so-called pressure detrending to avoid problems. This two levels approach is somewhat straightforward, however it is expensive when considering storage requirement since at least inlet and sometimes lateral boundaries are needed at every time steps to drive the the advanced simulation. In the same manner, recycle boundary condition can also be used, *i.e.* the flow at the outlet of an upstream domain serve as inlet of the computational domain and are also re-injected at the inlet of the upstream domain such as what was done in the periodical case.

Concerning the others boundary, at the outlet, a Neumann zero gradient boundary condition can be used (Iizuka and Kondo, 2004; Bechmann, 2006; Bechmann and Sørensen, 2010; Chow and Street, 2009). However, Bechmann (2006) reported some numerical problems in the region close to the outlet and had to use a buffer region. They also showed that, while more complex, a convective boundary condition such as used by Silva Lopes *et al.* (2007) and Uchida and Ohya (2003) gives better results. Concerning the lateral boundary conditions (sides), depending of the case free-slipping wall (Uchida and Ohya, 2003; Chow and Street, 2009) or periodic conditions are generally used (Iizuka and Kondo, 2004; Bechmann, 2006; Bechmann and Sørensen, 2010; Silva Lopes *et al.*, 2007). Finally, a top boundary similar to the homogeneous cases is generally used as described in Sec. 1.3.2.1, and most of the time a free shear boundary condition is used (Uchida and Ohya, 2003; Bechmann, 2006; Bechmann and Sørensen, 2010; Silva Lopes *et al.*, 2007; Chow and Street, 2009). However, in some cases a symmetry condition is adopted (Iizuka and Kondo, 2004) but this is more for CWE problems were the model is compared to wind tunnel data.

Finally, inlet lateral, outlet and top boundary conditions can also be prescribed following a nesting-like approach as described in Sec. 1.2.2.4 (Drobinski *et al.*, 2004, 2007). This is very appealing with regards to real cases and environmental modelling. As a side note this approach is also interesting when the flow is turning with height such as when the Coriolis acceleration is considered since inlet, outlet and sides of the domain are less well defined.

In conclusion, it is to note that many possible approaches exist to provide the model with suitable inlet, lateral and outlet boundary conditions.

1.3.3.2 Quick review of SGS models

Over an heterogeneous surface, the processes illustrated for the homogeneous surface ABL merge with the processes induced by surface heterogeneities increasing the level of complexity of flow features. Furthermore, surface heterogeneities first affect the flow close to the surface, *i.e.* the surface layer, a region already challenging for LES-NWM models as introduced previously (Piomelli, 2008). As a result, independently to the intrinsic abilities and limitation of each SGS model, a prerequisite is that the lower part of the ABL must be reproduced properly in homogeneous conditions if one wants to simulate complex flow features caused by inhomogeneities. This explains why most of the studies dedicated to the heterogeneous surface ABL, first validate the model for an homogeneous surface (Bechmann, 2006; Silva Lopes *et al.*, 2007; Chow and Street, 2009). However, this does not guarantee that the wall is correctly modelled in the context of heterogeneous surface as seen at the end of this section (Piomelli, 2008). Last but not least, it is noteworthy that all the approaches relying on an horizontal averaging of any kind are not anymore appropriate in the context of an heterogeneous surface ABL which further restrict the possible LES approaches to model ABL flows over an heterogeneous surface.

Cases similar to the one discussed in the CWE section, Sec. 1.1.3.2, are used to evaluate the LES models. Thus, the vast majority of studies tackling heterogeneous surface consider only the neutral ABL, few full scale experimental dataset exist and many studies rely on wind tunnel dataset for the validation of the models (with the limitation associated to them). The reader is referred to Sec. 1.1.3.2 for further discussion concerning the various available test cases. Here, it is to underline that most of the recent studies focusing on the evaluation of LES model over a full scale topography are based on the Askervein hill experiment (Silva Lopes *et al.*, 2007; Chow and Street, 2009; Bechmann and Sørensen, 2010). Those studies further allowed to better understand the flow above this very popular test case, confirming among other things the intermittency of separation in the lee-side of the hill.

Clark (1977) was among the first to implement a classical Smagorinsky SGS model considering the temperature and including of the topography by means of an oblique curvilinear vertical coordinate. This study was however focusing on gravity waves and a free-slip surface boundary condition was used. More recently, Murakami (1998) reviewed the challenges and compared the abilities of various LES over a bluff body. While this study focuses on CWE, it clearly illustrates the limitations of the classical SGS models, *i.e.* the over-dissipative nature of these pure eddy viscosity models, but more importantly, the need to adapt the model closure constant as a function of the flow fields (as already discussed previously). Murakami (1998) described the latter as particularly critical in the context of flow around bluff bodies, and thus by extension for flow above an heterogeneous surface. Indeed, flow fields induced by heterogeneities include various types of flow features such as separation, free shear layer, impinging, vortex shedding, etc. As a result, it is difficult to select one adequate value of the Smagorinsky constant knowing that each of the flow features, which location is a priori unknown, would ideally requires its proper value of the constant. In a general manner, when considering isolated surface heterogeneities such as a single hill, the results in the upwind region are little influenced by the difference of the SGS models used (albeit the homogeneous surface ABL is well reproduced and the inlet boundary is correctly prescribed), but there are generally large differences in the wake region (Murakami, 1998; Iizuka and Kondo, 2004; Silva Lopes *et al.*, 2007; Piomelli, 2008; Chow and Street, 2009; Bechmann and Sørensen, 2010). The standard Smagorinsky SGS model generally underestimates the length of the reverse flow region (Murakami, 1998; Iizuka and Kondo, 2004). Similarly, the classical TKE based SGS model predict a too low TKE level and a too high speed-up in the lee side of the hill (Chow and Street, 2009).

The over-dissipative nature of classical SGS models can be overcome by using a backscatter model or the Bardina scale-similarity approach as discussed in the previous section (Murakami, 1997, 1998; Brown *et al.*, 2001; Chow and Street, 2009). Similarly, this can be achieved using a dynamic SGS model that allow negative values of the model coefficient. As an example of the importance of such processes, Murakami (1998, Fig. 10) shows an instantaneous horizontal cross-section around a cube of the dynamically obtained Smagorinsky constant with various

dynamic SGS models. On that figure, it can be seen that the model coefficient is negative (indicating that backscatter of energy take place) in a non-negligible part of the cross-section. In that sense, (Chow and Street, 2009) demonstrated the enhancement obtained by using a reconstruction (deconvolution) model along with the classical TKE based SGS model. The additional information retrieved thanks to the reconstruction model, *i.e.* the RSFS stresses, clearly enhance the results, and even the simplest reconstruction model, which is said to be equivalent to the scale-similarity model, is found to greatly improve the results in the lee-side of the hill. In fact, results on par with the others more advanced dynamic models evaluated are obtained with this simpler model which thus appears as optimum.

The dynamic Smagorinsky approaches are very appealing for the LES of heterogeneous surface ABL due to their self-adaptation properties, and many studies have shown their clear advantages over classical models (Murakami, 1997, 1998; Iizuka and Kondo, 2004; Silva Lopes *et al.*, 2007; Piomelli, 2008). However, in addition to their higher computational cost, the dynamical computation of the constant generally induce numerical instability similar but worse than in the homogeneous context. Furthermore, cases generally do not feature homogeneous directions preventing from using ensemble average of the model constant. Murakami (1998) underlined the too intense fluctuations of the constant of the Germano-Lilly dynamic SGS model which affect the numerical stability of the model and the results. As a consequence, many studies have focused on this limitation using more advanced and mixed dynamic SGS models. Murakami (1998) and other subsequent studies such as Chow and Street (2009) found that the dynamics Smagorinsky SGS model mixed with a backscatter or scale similarity models notably increased the stability of the model while reducing by the computational cost. Advanced dynamic approaches such as the Lagrangian dynamic SGS model (Meneveau *et al.*, 1996) also have a similar positive effect. The latter is perfectly stable and also reduce the computational time compared to classical dynamic SGS models (Murakami, 1998; Silva Lopes *et al.*, 2007). However, the Lagrangian dynamic SGS model avoid backscatter effects which need to be explicitly included (as opposed to the classical dynamic approach). The addition of

the latter was proven to further improve the results while reduce the computational cost of the approach while improving the results (Murakami, 1998; Chow and Street, 2009).

A last challenging aspect of LES of the heterogeneous surface ABL is the representation of the fully aerodynamically rough surface along with the prediction of the flow in the first few meshes above the ground. Indeed, the wall model and the SGS model adaptations in the near-surface region not only must allow the correct prediction of MO similarity for an homogeneous surface, but also require to be able to go beyond since the latter are generally not valid in the context of heterogeneous surface (which is worsen when a coarse resolution is used) (Piomelli, 2008). As a result, the two part eddy viscosity SGS models of Sullivan *et al.* (1994) and Ding *et al.* (2001a) are not anymore valid since they fully rely on the MO similarity (and horizontal ensemble average) to obtain the inhomogeneous eddy viscosity and the isotropic factor. Hybrid RANS/LES approaches appear to be promising to address such a problem as demonstrated by Bechmann and Sørensen (2010). Close surface region, which is under-resolved by LES, is predicted based on a RANS model (using of a high resolution highly deformated meshes), which allows the model to go beyond MO similarity notably closer to the ground than if just a LES model was used. However, Bechmann and Sørensen (2010) failed to reproduce the intermittency of the recirculation, but they used a classical TKE based SGS model in the flow interior. Similar limitation are however found with dynamic approaches. As an example, Iizuka and Kondo (2004) illustrated that a dynamic SGS model was failing to reproduce a recirculation region in the back side of a hill due to the misrepresentation of the region close to the surface. Similarly, while Silva Lopes *et al.* (2007) used the advanced wall model of Marusic *et al.* (2001) along with a canopy model and a Lagrangian dynamic Smagorinsky SGS model, they still noticed problems in the prediction of the eddy viscosity close to the ground. This was said to be the cause of the models misrepresentation of the recirculation zone in the lee-side of the hill. While the intermittency of the recirculation was well reproduced, its intensity was increasing with a finer mesh (toward experimental results).

1.3.4 Summary of LES of ABL

In this section, a review of the main aspects of LES of the ABL was presented focusing on the various challenges and limitations of the different approaches introduced in the literature.

After briefly introducing the ABL in view of LES approaches, the LES of the homogeneous surface ABL was thoroughly discussed and it was seen that it is still an open field of research far from being trivial. A first section was dedicated to the common aspects of LES of the ABL over an homogeneous surface, *i.e.* boundary conditions, driving the flow, and initialization. The challenge of LES of a no-slip wall bounded flow were discussed along the large differences that exist between the LES-NWR and LES-NWM, and it was explained why the fully aerodynamically rough surface of the ABL is very challenging for LES. Both classical and advanced SGS models require a wall model which has profound implications in LES of the ABL. A panel of popular SGS models was then presented in the context of the adiabatic ABL. The classical SGS models, *i.e.* the Smagorinsky SGS model and the Deardorff TKE based SGS model, were first introduced along their main properties and limitations notably in the region close to the surface where the flow is under-resolved. These simple models are based on the sole eddy viscosity approximation. They are over-dissipative and the closure constant need to be adjusted manually. As a result, they are clearly biased in the near-surface region where they depart from the MO similarity theory. This drove a large interest from the research community for the last couple of decade, and while it was thought for longtime that the only way to avoid such a bias was to use more advanced SGS models or apply a dedicated treatment in this region of the computational domain, we saw that this shortcoming could be avoided by simply properly setting the grid and closure constants. Subsequently, advanced SGS models based on both implicit (two-part eddy viscosity, backscatter, hybrid RANS/LES SGS models) and explicit (scale similarity, dynamics Smagorinsky and reconstruction SGS models) filtering were introduced presenting the underlying philosophy of each approach along with the enhancement they bring and their limitations. These models generally address the limitations of the classical SGS model, at least in the near-surface region. As a general rule, the more an approach is advanced, the less it is biased, but this does not imply that they are more computationally

expensive. The dynamic Smagorinsky SGS models were found very promising notably when mixed with other approaches that better take into account the subgrid and subfiltered physical processes and their interaction with resolved flow such as backscatter of energy. However, due to their under-dissipative nature in the region close to the wall, they still require a fine tuning of the bottom boundary to properly perform. While many other approaches are discussed in the books of Lesieur *et al.* (2005); Sagaut (2006), this section was meant to illustrate the capabilities of various SGS model in the context of an adiabatic homogeneous surface ABL. It was clearly seen that it is still very challenging notably concerning the near-surface region which is an open subject of research.

The thermally stratified ABL over an homogeneous surface was then considered along the inclusion of thermal effects in SGS models. The challenges for LES of the various flow regimes were first introduced and it was seen that not only the SGS model but also the solver need to be properly designed. It was clearly underlined that convective conditions are generally easier to reproduce based on LES due to the dominance of buoyant production of turbulence and the large size of the eddies. At the opposite, it was seen that stable stratification is very challenging and that the interest from the research community has notably increased in the recent years. Various approaches to include thermal effects in SGS models were then presented focusing on the classical Smagorinsky and Deardorff TKE based SGS models.

Finally, we proceeded to a quick review of the LES of the ABL over an heterogeneous surface and real cases. The various common aspects were first discussed illustrating the important differences and limitation implied by the non-homogeneous surface: the flow at the inlet boundary need to be explicitly provided, cases do not generally feature homogeneous directions and MO similarity are not anymore always valid. It was thus shown that, regardless of the SGS model, the simple application of LES to such cases is tricky. The abilities of the various SGS models previously introduced were then discussed. It was seen that due to their intrinsic limitations, classical SGS models are clearly unable to predict much of the complex flow features induced by heterogeneities (notably in the lee-side). Advanced SGS models partly address these limitations especially concerning the dynamics Smagorinsky SGS models and hybrid RANS/LES

approaches. However, while being the most appealing and outperforming RANS models, they still present some difficulties in the region close to the wall leaving room for improvements.

To conclude it is to say that due to its abilities and the increase of the computational resources, LES is becoming more and more popular in ours days. Furthermore, LES models present interesting features allowing to address the various challenges of the processes within the mesoscale microscale range as discussed by Teixeira *et al.* (2008) and Shaw *et al.* (2009) and a promising approach is to use a LES model as a last level of nesting of a mesoscale model (Drobinski *et al.*, 2007). However, a gap remains before a straightforward application of LES for full scale real cases such as in the wind energy context. As an example, during the recent model intercomparison based on the Bolund experiment (Bechmann *et al.*, 2010), no LES model was present in the top ten results. Interestingly, while the opposite would have been expected, RANS models were outperforming all LES models.

1.4 General conclusion of the review

All along this chapter, the various approaches dedicated to the modelling of ABL flows were reviewed, illustrating their main properties, strengths and weaknesses. While wind energy applications were not at the centre of the various discussions, the ultimate goal was to define which of these approaches or combination could be the most appropriate to address the challenges faced by the wind energy industry.

A first section was dedicated to methods used in CWE to model the ABL. Second order RANS approaches such as the fine-tuned $k - \varepsilon$ models are found to be the most promising. They are currently more and more popular in the wind energy domain due to their balance between computational time and performance. However, turbulence is fully modelled and they are not well suited to reproduce unsteady and transient phenomena. As a result, they struggle when the flow is too complex notably in the lee-side of obstacles (Ayotte, 2008; Sumner *et al.*, 2010). Furthermore, most of the time, CWE implementations consider only the neutral surface layer neglecting the Coriolis effect. While these are good approximations when dealing with typical microscale engineering problems, it is not appropriate for larger scale problems ($>$

10 km) (Wyngaard, 2004; Shaw *et al.*, 2009). Furthermore, the ABL is effectively almost never in a neutral state. As a results, this introduces errors, notably when considering flow over complex terrain since stratification has a strong non-linear effect. Similarly, surface layer stratification has an important effect on the production of wind turbine (Shaw *et al.*, 2009).

A second section addressed environmental modelling approaches, *i.e.* mesoscale models. These approaches are dedicated to the simulation of large scale unsteady atmospheric flows considering the full ABL and the free atmosphere above a rotating sphere (Holton, 2004). They rely on very advanced and coupled solvers of the conservation equations (Steppeler *et al.*, 2003) and include parametrizations of all the main processes taking place in the full scale ABL. Due to their typical horizontal resolution (> 1 km), the ABL is modelled by means of ABL column model and the unsteady RANS one-and-a-half order $k-l$ turbulent closures are among the most popular. They are sufficiently skilled for a wide range of stratifications, while being relatively simple (Stull, 1988). Mesoscale approaches thus offer very promising features allowing to take into account the environment in which wind turbines operate (Shaw *et al.*, 2009). Furthermore, they are already essential tools for both forecasting and wind resource assessment (Landberg *et al.*, 2003a,b). However, their parametrization of the ABL and turbulence, *i.e.* column model, is generally too simplistic to be valid at a resolution higher than 1 km (Teixeira *et al.*, 2008; Shaw *et al.*, 2009). Below this scale, while the solver of conservation equations does not present theoretical limits, 3D turbulent closures are required for a realistic modelling of the ABL (Wyngaard, 2004).

In a last section, LES of the ABL was thoroughly discussed (see Sec. 1.3.4 for a summary). These approaches are able to almost fully resolve and reproduce the dynamic structure of the unsteady ABL. In that sense, they are closer to mesoscale models than CWE RANS approaches. They are well suited to address the multiscale nature of the ABL (Drobinski *et al.*, 2007). Only the subgrid part of the flow, which is generally very small except in the near-surface region for LES-NWM, is modelled by means of a SGS model. Momentum and sometimes internal energy are considered by the solver and the SGS model, and the Coriolis effect is also commonly included. Standard Smagorinsky and Deardorff TKE based SGS models are

very popular due to their relative simplicity. However, they are over-dissipative and present important limitations notably in the near-surface region where LES is under-resolved (Andren *et al.*, 1994). This can be partly addressed by using more advanced SGS model such as the very popular dynamic Smagorinsky SGS model. However, these latter approaches also require to be finely tuned to properly predict the flow in the surface layer, notably over an heterogeneous surface. As a result, and as opposed to CWE and environmental modelling, there are no general agreements on a best suited LES approach that feature the optimum balance between performance and simplicity (Piomelli, 2008). Furthermore, these approaches are significantly more computationally demanding than RANS models (a ten fold ratio), and due to the restrictions with regards to the resolution (~ 10 m), their computational cost was for a long time too high to allow their application on large domains (> 10 km) (Wyngaard, 2004; Shaw *et al.*, 2009).

Modern wind turbines feature a hub height at roughly 100 m agl with a rotor diameter of a similar scale. They are thus located in the upper part of the surface layer or even above in stable conditions. For their part, modern wind farm usually extend over more than 10 km, triggering both microscale and the mesoscale processes. Considering those simple facts, it is clear that wind energy facilities are within the microscale-mesoscale gap. The latter is sometimes referred to as "Terra incognita" (Wyngaard, 2004) due to the lack of understanding of the complex interactions between mesoscales and microscales processes. Indeed, both numerical and experimental research interest have for a long time mostly focused on the already challenging pure microscale and mesoscale issues as illustrated during this literature review. As a result, there is today a lack of numerical approach and experimental data that would allow the study of the microscale mesoscale transition (Wyngaard, 2004; Teixeira *et al.*, 2008), which is notably detrimental for wind energy applications (Shaw *et al.*, 2009).

In view of the specificities and abilities of the various models discussed in this literature review, it appears that a multiscale modelling approach integrating mesoscale and LES models may be the most natural and appropriate method to tackle the microscale mesoscale gap (Shaw *et al.*, 2009). Such a method would benefit from the environmental and large scale modelling abilities from the mesoscale model, while being highly skilled to simulate the flow at the microscale.

To that end, it is relevant to consider implementing a SGS modelling approach in a mesoscale model (along with all the other required components allowing 3D turbulence modelling) as recently proposed and proven to properly perform by few research groups (Cuxart *et al.*, 2000; Chow *et al.*, 2005; Klemp and Skamarock, 2004; Drobinski *et al.*, 2007). This would allow to seamlessly model atmospheric flows from the large scales to the microscales. However, for such an approach to perform properly, the solver of conservation equations of the mesoscale model must able to deal with the unsteady fine structures typical of microscales ($\sim$ 10 m). Furthermore, SGS model put aside, the new components of the mesoscale model such as the 3D turbulent diffusion also need to be thoroughly validated. It can be achieved based on a well known simple classical SGS model (such as the standard Smagorinsky of the TKE based SGS models) and relying on various test cases for which both the solution and the behaviour of classical SGS model are known. Once the new LES-capable mesoscale approach is demonstrated to perform on par with other reference LES models from the literature, it will be possible to enhance the SGS model following the promising approaches introduced in this review.

In order to follow this path, the MC2 mesoscale model from EC was elected as a basis. The dynamic kernel of MC2 is known to perform properly in a wide-range of scales ranging from blood vessels to the general circulation (Pinty *et al.*, 1995; Laprise *et al.*, 1997; Benoit *et al.*, 1997). Furthermore, Pelletier *et al.* (2005) started to implement the missing required components to allow MC2 to operate as a LES model. Among other things, the Smagorinsky SGS model and a modified TKE based SGS model as well as 3D turbulent diffusion were added to MC2 by Pelletier *et al.* (2005). However, this promising work was halted without evaluating validity and performances of neither the solver in the context of LES of the full ABL, nor the newly implemented components. The present study thus pursues Pelletier *et al.* (2005) achievements and is aimed at the validation and refinements of the LES-capable MC2 approach.

CHAPTER 2

MATHEMATICAL MODEL

The Compressible Community Mesoscale Model (MC2) is the fruit of more than 20 years of development at the "Recherche en Prévision Numérique" (RPN) research group of the Canadian Meteorological Centre (CMC), Environment Canada (EC). This state-of-the-art mesoscale model was first devoted to large scale applications such as weather forecasting, climate studies as well as numerical research.

MC2 solves the Euler equations of motion without approximations based on a Semi-Implicit, Semi-Lagrangian (SISL) time stepping. This represents the dynamic kernel of MC2. It have been refined and validated in the context of mesoscale modelling along the years (Robert *et al.*, 1985; Tanguay *et al.*, 1990; Bergeron *et al.*, 1994; Pinty *et al.*, 1995; Benoit *et al.*, 1997; Laprise *et al.*, 1997; Thomas *et al.*, 1998; Girard *et al.*, 2005). It is known to be suitable for a wide spectrum of atmospheric processes and other types of fluid. The dynamic kernel is complemented with models of all the relevant physical processes that require to be parametrized (*i.e.* turbulent diffusion). This component, which is also referred to as the physics (or physics library), is common to other CMC mesoscale models. Resolved processes are thus simulated through the dynamic kernel while modelled processes are parametrized in the physics.

The physics has been enhanced along the years notably by refining models and taking into account more processes (Mailhot and Benoit, 1982; Delage, 1988; Benoit *et al.*, 1989; Girard and Delage, 1990; Delage and Girard, 1992; Benoit *et al.*, 1997; Delage, 1997; Mailhot *et al.*, 1998; Bélair *et al.*, 1999). However, until recently it was only considering vertical exchanges relying on the horizontal homogeneity hypothesis (*i.e.* a column model). While such an approach is well suited in the mesoscale context (Stull, 1988; Holton, 2004; Cuxart *et al.*, 2006; Svensson and Holtslag, 2006), it does not allow the proper modelling of ABL flows for horizontal meshes smaller than one kilometre (Wyngaard, 2004). Work initiated by Pelletier *et al.* (2005) intended to include the required features to allow the MC2 to perform as a LES model.

In the present chapter, the mathematical model of both the dynamic kernel and the physics of MC2 is presented. In a first section, fundamental equations are developed relying on Favre averaging to obtain a system of equations in the form solved by MC2. Then, the model for turbulent processes is presented by detailing momentum and heat 3D turbulent diffusion, sub-grid scale (SGS) models, the 3D TKE equation, and lastly the column model. Finally, other components required to properly perform LES of the full ABL with MC2 are introduced.

2.1 Fundamental equations

Assuming the only force acting on a dry atmosphere are pressure, gravitation and friction, then the second law of Newton, the first thermodynamic principle, conservation of mass and the state equation can be written as follows (Stull, 1988; Holton, 2004)

$$\frac{d\boldsymbol{v}}{dt} + f\boldsymbol{k} \times \boldsymbol{v} + \frac{1}{\rho}\boldsymbol{\nabla} p + g\boldsymbol{k} = \mathbf{f}, \tag{2.1a}$$

$$\frac{dT}{dt} - \frac{1}{\rho c_p}\frac{dp}{dt} = \frac{Q}{c_p}, \tag{2.1b}$$

$$\frac{1}{\rho}\frac{d\rho}{dt} + \boldsymbol{\nabla} \cdot \boldsymbol{v} = 0, \tag{2.1c}$$

$$p = \rho R T. \tag{2.1d}$$

where $\boldsymbol{v}$ is the velocity vector, p the pressure, T the absolute temperature, ρ the density, f and Q non-conservative forces and heat sources, g the gravitational acceleration, f the Coriolis factor, and c_p the heat capacity of dry air at constant pressure.

Then, using the potential temperature definition

$$T = \theta\pi, \tag{2.2}$$

where π is the Exner function given by

$$\pi = \left(\frac{p}{p_0}\right)^{R/c_p}, \tag{2.3}$$

with p_0 is a reference pressure and R the gas constant for dry air, and Eq. (2.1) can be transformed in flux form in the perspective of filtering, with for any variable ψ

$$\rho\frac{d\psi}{dt} = \rho\frac{\partial\psi}{\partial t} + \rho\boldsymbol{v}\cdot\boldsymbol{\nabla}\psi = \frac{\partial\rho\psi}{\partial t} + \boldsymbol{\nabla}\cdot\rho\boldsymbol{v}\psi, \tag{2.4}$$

one can obtain the Navier-Stokes equations in flux form (Wilcox, 1994)

$$\frac{\partial\rho\boldsymbol{v}}{\partial t} + \boldsymbol{\nabla}\cdot\rho\boldsymbol{v}\boldsymbol{v} + f\boldsymbol{k}\times\rho\boldsymbol{v} + \boldsymbol{\nabla}p + \rho g\boldsymbol{k} = \rho\mathbf{f}, \tag{2.5a}$$

$$\frac{\partial\rho\theta}{\partial t} + \boldsymbol{\nabla}\cdot\rho\boldsymbol{v}\theta = \frac{\rho Q}{c_p\pi}, \tag{2.5b}$$

$$\frac{\partial\rho}{\partial t} + \boldsymbol{\nabla}\cdot\rho\boldsymbol{v} = 0, \tag{2.5c}$$

$$p = \rho RT. \tag{2.5d}$$

2.1.1 Filtered Navier-Stokes equations

Favre filtering allows to eliminate density fluctuations from equations while retaining their general character (Wilcox, 1994). For any variable ψ, this latter decomposition writes

$$\psi' = \psi - \widetilde{\psi} \qquad \text{with} \qquad \widetilde{\psi} = \frac{\overline{\rho\psi}}{\overline{\rho}} \tag{2.6}$$

where, as defined in Eq. (A II-8), $\widetilde{\psi}$ is the Favre filtered value of ψ, ψ' is the associated perturbation, and, for any variable ψ, the usual decomposition of the turbulent fields writes

$$\psi\text{`} = \psi - \overline{\psi} \tag{2.7}$$

where ψ‘ is the perturbation associated to the filtered value $\overline{\psi}$ as shown in Eq. (A II-11). Further details on the filtering of turbulent fields can be found is Sec. 2.

Thus, by decomposing $\boldsymbol{v}$, θ and the source terms using Favre filtering

$$\boldsymbol{v} = \widetilde{\boldsymbol{v}} + \boldsymbol{v}', \tag{2.8a}$$

$$\theta = \widetilde{\theta} + \theta', \tag{2.8b}$$

$$\mathbf{f} = \widetilde{\mathbf{f}} + \mathbf{f}', \tag{2.8c}$$

$$Q = \widetilde{Q} + Q', \tag{2.8d}$$

and ρ and p based on classical Reynolds decomposition

$$\rho = \overline{\rho} + \rho', \tag{2.8e}$$

$$p = \overline{p} + p', \tag{2.8f}$$

and further assuming that (Wilcox, 1994)

$$\widetilde{T} \approx \widetilde{\theta}\overline{\pi} = \widetilde{\theta}\left(\frac{\overline{p}}{p_0}\right)^{R/c_p}, \tag{2.9}$$

the flux form Favre filtered conservation equations are obtained (Wilcox, 1994)

$$\frac{\partial \overline{\rho}\widetilde{\boldsymbol{v}}}{\partial t} + \boldsymbol{\nabla}\cdot\left(\overline{\rho}\widetilde{\boldsymbol{v}}\widetilde{\boldsymbol{v}} + \overline{\rho\boldsymbol{v}'\boldsymbol{v}'}\right) + f\boldsymbol{k}\times\overline{\rho}\widetilde{\boldsymbol{v}} + \boldsymbol{\nabla}\overline{p} + \overline{\rho}g\boldsymbol{k} = \overline{\rho}\widetilde{\mathbf{f}}, \tag{2.10a}$$

$$\frac{\partial \overline{\rho}\widetilde{\theta}}{\partial t} + \boldsymbol{\nabla}\cdot\left(\overline{\rho}\widetilde{\boldsymbol{v}}\widetilde{\theta} + \overline{\rho\boldsymbol{v}'\theta'}\right) = \frac{\overline{\rho}\widetilde{Q}}{c_p\overline{\pi}}, \tag{2.10b}$$

$$\frac{\partial \overline{\rho}}{\partial t} + \boldsymbol{\nabla}\cdot\overline{\rho}\widetilde{\boldsymbol{v}} = 0, \tag{2.10c}$$

$$\overline{p} = \overline{\rho}R\widetilde{T}. \tag{2.10d}$$

Finally, by posing for any Favre averaged variables $\widetilde{\psi}$ that

$$\frac{\widetilde{d}\widetilde{\psi}}{dt} = \frac{\partial\widetilde{\psi}}{\partial t} + \widetilde{\boldsymbol{v}}\cdot\boldsymbol{\nabla}\widetilde{\psi}, \tag{2.11}$$

the Favre averaged advective form of the equations is obtained

$$\frac{\widetilde{d}\widetilde{\boldsymbol{v}}}{dt} + f\boldsymbol{k}\times\widetilde{\boldsymbol{v}} + \frac{1}{\overline{\rho}}\boldsymbol{\nabla}\overline{p} + g\boldsymbol{k} = \widetilde{\mathbf{f}} - \frac{1}{\overline{\rho}}\boldsymbol{\nabla}\cdot\overline{\rho\boldsymbol{v}'\boldsymbol{v}'} \quad = \widetilde{\mathbf{F}}, \tag{2.12a}$$

$$\frac{\widetilde{d}\widetilde{\theta}}{dt} = \frac{\widetilde{Q}}{c_p\overline{\pi}} - \frac{1}{\overline{\rho}}\boldsymbol{\nabla}\cdot\overline{\rho\boldsymbol{v}'\theta'} = \frac{\widetilde{\mathcal{Q}}}{c_p\overline{\pi}}, \tag{2.12b}$$

$$\frac{\widetilde{d}\ln\overline{\rho}}{dt} + \boldsymbol{\nabla}\cdot\widetilde{\boldsymbol{v}} = 0, \tag{2.12c}$$

$$\overline{p} = \overline{\rho}R\widetilde{T}. \tag{2.12d}$$

This system of equations is similar to Eq. (2.1). However, going from the advective to the flux form, then filtering and going back to the advective form, allowed to isolate two new terms on the right-hand side of Eq. (2.12). They are the turbulent momentum and heat turbulent fluxes which are unresolved (subfilter part) and that have to be modelled.

Finally, it is noteworthy that, in the present case, the same system of equations is obtained whether the so-called Favre averaging is based on time or space filtering. Indeed, as discussed in Sec. 2.2.4, since the grid is used as spatial filter, *i.e.* implicit filtering, Leonard tensor vanishes, and thus the subfilter stress tensor directly equals the Reynolds stress tensor (Pope, 2000). As a consequence, this set of equations can be used for both RANS and LES.

2.1.2 Modified set of equation

Using the state equation Eq. (2.1d), density can be suppressed from Eq. (2.1) (density becomes implicit) to obtain the following modified set of equations

$$\frac{d\boldsymbol{v}}{dt} + f\boldsymbol{k}\times\boldsymbol{v} + RT\boldsymbol{\nabla}q + g\boldsymbol{k} = \mathbf{f}, \tag{2.13a}$$

$$\frac{dT}{dt} - \frac{RT}{c_p}\frac{dq}{dt} = \frac{Q}{c_p}, \tag{2.13b}$$

$$\frac{c_v}{c_p}\frac{dq}{dt} + \boldsymbol{\nabla}\cdot\boldsymbol{v} = \frac{Q}{c_pT}, \tag{2.13c}$$

where $q = \ln(p/p_0)$ and p_0 is a reference pressure. Note that in the present study, it is considered that there is no external forcing. As a result, heat sources Q disappear as well as $\mathbf{f}$. Those terms are however retained in what follows.

By neglecting all viscous effects (molecular and turbulent), this system represents the complete Euler equations of motion. The Semi-Implicit Semi-Lagrangian (SISL) scheme of the MC2 is based on this set of equations (Thomas *et al.*, 1998; Girard *et al.*, 2005) (source of heat in the mass conservation equation are further considered as negligible in these studies).

2.1.2.1 Modified Favre filtered set of equation

Following the same procedure, an equivalent Favre averaged form of the modified system Eq. (2.13) can be obtained. Density is first substituted in Eq. (2.12) using Eq. (2.12d) to get

$$\frac{\widetilde{d}\widetilde{\boldsymbol{v}}}{dt} + f\boldsymbol{k}\times\widetilde{\boldsymbol{v}} + \frac{R\widetilde{T}}{\overline{p}}\boldsymbol{\nabla}\overline{p} + g\boldsymbol{k} = \widetilde{\mathbf{F}}, \tag{2.14a}$$

$$\frac{\widetilde{d}\ln\widetilde{\theta}}{dt} = \frac{\widetilde{\mathcal{Q}}}{c_p\widetilde{T}}, \tag{2.14b}$$

$$\frac{\widetilde{d}}{dt}\left(\ln\left(\frac{\overline{p}}{R\widetilde{T}}\right)\right) + \boldsymbol{\nabla}\cdot\widetilde{\boldsymbol{v}} = 0. \tag{2.14c}$$

Further considering that $\widetilde{T} \approx \widetilde{\theta}\overline{\pi}$ and using derivative chain rules[1], we obtain

$$\frac{\widetilde{d}\widetilde{\boldsymbol{v}}}{dt} + f\boldsymbol{k}\times\widetilde{\boldsymbol{v}} + R\widetilde{T}\boldsymbol{\nabla}\ln\overline{p} + g\boldsymbol{k} = \widetilde{\mathbf{F}}, \tag{2.15a}$$

$$\frac{1}{\widetilde{T}}\frac{\widetilde{d}\widetilde{T}}{dt} - \frac{1}{\overline{\pi}}\frac{\widetilde{d}\overline{\pi}}{dt} = \frac{\widetilde{\mathcal{Q}}}{c_p\widetilde{T}}, \tag{2.15b}$$

$$\frac{1}{\overline{p}}\frac{\widetilde{d}\overline{p}}{dt} - \frac{1}{\widetilde{T}}\frac{\widetilde{d}\widetilde{T}}{dt} + \boldsymbol{\nabla}\cdot\widetilde{\boldsymbol{v}} = 0. \tag{2.15c}$$

Then, introducing $\overline{q}$ such as

$$\overline{q} = \ln\left(\frac{\overline{p}}{p_0}\right) \quad \text{which implies} \quad \ln\overline{\pi} = \frac{R}{c_p}\overline{q}, \tag{2.16}$$

[1] $[f(g)]' = g'f'(g)$ and $[f/g]' = (f'g - fg')/g^2$

we obtain the system

$$\frac{\widetilde{d}\widetilde{\boldsymbol{v}}}{dt} + f\boldsymbol{k} \times \widetilde{\boldsymbol{v}} + R\widetilde{T}\boldsymbol{\nabla}\overline{q} + g\boldsymbol{k} = \widetilde{\mathbf{F}}, \tag{2.17a}$$

$$\frac{\widetilde{d}\widetilde{T}}{dt} - \frac{R\widetilde{T}}{c_p}\frac{\widetilde{d}\overline{q}}{dt} = \frac{\widetilde{\mathcal{Q}}}{c_p}, \tag{2.17b}$$

$$\frac{\widetilde{d}\overline{q}}{dt} - \frac{1}{\widetilde{\overline{T}}}\frac{\widetilde{d}\widetilde{T}}{dt} + \boldsymbol{\nabla} \cdot \widetilde{\boldsymbol{v}} = 0. \tag{2.17c}$$

At this point only the continuity equation Eq. (2.17c) needs to be adapted for the system Eq. (2.17) to be perfectly similar to Eq. (2.13). By substituting the temperature material derivative in Eq. (2.17c) using Eq. (2.17b), the continuity equation Eq. (2.17c) then becomes

$$\frac{\widetilde{d}\overline{q}}{dt} - \frac{1}{\widetilde{T}}\left[\frac{\widetilde{\mathcal{Q}}}{c_p} - \frac{R\widetilde{T}}{c_p}\frac{\widetilde{d}\overline{q}}{dt}\right] + \boldsymbol{\nabla} \cdot \widetilde{\boldsymbol{v}} = 0, \tag{2.18}$$

$$\frac{c_v}{c_p}\frac{\widetilde{d}\overline{q}}{dt} + \boldsymbol{\nabla} \cdot \widetilde{\boldsymbol{v}} = \frac{\widetilde{\mathcal{Q}}}{c_p\widetilde{\overline{T}}} \tag{2.19}$$

and thus, the final system of equation can be written as

$$\frac{\widetilde{d}\widetilde{\boldsymbol{v}}}{dt} + f\boldsymbol{k} \times \widetilde{\boldsymbol{v}} + R\widetilde{T}\boldsymbol{\nabla}\overline{q} + g\boldsymbol{k} = \widetilde{\mathbf{F}}, \tag{2.20a}$$

$$\frac{\widetilde{d}\widetilde{T}}{dt} - \frac{R\widetilde{T}}{c_p}\frac{\widetilde{d}\overline{q}}{dt} = \frac{\widetilde{\mathcal{Q}}}{c_p}, \tag{2.20b}$$

$$\frac{c_v}{c_p}\frac{\widetilde{d}\overline{q}}{dt} + \boldsymbol{\nabla} \cdot \widetilde{\boldsymbol{v}} = \frac{\widetilde{\mathcal{Q}}}{c_p\widetilde{T}}, \tag{2.20c}$$

which is equivalent to the system of equation Eq. (2.13) and thus equivalent to the form used by the model. However, under this form, density fluctuations are eliminated from filtered equations (Wilcox, 1994), and neglecting external forcing $\widetilde{\mathbf{f}}$ and heat source $\widetilde{Q}$ does not suppress the right hand side of the system of equations Eq. (2.20) as it further includes non-linear products $-1/\overline{\rho}\,\boldsymbol{\nabla} \cdot \overline{\rho\boldsymbol{v}'\boldsymbol{v}'}$ and $-1/\overline{\rho}\,\boldsymbol{\nabla} \cdot \overline{\rho\boldsymbol{v}'\theta'}$ that have to be modelled.

2.1.2.2 Changes of variables

To go further, the thermodynamic variables $\overline{q}$ and $\widetilde{T}$ are separated into the sum of a reference state and a deviation from this reference state as follows

$$\overline{q} = \overline{q}_* + \overline{q}'' \ = q_* + \overline{q}'' \ = \ln \frac{p_*}{p_0} + \ln \frac{\overline{p}}{p_*} = \ln \frac{\overline{p}}{p_0}, \tag{2.21}$$

$$\widetilde{T} = \widetilde{T}_* + \widetilde{T}'' = T_* + \widetilde{T}'', \tag{2.22}$$

where $T_* = \mathrm{const.}$ is a reference isothermal basic state, and q_* satisfies a stationary isothermal hydrostatic equilibrium, namely

$$\boldsymbol{\nabla}_H q_* = 0 \quad \text{and} \quad \nabla_z q_* = \frac{\partial q_*}{\partial z} = -\frac{g}{RT_*}, \tag{2.23}$$

which implies

$$\frac{\widetilde{d}q_*}{dt} = \widetilde{w}\frac{\partial q_*}{\partial z} = -\frac{g\widetilde{w}}{RT_*}. \tag{2.24}$$

Introducing this decomposition in the system Eq. (2.20) gives

$$\frac{\widetilde{d}\widetilde{\boldsymbol{v}}}{dt} + RT_*\boldsymbol{\nabla}\overline{q}'' - g\frac{\widetilde{T}''}{T_*}\boldsymbol{k} = \widetilde{\mathbf{F}} - f\boldsymbol{k}\times\widetilde{\boldsymbol{v}} - R\widetilde{T}''\boldsymbol{\nabla}\overline{q}'', \tag{2.25a}$$

$$\frac{\widetilde{d}\widetilde{T}''}{dt} - \frac{RT_*}{c_p}\frac{\widetilde{d}\overline{q}''}{dt} + \frac{g\widetilde{w}}{c_p} = \frac{\widetilde{\mathcal{Q}}}{c_p} - \frac{g\widetilde{T}''\widetilde{w}}{T_*c_p} + \frac{R\widetilde{T}''}{c_p}\frac{\widetilde{d}\overline{q}''}{dt}, \tag{2.25b}$$

$$\frac{c_v}{c_p}\frac{\widetilde{d}\overline{q}''}{dt} + \boldsymbol{\nabla}\cdot\widetilde{\boldsymbol{v}} - \frac{c_v}{c_p}\frac{g\widetilde{w}}{RT_*} = \frac{\widetilde{\mathcal{Q}}}{c_p(T_* + \widetilde{T}'')}. \tag{2.25c}$$

Furthermore, using a reference Brunt-Väisälä frequency N_* and sound speed c_* defined by

$$N_*^2 = g\left(\frac{\partial \ln T_*}{\partial z} + \frac{g}{c_pT_*}\right) = \frac{g^2}{c_pT_*}, \tag{2.26}$$

$$c_*^2 = \frac{c_p}{c_v}RT_*, \tag{2.27}$$

and using the mass conservation equation Eq. (2.25c) in order to replace the material derivative on the right-hand side of temperature equation Eq. (2.25b), we get

$$\frac{\widetilde{d}\widetilde{\boldsymbol{v}}}{dt} + RT_*\boldsymbol{\nabla}\overline{q'} - g\frac{\widetilde{T}''}{T_*}\boldsymbol{k} = \widetilde{\mathbf{F}} - f\boldsymbol{k}\times\widetilde{\boldsymbol{v}} - R\widetilde{T}''\boldsymbol{\nabla}\overline{q}'', \tag{2.28a}$$

$$\frac{\widetilde{d}\widetilde{T}''}{dt} - \frac{RT_*}{c_p}\frac{\widetilde{d}\overline{q}''}{dt} + \frac{T_*}{g}N_*^2\widetilde{w} = \frac{\widetilde{\mathcal{Q}}}{c_p}\left[1 + \frac{R\widetilde{T}''}{c_v(T_* + \widetilde{T}'')}\right] - \frac{R\widetilde{T}''}{c_v}\boldsymbol{\nabla}\cdot\widetilde{\boldsymbol{v}}, \tag{2.28b}$$

$$\frac{RT_*}{c_*^2}\frac{\widetilde{d}\overline{q}''}{dt} + \boldsymbol{\nabla}\cdot\widetilde{\boldsymbol{v}} - \frac{g}{c_*^2}\widetilde{w} = \frac{\widetilde{\mathcal{Q}}}{c_p(T_* + \widetilde{T}'')}. \tag{2.28c}$$

Finally, a buoyancy and a generalized pressure variables are introduced as

$$\widetilde{b} = g\frac{\widetilde{T}''}{T_*}, \tag{2.29}$$

$$\overline{P} = RT_*\overline{q}'', \tag{2.30}$$

and the system of five equations with five unknowns ($\widetilde{\boldsymbol{v}}$, $\widetilde{b}$ and $\overline{P}$) then becomes

$$\frac{\widetilde{d}\widetilde{\boldsymbol{v}}}{dt} + \boldsymbol{\nabla}\overline{P} - \widetilde{b}\boldsymbol{k} = \widetilde{\mathbf{F}} - f\boldsymbol{k}\times\widetilde{\boldsymbol{v}} - \frac{\widetilde{b}}{g}\boldsymbol{\nabla}\overline{P}, \tag{2.31a}$$

$$\frac{\widetilde{d}}{dt}\left(\widetilde{b} - \frac{N_*^2}{g}\overline{P}\right) + N_*^2\widetilde{w} = \frac{N_*^2}{g}\widetilde{\mathcal{Q}}\left[\frac{c_v g + c_p\widetilde{b}}{c_v g + c_v\widetilde{b}}\right] - \frac{R}{c_v}\widetilde{b}\,\boldsymbol{\nabla}\cdot\widetilde{\boldsymbol{v}}, \tag{2.31b}$$

$$\frac{1}{c_*^2}\frac{\widetilde{d}\overline{P}}{dt} + \boldsymbol{\nabla}\cdot\widetilde{\boldsymbol{v}} - \frac{g}{c_*^2}\widetilde{w} = \frac{N_*^2}{g}\widetilde{\mathcal{Q}}\left[\frac{1}{g + \widetilde{b}}\right]. \tag{2.31c}$$

Heat source from the mass conservation equations Eqs. (2.20c) and (2.25c) are commonly taken as negligible (Thomas *et al.*, 1998; Girard *et al.*, 2005), which leads to a simpler system identical to the one on which the MC2 model is based

$$\frac{\widetilde{d}\widetilde{\boldsymbol{v}}}{dt} + \boldsymbol{\nabla}\overline{P} - \widetilde{b}\boldsymbol{k} = \widetilde{\mathbf{F}} - f\boldsymbol{k}\times\widetilde{\boldsymbol{v}} - \frac{\widetilde{b}}{g}\boldsymbol{\nabla}\overline{P}, \tag{2.32a}$$

$$\frac{\widetilde{d}}{dt}\left(\widetilde{b} - \frac{N_*^2}{g}\overline{P}\right) + N_*^2\widetilde{w} = \frac{N_*^2}{g}\widetilde{\mathcal{Q}} - \frac{R}{c_v}\widetilde{b}\boldsymbol{\nabla}\cdot\widetilde{\boldsymbol{v}}, \tag{2.32b}$$

$$\frac{1}{c_*^2}\frac{\widetilde{d}\overline{P}}{dt} + \boldsymbol{\nabla}\cdot\widetilde{\boldsymbol{v}} - \frac{g}{c_*^2}\widetilde{w} = 0. \tag{2.32c}$$

where the internal energy conservation equation is also simpler than Eq. (2.31b) since it was obtained relying on the mass conservation equation Eq. (2.25c).

This system is independent of the coordinate system. It conveniently conserves a classical form as presented by Girard *et al.* (2005, Eqs. (5) and (6)) (Favre and Reynolds averaging put aside) while the formal inclusion of the filtering adds subfiltered non-linear terms that have to be modelled. The SISL approach implemented in MC2 can thus be applied straightforwardly to solve the filtered Euler equation of motion Eq. (2.32).

As seen in the next Chapter, the left-hand side of this system is quite general as it contains only material derivatives and linear forcing terms (acoustic and gravity waves) which allows for an implicit treatment (Girard *et al.*, 2005). On the other hand, the right-hand side contains non-linear and source term which require an explicit treatment. Taking the divergence of momentum, and eliminating the remaining variables thanks to the last two equations leads to an elliptic problem for $\overline{P}$. Subsequently, once $\overline{P}$ is obtained for the future time step, $\widetilde{b}$ and $\boldsymbol{v}$ can be deduced by appropriate back substitutions. This way, the system Eq. (2.32) is fully solved without any segregation of variables.

2.1.2.3 Summary

The system Eq. (2.32) can be rewritten in a matrix manner such as

$$\frac{\widetilde{d}\boldsymbol{\Psi}}{dt} + \boldsymbol{L} = \boldsymbol{R} + \boldsymbol{F}, \tag{2.33}$$

where the three first terms are computed during the solution of Euler equations

$$\boldsymbol{\Psi} = \begin{bmatrix} \widetilde{\boldsymbol{v}} \\ \widetilde{b} - \dfrac{N_*^2}{g}\overline{P} \\ \dfrac{\overline{P}}{c_*^2} \end{bmatrix}, \quad \boldsymbol{L} = \begin{bmatrix} \boldsymbol{\nabla}\overline{P} - \widetilde{b}\boldsymbol{k} \\ N_*^2\widetilde{w} \\ \boldsymbol{\nabla}\cdot\widetilde{\boldsymbol{v}} - \dfrac{g}{c_*^2}\widetilde{w} \end{bmatrix}, \quad \boldsymbol{R} = \begin{bmatrix} -f\boldsymbol{k}\times\widetilde{\boldsymbol{v}} - \dfrac{\widetilde{b}}{g}\boldsymbol{\nabla}\overline{P} \\ -\dfrac{R}{c_v}\widetilde{b}\boldsymbol{\nabla}\cdot\widetilde{\boldsymbol{v}} \\ 0 \end{bmatrix} \tag{2.34a}$$

and the forcing and source terms $\boldsymbol{F}$ are included afterwards in a fractional step manner

$$\boldsymbol{F} = \begin{bmatrix} \widetilde{\mathbf{F}} \\ \dfrac{N_*^2}{g}\widetilde{\mathcal{Q}} \\ 0 \end{bmatrix} = \begin{bmatrix} -\dfrac{1}{\overline{\rho}}\boldsymbol{\nabla}\cdot\overline{\rho\boldsymbol{v}'\boldsymbol{v}'} \\ -\dfrac{g\overline{\pi}}{\overline{\rho}\overline{T}_*}\boldsymbol{\nabla}\cdot\overline{\rho\boldsymbol{v}'\theta'} \\ 0 \end{bmatrix}. \tag{2.34b}$$

2.2 Turbulence modelling

The above system of equations, Eq. (2.32), can be fully solved (Girard *et al.*, 2005) at the exception of the non-linear velocity and temperature fluctuation products that appear after filtering Navier-Stokes equations. This is the well known turbulence closure problem (Stull, 1988; Wilcox, 1994; Pope, 2000). Those latter terms must be modelled and they write

$$\widetilde{\mathbf{F}} = -\frac{1}{\overline{\rho}}\boldsymbol{\nabla}\cdot\overline{\rho\boldsymbol{v}'\boldsymbol{v}'}, \tag{2.35}$$

$$\widetilde{\mathcal{Q}} = -\frac{c_p\overline{\pi}}{\overline{\rho}}\boldsymbol{\nabla}\cdot\overline{\rho\boldsymbol{v}'\theta'}. \tag{2.36}$$

The former, Eq. (2.35), represents the turbulent diffusion of momentum, *i.e.* the transport of momentum caused by turbulence, while the latter, Eq. (2.36), represents the turbulent diffusion of internal energy, *i.e.* the transport of heat caused by turbulence.

In this section, mathematical models of momentum and heat turbulent fluxes are presented[2].

2.2.1 Momentum turbulent diffusion

Momentum transfers solely due to turbulent diffusion can be expressed in Cartesian coordinates and tensorial notation such as

$$\left[\frac{d\widetilde{u}_i}{dt}\right]_{turb} = \frac{1}{\overline{\rho}}\frac{\partial}{\partial x_j}\left(-\overline{\rho u_i' u_j'}\right). \tag{2.37}$$

[2] Note that for convenience reasons, equations are based on a Cartesian coordinate system and tensorial notations are used in this section.

Turbulent momentum fluxes, also known as Reynolds stresses $\tau_{ij} = -\overline{\rho u_i' u_j'}$, need to be known in order to compute the mean properties of a turbulent flow. To close this problem, the eddy viscosity approximation is used. In the latter, the subfilter turbulent shear stresses τ_{ij} are related to the resolved rate of the strain S_{ij} (which trace S_{ii} is zero in incompressible conditions), *i.e.*

$$S_{ij} = \frac{1}{2}\left(\frac{\partial \widetilde{u}_i}{\partial x_j} + \frac{\partial \widetilde{u}_j}{\partial x_i}\right), \tag{2.38}$$

through a scalar turbulent eddy viscosity μ_t. This analogy with molecular viscosity was introduced by Boussinesq. Thus, it is often referred to as the Boussinesq (eddy viscosity) approximation, but it is sometimes called the gradient transport theory or the gradient diffusion assumption. In practice, the total viscosity becomes the sum of the molecular viscosity (property of the fluid) and the eddy viscosity (property of the flow). As a side note, considering that the ABL is a high Reynolds number flow, molecular viscosity is neglected in the present study. Under the above assumption, the Reynolds stress tensor can be expressed such as

$$\tau_{ij} = -\overline{\rho u_i' u_j'} = \underbrace{2\mu_t S_{ij}}_{\text{(I)}} \underbrace{- \frac{2}{3}\delta_{ij}\left(\mu_t S_{ll} + \overline{\rho} k\right)}_{\text{(II)}}, \tag{2.39}$$

where $\overline{\rho} k = 1/2\,\overline{\rho u_l' u_l'}$ is the subfiltered turbulent kinetic energy (TKE) (included since by definition it trace $\tau_{ll} = -2\overline{\rho} k$), and $\mu_t = \rho \nu_t = \rho K_M$ is the turbulent eddy viscosity.

In Eq. (2.39), term (I) can be called the deviatoric part of the Reynolds stress tensor (Mason and Thomson, 1987), and term (II) is the isotropic or volumetric part. Deviatoric stress distort fluid particle while isotropic stress tend to change their volume acting as a pressure (Pope, 2000).

Substituting Eq. (2.39) in Eq. (2.12a), it can be seen that the isotropic part of τ_{ij} can be subtracted from τ_{ij} and directly added to the pressure. The momentum conservation equation in Cartesian coordinate and tensorial notation which writes

$$\frac{\widetilde{d}\widetilde{u}_i}{dt} + f\varepsilon_{ij3}\widetilde{u}_j + \frac{1}{\overline{\rho}}\frac{\partial \overline{p}}{\partial x_i} + \delta_{i3} g = \frac{1}{\overline{\rho}}\frac{\partial}{\partial x_j}\left(-\overline{\rho u_i' u_j'}\right), \tag{2.40}$$

then becomes

$$\frac{\widetilde{d\widetilde{u}_i}}{dt} + f\varepsilon_{ij3}\widetilde{u}_j + \frac{1}{\overline{\rho}}\frac{\partial \overline{p}_{red}}{\partial x_i} + \delta_{i3}g = \frac{1}{\overline{\rho}}\frac{\partial}{\partial x_j}\left(2\overline{\rho}K_M S_{ij}\right), \tag{2.41}$$

with

$$\overline{p}_{red} = \overline{p} + \frac{2}{3}\overline{\rho}\left(K_M S_{ll} + k\right). \tag{2.42}$$

In that case, the problem can be directly solved for the reduce pressure $\overline{p}_{red}$ and only the non-diagonal terms of the Reynolds tensor (and part of the variances) need to be explicitly computed (Deardorff, 1972; Mason and Thomson, 1987; Wilcox, 1994; Pope, 2000). It conveniently reduces the number of term to compute, leading to the same results.

In the context of a compressible flow however, the use of such a reduced pressure is less convenient as density is constantly recomputed and the thermodynamic pressure is required. In this sense, such a variable change is not useful when density is implicit, and the isotropic part of the Reynolds tensor must be known and explicitly added to the pressure (Piomelli, 1999).

In the present model, viscous processes (molecular and turbulent) are neglected when solving the Euler equation of motion Eq. (2.32). Turbulent diffusion is then included afterwards in a fractional step manner (Benoit *et al.*, 1997) based on Eq. (2.35). This is thus equivalent to solve Eq. (2.33) considering only $\boldsymbol{\Psi}$, $\boldsymbol{L}$ and $\boldsymbol{R}$ and add $\boldsymbol{F}$ afterwards.

However, as discussed above, the isotropic part of Reynolds tensor, *i.e.* $-2/3\left(\overline{\rho}K_M S_{ll} + \overline{\rho}k\right)$, act as and impact directly the pressure. Thus, it must be added explicitly to the pressure. As a result, even if those terms are due to turbulence, they must to be removed from the Reynolds tensor (*i.e.* from $\boldsymbol{F}$) and included in $\boldsymbol{R}$ during the Euler solving step in Eq. (2.33). Thus, momentum turbulent diffusion terms that have to be included in the dynamic kernel write

$$\left[\frac{\widetilde{d\widetilde{u}_i}}{dt}\right]_{turb}^{dyn} = -\frac{2}{3\overline{\rho}}\frac{\partial}{\partial x_i}\left(\overline{\rho}K_M S_{ll} + \overline{\rho}k\right), \tag{2.43}$$

while the remaining diffusion terms are expressed as

$$\left[\frac{d\widetilde{u}_i}{dt}\right]_{turb}^{phy} = \frac{1}{\overline{\rho}}\frac{\partial}{\partial x_j}\left(2\overline{\rho}K_M S_{ij}\right). \tag{2.44}$$

Introducing Eqs. (2.43) and (2.44) in Eq. (2.33), $\boldsymbol{F}$ and $\boldsymbol{R}$ then become in Cartesian coordinate and tensorial notation

$$\boldsymbol{R} = \begin{bmatrix} f\widetilde{v} - \dfrac{\widetilde{b}}{g}\dfrac{\partial\overline{P}}{\partial x} - \dfrac{1}{\overline{\rho}}\dfrac{\partial}{\partial x}\left(\dfrac{2}{3}\left(\overline{\rho}K_M S_{ll} + \overline{\rho}k\right)\right) \\ -f\widetilde{u} - \dfrac{\widetilde{b}}{g}\dfrac{\partial\overline{P}}{\partial y} - \dfrac{1}{\overline{\rho}}\dfrac{\partial}{\partial y}\left(\dfrac{2}{3}\left(\overline{\rho}K_M S_{ll} + \overline{\rho}k\right)\right) \\ -\dfrac{\widetilde{b}}{g}\dfrac{\partial\overline{P}}{\partial z} - \dfrac{1}{\overline{\rho}}\dfrac{\partial}{\partial z}\left(\dfrac{2}{3}\left(\overline{\rho}K_M S_{ll} + \overline{\rho}k\right)\right) \\ -\dfrac{R}{c_v}\widetilde{b}\dfrac{\partial\widetilde{u}_i}{\partial x_i} \\ 0 \end{bmatrix}, \quad \boldsymbol{F} = \begin{bmatrix} \dfrac{1}{\overline{\rho}}\dfrac{\partial}{\partial x_i}\left(2\overline{\rho}K_M S_{i1}\right) \\ \dfrac{1}{\overline{\rho}}\dfrac{\partial}{\partial x_i}\left(2\overline{\rho}K_M S_{i2}\right) \\ \dfrac{1}{\overline{\rho}}\dfrac{\partial}{\partial x_i}\left(2\overline{\rho}K_M S_{i3}\right) \\ \dfrac{g\overline{\pi}}{\overline{\rho}T_*}\dfrac{\partial}{\partial x_i}\left(-\overline{\rho u_i'\theta'}\right) \\ 0 \end{bmatrix}.$$

In fact, in the present implementation of the 3D turbulent diffusion in MC2, the full subgrid velocity variances are included in $\boldsymbol{R}$ (*i.e.* the full terms from the Reynolds tensor diagonal). Thus, turbulent diffusion terms that are effectively included in the dynamic kernel write

$$\left[\frac{d\widetilde{u}_i}{dt}\right]_{turb}^{dyn} = \delta_{ij}\frac{1}{\rho}\frac{\partial}{\partial x_j}\left(-\overline{\rho u_i' u_j'}\right) \tag{2.45}$$

$$= \delta_{ij}\frac{1}{\overline{\rho}}\frac{\partial}{\partial x_j}\left(2\overline{\rho}K_M S_{ij} - \frac{2}{3}\overline{\rho}\left(K_M S_{ll} + k\right)\right), \tag{2.46}$$

while the remaining diffusion terms are expressed as

$$\left[\frac{d\widetilde{u}_i}{dt}\right]_{turb}^{phy} = (1-\delta_{ij})\frac{1}{\overline{\rho}}\frac{\partial}{\partial x_j}\left(-\overline{\rho u_i' u_j'}\right) \tag{2.47}$$

$$= (1-\delta_{ij})\frac{1}{\overline{\rho}}\frac{\partial}{\partial x_j}\left(2\overline{\rho}K_M S_{ij}\right). \tag{2.48}$$

Finally, after including Eqs. (2.46) and (2.48) in Eq. (2.33), $\boldsymbol{F}$ and $\boldsymbol{R}$ write

$$\boldsymbol{R} = \begin{bmatrix} f\widetilde{v} - \dfrac{\widetilde{b}}{g}\dfrac{\partial \overline{P}}{\partial x} + \dfrac{1}{\overline{\rho}}\dfrac{\partial}{\partial x}\left(2\rho K_M S_{11} - \dfrac{2}{3}\overline{\rho}\left(K_M S_{ll} + k\right)\right) \\ -f\widetilde{u} - \dfrac{\widetilde{b}}{g}\dfrac{\partial \overline{P}}{\partial y} + \dfrac{1}{\overline{\rho}}\dfrac{\partial}{\partial y}\left(2\rho K_M S_{22} - \dfrac{2}{3}\overline{\rho}\left(K_M S_{ll} + k\right)\right) \\ -\dfrac{\widetilde{b}}{g}\dfrac{\partial \overline{P}}{\partial z} + \dfrac{1}{\overline{\rho}}\dfrac{\partial}{\partial z}\left(2\rho K_M S_{33} - \dfrac{2}{3}\overline{\rho}\left(K_M S_{ll} + k\right)\right) \\ -\dfrac{R}{c_v}\widetilde{b}\dfrac{\partial \widetilde{u}_i}{\partial x_i} \\ 0 \end{bmatrix}, \tag{2.49}$$

$$\boldsymbol{F} = \begin{bmatrix} (1-\delta_{i1})\dfrac{1}{\overline{\rho}}\dfrac{\partial}{\partial x_i}\left(2\overline{\rho}K_M S_{i1}\right) \\ (1-\delta_{i2})\dfrac{1}{\overline{\rho}}\dfrac{\partial}{\partial x_i}\left(2\overline{\rho}K_M S_{i2}\right) \\ (1-\delta_{i3})\dfrac{1}{\overline{\rho}}\dfrac{\partial}{\partial x_i}\left(2\overline{\rho}K_M S_{i3}\right) \\ \dfrac{g\overline{\pi}}{\overline{\rho}T_*}\dfrac{\partial}{\partial x_i}\left(-\overline{\rho u_i'\theta'}\right) \\ 0 \end{bmatrix}. \tag{2.50}$$

2.2.2 Heat turbulent diffusion

Heat transfers solely due to turbulent diffusion can be expressed as

$$\left[\frac{d\widetilde{\theta}}{dt}\right]_{turb} = \frac{1}{\overline{\rho}}\frac{\partial}{\partial x_i}\left(-\overline{\rho u_i'\theta'}\right). \tag{2.51}$$

Following the same approach as for the momentum, turbulent heat flux vector, $\overline{\rho \boldsymbol{v}'\theta'}$, is assumed proportional to the mean temperature gradient so that

$$\overline{\rho u_i'\theta'} = -\frac{\mu_t}{\mathrm{Pr}_t}\frac{\partial \widetilde{\theta}}{\partial x_i}, \tag{2.52}$$

where Pr_t is the turbulent Prandtl number being the ratio between the momentum and thermal mixing coefficients. A turbulent temperature mixing coefficient can thus be defined such as

$$K_T = \frac{K_M}{\mathrm{Pr}_t}, \tag{2.53}$$

and heat transfer due to turbulent diffusion then become

$$\left[\frac{d\widetilde{\theta}}{dt}\right]_{turb}^{phy} = \frac{1}{\overline{\rho}}\frac{\partial}{\partial x_i}\left(\overline{\rho}K_T\frac{\partial\widetilde{\theta}}{\partial x_i}\right). \tag{2.54}$$

Finally, introducing Eq. (2.54) in Eq. (2.33) only modify $\boldsymbol{F}$, which can then be written as

$$\boldsymbol{F} = \begin{bmatrix} (1-\delta_{i1})\dfrac{1}{\overline{\rho}}\dfrac{\partial}{\partial x_i}\left(2\overline{\rho}K_M S_{i1}\right) \\ (1-\delta_{i2})\dfrac{1}{\overline{\rho}}\dfrac{\partial}{\partial x_i}\left(2\overline{\rho}K_M S_{i2}\right) \\ (1-\delta_{i3})\dfrac{1}{\overline{\rho}}\dfrac{\partial}{\partial x_i}\left(2\overline{\rho}K_M S_{i3}\right) \\ \dfrac{g\overline{\pi}}{\overline{\rho}T_*}\dfrac{\partial}{\partial x_i}\left(\overline{\rho}K_T\dfrac{\partial\widetilde{\theta}}{\partial x_i}\right) \\ 0 \end{bmatrix}. \tag{2.55}$$

2.2.3 Subgrid scale (SGS) models

Now that turbulent diffusion of momentum and heat have been described, the last quantities that need to be defined to close the problem are the turbulent eddy viscosity μ_t and the turbulent Prandtl number Pr_t, or in other words, the mixing coefficients of momentum K_M and heat K_T.

A simple yet representative model consists in defining the mixing coefficients as the product of a length scale l_t and a velocity scale u_t both representative of the turbulence, *i.e.* $\nu_t = l_t u_t$. This is also known as the mixing length approximation.

As seen in the literature review, those two quantities can take different forms. In the context of LES, the turbulent characteristic length scale is generally proportional to the 3D grid size

Δ, such as $l_t = C_t\Delta$. For the Smagorinsky type SGS models, the velocity scale is computed based on the product of the grid size by the modulus of the strain rate tensor, *i.e.* $u_t = \Delta S$ which leads to $\nu_t = C_t\Delta^2 S$ (with usually $C_t = C_S^2$). For SGS model including an equation for the TKE, we have $u_t = k^{1/2}$ which gives $\nu_t = C_t\Delta k^{1/2}$. Based on these simple considerations, several SGS model were proposed that further take into account both the no-slip rough surface and the thermal stratification to allow the reproduction of the full ABL with LES models.

In the present section, various aspects of five simple SGS models implemented in MC2 are described. Each of these SGS models integrates the basic features required to reproduce a dry ABL from the surface to the free atmosphere. A summary of the five SGS models is shown in Tab. 2.1, and their comparison for a shear and buoyancy driven ABL is presented in Sec. 4.4.1.

2.2.3.1 UKMO Smagorinsky SGS model

The Smagorinsky-Lilly approach is a local first order closure. This is the oldest and simplest SGS model (Lilly, 1962; Smagorinsky, 1963). A large amount of studies based on this SGS model have been published and the limitation of this approach are well understood and accepted by the community (Mason, 1994; Porté-Agel *et al.*, 2000; Pope, 2000).

The UK Meteorological Office (UKMO) has developed and validated an improved version of the Smagorinsky SGS model that integrates all the basic requirements to reproduce a complete ABL flow (from the surface to the free atmosphere) (Mason and Thomson, 1987; Mason, 1989; Mason and Thomson, 1992; Mason, 1994; Brown *et al.*, 1994; Hobson *et al.*, 1999; Mason and Brown, 1999; Brown *et al.*, 2000). It is thus able to deal with stable to unstable thermal stratification (and humidity and phase changes but this is out of the scope of the present study).

Following Brown *et al.* (1994) and Mason and Brown (1999), the momentum and heat mixing coefficients of the UKMO Smagorinsky SGS model are computed as follows

$$K_M = \lambda^2 f_m S, \tag{2.56}$$

$$K_T = \lambda^2 f_h S, \tag{2.57}$$

where λ is the neutral value of a characteristic length scale, f_m and f_h are stability functions that depend on the local gradient Richardson number Ri, and S is the modulus of the non-isotropic part of the strain rate tensor Eq. (2.38) that can be written as

$$S^2 = 2\left(S_{ij} - \frac{1}{3}\delta_{ij}S_{ll}\right)^2 \approx 2S_{ij}S_{ij} \tag{2.58}$$

$$= \frac{1}{2}\sum_{i,j=1}^{3}\left(\frac{\partial \widetilde{u}_i}{\partial x_j} + \frac{\partial \widetilde{u}_j}{\partial x_i} - \frac{2}{3}\delta_{ij}\frac{\partial \widetilde{u}_k}{\partial x_k}\right)^2 \tag{2.59}$$

In the literature, we usually have $S^2 = 2S_{ij}S_{ij}$ (Pope, 2000, Sec. 13.2.7). The divergence term, *i.e.* the trace of S_{ij}, which is zero in the incompressible context, is generally neglected. It is however no null in the compressible context. Thus, it is taken into account in order to explicitly remove the isotropic part of the tensor and strictly agrees with the definition of Reynolds stresses, Eq. (2.39) (Cuxart *et al.*, 2000; Pelletier *et al.*, 2005; Drobinski *et al.*, 2007).

Finally, in order to overcome the limitation related to the eddy viscosity approximation (that only relies on resolved fields to compute subgrid quantities and dissipate TKE), a stochastic backscatter model was also added to the classical UKMO Smagorinsky SGS model (Mason and Thomson, 1992). The latter proved to enhance the results in the surface layer and stably stratified regions (Mason and Thomson, 1992; Brown *et al.*, 1994; Andren *et al.*, 1994). The improvements are however negligible in convective conditions and in the mixed or Ekman layer (Mason and Brown, 1999; Brown *et al.*, 2000). As a first developmental step, this backscatter is not implemented in the present study and it shall be the topic of later studies.

2.2.3.1.1 Length scale

The characteristic length scale of the Smagorinsky SGS model is defined as the product of the Smagorinsky constant C_S and the characteristic grid size, *i.e.*

$$\lambda_0 = C_S\Delta. \tag{2.60}$$

This reference flow interior length scale is referred to as the filter width by the UKMO research group (Mason, 1994) (while other research groups consider Δ as the filter). This length scale is further matched asymptotically with a surface layer characteristic length scale such as

$$\frac{1}{\lambda^n} = \frac{1}{\lambda_0^n} + \frac{1}{\left(\kappa\left(z+z_0\right)\right)^n}, \tag{2.61}$$

where n is a surface matching parameter usually set to 2 (Mason and Thomson, 1992; Porté-Agel *et al.*, 2000).

Concerning the filter width Δ, following the UKMO approach, we have

$$\Delta = \max\left(\left(\Delta x \Delta y\right)^{1/2}, \left(\Delta x \Delta y \Delta z\right)^{1/3}\right), \tag{2.62}$$

$$= \max\left(\Delta_H, \Delta_{3d}\right), \tag{2.63}$$

where $\Delta_H = \left(\Delta x \Delta y\right)^{1/2}$ is the horizontal resolution, and $\Delta_{3d} = \left(\Delta x \Delta y \Delta z\right)^{1/3}$ is the 3D resolution. Δ is obtained locally and can thus evolve with height. Such a definition prevents the SGS model from being spuriously impacted when an anisotropic grid is used. Stretched grid in the vertical can thus be used while keeping λ unchanged.

2.2.3.1.2 Stability functions

The stability function used in the UKMO Smagorinsky SGS model, f_m and f_h, were obtained from experimental measurements. The functions described in Brown *et al.* (1994) and Mason and Brown (1999) are used here. They cover the whole range of stratification, *i.e.* from unstable (Mason, 1989; Mason and Brown, 1999) to stable stratification (Brown *et al.*, 1994), and are suitable for both neutral conditions and free convection limit. These functions are directly dependent of a local Richardson number, Ri, that can be defined as follow

$$\mathrm{Ri} = \frac{N^2}{S^2}, \tag{2.64}$$

where N^2 is the squared Brunt-Väisälä frequency of a dry atmosphere

$$N^2 = \frac{g}{\widetilde{\theta}} \frac{\partial \widetilde{\theta}}{\partial z}. \tag{2.65}$$

Concerning f_m and f_h, we have for unstable stratifications ($\mathrm{Ri} < 0$)

$$f_m = \left(1 - 16\mathrm{Ri}\right)^{1/2}, \tag{2.66}$$

$$f_h = \frac{1}{\mathrm{Pr}_N} \left(1 - 40\mathrm{Ri}\right)^{1/2}, \tag{2.67}$$

while in moderately stable conditions, *i.e.* Ri is subcritical ($0 \leq \mathrm{Ri} < \mathrm{Ri}_c$ with $\mathrm{Ri}_c = 0.25$)

$$f_m = \left(1 - \frac{\mathrm{Ri}}{\mathrm{Ri}_c}\right)^4, \tag{2.68}$$

$$f_h = \frac{1}{\mathrm{Pr}_N} \left(1 - \frac{\mathrm{Ri}}{\mathrm{Ri}_c}\right)^4 \left(1 - 1.2\mathrm{Ri}\right), \tag{2.69}$$

otherwise if $\mathrm{Ri}_c \leq \mathrm{Ri}$

$$f_m = f_h = 0. \tag{2.70}$$

The turbulent Prandtl number for neutral conditions is set to $\mathrm{Pr}_N = 0.7$. However, the effective turbulent Prandtl number Pr_t ($= K_M/K_T = f_m/f_h$) is a function of Ri. As seen in Mason and Brown (1999), this is believed to lead to better results in stably stratified regions in comparison with a classical approach where Pr_t is constant.

Stability functions are illustrated in Fig. 2.1, where it can be seen that both f_m and f_h increase notably when Ri become negative. The mixing is thus increased as the ABL become more unstable. At the opposite, subgrid mixing quickly vanish when Ri increases above zero.

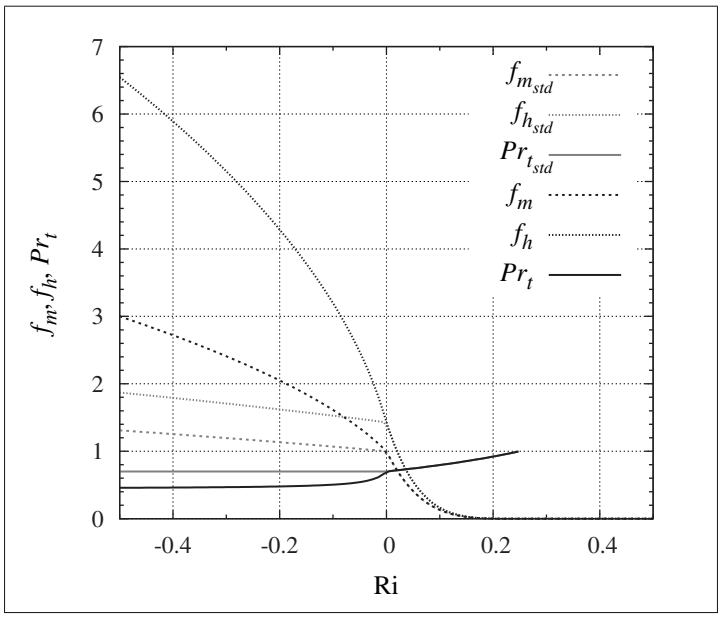

Figure 2.1 Momentum f_m and heat f_h stability functions, and turbulent Prandtl number Pr_t for the UKMO Smagorinsky SGS model (Brown *et al.*, 1994). "conventional" functions (Brown, 1999) are shown with a "$_{std}$" subscript

2.2.3.1.3 Closure constant

A theoretical value of the Smagorinsky constant C_S was first obtained by Lilly (1966) based on the Kolmogorov spectra model for an isotropic homogeneous turbulence, giving

$$C_S = \frac{1}{\pi}\left(\frac{2}{3C_{Kol}}\right)^{3/4}, \tag{2.71}$$

where C_{Kol} is the Kolmogorov constant generally taken equal to $1.5 - 1.6$ in the ABL (experimental measurements), thus giving $C_S = 0.173 - 0.165$ which is the theoretical best suited in shear-free well resolved regions of the flow where subgrid turbulence is isotropic. It is considered today as the traditional value (Porté-Agel *et al.*, 2000; Lesieur *et al.*, 2005). However, as discussed in Sec. 1.3.2.2.1.1, the value of C_S has to be reduced to enforce the local equilibrium relation in regions where the mean velocity gradient is non-zero (Sagaut, 2006), which

is achieved in the UKMO Smagorinsky SGS model though the matching of the mixing length scale, Eq. (2.61). In this study, $C_S = 0.15$ is used (Brown *et al.*, 1994; Hobson *et al.*, 1999).

Depending on the mesh properties, the filter width of the UKMO Smagorinsky SGS model may only be a function of the horizontal resolution Δ_H, *i.e.* Eq. (2.63). In such a case, we can define an equivalent 3D Smagorinsky constant, which allows to properly compare various SGS models regardless of the vertical grid properties, such as we have (far from the boundaries)

$$C_{S\,3d} = \frac{\Delta_H}{\Delta_{3d}} C_{S\,H}, \tag{2.72}$$

where $C_{S\,H} = C_S$. Hence, when considering the grids used in Moeng and Sullivan (1994) (on which results presented in Chap. 4 are partly based), we have $C_{S\,3d} = 0.216$ for the UKMO Smagorinsky SGS model.

2.2.3.2 Deardorff SGS model

The Deardorff (1980) SGS model is certainly the simplest TKE based SGS dedicated to the full ABL as discussed in Sec. 1.3.2.2.1.2. Thanks to the inclusion of a prognostic equation for the TKE (which is detailed in Sec. 2.2.4), production and dissipation of TKE are not anymore assumed equal, and non-local flow features may be better taken into account.

As most of the simple TKE based turbulent closures, Deardorff SGS model rely on the Kolmogorov relation to compute the momentum and heat mixing coefficients, which gives

$$K_M = C_k \lambda k^{1/2}, \tag{2.73}$$

$$K_T = \frac{K_M}{\mathrm{Pr}_t} = \frac{C_k \lambda}{\mathrm{Pr}_t} k^{1/2}, \tag{2.74}$$

where C_k is the TKE production closure constant and λ is a mixing length function of the mesh resolution and the flow stratification.

Finally, the dissipation rate of TKE is parameterized following the classical approach such as

$$\varepsilon = \frac{C_\varepsilon}{\lambda_\varepsilon} k^{3/2}, \tag{2.75}$$

where C_ε is the TKE dissipation closure constant and λ_ε the dissipation length scale that is considered equal to the mixing length in Deardorff SGS model (Sullivan *et al.*, 1994).

2.2.3.2.1 Length scales

The mixing length λ of Deardorff SGS model equals directly the grid size Δ in neutral and unstable conditions such as

$$\Delta = (\Delta x \Delta y \Delta z)^{1/3} = \Delta_{3d}, \tag{2.76}$$

while in stably stratified regions (Deardorff, 1980) it is reduced to

$$\mathcal{L}_N = 0.76 \frac{k^{1/2}}{N}, \tag{2.77}$$

where N is the Brunt-Väisälä frequency as described previously. This mixing length for stable stratification is similar to an inverse Richardson number, in that, it is the ratio of a velocity scale representing shear over a buoyant production. The reduction of λ in stable regions allows to reduce the SGS mixing in a similar manner as achieved with the stability function in the UKMO Smagorinsky SGS model. Even when buoyancy driven ABL is reproduced, this feature is necessary to model a complete ABL that includes a capping inversion (Sullivan *et al.*, 1994).

The mixing length is sometimes further reduced though a clipping with κz (Sullivan *et al.*, 1994), advocating that it allows to mimic the natural reduction of the turbulent eddies when getting close to the surface. However, Redelsperger *et al.* (2001) state that this van Driest-like damping (van Driest, 1956) does not have clear theoretical justification for LES. In addition, if this damping is applied to the present model, the length scale become too small close to

the surface and ABL flow is decoupled from the surface: shear instabilities are not anymore triggered. It is thus not used in the present study.

To summarize the length scales computation

$$\lambda = \begin{cases} \Delta, & \text{unstable} \\ \min(\Delta; \mathcal{L}_N), & \text{stable} \end{cases},$$
$$\lambda_\varepsilon = \lambda.$$

2.2.3.2.2 Turbulent Prandtl number

The turbulent Prandtl number used in Deardorff SGS model is a function of the stratification similarly as in the UKMO Smagorinsky SGS model. It is defined such as

$$\frac{1}{\mathrm{Pr}_t} = \left(1 + \frac{2\lambda}{\Delta}\right). \tag{2.78}$$

Thus, in unstable and neutral conditions, $\lambda = \Delta$, we have $\mathrm{Pr}_t = 1/3$ while in very stable conditions, $\lambda \ll \Delta$, momentum and mixing coefficient are equal with $\mathrm{Pr}_t = 1$.

2.2.3.2.3 Closure constants

Concerning the closure constants, they were first obtained theoretically by Lilly (1966). First, by considering turbulence in an equilibrium state (*i.e.* production and dissipation of TKE are equal which is a good approximation for a flow in equilibrium over an homogeneous surface in neutral condition (Stull, 1988)), he showed based on the SGS TKE prognostic equation that

$$C_k = C_\varepsilon^{1/3} C_S^{4/3} \tag{2.79}$$

then, using the Kolmogorov theory, he obtained

$$C_\varepsilon = \pi \left(\frac{2}{3C_{Kol}} \right)^{3/2}, \tag{2.80}$$

$$C_k = \frac{1}{\pi} \left(\frac{2}{3C_{Kol}} \right)^{3/2}, \tag{2.81}$$

and thus

$$\frac{C_\varepsilon}{C_k} = \pi^2. \tag{2.82}$$

These relations give $(C_k;\, C_\varepsilon) = (0.094;\, 0.93)$ with $C_{Kol} = 1.5$ and $(C_k;\, C_\varepsilon) = (0.086;\, 0.845)$ with $C_{Kol} = 1.6$. Deardorff (1973) and Deardorff (1980) used $(C_k;\, C_\varepsilon) = (0.1;\, 0.7)$, but Moeng and Wyngaard (1988) showed based on a spectra analysis that $(C_k;\, C_\varepsilon) = (0.1;\, 0.93)$ were better suited. These latter values are almost equal to the above theoretical values for $C_{Kol} = 1.5$. Other set of constants are also used depending on the model details such as $(C_k;\, C_\varepsilon) = (0.0667;\, 0.7)$ in MesoNH LES model (Cuxart *et al.*, 2000; Redelsperger *et al.*, 2001), $(C_k;\, C_\varepsilon) = (0.086;\, 0.845)$ in Schmidt and Schumann (1989) (which is also in agreement with the above theoretical values for $C_{Kol} = 1.6$), and finally, $(C_k;\, C_\varepsilon) = (0.15;\, 0.93)$ in WRF LES model (Klemp and Skamarock, 2004; Takemi and Rotunno, 2005).

In the current study, it was decided to use the commonly accepted set of constants: $(C_k;\, C_\varepsilon) = (0.1;\, 0.93)$ (Andren *et al.*, 1994; Sullivan *et al.*, 1994; Redelsperger *et al.*, 2001). Using Eq. (2.79), an equivalent Smagorinsky constant of $C_{S_{eqv}} = C_k^{3/4} C_\varepsilon^{-1/4} = 0.181$ is obtained. Finally, note that we always have $C_{S\,3d} = C_{S_{eqv}}$ for the Deardorff SGS model. Thus, when considering Moeng and Sullivan (1994) grids, we have $C_{S\,H} = 0.126$.

2.2.3.3 Hybrid TKE SGS model

The hybrid TKE SGS model integrates features of the Smagorinsky and Deardorff SGS models as well as from the classical column model from the RPN. In fact, the hybrid TKE SGS model can be viewed as a generalization for LES of the classical column closure.

Mixing coefficients and dissipation are defined as in Deardorff SGS model (*i.e.* based on the Kolmogorov relation) but as in the UKMO Smagorinsky SGS model, they also includes stability functions (that are the same as in the column model). We thus have

$$K_M = C'_k \lambda f_m k^{1/2}, \tag{2.83}$$

$$K_T = C'_k \lambda f_h k^{1/2}, \tag{2.84}$$

and the dissipation is parametrized similarly

$$\varepsilon = \frac{C'_\varepsilon}{\lambda_\varepsilon f_m} k^{3/2}, \tag{2.85}$$

where C'_k and C'_ε are closure constants similar to C_k and C_ε while all others quantities retain the same meaning as previously.

2.2.3.3.1 Length scales

As opposed to Deardorff SGS model, the mixing and dissipation length scales does not directly equal the filter width but they are proportional to it through a Smagorinsky like constant. The mixing length for neutral condition is thus defined as

$$\lambda = \min \left[\kappa \left(z + z_0 \right) ; \lambda_0 \right] \tag{2.86}$$

with its values in the flow interior λ_0 that writes

$$\lambda_0 = \min \left[C_S \Delta_H ; \lambda_e \right], \tag{2.87}$$

where the Smagorinsky-type constant is set to $C_S = 0.15$ in the present study, and an equilibrium length scale for neutral thermal stratification, $\lambda_e = 200$ m, is used as in the column model (Blackadar, 1962; Mailhot and Benoit, 1982). The latter intents to allow the hybrid TKE model to properly perform seamlessly from the microscale to the mesoscale but has no impact

on the results if $C_S\Delta < \lambda_e$. A clipping of the mixing length with $\kappa(z + z_0)$ is also carried out as in the column model. This van-Driest-like damping allow to better reproduce near-surface flow in LES (Sullivan *et al.*, 1994).

Finally, the dissipation length scale is always set equal to the mixing length, *i.e.* $\lambda_\varepsilon = \lambda$.

2.2.3.3.2 Stability functions

Stability functions are dependent of the local gradient Richardson number

$$\mathrm{Ri} = \frac{\dfrac{g}{\widetilde{\theta}}\dfrac{\partial\widetilde{\theta}}{\partial z}}{\left(\dfrac{\partial\widetilde{u}}{\partial z}\right)^2 + \left(\dfrac{\partial\widetilde{v}}{\partial z}\right)^2}. \tag{2.88}$$

They can be seen as an adaptation of the mixing length function of the thermal stratification. For unstable stratification ($\mathrm{Ri} \leq 0$) (Delage and Girard, 1992), we have

$$f_m^2 = \frac{f_h}{\mathrm{Pr}_N} = (1 - 40\mathrm{Ri})^{1/3}, \tag{2.89}$$

while for stable stratification ($\mathrm{Ri} > 0$) (Delage, 1997)

$$f_m = \frac{f_h}{\mathrm{Pr}_N} = (1 + 12\mathrm{Ri})^{-1}, \tag{2.90}$$

where the turbulent Prandtl number in neutral conditions is defined as $\mathrm{Pr}_N = 0.85$.

Fig. 2.2 shows the stability functions used in the hybrid TKE SGS model. It can be seen that shape of both stability functions and the turbulent Prandtl number are similar to the UKMO SGS model, Fig. 2.1. However, the increase of the mixing with Ri in unstable condition is notably lower than with the standard UKMO stability functions (but similar to the "conventional" UKMO stability function $f_{m_{std}}$ and $f_{h_{std}}$). At the opposite, for $\mathrm{Ri} > 0$, stability functions of the hybrid TKE SGS model feature a notably higher value than UKMO stability functions. No critical Richardson number is used and stability functions reach slowly 0. This latter be-

haviour is thought to be well suited in the mesoscale configuration as it allows mixing even if $\mathrm{Ri} > \mathrm{Ri}_c$ (Delage, 1997). Indeed, mesoscale grids are too large for the flow to become fully laminar within a mesh. At the opposite in LES, the use of a critical Ri_c is better suited as meshes are much smaller and turbulence can effectively disappear locally due to a local stable stratification (Delage, 1997; Brown *et al.*, 1994).

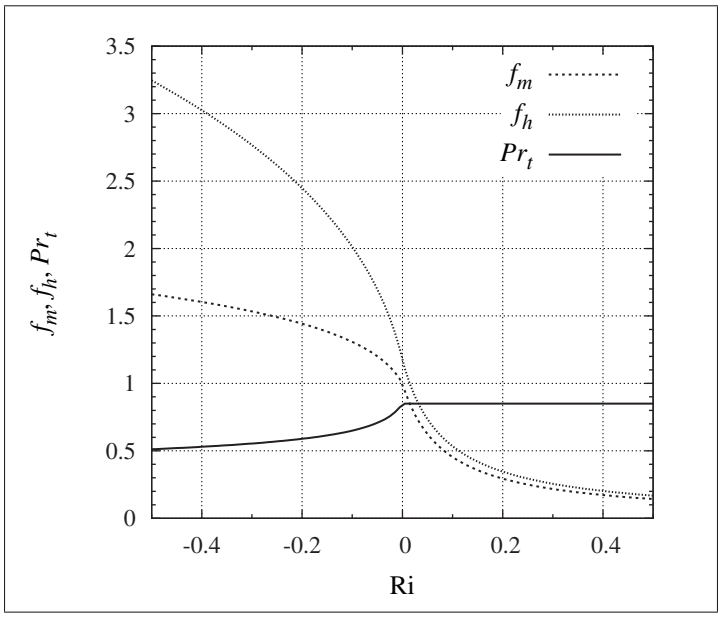

Figure 2.2 Momentum f_m and heat f_h stability functions, and turbulent Prandtl number Pr_t as a function of Ri for the column and hybrid TKE SGS models (Delage and Girard, 1992; Delage, 1997)

However to mitigate these differences, the TKE equation also includes a buoyancy term that further allows to enhance or inhibit turbulent mixing as a function of local thermal stratification, as seen in Sec. 2.2.4. In fact, Deardorff SGS model only rely on this term (and the solver) to take into account stratification at subgrid level when $\mathrm{Ri} < 0$, while mixing length is also reduced when $\mathrm{Ri} > 0$. It will thus be interesting to compare the results from the hybrid TKE SGS model with Deardorff and UKMO Smagorinsky SGS model..

2.2.3.3.3 Closure constants

The hybrid TKE SGS model production and dissipation closure constants are the same as for the column model. They are obtained by matching the column model with the surface layer similarity (Mailhot and Benoit, 1982; Redelsperger *et al.*, 2001), *i.e.* Sec. 2.3.3, such as

$$C'_k = \frac{1}{\alpha^{1/2}}, \tag{2.91}$$

$$C'_\varepsilon = C'^3_k = \frac{1}{\alpha^{3/2}}, \tag{2.92}$$

with the constant $\alpha = k/u_*^2$ at the surface. In the present model, following Wyngaard and Coté (1974) measurements, $\alpha = 3.75$ which gives $(C'_k;\, C'_\varepsilon) = (0.516;\, 0.138)$.

However, the Smagorinsky-type constant introduced to compute λ_0 could be directly included in the TKE equation closure constants leading to the following effective constants

$$C_k = C'_k C_S, \tag{2.93}$$

$$C_\varepsilon = \frac{C'^3_k}{C_S} = \frac{C'_\varepsilon}{C_S}, \tag{2.94}$$

which gives $(C_k;\, C_\varepsilon) = (0.077;\, 0.916)$ for the present model (and which interestingly returns perfectly $C_{S_{eqv}} = 0.15$ by using Eq. (2.79)). These values are similar but not identical to the ones used in the classical Deardorff SGS model as discussed previously. By further multiplying Eq. (2.93) by Eq. (2.94), it can be found that

$$C'_k = (C_k C_\varepsilon)^{1/4}, \tag{2.95}$$

$$C'_\varepsilon = (C_k C_\varepsilon)^{3/4}, \tag{2.96}$$

and thus

$$\alpha = \frac{1}{(C_k C_\varepsilon)^{1/2}}, \tag{2.97}$$

As a result, to recover Deardorff SGS model closure constants, *i.e.* $(C_k;\, C_\varepsilon) = (0.1;\, 0.93)$, it would be required to use $\alpha = 3.28$ leading to $(C'_k;\, C'_\varepsilon) = (0.552;\, 0.168)$ and $C_S = 0.181$.

Finally, note that we always have $C_{S\,H} = C_{S_{eqv}}$ for the hybrid TKE SGS model. Thus, when considering Moeng and Sullivan (1994) grids, we have $C_{S\,3d} = 0.216$ far from the boundaries.

2.2.3.4 Redelsperger SGS model

Redelsperger SGS model is identical to Deardorff SGS model, thus

$$K_M = C_k \lambda k^{1/2}, \tag{2.98}$$

$$K_T = \frac{K_M}{\mathrm{Pr}_t} = \frac{C_k \lambda}{\mathrm{Pr}_t} k^{1/2} \quad \text{with} \quad \frac{1}{\mathrm{Pr}_t} = \left(1 + \frac{2\lambda}{\Delta}\right), \tag{2.99}$$

and

$$\varepsilon = \frac{C_\varepsilon}{\lambda_\varepsilon} k^{3/2}. \tag{2.100}$$

However, mixing and dissipation length scales become height dependent in the region close to the surface. This matching was obtained by Redelsperger *et al.* (2001) thanks to a simple velocity spectra model dedicated to the surface layer (and that differs from Kolmogorov model spectra). The latter is based on a recent theory that describes the structure of the surface layer and that was validated experimentally and numerically (Drobinski *et al.*, 2004, 2007). This allows the SGS model to be mathematically consistent in the flow interior as well as at the surface. In other words, based on this approach production and dissipation closure constants of the column model are recovered at the surface while the SGS model is identical to Deardorff above the surface (Redelsperger *et al.*, 2001).

2.2.3.4.1 Length scales

In neutral conditions, mixing and dissipation length scales of Redelsperger *et al.* (2001) SGS model can be expressed as

$$\mathcal{L}_k = (1-\gamma)A_k z + \gamma\Delta, \tag{2.101}$$

$$\mathcal{L}_\varepsilon = (1-\gamma)A_\varepsilon z + \gamma\Delta, \tag{2.102}$$

where $\Delta = \Delta_{3d}$, A_k and A_ε are closure constants dependent on both the surface layer and the flow interior closure constants, $\gamma \in [0;1]$ is a weighting function that depends on both horizontal and vertical grid spacing and properties of the surface layer.

The above formula only considers neutral conditions. This approach can be generalized to a stratified surface layer considering stability functions used at the surface boundary condition, as presented in Redelsperger *et al.* (2001). However, as a first developmental step, the neural solution is considered here regardless of the stratification of the surface layer.

In the current implementation of Redelsperger SGS model, stratification is thus taken into account as in Deardorff SGS model, *i.e.* thanks to the buoyancy production term in the TKE equation and with a reduction of the length scale to $\mathcal{L}_N$ in stable condition. As a result, the mixing and dissipation lengths for unstable stratification ($\mathrm{Ri} < 0$) are defined as

$$\lambda = \mathcal{L}_k, \tag{2.103}$$

$$\lambda_\varepsilon = \mathcal{L}_\varepsilon, \tag{2.104}$$

while for stable stratification ($\mathrm{Ri} > 0$), we have

$$\lambda = \min(\mathcal{L}_k; \mathcal{L}_N), \tag{2.105}$$

$$\lambda_\varepsilon = \min(\mathcal{L}_\varepsilon; \mathcal{L}_N). \tag{2.106}$$

2.2.3.4.2 Closure constants

The constants A_k and A_ε were obtained by matching Redelsperger *et al.* (2001) SGS model with the similarity theory. They can be expressed as

$$A_k = \frac{1}{\alpha^{1/2}} \frac{\kappa}{C_k}, \tag{2.107}$$

$$A_\varepsilon = \alpha^{3/2} \kappa C_\varepsilon, \tag{2.108}$$

with the constant $\alpha = k/u_*^2$ at the surface. As a consequence, mixing and dissipation length scales are not anymore always equal. When $\alpha = 3.75$ (Wyngaard and Coté, 1974) and the set of closure constants from Deardorff SGS model are used [3] , *i.e.* $(C_k;\, C_\varepsilon) = (0.1;\, 0.93)$ (Moeng and Wyngaard, 1988), we obtain $(A_k;\, A_\varepsilon) = (2.7;\, 2.07)$. Thus, in the lower part of the ABL and in comparison to Deardorff SGS model, length scales are height dependent and dissipation of TKE become higher than production. Results based on Redelsperger SGS model may thus be less resolved close to the surface in comparison to Deardorff SGS model. Far from the boundaries, Redelsperger SGS model is identical to Deardorff, and thus $C_{S\,3d} = C_{S_{eqv}} = 0.181$ giving $C_{S\,H} = 0.126$ when considering Moeng and Sullivan (1994) grids.

2.2.3.4.3 Weighting function

The weighting function of Redelsperger *et al.* (2001) is similar to the "isotropic factor" introduced by Sullivan *et al.* (1994). However, while the latter can only be used for homogeneous surface flows relying on periodic lateral boundary conditions, the Redelsperger definition can be applied regardless of the surface properties and lateral boundary conditions. It is defined as

$$\gamma = 1 - \exp\left(-3 \frac{z_1 - z}{z_1 - z_c}\right), \tag{2.109}$$

where z_1 is the height of the first TKE level, and z_c is the critical height at which $\gamma \approx 0.95$ or, in other words, the height at which the model relies at 95 % on the flow interior closure.

[3] As a side note, in order to have $A_k = A_\varepsilon$, it is required that $\alpha = (C_k C_\varepsilon)^{-1/2}$. Thus, by using $(C_k;\, C_\varepsilon) = (0.1;\, 0.93)$, it would be need to have $\alpha = 3.28$ which is the same value as for the hybrid TKE SGS model to have the same constants as the Deardorff SGS model in the flow interior.

Redelsperger *et al.* (2001) defined the latter simply considering the smallest size of eddy that can be resolved in the horizontal and in the vertical. Thus, assuming that close to the surface the eddies characteristic height is κz (and the smallest eddy that can be represented is $2\Delta z$ high) and that they have a deformation height/width of $1/3$ (and the smallest eddy that can be represented is $2\Delta_H$ wide), they proposed that

$$z_c = \max\left(\frac{2\Delta z}{\kappa}; \frac{2\Delta_H}{3\kappa}\right). \tag{2.110}$$

Interestingly, this height is of the same order as the height at which 50 % of the flow is resolved.

2.2.3.5 Kosović SGS model

The gradient diffusion assumption cannot take into account some important phenomena observed in turbulence: the backscatter of TKE and the redistribution of SGS TKE among the normal SGS stress components (Mason and Thomson, 1992; Kosović, 1997).

2.2.3.5.1 Non-linear SGS model

Based on these considerations and the non-linear constitutive theory (Wilcox, 1994), Kosović (1997) introduced a SGS model allowing backscatter, but instead of relying on stochastic processes, a non-linear SGS model is used. The backscatter of TKE is fully deterministic since solely based on a non-linear combination of strain rate S_{ij} and rotation rate Ω_{ij} tensors such as

$$\begin{aligned}\tau_{ij} = -2C_k\Delta\overline{k}^{1/2}\overline{S}_{ij} - (C_S\Delta)^2\Bigg[C_1\left(\overline{S}_{ik}\overline{S}_{kj} - \frac{1}{3}\delta_{ij}\overline{S}_{mn}\overline{S}_{nm}\right) \\ + C_2\left(\overline{S}_{ik}\overline{\Omega}_{kj} - \overline{\Omega}_{ik}\overline{S}_{kj}\right)\Bigg],\end{aligned} \tag{2.111}$$

where S_{ij} is defined as in Eq. (2.38), and

$$\Omega_{ij} = \frac{1}{2}\left(\frac{\partial\widetilde{u}_i}{\partial x_j} - \frac{\partial\widetilde{u}_j}{\partial x_i}\right). \tag{2.112}$$

Concerning the closure constants, C_k is associate to the production of TKE and defined as

$$C_k = \pi^{1/3} \left(\frac{2}{3C_{Kol}} \right)^{1/2} C_S^{4/3} = \left(\frac{8\pi}{27} \right)^{1/3} C_S^{4/3}, \tag{2.113}$$

while C_S is a Smagorinsky-type constant defined as directly dependent on the backscatter of TKE (through another constant, C_b) such as

$$C_S = \pi^{-1} \left(\frac{2}{3C_{Kol}} \right)^{3/4} (1 + C_b)^{1/2} = \left(\frac{8\,(1 + C_b)}{27\pi^2} \right)^{1/2}, \tag{2.114}$$

finally, C_1 and C_2 are closure constants associated with the new non-linear terms and that write

$$C_1 = \frac{960^{1/2} C_b}{7\,(1 + C_b)\,\mathcal{S}(k_c)} \qquad \text{and} \qquad C_2 = C_1, \tag{2.115}$$

where $\mathcal{S}(k_c)$ is the velocity derivative skewness function taken equal to 0.5 (Kosović, 1997).

C_1, C_2 and C_S were determined by Kosović (1997) so that the model provides correct energy transfer and capture the normal stress effects observed in homogeneous sheared flows. They only depend on the backscatter constant, C_b, that needs to be defined. When the latter is increased, C_S also increases, which is consistent with the fact that the same total amount of fluctuations needs to be dissipated. A value of $C_b = 0.36$ was found optimal by Kosović (1997) based on experimental and DNS data, which leads to $C_S = 0.202$, $C_1 = C_2 = 2.343$ and $C_k = C_\varepsilon = 0.116$.

Finally, the dissipation rate of TKE is parameterized as in Deardorff (1980) SGS model giving

$$\varepsilon = \frac{C_\varepsilon}{\lambda_\varepsilon} k^{3/2}. \tag{2.116}$$

However, and as opposed to all the approaches based on Deardorff SGS model, the dissipation and production closure constants are set equal

$$C_\varepsilon = C_k, \tag{2.117}$$

and the definition of the dissipation length scale slightly differs.

2.2.3.5.2 Length scales

The mixing length is based on the filter width such as

$$\Delta = (\Delta x \Delta y \Delta z)^{1/3} = \Delta_{3d}. \tag{2.118}$$

However, and as opposed to the others SGS models, the dissipation length scales does not always equal to the mixing length scale and we have

$$\lambda_\varepsilon = \begin{cases} \Delta, & \text{unstable} \\ \left(\dfrac{1}{\Delta^2} + \dfrac{1}{\mathcal{L}_N^2} + \dfrac{1}{\mathcal{L}_S^2} \right)^{-1/2}, & \text{stable} \end{cases}, \tag{2.119}$$

with

$$\mathcal{L}_N = 0.76 \frac{k^{1/2}}{N}, \tag{2.120}$$

a length scale related to the stratification as proposed by Deardorff (1980), and

$$\mathcal{L}_S = 2.76 \frac{k^{1/2}}{S}, \tag{2.121}$$

an additional length scale which includes magnitude of the resolved shear in order to also take into account the shear production of TKE in stable regions for the computation of the dissipation length scale (Kosović, 1997).

2.2.3.5.3 Heat flux

In Kosović SGS model, a simple gradient diffusion approach is used to parameterize heat flux along with the classical definition of the heat mixing coefficient (with a constant turbulent Prandtl number set to $\mathrm{Pr}_t = 1/3$). This aspect of Kosović SGS model is thus identical to Dear-

dorff (1980) SGS model. Indeed, Kosović and Curry (2000) considered that the enhancement brought to momentum thanks to the non-linear SGS model are also profitable to heat processes thanks to the advection as shown by Sullivan *et al.* (1994).

2.2.3.5.4 Linear Kosović SGS model

If the backscatter constant is zero, $C_b = 0$, no backscatter effects are taken into account, and Kosović SGS stress model becomes similar the Deardorff (1980) SGS model

$$K_M = C_k \lambda k^{1/2}, \quad K_T = \frac{K_M}{\mathrm{Pr}_t} = \frac{C_k \lambda}{\mathrm{Pr}_t} k^{1/2} \quad \text{and} \quad \varepsilon = \frac{C_\varepsilon}{\lambda_\varepsilon} k^{3/2}, \tag{2.122}$$

with closure constants and mixing length that slightly differ. In that case, we have $C_S = 0.173$, $C_1 = C_2 = 0$, $C_k = C_\varepsilon = 0.0943$, $\mathrm{Pr}_t = 1/3$, $\lambda = \Delta$ and λ_ε computed as in Sec. 2.2.3.5.2.

For that model, Eq. (2.79) is not anymore true as $C_{S_{eqv}}$ becomes a function of the dissipation length scale (even in neutral conditions) such as

$$C_{S_{eqv}} = \left(\frac{C_k^3}{C_\varepsilon} \frac{\lambda_\varepsilon}{\Delta} \right)^{1/4}. \tag{2.123}$$

However, considering that λ_ε equals the filter width (as in unstable conditions), we obtain an equivalent constant $C_{S_{eqv}} = 0.3$ which is rather high as underlined in the studies from Mason and Brown (1999) and Brown *et al.* (2000), and may lead to much more smoothed results in comparison to the other models. However, this SGS model normally includes a backscatter component which may increase fluctuations.

Finally, note that we always have $C_{S\,3d} = C_{S_{eqv}}$ for the linear Kosović SGS model. Thus, when considering Moeng and Sullivan (1994) grids, we have $C_{S\,H} = 0.208$.

2.2.3.6 Summary of SGS models

The five subgrid scales presented in this section are summarized in Tab. 2.1.

Table 2.1 Summary of the key features of the five SGS models evaluated

Name	Mixing and dissipation	Closure constants	$C_{S_{eqv}}$	Filter width and length scales	Stratification
UKMO Smagorinsly (Mason and Brown, 1999)	$K_M = \lambda^2 f_m S$ $K_T = \lambda^2 f_h S$	$C_S = 0.15$ $\mathrm{Pr}_N = 0.7$ $\mathrm{Ri}_c = 0.25$	0.15	$\Delta = \begin{cases} (\Delta x \Delta y \Delta z)^{1/3}, & \Delta z > \Delta_H \\ (\Delta x \Delta y)^{1/2}, & \text{otherwise} \end{cases}$ $\lambda_0 = C_S \Delta$ $\lambda = \left(\frac{1}{\lambda_0^2} + \frac{1}{(\kappa (z + z_0))^2} \right)^{-1/2}$	$f_m = \begin{cases} (1 - 16\mathrm{Ri})^{1/2}, & \mathrm{Ri} < 0 \\ \left(1 - \frac{\mathrm{Ri}}{\mathrm{Ri}_c}\right)^4, & 0 \le \mathrm{Ri} < \mathrm{Ri}_c \end{cases}$ $f_h = \begin{cases} \frac{1}{\mathrm{Pr}_N} (1 - 40\mathrm{Ri})^{1/2}, & \mathrm{Ri} < 0 \\ \frac{1}{\mathrm{Pr}_N} \left(1 - \frac{\mathrm{Ri}}{\mathrm{Ri}_c}\right)^4 (1 - 1.2\mathrm{Ri}), & 0 \le \mathrm{Ri} < \mathrm{Ri}_c \end{cases}$ $f_m = f_h = 0, \quad \mathrm{Ri}_c < \mathrm{Ri}$
Deardorff (Deardorff, 1980)	$K_M = C_k \lambda k^{1/2}$ $K_T = \frac{C_k \lambda}{\mathrm{Pr}_t} k^{1/2}$ $\varepsilon = \frac{C_\varepsilon}{\lambda_\varepsilon} k^{3/2}$	$C_k = 0.1$ $C_\varepsilon = 0.93$ $\frac{1}{\mathrm{Pr}_t} = 1 + \frac{2\lambda}{\Delta}$	0.181	$\Delta = (\Delta x \Delta y \Delta z)^{1/3}$ $\mathcal{L}_N = 0.76 \frac{k^{1/2}}{N}$	$\lambda = \begin{cases} \Delta, & \text{unstable} \\ \min(\Delta, \mathcal{L}_N), & \text{stable} \end{cases}$ $\lambda_\varepsilon = \lambda$
Hybrid TKE (Pelletier *et al.*, 2005)	$K_M = C'_k \lambda f_m k^{1/2}$ $K_T = C'_k \lambda f_h k^{1/2}$ $\varepsilon = \frac{C'_\varepsilon}{\lambda_\varepsilon f_m} k^{3/2}$	$C_S = 0.15$ $C'_k = 0.516$ $C'_\varepsilon = 0.137$ $\mathrm{Pr}_N = 0.85$	0.15	$\Delta = \Delta_H = (\Delta x \Delta y)^{1/2}$ $\lambda_0 = \min(C_S \Delta, \lambda_e)$ $\lambda = \min(\kappa(z + z_0), \lambda_0)$ $\lambda_\varepsilon = \lambda$	$\begin{cases} f_m^2 = \frac{f_h}{\mathrm{Pr}_N} = (1 - 40\mathrm{Ri})^{1/3}, & \text{unstable} \\ f_m = \frac{f_h}{\mathrm{Pr}_N} = (1 + 12\mathrm{Ri})^{-1}, & \text{stable} \end{cases}$
Redelsperger (Redelsperger *et al.*, 2001)	$K_M = C_k \lambda k^{1/2}$ $K_T = \frac{C_k \lambda}{\mathrm{Pr}_t} k^{1/2}$ $\varepsilon = \frac{C_\varepsilon}{\lambda_\varepsilon} k^{3/2}$	$C_k = 0.1$ $C_\varepsilon = 0.93$ $\frac{1}{\mathrm{Pr}_t} = 1 + \frac{2\lambda}{\Delta}$ $A_k = 2.7$ $A_\varepsilon = 2.07$	0.181	$\Delta = (\Delta x \Delta y \Delta z)^{1/3}$ $\mathcal{L}_k = (1 - \gamma) A_k z + \gamma \Delta$ $\mathcal{L}_\varepsilon = (1 - \gamma) A_\varepsilon z + \gamma \Delta$ $\gamma = 1 - \exp\left(-3 \frac{z_1 - z}{z_1 - z_c}\right)$ $z_c = \max\left(\frac{2\Delta z}{\kappa}; \frac{2\Delta_H}{3\kappa}\right)$	$\lambda = \begin{cases} \mathcal{L}_k, & \text{unstable} \\ \min(\mathcal{L}_k, \mathcal{L}_N), & \text{stable} \end{cases}$ $\lambda_\varepsilon = \begin{cases} \mathcal{L}_\varepsilon, & \text{unstable} \\ \min(\mathcal{L}_\varepsilon, \mathcal{L}_N), & \text{stable} \end{cases}$
Linear Kosović (Kosović, 1997)	$K_M = C_k \lambda k^{1/2}$ $K_T = \frac{C_k \lambda}{\mathrm{Pr}_t} k^{1/2}$ $\varepsilon = \frac{C_\varepsilon}{\lambda_\varepsilon} k^{3/2}$	$C_k = 0.094$ $C_\varepsilon = 0.094$ $\mathrm{Pr}_t = 1/3$	0.3	$\Delta = (\Delta x \Delta y \Delta z)^{1/3}$ $\mathcal{L}_N = 0.76 \frac{k^{1/2}}{N}$ $\mathcal{L}_S = 2.76 \frac{k^{1/2}}{S}$	$\lambda = \Delta$ $\lambda_\varepsilon = \begin{cases} \Delta, & \text{unstable} \\ \left(\frac{1}{\Delta^2} + \frac{1}{\mathcal{L}_N^2} + \frac{1}{\mathcal{L}_S^2}\right)^{-1/2}, & \text{stable} \end{cases}$

2.2.4 Turbulent Kinetic Energy (TKE) prognostic equation

The turbulent kinetic energy (TKE), $\overline{\rho}k = 1/2\,\overline{\rho u_l' u_l'}$, is a quantity representative of the turbulent mixing intensity and transport. Solving a TKE prognostic equation permits to take into account non-local flow features while keeping the problem relatively simple. Indeed, as seen during the literature review, it almost alleviates the needs to solve an equation for each components of the Reynolds stress while retaining most of the important information on turbulence intensity and it transport (Sumner *et al.*, 2010). In the LES context, TKE prognostic equation represents the subgrid scale TKE, *i.e.* the unresolved part of the TKE, which is only a small part of the total TKE except in some location where the flow is less resolved such as close to the surface. As a consequence, in the LES context and as opposed to RANS, the inclusion of the TKE equation does not result in significant improvement notably for simple homogeneous cases (Mason, 1994; Andren *et al.*, 1994). It is however profitable for more complex cases (Chow and Street, 2009; Bechmann and Sørensen, 2010).

A simple approach to obtain the TKE equation is to multiply momentum conservation equations by the velocity perturbation, then filter this new equations based on Reynolds or Favre averaging and finally sum the equations of three components such that an equation for the evolution of $\overline{\rho u_k' u_k'}$ is obtained.

When considering stratified ABL flows (where buoyancy play an important role by producing or destructing TKE), the shallow convection approximation (also known as the Boussinesq buoyancy approximation) allows to greatly simplify the TKE prognostic equation while retaining all its representativeness. This approximation is generally accepted (Stull, 1988; Nieuwstadt *et al.*, 1992; Sullivan *et al.*, 1994; Holton, 2004) and it allows to neglect local density fluctuations except where they are multiplied by the gravity g. In practice, it is similar to replace ρ by $\overline{\rho}$ and g by $g(1 + \theta'/\overline{\theta})$ (Stull, 1988).

By applying shallow convection approximation to momentum conservation equation and, further considering the averaged ABL to be in hydrostatic equilibrium (which is a generally accepted approximation for the microscale (Stull, 1988; Holton, 2004)), the subgrid TKE prog-

nostic equation can be expressed as

$$\overline{\rho}\frac{\partial k}{\partial t} + \overline{\rho}\widetilde{u}_i\frac{\partial k}{\partial x_i} = \frac{g}{\widetilde{\theta}}\overline{\rho w'\theta'} - \overline{\rho u_i' u_j'}\frac{\partial \widetilde{u}_i}{\partial x_j} - \frac{\partial}{\partial x_i}\left(\overline{u_i' p'} + \overline{\rho u_i'\frac{u_k' u_k'}{2}}\right) - \mu\overline{\frac{\partial u_i'}{\partial x_j}\frac{\partial u_j'}{\partial x_i}}, \tag{2.124}$$

where all quantities retain the same meaning as previously.

The terms on the left hand side, *i.e.* the accumulation and the advection of subgrid TKE, can be combined to obtain the material (Lagrangian) derivative of the TKE. The latter is computed through the SISL time stepping approach by considering the TKE as a passive scalar.

The first term on the right is the buoyant production term (positive or negative). It directly depends on the closure of the turbulent heat-flux and can be written

$$\frac{g}{\widetilde{\theta}}\overline{\rho w'\theta'} = -\overline{\rho} K_T \frac{g}{\widetilde{\theta}}\frac{\partial \widetilde{\theta}}{\partial z} \tag{2.125}$$

$$= -\overline{\rho} K_T N^2. \tag{2.126}$$

The second source term on the right is the shear production (positive) which is also directly function of the closure

$$\overline{\rho u_i' u_j'}\frac{\partial \widetilde{u}_i}{\partial x_j} = \overline{\rho}\left(K_M S_{ij} - \frac{2}{3}\delta_{ij}\left(K_M S_{ll} + k\right)\right)\frac{\partial \widetilde{u}_i}{\partial x_j}. \tag{2.127}$$

The Kolmogorov relation is generally used to compute the momentum and heat mixing coefficient (*i.e.* $K_M = C_k \lambda k^{1/2}$ and $K_T = K_M/\mathrm{Pr}_t$) as seen in Sec. 2.2.3.

The third term is a transport term. It is the redistribution of TKE by pressure gradient and by velocity fluctuations. It can be approximated with the mixing length assumption (Tennekes and Lumley, 1972, Eq. (4.2.32)) such as

$$\frac{\partial}{\partial x_i}\left(\overline{u_i' p'} + \overline{\rho u_i'\frac{u_k' u_k'}{2}}\right) = \frac{\partial}{\partial x_i}\left(\overline{u_i'\left(p' + \rho k'\right)}\right) \approx -\frac{\partial}{\partial x_i}\left(\overline{\rho} K_k \frac{\partial k}{\partial x_i}\right), \tag{2.128}$$

with K_k being the turbulent diffusion coefficient for TKE directly dependent on the momentum mixing, $K_k = C_{tke} K_M$, where C_{tke} is a constant equal to 2.08.

Finally, the last terms is the viscous dissipation of TKE, also written ε. It is also parametrized following Kolmogorov relation as seen in Sec. 2.2.3.

$$\mu \overline{\frac{\partial u_i'}{\partial x_j} \frac{\partial u_j'}{\partial x_i}} = \overline{\rho}\varepsilon = \overline{\rho} \frac{C_\varepsilon}{\lambda_\varepsilon} k^{3/2}. \tag{2.129}$$

By replacing terms of Eq. (2.124) using Eqs. (2.125), (2.127), (2.128) and (2.129) and developing equations, one can obtain a TKE equation under a form which is very close to the one presented by Mailhot and Benoit (1982, Eq. (3.19)), *i.e.*

$$\frac{\partial k}{\partial t} + \overline{u}_i \frac{\partial k}{\partial x_i} = Ak + Bk^{1/2} - Ck^{3/2} + \frac{1}{\overline{\rho}} \frac{\partial}{\partial x_i} \left(\overline{\rho} K_k \frac{\partial k}{\partial x_i} \right), \tag{2.130}$$

where A and B are source-sink of TKE, C is the dissipation, and the last terms of the right hand side is the diffusion/redistribution of TKE, which is also referred to as D.

$$A = -\frac{2}{3} \left(\frac{\partial \widetilde{u}}{\partial x} + \frac{\partial \widetilde{v}}{\partial y} + \frac{\partial \widetilde{w}}{\partial z} \right) = -\frac{2}{3} \boldsymbol{\nabla} \widetilde{\boldsymbol{u}}, \tag{2.131}$$

$$\begin{aligned} B = & C_k \lambda \Bigg\{ -\frac{g}{\mathrm{Pr}_t \widetilde{\theta}} \frac{\partial \widetilde{\theta}}{\partial z} + \left(\frac{\partial \widetilde{u}}{\partial y} + \frac{\partial \widetilde{v}}{\partial x} \right)^2 + \left(\frac{\partial \widetilde{u}}{\partial z} + \frac{\partial \widetilde{w}}{\partial x} \right)^2 + \left(\frac{\partial \widetilde{v}}{\partial z} + \frac{\partial \widetilde{w}}{\partial y} \right)^2 \\ & + \frac{4}{3} \left[\frac{\partial \widetilde{u}}{\partial x} \left(\frac{\partial \widetilde{u}}{\partial x} - \frac{\partial \widetilde{v}}{\partial y} \right) + \frac{\partial \widetilde{v}}{\partial y} \left(\frac{\partial \widetilde{v}}{\partial y} - \frac{\partial \widetilde{w}}{\partial z} \right) + \frac{\partial \widetilde{w}}{\partial z} \left(\frac{\partial \widetilde{w}}{\partial z} - \frac{\partial \widetilde{u}}{\partial x} \right) \right] \Bigg\}, \end{aligned} \tag{2.132}$$

$$C = \frac{C_\varepsilon}{\lambda_\varepsilon}. \tag{2.133}$$

A and B are source-sink terms, C is the dissipation term, and the last term of the right hand side is the diffusion/redistribution of TKE, which is also referred to as D. Interestingly, the only new term in comparison to the 1D version presented in Sec. 2.2.5.3 (Mailhot and Benoit, 1982; Benoit *et al.*, 1989) is the velocity divergence (A). It is now present because of the inclusion of the isotropic part of the Reynolds tensor in the shear production term. The same remark can

be done for the Cuxart *et al.* (2000) approach. The other terms are the same but there are now generalized in three dimensions in order to include the horizontal contributions.

2.2.5 Classical column model

The turbulent diffusion presented in Sec. 2.2.1 and 2.2.2 is fully three dimensional and only the gradient-diffusion assumption was used to express turbulent heat and momentum fluxes. It is thus very general and similar to what can be found in the CFD domain.

In order to go from the 3D formulation to a simpler 1D column model, additional assumptions can be made that greatly simplify the problem.

- In locations where ground surface is homogeneous (ocean, plain), vertical mean gradients of all variables are significantly bigger than horizontal mean gradients except for pressure. As a results, an assumption often invoked is the horizontal homogeneity of all the variables ψ except pressure, *i.e.* $\partial\psi/\partial x = \partial/\partial y = 0$. This is often referred to as the boundary layer approximation in the literature. In such a case, turbulent diffusion can act in the vertical only, and we speak of 1D turbulent diffusion or column model.
- Considering that there is at least an order of magnitude between the mean vertical velocity and its fluctuations, it comes that subsidence is negligible, having thus $\widetilde{w} = 0$, $\partial\widetilde{w}/\partial x_i = 0$ and $\partial\widetilde{w}/\partial t = 0$[4].

As seen during the literature review, Sec. 1.2, turbulence closures from most of large scale and mesoscale models are based on these assumptions. Indeed, the latter is well suited for those approaches because of the coarse horizontal resolution used (that is at best of the order of the ABL height) and the aspect ratio of the meshes close to the surface (that is of the order of $\Delta x/\Delta z \approx 100$) that does not allow turbulent motion to be resolved but only fully modelled (Cuxart *et al.*, 2000; Wyngaard, 2004). The column model can thus be associated to an 1D unsteady RANS model.

[4] As a side note, horizontal homogeneity added to incompressibility hypothesis (*i.e.* considering the ABL in hydrostatic equilibrium, thus with $\overline{\rho}$ changing with height) also imposes the absence of subsidence through mass conservation. Thus, neglecting the subsidence and considering the horizontal homogeneity hypothesis mechanically imposes incompressibility.

Concerning MC2, a classical column model based on the TKE prognostic equation was first introduced by Mailhot and Benoit (1982). It has then been implemented in the operational regional forecast model from Environment Canada by Benoit *et al.* (1989). Along the years, this model has been heavily validated and refined (Delage and Girard, 1992; Benoit *et al.*, 1997; Delage, 1997; Mailhot *et al.*, 1998; Bélair *et al.*, 1999; Benoit *et al.*, 2002; Yu *et al.*, 2006). This one-and-a-half order RANS closure is somewhat similar to the hybrid TKE SGS model, Sec. 2.2.3.3, but it relies on the boundary layer approximation (it is thus 1D) and the definition of the mixing and dissipation length scales also differs. In this section, the classical column model is summarized.

2.2.5.1 Vertical turbulent diffusion

From the two assumptions above, the Reynolds stress tensor can be reduced to

$$\tau_{ij} = \tau_{i3}, \tag{2.134}$$

where i can only be 1 or 2 since the subsidence is neglected, *i.e.* $\widetilde{w} = 0$. This implies that no velocity variances, and thus, no isotropic terms of the Reynolds tensor are present in this 1D turbulence closure. Introducing the momentum mixing coefficient as previously

$$\overline{\rho u_i' u_j'} = \overline{\rho u_i' w'} = -\overline{\rho} K_M \frac{\partial \widetilde{u}_i}{\partial z}, \tag{2.135}$$

the column model momentum transfers solely due to turbulent mixing then becomes

$$\left[\frac{d\widetilde{u}_i}{dt}\right]_{turb}^{phy} = \frac{1}{\overline{\rho}} \frac{\partial}{\partial z} \left(\overline{\rho} K_M \frac{\partial \widetilde{u}_i}{\partial z} \right), \tag{2.136}$$

and

$$\left[\frac{d\widetilde{u}_i}{dt}\right]_{turb}^{dyn} = 0. \tag{2.137}$$

It is noteworthy that, while very simple, this closure leads to satisfactory results when applied in the frame of its assumptions (André *et al.*, 1978; Mailhot and Benoit, 1982). It is also still heavily used in large scale and mesoscale models (Cuxart *et al.*, 2006; Svensson and Holtslag, 2006; Bosveld *et al.*, 2008).

Concerning turbulent heat diffusion, similarly as for the momentum, only vertical gradient are considered when the boundary layer approximation is used. We thus have

$$\overline{\rho u_i' \theta'} = \overline{\rho w' \theta'} = -\overline{\rho} K_T \frac{\partial \widetilde{\theta}}{\partial z} \quad \text{with} \quad K_T = \frac{K_M}{\mathrm{Pr}_t}. \tag{2.138}$$

Thus, heat transfer due to the sole turbulent diffusion then becomes

$$\left[\frac{d\widetilde{\theta}}{dt}\right]_{turb}^{phy} = \frac{1}{\overline{\rho}} \frac{\partial}{\partial z} \left(\overline{\rho} K_T \frac{\partial \widetilde{\theta}}{\partial z} \right). \tag{2.139}$$

Finally as a summary, when the 1D turbulent diffusion is included in Eq. (2.33), $\boldsymbol{R}$ is unchanged with respect to Eq. (2.34) while $\boldsymbol{F}$ becomes

$$\boldsymbol{F} = \begin{bmatrix} \frac{1}{\overline{\rho}} \frac{\partial}{\partial z} \left(\overline{\rho} K_M \frac{\partial u}{\partial z} \right) \\ \frac{1}{\overline{\rho}} \frac{\partial}{\partial z} \left(\overline{\rho} K_M \frac{\partial v}{\partial z} \right) \\ 0 \\ \frac{g\overline{\pi}}{\overline{\rho} T_*} \frac{\partial}{\partial z} \left(\overline{\rho} K_T \frac{\partial \widetilde{\theta}}{\partial z} \right) \\ 0 \end{bmatrix}. \tag{2.140}$$

2.2.5.2 Column model closure

The closure of the column model is almost identical to the hybrid TKE SGS model, *i.e.* Eq. (2.83) and Eq. (2.84) are used to compute mixing coefficients K_M and K_T and Eq. (2.85) is used to compute dissipation rate of TKE, ε. Concerning thermal stratification, the same

stability functions are also used in the column model as presented in Eqs. (2.88), (2.89) and (2.90). Finally, the closure constants of the column model are also defined as in Eqs. (2.91) and (2.92), leading to $(C'_k;\, C'_\varepsilon) = (0.516;\, 0.138)$ when $\alpha = 3.75$ (Wyngaard and Coté, 1974).

In fact, the only difference between the hybrid TKE SGS model and the column model (beyond the boundary layer approximation) resides in the computation of the mixing length where the Smagorinsky-type constant is no longer present. Thus, in the column model, the mixing and dissipation length scale in neutral conditions are directly defined as

$$\lambda = \min\left[\kappa\left(z + z_0\right); \lambda_e\right], \tag{2.141}$$

$$\lambda_\varepsilon = \lambda, \tag{2.142}$$

where λ_e is the asymptotic value of 200 m (Blackadar, 1962).

Note finally that, other variant for the computation of the length scales are implemented in the column model such as the approach from Bougeault and Lacarrère (1989) or from Lenderink and Holtslag (2004). The former allows to better reproduce a rapidly growing convective ABL (Bélair *et al.*, 1999; Cuxart *et al.*, 2000) while the latter better account of the neutral to unstable transition. This is however out of the scope of the present study.

2.2.5.3 TKE equation of column model

The TKE equation of the column model is obtained similarly as in Sec. 2.2.4, however it is greatly simplified thanks to the boundary layer approximation. It can be written as

$$\frac{\partial k}{\partial t} = \frac{1}{\overline{\rho}}\frac{g}{\widetilde{\theta}}\overline{\rho w'\theta'} - \frac{1}{\overline{\rho}}\overline{\rho u_i' w}\frac{\partial \widetilde{u}_i}{\partial z} - \frac{\partial}{\partial z}\left(\overline{u_i'\left(p' + \rho k\right)}\right) - \varepsilon, \tag{2.143}$$

where i can only equal 1 or 2. Note that, the advection of TKE is usually neglected since horizontal velocity gradient are neglected as well as vertical velocity.

By replacing terms of Eq. (2.144) using Eqs. (2.135), (2.138), (2.83), (2.84), (2.128) and (2.129), a TKE equation identical to Mailhot and Benoit (1982, Eq. (3.19)) is obtained

$$\frac{\partial k}{\partial t} = Bk^{1/2} - Ck^{3/2} + \frac{\partial}{\partial z}\left(K_k \frac{\partial k}{\partial z}\right), \tag{2.144}$$

where

$$B = C_k \lambda \left(\left(\frac{\partial \widetilde{u}}{\partial z}\right)^2 + \left(\frac{\partial \widetilde{v}}{\partial z}\right)^2 - \frac{g}{\mathrm{Pr}_t \widetilde{\theta}} \frac{\partial \widetilde{\theta}}{\partial z} \right), \tag{2.145}$$

$$C = \frac{C_\varepsilon}{\lambda_\varepsilon}. \tag{2.146}$$

2.3 Surface layer similarity

Surface layer represents the lowest 10 % of the ABL. As discussed all along the literature review, because the ABL is a high Reynolds number flow and due to the intrinsic properties of the earth surface, ABL flows can hardly be resolved up to the viscous sublayer. As a result, a true no-slip surface boundary condition cannot be implemented and wall functions are needed to provide the model with surface boundary conditions.

2.3.1 Integrated surface layer

The Monin-Obukhov similarity is a generally accepted theory that describes the averaged surface layer profiles (Stull, 1988). Sometimes referred to as surface layer similarity, it relates mean surface layer vertical gradients of main variables to surface fluxes through stability function dependent of z/L_{MO} where the Monin-Obukhov length scale writes

$$L_{MO} = -\frac{u_*^3 \theta}{\kappa g \overline{w'\theta'}|_s}. \tag{2.147}$$

For the large majority of flow models dedicated to the ABL, Monin-Obukhov similarity theory is used for the surface boundary condition.

Based on this generally accepted theory, vertical turbulent fluxes are considered almost constant in the surface layer (Stull, 1988). However, while this leads to satisfactory results in neutral and unstable conditions, it was found that a linear variation with height is a better approximation in stable conditions (notably in the context of a mesoscale modelling where the first model level is relatively high in the surface layer) (Delage, 1997). Thus, similarity relationship implemented in MC2 are defined such as for $z < z_{i_e}$ we have

$$\frac{\partial \widetilde{U}}{\partial z} = \left(1 - \frac{z}{z_{i_e}}\right) \frac{u_*}{\kappa z} \phi_M, \tag{2.148}$$

$$\frac{\partial \widetilde{\theta}}{\partial z} = \left(1 - \frac{z}{z_{i_e}}\right) \frac{\theta_*}{\kappa z} \phi_H, \tag{2.149}$$

where $U = (u^2 + v^2)^{1/2} = \widetilde{U} + U'$ is the velocity magnitude, $u_* = \left(-\overline{w'U'}|_s\right)^{1/2} = (\overline{u'w'}|_s^2 + \overline{v'w'}|_s^2)^{1/4}$ is the surface layer fiction velocity, $\theta_* = -\overline{w'\theta'}|_s / u_*$ is the surface layer temperature scale, ϕ_M and ϕ_H are stability functions dependent of z/L_{MO} and z_{i_e} is a stability dependent ABL height defined as (Delage, 1997; Mailhot *et al.*, 1998)

$$z_{i_e} = \begin{cases} \infty, & \text{unstable} \\ \left(L_{MO} \dfrac{u_*}{|f|}\right)^{1/2}, & \text{stable} \end{cases}. \tag{2.150}$$

As a result, $(1 - z/z_{i_e})$ vanish in unstable conditions and the usual surface layer formula are recovered, while slightly more advanced expressions are used in stable conditions.

As a side note, by combining the definitions of Ri Eq. (2.88), and L_{MO} Eq. (2.147), with the basic surface layer equations, Eqs. (2.148) and (2.149), the following relationship (which is true in the surface layer for both stable and unstable conditions) can be obtained

$$\frac{z}{L_{MO}} = \left(1 - \frac{z}{z_{i_e}}\right) \frac{\phi_M^2}{\phi_H} \mathrm{Ri}, \tag{2.151}$$

It conveniently allows to go from z/L_{MO}, which is z-dependent, to Ri, which is a $z - less$ variable. As a result, z/L_{MO} dependent stability functions (used in the surface layer) can

be converted to Ri dependent stability functions in order to match the Ri dependent stability function used to scale the mixing coefficients in the ABL.

The velocity and temperature at given level z_{a_M} and z_{a_H} in the surface layer (which is traditionally called the anemometer level) can then be obtained by

$$U_a = \frac{u_*}{\kappa} \int_{z_{0_M}}^{z_{a_M}+z_{0_M}} \left(1 - \frac{z}{z_{i_e}}\right) \frac{\phi_M}{z} dz, \tag{2.152}$$

$$\theta_a - \theta_s = \frac{\theta_*}{\kappa} \int_{z_{0_H}}^{z_{a_H}+z_{0_H}} \left(1 - \frac{z}{z_{i_e}}\right) \frac{\phi_H}{z} dz, \tag{2.153}$$

where z_{0_M} is the momentum aerodynamic roughness height (usually noted z_0) and z_{0_H} is the temperature aerodynamic roughness height (taken as $z_{0_H} = \min(z_{0_M}/5.; 0.2)$ in MC2). Then, the above expressions can be expressed such as

$$U_a = \frac{u_*}{C_M} \quad \Rightarrow \quad -\overline{w'U'}|_s = C_M u_* U_a \quad = (C_M U_a)^2, \tag{2.154}$$

$$\theta_a - \theta_s = \frac{\theta_*}{C_H} \quad \Rightarrow \quad -\overline{w'\theta'}|_s = C_H u_* (\theta_a - \theta_s) = C_H C_M U_a (\theta_a - \theta_s), \tag{2.155}$$

with the integrated momentum and heat transfer coefficients defined as

$$C_M^{-1} = \frac{1}{\kappa} \int_{z_{0_M}}^{z_{a_M}+z_{0_M}} \left(1 - \frac{z}{z_{i_e}}\right) \frac{\phi_M}{z} dz = \frac{\Phi_M}{\kappa}, \tag{2.156}$$

$$C_H^{-1} = \frac{1}{\kappa} \int_{z_{0_H}}^{z_{a_H}+z_{0_H}} \left(1 - \frac{z}{z_{i_e}}\right) \frac{\phi_H}{z} dz \; = \frac{\Phi_H}{\kappa}. \tag{2.157}$$

Furthermore, considering that the wind does not change direction in the surface layer, which is a generally accepted assumption (Stull, 1988), Eq. (2.154) can be generalized to compute components of surface momentum flux such as

$$-\overline{w'u_i'}|_s = C_M u_* u_{a\,i} = C_M^2 U_a u_{a\,i}, \tag{2.158}$$

where $u_{a\,i}$ are the horizontal velocity components at z_{a_M}.

Surface fluxes can thus be expressed using the simple generic form

$$-\overline{w'\psi'}|_s = \beta_\psi \psi_a + \alpha_\psi, \tag{2.159}$$

where α_ψ is called the inhomogeneous part and β_ψ the homogeneous part. For momentum, $\beta_M = C_M^2 U_a$ and $\alpha_M = 0$, while for heat $\beta_T = C_H C_M U_a$ and $\alpha_T = -\beta_T \theta_s = -C_H C_M U_a \theta_s$.

Further assuming continuity of the vertical turbulent fluxes across z_{a_M} and z_{a_H} levels, we obtain

$$-\overline{w'u_i'}|_s = K_M \frac{\partial \widetilde{u}_i}{\partial z} = \beta_M u_{a\,i}, \tag{2.160}$$

$$-\overline{w'\theta'}|_s = K_T \frac{\partial \widetilde{\theta}}{\partial z} = \beta_T \theta_a + \alpha_T. \tag{2.161}$$

which can served as surface boundary condition for turbulent diffusion (Mailhot and Benoit, 1982; Mailhot *et al.*, 1998). This approach is used here to provide turbulent diffusion of heat and momentum with surface boundary values.

To close this section, note that the above approach is fully based on local values of velocity and temperature. This is well suited in the mesoscale context (column model) since the flow is fully modelled (not resolved) in the ABL. In the LES context however, while this approach is commonly used (Stoll and Porté-Agel, 2006; Drobinski *et al.*, 2007), it is not sufficient to enforce the spatially averaged surface layer (*i.e.* wind and temperature at z_{a_M} and z_{a_H}) to follow Monin-Obukhov similarity (Stoll and Porté-Agel, 2006) (see also Sec. 1.3.2.1.1.2).

2.3.2 Flux-profile relationships

The stability functions, also known as flux-profile relationship, are defined as in Delage and Girard (1992) for unstable surface layer, *i.e.*

$$\phi_M^2 = \phi_H = \left(1 - 40\frac{z}{L_{MO}}\right)^{-1/3}, \tag{2.162}$$

and as in Delage (1997) for stable conditions

$$\phi_M = \phi_H = 1 + 12\frac{z}{L_{MO}}. \tag{2.163}$$

These functions slightly differ from the ones usually used and widely spread from Businger *et al.* (1971) and Dyer (1974). However, as discussed by Delage and Girard (1992), these functions are suitable for the free convection limit and remain correct for calm wind situation in unstable cases. In addition, they are also sufficiently simple to allow the inclusion of a linear variation with height of the momentum and heat fluxes in the stable surface layer (Delage, 1997). They have been largely validated Delage and Girard (1992); Delage (1997); Cuxart *et al.* (2006); Svensson and Holtslag (2006) and were proven to perform successfully.

Based on Eq. (2.151), the dependence on z/L_{MO} can be conveniently transformed to a dependence on Ri when Eqs. (2.162) and (2.162) are used. The obtained Ri dependent stability functions are $z - less$ which allow their use in the ABL flow interior. They thus serve as stability functions in the hybrid TKE SGS model and the column model closures, *i.e.* Eqs. (2.89) and (2.90)[5]. This allows to consistently match the surface layer with the above (albeit in the column model and the hybrid TKE SGS model).

Finally, they can be integrated from the surface to a given height in the surface layer (*i.e.* from z_{0_M} and z_{0_H} to z_{a_M} and z_{a_H}) to obtain an algebraic expression of momentum and heat transfer coefficients Φ_M and Φ_H and thus C_M and C_H.

For an unstable surface layer, the integrated transfer coefficient of momentum Φ_M writes

$$\begin{aligned}\Phi_M = \ln\left(\frac{z_{a_M} + z_{0_M}}{z_{0_M}}\right) + \sqrt{3}\tan^{-1}\left(\frac{\sqrt{3}(x^2-1)x_0 - (x_0^2-1)x}{(x_0^2-1)(x^2-1) + 3xx_0}\right) \\ + \ln\left(\frac{(x_0+1)^2(x_0^2 - x_0 + 1)^{1/2}(x_0^2 + x_0 + 1)^{3/2}}{(x+1)^2(x^2 - x + 1)^{1/2}(x^2 + x + 1)^{3/2}}\right),\end{aligned} \tag{2.164}$$

[5] Note that for notation consideration (*i.e.* for mixing coefficient of the hybrid TKE SGS model to have the same form as the ones of UKMO SGS model), we have in the present study $f_m(\mathrm{Ri}) = \phi_M(\mathrm{Ri})^{-1}$ while traditionally $f_m(\mathrm{Ri}) = \phi_M(\mathrm{Ri})$ is used.

with

$$x = \left(1 - 40\frac{z_{a_M} + z_{0_M}}{L_{MO}}\right)^{1/6}, \qquad x_0 = \left(1 - 40\frac{z_{0_M}}{L_{MO}}\right)^{1/6}. \tag{2.165}$$

and the integrated transfer coefficient of heat Φ_H

$$\begin{aligned}\Phi_H = \ln\left(\frac{z_{a_H} + z_{0_H}}{z_{0_H}}\right) + \frac{3}{2}\ln\left(\frac{y_0^2 + y_0 + 1}{y^2 + y + 1}\right) \\ + \sqrt{3}\tan^{-1}\left(\frac{2\sqrt{3}(y - y_0)}{(2y_0 + 1)(2y + 1) + 3}\right),\end{aligned} \tag{2.166}$$

with

$$y = \left(1 - 40\frac{z_{a_H} + z_{0_H}}{L_{MO}}\right)^{1/3}, \qquad y_0 = \left(1 - 40\frac{z_{0_H}}{L_{MO}}\right)^{1/3}. \tag{2.167}$$

For a stable surface layer, heat and momentum transfer coefficients can be expressed as

$$\Phi_M = \ln\left(\frac{z_{a_M} + z_{0_M}}{z_{0_M}}\right) + \psi(z_{a_M} + z_{0_M}) - \psi(z_{0_M}), \tag{2.168}$$

$$\Phi_H = \ln\left(\frac{z_{a_H} + z_{0_H}}{z_{0_H}}\right) + \psi(z_{a_H} + z_{0_H}) - \psi(z_{0_H}), \tag{2.169}$$

with

$$\psi = \frac{1}{2}\left[a - \frac{z}{z_{i_e}} - \ln\left(1 + \frac{bz}{2} + a\right) - \frac{b}{2c^{1/2}}\sin^{-1}\left(\frac{b - 2cz}{d}\right)\right], \tag{2.170}$$

where

$$a = (1 + bz - cz^2)^{1/2}, \qquad b = d - \frac{2}{z_{i_e}}, \qquad c = \frac{d}{z_{i_e}} - \frac{1}{z_{i_e}^2}, \qquad d = \frac{48}{L_{MO}}. \tag{2.171}$$

2.3.3 TKE surface boundary conditions

From the above expressions, surface momentum and heat fluxes can be readily computed using Eqs. (2.154) and (2.155), and further assuming the continuity of the vertical turbulent fluxes

across the surface layer, we have

$$\overline{w'U'}|_s = -K_M \frac{\partial \widetilde{U}}{\partial z} = -u_*^2. \tag{2.172}$$

In addition, considering mixing coefficients definition of a generic TKE based models, *i.e.* Eq. (2.83), it is obtained that in the surface layer

$$C_k' \lambda k^{1/2} \frac{\partial \widetilde{U}}{\partial z} = u_*^2. \tag{2.173}$$

Then, using Eq. (2.148) to replace the vertical velocity gradient, and further assuming $\lambda = \kappa z$ (from the mixing length scale definition Eq. (2.86)), it can be obtained that

$$k = \alpha u_*^2, \tag{2.174}$$

with

$$C_k' = \frac{1}{\alpha^{1/2}}, \tag{2.175}$$

which, in addition to provide a surface boundary condition for the TKE, allows to obtain a flow interior TKE production closure constant (of the column model and the hybrid TKE SGS model) consistent with surface layer properties.

By further assuming that turbulence is in equilibrium in the surface layer, which implies that production and dissipation of TKE are equal, and considering that $\lambda = \lambda_\varepsilon$ (as in Deardorff and Hybrid TKE SGS models and the column model), and that as previously, $\lambda = \kappa z$ in the surface layer, we obtain

$$C_\varepsilon' = C_k' k^{-1} \left(\kappa z \frac{\partial \widetilde{U}}{\partial z} \right)^2, \tag{2.176}$$

which then becomes using Eqs. (2.148), (2.174) and (2.175)

$$C'_\varepsilon = \frac{1}{\alpha^{3/2}}. \tag{2.177}$$

Thus, both production and dissipation closure constants of a generic TKE based model are recovered by matching the flow interior closure with the surface.

2.4 Large scale forcing and periodicity

An interesting ability for LES of the ABL is the use of periodic lateral boundary conditions. It allows to easily reproduce theoretical cases without the requirement of an advanced prescription of the initial and boundary conditions, as discussed in the literature review, Sec. 1.3.2.1. However, when the flow is driven by a geostrophic wind, a large scale pressure gradient have to be present while such an approach implies that all main variables are periodical (which is not be the case for the full pressure). In this section, an approach is presented that allows large scale geostrophic forcing in presence of periodical lateral boundary conditions. The theoretical development of this approach was first introduced in by Girard in Pelletier *et al.* (2005) but it was implemented in the model during this study. Thermodynamic variable p and T can be decomposed into a large scale stationary ψ_{ls}, and small scales transient ψ''' variables, such as

$$q = q_{ls} + q''', \tag{2.178}$$

$$T = T_{ls} + T''', \tag{2.179}$$

where $q_{ls} = \ln(p_{ls}/p_0)$ with $p_{ls} = \rho_{ls} R T_{ls}$ and T_{ls} are the large scale thermodynamic reference state that satisfies both the geostrophic balance and hydrostatic equilibrium *i.e.*

$$f\boldsymbol{k} \times \boldsymbol{v}_g + RT_{ls}\boldsymbol{\nabla} q_{ls} + \boldsymbol{g} = 0. \tag{2.180}$$

By further differentiating Eq. (2.180) with respect to z one can get a general exact form of the so-called thermal wind relationship (which basically link a vertical gradient of geostrophic

wind with an horizontal temperature gradient)

$$\left(\frac{\partial}{\partial z} - \frac{N_{ls}^2}{g}\right)\boldsymbol{c}_g + \boldsymbol{\nabla}_H \ln\theta_{ls} = 0 \tag{2.181}$$

where

$$\boldsymbol{c}_g = \frac{f}{g}\boldsymbol{k}\times\boldsymbol{v}_g, \qquad N_{ls}^2 = g\frac{\partial \ln\theta_{ls}}{\partial z} \qquad \text{and} \qquad \theta_{ls} = T_{ls}\left(\frac{p_{ls}}{p_0}\right)^{-R/c_p}. \tag{2.182}$$

Then, introducing this decomposition in Eq. (2.13) to separate thermodynamic variables into large and small scales, horizontal gradients of the large scale variables can be eliminated thanks to Eqs. (2.180) and (2.181) (considering the large scale variable as stationary). The following system of equations can be obtained

$$\frac{d\boldsymbol{v}_H}{dt} + RT\boldsymbol{\nabla}_H q''' = \mathbf{f}_H - f\boldsymbol{k}\times(\boldsymbol{v}_H - \boldsymbol{v}_g) + g\frac{T'''}{T_{ls}}\boldsymbol{c}_g, \tag{2.183a}$$

$$\frac{dw}{dt} + RT\frac{\partial q'''}{\partial z} - g\frac{T'''}{T_{ls}} = \mathrm{f}_w, \tag{2.183b}$$

$$\begin{aligned}\frac{dT'''}{dt} - \frac{RT_{ls}}{c_p}\frac{dq'''}{dt} + \frac{T_{ls}}{g}N_{ls}^2 w = \frac{Q}{c_p} - \frac{RT'''}{c_v}\boldsymbol{\nabla}\cdot\boldsymbol{v} \\ + \frac{T_{ls}}{g}f\boldsymbol{v}_H\cdot\boldsymbol{k}\times\frac{\partial\boldsymbol{v}_g}{\partial z} - \frac{T_{ls}}{g}\boldsymbol{v}_H\cdot\boldsymbol{c}_g N_{ls}^2,\end{aligned} \tag{2.183c}$$

$$\frac{c_v}{c_p}\frac{dq'''}{dt} + \boldsymbol{\nabla}\cdot\boldsymbol{v} - \frac{g}{c_{ls}^2}w = \boldsymbol{v}_H\cdot\boldsymbol{c}_g\frac{g}{c_{ls}^2}. \tag{2.183d}$$

Finally, in order to allow this system to comply with periodicity of lateral boundary conditions, the following assumptions need to be done:

- Cartesian coordinates system (flat topography, no variable map scale factor);
- $\boldsymbol{v}_g$, T_{ls} and q_{ls} depend only on z, and $\boldsymbol{v}_g\,(z)$ has the same direction at all heights;
- Coriolis factor f is constant.

Furthermore, considering the order of magnitude of terms in Eq. (2.183), it comes that $\boldsymbol{c}_g$ term in the horizontal momentum equation, as well as terms containing $\boldsymbol{v}_H\cdot\boldsymbol{c}_g$ can be neglected.

The above assumptions lead to the simplified system

$$\frac{d\boldsymbol{v}_H}{dt} + RT\boldsymbol{\nabla}_H q''' = \mathbf{f}_H - f\boldsymbol{k}\times(\boldsymbol{v}_H - \boldsymbol{v}_g)\,, \tag{2.184a}$$

$$\frac{dw}{dt} + RT\frac{\partial q'''}{\partial z} - g\frac{T'''}{T_{ls}} = \mathrm{f}_w, \tag{2.184b}$$

$$\frac{dT'''}{dt} - \frac{RT_{ls}}{c_p}\frac{dq'''}{dt} + \frac{T_{ls}}{g}N_{ls}^2 w = \frac{Q}{c_p} - \frac{RT'''}{c_v}\boldsymbol{\nabla}\cdot\boldsymbol{v} + \frac{T_{ls}}{g}f\boldsymbol{v}_H\cdot\boldsymbol{k}\times\frac{\partial \boldsymbol{v}_g}{\partial z}, \tag{2.184c}$$

$$\frac{c_v}{c_p}\frac{dq'''}{dt} + \boldsymbol{\nabla}\cdot\boldsymbol{v} - \frac{g}{c_{ls}^2}w = 0. \tag{2.184d}$$

Interestingly, besides the new terms in the right-hand side of Eqs. (2.184a) and (2.184c), this system exhibits the same form as Thomas *et al.* (1998, Eqs. (8) and (9)) and as Eq. (2.28) (without Favre averaging and neglecting heat source term in mass conservation equation).

However, the meaning of the thermodynamic variables in Eq. (2.184) differs from Eq. (2.28). As a result, the problem of transforming Eq. (2.184) into the model equations remains. To that end, T_* and q_*, *i.e.* the isothermal and hydrostatic reference basic state defined by Eq. (2.23), are introduced such as

$$\begin{aligned}
q = q''' + q_{ls} \quad &= q'' + q_* \quad \Rightarrow \quad q''' = q'' + q_* - q_{ls}(z),\\
T = T''' + T_{ls}(z) = T'' + T_* \quad &\Rightarrow \quad T''' = T'' - a_{ls}(z)T_* \quad \text{with} \quad a_{ls}(z) = \frac{T_{ls} - T_*}{T_*}.
\end{aligned}$$

As a result

$$\frac{dq'''}{dt} = \frac{dq''}{dt} - w\frac{ga_{ls}}{RT_{ls}}, \qquad \frac{\partial q'''}{\partial z} = \frac{\partial q''}{\partial z} - \frac{ga_{ls}}{RT_{ls}},$$

$$\frac{dT'''}{dt} = \frac{dT''}{dt} - w\frac{\partial T_{ls}}{\partial z}, \qquad RT\frac{\partial q'''}{\partial z} - g\frac{T'''}{T_{ls}} = RT\frac{\partial q''}{\partial z} - g\frac{T''}{T_*}$$

and

$$\boldsymbol{\nabla}_H q''' = \boldsymbol{\nabla}_H q''.$$

Introducing the above relations in Eq. (2.184) to remove q_{ls}, T_{ls}, q''' and T''' from the left hand side, and then considering the terms including a_{ls} as negligible, *i.e.* $(T_{ls} - T_*) \ll T_*$, we obtain a system of equations identical to the model equations Eq. (2.28) that depends only on the usual variable but with two additional terms on the right-hand side of horizontal momentum and internal energy equations, *i.e.*

$$\frac{d\boldsymbol{v}_H}{dt} + RT\boldsymbol{\nabla}_H q'' = \mathbf{f}_H - f\boldsymbol{k} \times (\boldsymbol{v}_H - \boldsymbol{v}_g)\,, \tag{2.185a}$$

$$\frac{dw}{dt} + RT\frac{\partial q''}{\partial z} - g\frac{T''}{T_*} = \mathrm{f}_w, \tag{2.185b}$$

$$\frac{dT''}{dt} - \frac{RT_*}{c_p}\frac{dq''}{dt} + \frac{T_*}{g}N_*^2 w = \frac{Q}{c_p} - \frac{RT''}{c_v}\boldsymbol{\nabla}\cdot\boldsymbol{v} + \frac{T_*}{g}f\boldsymbol{v}_H \cdot \boldsymbol{k} \times \frac{\partial \boldsymbol{v}_g}{\partial z}, \tag{2.185c}$$

$$\frac{c_v}{c_p}\frac{dq''}{dt} + \boldsymbol{\nabla}\cdot\boldsymbol{v} - \frac{g}{c_*^2}w = 0. \tag{2.185d}$$

Further introducing the buoyancy b and the generalized pressure P, the system becomes identical to the model equations Eq. (2.32) with the two new terms on the right-hand side

$$\frac{d\boldsymbol{v}}{dt} + \boldsymbol{\nabla}P - b\boldsymbol{k} = \mathbf{f} - f\boldsymbol{k} \times (\boldsymbol{v} - \boldsymbol{v}_g) - \frac{b}{g}\boldsymbol{\nabla}P, \tag{2.186a}$$

$$\frac{d}{dt}\left(b - \frac{N_*^2}{g}P\right) + N_*^2 w = \frac{N_*^2}{g}\mathcal{Q} - \frac{R}{c_v}b\boldsymbol{\nabla}\cdot\boldsymbol{v} + f\boldsymbol{v}_H \cdot \boldsymbol{k} \times \frac{\partial \boldsymbol{v}_g}{\partial z}, \tag{2.186b}$$

$$\frac{1}{c_*^2}\frac{dP}{dt} + \boldsymbol{\nabla}\cdot\boldsymbol{v} - \frac{g}{c_*^2}w = 0. \tag{2.186c}$$

The additional terms in Eqs. (2.185) and (2.186) allow to take into account the large scale thermodynamic reference state while keeping thermodynamic variables fully periodic. They alleviate the need for

$$-f\boldsymbol{k} \times \boldsymbol{v}_g \quad \Rightarrow \quad \text{large scale pressure gradient.} \tag{2.187}$$

$$f\boldsymbol{v}_H \cdot \boldsymbol{k} \times \frac{\partial \boldsymbol{v}_g}{\partial z} \quad \Rightarrow \quad \text{large scale temperature advection (barotropic cases only).} \tag{2.188}$$

Finally, when the system Eq. (2.186) is written in a similar matrix form as Eq. (2.33), only $\boldsymbol{R}$ is changed with respect to Eq. (2.34), such as it full form can be written (with turbulence terms)

$$\boldsymbol{R} = \begin{bmatrix} f\left(\widetilde{v} - v_g\right) - \dfrac{\widetilde{b}}{g}\dfrac{\partial \overline{P}}{\partial x} + \dfrac{1}{\overline{\rho}}\dfrac{\partial}{\partial x}\left(2\rho K_M S_{11} - \dfrac{2}{3}\overline{\rho}\left(K_M S_{ll} + k\right)\right) \\ -f\left(\widetilde{u} - u_g\right) - \dfrac{\widetilde{b}}{g}\dfrac{\partial \overline{P}}{\partial y} + \dfrac{1}{\overline{\rho}}\dfrac{\partial}{\partial y}\left(2\rho K_M S_{22} - \dfrac{2}{3}\overline{\rho}\left(K_M S_{ll} + k\right)\right) \\ -\dfrac{\widetilde{b}}{g}\dfrac{\partial \overline{P}}{\partial z} + \dfrac{1}{\overline{\rho}}\dfrac{\partial}{\partial z}\left(2\rho K_M S_{33} - \dfrac{2}{3}\overline{\rho}\left(K_M S_{ll} + k\right)\right) \\ -\dfrac{R}{c_v}\widetilde{b}\dfrac{\partial \widetilde{u}_i}{\partial x_i} + f\left(-\widetilde{u}\dfrac{\partial v_g}{\partial z} + \widetilde{v}\dfrac{\partial u_g}{\partial z}\right) \\ 0 \end{bmatrix}. \tag{2.189}$$

2.5 Initial hydrostatic and geostrophic basic state

Usually, when dealing with mesoscale limited area models, initialization of the computation is done based on a larger scale gridded data solution (*i.e.* such as from the results of the general circulation model) in a nested manner. Three dimensional initial fields and lateral and top boundary conditions are thus obtained though the interpolation of a coarser result. In the context of the use and validation of a LES-capable mesoscale model, it is of particular interest to be able to manually provide an initial value for all the model main variables, *i.e.* $\boldsymbol{v}$, b and P in the case of MC2, based on a simplified atmospheric state. It allows to reproduce theoretical cases taking advantage of the periodicity of the lateral boundary conditions.

To provide such a basic initial atmospheric state, challenges differ for wind velocity components and thermodynamic variables. Indeed, in the context of theoretical cases based on periodical lateral boundary conditions where a permanent or quasi-steady states are reached, initialization of velocity does not generally requires much care since initial fields do not impact the final result but just the time to reach the permanent state (and thus only increases the total computational cost). The velocity fields develop by themselves in response to the imposed large scale forcing (large scale pressure and temperature gradients), and turbulence,

once triggered, will develop to define the ABL. A common practice is thus to initialize wind components with geostrophic wind and to add small random perturbation to ignite turbulent instabilities (Moeng and Sullivan, 1994; Porté-Agel *et al.*, 2000).

At the opposite, thermodynamic variables require that realistic coherent fields proper to the treated case are provided for their three dimensional initial fields and lateral and top boundary conditions. They need to take into account the reference thermal stratification through the vertical profile of pressure and temperature as well as the large scale horizontal gradient of those variables. In the context of theoretical cases where a permanent or quasi-steady state is reached, the atmosphere is generally initialized thermodynamically at rest. Thus, for barotropic ($\boldsymbol{v}_g = \text{const.}$) cases, it simply implies that both the geostrophic balance and the hydrostatic equilibrium have to be satisfied, while for more evolved baroclinic cases, the thermal wind relation can further be used (Holton, 2004).

In the present study, three dimensional initial fields of thermodynamic variables are obtained following a sounding like initialization approach: in a first step, from the hydrostatic equilibrium and considering a given description of the thermal stratification of the atmosphere, one vertical profile of both temperature and pressure are computed, and in a second step, based on the geostrophic balance, the three dimensional domain is populated starting from that profile. The initial fields thus satisfy the hydrostatic and geostrophic basic states such as

$$f\boldsymbol{k} \times \boldsymbol{v}_g + RT\boldsymbol{\nabla} q + \boldsymbol{g} = 0, \tag{2.190}$$

or if the vertical component is separated from the horizontal components

$$\frac{1}{\rho}\boldsymbol{\nabla}_H p = -f\boldsymbol{k} \times \boldsymbol{v}_g, \tag{2.191}$$

$$\boldsymbol{\nabla}_z q = \frac{\partial q}{\partial z} = -\frac{g}{RT}. \tag{2.192}$$

When the large scale forcing described in Sec. 2.4 are used, the second step of this approach is not needed since the large scale pressure gradient caused by the geostrophic wind is implicitly taken into account through new source terms added to momentum equations.

This sounding like initialization approach requires as input a description of thermal stratification of the atmosphere. A key and easy to interpret variable is the potential temperature: the sign of $\partial\theta/\partial z$ directly characterizes the stability regime. As a result, it was chosen as a starting point to obtain the profile of thermodynamic variables. Note that a profile of the Brunt-Väisälä frequency or of the absolute temperature could also be used.

From the θ definition Eq. (2.2) and the hydrostatic equilibrium Eq. (2.192), one can obtain

$$\left(\frac{p}{p_0}\right)^{R/c_p} \frac{\partial}{\partial z}\left(\ln\frac{p}{p_0}\right) = -\frac{g}{R\theta}, \tag{2.193}$$

which is in the form of the derivative of the composition of two function, *i.e.* $\left[f^{n+1}\right]' = (n+1)\, f' f^n$. It is thus equivalent to

$$\frac{\partial}{\partial z}\left(\left(\frac{p}{p_0}\right)^{R/c_p}\right) = \frac{\partial \pi}{\partial z} = -\frac{g}{c_p\theta}, \tag{2.194}$$

which is the hydrostatic equilibrium definition written in terms of the potential temperature and Exner function Eq. (2.3). At this point, integrating Eq. (2.194) from z_k to z gives a general relation which only depend on the vertical profile of θ, *i.e.*

$$\left[\pi\right]_{z_k}^{z} = -\int_{z_k}^{z} \frac{g}{c_p\theta(z')} dz'. \tag{2.195}$$

To go further, the vertical profile of θ can be approximated as linear with height such as

$$\forall\, z' \in \left[z_k; z_{k+1}\right], \quad \theta(z') = az' + b \quad \text{with} \quad \begin{cases} a = \dfrac{\theta(z_{k+1}) - \theta(z_k)}{z_{k+1} - z_k} \\ b = \theta(z_k) - az_k \end{cases}, \tag{2.196}$$

where in neutral conditions we have $\theta(z') = b$.

The right hand side of Eq. (2.195) can then be integrated to give

$$[\pi]_{z_k}^{z} = \begin{cases} -\dfrac{g}{c_p b}\left(z - z_k\right), & \text{if} \quad \dfrac{\partial \theta}{\partial z} = 0 \\ -\dfrac{g}{c_p a}\ln\left(\dfrac{az+b}{az_k+b}\right), & \text{otherwize} \end{cases}. \tag{2.197}$$

From Eqs. (2.3) and (2.30), the Exner function can be written in terms of generalized pressure

$$\pi = \exp\left(\frac{P - gz}{c_p T_*}\right). \tag{2.198}$$

As a consequence, the generalized pressure can then be written as

$$P = \begin{cases} c_p T_* \ln\left[\pi_k - \dfrac{g}{c_p b}\left(z - z_k\right)\right] + gz, & \text{if} \quad \dfrac{\partial \theta}{\partial z} = 0 \\ c_p T_* \ln\left[\pi_k - \dfrac{g}{c_p a}\ln\left(\dfrac{az+b}{az_k+b}\right)\right] + gz, & \text{otherwise} \end{cases}, \tag{2.199}$$

where π_k is the Exner function value at z_k.

Now, concerning the temperature, based on the definition of potential temperature Eq. (2.2), and Eqs. (2.196) and (2.197), it is possible to obtain

$$T = \begin{cases} b\left[\pi_k - \dfrac{g}{c_p b}\left(z - z_k\right)\right], & \text{if} \quad \dfrac{\partial \theta}{\partial z} = 0 \\ (az+b)\left[\pi_k - \dfrac{g}{c_p a}\ln\left(\dfrac{az+b}{az_k+b}\right)\right], & \text{otherwise} \end{cases}. \tag{2.200}$$

Finally, from Eq. (2.29), buoyancy corresponding to the input θ profile writes

$$b = \begin{cases} g\left\{\dfrac{b}{T_*}\left[\pi_k - \dfrac{g}{c_p b}\left(z - z_k\right)\right] - 1\right\}, & \text{if} \quad \dfrac{\partial \theta}{\partial z} = 0 \\ g\left\{\dfrac{az+b}{T_*}\left[\pi_k - \dfrac{g}{c_p a}\ln\left(\dfrac{az+b}{az_k+b}\right)\right] - 1\right\}, & \text{otherwise} \end{cases}. \tag{2.201}$$

Note however that this formula is not used since it may introduce some discrepancies caused by numerical error (*i.e.* as b is not directly linked to P but found analytically). Instead, based on the hydrostatic equilibrium Eq. (2.192) and the definition of the buoyancy Eq. (2.29), it is

also possible to obtain the following expression linking generalize pressure and buoyancy

$$b = \frac{g\dfrac{\partial P}{\partial z}}{g - \dfrac{\partial P}{\partial z}}. \tag{2.202}$$

On the one hand, the latter is more convenient since no hypothesis are needed concerning the profile of θ. It is thus more widely applicable. On the other hand, the discrete form of Eq. (2.202) is also more consistent with the solver internals and discretization. As a result, Eq. (2.202) is preferred to Eq. (2.201) to obtain the initial profile of b.

Finally, it is to underline that by approximating the full profile of potential temperature by n linear segment and starting the integration from the surface where the reference pressure is considered to be known (and thus the Exner function), a profile of the generalized pressure P and the buoyancy b consistent with the input potential temperature profile can be obtained. And although this procedure is a first approximation when dealing with real profile of potential temperature, it is well suited for theoretical profiles.

2.6 Summary of the mathematical model

In this chapter, the mathematical model of both the dynamic kernel and the physics of MC2 have been presented focusing on the relevant aspects of the method and new components implemented to allow MC2 to operate as a LES model of the full dry ABL over a flat surface. Indeed, the full mathematical model of MC2 is much more complex as geographical projection, topography, humidity, phase changes, etc. are fully included (Bergeron *et al.*, 1994; Benoit *et al.*, 1997; Mailhot *et al.*, 1998; Girard *et al.*, 2005).

In a first section, the Euler equations of motion have been expressed in the form solved by the model. However, as opposed to all previous presentation (Benoit *et al.*, 1997; Thomas *et al.*, 1998; Girard *et al.*, 2005), turbulent forcing are explicitly included in the development relying on Favre filtering (making the turbulent model fully compliant with the compressible solver).

The full mathematical model of turbulent processes was then described. Starting with turbulent diffusion of momentum and heat, it was underlined that in the context of 3D turbulence diffusion, due to the compressible solver where density is implicit, volumetric terms of the Reynolds tensor need to be explicitly modelled and included in the dynamic kernel as they act and impact directly on the pressure. Thus, only the deviatoric terms of the Reynolds tensor are processed as usual (which departs from the traditional procedure followed at the RPN that includes all modelled processes in the physics, see Sec. 3). The other aspects of the turbulent closure were also described such as the newly implemented SGS models, the modelling of the 3D subgrid TKE transport as well as the column model.

Finally, the mathematical justification of other required features for LES of the full ABL were introduced, *i.e.* the surface layer similarity theory, the large scale geostrophic forcing in presence of lateral periodicity, and the initial hydrostatic and geostrophic equilibrium derived from geostrophic wind and potential temperature profiles.

CHAPTER 3

NUMERICAL METHOD

The mathematical model of the LES-capable MC2 was presented in Chap. 2. The prognostic equations of MC2, Eq. (2.33), can be generalized to include terms used in the numerical treatment (Bergeron *et al.*, 1994), such as their general matrix form writes

$$\frac{d\boldsymbol{\Psi}}{dt} + \boldsymbol{L} = \boldsymbol{R} + \boldsymbol{E} + \boldsymbol{F} + \boldsymbol{H} + \boldsymbol{T} \tag{3.1}$$

where all the terms are a function of the main variables of the model $\boldsymbol{\Psi}$ (*i.e.* $\boldsymbol{v}$, b and P), and $d\boldsymbol{\Psi}/dt$ represents the material derivative of $\boldsymbol{\Psi}$, $\boldsymbol{L}$ is the linear part of the gravity and elastic waves, $\boldsymbol{R}$ includes the remaining Euler equation terms such as the non-linear terms, $\boldsymbol{F}$ contains the external forcing, *i.e.* the physical parametrization terms such as the turbulent diffusion, $\boldsymbol{H}$ contains the added horizontal numerical diffusion of $\boldsymbol{\Psi}$, $\boldsymbol{E}$ represents the nesting used to blend the model variables with the driving data near the lateral boundaries, and $\boldsymbol{T}$ is the Robert/Asselin time filter required for the SISL time scheme to be stable.

Under this form and based on finite differences, Eq. (3.1) is solved for $\boldsymbol{\Psi}$ by first considering only $d\boldsymbol{\Psi}/dt$, $\boldsymbol{L}$ and $\boldsymbol{R}$ (that represent the fully compressible Euler equations of motion without external forcing). This forms the so-called dynamic kernel. At the end of this first step, $\boldsymbol{\Psi}_D^+$ is obtained. The latter is then corrected by adding successively the other terms (in the following order: $\boldsymbol{E}$, $\boldsymbol{F}$ and $\boldsymbol{H}$, such as $\boldsymbol{\Psi}_{DE}^+$, $\boldsymbol{\Psi}_{DEF}^+$, and finally $\boldsymbol{\Psi}_{DEFH}^+$ are respectively obtained). This approach, which is illustrated in Fig. 3.1, is known as "successive corrections method". It is followed in MC2 to solve the full prognostic equations including the additional forcing.

Depending on the configurations of the model, *i.e.* real or theoretical cases, mesoscale or LES configuration, ... , some of the terms of Eq. (3.1) may vanish. As an example, gravity wave theoretical cases, such as presented in Pinty *et al.* (1995), only involve the dynamic kernel, the nesting and the time filter. In the present study, all computations are based on periodical lateral boundary conditions and feature an homogeneous surface. Thus, no data need to be provided at

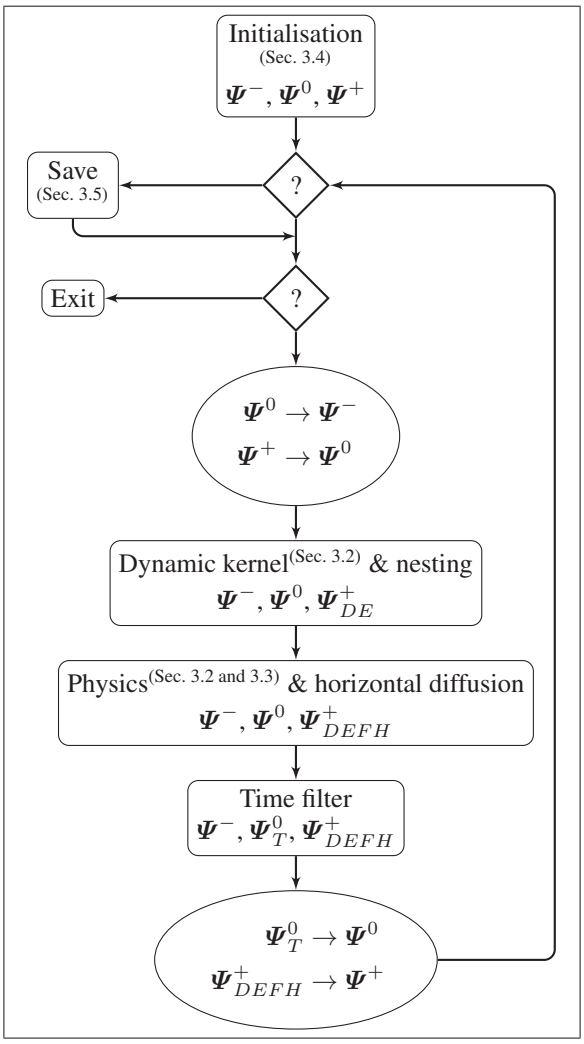

Figure 3.1 Diagram of MC2 time loop (adapted from Bergeron *et al.* (1994)). Sections associated to each step are indicated in parenthesis

the lateral boundary to drive the flow, *i.e.* no nesting is done and thus $\boldsymbol{E}$ disappears. Similarly in the context of the use of MC2 with a fully three dimensional turbulent diffusion (for either RANS or LES), no additional explicit numerical horizontal diffusion is required. Thus, $\boldsymbol{H}$ also vanishes. As a side note, this terms is also unnecessary when the model is used as a pure column model since all fields are perfectly homogeneous in the horizontal at all heights[1].

[1] Note that, in the present study, a so-called 3D sponge layer located in the upper part of the computational domain is used to smooth the fields of the main variables (see Sec. 3.2.3). The latter is imposed through $\boldsymbol{H}$.

Last but not least, concerning the implementation, MC2 (and more generally mesoscale models from EC) have been traditionally divided into two main components:

- the so-called "dynamics" taking care of simulated processes (Euler solver also referred to as the dynamic kernel) and terms related to the numerical treatment ($\boldsymbol{E}$, $\boldsymbol{H}$ and $\boldsymbol{T}$);
- the so-called "physics" (common to all model from EC and also referred to as the physics library) where all modelled processes, such as turbulent diffusion, are included.

These two components feature different spatial and time discretizations, and they rely on their proper boundary conditions. This has great implications on the implementation of the 3D turbulence modelling in MC2 (and in others mesoscale models from EC).

As a result of the above, in this chapter, after introducing the specificities of 3D turbulence modelling within the mesoscale models from EC in Sec. 3.1, the numerical method involved in the dynamics and then in the physics are described in Sec. 3.2 and Sec. 3.3 respectively. Both of these sections describe the time and space discretization as well as the boundary conditions proper to the various components along with other specific aspects. A special attention is given to the features implemented or modified in this study. Then, Sec. 3.4 is dedicated to numerical techniques used to provide the model with initial fields. Finally, Sec. 3.5 introduces various numerical aspects of the post-processing with regards to LES.

3.1 Turbulence modelling in EC mesoscale models

Turbulence is include to the solution through $\boldsymbol{F}$ in a fractional step manner following a successive correction approach. However, as illustrated in Sec. 2.2.1, turbulent diffusion terms related to the volumetric part of Reynolds tensor (present only when 3D turbulent processes are considered) *i.e.* the isotropic component, have to be included in the dynamic kernel as they act as a pressure (Piomelli, 1999). Then, after $\boldsymbol{\Psi}^{+}_{DE}$ from Fig. 3.1 is known, external and physical forcing $\boldsymbol{F}$, in which turbulent diffusion terms related to the deviatoric part of Reynolds tensor are included, are computed and added to $\boldsymbol{\Psi}^{+}_{DE}$ in order to obtain $\boldsymbol{\Psi}^{+}_{DEFH}$.

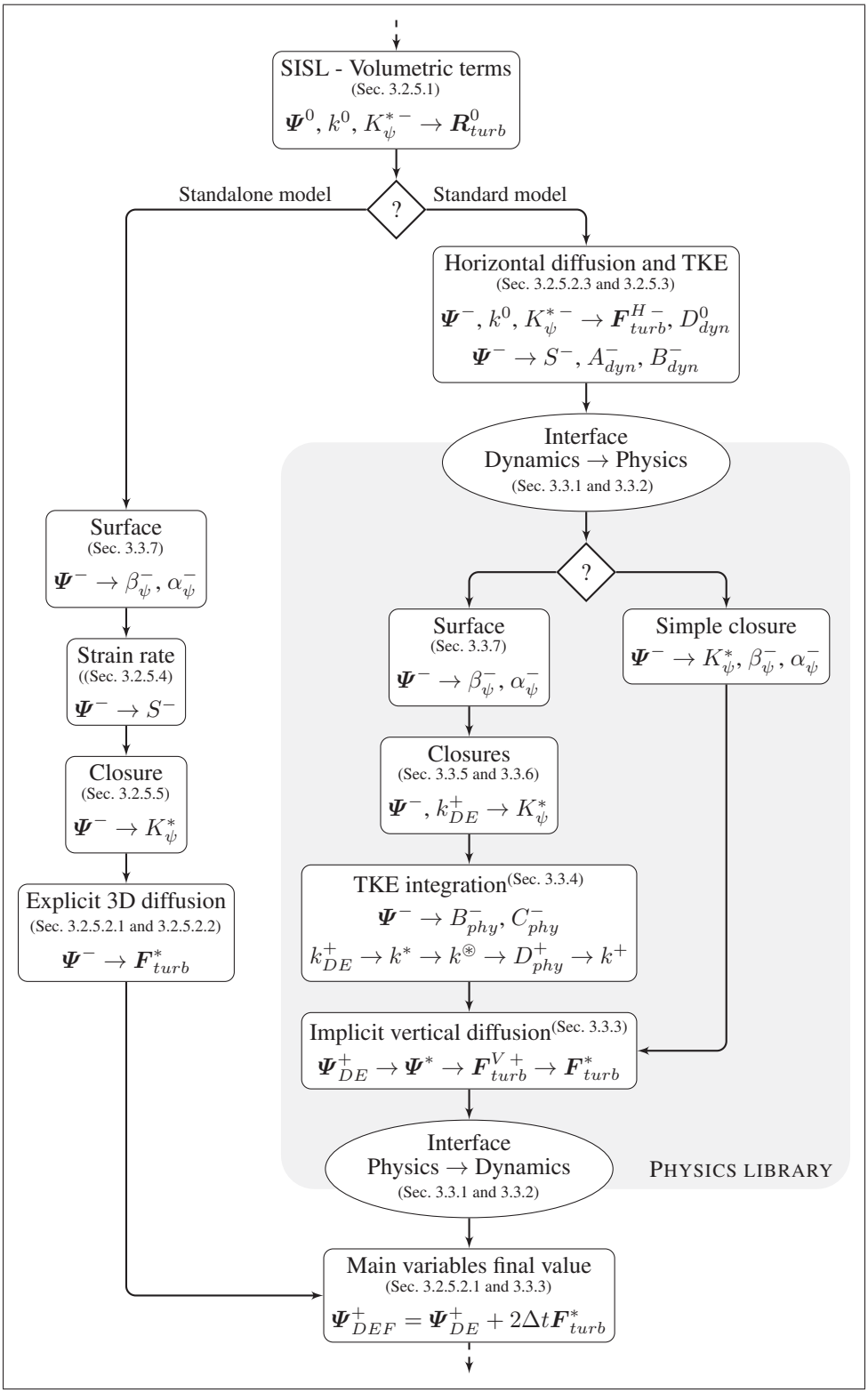

Figure 3.2 Diagram of the structure of the 3D turbulence modelling in MC2. Sections associated to each step are indicated in parenthesis

In the mesoscale models from EC and thus MC2, physical forcing have been traditionally computed separately (from the dynamic kernel), based on a so-called physics library. The latter is common to all models of EC and relies on its proper vertical coordinate and boundary conditions as seen later. Turbulent diffusion related to the deviatoric part of Reynolds tensor, and the full classical ABL column model are included within the physics library.

However, the physics library was designed with large scale and mesoscale modelling in mind. It fully relies on the boundary layer approximation, meaning that the ABL and the whole atmosphere are considered as horizontally homogeneous which largely affects the numerical methods used in the physics. Indeed, the 3D computational domain on which the Euler equations of motion are solved is considered as a set of independent 1D columns in the physics library, preventing the direct computation of horizontal gradient or interpolations (see Sec. 3.3 for further details).

As a result, when mesoscale cases are considered (*i.e.* relying on the ABL column model), all the turbulence modelling can be done seamlessly within the physics. At the opposite, for high resolution cases where a 3D turbulence modelling is required, many of the terms of the turbulent diffusion, the TKE equation and the closures can not be directly computed in the physics library. They need to be precomputed in the dynamics before being sent to the physics to complete the 3D turbulence modelling. Following this approach, there is thus a separation between all the horizontal and vertical turbulence related terms[2].

In addition to this separation in space, time discretization of horizontal and vertical turbulent diffusion differs. In order to fully take advantage of the large time step allowed by the SISL in the mesoscale context, vertical turbulent diffusion requires to be treated implicitly in time (Mailhot and Benoit, 1982). For its part, horizontal turbulent diffusion is considered only for very high resolution cases, *i.e.* where $\Delta x < 200$ m. In that context, $\Delta x / \Delta z$ become of the order of unity and the time step is notably smaller, while vertical resolution does not change significantly (in comparison to the horizontal resolution). As a result , numerical stability of

[2] This separation mainly concerns computation of the strain rate tensor, some of the terms of the TKE equation and turbulent diffusion terms related to the deviatoric part of Reynolds tensor.

horizontal turbulent diffusion is less sensitive to the time step than vertical turbulent diffusion in the context of mesoscale modelling. Thus, horizontal turbulent diffusion can be treated explicitly in time, while, considering that velocity and temperature vertical gradient are still dominant (horizontal turbulent diffusion terms are at least ten fold smaller than their vertical counterpart), the same implicit treatment as in the column model is retained for the momentum, heat and TKE vertical turbulent diffusion.

This approach, where the physics library is used (requiring a separated spatial and time numerical treatment of horizontal and vertical turbulent quantities), is referred to as the standard turbulence modelling in MC2.

Going a step further, and since the implicit treatment of the vertical turbulent diffusion is less critical in the context of very high resolution modelling with MC2, a solution to avoid such a partitioning (and the complications that come with it) is to handle the whole 3D turbulence modelling at the same place, *i.e.* explicit in time in the dynamics. This is referred to as the standalone turbulence model (since it does not rely anymore on the physics library). Both the standard and the standalone turbulence models are presented along this chapter. As a summary, the diagram shown in Fig. 3.2 illustrates the implementation of the 3D turbulence modelling in MC2 (the various terms introduced in that diagram are all detailed in this chapter).

3.2 Dynamics

The numerical method used to solve the fully compressible Euler equations of motion Eq. (2.31), *i.e.* the semi-Lagragian (SL) advection and the semi-implicit (SI) time discretization, have been refined along the years to obtain a versatile and robust solver as introduced in the various papers dedicated to MC2 (Robert *et al.*, 1985; Tanguay *et al.*, 1990; Bergeron *et al.*, 1994; Pinty *et al.*, 1995; Benoit *et al.*, 1997; Laprise *et al.*, 1997; Thomas *et al.*, 1998; Girard *et al.*, 2005). The report from Bergeron *et al.* (1994) is the most complete document describing thoroughly, not only the mathematical model, but also the complete numerical method, including discretizations and boundary conditions of the dynamic kernel of MC2. It is nevertheless partly outdated.

Numerical method of the current version of the model is detailed in Girard *et al.* (2005), and Thomas *et al.* (1998), while slightly older, present in details the current adiabatic kernel.

In this section, main aspects of numerical method used to solve the Euler equations of motion (which form the dynamic kernel of MC2) are first introduced, by presenting the SISL, spatial discretization and boundary conditions involved in the dynamics kernel. Then, and after presenting the implementation of the new large scale forcing, the remaining of the section is dedicated to the turbulence modelling achieved in the dynamics (outside the dynamics kernel). Thus, starting with volumetric terms, both the dynamics components of the standard 3D turbulence model (where horizontal turbulent diffusion and TKE terms are pre-computed in the dynamics), and the full standalone 3D turbulence model (where a full UKMO SGS model and the 3D turbulent diffusion are implemented in the dynamics) are then thoroughly presented.

3.2.1 Semi-Implicit Semi-Lagrangian (SISL) time stepping

The Semi-Lagrangian (SL) advection scheme approximates the material derivatives along a trajectory characterized by three time levels $(t - \Delta t,\, t,\, t + \Delta t)$, noted $(\psi^-,\, \psi^0,\, \psi^+)$ for any variable ψ hereafter, and two spatial locations: the arrival, *i.e.* the end, of the trajectory $\boldsymbol{x} = (x, y, z)$ which collocated with a grid point, and the upwind departure of the trajectory located at $(\boldsymbol{x} - 2\boldsymbol{\alpha}) = (x - 2\alpha, y - 2\beta, z - 2\gamma)$.

Following the SL approach, the discrete form of the material derivative can be expressed as

$$\frac{\delta_{tr}\boldsymbol{\Psi}}{2\Delta t} = \frac{\boldsymbol{\Psi}^+_{\boldsymbol{x}} - \boldsymbol{\Psi}^-_{\boldsymbol{x}-2\boldsymbol{\alpha}}}{2\Delta t}. \tag{3.2}$$

Variables at time t^- at the trajectory arrival location, *i.e.* $\boldsymbol{\Psi}^-_{\boldsymbol{x}}$, are known. However, in order to evaluate the various quantities at the upwind location and time t^-, *i.e.* $\boldsymbol{\Psi}^-_{\boldsymbol{x}-2\boldsymbol{\alpha}}$ required by Eq. (3.2), we also have to know the trajectory departure position $\boldsymbol{x} - 2\boldsymbol{\alpha}$ (that is not located on a grid point). This location is solely a function of the displacements along the Lagrangian trajectory (that are function of the velocity). As a result, the computation of the half displacement, *i.e.* $\boldsymbol{\alpha} = (\alpha, \beta, \gamma)$, is the first necessary step of the semi-Lagrangian method. For that

sake, a time extrapolation to t^+ of velocity at $\boldsymbol{x}$ is first achieved such as

$$\boldsymbol{v}_{\boldsymbol{x}}^{+} = 2\boldsymbol{v}_{\boldsymbol{x}}^{0} - \boldsymbol{v}_{\boldsymbol{x}}^{-}. \tag{3.3}$$

Then, a first computation of the displacement is done at the arrival of the trajectory, such as

$$\boldsymbol{\alpha'} = \Delta t \boldsymbol{v}_{\boldsymbol{x}}^{+}, \tag{3.4}$$

and this value is then used to evaluate velocity at the trajectory midpoint $\boldsymbol{v}_{\boldsymbol{x}-\boldsymbol{\alpha'}}^{0}$, allowing finally to obtain the value of the half displacements at the centre of the trajectory

$$\boldsymbol{\alpha} = \Delta t \boldsymbol{v}_{\boldsymbol{x}-\boldsymbol{\alpha'}}^{0}. \tag{3.5}$$

Values of the various variables and terms at upwind location, *i.e.* $\boldsymbol{\Psi}_{\boldsymbol{x}-2\boldsymbol{\alpha}}^{-}$, is then computed based on a piecewise cubic polynomial interpolations (Thomas *et al.*, 1998; Girard *et al.*, 2005).

As underlined by Thomas *et al.* (1998), the semi-Lagrangian time integration scheme can be interpreted as an Eulerian finite difference scheme which is shifted to the upwind grid cell (commonly known as upwind scheme). Similarly, Randall (2011, Sec. 5.12) also considers the semi-Lagrangian as being "equivalent to a generalized upstream scheme", thus featuring the same properties, *i.e.* it is monotone, but more importantly for LES, it is more diffusive than centred Eulerian schemes. Randall (2011) further adds that while the intensity of this numerical diffusion can be lowered by using higher-order interpolations (to compute variable at the upwind location), it cannot be avoided.

Robert *et al.* (1985) (see also Laprise *et al.* (1997)) further combined the semi-Lagrangian advection scheme with a semi-implicit algorithm to solve the remaining linear terms as averaged in time along the trajectory, which allows to filter the fastest gravity and sound waves ensuring the numerical stability of the SISL scheme while allowing relatively long time steps (Thomas

et al., 1998). The linear terms are thus expressed as

$$\overline{\boldsymbol{L}}^{tr} = \frac{(1+\epsilon)\,\boldsymbol{L}_{\boldsymbol{x}}^{+} + (1-\epsilon)\,\boldsymbol{L}_{\boldsymbol{x}-2\boldsymbol{\alpha}}^{-}}{2}, \tag{3.6}$$

where ϵ is an off-centring parameter.

As a result, following the SISL approach, the discrete form of the full model equations Eq. (2.33) (where all terms are detailed in Eq. (2.34)) can be written as

$$\frac{\delta_{tr}\boldsymbol{\Psi}}{2\Delta t} + \overline{\boldsymbol{L}}^{tr} = \overline{\boldsymbol{R}}^{tr0} + \boldsymbol{F}_{\boldsymbol{x}}^{*}, \tag{3.7}$$

where external forcing $\boldsymbol{F}_{\boldsymbol{x}}^{*}$ are evaluated at the arrival point and at an intermediate time level t^{*} as $\boldsymbol{F}$ may be based on quantities from different time levels (such as the mixing coefficient). For their part, the non-linear terms $\overline{\boldsymbol{R}}^{tr0}$ are spatially averaged along the trajectory at t^{0} (instead of been computed at the trajectory midpoint, *i.e.* $\boldsymbol{R}_{\boldsymbol{x}-\boldsymbol{\alpha}}^{0}$ (Tanguay *et al.*, 1990)). The latter can thus be written as

$$\overline{\boldsymbol{R}}^{tr0} = \frac{(1+\epsilon)\,\boldsymbol{R}_{\boldsymbol{x}}^{0} + (1-\epsilon)\,\boldsymbol{R}_{\boldsymbol{x}-2\boldsymbol{\alpha}}^{0}}{2}. \tag{3.8}$$

This spatial average introduces some mild numerical dissipation that allow to damp spurious mode excited by the SISL three time levels scheme (Thomas *et al.*, 1998). It thus increases the stability of the method with regards to non-linear forcing. Finally, posing $\Delta t^{\pm} = (1 \pm \epsilon)\,\Delta t$ and substituting Eqs. (3.2), (3.6) and (3.8) in Eq. (3.7) gives

$$\left[\boldsymbol{\Psi}^{+} + \Delta t^{+}\boldsymbol{L}^{+}\right]_{\boldsymbol{x}} = \left[\boldsymbol{\Psi}^{-} - \Delta t^{-}\boldsymbol{L}^{-} + \Delta t^{-}\boldsymbol{R}^{0}\right]_{\boldsymbol{x}-2\boldsymbol{\alpha}} + \left[\Delta t^{+}\boldsymbol{R}^{0} + 2\Delta t\boldsymbol{F}^{*}\right]_{\boldsymbol{x}} = \boldsymbol{Q} \tag{3.9}$$

This system of equations is then solved by first interpolating to upwind location $\boldsymbol{x} - 2\boldsymbol{\alpha}$ the first right-hand side term of Eq. (3.9), *i.e.* linear and non-linear terms, in order for $\boldsymbol{Q}$ to be fully known. Then, variables are eliminated by taking the divergence of the momentum equations (their spatial discretized form is used) which leads to an Helmholtz wave equation for P^{+} (Thomas *et al.*, 1998; Girard *et al.*, 2005).

This elliptic problem features a highly non-symmetric linear system of equations due to off-diagonal and cross-derivative terms. It is solved based on a robust iterative Generalized Minimal Residual (GMRES) Krylov solver, which is associated with an Alternative Direction Implicit (ADI) pre-conditioner method allowing to solve the Helmholtz equation more efficiently (Thomas *et al.*, 1998; Girard *et al.*, 2005). Once P at the arrival of the trajectory and at t^+ is known, *i.e.* $P^+_{\boldsymbol{x}}$, the remaining fields, *i.e.* $u^+_{\boldsymbol{x}}$, $v^+_{\boldsymbol{x}}$, $w^+_{\boldsymbol{x}}$, $b^+_{\boldsymbol{x}}$, are obtained by back substitution. At that point, $\boldsymbol{\Psi}^+_{ED}$ from Fig. 3.2 is known. Following this approach, the problem is fully solved without any segregation of variables contrary to the more classical CFD approaches such as the uncoupled pressure implicit with split operator (PISO) method. Finally, a weak Robert time filter (Asselin, 1972) is applied in order to damp numerical modes excited by the three time level scheme. This filter is fully part of the three time level SISL approach and even if it is applied after the physics (if activated).

Note that passive scalars Ψ, can be included in the problem such as

$$\frac{\delta_{tr}\Psi}{2\Delta t} = F^*_{\Psi\,\boldsymbol{x}}. \tag{3.10}$$

Thus, in such a case only the semi-Lagrangian advection is achieved to compute the material derivative of Ψ. Note that the TKE is advected following this approach.

Finally, concerning the present study, it is noteworthy that the isotropic part of the Reynolds tensor, Eq. (2.46), as well as the additional terms allowing large scale geostrophic forcing, Eq. (2.186), are included in $\boldsymbol{R}^0_{\boldsymbol{x}}$ as summarized on Eq. (2.189). The details of the spatial discretization of those terms is given in Sec. 3.2.5.1 and Sec. 3.2.4, respectively.

3.2.2 Spatial discretization

In the present model, a staggered grid is used (along with finite differences) in both horizontal and vertical directions as illustrated in Fig. 3.3 which shows the location of the main variables[3]. Variables from the continuous space are projected on the grid based on piecewise-constant

[3] Note that, as seen later a different discretization is used in the physics library of the model.

finite elements and the projection operator presented in Girard *et al.* (2005, Sec. 3.c and 3.d). As illustrated in Sec. 3.2.2.1 and Sec. 3.2.2.2, this formalism allows to define a correspondence between indices used in the code (integer only referred to as absolute index) and indices of the variable projected on the grid (referred to as projected indices and for which staggered variables with regards to the pressure feature a half index). It further allows to define the operation such as interpolations and derivatives in the discrete space as presented in Sec. 3.2.2.3.

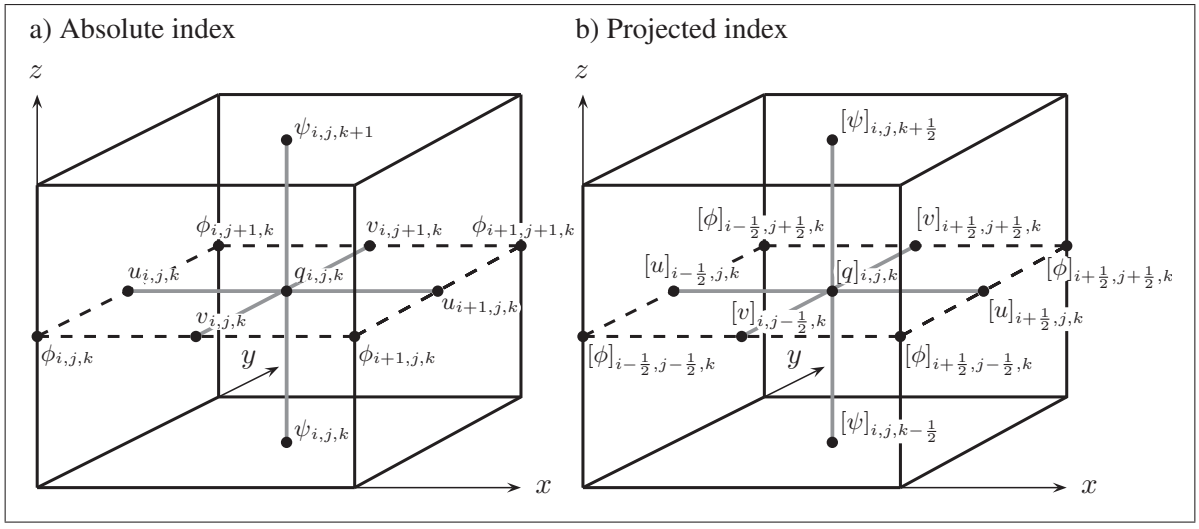

Figure 3.3 Mesh molecule illustrating the location of MC2 main variables: a) absolute index, and b) projected index. Coriolis and map scale factors are located in ϕ, while temperature, vertical velocity, TKE and mixing coefficients are in ψ

3.2.2.1 Horizontal discretization

In the horizontal, an Arakawa C-grid (Haltiner and Williams, 1980) is used along an uniform non-isotropic mesh (in the present study an uniform isotropic grid is always used, *i.e.* $\Delta x = \Delta y = \text{const.}$). As shown in Figs. 3.3 and 3.4, pressure (q and thus P) is located at the centre of the mesh, while the u velocity component is located at the centre of the east and west grid faces and the v velocity component is located at the centre of the south and north grid faces. Finally, vertical velocity and temperature (w, T and thus b) as well as TKE (k and K_M) are located at the centre of the upper and lower faces, *i.e.* above and below the pressure location.

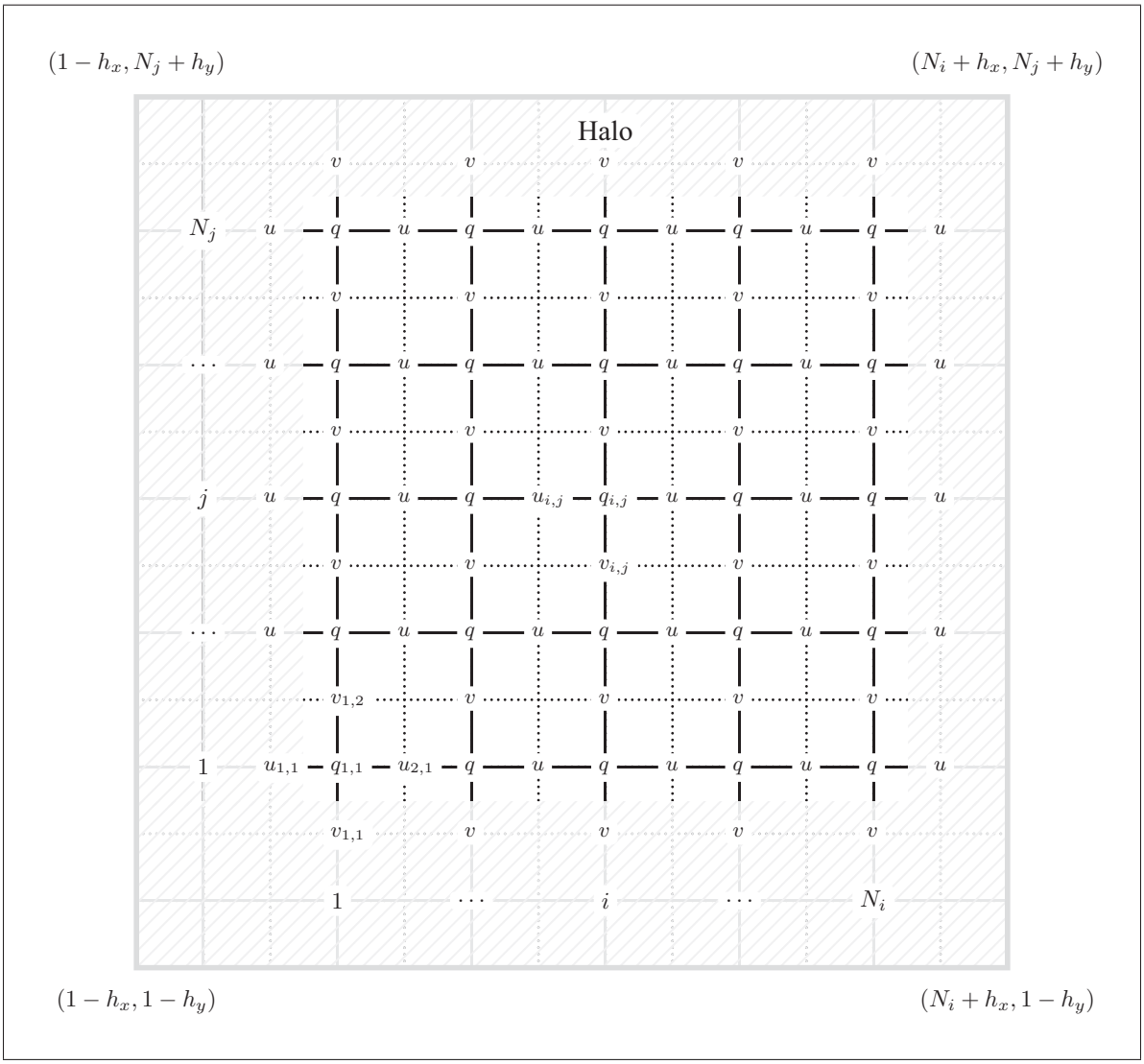

Figure 3.4 Horizontal full domain (computational domain with boundary conditions) along absolute index of q, u and v on the Arakawa C-grid (in this example we have: $N_i = N_j = 5$ and $h_x = h_y = 1$)

Following Girard *et al.* (2005) projection operator formalism, the correspondence between the absolute to the projected index, which is also illustrated in Fig. 3.3, writes

$$q_{i,j,k} = [q]_{i,j,k}\,, \qquad T_{i,j,k} = [T]_{i,j,k-1/2}\,, \qquad k_{i,j,k} = [k]_{i,j,k-1/2}\,,$$
$$u_{i,j,k} = [u]_{i-1/2,j,k}\,, \qquad v_{i,j,k} = [v]_{i,j-1/2,k}\,, \qquad w_{i,j,k} = [w]_{i,j,k-1/2}\,.$$

Table 3.1 Computational domain and array dimensions in absolute index

Variable	Computational domain			Array dimensions		
	x	y	z	x	y	z
q	$1 : N_i$	$1 : N_j$	$0 : N_k + 1$	$1 - h_x : N_i + h_x$	$1 - h_y : N_j + h_y$	$0 : N_k + 1$
T	$1 : N_i$	$1 : N_j$	$1 : N_k + 1$	$1 - h_x : N_i + h_x$	$1 - h_y : N_j + h_y$	$1 : N_k + 1$
u	$2 : N_i$	$1 : N_j$	$1 : N_k$	$1 - h_x : N_i + h_x$	$1 - h_y : N_j + h_y$	$1 : N_k + 1$
v	$1 : N_i$	$2 : N_j$	$1 : N_k$	$1 - h_x : N_i + h_x$	$1 - h_y : N_j + h_y$	$1 : N_k + 1$
w	$1 : N_i$	$1 : N_j$	$1 : N_k + 1$	$1 - h_x : N_i + h_x$	$1 - h_y : N_j + h_y$	$1 : N_k + 1$

Tab. 3.1 gives details on the computational domain size and total array dimensions, and Fig. 3.4 further illustrates the full horizontal grid along with boundary locations in quv-plane. N_i, N_j and N_k are the maximum indices in the three directions, and h_x and h_y the lateral halo size. On this figure, note that computational domain lateral borders are located on half indices *i.e.* at velocity locations $[u]_{1/2,j,k}$, $[u]_{N_i-1/2,j,k}$, $[v]_{i,1/2,k}$ and $[v]_{i,N_j-1/2,k}$ (which data is included in the boundary domain). Furthermore, a halo of h_x and h_y width is used as lateral boundary of the domain. The lateral boundaries is thus 3D. The latter is required to allow the computation of the various variables at the Lagrangian trajectories upwind/departure location, *i.e.* $\boldsymbol{\Psi}^{-}_{\boldsymbol{x}-2\boldsymbol{\alpha}}$ (for the mesh at an inlet). Sec. 3.2.3 further details the processing of the halo. Note finally that, a similar halo is also present on the lateral sides of each sub-domains when the domain is decomposed on several processor (decomposition is horizontal only and always based on a even number of sub-domain).

3.2.2.2 Vertical discretization

In the vertical, as illustrated in Figs. 3.3 and 3.5, a variant of a Charney-Phillips grid (Haltiner and Williams, 1980) is used with the possibility of a non uniform grid spacing. Far from the boundaries, such as presented in Fig. 3.3, pressure and horizontal velocity components are located on the full vertical levels, while vertical velocity, temperature, and TKE are located on staggered levels. For its part, momentum turbulent mixing coefficient is also located on staggered levels, while the heat turbulent mixing coefficient is computed on staggered levels and interpolated to full levels when needed.

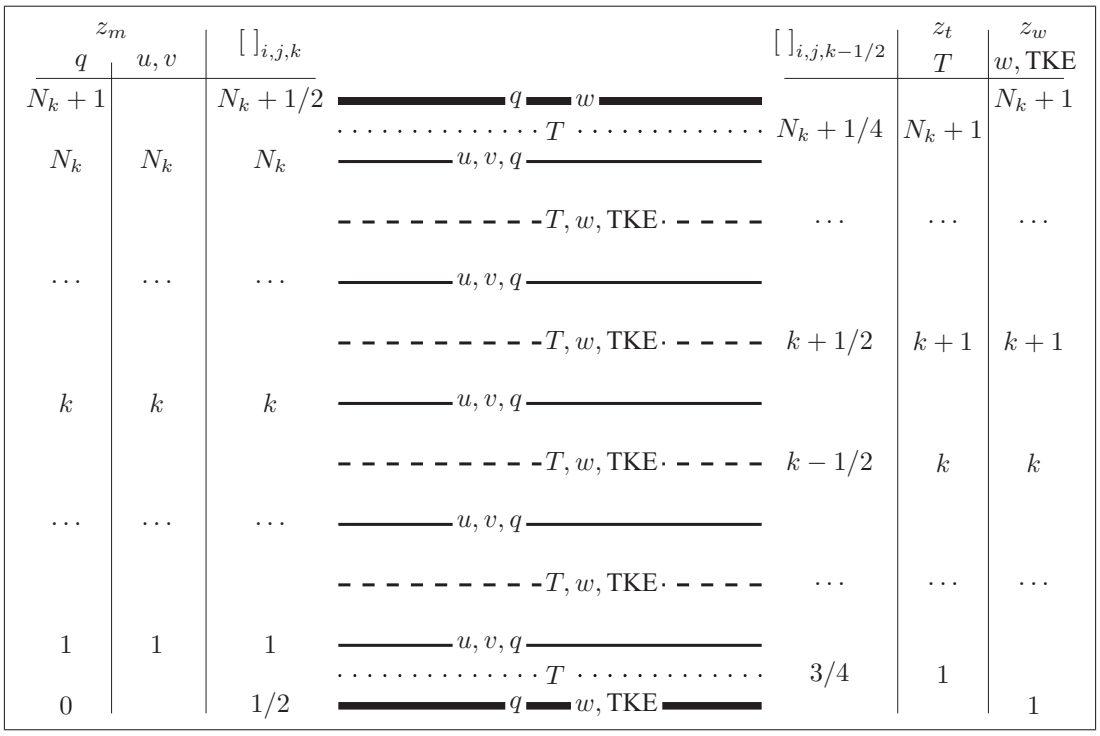

Figure 3.5 Vertical mesh of the dynamics along with the absolute and projected vertical indices of the main variables

The bottom and top boundary of the grid coincide with staggered levels. However, the pressure (instead of the temperature) and the vertical velocity (which is normal) are located on those two levels leading to $q_{i,j,0} = [q]_{i,j,1/2}$ and $q_{i,j,N_k+1} = [q]_{i,j,N_k+1/2}$. Concerning the temperature, its first (resp. last) level is located half way in between the bottom (resp. top) and the first (resp. last) full level, leading to $T_{i,j,1} = [T]_{i,j,3/4}$ and $T_{i,j,N_k+1} = [T]_{i,j,N_k+1/4}$. The organization of thermodynamic variables thus differs from the classical Charney-Phillips arrangement at the lower and upper boundaries in order to better accommodate the computation of their boundary conditions (see Sec. 3.2.3). On the contrary, discretization of velocity components is unchanged throughout the domain. Finally, the top and bottom boundary conditions of TKE (and mixing coefficients) are defined such as $k_{i,j,1} = [k]_{i,j,1/2}$ and $k_{i,j,N_k} = [k]_{i,j,N_k-1/2}$. TKE thus have one level less than velocity and temperature.

Fig. 3.5 further presents the height vectors of the full and staggered levels[4], *i.e.* temperature z_t (staggered), vertical velocity z_w (staggered), and momentum/pressure z_m (full) height vector. They are obtained by first setting the N_k+1 vertical velocity levels $z_{w\,k} = [z_w]_{k-1/2}$ with $z_{w\,1} = [z_w]_{1/2} = 0$ m and following a given definition of the vertical levels, *i.e.* uniform, stretched, ... , but that have to be monotonic. Then, momentum levels $z_{m\,k} = [z_m]_k$ are computed as being exactly in the middle of two z_w levels, such as

$$[z_m]_k = \frac{[z_w]_{k+1/2} + [z_w]_{k-1/2}}{2} = \frac{z_{w\,k+1} + z_{w\,k}}{2}, \tag{3.11}$$

with $z_{m\,0} = [z_m]_{1/2} = [z_w]_{1/2}$ and $z_{m\,N_k+1} = [z_m]_{N_k+1/2} = [z_w]_{N_k+1/2}$. Temperature level are finally defined as $z_{t\,k} = [z_t]_{k-1/2} = [z_w]_{k-1/2}$ except for the bottom and top levels that are computed as been half way in between the two first and last pressure levels respectively. Then, the vertical grid spacing are readily obtained such as

$$[\Delta z_m]_{k-1/2} = [z_m]_k \quad - [z_m]_{k-1}\,, \tag{3.12}$$

$$[\Delta z_t]_k = [z_t]_{k+1/2} - [z_t]_{k-1/2}\,, \tag{3.13}$$

$$[\Delta z_w]_k = [z_w]_{k+1/2} - [z_w]_{k-1/2}\,. \tag{3.14}$$

where we have $[\Delta z_t]_k = [\Delta z_w]_k$ away from the boundaries.

Finally, it is noteworthy that this approach introduces an asymmetry in the grid spacing and unless the vertical mesh is fully uniform, we have

$$[z_w]_{k-1/2} \neq \frac{[z_m]_k + [z_m]_{k-1}}{2}. \tag{3.15}$$

As a result, if a non uniform grid is to be used, care must be taken when interpolating variable from the momentum levels to temperature levels.

[4] Note that herein, these heights are Gal-Chen (Gal-Chen and Somerville, 1975) or generalized vertical coordinate and not geometrical heights. However, since they are equal in the context of flat terrain, it is not relevant to follow the formalism of vertical coordinate transformation.

3.2.2.3 Simple operations in the discrete space

Interpolations and derivatives in the discrete space are illustrated in this section based on the formalism, and horizontal and vertical discretizations introduced previously.

Staggered variables are brought to the center of the mesh based on a linear interpolation

$$\left[\overline{T}^{\mathrm{Z}}\right]_{i,j,k} = \frac{[T]_{i,j,k+1/2} + [T]_{i,j,k-1/2}}{2} = \frac{T_{i,j,k+1} + T_{i,j,k}}{2}, \tag{3.16}$$

$$[\overline{u}^{\mathrm{X}}]_{i,j,k} = \frac{[u]_{i+1/2,j,k} + [u]_{i-1/2,j,k}}{2} = \frac{u_{i+1,j,k} + u_{i,j,k}}{2}, \tag{3.17}$$

while the interpolation to go from plain to staggered levels writes

$$[\overline{u}^{\mathrm{Z}}]_{i-1/2,j,k-1/2} = \frac{[z_m]_k - [z_t]_{k-1/2}}{[z_m]_k - [z_m]_{k-1}} [u]_{i-1/2,j,k-1} + \frac{[z_t]_{k-1/2} - [z_m]_{k-1}}{[z_m]_k - [z_m]_{k-1}} [u]_{i-1/2,j,k}, \tag{3.18}$$

$$= \frac{z_{m\,k} - z_{t\,k}}{z_{m\,k} - z_{m\,k-1}} u_{i,j,k-1} + \frac{z_{t\,k} - z_{m\,k-1}}{z_{m\,k} - z_{m\,k-1}} u_{i,j,k}, \tag{3.19}$$

and further considering the definition of z_m levels, Eq. (3.11), this can also be expressed as

$$[\overline{u}^{\mathrm{Z}}]_{i-1/2,j,k-1/2} = [W_{z_t}]_{k-1/2} [u]_{i-1/2,j,k-1} + \Big(1 - [W_{z_t}]_{k-1/2}\Big) [u]_{i-1/2,j,k}, \tag{3.20}$$

$$= W_{z_t\,k}\, u_{i,j,k-1} + (1 - W_{z_t\,k})\, u_{i,j,k}, \tag{3.21}$$

with

$$[W_{z_t}]_{k-1/2} = \frac{[z_t]_{k+1/2} - [z_t]_{k-1/2}}{[z_t]_{k+1/2} - [z_t]_{k-3/2}} = \frac{z_{t\,k+1} - z_{t\,k}}{z_{t\,k+1} - z_{t\,k-1}}. \tag{3.22}$$

Note that at the bottom and top of the domain, special care is taken for vertical interpolation of temperature to fall on momentum/pressure levels, such as

$$\left[\overline{T}^{\mathrm{Z}}\right]_{i,j,1} = \frac{[z_t]_{i,j,3/2} - [z_m]_{i,j,1}}{[z_t]_{i,j,3/2} - [z_t]_{i,j,3/4}} [T]_{i,j,3/4} + \frac{[z_m]_{i,j,1} - [z_t]_{i,j,3/4}}{[z_t]_{i,j,3/2} - [z_t]_{i,j,3/4}} [T]_{i,j,3/2}, \tag{3.23}$$

$$= \frac{z_{t\,2} - z_{m\,1}}{z_{t\,2} - z_{t\,1}} T_{i,j,1} + \frac{z_{m\,1} - z_{t\,1}}{z_{t\,2} - z_{t\,1}} T_{i,j,2}. \tag{3.24}$$

Horizontal and vertical derivatives are given by

$$\left[\frac{\partial q}{\partial x}\right]_{i-1/2,j,k} \Rightarrow \left[\frac{\delta_x q}{\Delta x}\right]_{i-1/2,j,k} = \frac{[q]_{i,j,k} - [q]_{i-1,j,k}}{\Delta x} = \frac{q_{i,j,k} - q_{i-1,j,k}}{\Delta x}, \quad (3.25)$$

$$\left[\frac{\partial q}{\partial z}\right]_{i,j,k-1/2} \Rightarrow \left[\frac{\delta_z q}{\Delta z_m}\right]_{i,j,k-1/2} = \frac{[q]_{i,j,k} - [q]_{i,j,k-1}}{[\Delta z_m]_{k-1/2}} = \frac{q_{i,j,k} - q_{i,j,k-1}}{z_{m\,k} - z_{m\,k-1}}, \quad (3.26)$$

$$\left[\frac{\partial T}{\partial z}\right]_{i,j,k} \Rightarrow \left[\frac{\delta_z T}{\Delta z_t}\right]_{i,j,k} = \frac{[T]_{i,j,k+1/2} - [T]_{i,j,k-1/2}}{[\Delta z_t]_k} = \frac{T_{i,j,k+1} - T_{i,j,k}}{z_{t\,i,j,k+1} - z_{t\,i,j,k}}, \quad (3.27)$$

and slightly more complex derivative writes

$$\left[\frac{\partial u}{\partial x}\right]_{i,j,k-1/2} \Rightarrow \left[\frac{\delta_x \overline{u}^{\mathrm{Z}}}{\Delta x}\right]_{i,j,k-1/2} = \frac{[\overline{u}^{\mathrm{Z}}]_{i+1/2,j,k-1/2} - [\overline{u}^{\mathrm{Z}}]_{i-1/2,j,k-1/2}}{\Delta x}, \quad (3.28)$$

$$\left[\frac{\partial T}{\partial z}\right]_{i,j,k-1/2} \Rightarrow \left[\frac{\delta_z \overline{T}^{\mathrm{Z}}}{\Delta z_m}\right]_{i,j,k-1/2} = \frac{\left[\overline{T}^{\mathrm{Z}}\right]_{i,j,k} - \left[\overline{T}^{\mathrm{Z}}\right]_{i,j,k-1}}{[\Delta z_m]_{k-1/2}}. \quad (3.29)$$

Finally, coupled products such as the last terms on the right hand side of Eq. (2.32a) writes

$$\left[\frac{b}{g}\frac{\partial P}{\partial x}\right]_{i-1/2,j,k} \Rightarrow \left[\frac{\overline{b}^{\mathrm{XZ}}}{g}\frac{\delta_x P}{\Delta x}\right]_{i-1/2,j,k}. \quad (3.30)$$

3.2.2.4 Vertical mesh generator

In the context of normal use of the MC2 model (*i.e.* for mesoscale cases), the upper boundary of the computational domain is commonly located above 10 km, vertical grid is monotonically stretched upward to better take into account the high gradient in the ABL, and the width/height ratio of the near-surface cells is commonly higher than 100, *i.e.* 10 km/100 m. In addition, and partly due to its compressible solver, the MC2 model features a top boundary condition based on a multi-layer sponge as presented in Sec. 3.2.3 (always based on the ten upper levels here).

This heavily depart from the computational domains typically used to reproduce the full ABL based on LES (Nieuwstadt *et al.*, 1992; Moeng and Sullivan, 1994), which is generally only a couple of kilometres high with the ratio $\Delta x/\Delta z$ become of the order of unity in the regions of

interest (*i.e.* from the surface to above the inversion). The roof of the model is thus drastically lowered, and care must be taken for the upper boundary not to interact with the results (notably considering the sponge layer used here). Furthermore, monotonically upward stretched grids can not generally be used since a sufficiently high resolution is required to properly reproduce inversion processes where large and sharp gradients can also be found.

Considering that only vertical uniform or monotonically upward stretched grids were available in MC2, a new vertical mesh generator was developed based on the following criteria:

- function defining the vertical mesh must be growing and monotonic;
- surface as well as inversion are two regions where vertical gradients of various key quantities are large, and thus, regions where a finer grid is needed;
- sponge region need to be as far as possible from the inversion not to interact with it while been wide enough to be efficient without using too many levels.

From those simple criteria, and since surface layer momentum and temperature follow a log law, a vertical coordinate based on the log function Z_{log} is defined such as $\forall k \in [1; n_k]$, where $n_k = N_k + 1$, we have

$$\frac{ln\left(\frac{Z_{log}(k)}{r} + 1\right)}{ln\left(\frac{z_{top}}{r} + 1\right)} = \frac{k}{n_k}, \tag{3.31}$$

leading to

$$Z_{log}(k) = r\left[\left(\frac{z_{top}}{r} + 1\right)^{k/n_k} - 1\right], \tag{3.32}$$

where k is the height index, z_{top} the height of the top boundary, n_k the number of meshes in the vertical and r is a parameter. Here, z_{top} and n_k are provided as input and $r = z_{ref}/\alpha$ with α an input coefficient and z_{ref} a reference height also provided as input (taken to be roughly equal to the height of the ABL).

Based on this definition, the grid is further refined at the inversion (and indirectly in the upper ABL) thanks to a normal law used to reduce dZ_{log}/dk near the inversion, thus increasing locally the concentration of levels. The definition of this normal law writes

$$D_{nor}(k) = \frac{1}{\sqrt{2\pi\sigma^2}}\, e^{-\dfrac{(k-k_\mu)^2}{2\sigma^2}}, \tag{3.33}$$

where here k_μ is the normal law mean, *i.e.* location (in k index) of the normal law maximum, and, σ is the standard deviation of the normal law (also in k index) defining the width of the distribution. As seen later, k_μ is found iteratively while σ is a parameter provided as input.

The cumulative of D_{nor} is then subtracted from Z_{log}, but note that, in order for the resolution in the region of the inversion to be similar to the one at the surface, it is scaled. The scaled cumulative function writes

$$Z_{nor}(k) = \frac{\Delta Z_{log}(k_\mu) - \Delta Z_{log}(1)}{\max(D_{nor})} \int_0^k D_{nor}(k')dk'. \tag{3.34}$$

A blending is further added in order for the deviation from the logarithmic profile to return to zero at the top of the domain. The new vertical coordinate can then be expressed as

$$Z(k) = Z_{log}(k) - Z_{nor}(k) + \max(Z_{nor}) f(k), \tag{3.35}$$

where the blending function $f(k)$ must be increasing with k, monotonic and $\forall k \in [1; n_k]$, $f(k) \in [0; 1]$. $f(k) = (k/n_k)^2$ is used here. Finally, based on Eq. (3.35) and the criteria $Z(k_\mu - 1) < z_{ref} < Z(k_\mu)$, the location of the maximum of D_{nor}, *i.e.* k_μ, is computed. The new vertical mesh is then defined solely by Eq. (3.35) and the following parameters: α, σ, n_k, z_{ref} and z_{top}.

An illustration of the possible vertical grid along with their first and second derivatives can be seen in Fig. 3.6. On the left column of Fig. 3.6, grids have 60 meshes with $\alpha = 2$ and $z_{top} = 1500$ m. The top boundary is thus one third higher, while there are one third less meshes than in the uniform vertical grid previously used. A widening of the refined region at z_{ref} can be seen from $\sigma = 6$, where the normal law appears clearly, to $\sigma = 18$. In the latter case,

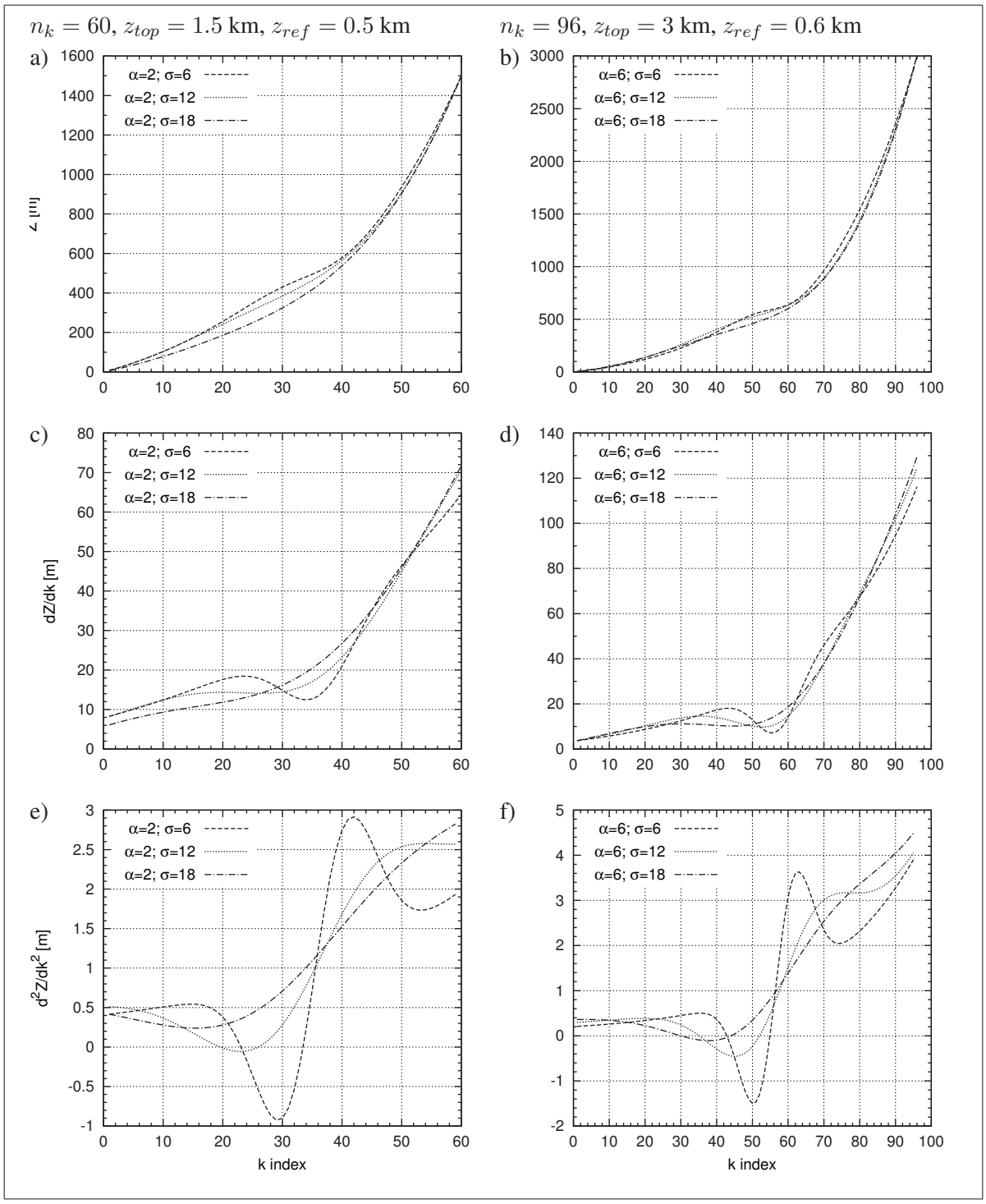

Figure 3.6 Illustration of the new vertical mesh, Eq. (3.35), along its first and second order derivatives for various sets of parameters: a), c) and e) $n_k = 60$, $z_{ref} = 0.5$ km and $z_{top} = 1.5$ km; b), d) and f) $n_k = 96$, $z_{ref} = 0.6$ km and $z_{top} = 3$ km

the local minimum of dz/dk at the inversion does not exist anymore: the resolution reaches a plateau below z_{ref} before stretching again. At the opposite, the grid most refined at the inversion, *i.e.* $\alpha = 2,\ \sigma = 6$, have roughly the same resolution at the surface and z_{ref} (as the uniform grid), while it is coarser in the mixed layer. On the right column of Fig. 3.6, grids have 96 meshes with $\alpha = 6$ and $z_{top} = 3000$ m. The top boundary is thus three times higher than the uniform grid, while the surface mesh is roughly three times finer and the same resolution or lower is found at the inversion. The increase of σ shows the very same pattern as previously. The grid based on $\alpha = 6,\ \sigma = 18$ is of particular interest as the resolution below z_{ref} is always finer than the uniform grid previously used.

The vertical mesh introduced here is interesting because, in addition to enhance resolution at the surface without affecting the mixed layer, it also allows the evaluation of the top boundary sponge influence on the results without adding computational cost. The main drawback is however that the height of the ABL needs to be a priori known (at least its maximum height). Furthermore, such meshes are less practical for cases where the inversion is evolving a lot during the integration, such as in convective conditions, while for any diurnal cycling, this constraint is diminished for large σ.

3.2.3 Boundary conditions

Boundary conditions involved to solve the Euler equations in MC2 are thoroughly presented by Bergeron *et al.* (1994), and their up-to-date description is included in Thomas *et al.* (1998) and Girard *et al.* (2005).

In the present section, the dynamic kernel set of boundary conditions used in the context of the current study are presented, *i.e.* for use in LES of thermally stratified barotropic ABL flows over a flat homogeneous surface and entrained by a constant geostrophic wind.

3.2.3.1 Surface boundary

The surface is considered as a free-slip rigid wall in the dynamic kernel. Thus, vertical velocity at the surface $[w]_{i,k,1/2}$, which is obtained diagnostically based on the kinematic condition Girard *et al.* (2005, Eq. (13)), depends on the slope of the terrain and horizontal velocity components. Then, surface pressure $[q]_{i,k,1/2}$ is computed diagnostically thanks to the non-hydrostatic prognostic equation of w at the first level (Girard *et al.*, 2005). Finally, an additional thermodynamic equation is solved to compute temperature perturbation at the first level $[T]_{i,k,3/4}$ (based on $[q]_{i,k,1/2}$ and $[q]_{i,k,1}$ explaining the $3/4$ vertical location of the first temperature). When the surface is flat, $[w]_{i,k,1/2} = 0$, and thus $dw/dt = 0$ at the surface. As a result, the diagnostic relation used to compute the surface pressure simplifies to the hydrostatic relation.

3.2.3.2 Top boundary

The top boundary is also based on a free-slip rigid wall but which is flat regardless of the configuration of the model. Thus, vertical velocity at the top $[w]_{i,k,N_k+1/2}$ is always zero at the top boundary and pressure $[q]_{i,k,N_k+1/2}$ is computed diagnostically relying on hydrostatic equilibrium. Concerning the top temperature perturbation, as for the surface, an additional thermodynamic equation is solved (Thomas *et al.*, 1998; Girard *et al.*, 2005).

Finally, it is noteworthy that the top boundary includes a so-called sponge layer of a given depth in which an explicit additional horizontal smoothing of all the main variables except the pressure (*i.e.* u, v, w and b) is applied. This region of enhanced horizontal diffusion allows to gradually dissipate the energy of the waves and eddies reaching the top boundary in order to prevent their spurious reflexion in the computational domain.

This horizontal smoothing is based on a nine point filtering as presented in Shuman (1957, Eq. (5)) (see also Haltiner and Williams (1980, Sec. 11.8)), and it is included in $\boldsymbol{H}$ from Eq. (3.1). As input parameters, this approach requires the number of levels on which the sponge is applied N_{sponge}, and a smoothing coefficient ν_{sponge} which can be interpreted as an horizontal viscosity. The latter coefficient is scaled from 0 at $k < N_k - N_{\text{sponge}}$ (base of the

sponge) to its maximum value at the top of the domain (top of the sponge) following a squared cosine. In the present study, $N_{\text{sponge}} = 10$, *i.e.* the sponge layer is located on the 10 uppermost levels, and a smoothing coefficient $\nu_{\text{sponge}} = 2$ is always used.

3.2.3.3 Lateral boundaries

The lateral boundary conditions have to let the flow in and out of the domain and connect with conditions outside the LAM area. As discussed in the previous section, due to the SL advection scheme, few points outside the computational domain are required to be able to compute the various quantities at the upwind location of the three time level trajectories. The variables in the halo further have to comply with the model differential equations as discussed by (Thomas *et al.*, 1998; Girard *et al.*, 2005). The optimum width of this halo, *i.e.* h_x and h_y, is a function of the CFL number. Thus, assuming that $\mathrm{CFL} < 1$ is the generally accepted criteria for SISL approaches such as MC2 (Bartello and Thomas, 1996; Thomas *et al.*, 1998; Girard *et al.*, 2005), $h_x = h_y = 3$ is used most of the time. Tab. 3.2 details the dimensions of the halo in absolute indices and the data involved when lateral periodicity is used.

Table 3.2 Horizontal boundary conditions domain and lateral periodicity

Variable		Boundary condition domain		Indices for lateral periodicity	
		x	y	x	y
East	q, T, w	$N_i + 1 : N_i + h_x$	$1 - h_y : N_j + h_y$	$1 : h_x$	$1 - h_y : N_j + h_y$
	u	$N_i + 1 : N_i + h_x$	$1 - h_y : N_j + h_y$	$1 : h_x$	$1 - h_y : N_j + h_y$
	v	$N_i + 1 : N_i + h_x$	$1 - h_y : N_j + h_y$	$1 : h_x$	$1 - h_y : N_j + h_y$
West	q, T, w	$1 - h_x : 0$	$1 - h_y : N_j + h_y$	$N_i - h_x + 1 : N_i$	$1 - h_y : N_j + h_y$
	u	$1 - h_x : 1$	$1 - h_y : N_j + h_y$	$N_i - h_x + 1 : N_i + 1$	$1 - h_y : N_j + h_y$
	v	$1 - h_x : 0$	$1 - h_y : N_j + h_y$	$N_i - h_x + 1 : N_i$	$1 - h_y : N_j + h_y$
North	q, T, w	$1 - h_x : N_i + h_x$	$N_j + 1 : N_j + h_y$	$1 - h_x : N_i + h_x$	$1 : h_y$
	u	$1 - h_x : N_i + h_x$	$N_j + 1 : N_j + h_y$	$1 - h_x : N_i + h_x$	$1 : h_y$
	v	$1 - h_x : N_i + h_x$	$N_j + 1 : N_j + h_y$	$1 - h_x : N_i + h_x$	$1 : h_y$
South	q, T, w	$1 - h_x : N_i + h_x$	$1 - h_y : 0$	$1 - h_x : N_i + h_x$	$N_j - h_y + 1 : h_y$
	u	$1 - h_x : N_i + h_x$	$1 - h_y : 0$	$1 - h_x : N_i + h_x$	$N_j - h_y + 1 : h_y$
	v	$1 - h_x : N_i + h_x$	$1 - h_y : 1$	$1 - h_x : N_i + h_x$	$N_j - h_y + 1 : h_y + 1$

In the present study, lateral boundary conditions are always periodical for all main variables. This greatly simplifies their processing, since it is only required to swap the lateral halo of each variables with the appropriate data from the opposite side of the computational domain, as detailed in Tab. 3.2. Then, trajectories can be computed similarly as in computational domain interior, and every variables has its lateral boundary conditions fully defined for the various time levels and locations on the Lagrangian trajectory.

3.2.4 Geostrophic forcing with lateral periodic conditions

The terms related to the large scale geostrophic forcing in presence of lateral periodic boundary conditions are illustrated in Eqs. (2.186) to (2.189). The mathematical formulation of such terms was first introduced in Pelletier *et al.* (2005), however they had never been implemented. As discussed in Sec. 2.4, they are included in $\boldsymbol{R}$ from Eq. (2.33) and noted $\boldsymbol{R}_{ls}$ hereafter. Thus, they are computed considering only the variables at the arrival of the trajectory at time t^0, namely $\boldsymbol{\Psi}^0_{\boldsymbol{x}}$, and included in $\boldsymbol{R}^0_{\boldsymbol{x}}$ from Eq. (3.9) (which is then interpolated at the upstream point of the trajectory to get $\boldsymbol{R}^0_{\boldsymbol{x}-2\boldsymbol{\alpha}}$). The information on the location in space (on the Lagrangian trajectory, $\boldsymbol{x}$ subscript) and time (0 superscript) are dropped hereafter.

The large scale geostrophic wind, $\boldsymbol{v}_g = (u_g, v_g)$, must be constant in time, horizontally homogeneous and with the same direction at all heights. It is located on plain levels, *i.e.* $u_{g\,i,j,k} = u_{g\,k} = [u_g]_k$ and $v_{g\,i,j,k} = v_{g\,k} = [v_g]_k$. Thus, the discrete form of the large scale geostrophic wind forcing terms writes

$$\boldsymbol{R}_{ls} = \begin{bmatrix} -\left[\overline{f}^{\mathrm{Y}} v_g\right]_{i-1/2,j,k} \\ \left[\overline{f}^{\mathrm{X}} u_g\right]_{i,j-1/2,k} \\ 0 \\ \left[\overline{f}^{\mathrm{XY}} \left(\overline{v}^{\mathrm{YZ}} \dfrac{\delta_z u_g}{\Delta z_m} - \overline{u}^{\mathrm{XZ}} \dfrac{\delta_z v_g}{\Delta z_m} \right)\right]_{i,j,k-1/2} \\ 0 \end{bmatrix}. \tag{3.36}$$

Concerning the computation of these expressions at the bottom and top boundaries, since $\boldsymbol{v}_g$ is located on the same levels as q and constant in the horizontal, the computation of $R_{u\,ls}$ and $R_{v\,ls}$ is straightforward. Concerning $R_{T\,ls}$, the computation of the vertical derivative at the bottom and top of the domain is also straightforward as it falls directly on temperature staggered levels $[T]_{i,j,3/4}$ and $[T]_{i,j,N_k+1/4}$. On the other hand, the velocity components required at those levels are simply set equal to their value at the first and last levels, *i.e.* $[\overline{u}^{\mathrm{XZ}}]_{i,j,3/4} = [\overline{u}^{\mathrm{X}}]_{i,j,1}$ and $[\overline{u}^{\mathrm{XZ}}]_{i,j,N_k+1/4} = [\overline{u}^{\mathrm{X}}]_{i,j,N_k}$. As a closure remark, f could be use instead of $\overline{f}^{\mathrm{X}}$, $\overline{f}^{\mathrm{Y}}$ and $\overline{f}^{\mathrm{XY}}$ as the Coriolis factor have to be constant when large scale geostrophic forcing are involved. Those notation were however retain to satisfy the projection formalism.

Finally, it is to note that $\boldsymbol{R}_{ls}$ is implemented taking into account the various metric factors arising from the mathematical transformation related to the inclusion of the topography. This was done so that all the new components included in $\boldsymbol{R}$ are not an exception with regards to metric factors, but not included here as they equal unity when the terrain is flat.

3.2.5 Turbulence modelling in the dynamics

Turbulent diffusion is normally achieved during the physical step. However, as illustrated in Sec. 2.2.1, momentum turbulent diffusion terms related to the volumetric part of the Reynolds tensor must be included in the dynamic kernel, *i.e.* in $\boldsymbol{R}$ from Eq. (2.33), as they act like a pressure. Furthermore, as discussed in Sec. 3.1, when the standard 3D turbulence modelling is followed, due to the specificities of the physics, the computation of the remaining terms requires a separation of their horizontal components (that feature horizontal gradients and derivatives), and their vertical components (that only feature vertical derivatives and interpolation). In this standard approach, the former need to be pre-computed in the dynamics before being included in the physics to complete the 3D turbulence modelling as introduced by Pelletier *et al.* (2005)[5]. An alternative approach introduced here is to fully achieve the turbulence modelling in the dynamics in a standalone manner (not relying on the physics).

[5] Note that in the early implementation of the 3D turbulence modelling in MC2, there was no distinction between the volumetric and the deviatoric part of the Reynolds tensor (Pelletier *et al.*, 2005). The approach was refined during this study as presented in the current chapter and validated in Chap. 4, by notably, further splitting properly the various terms and improving the vertical staggering.

In any case, it is noteworthy that the free-slip surface boundary condition used in the dynamic kernel does not apply here. Instead, the surface is considered as a no-slip rough wall modelled though wall functions, and the surface boundary condition is obtained considering the continuity of momentum and heat turbulent fluxes along the vertical at the bottom boundary (See Sec. 3.3.7 for more details).

In the present section, the numerical method used to obtain the turbulence related terms in the dynamics are presented. First, the discretization of the turbulent diffusion terms linked to the volumetric part of Reynolds tensor is described. Then, the numerical method used to compute turbulent diffusion terms that include the deviatoric part of the Reynolds tensor are discussed. In that subsection, the 3D turbulent diffusion fully implemented in the dynamics is first presented (*i.e.* the so-called standalone turbulence model), followed by the horizontal diffusion terms pre-computed in dynamics when relying on the standard turbulence modelling. Subsequently, the discretization of the horizontal terms of the TKE equation along with the computation of the strain rate tensor modulus are presented. Finally, the standalone UKMO Smagorinsky model implemented in the dynamics is introduced.

3.2.5.1 Volumetric part of the Reynolds tensor

The turbulent diffusion terms related to the volumetric part of Reynolds tensor are described in Eqs. (2.46) and (2.49). They are included with the non-linear terms $\boldsymbol{R}_{\boldsymbol{x}}^{0}$ from Eq. (3.9), and noted $\boldsymbol{R}_{turb}$ hereafter. They are thus computed considering only the variables at the arrival of the trajectory at time t^0, namely $\boldsymbol{\Psi}_{\boldsymbol{x}}^{0}$. The only exceptions are the mixing coefficient and the TKE that rely on their values from the previous time step and can be noted $K_{\psi}^{*\,-}$ and k^0 (because they are computed in the physics which is achieved after the solving Euler equation as illustrated in Fig. 3.2). The information on the location in space (on the Lagrangian trajectory, $\boldsymbol{x}$subscript), as well as the location in time (0 superscript) are thus dropped hereafter.

As a reminder, in the present implementation of the volumetric terms, the full subgrid velocity variances are included in the dynamic kernel (which is not fully the case when separating terms as done in Eq. (2.43) and (2.44)). Thus, the fully developed continuous form of $\boldsymbol{R}_{turb}$ in

cartesian coordinates is expressed as (similar to Eq. (2.49) but dropping Reynolds and Favre average notations and developing S_{ij})

$$\boldsymbol{R}_{turb} = \begin{bmatrix} \frac{1}{\rho}\frac{\partial}{\partial x}\left(2\rho K_M \frac{\partial u}{\partial x} - \frac{2}{3}\rho\left(K_M \frac{\partial u_i}{\partial x_i} + k\right)\right) \\ \frac{1}{\rho}\frac{\partial}{\partial y}\left(2\rho K_M \frac{\partial v}{\partial y} - \frac{2}{3}\rho\left(K_M \frac{\partial u_i}{\partial x_i} + k\right)\right) \\ \frac{1}{\rho}\frac{\partial}{\partial z}\left(2\rho K_M \frac{\partial w}{\partial z} - \frac{2}{3}\rho\left(K_M \frac{\partial u_i}{\partial x_i} + k\right)\right) \\ 0 \\ 0 \end{bmatrix} = \begin{bmatrix} -\frac{1}{\rho}\frac{\partial}{\partial x}\left(\overline{\rho u' u'}\right) \\ -\frac{1}{\rho}\frac{\partial}{\partial y}\left(\overline{\rho v' v'}\right) \\ -\frac{1}{\rho}\frac{\partial}{\partial z}\left(\overline{\rho w' w'}\right) \\ 0 \\ 0 \end{bmatrix}. \quad (3.37)$$

It is noteworthy that including the full vertical velocity variances in the dynamic kernel through $\boldsymbol{R}_{turb}$ avoid the need to achieve the vertical diffusion of w in the physics or elsewhere.

The air density is required to compute $\boldsymbol{R}_{turb}$. It is obtained from the state equation expressed in term of model variables such as

$$\rho = \frac{p_0 \exp\left(\frac{P - gz}{RT_*}\right)}{RT_*\left(\frac{b}{g} + 1\right)}. \quad (3.38)$$

Considering Eq. (3.37) and the horizontal and vertical arrangement of the main variables, it is convenient to compute density at the pressure location, so that its discrete form writes

$$[\rho]_{i,j,k} = \left[\frac{p_0 \exp\left(\frac{P - gz_m}{RT_*}\right)}{RT_*\left(\frac{\overline{b}^{\mathrm{z}}}{g} + 1\right)}\right]_{i,j,k} \quad (3.39)$$

Note that the density at the surface $[\rho]_{i,j,1/2}$ is extrapolated from $[\rho]_{i,j,1}$ and $[\rho]_{i,j,2}$. The density at the first level $[\rho]_{i,j,1}$ is computed from Eq. (3.39) considering for $\overline{b}^{\mathrm{z}}$ the special spacing of the first temperature level as described in Eq. (3.23).

Then, following the grid layout described in Sec. 3.2.2, the discrete form of Eq. (3.37) writes

$$\boldsymbol{R}_{turb} = \begin{bmatrix} \left[\dfrac{1}{\overline{\rho}^{\mathrm{X}}}\dfrac{\delta_x A_x}{\Delta x}\right]_{i-1/2,j,k} \\ \left[\dfrac{1}{\overline{\rho}^{\mathrm{Y}}}\dfrac{\delta_y A_y}{\Delta y}\right]_{i,j-1/2,k} \\ \left[\dfrac{1}{\overline{\rho}^{\mathrm{Z}}}\dfrac{\delta_z A_z}{\Delta z_m}\right]_{i,j,k-1/2} \\ 0 \\ 0 \end{bmatrix}, \tag{3.40}$$

where

$$[A_x]_{i,j,k} = \left[2\rho\overline{K_M}^{\mathrm{z}}\frac{\delta_x u}{\Delta x} - A\right]_{i,j,k}, \tag{3.41}$$

$$[A_y]_{i,j,k} = \left[2\rho\overline{K_M}^{\mathrm{z}}\frac{\delta_y v}{\Delta y} - A\right]_{i,j,k}, \tag{3.42}$$

$$[A_z]_{i,j,k} = \left[2\rho\overline{K_M}^{\mathrm{z}}\frac{\delta_z w}{\Delta z_w} - A\right]_{i,j,k}, \tag{3.43}$$

and

$$[A]_{i,j,k} = \left[\frac{2}{3}\rho\left(\overline{K_M}^{\mathrm{z}}\left(\frac{\delta_x u}{\Delta x} + \frac{\delta_y v}{\Delta y} + \frac{\delta_z w}{\Delta z_w}\right) + \overline{k}^{\mathrm{z}}\right)\right]_{i,j,k}. \tag{3.44}$$

The velocity divergence in A[6], which can be written $[D]_{i,j,k}$, is computed based on the operator implemented in the model and described in Girard *et al.* (2005, Eqs. (14a) and (33b)). At the bottom of the domain, $[A]_{i,j,1/2}$ is computed considering $[D]_{i,j,1/2} = [D]_{i,j,1}$ and both k and K_M are used directly (no interpolation needed), while at the top we set $[A]_{i,j,N_k} = [A]_{i,j,N_k+1/2} = 0$.

Concerning the surface and top values of A_x, A_y and A_z, velocity gradients at are considered to vanish. Furthermore since $[k]_{i,j,N_k-1/2}$ and $[K_M]_{i,j,N_k-1/2}$ are the highest level of k and K_M, we set $[A]_{i,j,N_k} = [A]_{i,j,N_k+1/2} = 0$. This is justified by the fact that both k and K_M as well as

[6] As a side note, strictly following Eq. (2.43), A_x, A_y and A_z would only include A

the divergence of velocity are negligible at the top of the domain (the flow is generally laminar in the free atmosphere, and gradients are largely smoothed by the sponge layer).

Then the computation of the derivative of A_x, A_y and A_z, *i.e.* Eq. (3.40), are straightforward with regards to the boundaries (except for the vertical velocity component that does not required density to be vertically interpolated at the surface and top boundary).

Finally, note that $\boldsymbol{R}_{turb}$ is implemented taking into account the various map scale and metric factors arising from the mathematical transformation related to the geographical projection and the inclusion of the topography through Gal-Chen oblique coordinates as presented in Girard *et al.* (2005). As a result, all the new components included in $\boldsymbol{R}^0_{\boldsymbol{x}}$ are not an exception with regards to topography and geographical projection. Those coefficients are not included in this presentation since they collapse when the terrain is flat and no geographical projection are used.

3.2.5.2 Deviatoric part of the Reynolds tensor and heat

The turbulent diffusion terms related to the deviatoric part of Reynolds tensor are described in Eqs. (2.48) and (2.50). They are included in $\boldsymbol{F}^*_{\boldsymbol{x}}$ from Eq. (3.7) (noted $\boldsymbol{F}_{turb}$ hereafter), and added to the solution following a successive correction approach as discussed in Sec. 3.2.1.

The standalone turbulent diffusion, as well as the terms of the standard turbulent model precomputed in the dynamics (*i.e.* horizontal components of turbulent diffusion) are explicit in time, meaning that main variables at the arrival of the trajectory and at time t^-, *i.e.* $\boldsymbol{\Psi}^-_{\boldsymbol{x}}$, are used to compute the corrections associated to the turbulent diffusion that are then applied on $\boldsymbol{\Psi}^+_{DE}$. However, similarly as for the volumetric terms, TKE and mixing coefficients (standalone model put a side) are based on their value obtained during the previous time step and noted $K^{*\,-}_{\psi}$ and k^0 (as illustrated in Fig. 3.2). The information on the location in space (on the Lagrangian trajectory, subscript $\boldsymbol{x}$), as well as the location in time (superscript) are dropped hereafter.

As a reminder, in the current implementation, the full velocity variances are removed from deviatoric terms $\boldsymbol{F}_{turb}$ and included in volumetric terms $\boldsymbol{R}_{turb}$ as discussed in Sec. 2.2.1. Thus, the fully developed continuous form of $\boldsymbol{F}_{turb}$ in cartesian coordinates is expressed as (similar

to Eq. (2.55) but dropping Reynolds and Favre average notations and developing S_{ij})[7]

$$\boldsymbol{F}_{turb} = \begin{bmatrix} \frac{1}{\rho}\left[\frac{\partial}{\partial y}\left(\rho K_M\left(\frac{\partial v}{\partial x}+\frac{\partial u}{\partial y}\right)\right)+\frac{\partial}{\partial z}\left(\rho K_M\left(\frac{\partial w}{\partial x}+\frac{\partial u}{\partial z}\right)\right)\right] \\ \frac{1}{\rho}\left[\frac{\partial}{\partial x}\left(\rho K_M\left(\frac{\partial u}{\partial y}+\frac{\partial v}{\partial x}\right)\right)+\frac{\partial}{\partial z}\left(\rho K_M\left(\frac{\partial w}{\partial y}+\frac{\partial v}{\partial z}\right)\right)\right] \\ \frac{1}{\rho}\left[\frac{\partial}{\partial x}\left(\rho K_M\left(\frac{\partial u}{\partial z}+\frac{\partial w}{\partial x}\right)\right)+\frac{\partial}{\partial y}\left(\rho K_M\left(\frac{\partial v}{\partial z}+\frac{\partial w}{\partial y}\right)\right)\right] \\ \frac{g\pi}{\rho T_*}\left[\frac{\partial}{\partial x}\left(\rho K_T\frac{\partial \theta}{\partial x}\right)+\frac{\partial}{\partial y}\left(\rho K_T\frac{\partial \theta}{\partial y}\right)+\frac{\partial}{\partial z}\left(\rho K_T\frac{\partial \theta}{\partial z}\right)\right] \\ 0 \end{bmatrix}, \tag{3.45}$$

$$= \begin{bmatrix} -\frac{1}{\rho}\left[\frac{\partial}{\partial y}\left(\overline{\rho u'v'}\right)+\frac{\partial}{\partial z}\left(\overline{\rho u'w'}\right)\right] \\ -\frac{1}{\rho}\left[\frac{\partial}{\partial x}\left(\overline{\rho u'v'}\right)+\frac{\partial}{\partial z}\left(\overline{\rho v'w'}\right)\right] \\ -\frac{1}{\rho}\left[\frac{\partial}{\partial x}\left(\overline{\rho u'w'}\right)+\frac{\partial}{\partial y}\left(\overline{\rho v'w'}\right)\right] \\ -\frac{g\pi}{\rho T_*}\left[\frac{\partial}{\partial x}\left(\overline{\rho u'\theta'}\right)+\frac{\partial}{\partial y}\left(\overline{\rho v'\theta'}\right)+\frac{\partial}{\partial z}\left(\overline{\rho w'\theta'}\right)\right] \\ 0 \end{bmatrix}. \tag{3.46}$$

Those expressions are the basis of the standalone turbulence model, *i.e.* when the full turbulence modelling is fully achieved in the dynamics, as presented in Sec. 3.2.5.2.1.

Concerning the standard turbulent model, as discussed in Sec. 3.1, there is a separation of horizontal terms $\boldsymbol{F}^H_{turb}$, that are pre-computed in the dynamics and sent to the physics afterwards, and the vertical terms $\boldsymbol{F}^V_{turb}$, that are computed in the physics, such as

$$\boldsymbol{F}_{turb} = \boldsymbol{F}^H_{turb} + \boldsymbol{F}^V_{turb}, \tag{3.47}$$

[7] Note that there are no terms related to the vertical turbulent diffusion of w in Eq. (3.45), since they are all included with the variances which are included in the dynamic kernel.

with

$$\boldsymbol{F}^H_{turb} = \begin{bmatrix} \frac{1}{\rho}\left[\frac{\partial}{\partial y}\left(\rho K_M\left(\frac{\partial v}{\partial x}+\frac{\partial u}{\partial y}\right)\right)+\frac{\partial}{\partial z}\left(\rho K_M\left(\frac{\partial w}{\partial x}\quad\right)\right)\right] \\ \frac{1}{\rho}\left[\frac{\partial}{\partial x}\left(\rho K_M\left(\frac{\partial u}{\partial y}+\frac{\partial v}{\partial x}\right)\right)+\frac{\partial}{\partial z}\left(\rho K_M\left(\frac{\partial w}{\partial y}\quad\right)\right)\right] \\ \frac{1}{\rho}\left[\frac{\partial}{\partial x}\left(\rho K_M\left(\frac{\partial u}{\partial z}+\frac{\partial w}{\partial x}\right)\right)+\frac{\partial}{\partial y}\left(\rho K_M\left(\frac{\partial v}{\partial z}+\frac{\partial w}{\partial y}\right)\right)\right] \\ \frac{g\pi}{\rho T_*}\left[\frac{\partial}{\partial x}\left(\rho K_T\frac{\partial \theta}{\partial x}\right)+\frac{\partial}{\partial y}\left(\rho K_T\frac{\partial \theta}{\partial y}\right)\quad\right] \\ 0 \end{bmatrix}, \tag{3.48}$$

which discretization is discussed in Sec. 3.2.5.2.3, and

$$\boldsymbol{F}^V_{turb} = \begin{bmatrix} \frac{1}{\rho}\left[\quad\frac{\partial}{\partial z}\left(\rho K_M\left(\quad\frac{\partial u}{\partial z}\right)\right)\right] \\ \frac{1}{\rho}\left[\quad\frac{\partial}{\partial z}\left(\rho K_M\left(\quad\frac{\partial v}{\partial z}\right)\right)\right] \\ 0 \\ \frac{g\pi}{\rho T_*}\left[\quad\frac{\partial}{\partial z}\left(\rho K_T\frac{\partial \theta}{\partial z}\right)\right] \\ 0 \end{bmatrix}, \tag{3.49}$$

which computation is detailed in Sec. 3.3.3. As a side note, the latter is identical to the turbulent diffusion of the classical column model as discussed in Sec. 2.2.5. Finally, the fractional step approach is followed to recombine $\boldsymbol{F}^H_{turb}$ and $\boldsymbol{F}^V_{turb}$ as described in Sec. 3.3.3.

3.2.5.2.1 Standalone turbulent diffusion

The standalone turbulence diffusion, *i.e.* Eq. (3.45), is implemented in the dynamics (outside of the dynamic kernel). It is fully explicit in time and only relies on the variables at the arrival location of the Lagrangian trajectory. $\boldsymbol{F}_{turb}$ from Eq. (3.45) thus rely on $\boldsymbol{\Psi}^-_{\boldsymbol{x}}$ and K^{*-}_{ψ} (it is

noted $\boldsymbol{F}^{-}_{turb}$). The final corrected main variables (turbulence aware) are obtained such as

$$\boldsymbol{\Psi}^{+}_{DEF} = \boldsymbol{\Psi}^{+}_{DE} + 2\Delta t \boldsymbol{F}^{-}_{turb}\left(\boldsymbol{\Psi}^{-}_{\boldsymbol{x}}\right). \tag{3.50}$$

where the total tendency can be written $\boldsymbol{F}^{*}_{turb} = \boldsymbol{F}^{-}_{turb}\left(\boldsymbol{\Psi}^{-}_{\boldsymbol{x}}\right)$. The information on the location in space and time on the trajectory is dropped hereafter.

Before proceeding to the computation of $\boldsymbol{F}_{turb}$, mixing coefficient are computed as illustrated in Sec. 3.2.5.4 and Sec. 3.2.5.5. The air density, the absolute and potential temperatures, and thus the Exner function and the full pressure need also to be known on staggered z_t levels. The pressure is first computed directly on z_m levels based on the usual formulae

$$[p]_{i,j,k} = \left[p_0 \exp\left(\frac{P - g z_m}{R T_*}\right)\right]_{i,j,k}, \tag{3.51}$$

then, its value on staggered levels, $[p_t]_{i,j,k-1/2}$, is obtained based on a cubic interpolation (routine provided in the model), and T, ρ, π and θ are computed on staggered levels such as

$$[T]_{i,j,k-1/2} = \left[\frac{T_*}{g}\left(b + g\right)\right]_{i,j,k-1/2}, \tag{3.52}$$

$$[\rho]_{i,j,k-1/2} = \left[\frac{p_t}{RT}\right]_{i,j,k-1/2}, \tag{3.53}$$

$$[\pi]_{i,j,k-1/2} = \left[\left(\frac{p_t}{p_0}\right)^{R/c_p}\right]_{i,j,k-1/2}, \tag{3.54}$$

$$[\theta]_{i,j,k-1/2} = \left[\frac{T}{\pi}\right]_{i,j,k-1/2}, \tag{3.55}$$

which are obtained straightforwardly from the surface $[\ \ ]_{i,j,3/4}$ to the top $[\ \ ]_{i,j,N_k+1/4}$.

Then, the various components of the turbulence diffusion, *i.e.* Eq. (3.45), are computed such as the discrete form of the streamwise velocity turbulent diffusion writes

$$[F_{u\,turb}]_{i-1/2,j,k} = \left[\frac{1}{\overline{\rho}^{\mathrm{XZ}}}\left(\frac{\delta_y A_u}{\Delta y} + \frac{\delta_z B_u}{\Delta z_w}\right)\right]_{i-1/2,j,k}, \tag{3.56}$$

with the turbulent fluxes expressed as

$$[A_u]_{i-1/2,j-1/2,k} = \left[\overline{\rho}^{\mathrm{XYZ}}\overline{K_M}^{\mathrm{XYZ}}\left(\frac{\delta_x v}{\Delta x}+\frac{\delta_y u}{\Delta y}\right)\right]_{i-1/2,j-1/2,k} = \left[-\overline{\rho u'v'}\right]_{i-1/2,j-1/2,k}, \quad (3.57)$$

$$[B_u]_{i-1/2,j,k-1/2} = \left[\overline{\rho}^{\mathrm{X}}\overline{K_M}^{\mathrm{X}}\left(\frac{\delta_x w}{\Delta x}+\frac{\delta_z u}{\Delta z_m}\right)\right]_{i-1/2,j,k-1/2} = \left[-\overline{\rho u'w'}\right]_{i-1/2,j-1/2,k}. \quad (3.58)$$

Similarly, the discrete form of the spanwise velocity turbulent diffusion is expressed as

$$[F_{v\,turb}]_{i,j-1/2,k} = \left[\frac{1}{\overline{\rho}^{\mathrm{YZ}}}\left(\frac{\delta_x A_v}{\Delta x}+\frac{\delta_z B_v}{\Delta z_w}\right)\right]_{i,j-1/2,k}, \quad (3.59)$$

with the turbulent fluxes expressed as

$$[A_v]_{i-1/2,j-1/2,k} = \left[\overline{\rho}^{\mathrm{XYZ}}\overline{K_M}^{\mathrm{XYZ}}\left(\frac{\delta_y u}{\Delta y}+\frac{\delta_x v}{\Delta x}\right)\right]_{i-1/2,j-1/2,k} = \left[-\overline{\rho u'v'}\right]_{i-1/2,j-1/2,k}, \quad (3.60)$$

$$[B_v]_{i,j-1/2,k-1/2} = \left[\overline{\rho}^{\mathrm{Y}}\overline{K_M}^{\mathrm{Y}}\left(\frac{\delta_y w}{\Delta y}+\frac{\delta_z v}{\Delta z_m}\right)\right]_{i,j-1/2,k-1/2} = \left[-\overline{\rho v'w'}\right]_{i-1/2,j-1/2,k}. \quad (3.61)$$

And the discrete form of the vertical velocity turbulent diffusion writes

$$[F_{w\,turb}]_{i,j,k-1/2} = \left[\frac{1}{\rho}\left(\frac{\delta_x A_w}{\Delta x}+\frac{\delta_y B_w}{\Delta y}\right)\right]_{i,j,k-1/2}, \quad (3.62)$$

with the turbulent fluxes expressed as

$$[A_w]_{i-1/2,j,k-1/2} = \left[\overline{\rho}^{\mathrm{X}}\overline{K_M}^{\mathrm{X}}\left(\frac{\delta_z u}{\Delta z_m}+\frac{\delta_x w}{\Delta x}\right)\right]_{i-1/2,j,k-1/2} = \left[-\overline{\rho u'w'}\right]_{i-1/2,j,k-1/2}, \quad (3.63)$$

$$[B_w]_{i,j-1/2,k-1/2} = \left[\overline{\rho}^{\mathrm{Y}}\overline{K_M}^{\mathrm{Y}}\left(\frac{\delta_z v}{\Delta z_m}+\frac{\delta_y w}{\Delta y}\right)\right]_{i,j-1/2,k-1/2} = \left[-\overline{\rho v'w'}\right]_{i,j-1/2,k-1/2}. \quad (3.64)$$

Finally, the discrete form of the temperature turbulent diffusion is expressed as

$$[F_{T\,turb}]_{i,j,k-1/2} = \left[\frac{g\pi}{\rho T_*}\left(\frac{\delta_x A_T}{\Delta x}+\frac{\delta_y B_T}{\Delta y}+\frac{\delta_z C_T}{\Delta z_m}\right)\right]_{i,j,k-1/2}, \quad (3.65)$$

with the turbulent fluxes written as

$$[A_T]_{i-1/2,j,k-1/2} = \left[\overline{\rho}^{\mathrm{X}}\overline{K_T}^{\mathrm{XZ}}\frac{\delta_x\theta}{\Delta x}\right]_{i-1/2,j,k-1/2} = \left[-\overline{\rho u'\theta'}\right]_{i-1/2,j,k-1/2}, \tag{3.66}$$

$$[B_T]_{i,j-1/2,k-1/2} = \left[\overline{\rho}^{\mathrm{Y}}\overline{K_T}^{\mathrm{YZ}}\frac{\delta_y\theta}{\Delta y}\right]_{i,j-1/2,k-1/2} = \left[-\overline{\rho v'\theta'}\right]_{i,j-1/2,k-1/2}, \tag{3.67}$$

$$[C_T]_{i,j,k} = \left[\overline{\rho}^{\mathrm{Z}}\overline{K_T}^{\mathrm{Z}}\frac{\delta_z\theta}{\Delta z_t}\right]_{i,j,k} = \left[-\overline{\rho w'\theta'}\right]_{i,j,k}. \tag{3.68}$$

3.2.5.2.2 Boundary condition of the standalone turbulent diffusion

Concerning the boundary condition of the standalone turbulent diffusion, much care must be taken to properly implement the bottom boundary, while the top boundary is less of concern since all the fields are almost totally smoothed by the sponge layer.

Indeed, at the top boundary, we assume that all gradients vanish and that $[K_M]_{i,j,N_k+1/2} = [K_T]_{i,j,N_k+1/2} = 0$ (which are virtual since outside of the domain). It then comes

$$[F_{u\,turb}]_{i-1/2,j,N_k} = [F_{v\,turb}]_{i,j-1/2,N_k} = [F_{w\,turb}]_{i,j,N_k+1/2} = [F_{T\,turb}]_{i,j,N_k+1/4} = 0. \tag{3.69}$$

At the bottom boundary, as discussed in Sec. 2.3, the continuity of heat and momentum vertical turbulent fluxes across the bottom boundary is assumed, and surface heat and momentum turbulent fluxes are obtained from the MO similarity. This Cauchy-type boundary condition (Mailhot and Benoit, 1982), which is illustrated on Eqs. (2.160) and (2.161), is used to obtain heat and momentum vertical turbulent fluxes at the lower boundary such as

$$\left[\overline{\rho}^{\mathrm{X}}\overline{K_M}^{\mathrm{X}}\frac{\delta_z u}{\Delta z_m}\right]_{i-1/2,j,1/2} = \left[\overline{\rho}^{\mathrm{X}}\overline{\beta_M}^{\mathrm{X}}u_a\right]_{i-1/2,j} = \left[-\overline{\rho u'w'}|_s\right]_{i-1/2,j}, \tag{3.70}$$

$$\left[\overline{\rho}^{\mathrm{Y}}\overline{K_M}^{\mathrm{Y}}\frac{\delta_z v}{\Delta z_m}\right]_{i,j-1/2,1/2} = \left[\overline{\rho}^{\mathrm{Y}}\overline{\beta_M}^{\mathrm{Y}}v_a\right]_{i,j-1/2} = \left[-\overline{\rho v'w'}|_s\right]_{i,j-1/2}, \tag{3.71}$$

$$\left[\overline{\rho}^{\mathrm{Z}}\overline{K_T}^{\mathrm{Z}}\frac{\delta_z\theta}{\Delta z_t}\right]_{i,j,1/2} = \left[\overline{\rho}^{\mathrm{Z}}\left(\beta_T\theta_a + \alpha_T\right)\right]_{i,j} = \left[-\overline{\rho w'\theta'}|_s\right]_{i,j}, \tag{3.72}$$

where $u_a = [u]_{i-1/2,j,1}$, $v_a = [u]_{i,j-1/2,1}$ and $\theta_a = [\theta]_{i,j,3/4}$ which are sometimes referred to variables at the "anemometer" level (Mailhot *et al.*, 1998). The homogeneous terms β_M and β_T and the inhomogeneous term α_T are two dimensional and horizontally located at the centre of the mesh, *i.e.* at pressure location. Their computation is detailed in Sec. 2.3 and Sec. 3.3.7.

Finally, concerning the other bottom boundary conditions, vertical velocity is assumed to vanish, *i.e.* $[w]_{i,j,1/2} = 0$, and $[K_M]_{i,j,1/2}$ and $[K_T]_{i,j,1/2}$ are computed based on the similarity as discussed in Sec. 3.2.5.5. Note that, care was taken to properly consider the unusual spacing of pressure and temperature at the bottom and top boundaries (see Eq. (3.23)).

Considering the above, the various terms involved in the turbulent diffusion bottom boundary are obtained as follow. Concerning $[F_{u\,turb}]_{i-1/2,j,1}$, the computation of $[A_u]_{i-1/2,j-1/2,1}$ and its derivative does not require special care. On the contrary, $[B_u]_{i,j-1/2,1/2}$ is expressed as

$$[B_u]_{i-1/2,j,1/2} = \left[\overline{\rho}^{\mathrm{X}}\overline{\beta_M}^{\mathrm{X}} u_a\right]_{i-1/2,j,1/2}, \tag{3.73}$$

leading to

$$\left[\frac{\delta_z B_u}{\Delta z_w}\right]_{i-1/2,j,1} = \frac{[B_u]_{i-1/2,j,3/2} - \left[\overline{\rho}^{\mathrm{X}}\overline{\beta_M}^{\mathrm{X}} u_a\right]_{i-1/2,j,1/2}}{[z_w]_{3/2} - [z_w]_{1/2}}. \tag{3.74}$$

Concerning $[F_{v\,turb}]_{i,j-1/2,1}$, similarly as for the streamwise velocity components the computation of $[A_v]_{i-1/2,j-1/2,1}$ and its derivative is straightforward, while we have

$$[B_v]_{i,j-1/2,1/2} = \left[\overline{\rho}^{\mathrm{Y}}\left(\overline{\beta_M}^{\mathrm{Y}} v_a\right)\right]_{i,j-1/2,1/2}, \tag{3.75}$$

leading to

$$\left[\frac{\delta_z B_v}{\Delta z_w}\right]_{i,j-1/2,1} = \frac{[B_v]_{i,j-1/2,3/2} - \left[\overline{\rho}^{\mathrm{Y}}\overline{\beta_M}^{\mathrm{Y}} v_a\right]_{i,j-1/2,1/2}}{[z_w]_{3/2} - [z_w]_{1/2}}. \tag{3.76}$$

Concerning $[F_{w\,turb}]_{i,j,1/2}$, both $[A_w]_{i-1/2,j,1/2}$ and $[B_w]_{i,j-1/2,1/2}$ include a vertical gradient of the horizontal velocity components at the surface. They can be computed such as

$$[A_w]_{i-1/2,j,1/2} = \left[\overline{\rho}^{\mathrm{X}}\overline{\beta_M}^{\mathrm{X}} u_a\right]_{i-1/2,j,1/2}, \tag{3.77}$$

$$[B_w]_{i,j-1/2,1/2} = \left[\overline{\rho}^{\mathrm{Y}}\overline{\beta_M}^{\mathrm{Y}} v_a\right]_{i,j-1/2,1/2}, \tag{3.78}$$

leading to

$$\left[\frac{\delta_x A_w}{\Delta x}\right]_{i,j,1/2} = \frac{\left[\frac{\delta_x}{\Delta x}\left(\overline{\rho}^{\mathrm{X}}\overline{\beta_M}^{\mathrm{X}} u_a\right)\right]_{i,j,1/2}}{\Delta x}, \tag{3.79}$$

$$\left[\frac{\delta_y B_w}{\Delta y}\right]_{i,j,1/2} = \frac{\left[\frac{\delta_y}{\Delta y}\left(\overline{\rho}^{\mathrm{Y}}\overline{\beta_M}^{\mathrm{Y}} v_a\right)\right]_{i,j,1/2}}{\Delta y}, \tag{3.80}$$

however, they are set to zero.

Finally, concerning $[F_{T\,turb}]_{i,j,3/4}$, the computation of $[A_T]_{i-1/2,j,3/4}$ and $[B_T]_{i,j-1/2,3/4}$ and their derivatives are straightforward, while $[C_T]_{i,j,1/2}$ can be expressed such as

$$[C_T]_{i,j,1/2} = \left[\overline{\rho}^{\mathrm{Z}}\left(\beta_T\theta_a + \alpha_T\right)\right]_{i,j,1/2}, \tag{3.81}$$

leading to

$$\left[\frac{\delta_z C_T}{\Delta z_m}\right]_{i,j,3/4} = \frac{[C_T]_{i,j,1} - \left[\overline{\rho}^{\mathrm{Z}}\left(\beta_T\theta_a + \alpha_T\right)\right]_{i,j,1/2}}{[z_m]_1 - [z_m]_{1/2}}. \tag{3.82}$$

3.2.5.2.3 Horizontal turbulent diffusion

When relying on the standard turbulence model, terms involving horizontal derivatives or interpolations, *i.e.* $\boldsymbol{F}^H_{turb}$ from Eqs. (3.47) and (3.48), have to be pre-computed in the dynamics (outside of the dynamic kernel) in a manner similar to the standalone turbulent diffusion as discussed in Sec. 3.1. Then, as described in Sec. 3.3.3, the output of the horizontal turbulent

diffusion is included in the physics library where the turbulence modelling is completed to obtain the total corrections from the turbulent diffusion $\boldsymbol{F}_{turb}$.

Numerical method used to compute the various terms of the horizontal diffusion are very similar to the standalone turbulent diffusion presented in Sec. 3.2.5.2.1, albeit simpler. Indeed, procedure followed are identical, while there are less terms to compute and boundary conditions are much simpler since only horizontal gradients are considered. The horizontal turbulent diffusion is explicit in time relying on the main variables at the arrival of the trajectory and at time t^-, *i.e.* $\boldsymbol{\Psi}_{\boldsymbol{x}}^-$. The tendency due to horizontal turbulent diffusion can thus be noted $\boldsymbol{F}_{turb}^{H\,-}$. Mixing coefficients are however based on the value obtained during the previous time step.

An important difference with the standalone model lies in the variables (mostly the pressure) computed before the horizontal turbulent diffusion is achieved. Indeed, the physics library is based on a sigma vertical coordinate (*i.e.* $\sigma = p/p_0$) obtained (at each time step) relying on the hydrostatic pressure computed considering variables at time t^+, *i.e.* $\boldsymbol{\Psi}_{DE}^+$ (see Sec. 3.3.2). As a result, each pressure level z_m of the dynamics has a corresponding sigma level $\sigma_m = p_h^+/p_0^+$ in the physics, and similarly for z_t with $\sigma_t = p_{ht}^+/p_0^+$.

Absolute and potential temperatures and air density computed in the physics on temperature levels at time t^- thus rely on p_{ht}^+, *i.e.* the hydrostatic pressure of temperature levels at time t^+, which is consistent with the implicit treatment of the vertical turbulent diffusion. As a result, for consistency reasons, ρ, π and θ used to pre-compute the horizontal diffusion terms in the dynamics are obtained based on p_{ht}^+ on temperature levels (as before). Their computation is thus very similar to Sec. 3.2.5.2.1, however p_{ht}^+ is used instead of p^-, such as

$$\left[T^-\right]_{i,j,k-1/2} = \left[\frac{T_*}{g}\left(b^- + g\right)\right]_{i,j,k-1/2}, \tag{3.83}$$

$$\left[\rho^-\right]_{i,j,k-1/2} = \left[\frac{p_{ht}^+}{RT^-}\right]_{i,j,k-1/2}, \tag{3.84}$$

$$\left[\pi^-\right]_{i,j,k-1/2} = \left[\left(\frac{p_{ht}^+}{p_0}\right)^{R/c_p}\right]_{i,j,k-1/2}, \tag{3.85}$$

and

$$\left[\theta^{-}\right]_{i,j,k-1/2} = \left[\frac{T^{-}}{\pi^{-}}\right]_{i,j,k-1/2}, \tag{3.86}$$

which are obtained straightforwardly from the surface $[\ \ ]_{i,j,3/4}$ to the top $[\ \ ]_{i,j,N_k+1/4}$. Then, the various pre-computed components of the horizontal turbulence diffusion, *i.e.* Eq. (3.48), are obtained (dropping the information on the time level hereafter). The discrete form of the streamwise velocity turbulent diffusion thus writes

$$\left[F^{H}_{u\,turb}\right]_{i-1/2,j,k} = \left[\frac{1}{\overline{\rho}^{\mathrm{XZ}}}\left(\frac{\delta_y A_u}{\Delta y} + \frac{\delta_z B_u}{\Delta z_w}\right)\right]_{i-1/2,j,k}, \tag{3.87}$$

with the turbulent fluxes discretized as

$$\left[A_u\right]_{i-1/2,j-1/2,k} = \left[\overline{\rho}^{\mathrm{XYZ}}\overline{K_M}^{\mathrm{XYZ}}\left(\frac{\delta_x v}{\Delta x} + \frac{\delta_y u}{\Delta y}\right)\right]_{i-1/2,j-1/2,k}, \tag{3.88}$$

$$\left[B_u\right]_{i-1/2,j,k-1/2} = \left[\overline{\rho}^{\mathrm{X}}\overline{K_M}^{\mathrm{X}}\left(\frac{\delta_x w}{\Delta x}\right)\right]_{i-1/2,j,k-1/2}. \tag{3.89}$$

Similarly, the discrete form of the spanwise velocity turbulent diffusion is expressed as

$$\left[F^{H}_{v\,turb}\right]_{i,j-1/2,k} = \left[\frac{1}{\overline{\rho}^{\mathrm{YZ}}}\left(\frac{\delta_x A_v}{\Delta x} + \frac{\delta_z B_v}{\Delta z_w}\right)\right]_{i,j-1/2,k}, \tag{3.90}$$

with the turbulent fluxes discretized as

$$\left[A_v\right]_{i-1/2,j-1/2,k} = \left[\overline{\rho}^{\mathrm{XYZ}}\overline{K_M}^{\mathrm{XYZ}}\left(\frac{\delta_y u}{\Delta y} + \frac{\delta_x v}{\Delta x}\right)\right]_{i-1/2,j-1/2,k}, \tag{3.91}$$

$$\left[B_v\right]_{i,j-1/2,k-1/2} = \left[\overline{\rho}^{\mathrm{Y}}\overline{K_M}^{\mathrm{Y}}\left(\frac{\delta_y w}{\Delta y}\right)\right]_{i,j-1/2,k-1/2}. \tag{3.92}$$

And the discrete form of the vertical velocity turbulent diffusion writes

$$\left[F^{H}_{w\,turb}\right]_{i,j,k-1/2} = \left[\frac{1}{\rho}\left(\frac{\delta_x A_w}{\Delta x} + \frac{\delta_y B_w}{\Delta y}\right)\right]_{i,j,k-1/2} = \left[F_{w\,turb}\right]_{i,j,k-1/2}, \tag{3.93}$$

with the turbulent fluxes discretized as

$$[A_w]_{i-1/2,j,k-1/2} = \left[\overline{\rho}^{\mathrm{X}}\overline{K_M}^{\mathrm{X}}\left(\frac{\delta_z u}{\Delta z_m} + \frac{\delta_x w}{\Delta x}\right)\right]_{i-1/2,j,k-1/2}, \tag{3.94}$$

$$[B_w]_{i,j-1/2,k-1/2} = \left[\overline{\rho}^{\mathrm{Y}}\overline{K_M}^{\mathrm{Y}}\left(\frac{\delta_z v}{\Delta z_m} + \frac{\delta_y w}{\Delta y}\right)\right]_{i,j-1/2,k-1/2}. \tag{3.95}$$

Finally, the temperature turbulent diffusion is discretized as

$$\left[F^H_{T\,turb}\right]_{i,j,k-1/2} = \left[\frac{g\pi}{\rho T_*}\left(\frac{\delta_x A_T}{\Delta x} + \frac{\delta_y B_T}{\Delta y}\right)\right]_{i,j,k-1/2}, \tag{3.96}$$

with the turbulent fluxes discretized as

$$[A_T]_{i-1/2,j,k-1/2} = \left[\overline{\rho}^{\mathrm{X}}\overline{K_T}^{\mathrm{XZ}}\frac{\delta_x \theta}{\Delta x}\right]_{i-1/2,j,k-1/2}, \tag{3.97}$$

$$[B_T]_{i,j-1/2,k-1/2} = \left[\overline{\rho}^{\mathrm{Y}}\overline{K_T}^{\mathrm{YZ}}\frac{\delta_y \theta}{\Delta y}\right]_{i,j-1/2,k-1/2}. \tag{3.98}$$

The same boundary conditions are used here as in the standalone turbulent diffusion, as described in Sec. 3.2.5.2.2. However, $F^H_{u\,turb}$, $F^H_{v\,turb}$ and $F^H_{T\,turb}$ do not require anymore a turbulent flux to be provided at the surface as they do not include the vertical diffusion terms. Only $F^H_{w\,turb}$ still requires a surface flux as bottom boundary. The latter term is identical as in the standalone model, it is thus computed following the same approach.

3.2.5.3 TKE equation pre-computed terms

The numerical integration of the TKE prognostic equation is achieved in the physics library, however, when not considering the ABL as horizontally homogeneous, a non-negligible part of TKE equation terms involve horizontal derivatives and interpolations. As a result, the latter have to be pre-computed in the dynamics before being sent to the physics. As a side note, no standalone version of the TKE equation was implemented in the present study.

The prognostic equation for the 3D TKE is presented in Eq. (2.130). In comparison, to the 1D TKE equation shown on Eq. (2.144) and implemented in the classical column model, the

advection and A (production) are new terms, while both B (production) and D (diffusion) are generalized, and C (dissipation) is unchanged. As a result, A and only the terms of B and D that involve horizontal derivatives and interpolations are pre-computed in the dynamics, while the remaining terms are computed in the physics as in the column model.

TKE material derivative is obtained following the SL approach as described in Sec. 3.2.1 considering the TKE as a passive scalar. Concerning the right-hand side of Eq. (2.130), by separating terms that are already implemented in the classical column model from the others (similarly as done for the turbulent diffusion), *i.e.* $A = A_{phy} + A_{dyn}$, $B = B_{phy} + B_{dyn}$, $C = C_{phy} + C_{dyn}$ and $D = D_{phy} + D_{dyn}$, we obtain (dropping Favre and Reynolds average formalism)

$$A_{dyn} = -\frac{2}{3}\left(\frac{\partial u}{\partial x} + \frac{\partial v}{\partial y} + \frac{\partial w}{\partial z}\right), \tag{3.99}$$

$$\begin{aligned} B_{dyn} =& C_k\lambda\Bigg\{\left(\frac{\partial u}{\partial y} + \frac{\partial v}{\partial x}\right)^2 + \frac{\partial w}{\partial x}\left(2\frac{\partial u}{\partial z} + \frac{\partial w}{\partial x}\right) + \frac{\partial w}{\partial y}\left(2\frac{\partial v}{\partial z} + \frac{\partial w}{\partial y}\right) \\ &+ \frac{4}{3}\left[\frac{\partial u}{\partial x}\left(\frac{\partial u}{\partial x} - \frac{\partial v}{\partial y}\right) + \frac{\partial v}{\partial y}\left(\frac{\partial v}{\partial y} - \frac{\partial w}{\partial z}\right) + \frac{\partial w}{\partial z}\left(\frac{\partial w}{\partial z} - \frac{\partial u}{\partial x}\right)\right]\Bigg\}, \end{aligned} \tag{3.100}$$

$$C_{dyn} = 0, \tag{3.101}$$

$$D_{dyn} = \frac{1}{\rho}\left(\frac{\partial}{\partial x}\left(\rho K_k \frac{\partial k}{\partial x}\right) + \frac{\partial}{\partial y}\left(\rho K_k \frac{\partial k}{\partial y}\right)\right), \tag{3.102}$$

and

$$A_{phy} = 0, \tag{3.103}$$

$$B_{phy} = C_k\lambda\left\{-\frac{g}{\mathrm{Pr}_t\theta}\frac{\partial\theta}{\partial z} + \left(\frac{\partial u}{\partial z}\right)^2 + \left(\frac{\partial v}{\partial z}\right)^2\right\}, \tag{3.104}$$

$$C_{phy} = \frac{C_\varepsilon}{\lambda_\varepsilon}, \tag{3.105}$$

$$D_{phy} = \frac{1}{\rho}\frac{\partial}{\partial z}\left(\rho K_k \frac{\partial k}{\partial z}\right). \tag{3.106}$$

Numerical integration of the TKE equation along the inclusion of A_{dyn}, B_{dyn} and D_{dyn} as well as the discretization of B_{phy}, B_{phy} and D_{phy} are presented in Sec. 3.3.4. Here, the pre-computation in the dynamics of A_{dyn}, B_{dyn} and D_{dyn} is presented.

As a general remarks, A_{dyn}, B_{dyn} and D_{dyn} are computed at the same location as the TKE, *i.e.* horizontally at the centre of the mesh and on staggered z_w levels. A_{dyn}, B_{dyn} terms only rely on variables at the arrival of the Lagrangian trajectory at time t^-, *i.e.* $\boldsymbol{\Psi}_{\boldsymbol{x}}^-$, while D_{dyn} is based on the TKE at time t^0 also at the arrival of the trajectory. The horizontal turbulent diffusion of TKE is thus explicit in time, and these terms can be noted A_{dyn}^-, B_{dyn}^- and D_{dyn}^0. Note however that, the mixing coefficient computed during the previous time step, *i.e.* $K_k^{*\,-}$, is used here. For its part, the multiplication with the mixing length λ in B_{dyn} is achieved within the physics.

As a result, the discrete form of A_{dyn}^-, B_{dyn}^- and D_{dyn}^0 can be written as (dropping the information on the time level hereafter)

$$[A_{dyn}]_{i,j,k-1/2} = \left[-\frac{2}{3}\left(\frac{\delta_x \overline{u}^{\mathrm{Z}}}{\Delta x} + \frac{\delta_y \overline{v}^{\mathrm{Z}}}{\Delta y} + \frac{\delta_z \overline{w}^{\mathrm{Z}}}{\Delta z_m}\right)\right]_{i,j,k-1/2}, \tag{3.107}$$

$$\begin{aligned}[B_{dyn}]_{i,j,k-1/2} = \Bigg[C_k \lambda \Bigg\{ &\left(\frac{\delta_y \overline{u}^{\mathrm{XYZ}}}{\Delta y} + \frac{\delta_x \overline{v}^{\mathrm{XYZ}}}{\Delta x}\right)^2 + \frac{\delta_x \overline{w}^{\mathrm{X}}}{\Delta x}\left(2\frac{\delta_z \overline{u}^{\mathrm{X}}}{\Delta z_m} + \frac{\delta_x \overline{w}^{\mathrm{X}}}{\Delta x}\right) \\ &+ \frac{\delta_y \overline{w}^{\mathrm{Y}}}{\Delta y}\left(2\frac{\delta_z \overline{v}^{\mathrm{Y}}}{\Delta z_m} + \frac{\delta_y \overline{w}^{\mathrm{Y}}}{\Delta y}\right) + \frac{4}{3}\Bigg[\frac{\delta_x \overline{u}^{\mathrm{Z}}}{\Delta x}\left(\frac{\delta_x \overline{u}^{\mathrm{Z}}}{\Delta x} - \frac{\delta_y \overline{v}^{\mathrm{Z}}}{\Delta y}\right) \\ &+ \frac{\delta_y \overline{v}^{\mathrm{Z}}}{\Delta y}\left(\frac{\delta_y \overline{v}^{\mathrm{Z}}}{\Delta y} - \frac{\delta_z \overline{w}^{\mathrm{Z}}}{\Delta z_m}\right) + \frac{\delta_z \overline{w}^{\mathrm{Z}}}{\Delta z_m}\left(\frac{\delta_z \overline{w}^{\mathrm{Z}}}{\Delta z_m} - \frac{\delta_x \overline{u}^{\mathrm{Z}}}{\Delta x}\right)\Bigg]\Bigg\}\Bigg]_{i,j,k-1/2},\end{aligned} \tag{3.108}$$

$$[D_{dyn}]_{i,j,k-1/2} = \left[\frac{1}{\rho}\left\{\frac{\partial}{\partial x}\left(\overline{\rho}^{\mathrm{X}}\overline{K_k}^{\mathrm{X}}\frac{\partial k}{\partial x}\right) + \frac{\partial}{\partial y}\left(\overline{\rho}^{\mathrm{Y}}\overline{K_k}^{\mathrm{Y}}\frac{\partial k}{\partial y}\right)\right\}\right]_{i,j,k-1/2}. \tag{3.109}$$

Concerning the boundary conditions of these expressions, a surface value of the TKE is provided through a Dirichlet boundary condition such as $[k]_{i,j,1/2} = 3.75u_*^2 + 0.2w_*^2$ as discussed in Sec. 3.3.7. Thus, $[A_{dyn}]_{i,j,1/2}$, $[B_{dyn}]_{i,j,1/2}$ and $[D_{dyn}]_{i,j,1/2}$ are set to zero. Finally, at the top boundary, $[k]_{i,j,N_k-1/2}$ is obtained from the prognostic equation of TKE, and $[k]_{i,j,N_k+1/2}$ (which is virtual) is always taken to be zero.

3.2.5.4 Modulus of the strain rate tensor

The strain rate tensor modulus is fully computed in the dynamics regardless of the version of the turbulent model used (*i.e.* standard or standalone). It is at the same location as the TKE, *i.e.* horizontally at the centre of the mesh and on staggered z_w levels. It is computed only relying on velocity components at the arrival of the trajectory at time t^-, *i.e.* $\boldsymbol{\Psi}_{\boldsymbol{x}}^-$, and noted S^- (the information on the location in time and on the trajectory is dropped hereafter).

As a reminder, the squared strain rate tensor modulus, Eq. (2.59), writes once fully developed

$$\begin{aligned} S^2 = &\left(\frac{\partial u}{\partial y}+\frac{\partial v}{\partial x}\right)^2+\left(\frac{\partial u}{\partial z}+\frac{\partial w}{\partial x}\right)^2+\left(\frac{\partial v}{\partial z}+\frac{\partial w}{\partial y}\right)^2 \\ &+\frac{1}{2}\left[\left(2\frac{\partial u}{\partial x}-\frac{2}{3}\frac{\partial u_k}{\partial x_k}\right)^2+\left(2\frac{\partial v}{\partial y}-\frac{2}{3}\frac{\partial u_k}{\partial x_k}\right)^2+\left(2\frac{\partial w}{\partial z}-\frac{2}{3}\frac{\partial u_k}{\partial x_k}\right)^2\right], \end{aligned} \tag{3.110}$$

where the summation apply on k index. The discrete form of S then writes

$$\begin{aligned} \left[S^2\right]_{i,j,k-1/2} = &\left[\left(\frac{\delta_y\overline{u}^{\mathrm{XYZ}}}{\Delta y}+\frac{\delta_x\overline{v}^{\mathrm{XYZ}}}{\Delta x}\right)^2+\left(\frac{\delta_z\overline{u}^{\mathrm{X}}}{\Delta z_m}+\frac{\delta_x\overline{w}^{\mathrm{X}}}{\Delta x}\right)^2+\left(\frac{\delta_z\overline{v}^{\mathrm{Y}}}{\Delta z_m}+\frac{\delta_y\overline{w}^{\mathrm{Y}}}{\Delta y}\right)^2\right. \\ &\left.+\frac{1}{2}\left\{\left(2\frac{\delta_x\overline{u}^{\mathrm{Z}}}{\Delta x}+A\right)^2+\left(2\frac{\delta_y\overline{v}^{\mathrm{Z}}}{\Delta y}+A\right)^2+\left(2\frac{\delta_z\overline{w}^{\mathrm{Z}}}{\Delta z_m}+A\right)^2\right\}\right]_{i,j,k-1/2}, \end{aligned} \tag{3.111}$$

with the velocity divergence $[A]_{i,j,k-1/2}$ that is identical to $[A_{dyn}]_{i,j,k-1/2}$ from Eq. (3.107).

Finally, concerning the boundaries of S, the surface value of $[S]_{i,j,1/2}$ is bypassed since $[K_M]_{i,j,1/2}$ and $[K_T]_{i,j,1/2}$ are imposed based on MO similarity through a Dirichlet boundary condition. Thus, $[S^2]_{i,j,1/2}=0$ is used. At the top, the computation of $[S^2]_{i,j,N_k-1/2}$ is straightforward and it is imposed that $[S]_{i,j,N_k+1/2}=0$ (which is virtual).

3.2.5.5 Standalone Smagorinsky SGS model

Heat and momentum turbulent mixing coefficient, K_M and K_T, need to be known prior to achieve the turbulent diffusion. Their computation is usually done in the physics library based on either one of the various SGS models described in Sec. 2.2.3, or on the column model

presented in Sec. 2.2.5. However, when relying on the standalone turbulence model, K_M and K_T also need to be computed in the dynamics (since physics is not anymore activated). As a first developmental step, only the UKMO Smagorinsky SGS model described in Sec. 2.2.3.1 was implemented in the dynamics (independently from its implementation in the physics).

Mixing coefficients are located on staggered z_w levels at the centre of the mesh. They are noted K_M^* and K_T^*, and computed only relying on variables at the arrival of the trajectory at time t^-, *i.e.* $\boldsymbol{\Psi}_{\boldsymbol{x}}^-$ (the information on the location in time and on the trajectory is dropped hereafter). Following the Smagorinsky SGS model presented in Sec. 2.2.3.1, their discrete form write

$$[K_M]_{i,j,k-1/2} = \left[\lambda^2 f_m S\right]_{i,j,k-1/2}, \tag{3.112}$$

$$[K_T]_{i,j,k-1/2} = \left[\lambda^2 f_h S\right]_{i,j,k-1/2}, \tag{3.113}$$

where the modulus of the strain rate tensor $[S]_{i,j,k-1/2}$ is computed as described in Sec. 3.2.5.4.

3.2.5.5.1 Length scale

The length scale is computed on staggered levels. Its value in the flow interior writes

$$[\lambda_0]_{k-1/2} = \min\left(500., \max\left(C_S\left(\Delta x \Delta y\right)^{1/2}, C_S(\Delta x \Delta y \left[\Delta z_m\right]_{k-1/2})^{1/3}\right)\right), \tag{3.114}$$

where the Smagorinsky constant is set to $C_S = 0.15$. Note that Δx, Δy, as well as C_S are constant and Δz_m only depends on the height. Thus, λ_0 is only a function of height, furthermore, if $[\Delta z_m]_{i,j,k-1/2} < (\Delta x \Delta y)^{1/2}$, λ_0 is constant throughout the domain.

Then, the final length scale (that includes an asymptotic surface matching and where z_0 that can be non-homogeneous in space) writes

$$[\lambda]_{i,j,k-1/2} = \left[\left(\frac{1}{\lambda_0^n} + \frac{1}{\left(\kappa\left(z_w + z_0\right)\right)^n}\right)^{-n}\right]_{i,j,k-1/2}, \tag{3.115}$$

where the asymptotic surface length scale matching coefficient is set to $n = 2$. The length scale is a simple geometric function that only depends on the grid and some coefficients. Thus, there is no need to recalculate λ at every time step.

3.2.5.5.2 Stability functions

Heat and momentum stability functions, f_m and f_h, are defined as illustrated in Sec. 2.2.3.1.2 and computed on staggered z_w levels. They depend on a local Richardson number, Eq. (2.64), which discrete form write

$$[\mathrm{Ri}]_{i,j,k-1/2} = \left[\frac{N^2}{S^2}\right]_{i,j,k-1/2}, \tag{3.116}$$

and which is computed on staggered z_w levels by first evaluating potential temperature on staggered levels as described in Sec. 3.2.5.2.1, and then the Brunt-Väisälä frequency such as

$$\left[N^2\right]_{i,j,k-1/2} = \left[\frac{g}{\theta}\frac{\delta_z\overline{\theta}^{\mathrm{z}}}{\Delta z_m}\right]_{i,j,k-1/2}. \tag{3.117}$$

At the top and bottom of the domain we have $[\mathrm{Ri}]_{i,j,1/2} = 0$ and $[\mathrm{Ri}]_{i,j,N_k+1/2} = 0$. Furthermore, it is imposed that $\mathrm{Ri} = 0$ if $S^2 < 10^{-30}$ in order to prevent overflow in the computation of Ri (since S^2 is always positive).

For unstable stratification ($\mathrm{Ri} < 0$), by developing Eqs. (2.56) and (2.57) replacing f_m and f_h by their respective expressions, the discrete form of the mixing coefficients writes

$$[K_M]_{i,j,k-1/2} = \left[\lambda^2\left(S^2 + 16N^2\right)^{1/2}\right]_{i,j,k-1/2}, \tag{3.118}$$

$$[K_T]_{i,j,k-1/2} = \left[\frac{\lambda^2}{\mathrm{Pr}_N}\left(S^2 - 40N^2\right)^{1/2}\right]_{i,j,k-1/2}. \tag{3.119}$$

Thus, while Ri still have to be explicitly computed, mixing coefficients for unstable conditions never show a division by S. In practice, this avoid possible division by zero and thus overflow errors when executing the model. This is of particular interest for cases or regions of the ABL

that do not present velocity gradients such as just after the initialization of theoretical cases. As a result, the above expression are implemented for the computation of heat and momentum mixing coefficients in unstable regions (instead of first computing stability functions, and then the mixing coefficients as presented in Sec. 2.2.3.1). However, to avoid any problems it is further imposed that $N^2 = 0$ if $N^2 > -10^{-30}$ (since N^2 is always negative in unstable conditions) and $S^2 = 0$ if $S^2 < 10^{-30}$ (since S^2 is always positive) in order to avoid underflow errors.

For subcritical stable stratification ($0 \leq \mathrm{Ri} < \mathrm{Ri}_c$), the ratio $(1 - \mathrm{Ri}/\mathrm{Ri}_c)$ is bounded such as

$$\mathrm{Ri}_{frac} = \max\left(0, \min\left(1, 1 - \frac{\mathrm{Ri}}{\mathrm{Ri}_c}\right)\right) \tag{3.120}$$

which leads to the mixing coefficients

$$[K_M]_{i,j,k-1/2} = \left[\lambda^2 S \mathrm{Ri}^4_{frac}\right]_{i,j,k-1/2}, \tag{3.121}$$

$$[K_T]_{i,j,k-1/2} = \left[\frac{\lambda^2}{\mathrm{Pr}_N} S \mathrm{Ri}^4_{frac}\left(1 - 1.2\mathrm{Ri}\right)\right]_{i,j,k-1/2}. \tag{3.122}$$

Finally, concerning the boundary values of the the mixing coefficients, at the top

$$[K_M]_{i,j,N_k+1/2} = 0 \qquad \text{and } [K_T]_{i,j,N_k+1/2} = 0, \tag{3.123}$$

while at the surface $[K_T]_{i,j,1/2}$ and $[K_T]_{i,j,1/2}$ (which are used to compute output diagnostic near-surface variables) are obtained based on the similarity such as

$$[\lambda]_{i,j,1/2} = \left[\kappa \frac{z_0}{\phi_M}\right]_{i,j}, \tag{3.124}$$

$$[K_M]_{i,j,1/2} = [u_* \lambda]_{i,j,1/2}, \tag{3.125}$$

$$[K_T]_{i,j,1/2} = \left[K_M \frac{\phi_M}{\phi_H}\right]_{i,j,1/2}, \tag{3.126}$$

where ϕ_M and ϕ_M are the flux profile relationship defined at Eqs. (2.162) and (2.163) and computed along the friction velocity u_* as discussed in Sec. 2.3 and Sec. 3.3.7.

3.3 Physics

The physics library have been actively developed for 30 years at the RPN and was successively integrated into the various mesoscale models from EC (Mailhot and Benoit, 1982; Delage, 1988; Delage and Girard, 1992; Delage, 1997; Benoit *et al.*, 1989, 1997; Mailhot *et al.*, 1998; Bélair *et al.*, 1999). It was created before MC2 existed. In a general manner, it includes a wide range of models for all phenomenon that require a parametrization. It is somewhat autonomous as it features its own vertical coordinate, discretization and boundary conditions and does not share memory and variables with the dynamics. Thus, as introduced in Sec. 3.1, all variables and parameters required by the physics need to be provided by the dynamics through a dedicated dynamics $\rightarrow$ physics interface and memory buses. Then, results from the modelling of physical processes are returned to the dynamics through a dynamics $\rightarrow$ physics interface under the form of corrections tendencies, *i.e.* $d\boldsymbol{\Psi}/dt$, that are added to the main variables.

In the present study, only momentum and heat turbulent processes as well as energy exchanges at the ground surface are of concern in the physics library. It is also noteworthy that a more recent version of the physics, that among other features a refined discretization, has been integrated with MC2 during this study.

As a result, this section focuses only on the components of interest, and most of the computations detailed here are based on the new discretization. However, in order to better appreciate the differences between the two versions of the physics, the spatial discretization of both original and new version of the physics library is presented in a first section along the sigma vertical coordinate and the processing applied at the interfaces between the physics and the dynamics. Then, the implicit vertical turbulent diffusion is presented along its aggregation with its horizontal counterpart allowing to obtain the total tendency from the 3D turbulent diffusion of main variables. Subsequently, the numerical integration of the turbulent kinetic energy equation is presented. Afterwards, the implementation of SGS models and classical column model closures are discussed. Finally, the computation of the surface layer scaling quantities and integrated surface coefficient used in the surface boundary condition is introduced.

3.3.1 Spatial discretization

In the physics, the three dimensional computational domain used to solve the Euler equations of motion is considered as a set of $N_i \times N_j$ independent columns. Thus, it is to underline that, in the physics, variables are not stored in 3D arrays but in 1D arrays. Each of these arrays contains a vertical slice of the 3D domain, thus 2D data (in a 1D array), and each slice are processed on a different computational processing unit (CPU) in the context of parallel computing. Finally, considering the differences in the discretization of the physics and the dynamics, a projection operator similar to $[\ ]_{i,j,k}$ but dedicated to the physics $\{\ \}_{\mathrm{i,j,k}}$ is introduced here[8].

3.3.1.1 Horizontal discretization

The $N_i \times N_j$ columns processed in the physics[9] are located at the mesh centre, *i.e.* the same horizontal location as the pressure. Thus, all the quantities sent to the physics must be located in either $[\ ]_{i,j,k-1/2}$ or $[\ ]_{i,j,k}$ while the outputs of the physics require to be interpolated back at the variable proper location.

As a consequence, both velocity components, and their associated horizontal turbulent diffusion (see Sec. 3.2.5.2.3) are interpolated at the centre of the mesh to obtain the input of the physics, *i.e.* $[\overline{u}^{\mathrm{X}}]_{i,j,k}$, $[\overline{v}^{\mathrm{Y}}]_{i,j,k}$, $\left[\overline{F^H_{u\,turb}}^{\mathrm{X}}\right]_{i,j,k}$ and $\left[\overline{F^H_{v\,turb}}^{\mathrm{Y}}\right]_{i,j,k}$ (horizontal terms of the TKE equation A_{dyn}, B_{dyn}, and D_{dyn} as well as the strain rate tensor modulus S are already located at the proper location). Similarly, the output of the physics, *i.e.* the total tendencies/corrections due to momentum turbulent diffusion, $F_{u\,turb}$ and $F_{v\,turb}$, have also to be interpolated back at the location of the velocity components before been applied as corrections, *i.e.* $\left[\overline{F_{u\,turb}}^{\mathrm{X}}\right]_{i-1/2,j,k}$ and $\left[\overline{F_{v\,turb}}^{\mathrm{Y}}\right]_{i,j-1/2,k}$. Note that on the contrary, no horizontal interpolation is needed for temperature in either way since it is already located at the centre of the mesh.

These interpolations were linear and done following Eq. (3.17). However, they are applied on both the input and output of turbulent diffusion at every time step which may introduce some

[8] While the three indices in $\{\ \}_{\mathrm{i,j,k}}$ are not mandatory since all computations in the physics are vertical only and $i = \mathrm{i}$ and $j = \mathrm{j}$, they are kept to retain the same formalism as in the previous sections.
[9] Note that no physics processing is done in the halo.

numerical diffusion and smoothing of turbulent diffusion tendency fields. It was thus decided to replace them by cubic interpolations such as taking u and $F_{u\,turb}$ as an example (interpolation in the streamwise direction), we have at the dynamics $\rightarrow$ physics interface

$$[\overline{u}^{\mathrm{x}}]_{i,j,k} = -\frac{1}{16}[u]_{i+3/2,j,k} + \frac{9}{16}[u]_{i+1/2,j,k} + \frac{9}{16}[u]_{i-1/2,j,k} - \frac{1}{16}[u]_{i-3/2,j,k}\,, \tag{3.127}$$

$$= -\frac{1}{16}u_{i+2,j,k} + \frac{9}{16}u_{i+1,j,k} + \frac{9}{16}u_{i,j,k} - \frac{1}{16}u_{i-1,j,k}. \tag{3.128}$$

and to go from the centre to the sides at the physics $\rightarrow$ dynamics interface

$$[F_{u\,turb}]_{i-1/2,j,k} = -\frac{1}{16}[F_{u\,turb}]_{i+1,j,k} + \frac{9}{16}[F_{u\,turb}]_{i,j,k} + \frac{9}{16}[F_{u\,turb}]_{i-1,j,k} - \frac{1}{16}[F_{u\,turb}]_{i-2,j,k}\,, \tag{3.129}$$

$$= -\frac{1}{16}F_{u\,turb\,i+1,j,k} + \frac{9}{16}F_{u\,turb\,i,j,k} + \frac{9}{16}F_{u\,turb\,i-1,j,k} - \frac{1}{16}F_{u\,turb\,i-2,j,k}. \tag{3.130}$$

A similar approach is followed for v in the spanwise direction, and for all the terms that need an horizontal interpolation at the interface between the dynamics and the physics.

Note finally that, at the lateral boundaries of the domain, the cubic interpolation is done straightforwardly considering lateral periodicity of the various fields.

3.3.1.2 Vertical staggering

The vertical discretization of the physics library is largely influenced by its vertical coordinate. Indeed, as further discussed in Sec. 3.3.2, a sigma coordinate $\sigma = p/p_0$ is used, which maximum value $\sigma = 1$ is located at the surface while the minimum is at the top of the domain. Thus, for convenience reasons when relying on such a coordinate, it is often chosen to have the lowest index of the arrays located at the top of the domain and the maximum index at the bottom boundary, *i.e.* the surface. This approach is followed in the physics library meaning that the vertical index are up-side-down compared to the dynamics as illustrated in Fig. 3.7.

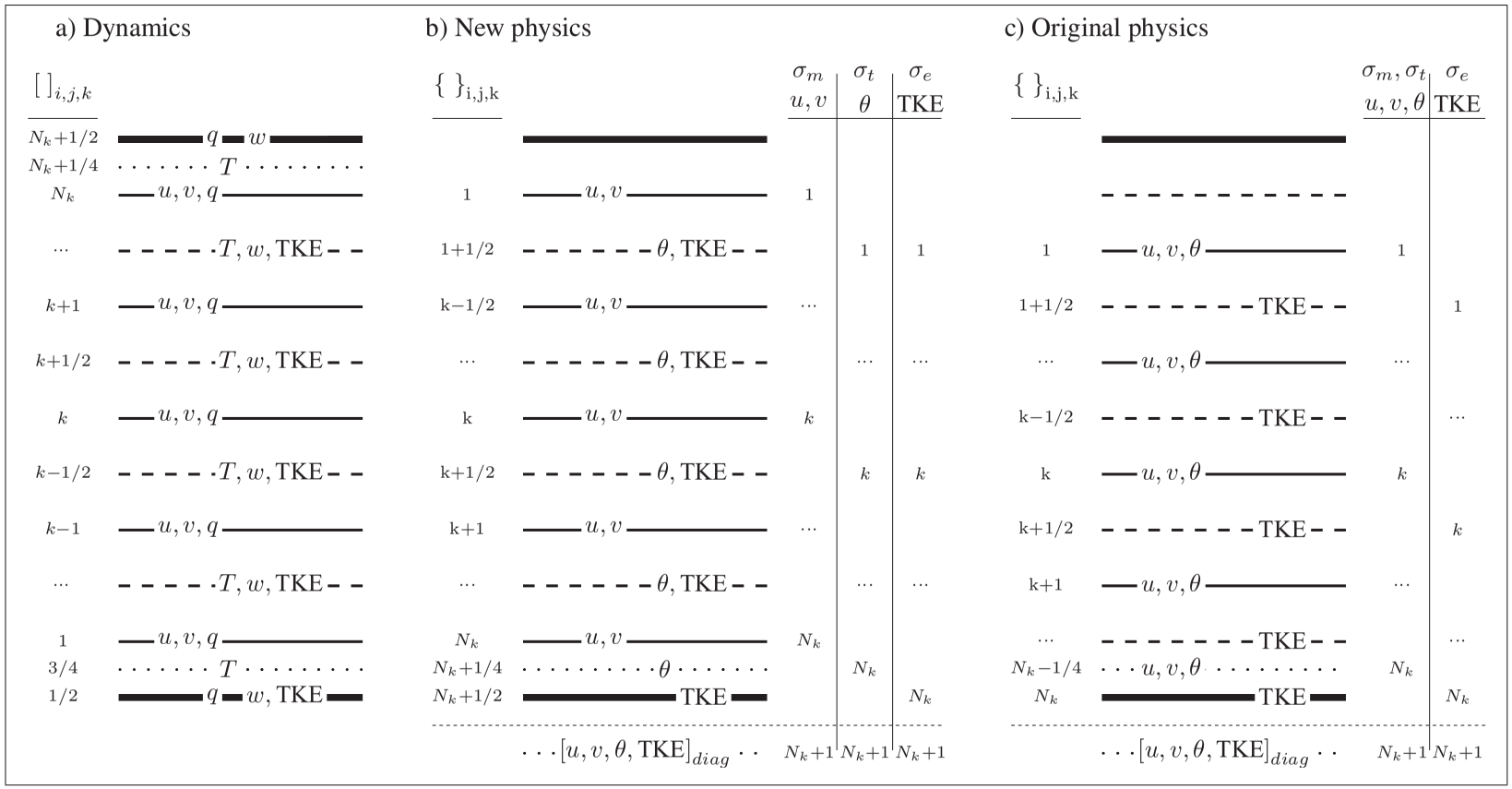

Figure 3.7 Vertical discretization grid of: a) the dynamics, b) the new physics, c) the original physics

Concerning the vertical location of the main variables, a staggered grid is used so that turbulent quantities such as the TKE are always staggered with regards to main variables as illustrated by Fig. 3.7. However, depending of the version of the physics (*i.e.* the legacy version (Benoit *et al.*, 1997; Mailhot *et al.*, 1998) in which an early version of the 3D turbulence modelling in MC2 was implemented (Pelletier *et al.*, 2005), or the new more advanced version integrated during this work), the location of the variable differs as shown in Fig. 3.7. Note finally that a special level of velocity components and temperature (at the maximum index in the physics) serves to store the surface layer diagnostic data, *i.e.* u_{diag}, v_{diag} and θ_{diag}. This last level is not part of the computational domain which thus has one level less than the dynamics.

In this section, both version of the physics vertical discretization are introduced along the formal projection operator on the physics mesh.

3.3.1.2.1 Original vertical staggering

The version of the physics (version 4.1) that is officially included in the last public version of MC2 (version 4.9.8) and in which the early version of the 3D turbulence modelling was implemented (Pelletier *et al.*, 2005), has its full levels (on which temperature and velocity components are located) matching the staggered levels of the dynamics (*i.e.* temperature levels), while its staggered level (where the TKE and mixing coefficient are located) correspond to momentum levels of the dynamics, as illustrated in Fig. 3.7 a).

As a result, a vertical interpolation on temperature level of the horizontal velocity components is needed to obtain the input of the physics (Benoit *et al.*, 1997). At the interface between the dynamics to the physics, we thus have

$$\{u\}_{\mathrm{i,j,k}} = [\overline{u}^{\mathrm{XZ}}]_{i,j,N_k+1-k+1/2}\,, \tag{3.131}$$

$$\{v\}_{\mathrm{i,j,k}} = [\overline{v}^{\mathrm{YZ}}]_{i,j,N_k+1-k+1/2}\,, \tag{3.132}$$

$$\{\theta\}_{\mathrm{i,j,k}} = [\theta]_{i,j,N_k+1-k}\,, \tag{3.133}$$

$$\{k\}_{\mathrm{i,j,k-1/2}} = [k]_{i,j,N_k+1-k}\,. \tag{3.134}$$

where $\{\}_{\mathrm{i,j,k}}$ is the projection operator to the physics grid and i, j and k are the projected indices on the physics grid. Note that all horizontal interpolations are cubic as discussed in Sec. 3.3.1.1. At the bottom level, temperature is properly located, while velocity components are extrapolated such as

$$\{u\}_{\mathrm{i,j},N_k-1/4} = (1-\alpha)\,[\overline{u}^{\mathrm{X}}]_{i,j,1} + \alpha\,[\overline{u}^{\mathrm{X}}]_{i,j,2} = [\overline{u}^{\mathrm{XZ}}]_{i,j,3/4}\,, \tag{3.135}$$

$$\{v\}_{\mathrm{i,j},N_k-1/4} = (1-\alpha)\,[\overline{v}^{\mathrm{Y}}]_{i,j,1} + \alpha\,[\overline{v}^{\mathrm{Y}}]_{i,j,2} = [\overline{v}^{\mathrm{YZ}}]_{i,j,3/4}\,, \tag{3.136}$$

where traditionally $\alpha = ([z_w]_{1/2} - [z_m]_1)/([z_m]_2 - [z_m]_1)$ is used instead of $\alpha = ([z_t]_{3/4} - [z_m]_1\,/([z_m]_2 - [z_m]_1)$ (that is the strict definition of a linear extrapolation) in order to lower the error associated with the linear extrapolation of variables that follow a log profile.

Subsequently and as in the horizontal directions, physics outputs, *i.e.* the total tendencies from turbulent diffusion, are then interpolated back to momentum components location, such as

$$[F_{u\,turb}]_{i-1/2,j,k} = \left\{\overline{F_{u\,turb}}^{\mathrm{XZ}}\right\}_{\mathrm{i-1/2,j},N_k+1-\mathrm{k}+1/2}\,, \tag{3.137}$$

$$[F_{v\,turb}]_{i,j-1/2,k} = \left\{\overline{F_{v\,turb}}^{\mathrm{YZ}}\right\}_{\mathrm{i,j-1/2},N_k+1-\mathrm{k}+1/2}\,, \tag{3.138}$$

$$[F_{T\,turb}]_{i,j,k-1/2} = \{F_{T\,turb}\}_{\mathrm{i,j},N_k+1-\mathrm{k}}\,, \tag{3.139}$$

where horizontal interpolations are cubic as discussed in Sec. 3.3.1.1.

This version of the physics and its coupling with the dynamics are described in Benoit *et al.* (1997), while all the underlying mathematical models and numerical methods are further presented in the official documentation of the physics (Mailhot *et al.*, 1998). The reader is thus referred to the latter documents for a thorough description of the physics library.

The implementation of the 3D turbulent diffusion in MC2 was at first done based on the original version of the physics as described in Pelletier *et al.* (2005). In that version of the model (dynamics 4.9.8 coupled with physics 4.1 plus 3D turbulence closure), the various horizontal terms are pre-computed in the dynamics so that neither horizontal nor vertical interpolation

are needed before sending them to the physics. Thus, unlike what was presented earlier in Sec. 3.2.5, the turbulent diffusion terms discussed in Sec. 3.2.5.2.3 are computed at the centre of the mesh but on temperature levels. Similarly, modulus of the strain rate tensor discussed in Sec. 3.2.5.4 and horizontal terms of TKE equation illustrated in Sec. 3.2.5.3 are computed at the centre of the mesh but on momentum levels. This is not further described here and the reader is referred to Pelletier *et al.* (2005) for further details.

In this original version of the physics library, the required vertical interpolations of momentum, and notably the extrapolation at the bottom of the domain to obtain $[\overline{u}^{\mathrm{XZ}}]_{i,j,3/4}$, are triggering a strong numerical mode with a zigzag pattern polluting the near surface region of the momentum related quantities as discussed in the last chapter of the present study, *i.e.* Sec. 4.1 and Sec. 4.4.2. This spurious phenomenon which is present in both the column and 3D turbulence models (since it is related to the vertical diffusion), was found to be amplified at high resolution during this study, affecting thus the suitability of the approach for use as a LES model.

3.3.1.2.2 New vertical staggering

In order to overcome numerical imperfections related to the original staggering of the physics, it was decided to couple the dynamics with a more advanced version of the physics (version 5.0.2) which can handle almost seamlessly the various possible vertical staggering of the dynamics (but that did not include 3D turbulence abilities). In fact, the turbulent diffusion of the various variables is now done according to their location in the dynamics.

Thus, momentum turbulent fluxes $\overline{u'w'}$ and $\overline{v'w'}$ are computed on staggered levels such as their divergence falls back on momentum levels. Similarly, heat flux $\overline{w'\theta'}$ is computed on momentum levels. As a results, all the main variables and pre-computed terms (as described in Sec. 3.2.5.2.3, Sec. 3.2.5.4 and Sec. 3.2.5.3) remain at the same height, *i.e.* velocity components on full levels, and temperature and TKE on staggered level as shown in Fig. 3.7 b), and only the heat mixing coefficient needs to be interpolated on momentum levels before processing heat turbulent diffusion. This new version of the physics is still based on a sigma vertical coordinate, and array indices are up side-down compared to the dynamics.

As a summary the following is done at the dynamics $\rightarrow$ physics interface

$$\{u\}_{\mathrm{i,j,k}} = [\overline{u}^{\mathrm{X}}]_{i,j,N_k+1-k}\,, \tag{3.140}$$

which is also the case for the pre-computed term $F^H_{u\,turb}$ from Eq. (3.87),

$$\{v\}_{\mathrm{i,j,k}} = [\overline{v}^{\mathrm{Y}}]_{i,j,N_k+1-k}\,, \tag{3.141}$$

which is also the case for the pre-computed term $F^H_{v\,turb}$ from Eq. (3.90),

$$\{\theta\}_{\mathrm{i,j,k-1/2}} = [\theta]_{i,j,N_k+1-k+1/2}\,, \tag{3.142}$$

which is also the case for the pre-computed term $F^H_{T\,turb}$ from Eq. (3.96),

$$\{k\}_{\mathrm{i,j,k-1/2}} = [k]_{i,j,N_k+1-k+1/2}\,, \tag{3.143}$$

which is also the case for the pre-computed terms A_{dyn}, B_{dyn} and D_{dyn} from Eqs. (3.107), (3.108) and (3.109), and the strain rate tensor modulus from Eq. (3.111).

Then, when returning the total tendencies (that include both vertical and horizontal turbulent diffusion) to the dynamics, we have

$$[F_{u\,turb}]_{i-1/2,j,k} = \left\{\overline{F_{u\,turb}}^{\mathrm{X}}\right\}_{\mathrm{i-1/2,j},N_k+1-\mathrm{k}}\,, \tag{3.144}$$

$$[F_{v\,turb}]_{i,j-1/2,k} = \left\{\overline{F_{v\,turb}}^{\mathrm{Y}}\right\}_{\mathrm{i,j-1/2},N_k+1-\mathrm{k}}\,, \tag{3.145}$$

$$[F_{T\,turb}]_{i,j,k-1/2} = \{F_{T\,turb}\}_{\mathrm{i,j},N_k+1-\mathrm{k}+1/2}\,, \tag{3.146}$$

which is achieve at the physics $\rightarrow$ dynamics interface, outside of the physics library. Note that all horizontal interpolations in the above equation are cubic as discussed in Sec. 3.3.1.1.

In order to couple this new version of the physics with the MC2 dynamics, the interface between the physics and the dynamics had to be adapted following the above rules. In addition, the new physics library was further modified to include the new features dealing with high resolution 3D turbulence modelling, such as the inclusion of the horizontal terms of turbulent diffusion and TKE equation, and several SGS models (in addition to others minor adaptations). Further details on the interface between the physics and the dynamics, and the modifications of the new physics are given all along this section, *i.e.* Sec. 3.3.

3.3.2 Sigma vertical coordinate

The physics library is based on a sigma vertical coordinate $\sigma_m = p_h^+/p_0^+$ as introduced in Sec. 3.3.1.2. It is obtained (at each time step) based on the hydrostatic pressure p_h^+, which is computed considering surface pressure p_0^+ and temperature profile of the output of the dynamic kernel at time t^+, *i.e.* $\boldsymbol{\Psi}_{DE}^+$. Thus, every dynamics pressure/momentum level z_m has a corresponding hydrostatic sigma level σ_m in the physics, and similarly for z_t with $\sigma_t = p_{ht}^+/p_0^+$ and for z_w with $\sigma_e = p_{ht}^+/p_0^+$ except at the first level where $\sigma_e = \sigma_m = 1$. The computation of the sigma levels used in the physics is fully part of the dynamics $\rightarrow$ physics interface.

3.3.2.1 From height to sigma coordinate

In the dynamics, in order to compute the hydrostatic pressure on momentum and temperature levels, *i.e.* p_h^+ and p_{ht}^+, absolute temperature T^+ at time t^+ (*i.e.* based on $\boldsymbol{\Psi}_{DE}^+$) is first computed on temperature levels such as

$$\left[T^+\right]_{i,j,k-1/2} = \left[\frac{T_*}{g}\left(b^+ + g\right)\right]_{i,j,k-1/2}, \tag{3.147}$$

then, the hydrostatic pressure is obtained integrating the hydrostatic relation from the surface to the top of the domain such as for each layer

$$\left[p_h^+\right]_{i,j,k} = \left[p_h^+\right]_{i,j,k-1}\left[\exp\left(-\frac{g\Delta z_m}{RT^+}\right)\right]_{i,j,k-1/2}, \tag{3.148}$$

with the surface pressure given by

$$\left[p_h^+\right]_{i,j,1/2} = \left[p_0 \exp\left(\frac{P^+}{RT_*}\right)\right]_{i,j,1/2}. \tag{3.149}$$

Finally, the pressure on temperature levels is obtained following

$$\left[p_{ht}^+\right]_{i,j,k-1/2} = \left(\left[p_h^+\right]_{i,j,k}\left[p_h^+\right]_{i,j,k-1}\right)^{1/2}, \tag{3.150}$$

with

$$\left[p_{ht}^+\right]_{i,j,3/4} = \left(\left[p_h^+\right]_{i,j,1}\left[p_h^+\right]_{i,j,1/2}\right)^{1/2}, \tag{3.151}$$

$$\left[p_{ht}^+\right]_{i,j,N_k+1/4} = \left(\left[p_h^+\right]_{i,j,N_k+1/2}\left[p_h^+\right]_{i,j,N_k}\right)^{1/2}. \tag{3.152}$$

Once the hydrostatic pressure is computed on the various sets of levels, the sigma coordinate σ_t and σ_m can be readily obtained such as

$$\left[\sigma_t\right]_{i,j,k-1/2} = \frac{\left[p_{ht}^+\right]_{i,j,k-1/2}}{\left[p_h^+\right]_{i,j,1/2}}, \tag{3.153}$$

$$\left[\sigma_m\right]_{i,j,k} = \frac{\left[p_h^+\right]_{i,j,k}}{\left[p_h^+\right]_{i,j,1/2}}, \tag{3.154}$$

which leads to the following once projected on the physics grid

$$\left\{\sigma_t\right\}_{\mathrm{i,j,k-1/2}} = \left[\sigma_t\right]_{i,j,N_k+1-k+1/2}, \tag{3.155}$$

$$\left\{\sigma_m\right\}_{\mathrm{i,j,k}} = \left[\sigma_m\right]_{i,j,N_k+1-k}. \tag{3.156}$$

For their part, the TKE sigma levels σ_e are at the same height as σ_t except the bottom level which is located at the surface, *i.e.* $N_k + 1/2$ instead of $N_k + 1/4$.

Finally, the top and bottom boundaries, *i.e.* σ_T and σ_B of the model are given by

$$\sigma_B = \{\sigma_m\}_{\mathrm{i,j},N_k+1/2} = \{\sigma_e\}_{\mathrm{i,j},N_k+1/2} = 1, \tag{3.157}$$

$$\sigma_T = \{\sigma_m\}_{\mathrm{i,j},1+1/2}\,. \tag{3.158}$$

3.3.2.2 From sigma to height coordinate

Once in the physics, the height of the sigma levels is retrieved by solving the hydrostatic relation for z, which takes the following form in σ coordinate

$$\frac{\partial \sigma}{\partial z} = -\frac{g\sigma}{RT} = -\frac{\rho g}{p_0}. \tag{3.159}$$

As a side note, the Exner function take the following convenient form in sigma coordinate

$$\pi = \sigma^{R/c_p}, \tag{3.160}$$

it is thus straightforward to go from absolute to potential temperature.

Concerning the vertical derivatives in a sigma coordinate, based on the above expression, the vertical gradient in height coordinate of a given variable ψ can be written as

$$\frac{\partial \psi}{\partial z} = \frac{\partial \psi}{\partial \sigma}\frac{\partial \sigma}{\partial z} = -\frac{g\sigma}{RT}\frac{\partial \psi}{\partial \sigma} = -\frac{\rho g}{p_0}\frac{\partial \psi}{\partial \sigma}. \tag{3.161}$$

As a result, the vertical diffusion of ψ takes the following convenient form

$$\frac{1}{\rho}\frac{\partial}{\partial z}\left(\rho K_\psi \frac{\partial \psi}{\partial z}\right) = \frac{\partial}{\partial \sigma}\left(\check{K}_\psi \frac{\partial \psi}{\partial \sigma}\right). \tag{3.162}$$

where we have

$$\check{K}_\psi = \left(\frac{g\sigma}{RT}\right)^2 K_\psi. \tag{3.163}$$

Finally, the vertical grid spacing at a given height is obtained directly by

$$\{\Delta z_m\}_{\mathrm{i,j,k+1/2}} = -\frac{R\,\{T\}_{\mathrm{i,j,k+1/2}}}{g} \ln\left(\frac{\{\sigma_m\}_{\mathrm{i,j,k+1}}}{\{\sigma_m\}_{\mathrm{i,j,k}}}\right). \tag{3.164}$$

3.3.3 Implicit vertical turbulent diffusion

The vertical turbulent diffusion solved in the physics is illustrated in Eq. (3.49) and detailed in Appendix III. These terms are shared by both the column and the 3D turbulence model. For any variable ψ (being either u, v or θ), the sole impact of the vertical turbulent diffusion on the main variables can be expressed as (similarly as Eqs. (2.48) and (2.54))

$$\left[\frac{d\psi}{dt}\right]^V_{turb} = \frac{1}{\rho}\frac{\partial}{\partial z}\left(\rho K_\psi \frac{\partial \psi}{\partial z}\right) \equiv F^V_{\psi\,turb}, \tag{3.165}$$

where, following the formalism from Eqs. (2.33) to (2.36) and Sec. 3.2.5, $[d\psi/dt]^V_{turb}$ is equivalent to $F^V_{u\,turb}$, $F^V_{v\,turb}$ and $T_* F^V_{T\,turb}/g\pi$ for u, v and θ equations respectively (see Eq. (3.49)).

After transforming Eq. (3.165) in sigma coordinates following Eq. (3.162), the discrete form in time of the implicit vertical diffusion can be written as

$$\frac{\psi^+ - \psi^*}{2\Delta t} = \frac{\partial}{\partial \sigma}\left(\check{K}^*_\psi \frac{\partial \psi^+}{\partial \sigma}\right) \equiv F^{V\,+}_{\psi\,turb}(\psi^*)\,, \tag{3.166}$$

where $\check{K}^*_\psi$ is obtained following Eq. (3.163) with K^*_ψ first computed as described in Sec. 3.3.5 and Sec. 3.3.6 prior to solve Eq. (3.166).

The above equation is solved for $\Delta\psi = \psi^+ - \psi^*$ as discussed by Mailhot and Benoit (1982), Benoit *et al.* (1989) and Mailhot *et al.* (1998), and the solution obtained is added as a correction to the output of the dynamic kernel, such that the final value (turbulence aware) of the main variables is obtained. Note however that, the initial value ψ^* required to solve Eq. (3.166) differs depending of the approach.

In the column model, following a fractional step approach, ψ^* is directly taken to be the output from the dynamic kernel, *i.e.* $\boldsymbol{\Psi}^+_{DE}$, such as following the matrix form introduced at Eq. (2.33), the final value of the main variables is expressed as

$$\boldsymbol{\Psi}^+_{DEF} = \boldsymbol{\Psi}^+_{DE} + 2\Delta t \boldsymbol{F}^{V+}_{turb}\big(\boldsymbol{\Psi}^+_{DE}\big)\,, \tag{3.167}$$

and thus the total tendency writes

$$\boldsymbol{F}^*_{turb} = \boldsymbol{F}^{V+}_{turb}\big(\boldsymbol{\Psi}^+_{DE}\big)\,. \tag{3.168}$$

In the context of three dimensional turbulence modelling, by generalizing the fraction-step philosophy, the horizontal turbulent diffusion pre-computed term, $\boldsymbol{F}^{H-}_{turb}\big(\boldsymbol{\Psi}^-\big)$, is added to $\boldsymbol{\Psi}^+_{DE}$ in order to compute an initial value ψ^* for the vertical turbulent diffusion Eq. (3.166). Thus, using the matrix form as above, the initial value of Eq. (3.166) writes as follow when the 3D turbulent diffusion is involved

$$\boldsymbol{\Psi}^* = \boldsymbol{\Psi}^+_{DE} + 2\Delta t \boldsymbol{F}^{H-}_{turb}\big(\boldsymbol{\Psi}^-\big)\,, \tag{3.169}$$

and the final value of the main variables is obtained such as

$$\boldsymbol{\Psi}^+_{DEF} = \boldsymbol{\Psi}^* + 2\Delta t \boldsymbol{F}^{V+}_{turb}(\boldsymbol{\Psi}^*)\,. \tag{3.170}$$

and thus the total tendency writes

$$\boldsymbol{F}^*_{turb} = \boldsymbol{F}^{H-}_{turb}\big(\boldsymbol{\Psi}^-\big) + \boldsymbol{F}^{V+}_{turb}(\boldsymbol{\Psi}^*)\,. \tag{3.171}$$

As a side note, this formulation is compatible with Eq. (3.166) since $\boldsymbol{F}^{H-}_{turb}$ vanish in the 1D context, and thus $\boldsymbol{\Psi}^* = \boldsymbol{\Psi}^+_{DE}$ is recovered.

The boundary conditions involved to solve Eq. (3.166) are defined similarly as presented in Sec. 3.2.5.2.1, but they further include the sigma coordinate transformation such as they write

$$\check{K}_{\psi}^{*}\frac{\partial\psi^{+}}{\partial\sigma}\bigg|_{\sigma_T} = 0, \tag{3.172}$$

$$\check{K}_{\psi}^{*}\frac{\partial\psi^{+}}{\partial\sigma}\bigg|_{\sigma_B} = -\check{\beta}_{\psi}^{-}\left(\psi_{a}^{+}-\psi_{s}^{-}\right), \tag{3.173}$$

where

$$\check{\beta}_{\psi}^{-} = \left(\frac{g}{RT_{s}^{-}}\right)\beta_{\psi}^{-}, \tag{3.174}$$

and ψ_{a}^{+} (unknown) is either $\{u^{+}\}_{\mathrm{i,j},N_k}$, $\{v^{+}\}_{\mathrm{i,j},N_k}$ or $\{\theta^{+}\}_{\mathrm{i,j},N_k+1/4}$, and β_{ψ}^{-} and $\alpha_{\psi}^{-} = -\beta_{\psi}^{-}\psi_{s}^{-}$ are the associated homogenous and inhomogeneous surface terms computed as in Sec. 2.3 and Sec. 3.3.7 prior to solve Eq. (3.166).

Finally, the spatial discretization of the above equations, as well as further details regarding the original solver can be found in Mailhot and Benoit (1982), in Benoit *et al.* (1989, Appendix B and C) and in Mailhot *et al.* (1998). Here, it is however to underline that, in the new version of the physics, variables are vertically located as in the dynamics. Thus, while the exact same solver as in the original version of the physics is used, there is half a vertical layer offset for momentum diffusion (thus momentum diffusion discretization is similar to the TKE diffusion in the original version of the model). At the opposite, turbulent diffusion of heat is unchanged with regards to the original version of the physics, but the heat mixing coefficient is interpolated on σ_m levels prior to solve Eq. (3.166).

3.3.4 Numerical integration of turbulent kinetic energy equation

The integration of the TKE equation Eq. (2.130) from t^{0} to t^{+} is achieved by splitting the process into several fractional steps similarly as the turbulent diffusion. This approach is used to solve the 1D TKE equation in the physics (Mailhot and Benoit, 1982; Benoit *et al.*, 1989), and

it is generalized to the 3D context where horizontal and vertical terms are further split (Pelletier *et al.*, 2005) (see also Sec. 3.2.5.3).

In this generalized fractional-step method, k^+_{DE} is first computed following the SL advection scheme as described in Sec. 3.2.1 (considering the TKE as a passive scalar, see Eq. (3.10))[10]. Then, the remaining non-diffusive terms B^-_{phy} and C^-_{phy} are computed based on variables at time t^- following Eqs. (3.104) and (3.105), and all terms are brought together, such as

$$A^- = A^-_{dyn}, \qquad B^- = B^-_{dyn} + B^-_{phy}, \qquad C^- = C^-_{phy}. \tag{3.175}$$

The non-diffusive part of the TKE equation then writes (dropping the superscript)

$$\frac{\partial k^*}{\partial t} = Ak^* + Bk^{*\,1/2} - Ck^{*\,3/2}, \tag{3.176}$$

which is solved for an intermediate solution k^* considering A, B and C independent of time and using k^+_{DE} as initial value, such as

$$\int_{t^0}^{t^+} dt = \int_{k^+_{DE}}^{k^*} \frac{d\eta}{A\eta + B\eta^{1/2} - C\eta^{3/2}}. \tag{3.177}$$

The right hand side integral is obtained analytically (quadratic equation). In comparison to the 1D version (Mailhot and Benoit, 1982; Benoit *et al.*, 1989), A is new in the 3D model. Thus, the computation of the above integral required a new analytic solver as discussed by Pelletier *et al.* (2005). Note also that, C can now take a different form depending on the closure (*i.e.* column model, hybrid TKE SGS model, Deardorff SGS model, ...).

Subsequently, the TKE horizontal diffusion tendency D^0_{dyn} (that is explicit in time, see Sec. 3.2.5.3) is added to k^*, and a second intermediate value is obtained such as

$$k^{\circledast} = k^* + 2\Delta t D^0_{dyn}\left(k^0\right). \tag{3.178}$$

[10] This step is bypassed when relying on the column model as TKE advection is neglected.

Finally, the vertical diffusion of TKE is solved implicitly for $\Delta k = k^+ - k^{\circledast}$ using $k^{\circledast}$ from the above equation as initial value. In this last step, a similar approach as for the momentum and temperature (see Sec. 3.3.3) is followed but with an appropriate mixing coefficient, *i.e.* $K_k = 2.08 K_M$ (see Sec. 2.2.4), and top and bottom boundary conditions. Note also that in the new version of the physics there is half a level vertical offset compared to the original version of the model (thus discretization of the TKE vertical diffusion in the new physics version is similar to momentum and heat vertical diffusion in the original version of the model). As a summary, the discrete form in time of the latter equation in sigma coordinate can be written

$$\frac{k^+ - k^{\circledast}}{\Delta t} = \frac{\partial}{\partial \sigma}\left(\check{K}_k^* \frac{\partial k^+}{\partial \sigma}\right) \equiv D_{phy}^+(k^{\circledast}) \tag{3.179}$$

where $\check{K}_k^*$ is obtained as in Eq. (3.163), and the top and bottom boundary conditions write

$$\check{K}_k^+ \frac{\partial k^+}{\partial \sigma}\bigg|_{\sigma_T} = 0, \tag{3.180}$$

$$k^+\big|_{\sigma_B} = k_a^0, \tag{3.181}$$

where $k_a^0 = 3.75 u_*^2 + 0.2 w_*^2$ (Wyngaard and Coté, 1974) and the TKE is clipped by a minimum value, *i.e.* $k^+ = \max\left(k^+, 10^{-4}\right)$.

The tendency from the vertical diffusion of TKE is then known, and the final value of the TKE at time t^+ is obtained such as

$$k^+ = k^{\circledast} + 2\Delta t D_{phy}^+(k^{\circledast})\,. \tag{3.182}$$

Note that, as for the vertical diffusion of heat and momentum, the above equation involved when the 3D turbulent model is used, is consistent with the column model, since when relying on the latter $D_{dyn}^0(k^0)$ vanish and we have $k^{\circledast} = k^*$.

3.3.5 SGS models

The mathematical model of the five SGS models evaluated during the present study was introduced in Sec. 2.2.3 where Tab. 2.1 presented their detailed overview. They serve to compute the mixing coefficients which are located at the same place as the TKE as shown in Fig. 3.7, *i.e.* vertically on staggered σ_e levels and horizontally at the centre of the mesh (as all the column of the physics)[11]. In a general manner, main variables at time t^- are used here, *i.e.* $\boldsymbol{\Psi}^-$. The information on their location in time (superscript) is thus dropped hereafter.

In this section, the implementation of the five SGS models in the physics library is discussed. However, before entering into the details of each SGS model, it is convenient to introduce the computation of some quantities common to several SGS models.

The TKE and the strain rate tensor modulus are located on staggered levels at the centre of the mesh, *i.e.* $\{k\}_{\mathrm{i,j,k+1/2}}$ and $\{S\}_{\mathrm{i,j,k+1/2}}$, they can thus be used straightforwardly to compute mixing coefficients. Concerning their time level, S is pre-computed in the dynamics based on variables at time t^-, it can thus be noted S^-. On the other hand, the time integration of TKE is achieved after the mixing coefficient are computed as illustrated in Fig. 3.2. As result, mixing coefficients are computed based on k_{DE}^+ in agreement with the fractional step philosophy (Mailhot *et al.*, 1998).

The height (agl) of σ_e levels (*i.e.* $\{z_w\}_{\mathrm{i,j,k+1/2}}$) and the vertical resolution $\{\Delta z_m\}_{\mathrm{i,j,k+1/2}}$ are also required by several SGS models to define the mixing and dissipation length scales, and some of the vertical gradients. The former is obtained as discussed in Sec. 3.3.2, while the latter is computed as in Eq. (3.164). The filter width Δ, is given by

$$\{\Delta\}_{\mathrm{k+1/2}} = \left(\Delta x \Delta y \{\Delta z_m\}_{\mathrm{k+1/2}}\right)^{1/3}, \tag{3.183}$$

which is only a function of height.

[11] As a side note, K_T is computed on staggered σ_e levels, however, it is interpolated on σ_m before proceeding to the vertical turbulent diffusion of temperature as discussed in Sec. 3.3.3.

Concerning gradients, based on the physics discretization formalism, the Brunt-Väisälä frequency is expressed on staggered σ_e levels as

$$\left\{N^2\right\}_{\mathrm{i,j,k+1/2}} = \left\{\frac{g}{\theta}\frac{\delta_z \overline{\theta}^{\mathrm{z}}}{\Delta z_m}\right\}_{\mathrm{i,j,k+1/2}}, \tag{3.184}$$

where θ is interpolated on σ_m levels for the vertical derivative of $\overline{\theta}^{\mathrm{z}}$ to be located on σ_e levels.

In the following, the discrete form of the remaining quantities required by each SGS model is detailed. It is however noteworthy that the physics library is largely relying on single precision floats and integers (32 bit). Thus, as presented in this section, some limits and bounds have to be imposed to avoid not only overflow and underflow, but also spurious phenomenon arising for situations such as after initializing a perfectly neutral theoretical case with no shear.

3.3.5.1 UKMO Smagorinsky SGS model

The implementation of the UKMO Smagorinsky SGS model in the physics library is very similar to the standalone SGS model included in the dynamics and presented in Sec. 3.2.5.5. Indeed, while two separated routine perform these computations, both versions rely on the same numerical method, boundary conditions and limits to avoid overflow and underflow.

Following Eqs. (2.56) and (2.57), the discrete form of UKMO Smagorinsky SGS model mixing coefficients on σ_e levels can be written

$$\left\{K_M\right\}_{\mathrm{i,j,k+1/2}} = \left\{\lambda^2 f_m S\right\}_{\mathrm{i,j,k+1/2}}, \tag{3.185}$$

$$\left\{K_T\right\}_{\mathrm{i,j,k+1/2}} = \left\{\lambda^2 f_h S\right\}_{\mathrm{i,j,k+1/2}}, \tag{3.186}$$

where the length scale λ is constant in time and function of height agl. It is thus computed once during initialization and it writes

$$\left\{\lambda\right\}_{\mathrm{i,j,k+1/2}} = \left\{\left(\frac{1}{\lambda_0^n} + \frac{1}{\left(\kappa\left(z_w + z_0\right)\right)^n}\right)^{-n}\right\}_{\mathrm{i,j,k+1/2}}, \tag{3.187}$$

where $n = 2$ and the length scale value in the flow interior λ_0 is given by

$$\{\lambda_0\}_{\mathrm{k+1/2}} = \min\left(500., \max\left(C_S\left(\Delta x \Delta y\right)^{1/2}, C_S\left\{\Delta\right\}_{\mathrm{k+1/2}}\right)\right), \tag{3.188}$$

with the Smagorinsky constant $C_S = 0.15$.

Heat and momentum stability functions, f_m and f_h are defined as illustrated in Sec. 2.2.3.1.2. They are computed following the approach presented in Sec. 3.2.5.5.2. Thus, after the Brunt-Väisälä frequency is computed on staggered levels σ_e based on Eq. (3.187), the local Richardson number defined on Eq. (2.64) is computed such as

$$\{\mathrm{Ri}\}_{\mathrm{i,j,k+1/2}} = \left\{\frac{N^2}{S^2}\right\}_{\mathrm{i,j,k+1/2}} \tag{3.189}$$

Furthermore, it is imposed $\mathrm{Ri} = 0$ if $S^2 < 10^{-30}$ in order to prevent overflow, and at the top and bottom of the domain $\{\mathrm{Ri}\}_{\mathrm{i,j,1/2}} = \{\mathrm{Ri}\}_{\mathrm{i,j},N_k+1/2} = 0$.

Finally, mixing coefficients are computed exactly as in Sec. 3.2.5.5.2 considering the proper vertical indexing of the physics as described in Sec. 3.3.1. Finally, note that the same limits in S and N as in Sec. 3.2.5.5.2 are used here to avoid overflow and underflow errors.

3.3.5.2 Deardorff SGS model

The Deardorff (1980) SGS model was introduced in Sec. 2.2.3.2. The discrete form on staggered levels of its momentum and heat mixing coefficients writes

$$\{K_M\}_{\mathrm{i,j,k+1/2}} = \left\{C_k \lambda k^{1/2}\right\}_{\mathrm{i,j,k+1/2}}, \tag{3.190}$$

$$\{K_T\}_{\mathrm{i,j,k+1/2}} = \left\{\frac{K_M}{\mathrm{Pr}_t}\right\}_{\mathrm{i,j,k+1/2}}, \tag{3.191}$$

and the dissipation rate of TKE writes

$$\{\varepsilon\}_{\mathrm{i,j,k+1/2}} = \left\{ \frac{C_\varepsilon}{\lambda_\varepsilon} k^{3/2} \right\}_{\mathrm{i,j,k+1/2}}, \tag{3.192}$$

where $C_k = 0.1$, $C_\varepsilon = 0.93$, Pr_t is computed directly using Eq. (2.78) and λ is defined as

$$\{\lambda\}_{\mathrm{i,j,k+1/2}} = \begin{cases} \{\Delta\}_{\mathrm{k+1/2}}, & \text{unstable} \\ \min(\{\Delta\}_{\mathrm{k+1/2}}, \{\mathcal{L}_N\}_{\mathrm{i,j,k+1/2}}), & \text{stable} \end{cases},$$

$$\{\lambda_\varepsilon\}_{\mathrm{i,j,k+1/2}} = \{\lambda\}_{\mathrm{i,j,k+1/2}},$$

and

$$\{\mathcal{L}_N\}_{\mathrm{i,j,k+1/2}} = \left\{ 0.76 \frac{k^{1/2}}{N} \right\}_{\mathrm{i,j,k+1/2}}. \tag{3.193}$$

In order to avoid underflow/overflow errors as well as spurious phenomenon arising after the initialization of neutral theoretical cases, the following limits are imposed during the computation of the Brunt-Väisälä frequency

$$\left\{ \frac{\delta_z \overline{\theta}^{\mathrm{Z}}}{\Delta z_m} \right\}_{\mathrm{i,j,k+1/2}} = 0, \qquad \text{if} \quad \left\{ \left| \frac{\delta_z \overline{\theta}^{\mathrm{Z}}}{\Delta z_m} \right| \right\}_{\mathrm{i,j,k+1/2}} < 5 \times 10^{-6}, \tag{3.194}$$

and $N^2 = \max\left(N^2, 10^{-15}\right)$.

3.3.5.3 Hybrid TKE SGS model

The hybrid TKE SGS model was introduced in Sec. 2.2.3.3. Its mixing coefficients and dissipation are defined as in Deardorff SGS model, but as in the UKMO Smagorinsky SGS model, they also include a Smagorinsky-type constant and stability functions (that are the same as in the column model). The discrete form on staggered levels of the hybrid TKE SGS model

mixing coefficients thus writes

$$\{K_M\}_{\mathrm{i,j,k+1/2}} = \left\{C'_k \lambda f_m k^{1/2}\right\}_{\mathrm{i,j,k+1/2}}, \tag{3.195}$$

$$\{K_T\}_{\mathrm{i,j,k+1/2}} = \left\{C'_k \lambda f_h k^{1/2}\right\}_{\mathrm{i,j,k+1/2}}, \tag{3.196}$$

and the dissipation is parametrized similarly

$$\{\varepsilon\}_{\mathrm{i,j,k+1/2}} = \left\{\frac{C'_\varepsilon}{\lambda_\varepsilon f_m} k^{3/2}\right\}_{\mathrm{i,j,k+1/2}}, \tag{3.197}$$

where the closure constants $C'_k = 0.516$ and $C'_\varepsilon = 0.137$ are used.

The mixing length scales is proportional to the filter width through a Smagorinsky like constant

$$\{\lambda\}_{\mathrm{i,j,k+1/2}} = \{\min\left[\kappa\left(z_w + z_0\right), \lambda_0\right]\}_{\mathrm{i,j,k+1/2}}, \tag{3.198}$$

with $\lambda_0 = \min\left[C_S \Delta_H, \lambda_e\right]$, $C_S = 0.15$ and $\lambda_e = 200$ m.

Stability functions are dependent of the gradient Richardson number as defined in Eq. (2.88). The latter is computed on staggered levels and writes

$$\{\mathrm{Ri}\}_{\mathrm{i,j,k+1/2}} = \left\{\frac{\dfrac{g}{\overline{\theta}}\dfrac{\delta_z \overline{\theta}^{\mathrm{Z}}}{\Delta z_m}}{\left(\dfrac{\delta_z u}{\Delta z_m}\right)^2 + \left(\dfrac{\delta_z v}{\Delta z_m}\right)^2}\right\}_{\mathrm{i,j,k+1/2}}. \tag{3.199}$$

where the numerator is equal to N^2 (obtained as in Eq. (3.184)). Note that the same limits as in Deardorff SGS model are imposed for the computation of the latter, and 10^{-6} is added to the denominator of Ri (done in the official version of the physics) in order to avoid underflow/overflow errors as well as spurious phenomenon mostly during the initialization.

Then, stability functions are obtained straightforwardly on staggered levels based on Eqs. (2.89) and (2.90) where the turbulent Prandtl number $\mathrm{Pr}_N = 0.85$ is used. However, the product of

the mixing length by the stability function is further bounded in unstable conditions such as

$$\{\lambda f_m\}_{\mathrm{i,j,k+1/2}} = \min\left(\{\lambda f_m\}_{\mathrm{i,j,k+1/2}}, 5000\right). \tag{3.200}$$

Finally, the dissipation length scale is obtained such as

$$\{\lambda_\varepsilon f_m\}_{\mathrm{i,j,k+1/2}} = \max\left(\{\lambda f_m\}_{\mathrm{i,j,k+1/2}}, 10^{-6}\right). \tag{3.201}$$

3.3.5.4 Redelsperger SGS model

As introduced in Sec. 3.3.5.4, Redelsperger *et al.* (2001) SGS model is similar to Deardorff SGS model: the discrete form of the mixing coefficient and TKE dissipation rate are identical to Eqs. (3.190), (3.191) and (3.192), and the same definition is used for the mixing and dissipation length scales in the flow interior (along with the limits to avoid overflow/underflow) as well as the closure constants $(C_k;\, C_\varepsilon) = (0.1;\, 0.93)$.

However, in the vicinity of the surface, mixing and dissipation length scales become height dependent such as in neutral condition we have

$$\{\mathcal{L}_k\}_{\mathrm{i,j,k+1/2}} = \{(1-\gamma)A_k z_w + \gamma\Delta\}_{\mathrm{i,j,k+1/2}}, \tag{3.202}$$

$$\{\mathcal{L}_\varepsilon\}_{\mathrm{i,j,k+1/2}} = \{(1-\gamma)A_\varepsilon z_w + \gamma\Delta\}_{\mathrm{i,j,k+1/2}}, \tag{3.203}$$

where the additional closure constants $A_k = 2.7$ and $A_\varepsilon = 2.07$, and $\gamma \in [0, 1]$ is a weighting function defined latter.

In the present version of Redelsperger SGS model, no care is taken to adapt A_k and A_ε depending on the thermal stratification of the surface layer. As a result, stratification is only taken into account as in Deardorff SGS model, and $\{\lambda\}_{\mathrm{i,j,k+1/2}}$ and $\{\lambda_\varepsilon\}_{\mathrm{i,j,k+1/2}}$ are obtained based on the

switch presented on Eq. (2.103) to (2.106), *i.e.* for unstable stratification ($\mathrm{Ri} < 0$)

$$\{\lambda\}_{\mathrm{i,j,k+1/2}} = \{\mathcal{L}_k\}_{\mathrm{i,j,k+1/2}}\,, \tag{3.204}$$

$$\{\lambda_\varepsilon\}_{\mathrm{i,j,k+1/2}} = \{\mathcal{L}_\varepsilon\}_{\mathrm{i,j,k+1/2}}\,, \tag{3.205}$$

while for stable stratification ($\mathrm{Ri} > 0$)

$$\{\lambda\}_{\mathrm{i,j,k+1/2}} = \{\min(\mathcal{L}_k, \mathcal{L}_N)\}_{\mathrm{i,j,k+1/2}}\,, \tag{3.206}$$

$$\{\lambda_\varepsilon\}_{\mathrm{i,j,k+1/2}} = \{\min(\mathcal{L}_\varepsilon, \mathcal{L}_N)\}_{\mathrm{i,j,k+1/2}}\,. \tag{3.207}$$

where $\mathcal{L}_N$ is computed as in Deardorff SGS model, *i.e.* Eq. (3.193) (relying on the same limits).

The weighting function γ is defined as

$$\{\gamma\}_{\mathrm{i,j,k+1/2}} = \left\{1 - \exp\left(-3\frac{z_1 - z_w}{z_1 - z_c}\right)\right\}_{\mathrm{i,j,k+1/2}}, \tag{3.208}$$

where $z_1 = \{z_w\}_{\mathrm{i,j},N_k-1/2}$ is the height of the first TKE level above the surface, and $\{z_c\}_{\mathrm{i,j,k+1/2}}$ is a critical height computed as

$$\{z_c\}_{\mathrm{i,j,k+1/2}} = \max\left(\frac{2\,\{\Delta z_m\}_{\mathrm{i,j,k+1/2}}}{\kappa}, \frac{2\Delta_H}{3\kappa}\right). \tag{3.209}$$

3.3.5.5 Linear Kosović SGS model

The linear Kosović SGS model is described in Sec. 2.2.3.5.4. In that simplified version, no backscatter effects are taken into account, *i.e.* $C_b = C_1 = C_2 = 0$, and Kosović SGS stress model become linear and similar to the Deardorff (1980) SGS model. Mixing coefficients and dissipation are identical to Eqs. (3.190), (3.191) and (3.192), while the closure constants and length scales slightly differ.

The mixing length is based on the filter width as in Deardorff SGS model, *i.e.* $\lambda = \Delta$. But on the contrary, the dissipation length scales does not always equal λ, and we have

$$\left\{\lambda_\varepsilon\right\}_{\mathrm{i,j,k+1/2}} = \begin{cases} \left\{\Delta\right\}_{\mathrm{i,j,k+1/2}}, & \text{unstable} \\ \left\{\left(\dfrac{1}{\Delta^2} + \dfrac{1}{\mathcal{L}_N^2} + \dfrac{1}{\mathcal{L}_S^2}\right)^{-1/2}\right\}_{\mathrm{i,j,k+1/2}}, & \text{stable} \end{cases}, \tag{3.210}$$

where $\left\{\mathcal{L}_N\right\}_{\mathrm{i,j,k+1/2}}$ is computed as in Deardorff SGS model, Eq. (3.193), and relying on the same limits. For its part, $\left\{\mathcal{L}_S\right\}_{\mathrm{i,j,k+1/2}} = \left\{2.76k^{1/2}/S\right\}_{\mathrm{i,j,k+1/2}}$ is obtained straightforwardly on staggered levels.

Finally, concerning the closure constants, $C_k = C_\varepsilon = 0.0943$ (as opposed to the other SGS models) and the turbulent Prandtl number is taken to be $\mathrm{Pr}_t = 1/3$.

3.3.6 Classical column closure

The classic column model is almost identical to the Hybrid TKE SGS model presented in Sec. 3.3.5.3, albeit simpler. Indeed, as introduced in Sec. 2.2.5.2, both models share the same definition for the mixing coefficients, Eqs. (3.195) and (3.196), the TKE dissipation rate, Eq. (3.197), the Ri and stability functions, Eqs. (3.199), (2.89) and (2.90), and finally the closure constants $(C_k'; C_\varepsilon') = (0.516; 0.138)$, Eqs. (2.91) and (2.92).

In fact, the only difference between the hybrid TKE SGS model and the column model (beyond the boundary layer approximation) is in the mixing length: the Smagorinsky-type constant is no longer present in the column model, and we have

$$\left\{\lambda\right\}_{\mathrm{i,j,k+1/2}} = \left\{\min\left[\kappa\left(z + z_0\right), \lambda_e\right]\right\}_{\mathrm{i,j,k+1/2}}, \tag{3.211}$$

$$\left\{\lambda_\varepsilon\right\}_{\mathrm{i,j,k+1/2}} = \left\{\lambda\right\}_{\mathrm{i,j,k+1/2}}, \tag{3.212}$$

where $\lambda_e = 200$ m (Blackadar, 1962).

3.3.7 Surface layer similarity theory

In the official versions of the physics library (both the legacy that came with MC2 and the new versions), surface layer parameters, such as the friction velocity, the surface sensible heat flux or the Monin-Obukhov length scale, are evaluated following the mathematical model introduced in Sec. 2.3. They are thus computed considering only the modulus of velocity U_a at a given level z_{a_M} in the surface layer and the temperature difference $(\theta_a - \theta_s)$ between the surface, $z = 0$ m, and a given height z_{a_H} in the surface layer (along with the momentum and temperature aerodynamic roughness lengths, z_{0_M} and z_{0_H}, respectively).

In the present study, all the cases reproduced require a surface sensible heat flux $\overline{w'\theta'}|_s$ to be imposed (as opposed to the surface temperature) which is a common approach for LES theoretical cases (Nieuwstadt *et al.*, 1992; Kosović and Curry, 2000). Thus, the approach to compute the surface layer parameters had to be adapted, such as at each time step, based on the velocity and temperature at the first level above the surface at time t^-, *i.e.*

$$\begin{aligned}
&\{U_a\}_{\mathrm{i,j}} = \left\{(u^{-2} + v^{-2})^{1/2}\right\}_{\mathrm{i,j},N_k} \quad \text{(located at } \{z_{a_M}\}_{\mathrm{i,j}} = \{z_m\}_{\mathrm{i,j},N_k}\text{)},\\
&\{\theta_a\}_{\mathrm{i,j}} = \left\{\theta^-\right\}_{\mathrm{i,j},N_k+1/4} \quad \text{(located at } \{z_{a_H}\}_{\mathrm{i,j}} = \{z_t\}_{\mathrm{i,j},N_k+1/4}\text{)},
\end{aligned}$$

and the given input parameters $\left\{\overline{w'\theta'}|_s\right\}_{\mathrm{i,j}}$, $\{z_{0_M}\}_{\mathrm{i,j}}$ and $\{z_{0_H}\}_{\mathrm{i,j}}$, we need to compute $\{u_*\}_{\mathrm{i,j}}$ and $\{L_{MO}\}_{\mathrm{i,j}}$, that will then allow to obtain all others surface layer quantities such as the homogeneous and inhomogeneous boundary condition terms.

In this section, this modified approach is described for the unstable surface layer. Note that the spacial indices and time level information is dropped hereafter (since all fields are 2D and located at the centre of the mesh and only variables at time t^- are used as input).

Starting with the definition of u_* and L_{MO} as presented in Sec. 2.3, a system of two equations and two unknowns (u_* and L_{MO}) can be obtained such as

$$L_{MO} = -\frac{u_*^3 \theta_a}{\kappa g \overline{w'\theta'}|_s}, \tag{3.213}$$

$$u_* = \frac{U_a \kappa}{\Phi_M}, \tag{3.214}$$

where Φ_M is a function of z_m/L_{MO} defined as in Eqs. (2.164).

This system can be solved for $1/L_{MO}$ thanks to the Newton-Raphson method[12]. For that purpose, u_* as defined in Eq. (3.214) is first substituted in Eq. (3.213) to obtain

$$\frac{1}{L_{MO}} = -\frac{g \overline{w'\theta'}|_s}{\kappa^2 U_a^3 \theta_a} \Phi_M^3. \tag{3.215}$$

Then, the function, which root is searched, can be defined such as

$$f\left(\frac{1}{L_{MO}}\right) = -\frac{g \overline{w'\theta'}|_s}{\kappa^2 U_a^3 \theta_a} \Phi_M^3 - \frac{1}{L_{MO}}, \tag{3.216}$$

and which derivative writes

$$f'\left(\frac{1}{L_{MO}}\right) = -\frac{3 g \overline{w'\theta'}|_s}{\kappa^2 U_a^3 \theta_a} \Phi'_M \Phi_M^2 - 1. \tag{3.217}$$

where Φ_M is defined as in Eq. (2.164), and Φ'_M is given by

$$\Phi'_M = L_{MO}\left(x^{-1} - x_0^{-1}\right) \tag{3.218}$$

with x and x_0 defined as in Eq. (2.165) (see also Delage and Girard (1992) Appendix).

[12] Following the Newton-Raphson method, the root of a given a function f defined over the reals x and which derivative write f', can be evaluated iteratively such as $x_{n+1} = x_n - f(x_n)/f'(x_n)$.

Finally, after four iterations of the Newton-Raphson method (Delage and Girard, 1992), *i.e.*

$$\left(\frac{1}{L_{MO\,n+1}}\right) = \left(\frac{1}{L_{MO\,n}}\right) - \frac{f\left(\frac{1}{L_{MO\,n}}\right)}{f'\left(\frac{1}{L_{MO\,n}}\right)}, \tag{3.219}$$

an approximated value of L_{MO} is obtained. Then, both Φ_M and Φ_H, Eqs. (2.164) and (2.166), become fully known as well as u_* that is retrieved thanks to Eq. (3.214).

At that point, other variables such as the surface temperature θ_s can be computed, *i.e.*

$$\theta_s = \theta_a + \frac{\Phi_H \overline{w'\theta'}|_s}{\kappa u_*}, \tag{3.220}$$

but also, and more importantly, the surface transfer coefficients C_M and C_H, Eqs. (2.156) and (2.157)), as well as the homogeneous and inhomogeneous momentum and temperature surface boundary terms that write

$$\beta_M = C_M u_* = \frac{\kappa u_*}{\Phi_M} = \frac{\kappa^2 U_a}{\Phi_M^2} \quad \text{and} \quad \alpha_M = 0, \tag{3.221}$$

$$\beta_T = C_H u_* = \frac{\kappa u_*}{\Phi_H} = \frac{\kappa^2 U_a}{\Phi_M \Phi_H} \quad \text{and} \quad \alpha_T = -\frac{\kappa^2 U_a}{\Phi_M \Phi_H}\theta_s. \tag{3.222}$$

This then allows to provide surface boundary to the various turbulent quantities and processes such as the momentum and heat turbulent diffusion. This method to compute surface layer parameters (that was at first only included in the physics) was also fully implemented in the dynamics to provide the standalone turbulence model with surface boundaries.

Finally, it is to underline that the same surface boundary condition as described above is used in conjunction with the five SGS models. Thus, the particular stability functions used for the surface boundary condition of the UKMO LEM model (Gray *et al.*, 2001) are not used here. Similarly, for consistency reasons, the SGS model proposed by Redelsperger *et al.* (2001) for non-neutral condition would require to be adapted according to the stability functions from Delage and Girard (1992) and Delage (1997) (if it were used).

3.4 Initialization

The initialization is the first necessary step allowing to properly perform numerical simulation of ABL flows relying on either the classical column model or the LES model. As previously discussed in Sec. 2.5, three dimensional initial fields of the main model thermodynamic variables, *i.e.* P and b, need to be populated such as the atmosphere is in equilibrium. The approach followed here is the same regardless of the model used. At the opposite, velocity component u, v, w initialization is more model dependent. Note that in any cases, the three time levels t^-, t^0 and t^+, of all the main variables $\boldsymbol{\Psi}$ of the model have to be initialized, but not the TKE which is set to a default value at the first time step.

In this section, the numerical details of the initialization step are further discussed by first presenting the initialization of the 3D thermodynamic fields introduced in Sec. 2.5. Then, the initialization of velocity components is discussed.

3.4.1 Initialization of thermodynamic fields

As introduced in Sec. 2.5, thermodynamic variables three dimensional initial fields are obtained following a sounding like initialization approach. Thus, considering the hydrostatic equilibrium and a given reference vertical profile of potential temperature, the profiles of the generalized pressure P and the buoyancy b are first computed. Then, since the geostrophic balance is implicitly taken into account through the additional large scale forcing terms described in Sec. 2.4 and Sec. 3.2.4, this column is directly used to populate the three dimensional domain. The initial fields thus satisfy directly the hydrostatic basic states and indirectly the geostrophic equilibrium.

The first step of this approach is to interpolate the input profile of potential temperature θ_i (that does not necessarily comply with the vertical grid layout) on pressure levels z_m to get $[\theta_i]_k$ (so that the vertical gradient of the latter falls on staggered levels). Then, the discrete form of Eq. (2.197) is integrated from the bottom $[\ ]_{1/2}$ to the top $[\ ]_{N_k+1/2}$ of the domain considering

that $[\pi]_{1/2} = 1$ such as a profile of the Exner function is obtained, *i.e.*

$$[\pi]_k = \begin{cases} [\pi]_{k-1} - \dfrac{g}{c_p b}\left([z_m]_k - [z_m]_{k-1}\right), & \text{if } \left[\dfrac{\delta_z \theta_i}{\Delta z_m}\right]_{k-1/2} = 0 \\ [\pi]_{k-1} - \dfrac{g}{c_p a}\ln\left(\dfrac{a\,[z_m]_k + b}{a\,[z_m]_{k-1} + b}\right), & \text{otherwise} \end{cases}, \tag{3.223}$$

where

$$a = \left[\frac{\delta_z \theta_i}{\Delta z_m}\right]_{k-1/2}, \tag{3.224}$$

$$b = [\theta_i]_{k-1} - a\,[z_m]_{k-1}\,. \tag{3.225}$$

Subsequently, from Eq. (2.198), which discrete form writes

$$[P]_k = [c_p T_* \ln(\pi) + g z_m]_k\,, \tag{3.226}$$

the profile of the generalized pressure P is recovered.

Then, the buoyancy is obtained directly based on Eq. (2.202) which discrete form writes

$$[b]_{k-1/2} = \left[\frac{g\dfrac{\delta_z P}{\Delta z_m}}{g - \dfrac{\delta_z P}{\Delta z_m}}\right]_{k-1/2}. \tag{3.227}$$

And finally, the full 3D domain is initialized (including the halo) such as

$$\forall\,(i,j \in [(1-h_x, 1-h_y) : (N_i + h_x, N_j + h_y)] \quad \Rightarrow \quad \begin{cases} [P]_{i,j,k} &= [P]_k \\ [b]_{i,j,k} &= [b]_k \end{cases}. \tag{3.228}$$

3.4.2 Initialization of velocity components

All cases reproduced in this study are unsteady theoretical full ABL cases based on periodical lateral boundary conditions with stationary large scale and surface forcing. They tend to a permanent or quasi-steady state. As a consequence, the initial value of velocity components should not affect the final permanent or quasi-steady results as opposed to the thermodynamic variables. Nevertheless, if the evolution to reach that permanent state, or if the results are compared before the permanent state is reached, it is important to use a similar initialization.

For such theoretical cases, the initial value of velocity components is commonly taken equal to the geostrophic wind (Moeng and Sullivan, 1994) such as

$$\boldsymbol{v}(t=0) = \boldsymbol{v}_g, \tag{3.229}$$

and with w set to 0 m/s. Thus, unless specified, this approach is followed when relying on the classical column model.

In the LES context, some sort of perturbation further need to be added to velocity components in order to trigger shear instabilities and ignite the energy cascade process that then allow a self-sustained turbulent regime to develop. As a result, following Andren *et al.* (1994) and Moeng and Sullivan (1994), TKE scaled random perturbations $\boldsymbol{\varpi} = (\varpi_u, \varpi_v, \varpi_w)$ are introduced in the initial velocity components (u, v, and w) such as

$$\boldsymbol{v}(t=0) = \boldsymbol{v}_g + \boldsymbol{\varpi}\sqrt{\frac{k}{\|\boldsymbol{\varpi}^2\|}}, \tag{3.230}$$

where, in order to avoid having to provide the TKE (that is a priori unknown), k is replaced by a linear or quadratic function that is going from its maximum $k = 3\varpi_{max}^2$ at the surface to $k = 0$ at a given height z_{ref} (often taken to be of the order of z_i). We thus have

$$\boldsymbol{v}(t=0) = \boldsymbol{v}_g + \boldsymbol{\varpi}\left[1 - \min\left(1, \frac{z}{z_{ref}}\right)\right]\sqrt{\frac{3\varpi_{max}^2}{\varpi_u^2 + \varpi_v^2 + \varpi_w^2}}. \tag{3.231}$$

Perturbation of the three velocity components are obtained thanks to the default FORTRAN random number generator. They are distributed between $-\varpi_{max}$ and $+\varpi_{max}$, and care was taken for the seed of the random number generator to be different for each run of the model (and each processor). The seed is computed such as

$$\text{seed} = \text{CPU index} \times 10^5 + \text{minute} \times 10^4 + \text{second} \times 10^3 + \text{millisecond} \tag{3.232}$$

Concerning the value of ϖ_{max}, Moeng and Sullivan (1994) used ± 0.1 m/s and Andren *et al.* (1994) used ± 0.5 m/s. However, the present model is fully compressible. As a consequence, temperature may be prone to spurious effects if initial velocity fields do not satisfy the mass conservation. The following simple development illustrates such a problem.

Starting with the velocity divergence that can be expressed as

$$\boldsymbol{\nabla} \cdot \boldsymbol{v} = \boldsymbol{\nabla}_H \cdot \boldsymbol{v} + \frac{\partial w}{\partial z}, \tag{3.233}$$

and assuming that the flow is divergence free, *i.e.* $\boldsymbol{\nabla} \cdot \boldsymbol{v} = 0$, it comes that the vertical velocity at the first z_w level above the surface, *i.e.* $[w]_{3/2}$, can be expressed as

$$[w]_{3/2} = \left[-\Delta z_w \left(\frac{\delta_x u}{\Delta x} + \frac{\delta_y v}{\Delta y} \right) \right]_1 . \tag{3.234}$$

Then, considering that the temperature of an air parcel displaced vertically and adiabatically follows the dry adiabatic lapse rate such as

$$\left[\frac{\delta_z T}{\Delta z_t} \right]_1 = -\frac{g}{c_p}, \tag{3.235}$$

and that at the first level $[\Delta z_t]_1 = [w]_{3/2} \, \Delta t$, we get

$$[\Delta T]_1 = -\frac{g}{c_p} [w]_{3/2} \, \Delta t. \tag{3.236}$$

Finally, substituting Eq. (3.234) in the above, an estimate of ΔT as a function of the horizontal velocity divergence is obtained such as

$$[\Delta T]_1 = \frac{g}{c_p}\left[\Delta z_w \left(\frac{\delta_x u}{\Delta x} + \frac{\delta_y v}{\Delta y}\right)\right]_1 \Delta t. \tag{3.237}$$

By using values representative of LES of the ABL for the various quantities, *i.e.*

$$[\Delta z_w]_1 \sim 10 \text{ m} \quad (\equiv [\Delta x]_1 \equiv [\Delta y]_1), \tag{3.238}$$

$$\Delta t \sim 1 \text{ s}, \tag{3.239}$$

and considering random horizontal velocity perturbations with $\varpi_{max} = 0.1$ m/s such as

$$\left[\left(\frac{\delta_x u}{\Delta x} + \frac{\delta_y v}{\Delta y}\right)\right]_1 \sim 10^{-2} \text{ s}^{-1}, \tag{3.240}$$

we obtain a temperature variation

$$[\Delta T]_1 \sim 1 \text{ K}, \tag{3.241}$$

which clearly illustrates the importance for random perturbation to satisfy mass conservation in order not to impact temperature profile (in the context of a compressible solver). Such spurious temperature differences, that were also observed in the results from MC2 when using $\varpi_{max} = 0.1$ m/s, are of concern notably in the context of a perfectly neutral cases, since they pollute the ABL temperature profile (and indirectly all the others quantities).

To avoid such a problem, the constraint of mass conservation must also be a criterion of the initialization. This could be achieved by relying on the kinematic decomposition of flow fields in a rotational and potential parts such as presented in Panton (1996, Chap. 17). In the meantime, small enough perturbations, such as $\varpi_{max} = 0.01$ m/s, were found sufficient to notably reduce this initialization problem while still triggering turbulence. Thus, due to the more sensitive compressible solver, the perturbations required to ignite turbulence are at least an order of

magnitude smaller than in Moeng and Sullivan (1994) and Andren *et al.* (1994) studies while properly triggering turbulent processes.

In addition of the above and to avoid any problems, it was decided to use $\varpi_{max} = 0.01$ m/s in conjunction with a temporary heating surface (during an initialization period at the integration beginning) as proposed by Moeng and Sullivan (1994). This approach allows perturbations to propagate and organize faster due to the strong effect of convection, while the latter phenomena evacuates spurious temperature perturbations that arise close to the surface (Moeng and Sullivan, 1994). It is thus more robust than solely relying on random numbers.

3.5 Post-processing

The post-processing is the last necessary step that allows to appreciate and compare LES results. Indeed, while RANS approaches provide almost directly usable results (only a time average needed), a more advanced post-processing is required for LES outputs to be valuable.

In this section, the main outcomes of the post-processing are illustrated. First, the general organization and philosophy of the post-processing are introduced. Then, more details on the computation of the resolved and subgrid turbulent quantities are presented. Note that further specific details on the post-processing may be found in Chap. 4.

3.5.1 General organization of the post-processing

Concerning the organization of the post-processing, no treatment is achieved during the computations. Instead, snapshots of the unsteady raw results are saved at constant time intervals Δt_{out} during the computation (as in Moeng and Sullivan (1994) and Andren *et al.* (1994)). Then, all the post-processing is achieve based on these snapshots in an independent manner after the integration is completed. The following 3D quantities are thus written to the output files at every Δt_{out} (and used in the post-processing): P, $\widetilde{u}$, $\widetilde{v}$, $\widetilde{w}$, $\widetilde{\theta}$, k, K_M, K_T and S; as

well as the following 2D quantities that are all surface parameters: u_*, $w'\theta'|_s$, θ_s, and L_{MO}[13]. The post-processing is based on Open-Source software and codes, for the most part relying on FORTRAN, C, Octave (an open-source MATLAB like interpreter) and Gnuplot.

The larger drawback of this off-line post-processing approach is the huge disk space required to store all the unsteady data which is somewhat restrictive. Indeed, as an example, roughly 20 GB are required for the results of one typical LES computation, *i.e.* with a 96^3 mesh, $\Delta t = 1.5$ s, $\Delta t_{out} = 150$ s and that is run for a third of an inertial period (*i.e.* ~ 22500 s which gives 150 snapshots of the flow in the output data). In addition, considering that each cases are reproduced at least fives times, it comes that the full data for 96^3 cases requires not less than 100 GB of disk space for a single experiment. On the other hand, however, this post-processing approach allows for more flexibility and to fully take advantage of the results. Indeed, computations are worth to achieve even if the full post-processing is not implemented yet, and the post-processing can be refined and reachieved as many times as required.

Concerning the model output data format, MC2 is relying on the binary RPN standard file format, also referred to as FST files. This format is similar to the World Meteorology Organization (WMO) GRIB format, *i.e.* the files contain only 1D or 2D horizontal records. Thus, a 3D field with N_k vertical levels is represented as N_k 2D records in a FST file. As a result, for convenience reasons 3D fields are reconstructed before the data is used in the post-processing. In addition to those specificities, such a format requires appropriate readers and it can not be used straightforwardly in the usual post-processing software such as MATLAB or Octave. Thus, a standalone converter of FST file to binary or ASCII common data formats was developed. However, this approach appeared to be a too restrictive solution with regards to LES (due to the additional disk space required by the converted data). As a consequence, a reader of FST files was also developed directly in Octave so that the data could be used straightforwardly in the latter toolboxes as conventional data files.

[13] Note that others quantities are also written in the output FST files, such as the buoyancy b, the mixing and dissipation length scales λ and λ_e, or the homogeneous and inhomogeneous surface terms β_ψ and α_ψ. However, they are not directly used in the post-processing of turbulent quantities, but for validation purpose.

Finally, it is noteworthy that the same post-processing is applied to every results, *i.e.* classical column model and LES model. Thus, only the subgrid part of the vertical momentum and heat turbulent fluxes are non-zero when applied to column model results. Furthermore, as discussed in the next chapter, series of at least five LES computations are achieved (where only initial random velocity perturbations are changed) for each model configurations/cases in order to better appreciate the convergence and statistical behaviour of the solution. As a result, the usual post-processing is applied to each computation of a series, and its non-dimensional output is combined afterwards to obtain the ensemble averaged result and its statistical properties such as the minimum and maximum from the series of results at each height or the root mean square (RMS) of the scatter of the series across the vertical.

3.5.2 Resolved and subgrid turbulent quantities

The computation of the various resolved and subgrid turbulent quantities, such as momentum and heat turbulent fluxes and variances as well as the resolved third order moments and correlation coefficients is done on the staggered TKE levels horizontally at the centre of the mesh. Thus, according to the location of the model variables, turbulent quantities are post-processed on z_w levels when relying on the new physics library (or the standalone turbulence model), while this is done on z_m levels when the original version of the physics is used. Similarity, the non-dimensional vertical gradient of velocity and temperature are computed on staggered z_t levels (z_m when the original version of the physics is used) at the centre of the mesh.

Concerning result parameters used to normalize the various turbulent quantity profiles, most of them, *i.e.* u_*, $w'\theta'|_s$, θ_s, and L_{MO}, are directly retrieved from the output data of the model and averaged horizontally and in time. At the opposite, some others key quantities, such as z_i, $\overline{w'\theta'_i}$ and $\Delta\theta_1$ depends on the post-processing. Indeed, the height of the ABL z_i correspond to the location of the minimum total sensible heat flux at the inversion $\overline{w'\theta'_i}$ which is computed by adding the horizontally and times averaged resolved and subgrid part of the turbulent heat flux as discussed hereafter. Similarly, $\Delta\theta_1$ are computed based on the difference between the horizontally and time averaged temperature at the surface and the first level.

In the following, all the discussions refers to the post-processing involved when the new physics library or the standalone turbulence model are used. Indeed, the post-processing used in conjunction with the original version of the physics is very similar albeit offset by half a vertical layer. Finally, before discussing the numerical method used to obtain the various resolved and subgrid turbulent quantities, it is noteworthy that velocity components form the output of the model are horizontally unstaggered and located at the centre of the mesh, *i.e.* all the data in the output FST files is horizontally located at the pressure location.

Subgrid turbulent fluxes are obtained following a similar approach as described in Sec. 3.2.5.2.1, *i.e.* Eqs. (3.57), (3.58), (3.60), (3.61), (3.63), (3.63), (3.66), (3.67) and (3.68). They are further averaged horizontally and in time. However, horizontal velocity components are interpolated to the appropriate horizontal location when needed (due to their unstaggering in the output data). Concerning the temperature, the subgrid heat flux is also computed on staggered levels. However, subgrid heat flux are first computed on momentum level (by interpolating K_T on momentum level as in the vertical turbulent diffusion implemented in the model), and then the flux is interpolated on staggered levels.

Subgrid scale variances are obtained similarly as in Sec. 3.2.5.1, *i.e.* Eq. (3.41) to (3.43) (where A is obtained as A_{dyn} from Eq. (3.107)), albeit they are computed on staggered z_w levels here (instead of z_m as in Sec. 3.2.5.1). Thus, u, v and w from the output data are interpolated at the appropriate location before the computation of the variances. Subgrid scale variances are then horizontally and time averaged.

Resolved part of turbulent fluxes and variances averaged in time are obtained following the same approach as Andren *et al.* (1994), *i.e.*

$$\overline{\left\langle \overline{u_i' u_j'} \right\rangle} = \overline{\left\langle \left(\widetilde{u}_i - \left\langle \widetilde{u}_i \right\rangle\right) \left(\widetilde{u}_j - \left\langle \widetilde{u}_j \right\rangle\right) \right\rangle}, \tag{3.242}$$

$$\overline{\left\langle \overline{u_i' \theta'} \right\rangle} = \overline{\left\langle \left(\widetilde{u}_i - \left\langle \widetilde{u}_i \right\rangle\right) \left(\widetilde{\theta} - \left\langle \widetilde{\theta} \right\rangle\right) \right\rangle}, \tag{3.243}$$

where $\langle\widetilde{u_i}\rangle$ is the horizontally averaged instantaneous revolved velocity component $\widetilde{u_i}$, and $\left\langle\overline{u_i'u_j'}\right\rangle$ and $\overline{\left\langle\overline{u_i'u_j'}\right\rangle}$ are respectively the instantaneous and time averaged turbulent flux/variance profiles. They are computed at the same location as their subgrid counterpart, *i.e.* on z_w levels at the centre of the mesh, based on the same time interval. Thus, w and T can be used directly, while u and v are interpolated on staggered level z_w prior to compute resolved turbulent quantities based on Eq. (3.243).

Concerning the profiles of non-dimensional shear, as proposed in Stull (1988), the velocity shear is computed based on the modulus of the velocity. Thus, we first compute $\widetilde{U} = (\widetilde{u}^2 + \widetilde{v}^2)^{1/2}$, that is then horizontally and time averaged to get $\left\langle\overline{\widetilde{U}}\right\rangle$, and finally the vertical gradient of the latter quantity is computed, such as

$$\phi_M = \frac{\kappa z}{\langle\overline{u_*}\rangle}\frac{\partial}{\partial z}\left(\overline{\left\langle(\widetilde{u}^2+\widetilde{v}^2)^{1/2}\right\rangle}\right). \tag{3.244}$$

Some authors first compute each components of the shear and combined them afterwards (Andren *et al.*, 1994). Thus, horizontal velocity components are averaged in space and time, then their vertical gradients are computed, which are finally combined such as

$$\phi_M = \frac{\kappa z}{\langle\overline{u_*}\rangle}\left(\frac{\partial\overline{\langle\widetilde{u}\rangle}}{\partial z}^2 + \frac{\partial\overline{\langle\widetilde{v}\rangle}}{\partial z}^2\right)^{1/2}. \tag{3.245}$$

Both approaches lead to identical results in the region of interest, *i.e.* the lowest third of the ABL, since there are almost no changes in the wind direction in the surface layer. At the opposite, the results diverge in the upper part of the ABL (which is not of concern).

Finally, concerning the spectral analysis of the results, all the velocity spectra presented in this study are time averaged one dimensional longitudinal velocity spectra. They are computed, at each vertical levels of the domain and each Δt_{out}, from the spanwise averaged squared amplitude of the longitudinal (one-dimensional) Fourier transforms of the resolved perturbation of each velocity component. Spectra are then averaged in time such as $\overline{E_{u_i}(k_x)}$ is obtained at

each height. In addition, it is to note that an ensemble average is also done from each velocity spectra of the series of results for which only the initial random velocity perturbations differ.

3.6 Summary

In this chapter, the various aspects of the numerical method involved in the LES-capable version of MC2 were thoroughly presented. The chapter was subdivided in four sections, each presenting one of the main components of the approach, *i.e.* the dynamics, the physics, the initialization and the post-processing. In sections dedicated to the dynamics and the physics, the inclusion of the 3D turbulent modelling with regards to the main specificities of the model was clearly illustrated in addition to present the general numerical aspects of the method such as the SISL dynamic kernel, space and time discretizations, boundary conditions and the general structure of the model (and its main components). An important aspect was the description of the practical splitting of the various turbulence related terms which have large influences on the structure of the code as summarized in Fig. 3.2.

The compressible solver implies that volumetric and deviatoric parts of the Reynolds tensor are split (see Sec. 2.2.1), the former being included in the dynamic kernel while the latter processed as usual in the physics. Similarly due to the separation between the dynamics and the physics, and the 1D implementation of the physics, the horizontal and vertical terms of both turbulent diffusion and TKE equation must also be split. The horizontal components are explicit in time and computed in the dynamics (outside of the dynamic kernel). Then, they are sent to the physics to complete the turbulence modelling by including the vertical terms that are implicit in time. These two separations require special care so that each term is properly computed (based on the data at the proper time level) and recombined as illustrated in this chapter.

To avoid such a vertical-implicit/horizontal-explicit partitioning of turbulent diffusion terms required in this standard version of the 3D turbulence model (and all the complications that come with it), a standalone turbulence model (based on the same mathematical model but not relying on the physics library anymore) was also developed and implemented. The latter is

based on the same UKMO Smagorinsky SGS model (as implemented in the physics), but the 3D turbulent diffusion is fully explicit in time and not split depending on the direction.

The implementation of several features necessary to reproduce and compare full ABL theoretical cases based on LES was introduced in the present chapter, such as the large scale geostrophic forcing, the initialization and the post-processing. Concerning the initialization, after introducing the numerical method used to obtain thermodynamic variable initial fields, momentum initialization based on random velocity perturbations was discussed in the context of a compressible solver. Concerning the post-processing, its organization was discussed considering MC2 output data specificities, and numerical method used to obtain the various resolved and subgrid turbulent quantities were introduced.

Finally, compared to the early version of the LES-capable MC2, the volumetric/deviatoric splitting is an original contribution. Concerning the computation of the deviatoric terms, it is noteworthy that a new (more recent) version of the physics featuring, among other things, a refined vertical staggering, was integrate to MC2 during this study. It allowed to remove numerical imperfections related to the previous versions, but required the 3D turbulence modelling (both horizontal and vertical terms) to be reimplemented (since the discretization of the new version of the physics changed and it did not originally include 3D turbulence modelling features). In addition, the surface boundary was adapted to allow the imposition of a heat flux, SGS models existing in the original version of the model (*i.e.* the UKMO Smagorinsky, the hybrid TKE and the linear Kosović SGS models) were refined, and two new SGS models were added (*i.e.* the Deardorff and the Redelsperger SGS models). Finally, the large scale geostrophic forcing, the sounding-like initialization of momentum and thermodynamics variables, and the post-processing were also fully implemented during this study.

CHAPTER 4

RESULTS AND VALIDATION

The present chapter focuses on the presentation and discussion of the results obtained using the various configurations of the model introduced in Chap. 2 and Chap. 3. It thus serves to validate the approach as a whole, as well as all the new components and enhancements introduced during the present study. It is noteworthy that no thorough validation of the preliminary version of the LES-capable MC2 model (Pelletier *et al.*, 2005) had been undertaken previous to this study. However, considering the nature of MC2 and its primary endeavours, a comprehensive evaluation of both the SISL approach and the turbulent modelling is required in the context of LES of the full ABL. In that sense, the approach followed in this study is to rely on relevant reference cases well established in the literature.

In a first section, as a preliminary validation step, the generalized Ekman boundary layer analytical model developed by Berger and Grisogono (1998) is used to validate the new geostrophic forcing terms, and various numerical aspects of the vertical turbulent diffusion from the original and the new version of the physics library as well as from the standalone model. Then, Moeng and Sullivan (1994) and Sullivan *et al.* (1994) shear and buoyancy driven full ABL cases (*i.e.* from the earth surface to the free atmosphere fully considering the temperature) are used as a direct benchmark for the first evaluation of the LES-capable MC2, discussing and comparing, among other things, relevant turbulence statistics, flow structure and velocity spectra across the ABL. Both the column model and the LES model are evaluated in this section. In a third section, relying on the shear and convective cases previously reproduced but further evaluating the post-processing parameters, numerical parameters of the model are studied, *i.e.* horizontal grid, vertical grid, and time step. Finally, the new components and enhancements of the method are evaluated in the context of LES of the full ABL, *i.e.* the five SGS models, the original and new version of the physics library and the standalone model.

Note finally that in this chapter, unless specified, all profiles displayed and quantities discussed are generally time and horizontally averaged across the domain such as any Favre averaged variable ψ would be written $\overline{\left\langle \widetilde{\psi} \right\rangle}$. However in this chapter, in order to lighten notations, it was decided to always drop Favre averaging formalism (as in the previous chapter), thus $\overline{\left\langle \widetilde{\psi} \right\rangle}$ becomes $\overline{\langle \psi \rangle}$. Furthermore, time and space average formalism were also droped such as $\overline{\left\langle \widetilde{\psi} \right\rangle}$ is simply referred to as ψ. Finally, turbulent fluxes are written as $\overline{u'w'}$ instead of $\overline{\langle \overline{\rho u'w'}/\overline{\rho} \rangle}$. This greatly simplifies notation in figures and the text.

4.1 Ekman boundary layer

Berger and Grisogono (1998) developed an analytical model of a generalized ideal Ekman boundary layer for which horizontal pressure gradient (*e.g.* geostrophic wind, $\boldsymbol{v}_g$) as well as the mixing coefficient, K_M, are both a function of the height agl (as opposed to the simpler classical Ekman boundary layer for which $\boldsymbol{v}_g$ and K_M are constant with height). At first, Berger and Grisogono (1998) analytical model was elected in order to validate the new large scale geostrophic forcing in presence of periodic lateral boundary conditions as describe in Sec. 2.4. However, it proved to be helpful all along thid study. Indeed, it also served us to diagnose and solve a discretization problem within the existing model. Finally, it was also used to validate the vertical component of a standalone version of the turbulent diffusion (implemented directly within the dynamics of the model).

In this section, after a brief description of Berger and Grisogono (1998) analytical solution, the model setup used to reproduce that case is presented. Finally, results and enhancements of the various configuration of the model are discussed with regards to the analytical solution.

4.1.1 Case description and model setup

In the present study, both barotropic ($\boldsymbol{v}_g = \text{const.}$) and baroclinic ($\boldsymbol{v}_g$ evolve with height)[1] cases are reproduced. They are based the geostrophic wind $\boldsymbol{v}_g$ profiles provided by Berger

[1] Note that, an advection of temperature is also present in a real baroclinic atmosphere, however the effects of the vertically evolving $\boldsymbol{v}_g$ is only taken into account in the momentum equation by Berger and Grisogono (1998) non-dynamic model. The same hypothesis was thus used here.

and Grisogono (1998, Tab. 2) (*i.e.* $dp/dn|_1$, $dp/dn|_2$ and $dp/dn|_3$ with $dp/dn \equiv dp/dy$ in the present study). Their generic expression can be written

$$\boldsymbol{v}_g = (u_g, 0) \qquad \text{with} \qquad u_g = F + Ge^{-\gamma z}, \tag{4.1}$$

where $\gamma = \sqrt{f/2K_M}$, F and G are constants (see Berger and Grisogono (1998, Tab. 2)).

The eddy viscosity is set to a constant throughout the domain. Thus, the analytical velocity profile is given by Berger and Grisogono (1998, Eqs. (22) to (24)). It is similar to the standard Ekman solution and writes

$$u = u_g \left(1 - e^{-\gamma z} \cos \gamma z\right) \qquad \text{and} \qquad v = u_g \left(e^{-\gamma z} \sin \gamma z\right). \tag{4.2}$$

Note that $z = 1/\gamma$ corresponds to the height at which the velocity first reaches geostrophic wind direction (Holton, 2004)). Here, we have $K_M = 1.3$ m^2/s and thus $1/\gamma \sim 500$ m.

To reproduce this theoretical case with MC2, no changes were made within the dynamic kernel of the model, but its operating mode was adapted. In fact, Berger and Grisogono (1998) solution comes in the form of a profile not invoking neither the internal energy nor the vertical velocity. Thus, while in the present model internal energy and vertical velocity conservation equations are still solved, a proper initialization with appropriate boundary conditions was developed not to invoke them. For that purpose, the atmosphere was initialized in a hydrostatic isothermal equilibrium minimizing generalized pressure and buoyancy perturbation ($P = 0$ and $b = 0$, see Eqs. (2.30) and (2.29)), while keeping the atmosphere in a stable static stability state to inhibit vertical motion. The default bottom and top boundary conditions of the model were used and lateral boundary conditions were periodical. However, as discussed in Sec. 2.4 and Sec. 3.2.4, the large scale pressure gradient, *i.e.* u_g profile, was imposed through the use of the new geostrophic forcing terms, Eq. (2.184), in order for the horizontal pressure field to be periodical. Both terms in momentum and internal energy equations (allowing temperature advection for baroclinic cases) were implemented but only the ones in momentum equations were activated to properly reproduce Berger and Grisogono (1998) cases.

Concerning the turbulent modelling, the rightmost branch of Fig. 3.2 is followed, *i.e.* the simplified turbulent model of the physical library: the mixing coefficients are set constant ($K_M = 1.3$ m^2/s and $K_T = 0$ m^2/s) and the surface boundary condition of momentum turbulent diffusion is adapted. As discussed in Sec. 2.3, the turbulent diffusion surface boundary condition of MC2 is based on the continuity of the fluxes across a given height in the surface layer (Cauchy boundary condition) which writes for any variable ψ

$$K_\psi \left.\frac{\partial \psi}{\partial z}\right|_{z=0} = \beta_\psi \psi_1 + \alpha_\psi, \tag{4.3}$$

where β_ψ and α_ψ are the homogeneous and the inhomogeneous boundary condition terms, and ψ_1 is the value of ψ at the first level above the surface (see Sec. 2.3 for further details). It is noteworthy that stress is computed at $z = 0$ m agl, while it is the speed at the first grid point level that is multiplied by β_ψ when solving turbulent diffusion.

Reverting this expression and computing the velocity vertical derivative based on the analytical solutions, Eq. (4.2), surface flux value can be imposed through either α_ψ or β_ψ, such as

$$\begin{cases} \alpha_u = K_M \left.\dfrac{\partial u}{\partial z}\right|_{z=0} ;\ \beta_u = 0, \\ \alpha_v = K_M \left.\dfrac{\partial v}{\partial z}\right|_{z=0} ;\ \beta_v = 0, \end{cases} \quad \text{or} \quad \begin{cases} \alpha_u = 0\,;\ \beta_u = \dfrac{K_M}{u_1} \left.\dfrac{\partial u}{\partial z}\right|_{z=0}, \\ \alpha_v = 0\,;\ \beta_v = \dfrac{K_M}{v_1} \left.\dfrac{\partial v}{\partial z}\right|_{z=0}. \end{cases}$$

Note that using non-zero β_ψ implies that surface stress is proportional to velocity (at the first model level) which allows to damp inertial oscillation faster in comparison with the use of a constant surface stress when using α_ψ alone. Thus, even if both ways lead to the same final result, the one based on non-zero β_ψ may converge faster to a steady solution.

Finally, because the solution is horizontally homogeneous, numerical results should not be influenced by neither horizontal resolution nor domain size (in the limit of an acceptable Courant–Friedrichs–Lewy (CFL) number). Indeed, the same results were obtained by using several horizontal grid configurations (not shown here). The smallest possible horizontal grid, *i.e.* a 3 by 3 grid with $\Delta x = 0.5$ km, was elected along a time step of 40 s (giving $\mathrm{CFL} = 0.69$).

In the vertical direction, a more classical definition of the grid (with respect to mesoscale models) is first used, Sec. 4.1.2. It features a total of 45 grid points in the vertical direction, 23 being in the first 1.5 km, and a top level at 15 km. The first momentum level is located at 10 m with a vertical resolution of 20 m close to the surface. Subsequently in Sec. 4.1.3, various stretched and homogeneous vertical grids with a top level going from 2 to 15 km are used to evaluate the sensitivity of the various configuration of the model to the vertical mesh.

4.1.2 Model results

Fig. 4.1 summarizes the results obtained for the Ekman theoretical cases with three profiles of geostrophic wind forcing. It is interesting to note that analytical profiles and numerical results of velocity magnitude and direction superpose.

The departure of the velocity from the geostrophic wind can be appreciated comparing Fig. 4.1 a) and c). Concerning the inertial oscillation, Fig. 4.1 b), note that the computations are initialized with the exact analytical solution explaining the low amplitude oscillation and the value of $C_u = 1$ at $t = 0$ s. Ten inertial oscillations are required to damp the oscillation by 95 %. Starting from the geostrophic wind or any velocity profile leads to the same final steady state solution but requires a longer time to converge (not shown here).

The value of C_u to which the model converge is however slightly higher than the theoretical value of unity. This tiny (0.37 %) difference might be caused by the discrete nature of the numerical results that is leading to numerical discrepancy during the computation and the post-processing. The latter difference is reduced by refining the vertical mesh (not shown here). Those results are thus very satisfactory and they confirm that:

- the new geostrophic forcing terms properly perform when used in conjunction with periodical boundary conditions;
- the chosen approach for the initialization of thermodynamical ABL state allows not to excite neither internal energy nor vertical velocity;
- surface boundary conditions is properly implemented.

To sharply evaluate the various configurations of the model, Fig. 4.2 presents the difference between analytical and numerical results for the two baroclinic cases $dp/dy|_2$ and $dp/dy|_3$. Note that, $dp/dy|_1$ case (classical Ekman ABL) exhibits an error shape which is very similar to the one of $dp/dy|_3$. On each of the four graphics from Fig. 4.2 are presented four curves showing results obtained based on the various configurations of the model. Results labels have the following meaning:

Original: model based on the original version of the physics library (staggering between the vertical discretization of the physics and the dynamics). A vertical interpolation (extrapolation at the lowest level) of the velocity components is needed at the interface of the two components of the model (see Sec. 3.3.1.2.1 for more details).

Original+: model based on the original version of the physics library (as for the Original configuration) but for which solely the extrapolation of the first momentum level at the interface between physics and dynamics is refined, *i.e.* the latter is now perfectly linear (*c.f.* Eqs. (3.135) and (3.136)).

New: model based on the new version of the physics library. Momentum levels are collocated in every parts of the model and no more vertical interpolation is needed (see Sec. 3.3.1.2.2).

Standalone (SA): model based on the standalone turbulent diffusion implemented directly within the dynamics (the physics library is not anymore used, see Sec. 3.2.5.2.1).

The exact same grid as before is used here. Finally given the small amplitude of the differences, and to avoid the effects of the inertial oscillation, a time average of $5\,T_{inert}$ (from $7\,T_{inert}$ to $12\,T_{inert}$ with $T_{inert} = 2\pi/f = 60928$ s) was used to compute the differences between numerical and analytical results. showing the inertial oscillation

The first thing to note in Fig. 4.2 is that while the general averaged trend of the difference between the theory and numerical results is roughly equivalent below 0.3 km agl, notably for the direction, the numerical results are very sensitive to the vertical discretization of the physics library. A strong numerical mode (zigzag), increasing as the surface is approached, is exhibited

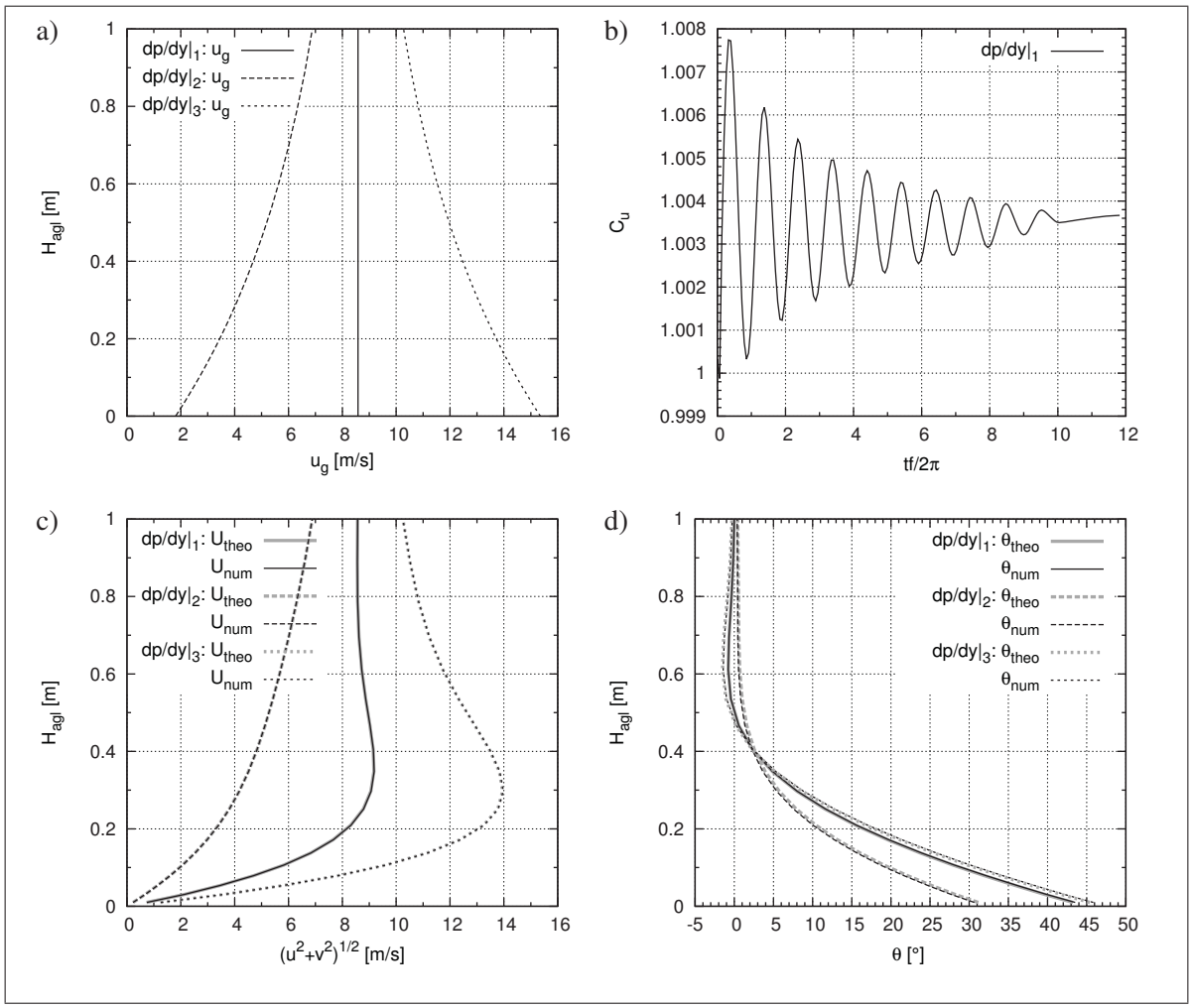

Figure 4.1 Berger and Grisogono (1998) theoretical case: a) geostrophic wind profile; b) integrated velocity coefficient; and analytical (theo) and modelled (num) profiles of: c) horizontal wind velocity modulus; d) wind direction

in the results based on the Original model for velocity direction and magnitude for both cases. This translates into an error of a few percents close to the surface. Note that the discrepancies caused by this mode in momentum fluxes are higher (not shown here). This zigzag is notably affected by the surface wind extrapolation required at the interface between physics library and dynamics as seen on the curve labelled Original+, which show a reduced zigzag.

In fact, in order to totally remove this numerical mode, the harmonization of the vertical discretization of the various parts of the method is required as seen on the results from the New

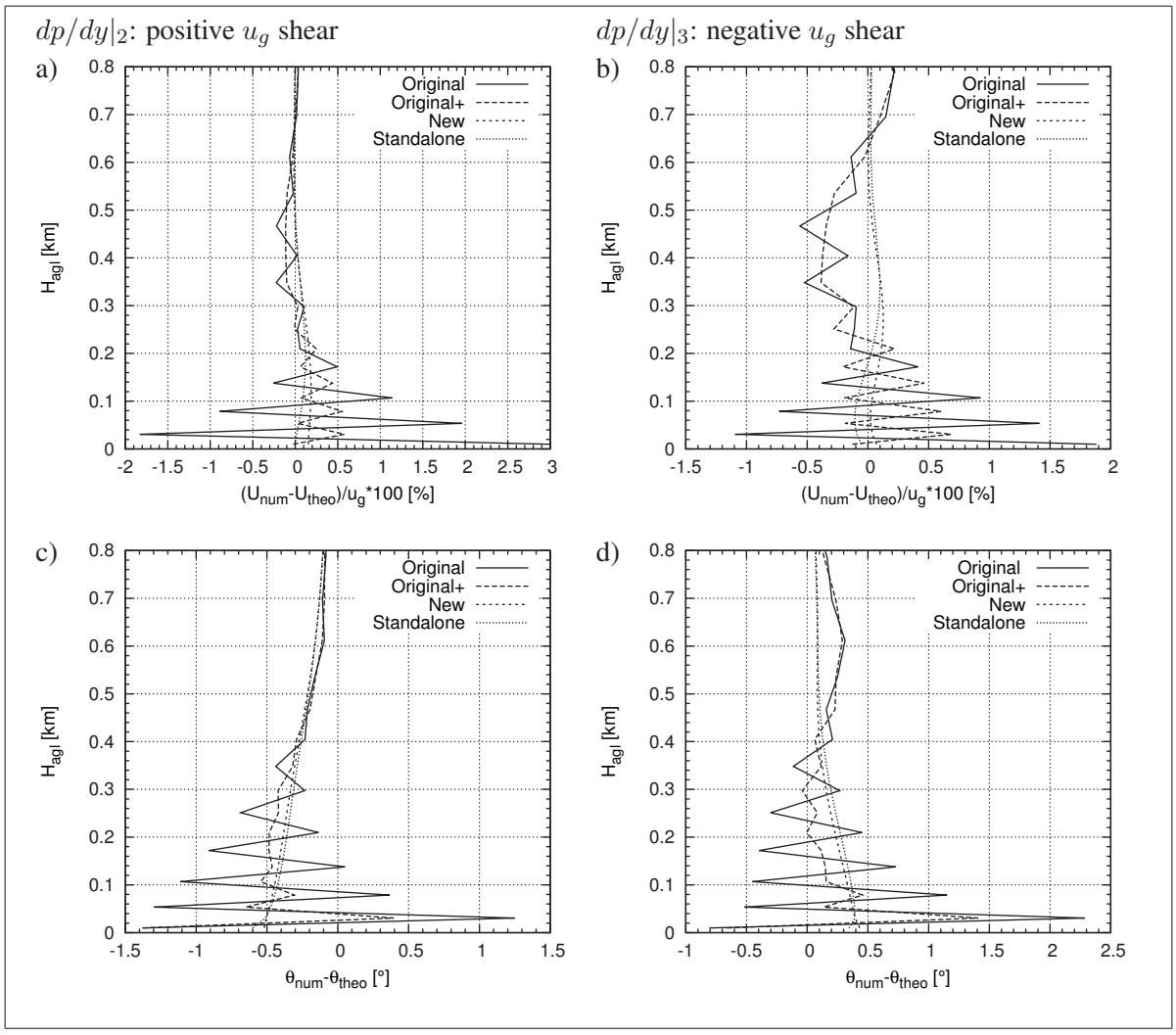

Figure 4.2 Velocity modulus and direction differences between modelled (num) and analytical (theo) solution: a) and c) $dp/dy|_2$; b) and d) $dp/dy|_3$

model, Fig. 4.2. Indeed, velocity magnitude error for the New results are no larger than 0.15 % of u_g, which clearly demonstrates the necessity to avoid interpolations (and extrapolations at the lowest level) of momentum when going back and forth (from/to the dynamics to/from the physics library). These results are really promising since discrepancies caused by this numerical imperfection are totally removed in the New version of the model.

The other important point regards the results of the Standalone model. Indeed, while the vertical turbulent diffusion and its boundary conditions are totally new in that version of the model

(fully explicit in time and implemented directly within the dynamics in height coordinates), results are very similar to the ones obtained using the properly discretized version of the physics library, *i.e.* results labelled New. Velocity magnitude error from the Standalone and New models almost superposes at all heights, and the main difference lies in the slight shift close to the surface. This discrepancy is likely to be caused by the vertical coordinate transformation still needed at the interface between the dynamics and the physics library in the New model (*i.e.* going from height coordinate to sigma coordinate, see Chap. 3).

4.1.3 Vertical mesh impact

To further illustrate the impact of the vertical mesh on the two main versions of the full model, *i.e.* the Original and the New, Fig. 4.3 shows results obtained for the negative u_g shear case ($dp/dy|_3$) based on the three different vertical meshes allowing to appreciate the impact of the stretching as well as the resolution notably close to the surface. They are labelled as follow:

Stretched: mesh identical to the one previously used.

Uniform 20 m: grid with an uniform resolution across the domain. It has a top level at 2 km and 96 meshes in the vertical. As a result, close to the surface, levels height and resolution are similar to the stretched grid.

Uniform 40 m: same grid as Uniform 20 m mesh but with a top level at 2 km and with 48 meshes in the vertical. As a result, the vertical resolution is twice as coarse in the near-surface region and equivalent to the stretched grid in the middle of the Ekman layer.

Uniform SA: mesh identical to Uniform 20 m grid but based on the Standalone model.

Concerning the results based on the Original model (*i.e.* original version of the physics), Fig. 4.3 a) and c), the numerical mode is reduced when the resolution is increased close to the surface for both velocity modulus and direction. Velocity modulus error close to the surface is roughly divided by two when going from the 40 m to the 20 m resolution uniform grids. However, the zigzag tends to propagate up to the top of the boundary layer (*i.e.* ~ 500 m), regardless of the grid. Both Uniform 20 m and Stretched grid results perfectly superpose close to the surface for both velocity modulus and angular deviation indicating that the zigzag is

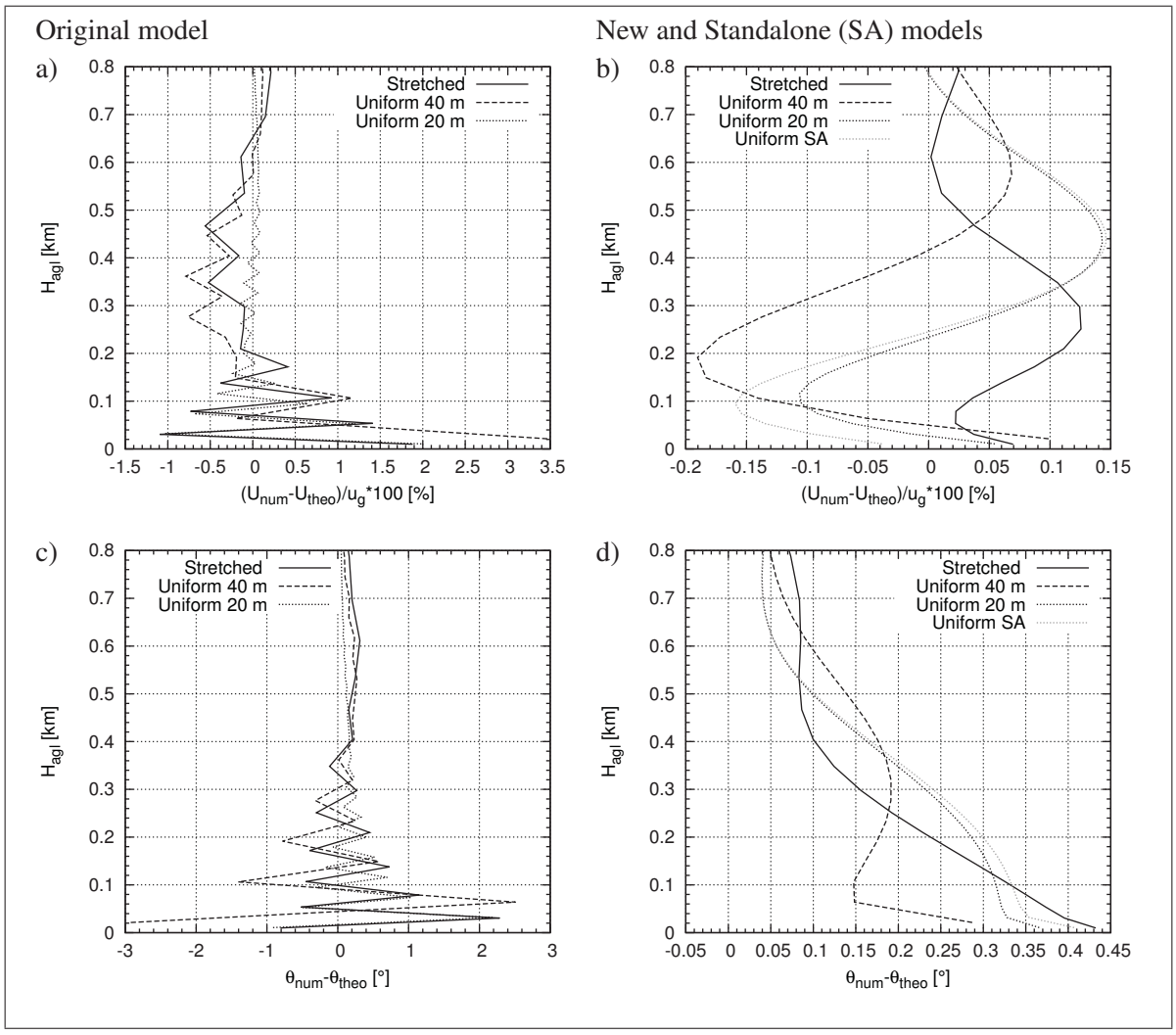

Figure 4.3 Velocity modulus and direction differences between modelled (num) and analytical (theo) solution for $dp/dy|_3$: a) and c) Original model; b) and d) New and Standalone models

strongly a function of the first mesh height. In the upper part of the boundary layer, the Uniform 20 m grid error oscillates between ± 0.15 % of u_g while the Stretched and the Uniform 40 m grid results are similar with a maximum departure from the analytical velocity modulus of around -0.5 % at 400 m agl. By noting that the resolution of the Stretched grid becomes coarser than 40 m above 300 m agl, one can conclude that the error at this height and above is more likely to be the consequence of the resolution and not the stretching of the grid.

Fig. 4.3 b) and d), present results for identical grids but relying on the properly staggered physics, *i.e.* the New model (and results from the Standalone model using the Uniform 20 m grid). It confirms that with these versions of the model, the numerical mode is totally avoided regardless of the grid, and that differences with analytical solution are notably reduced close to the surface. The latter is at least one order of magnitude smaller than with the Original model as seen in Fig. 4.3 a) and c). In addition, and independently of the zigzag, the velocity modulus error is always reduced and appears to be less a function of the mesh with the New model in comparison of the Original model. Interestingly in Fig. 4.3 b) and d), both Uniform grids show a similar velocity modulus error shape with an amplitude of roughly 0.25 % of u_g within the boundary layer. Surface error is however two times higher for the Uniform 40 m grid which shape is shifted by -0.1 % and slightly smoothed. Finally, the Stretched grid velocity modulus error is similar to the Uniform 20 m grid results very close to the surface but the shape of the error above notably differs with an amplitude of only 0.12 % of u_g.

Concerning the velocity direction error Fig. 4.2 c) and d), further than the improvement due to the proper discretization of the turbulent diffusion, conclusions are less easily drawn. Indeed, the general trend (not considering the zigzag) of this error is very similar for all the models. In Fig. 4.3 d), the impact of the grid configuration is not clear, since, besides an notable reduction of the near-surface error for the coarse grid (the opposite would have been expected), no significant differences are noted between results.

Finally, concerning the Standalone model, Fig. 4.2 confirms the remarks made in the previous section. Its results are very close to the New model results regardless of the geostrophic wind profile and the vertical grid. In fact, the Standalone model velocity modulus error appears to tend to zero close to the surface while there is a little offset for the New model results. This is true, independently of the geostrophic wind profile (see Fig. 4.2 a) and b)) and of the grid (see Fig. 4.3 b)). Others geostrophic wind profiles and grids were tested with the same conclusion.

4.1.4 Conclusion

To conclude this section, while the Berger and Grisogono (1998) cases were relatively simple, they have been very helpful to appreciate and enhance several aspects of the model. Promising results have been obtained. As a summary, it was shown that:

- momentum components of the large scale geostrophic forcing properly perform in presence of periodical lateral boundary condition for both barotropic and baroclinic cases;
- all model configurations tested were able to reproduce satisfactorily the barotropic and baroclinic Ekman boundary layer with a maximum normalize absolute error lower than 3 % of u_g for the Original model (original physics library) and lower than 0.2 % of u_g for the enhanced version of the model (New and Standalone);
- near-surface results are sensitive to the vertical extrapolation of momentum required at the interface between the physics and the dynamics in the Original model. It generates a numerical mode which is removed by using a contiguous discretization in the various parts of the code as seen in the results from the New and Standalone models;
- error from Standalone and New model models is very little affected by neither the vertical resolution nor its vertical stretching of the mesh;

4.2 LES of the full ABL: Moeng and Sullivan (1994) benchmark

In the context of developing and finely validating a LES-capable mesoscale model, well documented and representative microscale flow regimes have to be considered. In the present case, this represents a two fold challenge, since, in addition to the various new features implemented (*i.e.* new SGS models, new discretization in the physics library, new initialization and adapted surface and lateral boundary conditions), the dynamic kernel of the MC2 which is compressible has almost never been used at such fine scales. As a result, it is required to evaluate the dynamical behaviour of the LES-capable MC2 at very fine scales, as well as to validate the implementation of SGS models along with the various new features that allow LES with MC2.

While the best way to achieve such a validation would have been to compare with experimental data, it was decided to focus on more theoretical numerical experiments which are based on reference LES models that were, at first, intercompared with other models and evaluated against experimental data. This approach, which is common in LES, was essentially motivated by the richness of numerical results in the literature, their high level of detail (in comparison to experimental data) and the more simple model setup required to reproduce a theoretical full ABL. Hence, the shear and buoyancy driven full dry ABL cases presented by Moeng and Sullivan (1994) and Sullivan *et al.* (1994) were elected as a basis of reference.

As a summary, Moeng and Sullivan (1994) and Sullivan *et al.* (1994) studied a range of full ABL, *i.e.* from the surface to the free atmosphere, over an homogeneous surface going from a shear only driven case (referred to as shear case), to a strongly buoyancy driven case (referred to as convective case hereafter), based on a LES model presented in Sec. 1.3.2.2.1.2 and 1.3.2.3.2. Those cases are simple, yet feature a relatively complete representation of the ABL since they all incorporate the full ABL covered by a temperature inversion, and density is a function of height. A full featured ABL is thus involved, albeit the latter is dry. This is clearly more challenging than using a model only based on momentum equations, and results better reflect how the model would behave for real cases where the full complexity of the ABL need to be invoked. The study of Ding *et al.* (2001a) and Churchfield *et al.* (2010) are also based on the exact same cases and while the general approach are similar, different LES models are used.

Moeng and Sullivan (1994) and Sullivan *et al.* (1994) studies were elected because in addition to the range of ABL evaluated, the numerical protocol is well described and many flow features are studied in addition to the classical turbulent quantities. Furthermore, flow structure is shown at various heights of interest in the ABL for the various cases. Last but not least, the method and SGS model used in Moeng and Sullivan studies have been thoroughly evaluated as discussed in the literature review (Nieuwstadt *et al.*, 1992; Andren *et al.*, 1994; Mason, 1994; Sullivan *et al.*, 1994; Porté-Agel *et al.*, 2000; Pope, 2000; Ding *et al.*, 2001a; Chow *et al.*, 2005; Churchfield *et al.*, 2010) which increases the confidence level of the results they obtained and will allow to further evaluate ours results.

In this section, a first evaluation of the LES-capable MC2 approach is done based on the shear and convective cases of Moeng and Sullivan (1994) and Sullivan *et al.* (1994). Thus, in a first part, flow set-up and computational procedure are presented underlining the challenges of those microscale cases with regards to the present method. Then, after discussing the time evolution of key variables obtained with the present model, a direct and thorough comparisons with Moeng and Sullivan (1994) and Sullivan *et al.* (1994) is made. Finally, the flow structure, the near-surface results and the spectral analysis of the solution are studied in order to thoroughly evaluate various aspects of the model abilities. It is to underline that in general results from the most well known and simple SGS model are presented in this section, *i.e.* the UKMO Smagorinsky SGS model presented in Sec. 2.2.3.1 (also referred to the Smagorinsky SGS model hereafter). All cases were also reproduced based on the hybrid TKE SGS model described in Sec. 2.2.3.3 (for debugging purposes). However, as presented in Sec. 4.4.1, both results are very similar, if not identical. As a result and for clarity reasons, only the UKMO Smagorinsky SGS model results are most of the time shown on the figures (except when the subgrid TKE is needed), while result parameters are shown in all the tables of this section. The standard ABL column model implemented in MC2 is also used as a reference.

Finally and before going any further, it is noteworthy that the exact same numerical parameters (grid configuration/boundary conditions/initialization/...) and post-processing (time interval/sampling method/...) as in Moeng and Sullivan (1994) are used in the present section. In what follows, this later study is also referred to as MS94. The next section focuses on the study of the latter parameters. However, it can be already said here that Moeng and Sullivan numerical parameters are found to be perfectly appropriate while the post-processing parameters would require refinements due to some scatter problems further discussed in Sec. 4.3.1. As a result, and to clearly illustrate the latter fact in the present section, all results shown here are based on the ensemble average of five realizations of the exact same model configuration but for which only the initial random velocity perturbations are changed. The scatter or envelope between the various results of the series is also displayed in the form of error bars on all the figures of this section.

4.2.1 Flow set-up: initialization and boundary conditions

As a general rule for this first evaluation of the model, the procedure presented by Moeng and Sullivan (1994) is closely followed with few exceptions. The reader is referred to Tab. 4.1 that summarizes the numerical parameters of each case reproduced here: S_S (resp. S_M) refers to shear case S results based on the Smagorinsky (resp. the hybrid TKE) SGS model, while S_{1d} refers to the same case based on the column model (and similarly for the convective case B).

Table 4.1 Numerical parameters of Moeng and Sullivan (1994) shear and convective cases (S and B respectively) presented in Sec. 4.2

Name	Model	L_{x_i} [km]	L_z [km]	$N_x \times N_y \times N_z$	u_g [m/s]	$\overline{w'\theta'}_s$ [K m/s]	Δt [s]	Realizations
S_{1d}	$k-l$ column	0.3	1	$3 \times 3 \times 96$	15	0.0	2	1
S_S	Smagorinsky SGS	3	1	$96 \times 96 \times 96$	15	0.0	1.5	5
S_M	TKE hybrid SGS	3	1	$96 \times 96 \times 96$	15	0.0	1.5	5
B_{1d}	$k-l$ column	0.3	2	$3 \times 3 \times 96$	10	0.24	4	1
B_S	Smagorinsky SGS	5	2	$96 \times 96 \times 96$	10	0.24	4	5
B_M	TKE hybrid SGS	5	2	$96 \times 96 \times 96$	10	0.24	4	5

To sum-up the procedure, a constant geostrophic wind $\boldsymbol{v}_g = (u_g, 0)$ is imposed through appropriate source terms added to momentum equation as described in Sec. 2.4 and Sec. 3.2.4, and already validated in Sec. 4.1. Lateral boundary condition are periodical for all the main variables of the model. A sensible heat flux $\overline{w'\theta'}_s$ is imposed at the surface together with an homogeneous surface roughness length[2] of $z_0 = 0.16$ m. The turbulent diffusion surface boundary conditions are applied locally through MO similarity theory as described in Sec. 2.3 and Sec. 3.3.7 (Mailhot and Benoit, 1982; Delage and Girard, 1992), and Moeng's approach (but only with local quantities) is followed to compute surface stresses (Stoll and Porté-Agel, 2006). The surface temperature, T_s, is then diagnosed from L_{MO}, $\overline{w'\theta'}_s$ and u_* at every time step (see Sec. 3.3.7). The top boundary of the physics is kept unchanged with regards to the

[2] No value of the roughness length is given in Moeng and Sullivan (1994). It can be obtained by using velocity and friction velocity from Moeng and Sullivan (1994, Tab. 2). However, on that table, the non-dimensional velocity u/u_* is displayed for S and SB (as opposed to what stated in the legend), while velocity u is shown for B. This is confirmed by Sullivan *et al.* (1994, Fig. 3) who reproduced the same cases with the same model. The roughness length is thus $z_0 = 0.16$ m and velocity at the first level for S is $u = 4.35$ m/s.

original mesoscale model (Mailhot and Benoit, 1982). In the dynamics, the same surface and top boundaries as in the mesoscale configuration are also used (see Sec. 3.2.3), and a ten layer sponge, *i.e.* roughly ~ 100 m effective thickness, is applied at the top of the computational domain to prevent waves from being reflected downward. This sponge is based on the smoothing approach proposed by Shuman (1957).

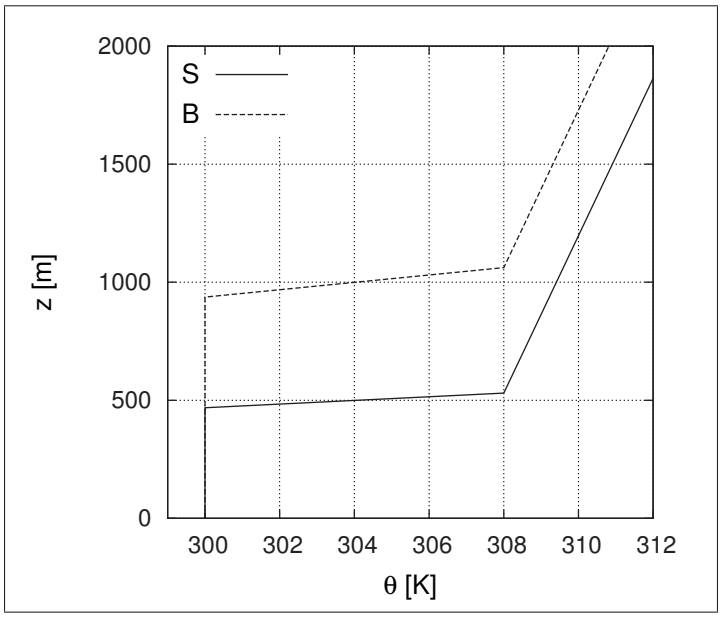

Figure 4.4 Initial potential temperature profile of Moeng and Sullivan (1994) shear and convective cases

Concerning the initialization of the thermodynamical atmospheric state, a profile of potential temperature was used as described in Sec. 2.5 and Sec. 3.4.1 to compute the buoyancy b and the generalized pressure P. The exact same profile of θ as Moeng and Sullivan (1994) was used here. As illustrated in Fig. 4.4, it features a neutral region, $\theta = 300$ K, going from the surface to z_i. This adiabatic layer is covered by a temperature inversion of $\Delta T = 8$ K in $6\,\Delta z$ ($6\Delta z = 62.5$ m for shear and moderate buoyant cases and $6\,\Delta z = 125$ m for highly buoyant case). This leads to a lapse rate at the inversion of 0.128 K/m and 0.064 K/m for the shear and the convective case respectively. Finally, the remaining above atmosphere is set to a potential temperature lapse rate of 0.003 K/m.

Finally, following Moeng and Sullivan (1994) and Andren *et al.* (1994) philosophy, momentum is initialized equal to the geostrophic wind to which a random perturbation vector, $\boldsymbol{\varpi} = (\varpi_u, \varpi_v, \varpi_w)$, scaled with the TKE is added as described in Sec. 3.4.2. Furthermore, following Moeng and Sullivan (1994), a positive surface sensible heat flux is imposed during a spin-up period for all the cases reproduced. This flux is constant during the whole convective run (*i.e.* $\overline{w'\theta'}_s = 0.24$ K m/s), while it is set to 0.05 K m/s during the first 3000 s and then turn off for the shear cases. Heating the surface during the initialization period triggers convective instabilities which on the one hand, allows organized perturbations to efficiently propagate across the ABL, and on the other hand, evacuate the spurious temperature perturbations related to the slightly mass divergent random velocity perturbation added to the initial field. Note finally that the same procedure is used for the 1D computation, *i.e.* with the heating surface but without the initials random velocity perturbations, to consistently compare time evolution with LES.

4.2.2 Time evolution

Moeng and Sullivan (1994) and Sullivan *et al.* (1994) considered the flow as being in a statistically quasi-steady state after a six large eddy turnover time, *i.e.* $\tau_* = z_i/u_*$ or $\tau_* = z_i/w_*$, for all their cases (S, B and SB). In such a situation, dimensional first order moments, *i.e.* velocity components (and temperature for convective cases), are constantly evolving, while higher order as well as non-dimensional first order moments should be almost constant. Their post-processing was based on a time interval of $5\,\tau_*$ stating at $12\,\tau_*$.

In the context of the shear case S, horizontal velocity components are expected to follow an inertial oscillation as presented in Sec. 4.1 (with the same frequency but a different signature). However, compared to Andren *et al.* (1994), the inertial oscillation of Moeng and Sullivan (1994) cases should feature a smaller amplitude due to the presence of the temperature inversion that acts as a damper (Moeng and Sullivan, 1994). In the context of the convective case B, a constant heat flux is imposed at the surface. As a result, energy is permanently brought in the ABL (and in the whole computational domain) causing both the temperature in the whole ABL

and its height to rise constantly. Thus, while horizontal velocity components are also expected to oscillate, the dominant effect should be the increase in temperature.

In order to better appreciate the time evolution of the flow for the shear and the convective cases, Figs. 4.5 and 4.6 shows the evolution of the velocity integral coefficients, C_u and C_v, the drag coefficient C_g, and the total TKE coefficient, C_{TKE} for half an inertial period, $T_{inert} = 2\pi/f$ (which is equivalent to 30464 s when strictly at 45 deg. North, *i.e.* $f = 0.0001031$ s^{-1})[3]. These quantities are commonly used as a reference (Nieuwstadt *et al.*, 1992; Andren *et al.*, 1994; Mason, 1994) to diagnose the time evolution of ABL flows, and they write

$$C_u = -\frac{f}{\overline{u'w'}_s}\int_0^{z_{top}} (v - v_g)\, dz, \tag{4.4a}$$

$$C_v = +\frac{f}{\overline{v'w'}_s}\int_0^{z_{top}} (u - u_g)\, dz, \tag{4.4b}$$

$$C_{TKE} = \frac{f}{{u_*}^3}\int_0^{z_{top}} k_{tot}\, dz, \tag{4.4c}$$

$$C_g = \frac{u_*}{\|\boldsymbol{v}_g\|}. \tag{4.4d}$$

where the various quantities are horizontally averaged before computing the integrals.

Curves in Figs. 4.5 and 4.6 were obtained from the ensemble average of several computations for which only initial random velocity perturbations were changed: one computation for the pure 1D cases (S_{1d} and B_{1d}), and five for the large grid LES cases (S_M and B_M)[4]. Furthermore, in order to better appreciate the scatter of the various solutions, the envelope of all the realizations of each case is presented as a background grey shaded area. Note that changing the initialization parameters, such as slightly increasing/reducing the random velocity perturbations (or not heating the surface during the spin-up period of S) case had no impact on the spread of the LES results (not shown here).

[3] The initialization spin-up period is not included in Fig. 4.5 explaining why the graphs do not start at zero.

[4] Only the hybrid TKE SGS model S_M results are shown in Figs. 4.5 and 4.6 since the total TKE, k_{tot}, is required to fully compute C_{TKE}. However, results from the UKMO Smagorinsky SGS model are very similar, albeit only the resolved C_{TKE} can be obtained instead of C_{TKE} based on the total TKE.

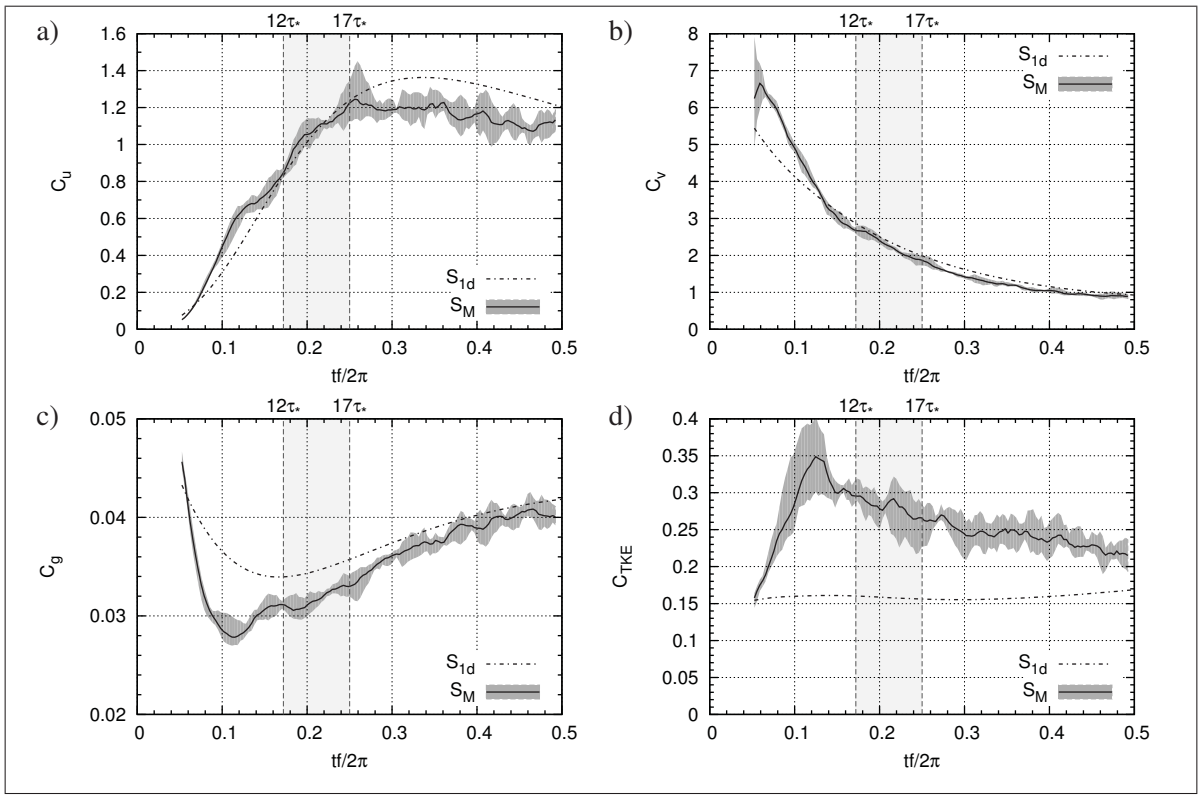

Figure 4.5 Time evolution of integral coefficients, Eq. (4.4), from the shear case: a) and b) velocity integral coefficients; c) geostrophic drag coefficient; d) TKE integral coefficient. Dark grey overlaid regions show the scatter of the results. Light grey overlaid background areas show the post-processing time intervals

While a higher number of computations would have been needed to statistically quantify the spread of the results, taking the averaged result of the five runs allowed to filter most of the higher frequency oscillations related to unsteady turbulent phenomena. On the one hand, it permitted to compare the average behaviour of the LES model with the column model. And, on the other hand, it further allowed to better appreciate the oscillations that are caused by unsteady turbulent phenomena. Finally, as confirmed in the following sections, such an approach was required to properly compare ours results with Moeng and Sullivan (1994) and to study the impact of various numerical parameters.

In Figs. 4.5 and 4.6, all results are surprisingly close considering the differences in the column model and LES approaches, and it can be said that models are in good agreement for both

the shear and the convective cases. For the two cases, both velocity components, shown in Figs. 4.5 and 4.6 a) and b), are evolving rapidly before C_u reaches a maximum value at roughly $0.3 - 0.4\,T_{inert}$. Then, the evolution of C_u and C_v slows down and tends to converge to an equilibrium value (more details in a Sec. 4.3.1). The time evolution is more significant for C_v which makes its prediction more challenging.

The evolution is also very rapid for C_g and C_{TKE} before $0.15\,T_{inert}$ as seen in Figs. 4.5 and 4.6 c) and d). C_g (and thus u_*) first drop to a minimum value and then increase regularly. At the opposite, C_{TKE} quickly reaches a maximum, and then decreases slowly for the shear case, while it oscillates around a plateau for the convective case. Minimum of C_g and maximum of C_{TKE} coincide in time, which corresponds to the on-set of the organized turbulent regime as described in the literature (Mason and Thomson, 1987; Andren *et al.*, 1994; Mason, 1994). The latter is located at roughly $1.1\,T_{inert}$ for S and $0.2\,T_{inert}$ for B, which is slightly after six large eddy turnover time τ_* suggested by Moeng and Sullivan (1994). Those remarks hold for both the shear and the convective cases, with extrema taking place later for the convective case due to the different nature of the flow.

While they are in agreement, some differences between the 1D and the LES model are to underline. C_u and C_v are generally very close for both models in both cases. C_u is however somewhat underestimate (overestimated) by the LES model after $0.25\,T_{inert}$ for the shear (convective) case but both models tend to converge to the same value after $0.5\,T_{inert}$ (more details in a Sec. 4.3.1). At the opposite, C_g for the shear case, and C_{TKE} for both cases, exhibit more noticeable differences between 3D and 1D results.

Concerning C_g, and thus the friction velocity, Figs. 4.5 c) and 4.6 c), it is generally lower for LES results with a notably lower and earlier minimum value for the shear case. In fact, since no special treatment is done close to the surface for SGS model to properly perform (notably in neutral conditions), u_* is underestimated by the LES model (Andren *et al.*, 1994; Sullivan *et al.*, 1994; Porté-Agel *et al.*, 2000). At the opposite, the 1D model is shown to correctly reproduce similarity profiles (Stull, 1988). Thus, the underestimation of u_* by LES model after

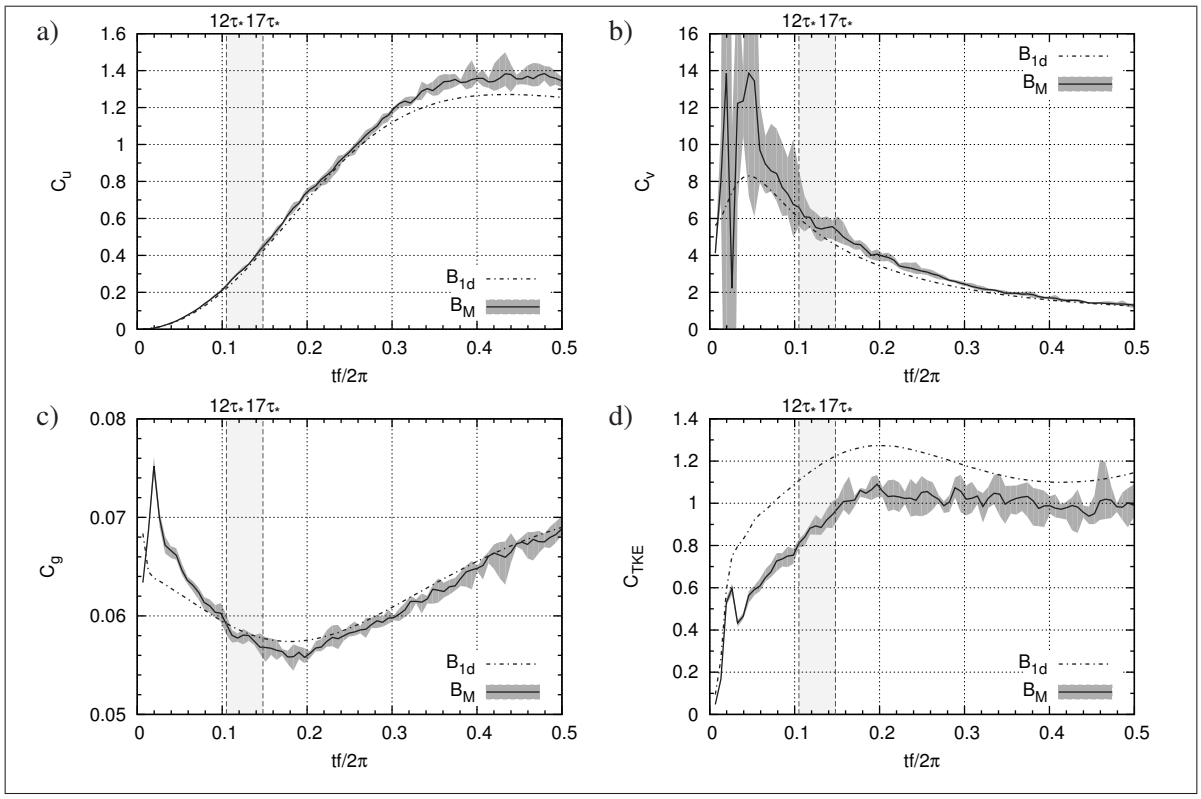

Figure 4.6 Same as Fig. 4.5 but from the convective case

$0.25\,T_{inert}$ in Fig. 4.5 c), and to a lesser extent in Fig. 4.6 c), is related to the above mentioned facts. Differences between column and LES results are lower in convective conditions since LES model suffers less from this shortcoming as shown by Sullivan *et al.* (1994, Fig. 2 and 3).

Concerning C_{TKE} of the shear case, Fig. 4.5 d), the total TKE level is notably lower and no stringent maximum is present in the 1D results. This peak and time evolution of S_M (and S_S - not shown here) is typical of a LES results based on a dissipative only SGS model (Mason, 1994). In fact, it is noteworthy that C_{TKE} is based on the sum of the resolved and subgrid part of the TKE. In the column model, the whole TKE is modelled while only a marginal part of the total TKE is modelled in the LES model (roughly 5 % for S and B cases when the turbulent regime is well established). The 1D model thus leads to a less realistic estimation of the TKE notably in the mixed layer and the upper ABL when considering its parametrization level (one-and-a-half order). In addition, the integrated TKE is normalized by u_*^3 to get C_{TKE}. The lower

u_* of the LES model thus leads to a higher C_{TKE}. In fact, the dimensional integrated TKE of both models converge to similar values as computation evolves (not shown here). By defining a new TKE integral coefficient that takes into account the real ABL height z_i such as

$$C'_{TKE} = \frac{1}{z_i u_*^2} \int_0^{z_{top}} k_{tot} dz = \frac{u_*}{z_i f} C_{TKE}, \tag{4.5}$$

a value on par with Andren *et al.* (1994, Fig. 2) is obtained for the shear case.

Concerning the convective case, differences between models are also to note in C_{TKE}, Fig. 4.6 d). Here, there is almost a constant offset in C_{TKE} between the 1D model and the LES model, and both curves follow the same pattern. Only a small peak during the initialization period of the LES model contradicts those facts. Interestingly, C_{TKE} of the LES model oscillate around 1 after $0.2\,T_{inert}$. This results compares well with Nieuwstadt *et al.* (1992, Fig. 1) when defining a new TKE integral coefficient that takes into account the convective velocity scale, such as

$$C'_{TKE} = \frac{k}{w_*^2} \simeq \frac{u_*^3}{z_i f w_*^2} C_{TKE}, \tag{4.6}$$

which is fully valid in ours case since a uniform mesh is used in the vertical direction.

The last aspect of Figs. 4.5 and 4.6 to be discussed here regards the scatter between LES results (the grey shaded area in the figures). As a reminder, the LES model was run five times for each LES cases changing only the initial random velocity perturbations. All realizations of both the shear and convective cases clearly follow the same trend for the four quantities displayed in Figs. 4.5 and 4.6. Results oscillate rapidly around an equilibrium value which is in agreement with the average of the five runs (oscillation of each result is included in the grey area but roughly centred on the average curve). The latter oscillations have a notably higher frequency than the inertial oscillation and their amplitudes stay roughly constant after the on-set of turbulence. Finally, comparing the UKMO Smagorinsky and hybrid TKE SGS model results (not shown here), the spread of the five results is generally larger than the differences between the ensemble average result of the two SGS model which is in agreement with Nieuwstadt *et al.* (1992) and Andren *et al.* (1994).

To conclude this section, both 1D and LES models are in agreement and predict the same time evolution of the reference flow variables. Achieving the ensemble average of several LES computations, for which only initial random velocity perturbations were different, permitted to better appreciate the general behaviour of the LES model. The time evolution of integrated quantities studied in this section, Figs. 4.5 and 4.6, clearly shows that the on-set of the organized turbulent regime is occurring after six large eddy turnover time τ_* as suggested by Moeng and Sullivan (1994). Both the convective and the shear cases are in quasi-steady state during the time interval used by Moeng and Sullivan (1994) for the post-processing (*i.e.* from 12 to $17\,\tau_*$, hence from 0.172 to $0.25\,T_{inert}$ for the S case, and from $0.105\,T_{inert}$ to $0.148\,T_{inert}$ for B case). Only the shear case appears to tend to a steady solution after at least $0.5\,T_{inert}$ as further discussed in Sec. 4.3.1. As a consequence, managing to reproduce Moeng and Sullivan (1994) results is a good indication of a well modelled time evolution.

To mitigate these thoughts, however, the inertial oscillation has a strong effect only on the first order moments and related scaling parameters such as u_* (Sorbjan, 2003). This is also later confirmed in Sec. 4.3.1, along with the fact that non-dimensional profiles of all quantities reach a roughly steady state after the turbulent regime is well established. This allows Moeng and Sullivan (1994) to notably shorten the duration of the integrations while retaining the general character of the results. Those points are studied more in detail in the next sections.

4.2.3 Direct comparison with Moeng and Sullivan (1994)

The first evaluation of the LES-capable MC2 model is achieved in this section. For that sake, a direct comparison with the shear and convective cases of MS94 is intended. As a consequence and as mentioned earlier, the guidelines presented by MS94 are followed as closely as possible in order to be able to compare both dimensional and non-dimensional quantities as well as other more specific aspects of the solution. In view of Figs. 4.5 and 4.6, the same start/end time as MS94 are used to compute statistics (namely from/to $10445/15225$ s for the shear cases and $6450/9000$ s for the convective case, which is equivalent to $12\,\tau_*$ to $17\,\tau_*$ in Moeng's results) regardless of the τ_* obtained with the present methods (cf. Figs. 4.5 and 4.6). Such an interval

is short in comparison to the inertial oscillation period, *i.e.* $0.08\,T_{inert}$ for the shear case and $0.04\,T_{inert}$ for the convective case. Furthermore, as illustrated in the previous section, the time evolution of horizontal velocity components (notably v) and others first order moments is non negligible making their comparison more tricky.

All the results shown and discussed in this section are based on the $k-l$ column model, named S_{1d}, and the Smagorinsky SGS model, named S_S, described respectively in Sec. 2.2.5 and Sec. 2.2.3.1. All cases were also reproduced based on the hybrid TKE SGS model described in Sec. 2.2.3.3 and named S_M. The configuration described in Tab. 4.1 is used. Results based on others SGS models and configurations are presented and discussed in later sections.

Table 4.2 Result parameters for model setups shown in Tab. 4.1

Name	u_* [m/s]	w_* [m/s]	z_i [m]	L_{MO} [m]	θ_s [K]	$\overline{w'\theta'}_i$ [K m/s]	U_1 [m/s]	$\Delta\theta_1$ [K]
S_{1d}	0.520	0.0	516	∞	300.55	-0.0330	4.45	-0.0024
S_S	0.468	0.0	474	∞	300.36	-0.0032	4.17	-0.0008
S_M	0.474	0.0	459	∞	300.38	-0.0034	4.01	-0.0009
Moeng *et al.*	0.50	0.0	478	∞	NA	-0.007	4.35	0.0
B_{1d}	0.590	1.963	989	-39.2	307.31	-0.017	5.65	4.93
B_S	0.573	1.956	981	-27.3	307.90	-0.023	5.35	5.11
B_M	0.579	1.962	989	-28.8	307.79	-0.028	5.29	4.99
Moeng *et al.*	0.56	2.02	1030	-57.2	NA	-0.040	5.1	2.8

Furthermore, slightly different results are obtained from computations based on the same model but which are initialized with different random velocity perturbations. As a result, the ensemble average of five S_S and B_S runs was made to obtain all result parameters and figures of the present section. The error bars in the figures show the envelope, *i.e.* the scatter, of the series of results based on the same model. They are referred to as scatter hereafter. This approach was found necessary in order to reduce the uncertainty in the results associated with the variability of the phenomena, while retaining the same post-processing time interval as MS94. This thus allowed a direct comparison with MS94, however it also raised questions concerning the unicity of MS94 and Sullivan *et al.* (1994) results. Those aspects are further studied in Sec. 4.3.1.

In this section, after briefly discussing the general aspect of the results, the shear case is first thoroughly investigated followed by the convective case. The results obtained are mostly discussed and validated with regards to Moeng and Wyngaard (1989), Moeng and Sullivan (1994) and Sullivan *et al.* (1994) but other studies are invoked when required. In that sense, Figs. 4.7, 4.8, 4.9 and 4.10 are direct comparisons to Moeng and Sullivan (1994, Figs. 8, 9, 10) and Sullivan *et al.* (1994, Figs. 11, 12 and 13) (profiles from these figures were digitized and are labelled Moeng *et al.* and Sullivan *et al.* in Figs. 4.7, 4.8, 4.9 and 4.10). Furthermore, result parameters are summarized in Tab. 4.2 along with the ones obtained by Moeng and Sullivan (1994)[5]. Finally, The scatter of the result parameters is shown in Tab. 4.3.

Table 4.3 Scatter of the result parameters from Tab. 4.2, Eq. (4.9)

Name	$o(u_*)$ [m/s]	$o(w_*)$ [m/s]	$o(z_i)$ [m]	$o(L_{MO})$ [m]	$o(\theta_s)$ [K]	$o\left(\overline{w'\theta'}_i\right)$ [K m/s]	$o(U_1)$ [m/s]	$o(\Delta\theta_1)$ [K]
S_S	0.014	0.0	32	∞	0.011	0.0015	0.13	0.010
S_M	0.010	0.0	32	∞	0.009	0.0020	0.11	0.009
B_S	0.008	0.014	21	1.81	0.045	0.008	0.10	0.029
B_M	0.007	0.000	0	1.43	0.052	0.005	0.09	0.020

Before going in the detail of the two cases, it can be said from Tab. 4.2 and Figs. 4.7 to 4.9, that, in a general manner, both scale parameters as well as the various profiles compare well with MS94 and Sullivan *et al.* (1994) for the column and the LES models and for both the convective and the shear case. Dimensional profiles of horizontal velocity components are also in agreement with MS94 which is promising in view of the time evolution of both quantities during the post-processing time interval. Scatter between S_S/B_S results (as shown by the intervals on the curves and in Tab. 4.3) are generally not negligible, and only the first order moments show small scatter in comparison to the mean profile values. Indeed, vertical momentum flux of the convective case, Fig. 4.8 b), and, variance and third order moment of both cases, Figs. 4.8 c) and d) and Figs. 4.9 a) and b), exhibit a rather large spread. As a result, MS94 results fall most

[5] Note however that U_1 of the shear case from that paper was corrected according to Sullivan *et al.* (1994, Fig. 3) (see note in Sec. 1.3.2.2.1.2). "NA" is reported for θ_s since this value was not accessible from neither Moeng and Sullivan (1994) nor Sullivan *et al.* (1994).

of the time within the interval of the results obtained in this study. However, it can already be said that due to this uncertainty, it is not always easy to draw quantitative conclusions. Those facts seem to indicate that a longer period would be needed to compute more steady statistics.

4.2.3.1 Shear case

Concerning the shear case, the longitudinal velocity component, u, is slightly larger than MS94 across the whole ABL for S_S as seen in Fig. 4.7 a). The difference with MS94 is nearly constant through the ABL invoking a possible cause located in the near-surface region (Andren *et al.*, 1994). Concerning the lateral velocity component, v, differences are less significant and LES results nearly superpose. When considering z_i as shown in Tab. 4.2, the geostrophic wind is reached at a lower height by S_S than MS94. The difference between the various S_S results for both velocity component is very small across the ABL. The column model S_{1d}, for its part, exhibits a higher shear for both components close to the surface which results in lower velocities between 0.1 and $0.5\,z_i$. While this can appear odd here, the velocity profile of the 1D model is closer to the logarithmic solution as discussed in the literature review, Sec. 1.3. It may thus be in better agreement with the analytical solution close to the surface. In the upper ABL, the 1D model features a smoother transition to the free atmosphere, and it reaches the geostrophic wind at higher altitude. In a general manner and given the time evolution of Moeng and Sullivan (1994) shear case, both velocity components obtained with both the column and the LES models are in good agreement with MS94 across the whole ABL.

The vertical momentum flux, Fig. 4.8 a), is in good agreement with MS94 for LES model and only the 1D solution deviates from the other results at the inversion where 1D momentum fluxes are higher. Indeed, in the absence of horizontal mixing and resolved turbulent perturbations, vertical momentum flux needs to be higher to transport an equivalent amount of energy in that region. It has a shape similar to Andren *et al.* (1994). As underlined by André *et al.* (1978), $\overline{u'w'}$ has a quasi-linear shape with height while $\overline{v'w'}$ has a parabolic shape. The scatter between the five S_S runs, which is at its maximum in the middle of the ABL is not negligible,

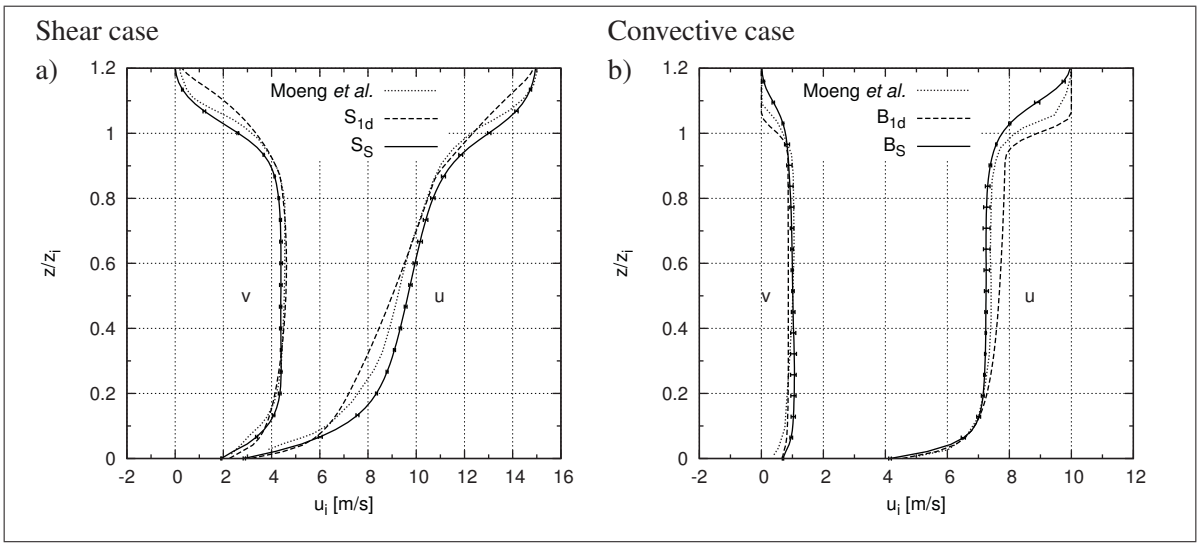

Figure 4.7 Dimensional profiles of horizontal velocity components: a) shear case; b) convective case. Scatter of the results is shown by error bars which are plotted every third mesh point

notably concerning $\overline{u'w'}$. As illustrated in the TKE profiles Fig. 4.8 e) and the sensible heat flux Fig. 4.10 a), this scatter is mostly originating from the resolved part of momentum fluxes.

Variances, Fig. 4.8 c), exhibit the same shape as MS94[6]. Column model results are not displayed since the computation of the variance goes beyond the abilities of the $k-l$ column model. In fact, since no resolved part exists, variances are isotropic and equal to $2/3\,k$ which is a very rough estimate of the variances. Concerning the LES results, above $0.3\,z_i$ and the inversion region put aside, MS94 results are within the scatter of S_S except for $\overline{w'^2}$ which is generally slightly lower than MS94 across the ABL. The scatter of S_S results is notable for $\overline{u'^2}$ while it is negligible for the two others components. Below $0.3\,z_i$, $\overline{u'^2}$ and $\overline{v'^2}$ are higher than MS94 especially for the former ($\overline{u'^2}_{max}/u_*^2 \sim 0.7$). The calculated values are however consistent with Andren *et al.* (1994) intercomparison results, where $0.6 < \overline{u'^2}/u_*^2 < 0.7$ and $0.2 < \overline{v'^2}/u_*^2 < 0.30$ for the non-backscatter models. As a reminder that, the "nose" exhibited in the latter results (also present in S_S) is typical of the dissipative SGS models but it is

[6] Note that subgrid TKE is required in order to compute total variances and TKE, and compare with MS94. However, it is not provided by the Smagorinsky SGS model. As a result, considering how close results from Smagorinsky and the hybrid TKE SGS models are (see Sec. 4.4.1), subgrid TKE from S_M and B_M is used to compute the total TKE and variances of S_S and B_S in Fig. 4.8 c), d), e) and f).

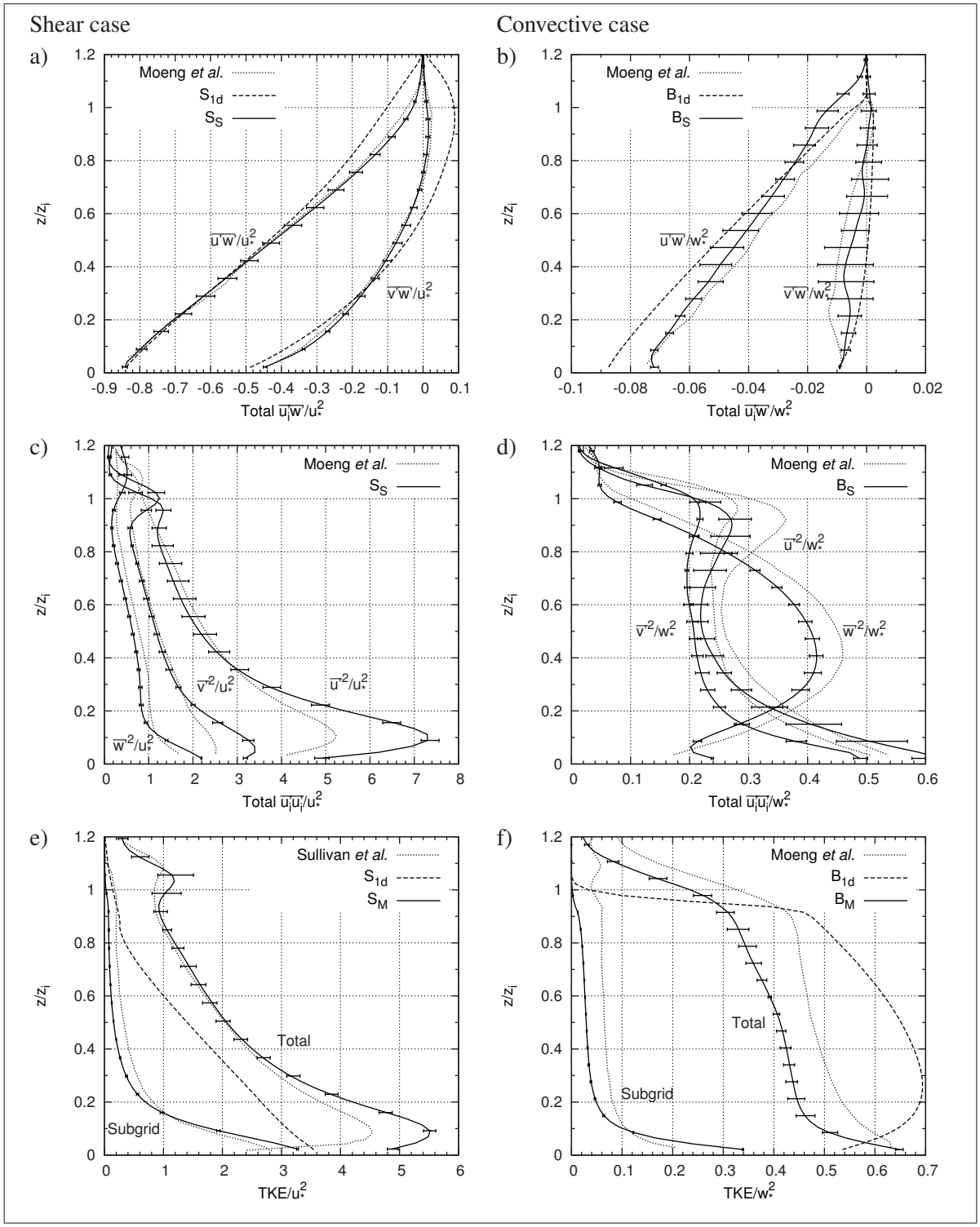

Figure 4.8 Profiles of second order moments from the shear (left) and convective (right) cases: a) and b) total vertical momentum fluxes; c) and d) total velocity variances; e) and f) total and subgrid TKE

erroneous (Andren *et al.*, 1994; Mason, 1994; Sullivan *et al.*, 1994; Porté-Agel *et al.*, 2000; Pope, 2000; Ding *et al.*, 2001a). In Andren *et al.* (1994) study, Moeng's $\overline{u'^2}$ featured the lowest maximum value while Mason's non-backscatter model, which is based on a Smagorinsky SGS model equivalent to the one used here, is the highest (and equal to the values obtained here). Concerning the vertical velocity variances, S_S results also feature an inflection point at around $0.25\,z_i$ with the value $\overline{w'^2}/u_*^2 = 0.8$. The height range of this plateau is in agreement with MS94 but the present value is generally lower. Finally, at the inversion, the local maximum is more marked in S_S than MS94 and they are also lower in height ($1.0\,z_i$ here instead of $1.1\,z_i$ for MS94). This overshoot in the variances is coming from their resolved part. It is thus reproduced thanks to the dynamics of the method (fully compressible).

The TKE profiles, Fig. 4.8 e), are also in agreement with the reference data from Sullivan *et al.* (1994). Note that, as for the unresolved part of the variances, the results from a computation based on the same general model (MC2) but using a TKE based SGS, S_M, are shown here since the Smagorinsky model does not provide the TKE. The total TKE differences between S_M and MS94 is similar to $\overline{u'^2}$ and $\overline{v'^2}$. As a summary, LES results are in good agreement above $0.3\,z_i$, while the proposed model features higher values below $0.3\,z_i$. Total TKE of S_M also exhibit a "nose" such as the horizontal velocity variances. Interestingly, the SGS part of the TKE is lower than MS94 above $0.2\,z_i$ meaning that the resolved part of the TKE is larger above that height for the present model. Note also that, Fig. 4.8 e) clearly shows that the scatter between S_M results is coming from the resolved part of the variances. This is also the case for the other variables (not shown here). Concerning the 1D results, the TKE profile varies linearly with height and is located in between the total and the unresolved TKE from S_M.

Vertical fluxes of velocity variance, Fig. 4.9 a), have also the same shapes as MS94 with maximum/minimum at the same heights. Both $\overline{w'v'^2}$ and $\overline{w'^3}$ are very close to MS94 (within the scatter of the results) and $\overline{w'u'^2}$ clearly reproduce the local minimum at $0.08\,z_i$ and the local maximum at $0.25\,z_i$. However, mean values for the latter is nearly two times larger than those of MS94. The scatter exhibited in the vertical flux of velocity variances is higher than in sec-

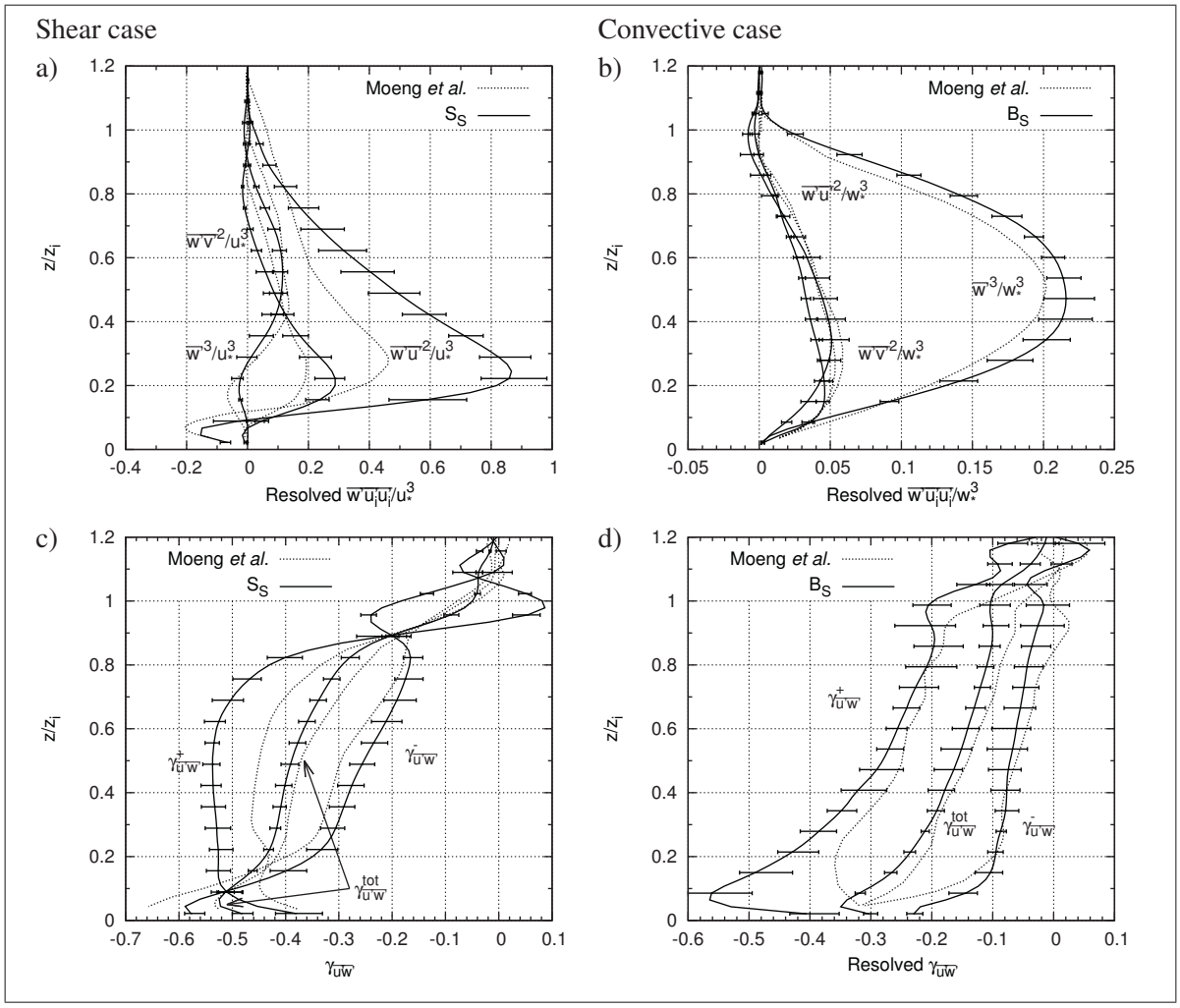

Figure 4.9 Profiles of resolved third order moments from the shear (left) and convective (right) cases: a) and b) velocity variances vertical fluxes; c) and d) correlation coefficients of vertical momentum fluxes

ond order moment (which was higher than in first order moment). The scatter of turbulent quantities thus appears to increase with their order.

Concerning the correlation coefficients of vertical momentum fluxes, Fig. 4.9 c), on the one hand, the total coefficient nearly superpose with MS94. However, on the other hand, the updraft and downdraft correlations, besides having a similar shape, exhibit significantly different values. Indeed, mean updraft momentum flux are more correlated than MS94 and nearly constant from 0.1 to $0.7\ z_i$ while mean downdraft are less correlated than MS94. However, scatter

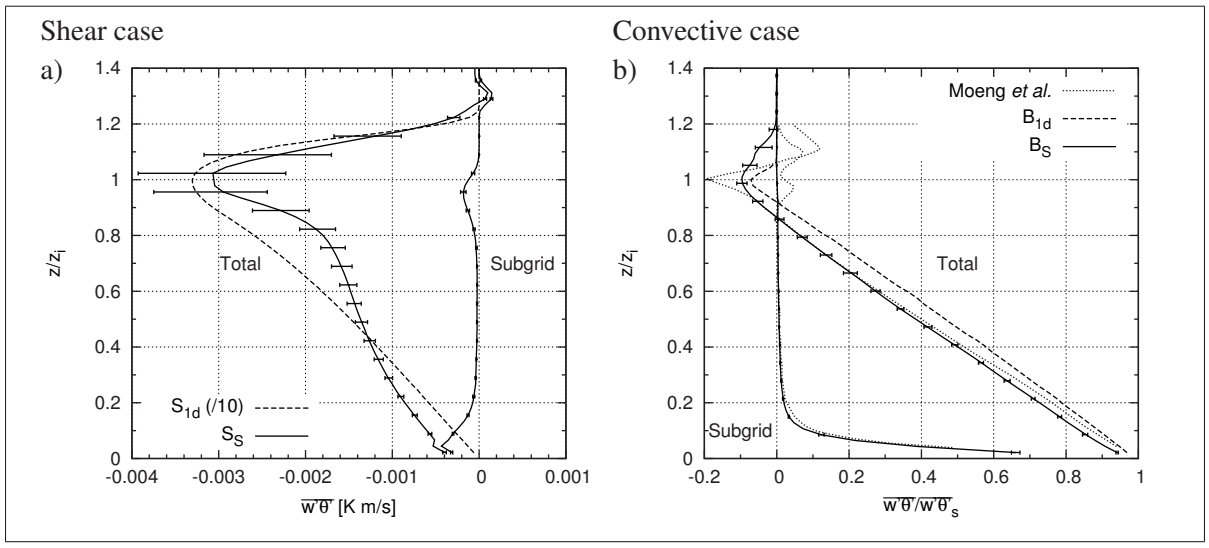

Figure 4.10 Profiles of total and subgrid sensible heat flux: a) shear case; b) convective case

between results is high especially for $\gamma_{\overline{uw}}^{+}$. Furthermore, while correlation for downdraft becomes lower than the one for updraft at $0.9\,z_i$, the total correlation coefficient, $\gamma_{\overline{uw}}^{tot}$, tends to 0 at $1.2\,z_i$ such as MS94. However and as opposed to MS94, both updraft and downdraft correlations show two crisscross between 0.9 and $1.2\,z_i$. It thus clearly suggests that processes taking place in that region are different from MS94. By further taking in consideration the local maximum of horizontal velocity variances at the inversion, the implemented model features a notably higher level of resolved fluctuation than MS94. This is attributable to the dynamics of the model which appears to be more sensitive to the sharp temperature inversion.

Finally, concerning the sensible heat flux profile, Fig. 4.10 a), only the minimum value at the inversion was given by MS94, but no profile is shown. In fact, such a profile is rarely found in the literature for neutral case since temperature is not of prime interest for such a case and heat flux are usually negligible. For the shear case of MS94, heat flux is expected to evolve from zero at the surface to a minimum value at the inversion because of the entrainment of hot air from the free atmosphere. S_S and S_{1d} results are correctly following this behaviour. It is also interesting to underline the small region just above the inversion with positive subgrid heat flux. This region exists in both column model and LES model results. As seen later in

Fig. 4.27 b, it coincides with a region in the potential temperature profile that has a neutral (or slightly unstable) stratification. While not present in the initial profile, this layer is created right at the junction between the temperature inversion and the free atmosphere. Such a feature was also observed by Sorbjan (2005b, Fig. 7 a) and 11 a)) using a LES model based on Deardorff (1980) SGS model that includes internal energy conservation equation.

The predicted minimum heat flux at the inversion (see Tab. 4.2) is two times smaller for S_S and 20 times higher for S_{1d} than in MS94. The very high value for S_{1d} is the consequence of the lack of horizontal mixing and resolved motion at the inversion requiring an unrealistic increase of the flux. Concerning the LES results, the scatter of the results is roughly equal to a quarter of the heat flux, which is very high. Furthermore, the sensible heat flux values are very small. As a result, the difference with MS94 is not critical. An aspect more of concerns however, is the slight increase of the subgrid scale heat flux close to the surface. Indeed, as no surface forcing is applied the later should be zero. After investigating this aspect by forcing the subgrid heat flux to zero below $0.5\ z_i$, it was found that this had no influence on the solution.

To summarize MS94 shear case results are satisfactorily reproduced using both the LES and the column model. The column model however shows limitation at the inversion in comparison to the LES models, and close to the surface the velocity profile also departs from both LES models (see Sec. refsec:surface.MS1994). The present LES model is in very good agreement with MS94 from 0.3 to $0.9\ z_i$. In the inversion region, S_S results feature more resolved motion than MS94 impacting notably the resolved variances. The predicted friction velocity u_* is slightly lower than MS94 and the near-surface "nose" of the TKE, $\overline{u'^2}$ and $\overline{v'^2}$ is more significant than MS94. These latter facts tend to indicate that MC2 is more dissipative than MS94, at least close to the surface. Indeed, as noticed by Mason and Thomson (1992) and later Brown *et al.* (2000), increasing the dissipation of an LES model (by increasing the Smagorinsky constant or using a more dissipative advection scheme), has effects very similar to those noticed above. Finally, the scatter of the results is mainly coming from the resolved part of the turbulent quantities. The higher their order, the higher the scatter. In some cases, such as for the third order moments of the heat flux, the scatter peaked at more than 15 % of the value of the variables.

4.2.3.2 Convective case

The horizontal velocity components for the convective case shown in Fig. 4.7 b), are in good agreement with MS94 in the whole ABL. The transition from the ABL to the free atmosphere, namely the inversion, is however higher and thicker for B_S featuring a less steep slope. According to Tab. 4.2, z_i is lower than MS94 by 50 m for B_S. This has the effect of shifting by $0.05\, z_i$ upward the non-dimensional profiles of B_S. It thus indicates that in fact velocity transition to the free atmosphere of both LES models are roughly at the same height.

For the longitudinal component u, Fig. 4.7 b), all results nearly superpose below $0.15\, z_i$. Both LES models predicts a quasi uniform vertical profile of u while the 1D model predict a slight increase of u with height across the ABL. The values of u obtained by MS94 are slightly higher than B_S but the difference is most often not larger than the scatter of B_S. Concerning the lateral component v, the column model result is perfectly uniform in the vertical direction with a surface value equal to the one of B_S (the same surface boundary condition is used for both models). MS94 results feature a slightly different profile of v close to the surface with lower speeds. B_S results have a maximum value in the lower half of the ABL, then v decreases by 0.2 m/s across the ABL, while the v component of MS94 increases by a similar amount across the ABL and has a maximum just under the inversion.

Vertical momentum flux profiles of the convective case, Fig. 4.8 b), exhibit a rather large scatter between results from the same model (in comparison to the maximum value which is small). Indeed, the scatter of $\overline{v'w'}/w_*^2$ reaches twice the value of that flux in the middle of the ABL. The following general conclusion can however be drawn: B_S momentum fluxes are reaching zero at $1.15\, z_i$, while it is roughly at $1.05\, z_i$ for MS94 and B_{1d}. This difference is lowered when considering the dimensional height instead of z/z_i. The 1D results has a $\overline{u'w'}/w_*^2$ surface value higher by 10 % than the LES model results which are in agreement in that region. Note that the slight deviation of $\overline{u'w'}/w_*^2$ at the surface for B_S can tentatively be attributed to the difference between the similarity function used at the surface (Delage and Girard, 1992) and in the atmosphere (Brown *et al.*, 1994).

Variances, Fig. 4.8 d), have nearly an identical shape to the one of MS94 but they generally have lower valued by a nearly constant offset across the ABL. The values obtained here are however in agreement with the results from a previous study of Moeng based on the same model as in MS94 (see Moeng and Wyngaard (1989, Fig. 2)). Furthermore, they are also in agreement with results from the convective intercomparison of Nieuwstadt *et al.* (1992). In that study based on a freely convective ABL, a maximum value of $\overline{w'^2}/w_*^2 \simeq 0.4$ is obtained at $\sim 0.4\, z_i$ by LES models (in agreement with experimental data) and $\overline{u'^2}/w_*^2$ is around 0.2 at the same height ($\overline{u'^2} = \overline{v'^2}$ since a freely convective case is reproduced in that study). Those latter values were also found to be representative by Stull (1988, p. 125, 370 and 375) and more recently by Brown (1999) for freely convective cases.

Note nevertheless that geostrophic wind is non-zero in MS94 B case, and thus both shear and buoyancy produce turbulence. But since $-z_i/L_{MO} \gg 4$, the latter process is clearly dominant and free convection scaling apply (Deardorff, 1980). The presence of shear slightly changes the flow dynamics (compared to a free convective case), as demonstrated by MS94 and Sorbjan (2005a). It introduces some anisotropy in the horizontal momentum fluctuations resulting in a higher value of $\overline{u'^2}/w_*^2$ compared to $\overline{v'^2}/w_*^2$. Differences between those two terms exhibit the very same features in our case as in MS94 but it is less pronounced in the upper part of the ABL, just below the inversion.

In that sense, Sorbjan (2005a) also reproduced convective ABL based on LES going from free to forced convection. This study clearly illustrated that increasing the shear production (by increasing the geostrophic wind), tends to increase $\overline{u'^2}$ and $\overline{v'^2}$ at the surface and at the peak just below the inversion as well as slightly increase $\overline{w'^2}$ maximum value in the mixed layer. The profile of the two former quantities is also less uniform in the vertical direction in such a case, notably close to the surface.Present LES results are thus in good agreement with free convection variances results, due to the large value of the surface sensible heat flux (making convection clearly the dominant process). However, the above mentioned features are less noticeable, and variances value would be expected to be slightly higher than for a freely convective case. It thus tends to show that the present model features too low variances values.

Finally concerning the scatter, while generally smaller than for the vertical momentum flux, it is not negligible notably for $\overline{u'^2}$ below $0.3\,z_i$ and above $0.7\,z_i$.

Concerning the TKE profile shown in Fig. 4.8 f), the results from the TKE based SGS model, B_M, are shown here along with the column model results, B_{1d}. Furthermore, since no TKE profiles are directly provided in MS94, Moeng and Wyngaard (1989) results (which are based on the same case and LES model as MS94) are used as reference. Column model results present a notably higher level of TKE than the LES results. On the other hand and in comparison to Moeng and Wyngaard (1989), B_M results feature a notably lower TKE level, which is mainly cause by a lower subgrid scale TKE level (50 % lower than Moeng's results). The resolved TKE is also slightly lower. This lower subgrid TKE may also be the cause of lower variances values in the mixed layer. Interestingly, the subgrid TKE vanishes at the top of the ABL for B_M, while it retains a value similar to the one of the mixed layer for MS94. Thus, resolved TKE contribute to 100 % of the TKE above the inversion for B_M.

Vertical fluxes of velocity variances, Fig. 4.9 b), are for their part close to MS94. Most of the time, the latter fall within the scatter of the present results. Interestingly, $\overline{w'^3}$ is slightly higher than MS94 while it was the opposite for $\overline{w'^2}$, which may lead to a different vertical velocity skewness shape ($\overline{w'^3}/\overline{w'^2}^{3/2}$) in comparison to MS94 (not shown here). B_S results are also in agreement with Nieuwstadt *et al.* (1992). On the latter study, differences between models is notably larger for the third order moments than for the variances. Here the scatter of velocity variances vertical flux from B_S model is generally of the same order as the one of the momentum flux and the variances. It is higher for $\overline{w'^3}$ in the mixed layer. Concerning vertical flux of $\overline{u'^2}$ and $\overline{v'^2}$, there are hardly differentiable in MS94 and the differences are more notable here but values are generally lower. The scatter of those variable is lower than $\overline{w'^3}$.

The correlations of vertical momentum flux, Fig. 4.9 d), are also in agreement with MS94 while they are generally slightly lower for B_S. In fact, the only obvious difference with B_S is in $\gamma^+_{\overline{uw}}$ below $0.3\,z_i$ where, instead of smoothly returning to -0.3, updraft correlation keeps decreasing to reach -0.55 at $0.09\,z_i$. It then suddenly increases as the surface is getting closer.

At the inversion, MS94 correlations are crossing at $1.1\,z_i$ while in our case there are just doing a bottleneck at $1.05\,z_i$ and they cross at $1.2\,z_i$. This time, only one small criss-cross is present in our results between 1.2 and $1.25\,z_i$ (not shown here).

Finally, concerning the heat flux, Fig. 4.10 b), both B_{1d} and B_S predict a linear profile going from roughly one at the surface to a slightly negative minimum value at the inversion cause by the entrainment. A constant shift is however observed between B_S and B_{1d} (LES model showing lower values). Interestingly, very close to the surface Moeng and Wyngaard (1989) total heat flux (which is coming from the same case and model as MS94) is closer to B_{1d} (which is closer to one), while it superposes with B_S between 0.3 and $0.9\,z_i$. Both LES models predict the same subgrid heat flux in the whole ABL. Above $0.9\,z_i$, subgrid scale flux profile from Moeng and Wyngaard (1989) is rather unusual (see Moeng and Sullivan (1994, Fig. 18) and Nieuwstadt *et al.* (1992, Fig. 2) for more common subgrid scale heat flux profiles). However, the low value of that part of the flux in comparison to the resolved part does not prevent us to draw conclusions. The present LES results exhibit a less sharp countergradient flux with a lower magnitude (half MS94 value as shown in Tab. 4.2). Such a profile of the heat flux at the inversion is more representative of a convective ABL featuring a less sharp (weaker) inversion that allows more turbulent mixing and thus a smoother transition between ABL and free atmosphere as illustrated in Sorbjan (2005a, Figs. 7 b) and 12 a)). Furthermore, by applying similarity function dedicated to the inversion that are proposed in the latter paper (see of Sorbjan (2005a, Eq. (9a))) one can quantitatively evaluate the entrainment heat flux. For MS94 B case, Sorbjan (2005a) similarity functions lead to an entrainment heat flux value of roughly -0.05 K m/s which is twice the obtained value with B_S but in agreement with MS94 value. This difference can only be attributed to the resolved part of the flux (since subgrid scale heat flux in negligible at the inversion), and thus to the dynamics of the model.

In conclusion of the direct comparison with Moeng and Sullivan (1994) convective case, results are generally well reproduced, however, the scatter from the present LES model is sometimes very high preventing to always properly compare results with Moeng and Sullivan (1994). All profiles have a very similar shape to the reference study but the ABL height is 5 % lower for B_S.

Furthermore, variances and TKE obtained with B_S/B_M are also lower than Moeng and Sullivan (1994). This is partly due to a lower subgrid scale TKE than Moeng and Sullivan (1994) in the mixed layer. Finally, the inversion appear to be smoother than Moeng and Sullivan (1994). This is particularly noticeable in the sensible heat flux. In consideration of Sorbjan (2005a) similarity functions, it was found that B_S predict a 50 % too low entrainment flux for the case considered which was found to be coming from the dynamics of the model.

4.2.4 Flow structure

An aspect of LES which is of interest, is the ability of such an approach to resolve and reproduce eddies, their evolution and their interaction throughout the whole ABL (with some limitation in the surface layer). The spatial distribution of turbulent structure can thus be explicitly studied which is an important advantage over column models. The early LES studies allowed to better explore qualitatively and quantitatively these aspects of the ABL. In our days, measurement facilities such as SODAR and LIDAR allow to fully appreciate experimentally such a process and enforce the early LES findings, see Drobinski *et al.* (2004) for an example.

In the present section, instantaneous turbulent fields from the S and B cases are discussed with regards to the literature. Main features of the flow are illustrated along with the differences between the shear and convective ABL. To better appreciate and compare flow features, Moeng and Sullivan (1994, Figs. 1 to 6) are reproduced here using the results from the LES based on the Smagorinsky SGS model, *i.e.* S_S and B_S. Those figures were also reproduced by Churchfield *et al.* (2010) based on a Smagorinsky model and a finer mesh than MS94.

4.2.4.1 Shear case

The shear case, reproduced here, includes features from: classical Ekman cases, channel flows, and full scale real ABL. Hence, depending of the height in the ABL, the striking feature should resemble one of the above mentioned flow types (Moeng and Sullivan, 1994). Flow structure of shear driven ABL is often discussed by authors but, most of the time, only for the near-surface region (with the objective to better appreciate the impact of model parameters such

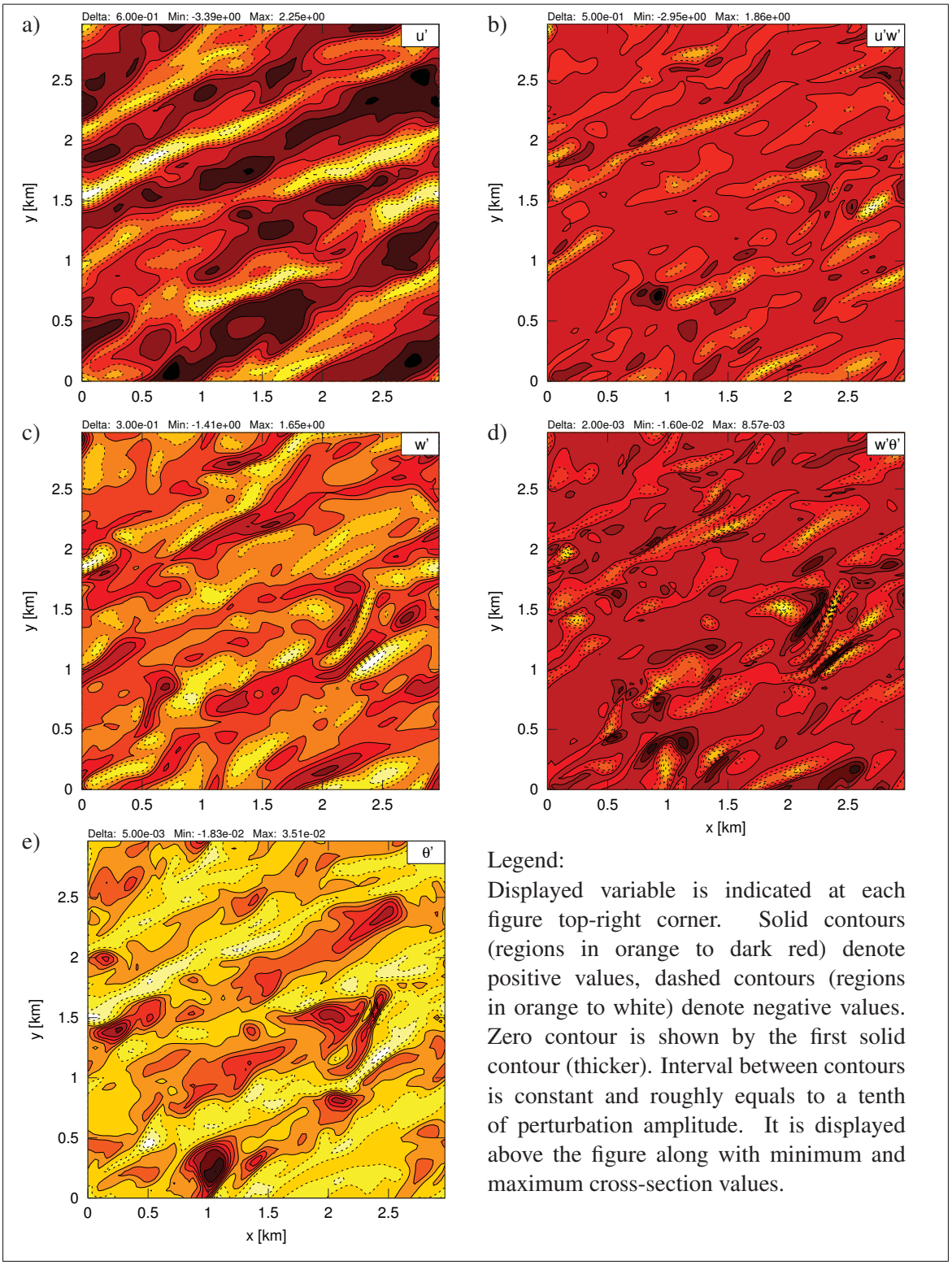

Figure 4.11 Instantaneous resolved-scales horizontal cross-sections from S_S at $0.2\,z_i$ and at time $t = 10170$ s (*i.e.* $17\,\tau_*$): a) u'; b) $u'w'$; c) w'; d) $w'\theta'$; e) θ'

as the mesh or SGS model) (Sullivan *et al.*, 1994; Ding *et al.*, 2001a; Senocak *et al.*, 2007; Silva Lopes *et al.*, 2007). Furthermore, temperature and heat are almost never studied for shear cases. Here, the whole domain is investigated for both momentum and heat.

Fig. 4.11 shows the horizontal cross-section at $0.2\,z_i$ (*i.e.* ~ 100 m agl, where the flow is more than 90 % resolved, see Fig. 4.19 a)) of the longitudinal and vertical velocity perturbation, potential temperature perturbation and resolved vertical momentum and heat fluxes. A spatial average of the horizontal cross-section is made to obtain reference values used to compute the perturbations. On this figure, well defined elongated structures (streaks) oriented along the flow direction can clearly be observed. They span nearly across the whole domain. In spanwise direction, low and high speed regions are alternating. The size of those structure is very similar to those shown by MS94. Those near-surface streaks are caused by shear instabilities. They occur in updraft/downdraft pairs (elongated in the flow direction). In high velocity regions, the flow tends to go downwards (sweeps process, u^+w^-, featuring high-speed negative momentum flux), while in low speed region, the flow is clearly going upwards (ejections process, u^-w^+, featuring low-speed negative momentum flux) (Drobinski *et al.*, 2004). As noted by MS94, ejection regions concentrate large negative $u'w'$ values (see Fig. 4.11 b)).

The near-surface streaks were for the first time observed by means of LES by Deardorff (1972) and they were later extensively described for the neutral ABL by Mason and Thomson (1987) who further used two dimensional correlations to characterize the latter. It is also a well known feature of the near-wall region of channel flow (Sagaut, 2006). More recent studies as well as experimental data (wind tunnel and full scale data) confirm the presence of such eddies in the surface layer (Mason, 1994; Sullivan *et al.*, 1994; Ding *et al.*, 2001a; Drobinski *et al.*, 2004; Senocak *et al.*, 2007; Churchfield *et al.*, 2010; Silva Lopes *et al.*, 2007). They are present in all flow variables but they are more noticeable in longitudinal velocity fluctuations.

Potential temperature fluctuations at $0.2\,z_i$, Fig. 4.11 e), are relatively small (~ 0.04 K) and they can be assumed to be solely due to the advection caused by w' fluctuations. Indeed,

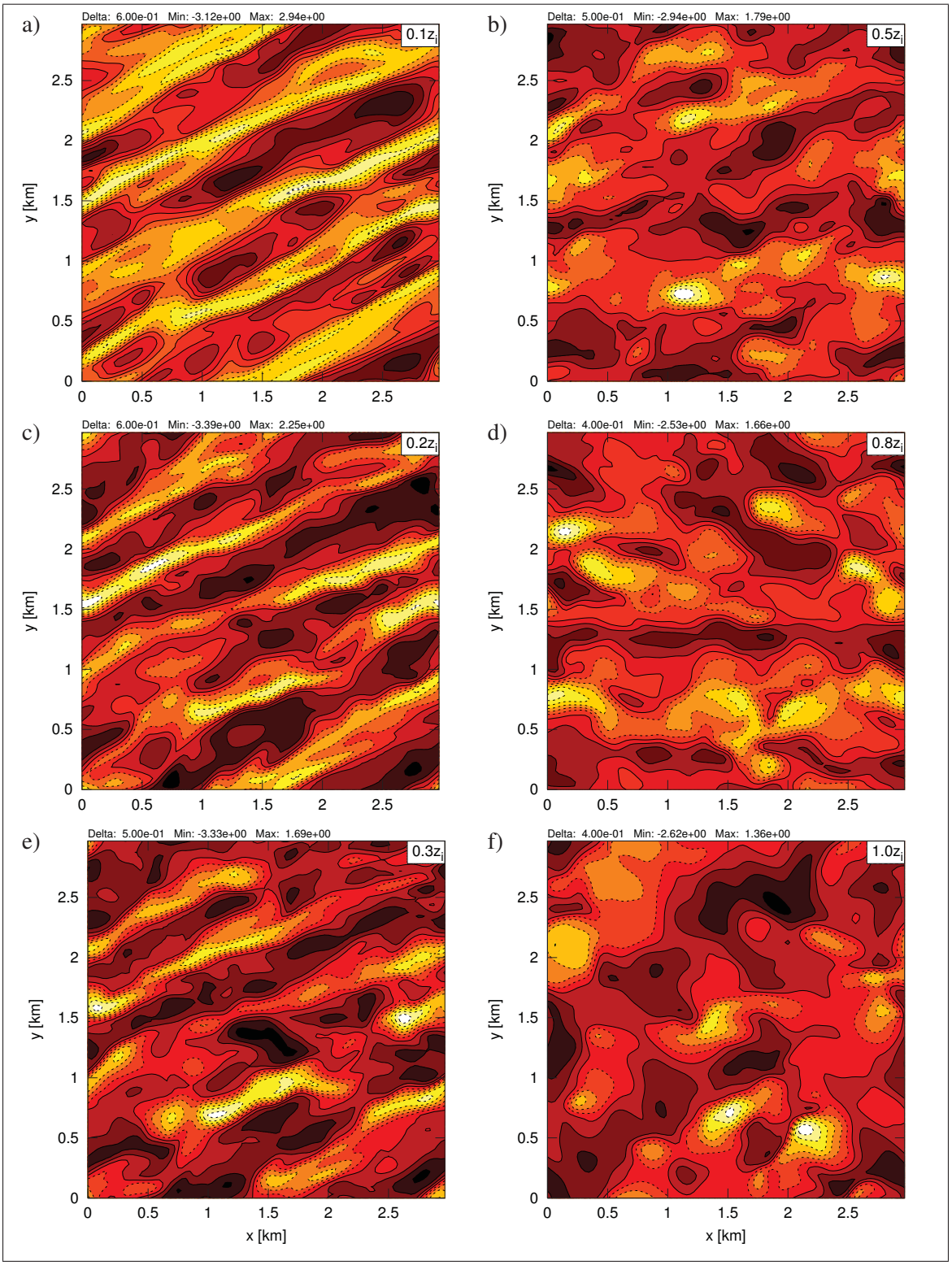

Figure 4.12 Instantaneous horizontal cross-sections of resolved streamwise velocity fluctuations u' from S_S at time $t = 10170$ s at various heights: a) $0.1\ z_i$; b) $0.5\ z_i$; c) $0.2\ z_i$; d) $0.8\ z_i$; e) $0.3\ z_i$; f) $1.0\ z_i$. Contours legend as in Fig. 4.11

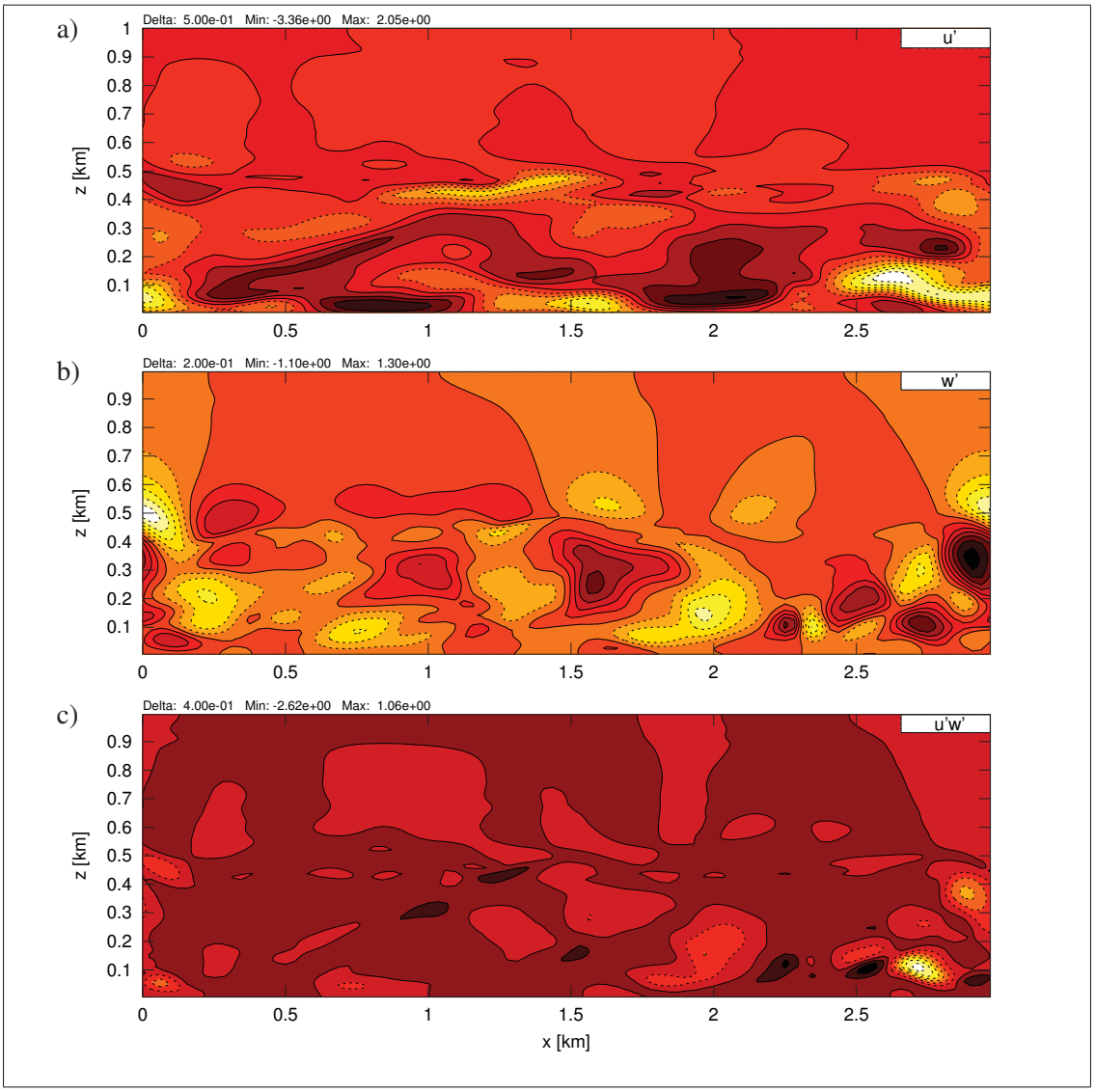

Figure 4.13 Instantaneous resolved-scales vertical cross-sections (x-z plane at $L_y/2$) from S_S at time $t = 10170$ s: a) u'; b) w'; c) $u'w'$. Contours legend as in Fig. 4.11

vertical velocity and temperature patterns are roughly similar and updraft (downdraft) regions are generally located where temperature is lower (higher) than the environment.

Fig. 4.12 shows instantaneous horizontal cross-sections of longitudinal velocity fluctuations at various heights in the ABL for the shear case. In this figure, contour intervals as well as colour scheme are proper to each figure as opposed to MS94. It can be clearly seen that as z increases streak structures gradually disappear while they turn toward geostrophic wind direction. The

min/max values of fluctuations are also reduced as z increases (see min/max values displayed above the figures). At $z/z_i = 0.5$ and above, Fig. 4.12 b), streaks are no longer visible and they are replaced by more spatially random structures. Mason and Thomson (1987), Moeng and Sullivan (1994) and Churchfield *et al.* (2010) obtained the very same features (with finer details for Churchfield *et al.* (2010) due to the finer mesh used). In the middle of the ABL, the flow is almost fully resolved by the numerical mesh. Flow fields are smooth and few structure of the size of the mesh are present which indicates, as underlined by Mason and Thomson (1987), Mason (1994) and Klemp and Skamarock (2004); Takemi and Rotunno (2005), that SGS model constants are correctly set and solution in not prone to discretization errors. Finally, at the inversion, Fig. 4.12 f) no predominant direction can be observed and auto-correlation is almost circular (not shown here).

The next figures discussed, Figs. 4.13 and 4.14, are vertical x-z cross-sections at $y = 1.5$ km for the same variables as in Fig. 4.11. Perturbations are computed from the horizontal spatial average at each height. Longitudinal velocity perturbations, Fig. 4.13 a), exhibit small elongated structures organized in high/low speed pairs and mostly concentrate close to the surface, *i.e.* below 200 m, which is in agreement with Fig. 4.12 and the observation of MS94. Vertical velocity perturbations, Fig. 4.13 b), feature structures ranging up to scales equal to the ABL height. They are located in updraft-downdraft pair with strong perturbations going up to ± 1 m/s found above $0.1\ z_i$. Eddies are also observed at the inversion. The influence of the latter goes up to the top of the domain and zero contour lines reach the top of the domain almost vertically. A strong negative correlation of $u'w'$ can be observed in updraft/downdraft regions (*e.g.* for x around 2 km in the middle of the ABL and for x between 2.5 km and 3 km) in Fig. 4.13 c). Regions of negative (positive) vertical velocity coincide with regions of positive (negative) u' fluctuation. This latter fact is also in agreement with the previous findings, MS94 and Mason and Thomson (1987).

A last interesting feature of Fig. 4.13 a) to c) is the organized series of structures seen in the ABL at $x > 2.25$ km and that reaches the inversion at $x = 3$ km. The latter is present in u' and w' vertical cross sections Fig. 4.11 a) and b), and the correlation $u'w'$ is fairly high as seen in

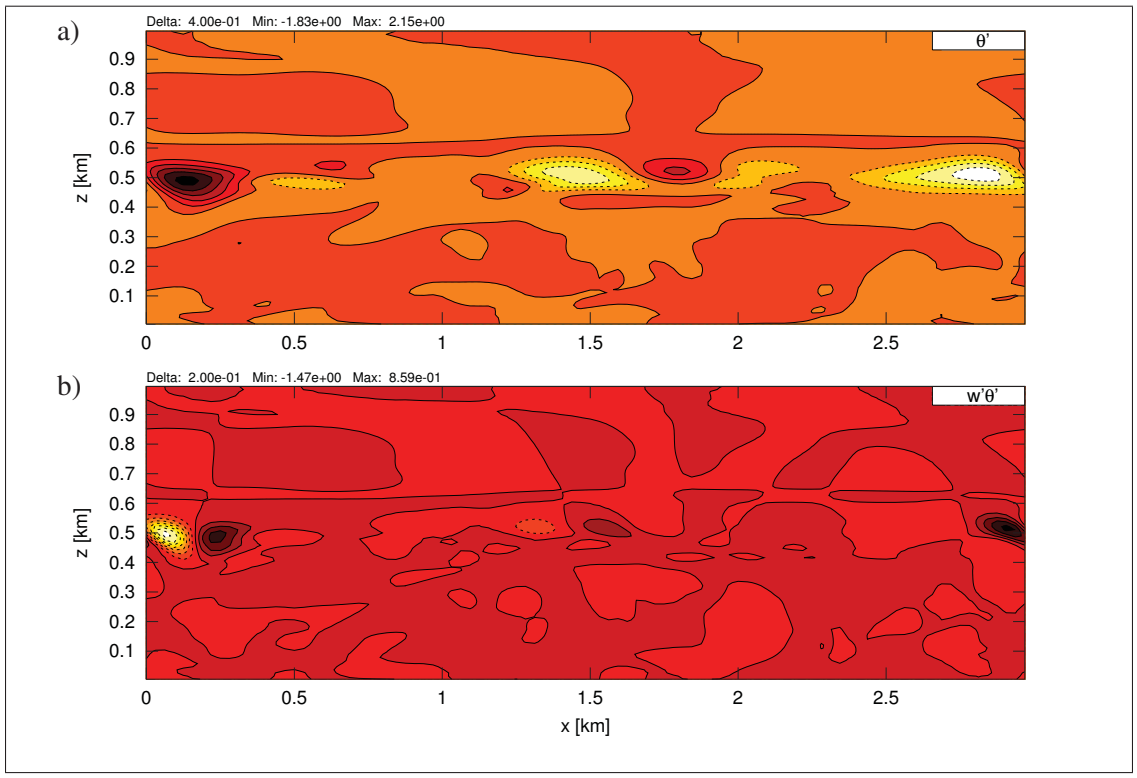

Figure 4.14 Instantaneous resolved-scales vertical cross-sections (x-z plane at $L_y/2$) from S_S at time $t = 10170$ s: a) θ'; b) $w'\theta'$. Contours legend as in Fig. 4.11

Fig. 4.11 c). Those organized structures feature the same pattern and may be a gravity wave triggered by surface shear instabilities.

Potential temperature perturbations, Fig. 4.14 a), show strong negative/positive extrema of a few degrees all along the inversion. They are going by pair and hot regions appears to be correlated with downdraft invoking entrainment of hot air from above the inversion (*e.g.* for $x < 250$ m). This results in strong negative heat flux $w'\theta'$, Fig. 4.14 b). In Fig. 4.14 a) and b), a nearly strait line is seen at ~ 620 m (just above the inversion). It coincide with a neutral (or slightly unstable) region located just above the inversion as seen in Fig. 4.10 a) and 4.27 b). While the latter can appear to be spurious, it was also observed by Sorbjan (2005a, Figs. 7 a) and 11 a)) relying on Deardorff SGS model (Deardorff, 1980).

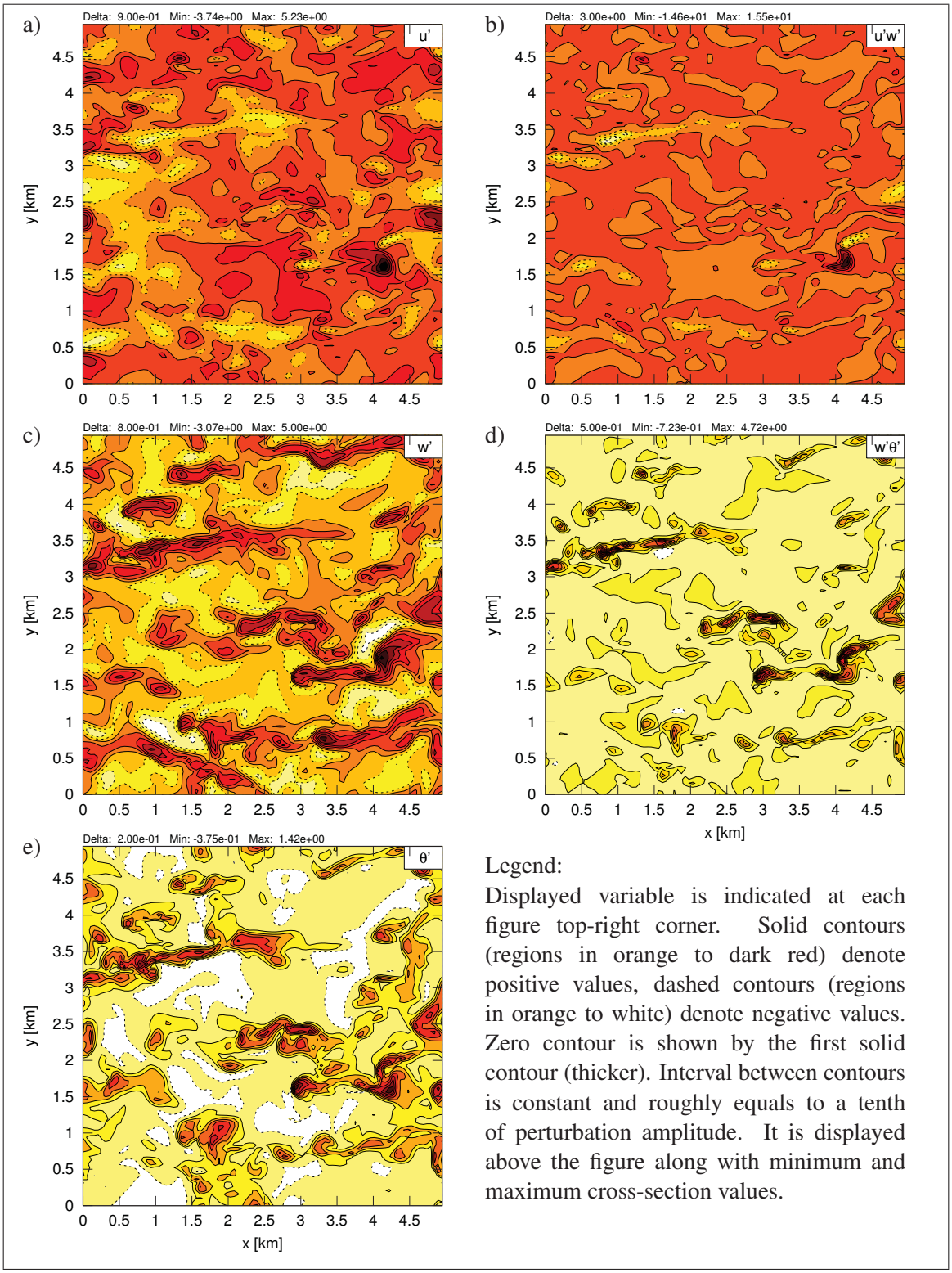

Figure 4.15 Instantaneous resolved-scales horizontal cross-sections from B_S at $0.2\,z_i$ and at time $t = 2200$ s (*i.e.* $17\,\tau_*$): a) u'; b) $u'w'$; c) w'; d) $w'\theta'$; e) θ'

4.2.4.2 Convective case

As already previously observed, buoyancy driven ABL presents notably different features compared to a shear driven ABL. For such a case, vertical velocity w and potential temperature θ are more of interest than horizontal velocity components. In MS94 B case, buoyancy is clearly the dominant process as $-z_i/L_{MO} \gg 4.5$ but a slight shear is also present, notably close to the surface and at the inversion. As discussed by Moeng and Sullivan (1994); Churchfield *et al.* (2010) and more extensively by Sorbjan (2005a), in such a case the flow structure is expected to slightly differ close to the surface and at the inversion in comparison to free convective cases while main patterns and structures (and scalings) should be largely similar. Free convection results can thus be used as a basis of comparison. In this section, as for the shear case, the cross-section for the same variable and at the same location as MS94 are discussed.

Fig. 4.15 show the horizontal cross-section at $0.2\ z_i$ (*i.e.* just above the surface layer and where the flow is more than $95\ \%$ resolved, see Fig. 4.19) of longitudinal and vertical velocity perturbation, potential temperature perturbation and resolved vertical momentum and heat fluxes. It is similar to Fig. 4.11 and was obtained in the same manner. Structures appear smaller than for the shear case, but the domain as well as the meshes of the convective case are $40\ \%$ larger. Flow structure is primary determined by a few narrow and powerful updrafts that concentrate most of the positive vertical velocity and potential temperature fluctuations, Fig. 4.15 b) and e). Strong positive correlation thus exist between those two variables in the updrafts as seen on $w'\theta'$ cross-sections, Fig. 4.15 d). Elsewhere, $w'\theta'$ is close to zero. Those updraft structures are isolated and surrounded by large smooth downdraft. Finally, almost all the large negative $u'w'$ at $0.2\ z_i$ is also found in these updrafts. The above described results are very similar to the one of Moeng and Sullivan (1994) and Churchfield *et al.* (2010).

Mason (1989) and Sorbjan (2005a) clearly obtained similar strong updrafts in freely convective conditions. However, the well defined closed cells they found close to the surface (similar to the Rayleigh-Bénard convection structures), as shown by Mason (1989), are not found in the convective case reproduced here, Fig. 4.15. In fact, narrow near-surface updrafts are oriented

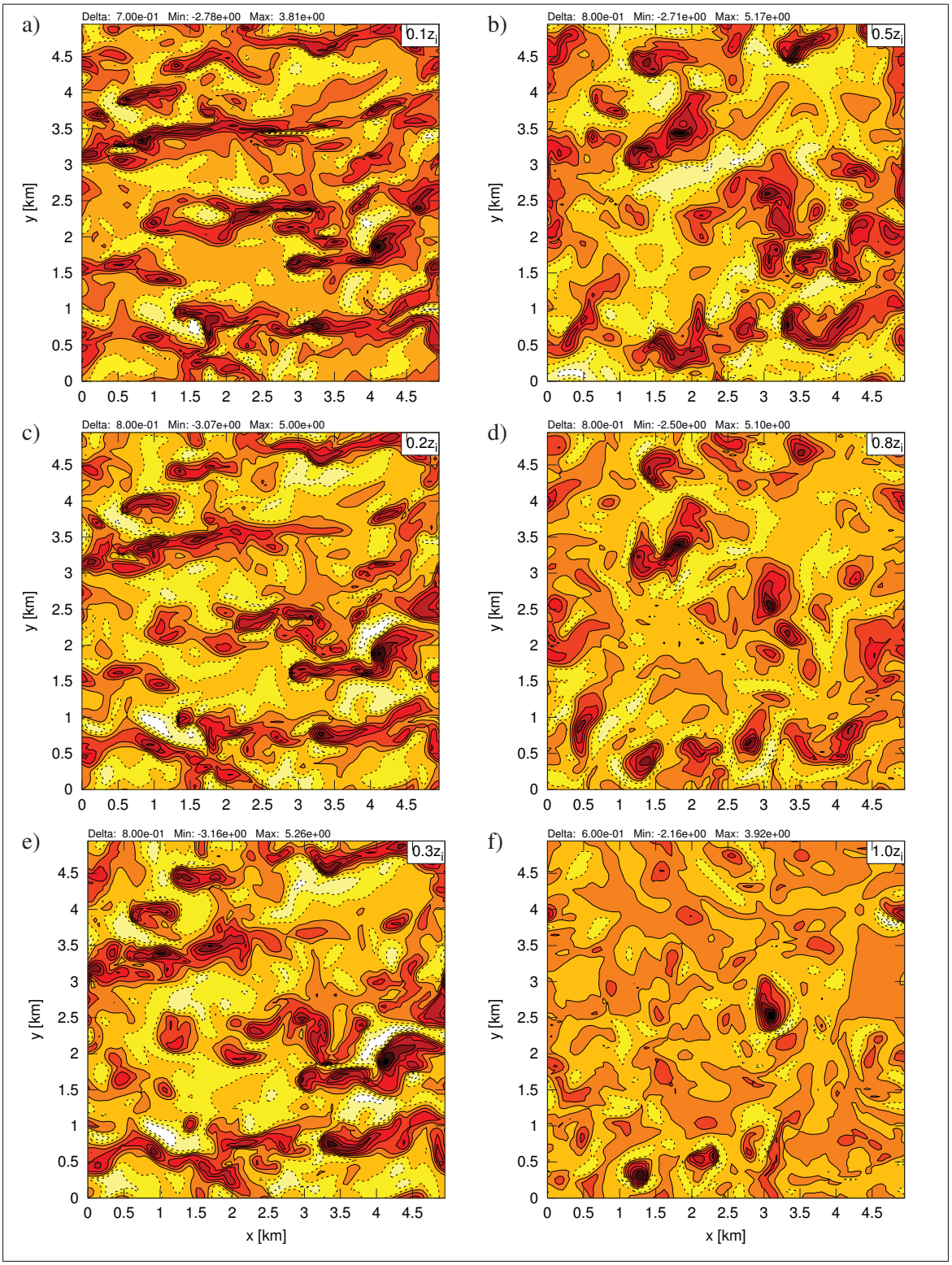

Figure 4.16 Instantaneous horizontal cross-sections of resolved vertical velocity fluctuations w' from B_S at time $t = 2200$ s at various heights: a) $0.1\ z_i$; b) $0.5\ z_i$; c) $0.2\ z_i$; d) $0.8\ z_i$; e) $1.0\ z_i$. Contours legend as in Fig. 4.15

along the flow direction similarly to Moeng and Sullivan (1994) and Churchfield *et al.* (2010). This is due to the additional surface shear which cause the convective instabilities to have their organization influenced by shear instabilities that tend to have a streak like structure. The difference observed at $0.2\,z_i$ with free convective case is thus normal.

Fig. 4.16 shows instantaneous horizontal cross-sections of vertical velocity fluctuations at various height for the convective case B_S. On this figure, contour intervals as well as colour scheme are proper to each figures as opposed to MS94. It can be observed that strong convective plumes (called "spokes" by Mason (1989)) generally span the whole ABL vertically, illustrating their non-local effect. Few of them are however strong enough to overshoot the inversion as illustrated in Fig. 4.16 d) and f). A clear example of such a strong updraft, that overshoot the inversion, can be seen at $x = 3$ km, $y = 2.5$ km in Fig. 4.16 a) to f). Intensity of w fluctuation is higher in the mixed layer than close to the surface and at the inversion. This is in agreement with MS94 and Churchfield *et al.* (2010). In comparison with free convective case as shown in Fig.2 c), d), g) and i) from Mason (1989), despite the differences previously discussed in the near-surface region, the flow structure in the upper half of the ABL is very similar confirming the free convective nature of the flow from B case in that region.

The next figures, Fig. 4.17 and Fig. 4.18, show vertical x-z cross-sections at $y = 2.5$ km for the same variables as in Fig. 4.15. Perturbations are computed from the spatial average of the horizontal cross-section at each height. Longitudinal velocity perturbation, Fig. 4.17 a), show structures that appear to be smaller in size and more randomly located than MS94. Very close to the surface (*i.e.* below 0.1 km) structures present some similarity with the shear case. Concerning vertical velocity perturbation, Fig. 4.17 b) shows few strong updraft confirming previous observations (two are seen at $x = 0$ km and $x = 3$ km). Their structure clearly span the entire ABL and overshoot the inversion for the one at $x = 3$ km. Compared to a free convective case where convective plumes are rising vertically, here updrafts are slightly affected by shear which cause their deformation close to the surface. Finally, updrafts also concentrate most of large $u'w'$ (positive or negative) as seen in Fig. 4.17 b).

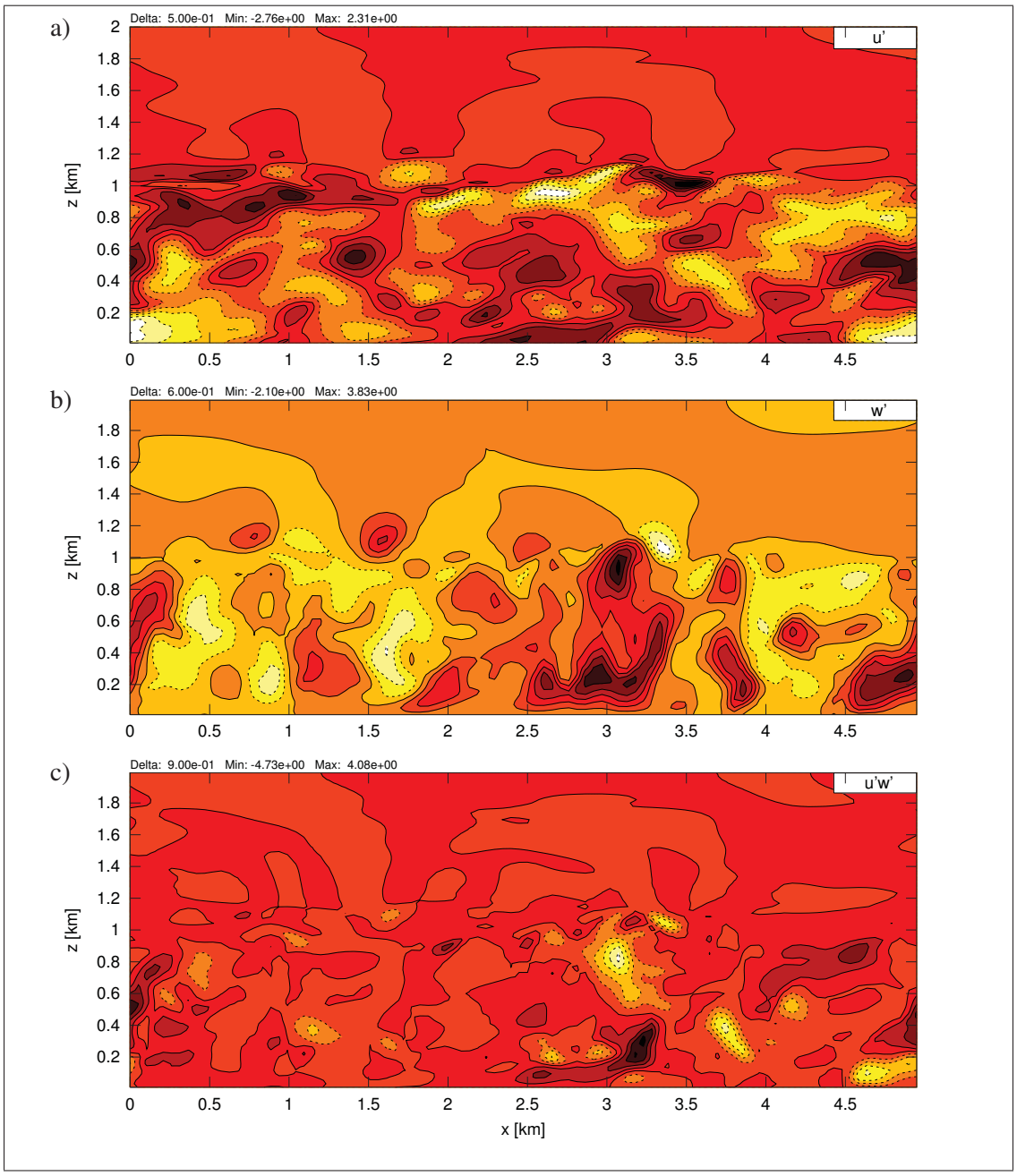

Figure 4.17 Instantaneous resolved-scales vertical cross-sections (x-z plane at $L_y/2$) from B_S at time $t = 2200$ s: a) u'; b) w'; c) $u'w'$. Contours legend as in Fig. 4.15

In Figs. 4.18 a) and b) which is equivalent to Moeng and Sullivan (1994, Figs. 6 d) and e)), the contour scale in notably different from MS94. The features obtained here are however qualitatively equivalent to MS94 in the mixed layer, *i.e.* positive perturbation regions located

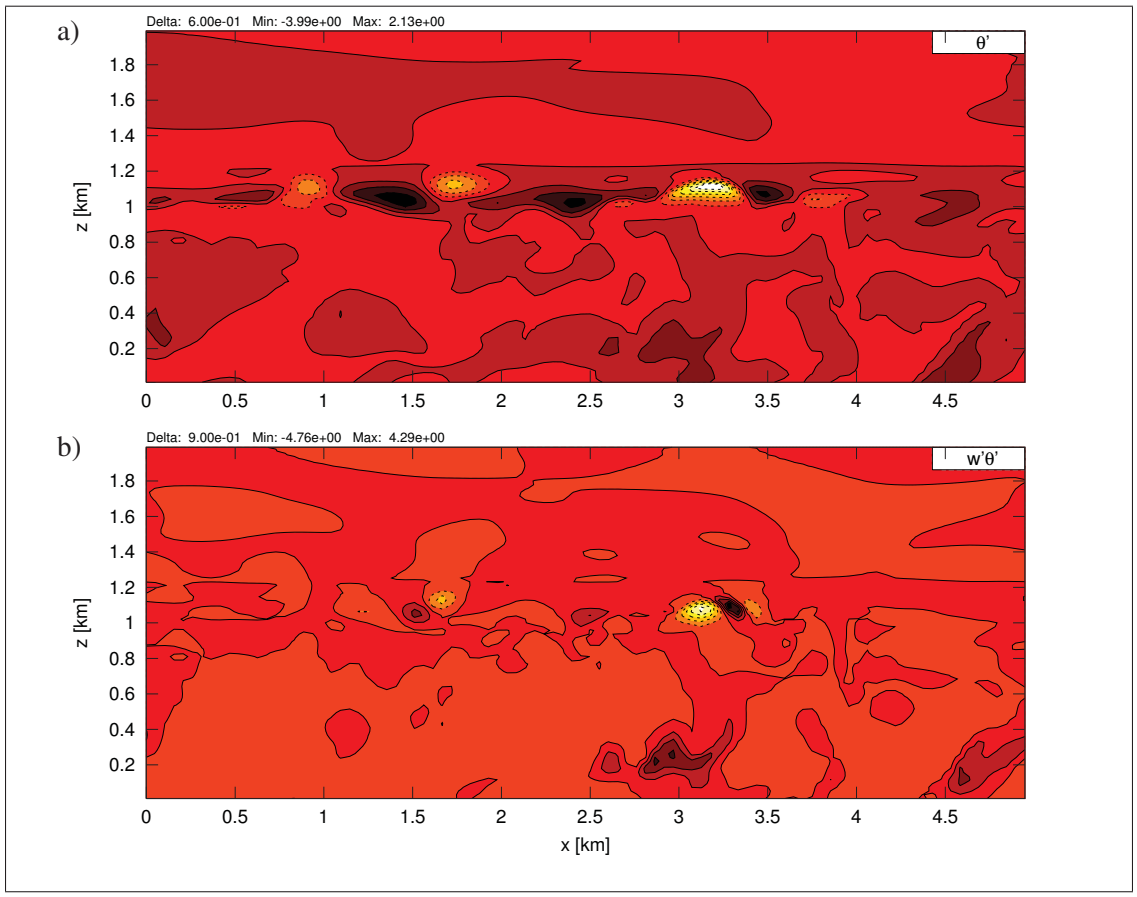

Figure 4.18 Instantaneous resolved-scales vertical cross-sections (x-z plane at $L_y/2$) from B_S at time $t = 2200$ s: a) θ'; b) $w'\theta'$. Contours legend as in Fig. 4.15

in updraft regions (see at $x = 3$ km). And a strong positive relationship is observed between vertical velocity and potential temperature leading to strong a positive $w'\theta'$ within the updrafts.

Another striking feature in Fig. 4.18 is the presence along the inversion of alternating strong positive/negative temperature perturbations (from -4 K to 2 K) to which correspond pairs of positive/negative heat flux. Those strong negative temperature perturbations are due to the updrafts that hit the inversion bringing with them air cooler than the environment (see at $x = 3$ km in Fig. 4.18 a)). Furthermore, hot air is pushed down (by continuity) which correspond to the strong positive temperature perturbations. This is the entrainment process (Deardorff, 1974; Stull, 1988; Sommeria, 1976; Sorbjan, 2005a). Finally, a neutral region is also found for

the B_S case just above the inversion (at $z = 1.225$ km). It is however, less notable than for the shear case. Sorbjan (2005a) free and force convective cases also present such a feature.

4.2.5 Near-surface behaviour

The ABL region close to the surface, *i.e.* the surface layer, is an area where LES models are prone to large errors due to the lack of flow resolution as shown in Fig. 4.19. For the shear case, only 60 % of the vertical momentum flux is resolved at the top of the surface layer, *i.e.* $0.1\, z_i$, while it is roughly 90 % for the buoyant case. This implies that the surface layer results are heavily influenced by the SGS model notably in neutral conditions. As discussed during the literature review, it can be seen as the Achilles' heel of LES models dedicated to the ABL. Furthermore, depending of the SGS model used and their adaptation, this error features a particular shape, as clearly illustrated in Porté-Agel *et al.* (2000); Chow *et al.* (2005).

The similarity theory provides analytical solutions (derived from empirical data) that were proven to be representative for the mean wind and temperature profiles in the surface layer of the ABL (Stull, 1988; Andren *et al.*, 1994; Chow *et al.*, 2005; Sorbjan, 2005a) over a homogeneous terrain. This theory is thus generally used to provide boundary condition of ABL flow models (which is the case for both the column model and the LES model presented here). However and as a side note, this latter practice is more controversial for use in LES since these law are only valid when considering the ensemble averaged velocity and temperature profiles (not unsteady) (Porté-Agel *et al.*, 2000; Redelsperger *et al.*, 2001; Drobinski *et al.*, 2004). The similarity theory is however a good reference for comparisons and one would expect to see a good agreement of numerical results with similarity in the surface layer.

In this subsection, near-surface results of the shear and convective cases are discussed and compared against both similarity theory and literature results. The same post-processing approach as in the previous section is used and the error bars show the envelope of the results based on the same model but with difference initial random velocity perturbations.

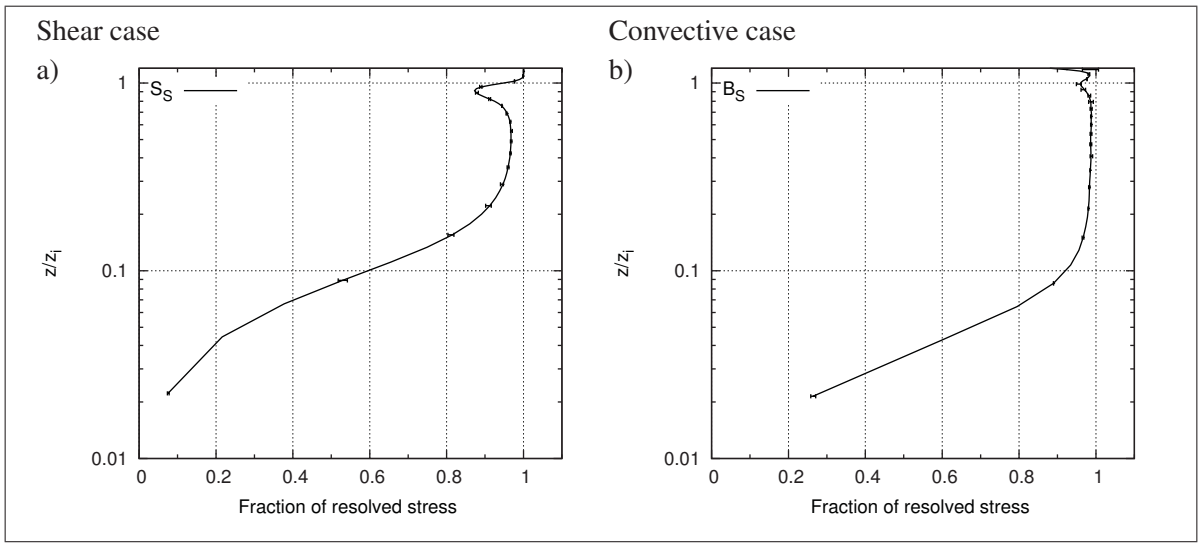

Figure 4.19 Ratio of resolved over total vertical momentum flux: a) shear case; b) convective case. Scatter as in Fig. 4.7

4.2.5.1 Non-dimensional wind velocity and shear

Fig. 4.20 shows vertical profile of non-dimensional wind velocity and shear for the neutral and convective cases. It includes theoretical solution from the similarity theory, results from the 1D column model, the Smagorinsky SGS model and from MS94 (*e.g.* Sullivan *et al.* (1994) more precisely) for both cases. Note that for the convective case, while error bars are plotted, the scatter between results is too small to be observed. Indeed, as underlined earlier, the spread between all results from the same model become negligible close to the surface.

From Fig. 4.20 a) and b), it is interesting to underline the differences between the column model and LES results, especially for the shear case. Indeed, for that case, in Fig. 4.20 a) (left) S_{1d} non-dimensional wind profile is closely following the log law profile up to $0.2\,z_i$ (100 m), while LES results clearly depart for the similarity above $0.02\,z_i$. This is in agreement with the non-dimensional wind shear, ϕ_M, shown in Fig. 4.20 b) (left): the 1D result follows the similarity up to $0.1\,z_i$ and then gradually deviates. At the opposite, the bias with the similarity for the LES results quickly rise from zero at the surface to a maximum at around $0.1\,z_i$ (height at which more the 50 % of the flow become resolved) and then decrease again up to $0.3\,z_i$.

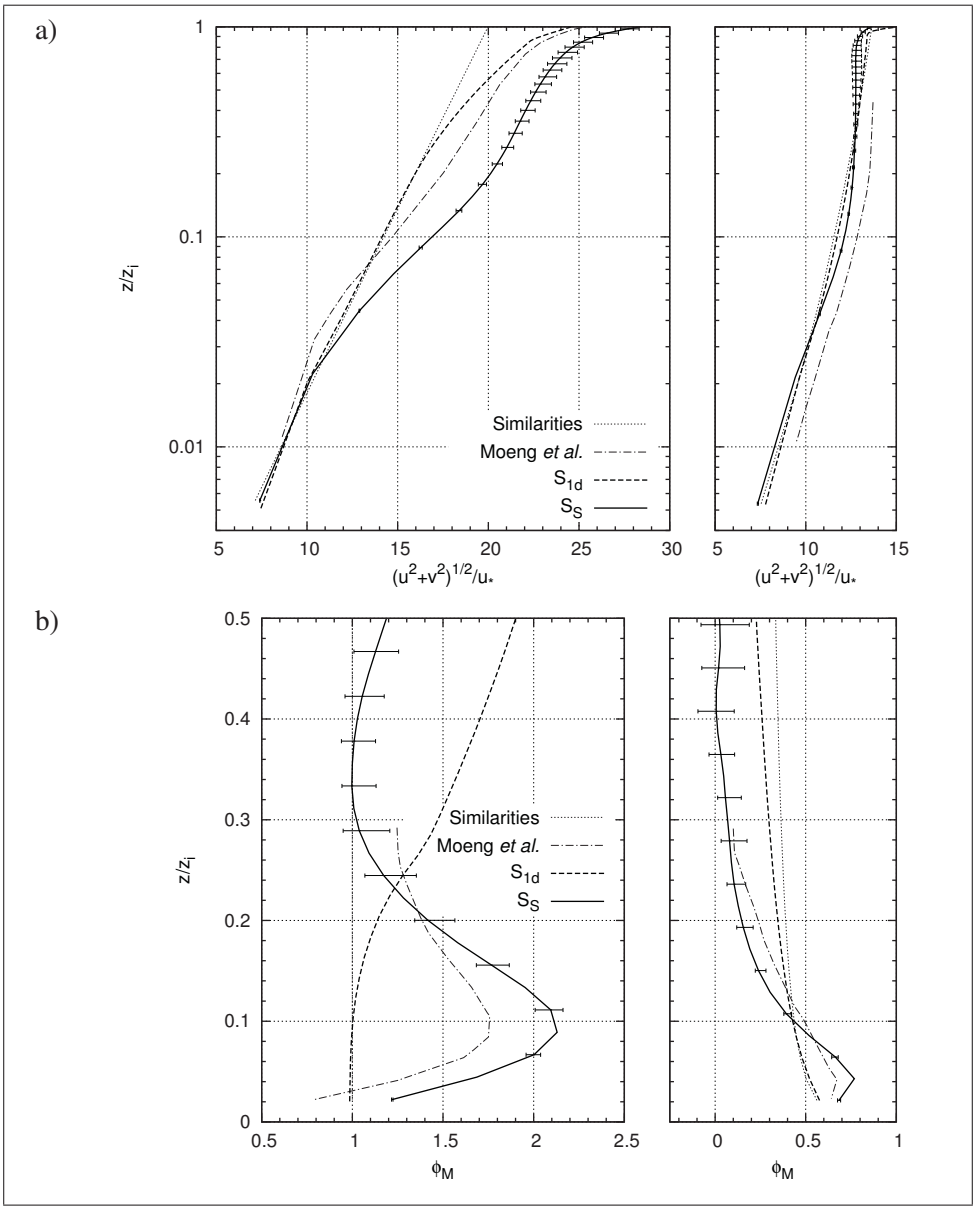

Figure 4.20 Near-surface profiles from the shear (left) and convective (right) cases: a) wind velocity; b) wind shear. Scatter is plotted every second mesh point

Concerning the convective case, the picture is changed since the near-surface flow is notably more resolved, and LES approaches rely less on the SGS model details than for the shear case. In Fig. 4.20 a) (right), results from all models are much closer (in comparison to the neutral case) and in agreement with similarity theory. Only MS94 results appears to feature

a constant shift with the present results. This shift is caused by the slightly higher value of v obtained here (for both the column and the LES model) and the lower value of u_* obtained by MS94. The non-dimensional wind shear of the convective case Fig. 4.20 b) (right) also feature a much better agreement between all results and similarity than the shear case. The column model superposes with similarity up to $0.1\ z_i$, while both LES approaches are in agreement and slightly overestimate (underestimate) the shear below (above) this height.

To explain the different behaviour of the LES and the column model close to the surface, few facts can be considered. On the one hand, 1D closure fluxes are fully modelled. They most of the time relying on the K-closure. On the other hand, LES turbulent fluxes are the sum of resolved and subgrid scale components. The first order SGS model also explicitly follows the flux-profile relationships, however, they are based on the hypothesis that the turbulence is homogeneous and isotropic (*i.e.* Kolmogorov hypothesis). This makes the definition of the mixing length and closure constant to differs between the two approaches as illustrated by Redelsperger *et al.* (2001): closure constants from column model are computed by matching similarity theory at the surface, while Kolmogorov hypothesis are used for SGS model.

Furthermore, due to the presence of the wall, eddy characteristic size becomes proportional with the distance to the wall as the latter is approached. As a consequence, if the LES does not resolve down to the viscous sublayer, the first few cells close to the surface have grid size that become approximately equivalent or larger than the largest eddies letting the flow to be fully unresolved, as illustrated in Fig. 4.19. This is far beyond the validity limit of the hypothesis used to obtains the SGS model definition. As a result, close to the surface, solution heavily rely on the SGS model while it is not anymore valid.

Considering the specific case of dissipative only SGS models such as the standard Smagorinsky SGS model and the TKE based SGS model, their over-dissipative nature tend to reduce the level of energy of the smallest resolved structures, as discussed by Porté-Agel *et al.* (2000). In the near-surface region, this tend to over reduce the resolved vertical turbulent mixing, which allows a higher vertical shear of horizontal velocity, resulting in a too low friction velocity. The

nose shape in the dimensionless wind shear is thus very typical of LES based on dissipative only SGS models (Andren *et al.*, 1994; Sullivan *et al.*, 1994; Porté-Agel *et al.*, 2000; Ding *et al.*, 2001a; Redelsperger *et al.*, 2001; Chow *et al.*, 2005; Piomelli, 2008). To avoid this error, the latter SGS model requires an adaptation to properly take into account the surface (wall) as it is illustrated in Andren *et al.* (1994); Sullivan *et al.* (1994); Piomelli (2008).

Researchers devoted many efforts to avoid this shortcoming, and while some solution were proposed at an early stage (Schumann, 1975), it is still an open field of research (Piomelli, 2008) that receive a lot of attention (Andren *et al.*, 1994; Sullivan *et al.*, 1994; Porté-Agel *et al.*, 2000; Ding *et al.*, 2001a; Redelsperger *et al.*, 2001; Chow *et al.*, 2005; Piomelli, 2008; Brasseur and Wei, 2010). Results from the proposed approach exhibit the very same features as equivalent models in the literature (Andren *et al.*, 1994; Sullivan *et al.*, 1994).

4.2.5.2 Non-dimensional temperature and temperature gradient

Similarly as in the previous section, but only for the convective case, Fig. 4.21 a) and b) compare respectively the non-dimensional potential temperature profile and the vertical gradient of potential temperature of B_{1d} and B_S with the similarity theory and MS94 (*e.g.* Sullivan *et al.* (1994) more precisely). In Fig. 4.21 a), all non-dimensional temperature profiles are in good agreement with a departure from the similarity always lower than half θ_* (*i.e.* 0.25 K). The present results however feature a nearly constant shift of roughly $+5\,\theta_*$, *i.e.* $+2.2$ K, with MS94. In fact, roughness length for temperature is five times smaller than the aerodynamic roughness z_0 in the present model (see Sec. 2.3). This quantity is used to diagnose the surface temperature (since a surface sensible heat flux is imposed) which explains the shift in the results. By off-line computing θ_s based on a temperature roughness that equals z_0 and relying on values from B_S in Tab. 4.2, one can obtain $\Delta\theta_1 = 2.9$ K, which is on part with the value obtained by MS94. However, considering the accessible information from Moeng and Sullivan (1994); Sullivan *et al.* (1994), surface temperature can not be directly compared [7].

[7] No surface temperature was provided by neither MS94 nor Sullivan *et al.* (1994), and only the non-dimensional profile of potential temperature, $(\theta - \theta_s)/\theta_*$, was accessible along with the surface layer temperature scale, $\theta_* = \overline{w'\theta'}_s/u_*$.

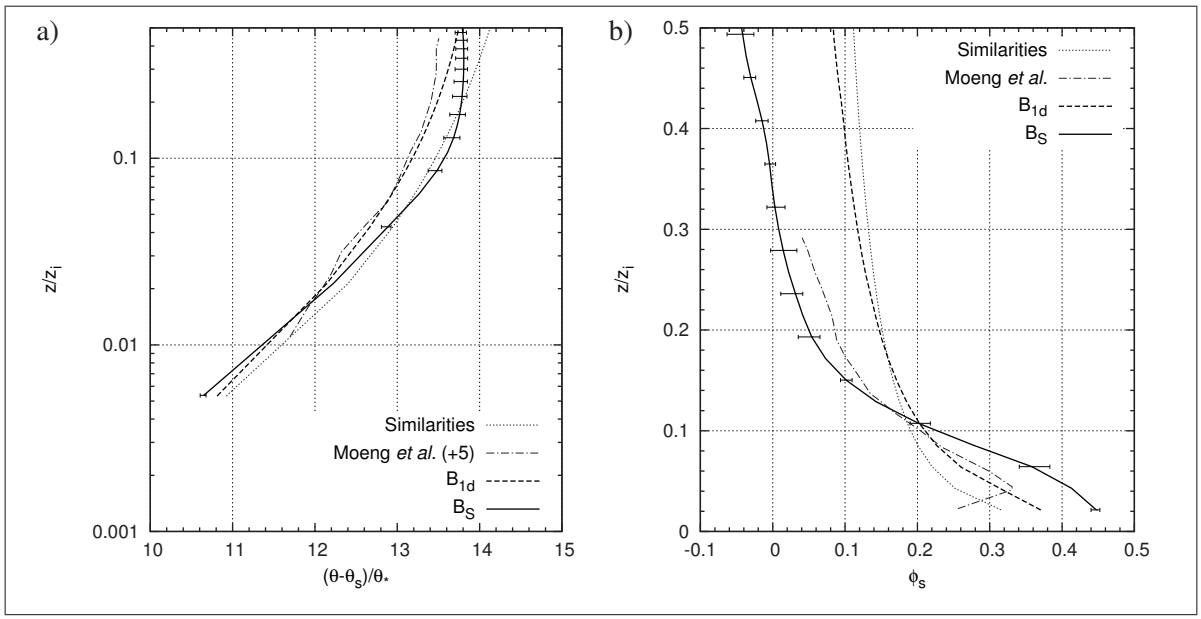

Figure 4.21 Near-surface profiles from the convective case: a) potential temperature; b) potential temperature vertical gradient. Scatter as in Fig. 4.20

Concerning the profile of dimensionless vertical gradient of potential temperature in Fig. 4.21 b), a good agreement is also obtained between all the approaches: column model result is closer to the similarity, while both LES results show the same features (MS1994 results being slightly better). Temperature gradient is overestimated (underestimated) below (above) $0.11\,z_i$ for MS94 and B_S. This figure confirms that the shift in MS94 result in Fig. 4.21 a) is roughly constant since the vertical temperature gradient from both LES model is similar.

As a conclusion, a good agreement is obtained for near-surface potential temperature between similarity, B_{1d}, B_S and MS94. As for the momentum, potential temperature obtained by means of the column model is the closest to the similarity, then come MS94 results closely followed by B_S. Only the post-processed surface temperature of B_S and B_{1d}, which are diagnosed, differs from MS94 due a different roughness associated to heat processes in MC2.

4.2.6 Velocity spectra

Turbulent flow energy and velocity spectra contain an large amount of information as thoroughly explained by Pope (2000). Some of this information can only be retrieved by means of a spectral analysis. As a result and for the sake of completeness, the analysis and evaluation of a LES method requires the latter analysis (Nieuwstadt *et al.*, 1992; Andren *et al.*, 1994).

In the present section, theoretical spectral model and numerical results from other authors are first introduced. They serve as a basis of reference in a second section where velocity spectra from S_S and B_S cases are evaluated. In that second section, shear results are first discussed followed by the results from the convective case.

4.2.6.1 Velocity spectra comparison background

As introduced in Appendix II, an energy cascade from the big eddies, that produce and transport the kinetic energy, to the smallest ones, that dissipate it, take place in turbulent flows. This cascade can be conveniently represented under a spectral form as seen in Fig. II-1.

Inertial subrange

In the high wave numbers, *i.e.* the smallest structures, one can demonstrate from the two first Kolmogorov hypothesesthat, regardless of the thermal stratification, energy spectra in the inertial subrange is equal to $E(k) = C_{Kol}\varepsilon^{2/3}k^{-5/3}$ where k is the wave number and C_{Kol} is the universal Kolmogorov constant (found experimentally to be equal to $1.5 - 1.6$). In the context of isotropic turbulence, one dimensional velocity spectra (longitudinal and transverse) also retain the same slope (for any velocity components) and only the proportionality constant is changed (cf. Pope (2000, Sec. 6.5.2)). The streamwise and spanwise velocity component longitudinal spectra can be expressed as

$$k_x E_u(k_x) = C_1\varepsilon^{2/3}k_x^{-2/3} \tag{4.7}$$

$$k_x E_v(k_x) = C_1'\varepsilon^{2/3}k_x^{-2/3} \tag{4.8}$$

where $k_x = 2\pi N_i / L_x$ is the longitudinal wave number, $C_1 = 18/55\, C_{Kol}$ and $C_1' = 24/55\, C_{Kol}$ (*i.e.* $C_1'/C_1 = 4/3$ thus $E_u(k_x) = 3/4\, E_v(k_x)$). The Kolmogorov spectra model was verified experimentally by many authors and shown to exist regardless of the thermal stratification and the height in the ABL (Stull, 1988; Nieuwstadt *et al.*, 1992; Andren *et al.*, 1994; Mason and Brown, 1999; Porté-Agel *et al.*, 2000; Brown *et al.*, 2000; Drobinski *et al.*, 2004). Furthermore, Busch and Panofsky (1968) found based on full scale ABL measurements, that in the inertial subrange, the ratio of $4/3$ between C_1 and C_1' (*i.e.* ratio between E_u and E_v) clearly hold and that the ratio between E_u and E_w was likely to be of a same amount (leading to $E_u(k_x) = 4/3\, E_v(k_x) = 4/3\, E_w(k_x) = 18/55\, E(k)$) (Drobinski *et al.*, 2004).

In the context of LES, one could further consider the properties of the LES filter involved (as illustrated in Fig. II-4) as well as the finite and discrete nature of the numerical results, to obtain an analytical expression of the theoretical energy spectra of the inertial subrange (Moeng and Wyngaard, 1988; Pope, 2000). The latter is more consistent with model results notably close to the cut-off wave number where it exhibits a smaller slope than $-5/3$ (see Fig. II-4 and Moeng and Wyngaard (1988)). This approach is however rarely followed in the literature and the $-5/3$ is most of the time preferred (Nieuwstadt *et al.*, 1992; Andren *et al.*, 1994; Mason and Brown, 1999; Porté-Agel *et al.*, 2000; Brown *et al.*, 2000; Drobinski *et al.*, 2004).

Low wave numbers and transition

Spectra shape in the low wave numbers is largely influenced by the distance from the ground (Drobinski *et al.*, 2004) and large scale flow properties and forcing (Nieuwstadt *et al.*, 1992; Andren *et al.*, 1994; Drobinski *et al.*, 2004). As opposed to the inertial subrange, no universal theory exists and the picture is less clear. In the mixed layer (*i.e.* region between the surface layer and the inversion), there are however evidence that the longitudinal energy spectra of low wave numbers become constant with k_x (Busch and Panofsky, 1968; Drobinski *et al.*, 2004) for all velocity components (*i.e.* $k_x E_u(k_x) \propto k_x E_v(k_x) \propto k_x E_w(k_x) \propto k_x^{+1}$). Closer to the surface (lowest part of the mixed layer and surface layer), a region with the same constant slope (*i.e.* $k_x E_{u_i}(k_x) \propto k_x^{+1}$) has also been observed in the lowest wave numbers for all velocity

components as discussed by Drobinski *et al.* (2004). However, in the surface layer (and above 10 m) transition from the lowest wave numbers to the inertial subrange can feature a plateau with $k_x E_{u_i}(k_x) \propto k_x^0$ (see Drobinski *et al.* (2004, Fig. 9)). According to the latter study, the plateau starts at $k_x = u_*/uz_i$ which gives $k_x = 2.4 \times 10^{-4}$ m^{-1} for S_S using Tab. 4.2 parameters. Thus, $L_x \simeq 24$ km using $k_{x_{min}} = 2\pi/L_x$ which, in other words, would be the domain size required for $k_x E_{u_i}(k_x)$ to reach the $+1$ slopes at the first level above the surface. Following Drobinski *et al.* (2004) suggestions, surface layer spectra from S_S and B_S should only feature $k_x E_{u_i}(k_x) \propto k_x^0$, while $k_x E_{u_i}(k_x) \propto k_x^{+1}$ is not likely to be present as L_x (the horizontal domain size) of both shear and convective cases is too small.

In the surface layer, E_w also shows an increase of the energy with height (Mason and Brown, 1999; Brown *et al.*, 2000) in the low wave numbers while E_u and E_v does not have such an increase. This feature is clearly illustrated by Mason and Brown (1999); Brown *et al.* (2000); Ding *et al.* (2001a) for both shear and convective cases using various configurations of a standard Smagorinsky SGS model. In that sense, the latter studies can serve as reference to quantitatively evaluate the results of the present model.

Finally, concerning the transition to the inertial subrange, it is known to evolve with height such as, in neutral conditions, its location should be roughly constant with zk_x such as $zk_x \simeq 0.6-1$ for $E_u(k_x)$ and $zk_x \simeq 2.7 - 3.1$ for $E_w(k_x)$ (Porté-Agel *et al.*, 2000; Drobinski *et al.*, 2004). Furthermore, it was shown experimentally in neutral conditions that by plotting velocity spectra against zk_x on a log-log graph and normalizing them by zu_*^2 such as presented by Porté-Agel *et al.* (2000), a merge of the spectra in two linear region, $E_u(k_x) \propto k_x^{-1}$ and $E_u(k_x) \propto k_x^{-5/3}$ is observed. The transition between the two linear region is located at the transition to the inertial subrange. Those features conveniently allow for a quantitative comparison of, at the same time, the velocity spectra at various wave numbers as well as at various heights. Porté-Agel *et al.* (2000) successfully applied these criteria (primarily obtained for a turbulent pipe flow) to analyze various LES of a neutral ABL. In his study, Smagorinsky SGS model ranging from the standard one (based on various C_S values) to a state-of-the-art scale-dependent dynamic SGS model were analyzed. Although the ABL they are simulating is more idealized (only mo-

mentum is solved, friction velocity is imposed and constant, and Coriolis factor is not present), it is an interesting basis of comparison that illustrates the limitation of the Smagorinsky SGS model (*i.e.* departure from the theory above) and the spectral signature of the latter model.

Summary

As a summary of the above and regardless of the stratification and the velocity components:

- $k_x E_{u_i}(k_x) \propto k_x^{-2/3}$ is a good reference in the inertial subrange at all heights;
- $k_x E_{u_i}(k_x) \propto k_x^{+1}$ is a good reference in the low wave numbers but only in the mixed layer. Surface layer low wave number velocity spectra shape are more complex (see Drobinski *et al.* (2004, Fig. 9)).

Note however that the above mentioned reference spectra slope (notably in the low wave numbers) are based on theoretical consideration and experimental measurements. When considering LES results found in the literature, the picture is however somewhat changed due to the limitation inherent to the methods and SGS models (Mason, 1989; Nieuwstadt *et al.*, 1992; Andren *et al.*, 1994; Mason and Brown, 1999; Porté-Agel *et al.*, 2000; Brown *et al.*, 2000; Ding *et al.*, 2001a; Cuxart *et al.*, 2000). As an example, the over-dissipative nature of the Smagorinky SGS model tend to make velocity spectra falloff in the high wave number much quicker than observed and predicted by Kolmogorov theory (Mason and Thomson, 1992; Porté-Agel *et al.*, 2000). As a result, in the discussion of the velocity spectra from S_S and B_S, while experimental and theoretical results serve as reference, LES results from other studies based on similar cases and SGS models are always taken into account.

4.2.6.2 Spectra processing and figures

All the velocity spectra presented in this section, Figs. 4.22 to 4.25, are one dimensional longitudinal velocity spectra, *i.e.* $E_{u_i}(k_x)$. They are referred to as "spectra" and denoted E_{u_i}. At each height, spectra are computed from the spanwise average of the squared amplitude of the longitudinal (one-dimensional) Fourier transforms of a given velocity component perturbation.

They are then averaged in time (same time windows as MS94). In addition, the ensemble average of five results for which only initial random velocity perturbations differ is also done. Finally, spectra are normalized based on parameters presented in Tab. 4.2.

Every figures include both shear case S_S and convective case B_S results. In Figs. 4.22, 4.23 and 4.24 spectra are normalized by $1/z_i$ and u_*^2/k_x (w_*^2/k_x for the convective case), while $1/z$ and zu_*^2 (zw_*^2 for the convective case) is used in Fig. 4.25 in order to observe a merging of the spectra (Porté-Agel *et al.*, 2000) and further evaluate the location of the transition to the inertial subrange at various heights(Drobinski *et al.*, 2004). Fig. 4.22 show spectra of the three velocity components at several heights from the surface to the upper mixed layer. To better compare spectra of the various velocity components at the same height, Fig. 4.23 shows, on the same graph, E_u, E_v and E_w in the centre of the ABL (centre of the mixed layer) along with the discrete top-hat filtered Kolmogorov spectra corresponding to the inertial subrange of E_u and E_v (grey curves, see Moeng and Wyngaard (1988) for a detailed expression of the latter). Finally, Fig. 4.24 presents a comparison of E_w with Mason and Brown (1999); Brown *et al.* (2000). This figure further illustrates E_w spectra at several heights along with the associated scatter of the five results used in the ensemble average.

The discussions of the results are organized using the following criteria: low/high wave numbers and well resolved/near-surface regions. The inertial subrange is initially discussed, first in the well resolved region and then in the near-surface region. Low wave numbers and the transition to the inertial subrange are then assessed following the same sequence. Finally, Fig. 4.25 comes as a summary as scaling mix both wave numbers and height agl.

4.2.6.3 Shear case

Concerning the shear case in the well resolved region, *i.e.* the mixed layer, all spectra reach the inertial subrange slope and superpose each over the others but the curves quickly falloff in the higher wave numbers as shown on dash-dot and solid black curves in Fig. 4.22 a), c) and e) and Fig. 4.25 a), c) and e), in Fig. 4.23 a), and finally in Fig. 4.24 a).

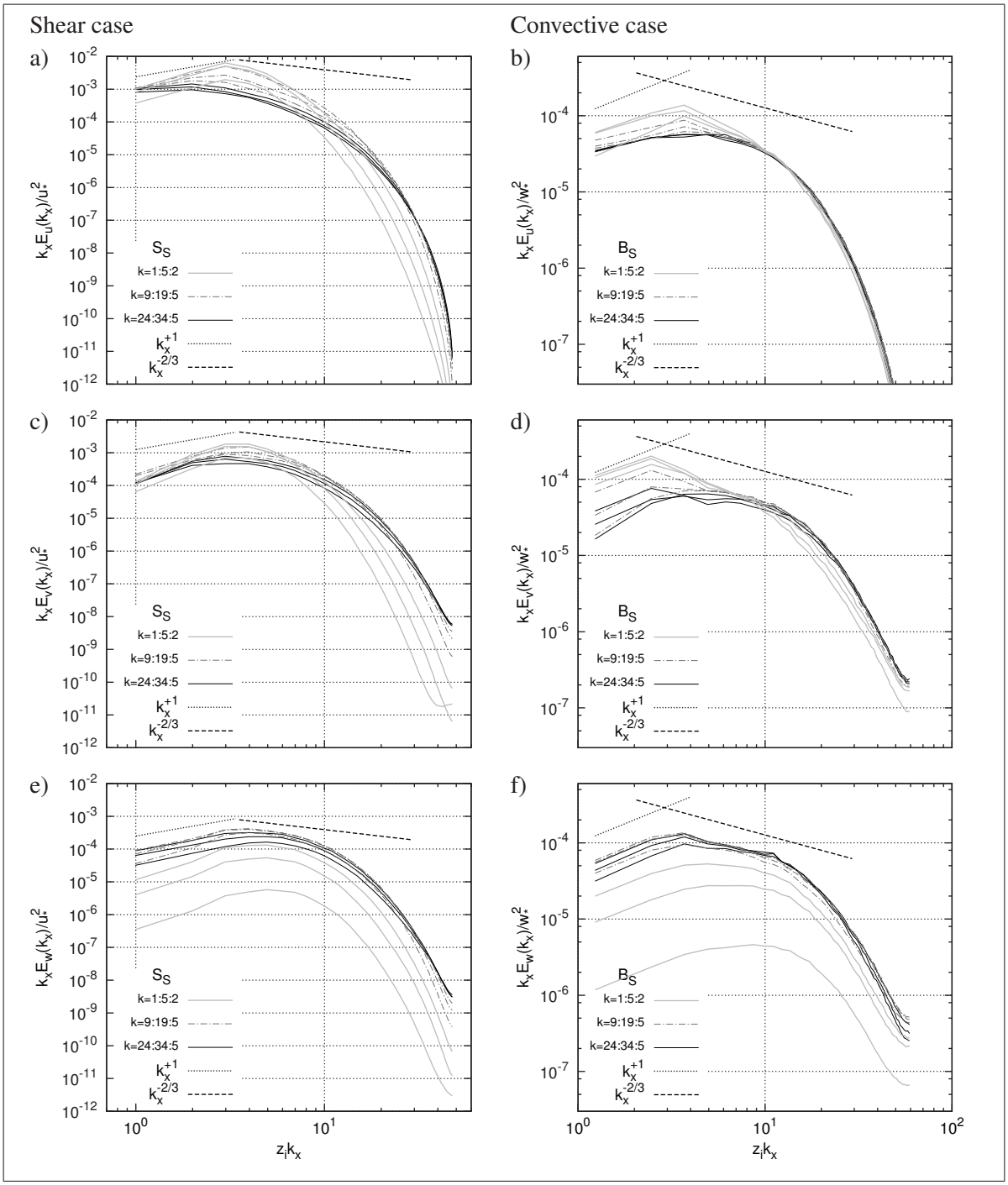

Figure 4.22 Longitudinal spectra of the three velocity components: a), c) and e) shear case; b), d) and f) convective case. Grey solid lines show spectra at $k = 1, 3, 5$ vertical levels indices (surface layer), dash-dot black spectra at $k = 9, 14, 19$ (lower mixed layer) and black solid spectra at $k = 24, 29, 34$ (upper mixed layer). Reference lines, k_x^{+1} and $k_x^{-2/3}$, are located arbitrarily

This is in good agreement with spectra shown in the literature (based on similar SGS model and numerical parameters) (Andren *et al.*, 1994; Brown *et al.*, 2000; Ding *et al.*, 2001a), and it indicates that the mesh is refined enough for the filter to be located at the beginning of the inertial subrange. A coarser mesh might not be fined enough while a finer mesh would definitely allows to better reproduce the $-5/3$ slope (Andren *et al.*, 1994).

A more detailed picture of the mixed layer is presented in Fig. 4.23 a) where E_u, E_v and E_w from the middle of the ABL are shown on the same graph along with the discrete top-hat filtered Kolmogorov spectra computed relying on the averaged dissipation at the proper height (see Appendix 2.2.2; Moeng and Wyngaard (1988); Pope (2000)). On that figure, it can be seen that, while S_S results depart from the theory at high wave numbers (notably for E_u), the predicted energy level in the inertial subrange is in agreement with Kolmogorov theory, *i.e.* theoretical spectra are nearly tangent to the energy spectra obtained from the LES results (notably for E_w, E_u and E_v feature more energy). In addition, an offset of around $4/3$ is also present between E_u and E_v/E_w (for $10 < zk_x < 30$), but E_u falloff is more rapid than E_v and E_w that are parallel and very close in the whole inertial subrange as predicted by the theory.

Comparing Fig. 4.23 a) with Moeng and Wyngaard (1988, Fig. 4) (that shows a much better fit with the discrete filtered Kolmogorov spectra, albeit for a convective case), S_S results appear to feature a much higher dissipation of the finest scales. Indeed, the falloff of all the spectra is much quicker for S_S which feature notably less energy in the high wave numbers than Moeng's spectra. However, it is noteworthy that Moeng's approach is based on a mixed pseudo-spectra finite-difference method, *i.e.* finite differencing in the vertical and pseudo-spectral differencing in the horizontal. The latter require an explicit filtering of the main variables of the model allowing a better control. Furthermore, these approaches are known to better conserve the energy of eddies up to the cut-off wave number. This contrast with finite differencing approach that implicitly include a filter on which no control is allowed and that also dissipate the energy of eddies larger than the cut-off. It thus partly explains the differences between S_S and Moeng and Wyngaard (1988, Fig. 4) in the highest wave numbers.

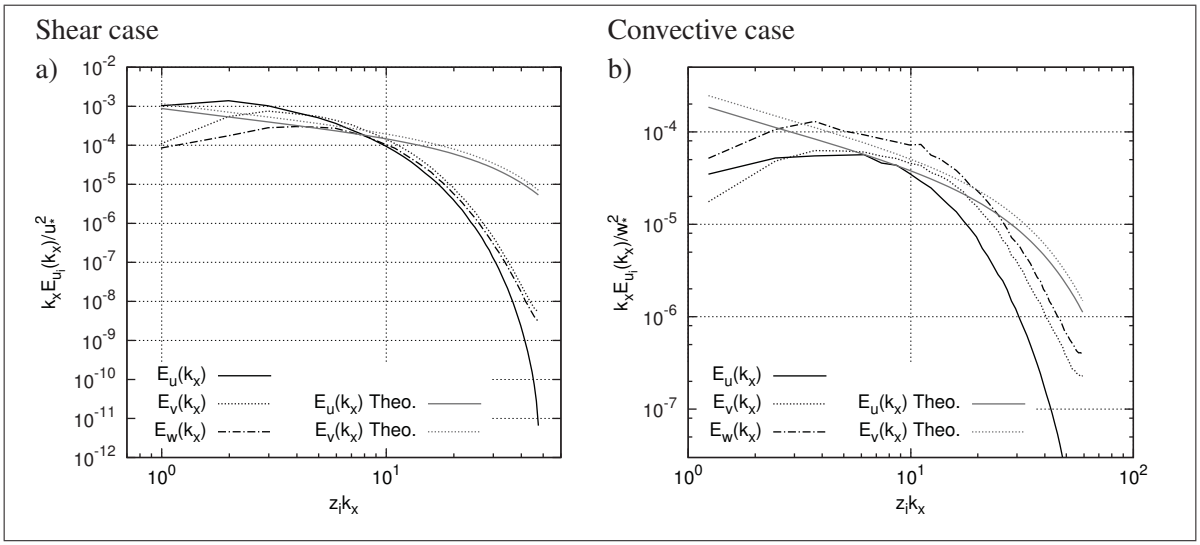

Figure 4.23 Longitudinal spectra of the three velocity components in the centre of the ABL: a) shear case ($k = 24 \sim z = 250$ m); b) convective case ($k = 24 \sim z = 500$ m). Reference spectra (Theo.) shows the discrete top-hat filtered Kolmogorov spectra

Furthermore, as shown by Andren *et al.* (1994), model with lower SGS eddy diffusivity, K_M, leads to a spectral peak that is moved to higher wave numbers, with a steeper falloff (*i.e.* differences between Andren/Moeng/Nieuwstadt and Mason/Brown/Schumann/Graf in Andren *et al.* (1994, Fig. 15)). S_S results feature a lower K_M than Moeng and Sullivan (1994) (not shown here, but compared with Sullivan *et al.* (1994, Fig. 1)), thus further explaining the steeper falloff in comparison to Moeng and Wyngaard (1988, Fig. 4).

In the near-surface region, grey solid curves in Fig. 4.22 a), c) and e), Fig. 4.25 a), c) and e) and in Fig. 4.24 a), the spectra falloff happens sooner than in the mixed layer. Indeed, in Fig. 4.22 a), c) and e) the $-5/3$ slope region is almost absent and the spectra are not merging at the high wave numbers. Comparing with Brown *et al.* (2000) and Ding *et al.* (2001a), it can be seen that a very similar evolution of the spectra with height is obtained for S_S (albeit E_u falloff is quicker in the present results). It thus clearly shows that, as expected in this region of the ABL (see Sec. 4.2.5), the mesh is too coarse in order to properly resolve and reproduce the near surface flow, and that the SGS model is clearly used beyond the limit of it validity envelope (Andren *et al.*, 1994; Porté-Agel *et al.*, 2000; Brasseur and Wei, 2010).

Concerning the lowest wave numbers in Fig. 4.22 a), c) and e), the slope of E_u evolves with height from $k_x E_u \propto k_x^2$ at the surface to $k_x E_u \propto k_x^0$ in the mixed layer; the slope of $k_x E_v$, while constant with height, is roughly equal to k_x^2; and finally, $k_x E_w \propto k_x$ is clearly reproduced in the mixed layer, but it increases to k_x^2 at lower height, see Fig. 4.22 e) and Fig. 4.25 e). Those values, while of the same order of magnitude, does not reproduce the reference slope except for E_w in the mixed layer. However, as Andren *et al.* (1994); Ding *et al.* (2001a), the spectra peak of E_u is most of the time located at the lowest wave number at that height (leading to a slope of k_x^0). Furthermore, as Ding *et al.* (2001a); Mason and Brown (1999); Brown *et al.* (2000), E_u and E_v show a slight decrease of the energy with height (lowest wave number and spectra peak) as opposed to E_w that features a clear increase of energy with height for the lower wave numbers (which is in agreement with the profile of the resolved variances). Thus, as in the previously mentioned studies, surface spectra cross mixed layer spectra in the middle range wave numbers for E_u and E_v, while surface spectra never cross mixed layer spectra for E_w.

In order to further study the impact of height above the ground on the whole spectra, Fig. 4.24 a) shows E_w obtained from S_S at various heights (from the surface up to above the inversion) along with results from Brown *et al.* (2000, Fig. 7 (Y08)). It this study, Andren *et al.* (1994) test case was reproduced based on the standard Smagorinsky model studying various numerical parameters. The Y08 case results were chosen for comparison as they have the closest parameters to S_S with $\Delta x = 53.3$ m and $C_S = 0.15$. Results from Brown *et al.* (2000) nearly superpose with S_S However, Brown *et al.* (2000) Y08 case feature a coarser resolution than S_S with an equal Smagorinsky constant, which implies, seeing Fig. 4.24 a), that the present model is more dissipative (Mason and Brown, 1999). The low wave number in the mixed layer tend also to show more energy in Brown *et al.* (2000), but this might be due to the fact that their case feature a notably different upper ABL (ABL is taller without inversion). Finally in Fig. 4.24 a) and aside from the comparison with Brown, it is interesting to comment on the shape of the spectra above the inversion. Indeed, the latter shows an earlier falloff which is extremely fast confirming that there are no small structures and that the flow is almost laminar in the free atmosphere.

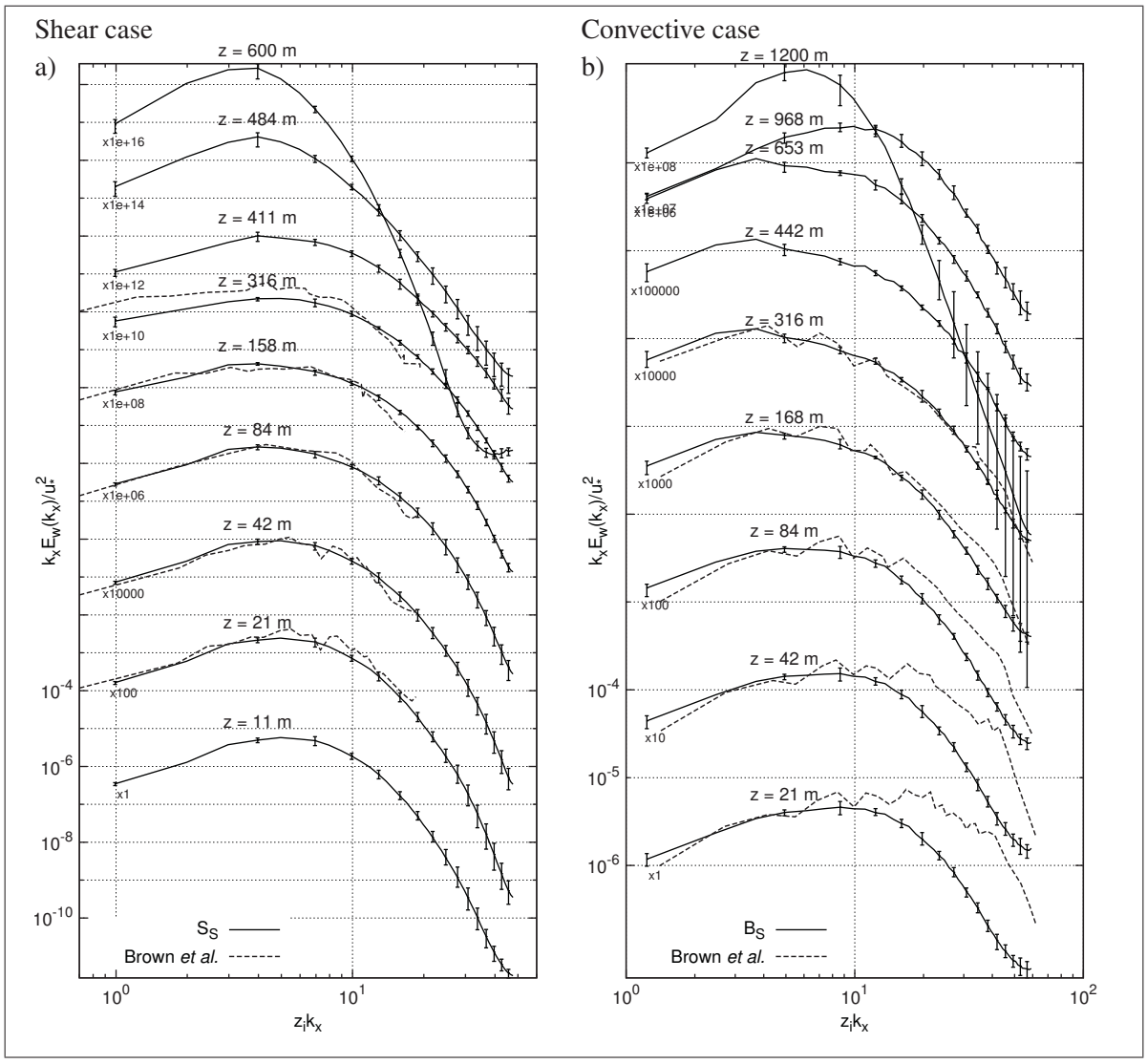

Figure 4.24 Longitudinal spectra of vertical velocity at various heights: a) shear case; b) convective case. A vertical shift is applied as shown on the left of each spectra. Scatter is plotted every third mesh point

The scatter, as shown for E_w in Fig. 4.24 a) (E_u and E_v present similar features), is generally not significant notably close to the surface in the low wave numbers, and in the mixed layer for all wave numbers. It is the highest in the surface layer at high wave number, and at the inversion and above for almost all wave numbers. Interestingly, the scatter obtained for both the velocity variances and the TKE profiles in Fig. 4.8 c) and e) is slightly larger in the mixed layer than at the surface, which tends to differ from the scatter of the spectra.

Finally, in Fig. 4.25 a) c) and e), a merge of the spectra is observed for all velocity components similarly to what obtained by Porté-Agel *et al.* (2000, Fig. 5 b)) with a standard Smagorinsky SGS model. Two linear regions (with a slope around k_x^{-1} and $k_x^{-5/3}$) are present in the merge spectra of E_u and E_v with a clear transition located at $0.6\,zk_x$. This transition, which also represent the height at which spectra reach effectively the inertial subrange, roughly coincide with the peak of the spectra at $z/z_i = 0.2$ (*i.e.* $k = 9$). At that height, 90 % of the flow is resolved (see Fig. 4.19 a)). Below that height, spectra do not reach the inertial subrange, while above that height, they feature a clear transition to the inertial subrange located between $0.6\,zk_x$ and $1.0\,zk_x$. This is in agreement with the suggestion of Drobinski *et al.* (2004) as illustrated by the reference curves k_x^{-1} and $k_x^{-5/3}$ (that were located in order to cross at the expected transition to the inertial subrange in neutral conditions (Porté-Agel *et al.*, 2000; Drobinski *et al.*, 2004)). Results of the spanwise velocity component are in very good agreement with reference slopes and transition location (albeit the slope for $zk_x > 0.6$ is slightly higher). Streamwise velocity component merge spectra is also in agreement with the k_x^{-1} slope below $0.6\,zk_x$, however, the slope in the inertial subrange is too high (in agreement with the previous remarks).

Comparing Fig. 4.25 a) and c) with Porté-Agel *et al.* (2000, Figs. 5 a) and b)) that feature a domain twice as large, a notably coarser resolution with $\Delta x = 116$ m, and $C_S = 0.1$ and 0.17, while the general feature are recovered, slope of the spectra in the low wave number differ and spectra falloff seem to append sooner notably for E_u. Considering the Δx and C_S values used by Porté-Agel *et al.* (2000), and following the analysis from Mason and Brown (1999); Brown *et al.* (2000), it can be conclude that the present method appears to be more dissipative. However, it is noteworthy that as Moeng and Wyngaard (1988), Porté-Agel *et al.* (2000) is based on a mixed pseudo-spectra finite-difference method, which may be the explanation for the faster falloff of the spectra obtained with the present model.

Concerning the longitudinal spectra of the vertical velocity component, a merging of the curve is also observed in Fig. 4.25 e). In the low zk_x, spectra collapse perfectly at the lowest wave number to a line with a slope of $2/3$ (which contrast with E_u and E_v). The same feature is obtained by rescaling Brown *et al.* (2000) results shown in Fig. 4.24 a). The merging spectra

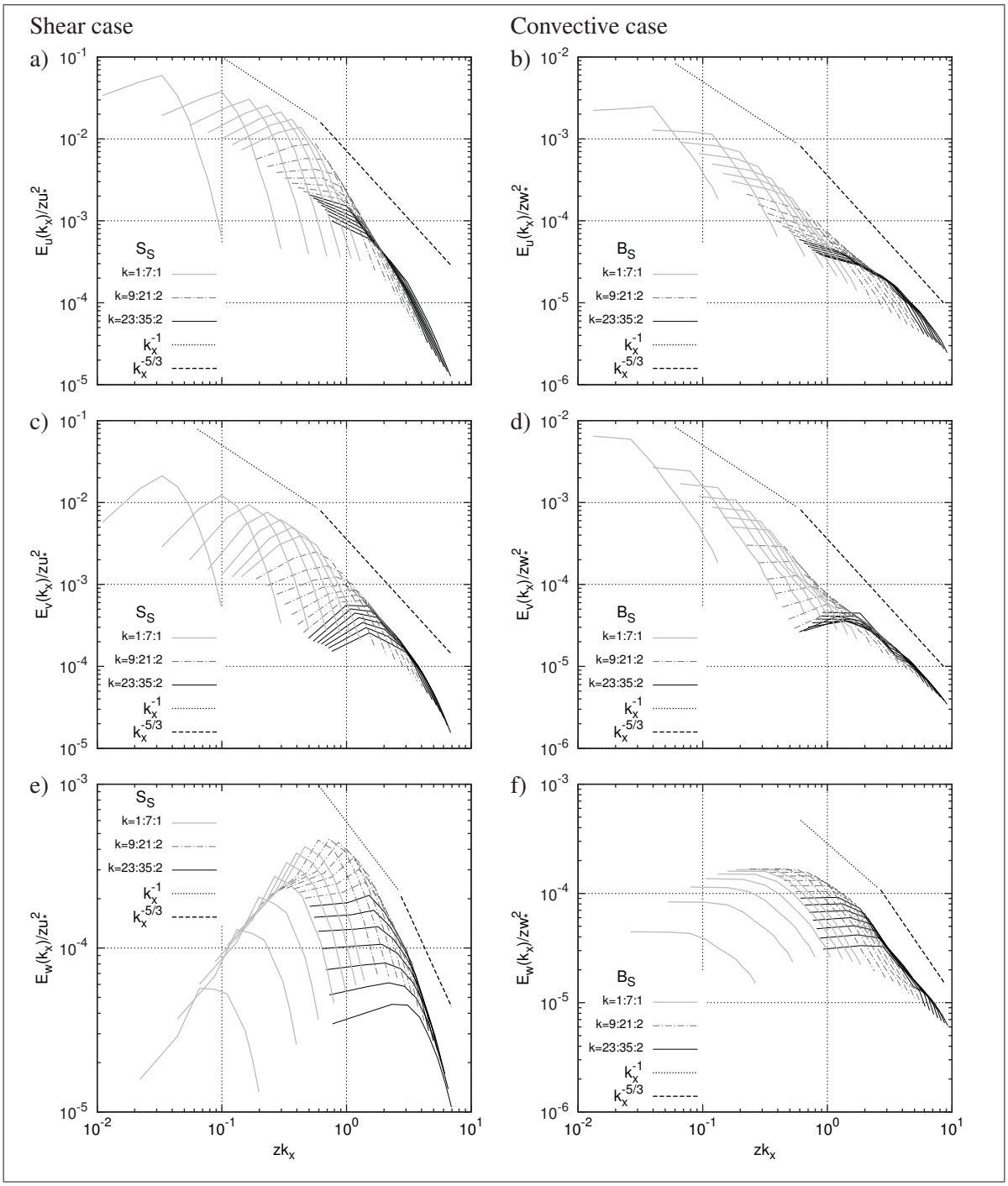

Figure 4.25 Longitudinal spectra of the three velocity components plotted against zk_x: a), c) and e) shear case; b), d) and f) convective case. Grey solid spectra show level indices $k = 1$ to 7 (surface layer), dash-dot spectra $k = 9$ to 21 every first index (lower mixed layer) and black solid spectra $k = 23$ to 35 every first index (upper mixed layer). Only the nine lowest wave numbers are shown

reaches a maximum at around $0.6\,zk_x$, followed by a decrease with a slope of k_x^{-1} that change to $k_x^{-5/3}$ after $1.2\,zk_x$. The constant slope regions are not well defined and two transitions (at $1.2\,zk_x$ and $3\,zk_x$) seems to be present (with a slightly higher slope than $k_x^{-5/3}$ in between).

As a conclusion it is to say that, besides the faster E_u falloff in the highest wave numbers, spectra from the shear case S_S are in agreement with theory and results found in the literature for similar SGS model, *i.e.* Andren *et al.* (1994); Brown *et al.* (2000); Porté-Agel *et al.* (2000); Ding *et al.* (2001a); Drobinski *et al.* (2004). However, the present model appears to be more dissipative than the model used for the comparisons. This is not of concern in the well resolved regions (Brown *et al.*, 2000), but the near-surface region may be affected, and it is most likely to be the cause of the higher deviation from the similarity theory at the surface than Moeng and Sullivan (1994); Sullivan *et al.* (1994).

4.2.6.4 Convective case

Concerning the convective case in the well resolved region, all spectra clearly merge each others in the higher wave numbers reaching the inertial subrange slope as shown on dash-dot and solid black curves in Fig. 4.22 b), d) and f), in Fig. 4.25 b), d) and f), in Fig. 4.23 b), and finally in Fig. 4.24 b). In that sense, E_w shown in Fig. 4.22 f), features a better well defined and prolonged $k_x^{-5/3}$ slope (from 4 to $12\,z_i k_x$) than the slightly less clear one of E_u and E_v, Fig. 4.22 b) and d). Thus, within the mixed layer the filter is correctly located in the inertial subrange. This is also in agreement with results shown in the literature (Mason, 1989; Nieuwstadt *et al.*, 1992; Brown *et al.*, 2000; Cuxart *et al.*, 2000). In comparison to the shear case, the inertial subrange slope is better defined and the spectra falloff is notably slower.

In Fig. 4.23 b), E_u and E_v are perfectly tangent with the discrete filtered Kolmogorov spectra and the offset between E_u and E_v in the inertial subrange is in good agreement with the theory (except for E_w that should superpose E_v) and very similar to the one obtained by Moeng and Wyngaard (1988); Mason (1989) (that feature a E_w with more energy than E_v). The falloff of spectra tail is quicker than the theory (but to a lesser extent than in the shear case). Furthermore, the longitudinal spectra of the streamwive velocity component show a steeper falloff at high

wave number than the other two components that are nearly parallel (as for the shear case). Mason (1989, Fig. 20) results show the same feature for E_u. A quantitative comparison of E_w with Brown *et al.* (2000, Fig. 6 (D14)) is presented in Fig. 4.24 b). On that figure, results in the mixed layer nearly superpose with Brown *et al.* (2000). Brown's D14 case is based on a similar horizontal resolution as B_S ($\Delta x = 44.4$ m), but with a Smagorinsky constant twice as large as in B_S ($C_S = 0.32$). As a result, when considering the impact of C_S on the spectra in convective conditions as illustrated by Nieuwstadt *et al.* (1992); Mason and Brown (1999), it can be concluded that the present model dissipates small structures at a higher rate than Brown *et al.* (2000) and by extension than all the model presented in Nieuwstadt *et al.* (1992) intercomparison (which includes the UKMO Smagorinsky SGS model).

In the near surface region, grey solid lines in Fig. 4.22 b), d) and f) and Fig. 4.25 b), d) and f), E_w shows a clear increase of the energy with height for all wave numbers, while E_u and E_v are merging with the spectra from the mixed layer in the high wave numbers. In the surface layer, the latter two spectra do not feature a clear $k_x^{-5/3}$ slope in comparison to E_w. It thus indicates that in the near-surface region, while the filter is not located in the inertial subrange, little structures are less dissipated by the SGS model than for the shear case. This is coherent with the fact that the near-surface region is more resolved in the convective case, and thus, less prone to the SGS model limitation at low resolution, see Fig. 4.19.

Compared to the freely convective ABL results from Brown *et al.* (2000) shown in Fig. 4.24 b), the near-surface spectra in the high wave numbers are in less good agreement than for the shear case. Indeed, all Brown *et al.* (2000) E_w spectra collapse in the highest wave numbers (see Brown *et al.* (2000, Fig. 6) in comparison to Fig. 4.22 f)) which was not observed in the shear case results. Brown *et al.* (2000) results shown are for a freely convective ABL (no mean horizontal velocity) similar to the one of Nieuwstadt *et al.* (1992). However, as previously illustrated in Sec. 4.2.4, the added near-surface shear in B_S (caused by the mean horizontal motion) tends to generate structures with features from both purely neutral and freely convective cases. This thus appears to be a good explanation for a signature similar to the shear case in the near-surface E_w of B_S (in comparison to Brown *et al.* (2000)).

Concerning the low wave numbers, from Fig. 4.22 b), d) and f) and Fig. 4.25 b), d) and f), it can be seen that $k_x E_w \propto k_x$ is clearly reproduced at all height which perfectly agree with the theory, while the slope of E_u and E_v evolve with height and agree slightly less with the theoretical value. Lowest wave number slopes of the two latter spectra evolve from roughly $k_x E_u \propto k_x E_v \propto k_x$ close to the surface to $k_x E_u \propto k_x^{1/2}$ and $k_x E_v \propto k_x^2$ in the mixed layer. A clear change in slope between the low wave numbers and the inertial subrange is thus visible for all spectra at all heights. In the mixed layer, Fig. 4.23 b), low wave numbers E_w feature a higher level of energy than E_u and E_v. The transition to the inertial subrange of the former is also earlier and more direct than for the latter spectra. Those features are on part with what obtained by Mason and Brown (1999) (comparison of Fig. 4 and 5 of that study).

At the lowest wave number, energy in all the spectra evolve with height, see Fig. 4.22 b), d) and f). E_u and more notably E_v have an energy that decrease with height, while E_w feature the same clear increase of the energy with height as for the shear case. Fig. 4.24 b) shows that at the lowest wave numbers, E_w energy increase is in good agreement with Brown *et al.* (2000) from the surface to the mixed layer. Finally on that figure, the shape of E_w at the inversion feature an elongated linear region in the low wave numbers in agreement with results of all model in Nieuwstadt *et al.* (1992). Above the inversion, E_w show the exact same shape as for the shear case: the fall down of the spectra is earlier than in the ABL and extremely rapid.

The scatter of the spectra, shown for E_w in Fig. 4.24 b), is generally not significant, notably in the upper surface layer and the mixed layer for the whole range of wave numbers. The surface layer and the inversion generally feature a higher scatter. However, the most striking feature in Fig. 4.24 b), is the very high value of the scatter above the inversion notably in the high wave numbers. This tends to indicate that the vertical inversion oscillation may impact the flow up to $1.2\, z/z_i$ but most certainly only for the results featuring the highest inversion.

The last results to comment, Fig. 4.25 b) d) and f), show the spectra using a variant of the scaling. No LES studies of the ABL were found that scale spectra in convective condition base on such a scaling. However, the behaviour of the results in the inertial subrange is expected to

be on part with the shear case: spectra should merge in a curve that follows the $k_x^{-5/3}$ slope for all velocity components before falling down. In the low wave numbers, while a slope of k_x^{-1} is expected to be observed, no information was found concerning neither the merge spectra in the low wave number, nor the transition to the inertial subrange. It was however chosen to display reference curves located similarly as for the shear case.

In Fig. 4.25 b) d) and f), it can be seen that all velocity components spectra clearly merge similarly as for the shear case. For the convective case, the inertial subrange region is notably better reproduced and elongated for all velocity components. A linear region of a slope around k_x^{-1} is also present in the low wave numbers of E_u and E_v, but the transition to the inertial subrange is not well defined. The latter appears to be located at $0.3\,zk_x$ which also correspond to the peak of the merge spectra of E_w. The E_u and E_v spectra that first reach the merge inertial subrange spectra are located at height $0.1\,z_i$. Interestingly, $0.1\,z_i$ is also the height above which more than 90 % of the flow is resolved, see Fig. 4.19 b) (as for the shear case).

Concerning the vertical velocity spectra, a merge of the curves is also observed and two linear regions can be observed. One not well defined with a slope of k_x^{-1} between $0.6\,zk_x$ and $2\,zk_x$ followed by a well defined linear region with a slope of $k_x^{-5/3}$. In the low zk_x, no merge is observed in E_w. Slope of individual spectra is zero as predicted by the theory and spectra are parallel. By rescaling Brown *et al.* (2000) results shown in Fig. 4.24 b), a similar merge as for the shear case is obtained in the low wave numbers.

As a conclusion, longitudinal velocity spectra from the convective case modelled by means of the UKMO Smagorinsky SGS model, B_S, present feature similar to the ones of the neutral case. Results are generally in good agreement with reference spectra and literature results based on similar cases and approaches (Mason, 1989; Nieuwstadt *et al.*, 1992; Mason and Brown, 1999; Brown *et al.*, 2000; Cuxart *et al.*, 2000). The inertial subrange is well reproduced by all velocity components (better than for S_S). The faster falloff of E_u than E_v and E_w is also observed in the highest wave numbers (as for S_S). Finally, it was also found that the present model is more dissipative than the equivalent approaches found in the literature.

4.2.7 Conclusion of Moeng and Sullivan (1994) benchmark

As a summary of this first direct evaluation of the proposed LES-capable mesoscale model, it is worth commenting both the obtained results and the cases selected for the benchmark. Obtained results are very promising since first, second and third order moments, as well as the velocity spectra are in good agreement with literature reference studies based on similar SGS models. On the one hand, in the mixed layer and at the top of the ABL, results almost superpose with the comparison data for both the shear and the convective cases. On the other hand, in the near-surface region which is the most challenging region of the flow, results present characteristics similar to others LES results based on dissipative only SGS models (*i.e.* Smagorinsky): surface velocity vertical shear is clearly over-predicted in comparison to experimental data. This over-prediction appears to be slightly larger than in the numerical results used as reference. In fact, as observed during the spectral analysis, the proposed model tends to over-dissipate the smallest resolved eddies (more clearly seen for the shear case). Therefore, the small structures feature less energy which is worsening the limitation of the Smagorinsky SGS model notably in the near-surface region. Since the UKMO Smagorinsky SGS model and the numerical parameters used here are similar to the ones from the models used for comparisons, the increase of the dissipation rate observed for the present model can uniquely be attributed to the the SISL time and advective scheme of the numerical method.

Concerning the shear and convective benchmark cases from MS94 , it was seen that both cases appear to be in a quasi-steady state during MS94 post-processing time interval, but further evaluation of the time evolution is needed for a strict confirmation. Furthermore, non negligible differences were observed between results based on the exact same model but for which only initial random velocity perturbations were changed. These differences, also called scatter, were sometimes high. To lower uncertainty and allow better comparisons, it was decided to achieve an ensemble average of five computations based on the same model and time interval as MS94. The scatter was very large in some parts of the domain advocating the needs for a longer time interval for post-processing. These latter points are studied in further details in the next section along with the impacts of the numerical parameters of the method.

4.3 LES of the full ABL: numerical parameters

Since the beginning of the study, only results based on one set of numerical parameters for the computations and the post-processing were evaluated. Indeed, in the previous section, it was chosen to closely follow the well documented comparison cases of a full ABL from Moeng and Sullivan (1994); Sullivan *et al.* (1994). As a result, with the exception of the time step, all the other parameters were kept the same as in these referenced studies. This first evaluation was promising. However, some aspects such as the scatter of the results, the sensitivity of the results to the mesh and time step were found to require an further evaluation.

In this section, the post-processing parameters, *i.e.* the location and size of the time windows involved to compute flow statistics, are first studied assessing the evolution and convergence as well as the scatter of both the shear and convective cases discussed previously. This will allow to define the optimum post-processing parameters that will be used afterwards. Then, the impact of the horizontal grid, the vertical grid and the time step are evaluated. It is noteworthy that all the evaluations presented in this section were achieved using two different SGS model (for validation purpose as in the previous section): the UKMO Smagorinsky and the hybrid TKE SGS models. However, as presented in Sec. 4.4.1, both results are very similar. As a result for clarity reasons, only the UKMO Smagorinsky SGS model results are systematically shown on the figures (except when the subgrid TKE is needed), while parameters and the scatter of both series of results is shown in all the tables of this section.

4.3.1 Post-processing parameters

In the previous section, the shear and convective cases from Moeng and Sullivan (1994) appeared to be in a quasi-steady state with a turbulent regime fully developed during the time interval used for the post-processing (see Figs. 4.5 and 4.6). However, while there were strong evidences, this could not be fully demonstrated solely based on the results shown previously.

It was also shown that, by using the same procedure and time interval as Moeng and Sullivan (1994), computations based on the same model and configuration but for which only the ini-

tial velocity perturbations were changed, led to different results. This scatter was illustrated by errors bars in all the figures of the previous section. These differences, while generally not critical, can significantly affected some of the higher order variables. As a consequence, comparisons with MS1994 were not always easy to interpret (*e.g.* the momentum flux of the convective case in Fig. 4.8 b)) and it was sometimes hard to draw clear conclusions. Moreover, differences in the results based on various configuration of the model are almost always smaller than the scatter of the results (further illustrated in Sec. 4.3.1.1.2 and 4.3.1.2.2).

The aim of the present section is thus twofold: study the impact of the time evolution of the flow on the turbulence statistics, and evaluate post-processing parameters (location and length of the post-processing time windows) allowing to keep the scatter of the results below an acceptable level for all variables at all height in the ABL. As a consequence, the time evolution of the flow is first studied based on three time windows. Then, the scatter of the results is further evaluated using the same three time intervals. The shear case is first studied followed by the convective case. As seen in Tab. 4.4, results from various model configurations (grid and domain size) are used here to increase the number of samples. The thorough comparison of the results from those latter configurations is discussed in Sec. 4.3.2. Here, we focus on the impact of the post-processing time interval location and length on the results convergence and scatter.

Table 4.4 Numerical parameters of the shear and convective cases discussed in Sec. 4.3.1 and Sec. 4.3.2, and used as reference all along Sec. 4.3 and Sec. 4.4

Name	Model	$N_x \times N_y \times N_z$	L_{x_i} [km]	L_z [km]	Δt [s]	Iteration max.	Realizations
S_{1d}	$k-l$ column	$3 \times 3 \times 96$	0.3	1	2	60000	1
S_S^s	Smagorinsky SGS	$50 \times 50 \times 96$	2	1	2	30000	10
S_S^m		$64 \times 64 \times 96$	2	1	1.5	40000	5
S_S^l ($\equiv S_S$)		$96 \times 96 \times 96$	3	1	1.5	15000	5
S_M^s	Hybrid TKE SGS	$50 \times 50 \times 96$	2	1	2	30000	10
S_M^m		$64 \times 64 \times 96$	2	1	1.5	40000	5
S_M^l ($\equiv S_M$)		$96 \times 96 \times 96$	3	1	1.5	15000	5
B_{1d}	$k-l$ column	$3 \times 3 \times 96$	0.3	2	4	10000	1
B_S	Smagorinsky SGS	$96 \times 96 \times 96$	5	2	4	10000	5
B_M	Hybrid TKE SGS	$96 \times 96 \times 96$	5	2	4	10000	5

4.3.1.1 Shear case

The evolution and scatter of the results from the shear case are studied here. Fig. 4.26 is similar to Fig. 4.5 but it shows the time evolution of integral coefficients, Eq. (4.4), for a full inertial period and for the four model configurations described in Tab. 4.4. The envelope of the scatter of the various results is displayed in coloured shaded area. The three time intervals are shown by the background light grey shaded area in Fig. 4.26, and they are defined as:

MS1994: from $0.172\,T_{inert}$ to $0.250\,T_{inert}$, *i.e.* from 10445 s to 15255 s.
LONG: from $0.172\,T_{inert}$ to $0.369\,T_{inert}$, *i.e.* from 10445 s to 22500 s.
TINERT: from $0.492\,T_{inert}$ to $0.985\,T_{inert}$, *i.e.* from 30000 s to 60000 s.

The interval MS1994 is the same as in the previous section[8]. The interval LONG starts at the same location as MS1994, but it is 2.5 times longer. Finally, the interval TINERT allows to capture half an inertial period while not overlapping with MS1994 and LONG. It is located far from the beginning of the integration (further reducing the possible influence of the initialization on the results). In addition, the inertial oscillation is almost damped after $0.5\,T_{inert}$.

4.3.1.1.1 Steadiness of the solution

From Fig. 4.26, it can be seen that results from all model configurations follow the same time evolution. This figure is similar to Fig. 4.5 but it now can be seen that the shear case features a much damped inertial oscillation in comparison to Andren *et al.* (1994). This high damping is caused by the presence of a strong and low height inversion that prevents the flow from oscillating freely around the equilibrium Ekman spiral compared to a case where there would be no inversion such as the one of Andren *et al.* (1994).

The general evolution of C_u, C_v, C_g and C_{TKE} in the first half of the inertial period was already commented in Sec. 4.2.2. Here, as discussed later, only the results from the small grid, *i.e.* S^s_S, depart from the other LES results before $0.2\,T_{inert}$ as seen in Fig. 4.26 a), c) and d).

[8] Note that the acronym MS1994, which refers to the time interval used by Moeng and Sullivan (1994), is different from MS94 used in the previous section, which refers to Moeng and Sullivan (1994) study.

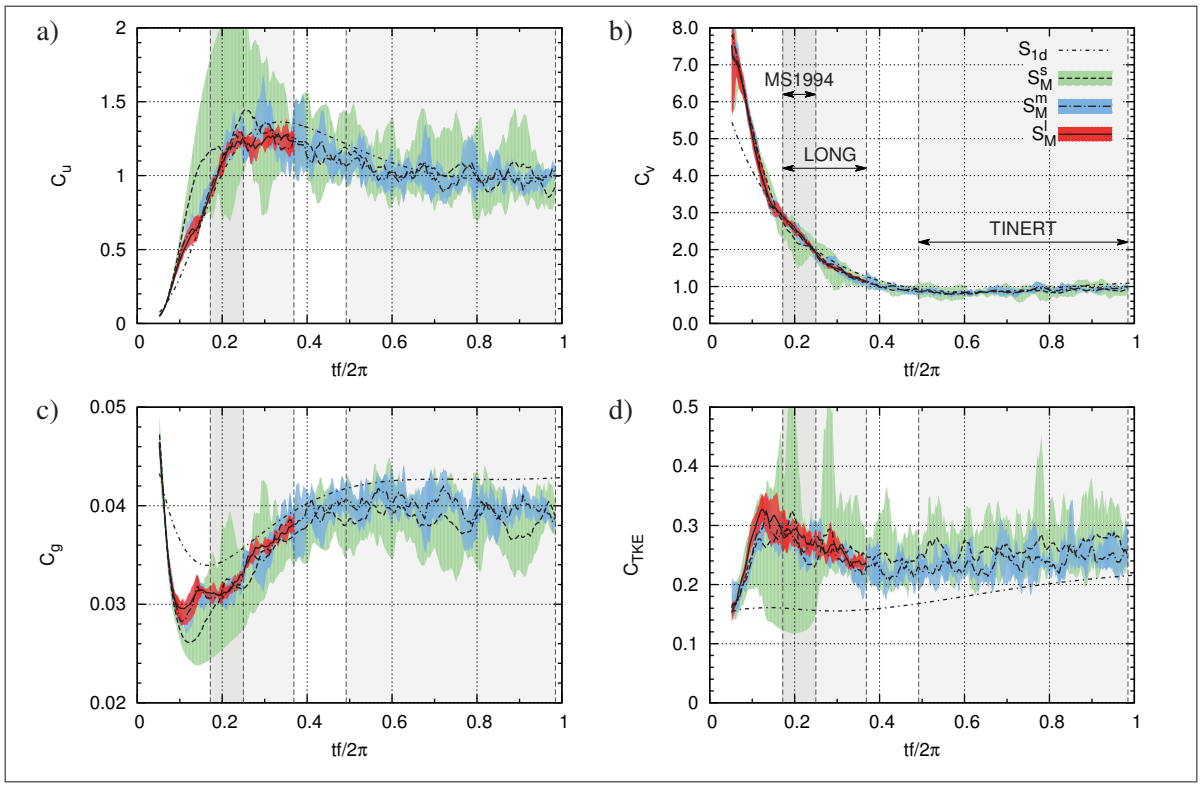

Figure 4.26 Time evolution of integral coefficients, Eq. (4.4), from the shear case: a) and b) velocity integral coefficients; c) geostrophic drag coefficient; d) TKE integral coefficient. The coloured overlaid regions show the scatter of the results. Grey overlaid background areas show post-processing time intervals

After $0.5\,T_{inert}$, S_{1d}, S_S^s and S_S^m trends are in very good agreement. Both C_u and C_v converge to one that is reached after $0.8\,T_{inert}$. Concerning C_g and C_{TKE}, both feature a plateau after $0.5\,T_{inert}$, but the former slightly increase while the latter slightly decrease. The plateau value and trend is the same for all LES results, while S_{1d} show a nearly constant offset: C_g, and thus u_*, is 10 % higher than in LES results, and C_{TKE} is 20 % lower. Those features were already discussed previously (see Sec. 4.2.2). They have the same origins after $0.5\,T_{inert}$ than before: the higher friction velocity obtained with the column model is due to its thankful closer reproduction of the similarity theory in comparison the the under resolved close surface LES results. At the opposite, the fully parametrized turbulent mixing of the 1D model under predict the TKE in the mixed layer leading to an under estimation of C_{TKE}.

Table 4.5 Result parameters from the shear case for model setups shown in Tab. 4.4 and the three time intervals

Name	Interval	u_* [m/s]	z_i [m]	θ_s [K]	$\overline{w'\theta'}_i$ [K m/s]	U_1 [m/s]	$\Delta\theta_1$ [K]
S_{1d}	MS1994	0.520	516	300.55	-0.0330	4.45	-0.0024
	LONG	0.547	516	300.76	-0.0311	4.50	-0.0023
	TINERT	0.639	589	302.38	-0.0226	5.58	-0.0016
S_S^s	MS1994	0.461	432	300.37	-0.0033	3.98	-0.0006
	LONG	0.487	452	300.38	-0.0033	4.10	-0.0006
	TINERT	0.566	454	300.63	-0.0058	4.95	-0.0008
S_S^m	MS1994	0.468	451	300.37	-0.0029	4.18	-0.0008
	LONG	0.499	453	300.38	-0.0036	4.29	-0.0008
	TINERT	0.587	465	300.67	-0.0062	5.17	-0.0011
S_S^l	MS1994	0.468	474	300.36	-0.0032	4.17	-0.0008
	LONG	0.499	459	300.38	-0.0037	4.29	-0.0009
S_M^s	MS1994	0.470	472	300.39	-0.0043	3.90	-0.0007
	LONG	0.503	476	300.41	-0.0045	4.08	-0.0007
	TINERT	0.579	459	300.75	-0.0071	4.89	-0.0010
S_M^m	MS1994	0.470	459	300.38	-0.0030	3.95	-0.0009
	LONG	0.512	461	300.40	-0.0048	4.17	-0.0010
	TINERT	0.601	465	300.77	-0.0076	5.06	-0.0012
S_M^l	MS1994	0.474	459	300.38	-0.0034	4.01	-0.0009
	LONG	0.515	465	300.40	-0.0047	4.20	-0.0010

As a result of the above discussion in Fig. 4.26, it is to say that the shear case appears to reach a permanent state where averaged u, u_* and k (*i.e.* C_v, C_g and C_{TKE}) are almost constant after $0.5\,T_{inert}$ and the v component take more time to stabilize. TINERT interval results are thus representative of that state. They would not change significantly by changing the size and location of the time windows, albeit it is wide enough and located after $0.5\,T_{inert}$.

Tab. 4.5 shows result parameters for the three time intervals and all model configurations of Tab. 4.4. In Tab. 4.5, friction velocity and velocity modulus at first level increase from MS1994 to TINERT intervals for all cases. S^m and S^l values are very similar while S^s values are smaller (see Sec. 4.3.2 for explanation). Concerning the others parameters of the LES results: no clear trend can be concluded for z_i as well as for $\Delta\theta_1$, while θ_s shows a slight increase from MS1994 to TINERT, and $\overline{w'\theta'}_i$ becomes twice as large for TINERT than for MS1994.

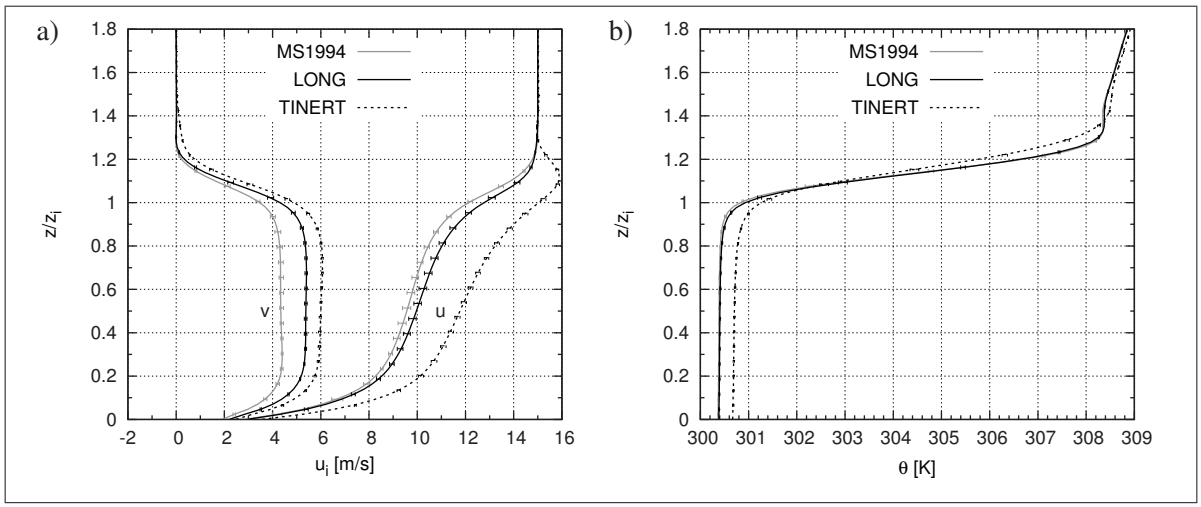

Figure 4.27 Dimensional profiles from S_S^m along with the scatter for the three time intervals: a) horizontal velocity components; b) potential temperature

Those changes in result parameters are coherent with the evolution of the various profiles shown in Fig. 4.27 and 4.28, as discussed hereafter. But, it can be already noted that only dimensional profiles of velocity components differ notably from Moeng and Sullivan (1994) (most visible during TINERT). In fact, in Fig. 4.27 a), both velocity components steadily increase with time across the whole ABL. They appear to stabilize to a permanent state during TINERT interval. As a results of the increase of momentum in the mixed layer, the surface wind also gets higher, which make the surface shear u_* to increase. An overshoot develops in u just above z_i for TINERT interval. This overshoot is naturally present at the top of the classical Ekman spiral (see Fig. 4.1 c)), but it may be amplified by the unbalance in the terms of the momentum equations (Coriolis and momentum diffusion terms) cause by the sudden reduction of the subgrid turbulent mixing (which vanish) in the inversion (similarly as in stable surface layer (Stull, 1988; Cuxart *et al.*, 2006; Beare *et al.*, 2006)).

Concerning the ABL height, the sharp inversion prevents its proper vertical evolution. Indeed, as seen in Fig. 4.27 b), the height and temperature lapse rate of the inversion evolve slowly in time. The small negative sensible heat flux across the inversion, which is caused by the entrainment of hot air from above, brings some energy in the adiabatic ABL causing a small

increase of the whole mixed layer temperature. Since no heat is coming from the surface, and assuming that the only source of heat in the mixed layer comes from above, one can obtain the mixed layer averaged temperature increase, *i.e.* $-\overline{w'\theta'}_i/z_i$, based on the values from Tab. 4.5. Considering S_S^m case, it gives a mixed layer averaged temperature increase of roughly 0.06 K between the MS1994 and LONG and of 0.3 K between the LONG and TINERT. This is in very good agreement with the value obtained from the computations (averaging θ from the surface to z_i) which thus justify the whole increase of potential temperature in the mixed layer.

Finally, it is to note that the resolved part of $\overline{w'\theta'}_i$ increases with time mostly because of the slightly smoother and less stable inversion that allows more mixing (see variance peaks in Fig. 4.28 e)). For its part, the small neutral region above the inversion, *i.e.* at $z/z_i = 1.4$ in Fig. 4.27 b), is also present for the three time intervals. This feature was also obtained by Sorbjan (2005b, Fig. 7 a) and 11 a)). However, it is more clearly defined for MS1994 and LONG intervals. Indeed, from Fig. 4.28 d), the total sensible heat flux above the inversion become positive at that height for MS1994 and LONG, while it is still clearly negative for TINERT where it smoothly reaches zero (not shown on the figure). This difference can also be attributed to the increase of the mixing across the inversion with time.

Concerning the non-dimensional profiles of the first, second and third order moments, it can be seen in Fig. 4.28 that there is nearly no changes between the three time intervals. Indeed, at the exception of few differences that are always within the scatter of the MS1994 interval, all results are in good agreement demonstrating that even during the interval MS1994, the turbulence is fully developed and the initialization has no more influences.

In fact, the biggest change is the increase with time of total heat and momentum fluxes toward a more linear profile with height as seen in Fig. 4.28 c) and d). According to Porté-Agel *et al.* (2000), it indicates that turbulence is more developed during TINERT interval. Furthermore, since subgrid scale flux is almost unchanged, this increase comes from the resolved part. The same can be observed on variances (not shown here). As a result of this increase, the flow is slightly more resolved for the TINERT interval.

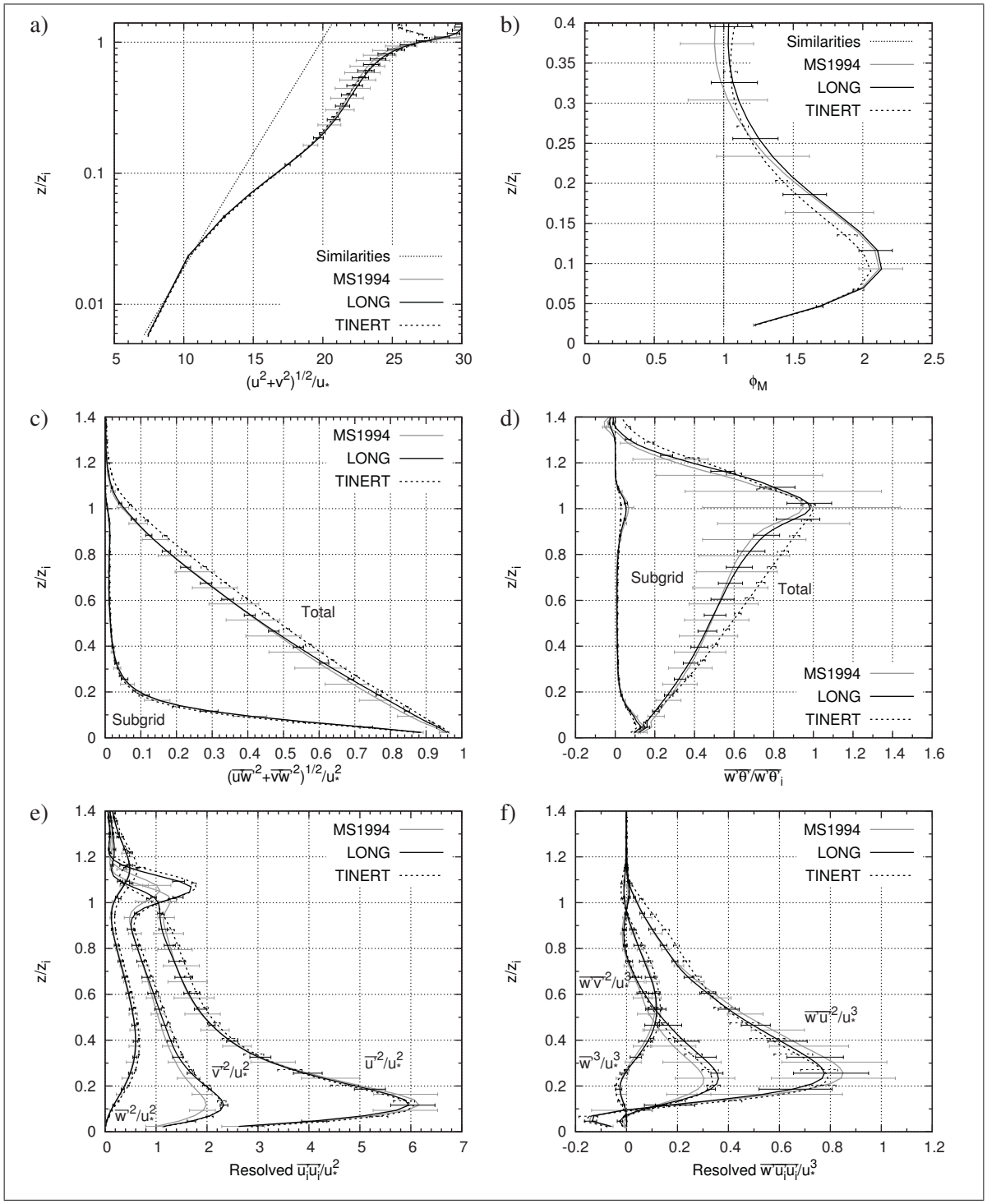

Figure 4.28 Profiles from S_S^m along with the scatter for the three time intervals: a) velocity modulus (using a log scale in ordinate); b) horizontal velocity vertical gradient; c) total and subgrid momentum flux; d) total and subgrid sensible heat flux; e) resolved velocity variances; f) resolved vertical flux of velocity variances

In the near-surface region, velocity and non-dimensional velocity gradient profiles, perfectly superpose for the first few meshes above the surface, *i.e.* roughly up to $0.1\,z_i$, Figs. 4.28 a) and b). This is consistent with the fact that subgrid scale part of the turbulent quantities is almost unchanged between the various intervals. At the top of the surface layer and above, little discrepancies between results appear which are caused by the resolved part as described above. The bias with the similarity theory of ϕ_M become lower with time since the flow is more resolved, see Fig. 4.27 b). Finally, $\overline{v'^2}$ show an increased near-surface peak for LONG and TINERT which can also been explained by the notable increase of that velocity component.

At the inversion, besides the doubling of the resolved part of $\overline{w'\theta'}$, it was also noted in Fig. 4.27 that for TINERT intervals, u overshoot the geostrophic wind while the gradient of v across the inversion increases and reaches a maximum value during the permanent state. This has the consequence to noticeably increase the local maximum in resolved $\overline{v'^2}$ at the inversion while $\overline{u'^2}$ peak is removed as seen in Fig. 4.28 c). The vertical velocity variance at that height also increases a little contributing to the increase of the resolved heat flux at the inversion.

The last comparison shown in Fig. 4.29 presents the streamwise and vertical velocity longitudinal spectra at various heights. In the lower half of the ABL, energy of both u and w spectra in the high wave numbers increases with time to reach its maximum for TINERT interval. This energy increase is to be correlated with the increase of heat and momentum flux resolved parts. In the middle of the ABL, spectra are almost unchanged. In the upper part of the ABL, spectra feature a lower level of energy in the high wave numbers which is caused by the wider transition to the inversion that tend to render the top of the ABL more stable. In the low wave numbers, u and w spectra tend to feature slightly more energy in the near-surface region while w spectra show more energy in the upper ABL. However, those changes are not significant in comparison to the increase of energy in the high wave numbers.

As a conclusion of the time evolution of the shear case, it can be said that although the dimensional first order moments features notable evolution (that converge to an almost permanent state after $0.5\,T_{inert}$), the non-dimensional profiles are almost unchanged. This confirms that

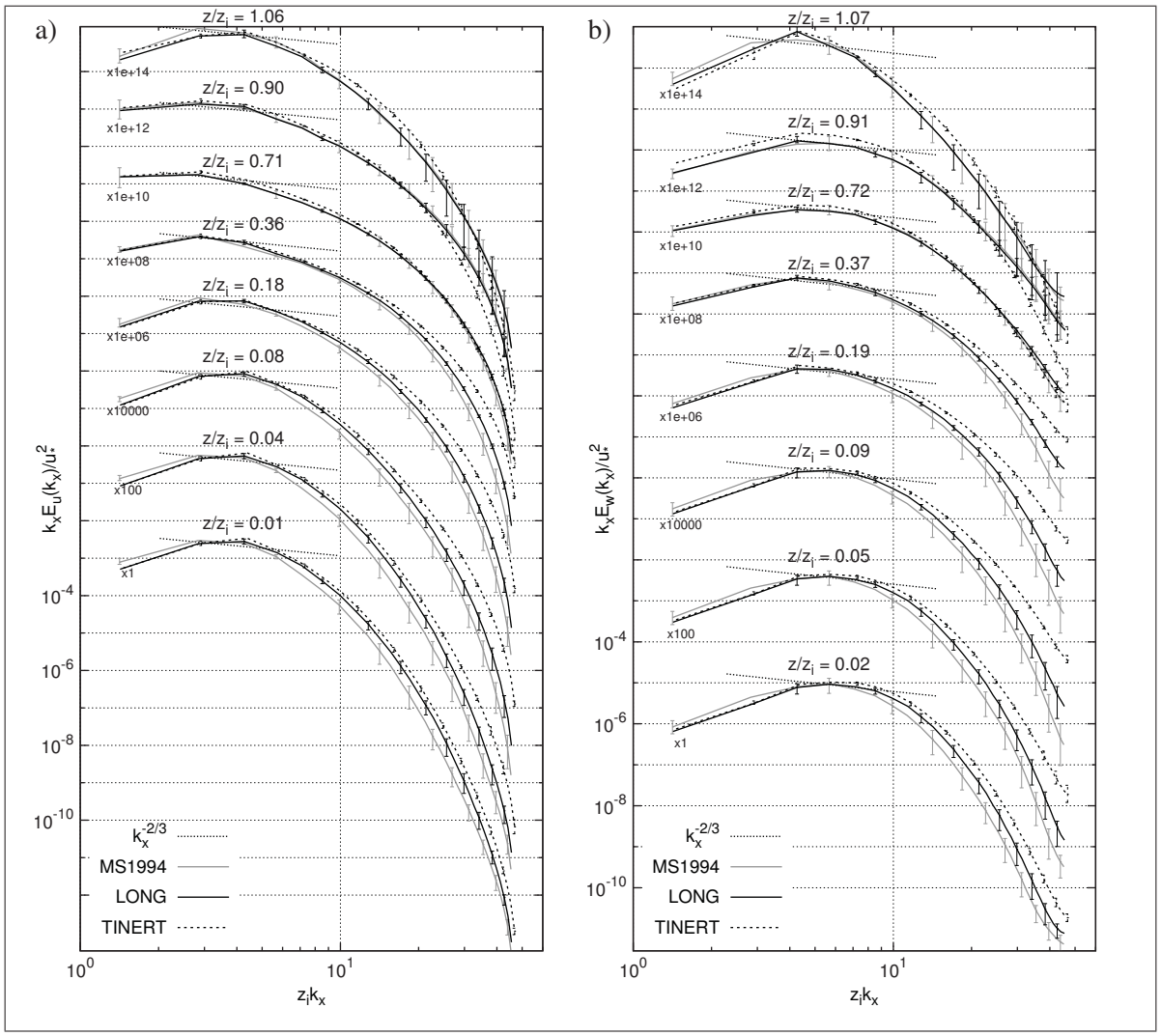

Figure 4.29 Longitudinal velocity spectra from S_S^m along with the scatter for the three time intervals: a) streamwise component; b) vertical component

the turbulence, but not the first order moments, is already fully developed during MS1994 interval (which is characteristic of a quasi-steady state). However, an increase of the resolved part of momentum and heat fluxes as well as an increase of the energy of small resolved eddies in the lower half of the ABL was noted for TINERT time interval.

4.3.1.1.2 Scatter of the results

Now that the time evolution of the various quantities has been studied, the scatter of the results is discussed in this section based on the same three time intervals, MS1994, LONG and TINERT. As a reminder, the scatter represents the difference between several simulations of the same case but for which only the initial random perturbations of the velocity field are changed. The number of realizations per model configurations is shown in Tab. 4.4. The scatter was already introduced in Sec. 4.2 (but not discussed) and displayed as error bars in all the figures of the previous section, *i.e.* in Figs. 4.27, 4.28 and 4.29 for the three time intervals.

In order to have a better overview of this scatter, Tab. 4.6 further presents the scatter of the result parameters that are displayed in Tab. 4.5, *i.e.* for any variable ψ

$$o\left(\psi\right) = \max\left(\psi\right) - \min\left(\psi\right), \tag{4.9}$$

and Tab. 4.7 shows the root mean square from the surface to $1.2\,z_i$ of the dimensional scatter of six variables of interest, *i.e.* for any variable ψ

$$\sigma\left(\psi\right) = \left[\frac{1}{1.2z_i}\int_0^{1.2z_i} o\left(\psi\right)^2 dz\right]^{1/2}. \tag{4.10}$$

The data of those two tables is shown in Fig. 4.30 to visually appreciate scatter trends as a function of the time interval. Note that the scatter from S^s is divided by ten in Fig. 4.30.

From the various figures and tables illustrating the scatter of the results, it can be clearly seen that the scatter generally decreases with the time interval length. Between MS1994 and LONG, this reduction is clearer for the results based on the smallest domain and/or lowest resolution, *i.e.* S^l and S^m. Tab. 4.6 and 4.7 and Fig. 4.30 further shows reduction of the scatter of S^s for TINERT interval, while this improvement is not as clear for S^m. It thus appears that the coarser the mesh, the more scatter there are, and the more noticeable the reduction is when the time interval is lengthen.

Table 4.6 Scatter of the result parameters from Tab. 4.5, Eq. (4.9), for the shear case and for the three time intervals

Name	Interval	$o(u_*)$ [m/s]	$o(z_i)$ [m]	$o(\theta_s)$ [K]	$o(\overline{w'\theta'}_i)$ [K m/s]	$o(U_1)$ [m/s]	$o(\Delta\theta_1)$ [K]
S^s_S	MS1994	0.124	295	0.054	0.0054	1.61	0.00055
	LONG	0.084	137	0.050	0.0043	0.95	-0.00003
	TINERT	0.020	53	0.113	0.0014	0.13	-0.00013
S^m_S	MS1994	0.037	32	0.009	0.0026	0.39	0.00026
	LONG	0.013	21	0.015	0.0007	0.13	0.00010
	TINERT	0.007	21	0.027	0.0002	0.05	0.00002
S^l_S	MS1994	0.014	32	0.011	0.0015	0.13	-0.00005
	LONG	0.015	11	0.010	0.0007	0.14	0.00001
S^s_M	MS1994	0.118	74	0.033	0.0074	1.52	0.00059
	LONG	0.049	42	0.037	0.0025	0.58	0.00014
	TINERT	0.016	32	0.059	0.0009	0.13	0.00005
S^m_M	MS1994	0.017	21	0.005	0.0007	0.16	0.00003
	LONG	0.004	21	0.007	0.0008	0.05	0.00002
	TINERT	0.005	21	0.020	0.0007	0.04	0.00000
S^l_M	MS1994	0.010	32	0.009	0.0020	0.11	0.00002
	LONG	0.007	11	0.012	0.0005	0.09	0.00000

The small grid S^s results feature a very large scatter notably before $0.5\,T_{inert}$, *i.e.* MS1994 and LONG intervals. From Tabs. 4.6 and 4.7, it can be seen that S^s scatter is at least an order of magnitude higher than the medium and large grid results for both MS1994 and LONG intervals. In fact, after a closer inspection it was found that, the coarser grid is at the limit of suitability to reproduce the shear case with the current model. Indeed, the turbulent regime of few S^s computations appears to be delayed before reaching a permanent regime (in comparison to S^m and S^l results). This explain the wide envelope of C_u and C_{TKE} and the low level of the envelope of C_g (*i.e.* u_*) for S^s cases between 0.15 and $0.35\,T_{inert}$. In addition, spurious event of turbulence extinction (followed by a prompt ignition illustrated by the three clear peaks in the scatter of S^s in Fig. 4.26 d)) are also observed mostly during the first half of computation.

The ignition and self-sustainability of the fully developed turbulent regime is thus affected by a too coarse grid. The delay observed in the ignition may unfortunately prevent from using the coarse grid results, S^s, before $0.35\,T_{inert}$ (if not before $0.5\,T_{inert}$), as they may not be representative of a fully developed ABL flow. This discards MS1994 and LONG intervals with

Table 4.7 Root mean square of the dimensional scatter from 0 to $1.2\,z_i$, Eq. (4.10), of selected variables (shown on Figs. 4.27, 4.28 and 4.29) for the shear case and for the three time intervals

Name	Interval	$\sigma(u)$ [m/s] $\times 10^{0}$	$\sigma(w)$ [m/s] $\times 10^{-6}$	$\sigma(\overline{u'w'})$ [m^2/s^2] $\times 10^{-2}$	$\sigma(\overline{u'^2})$ [m^2/s^2] $\times 10^{-1}$	$\sigma(\overline{w'^2})$ [m^2/s^2] $\times 10^{-1}$	$\sigma(\overline{w'\theta'})$ [K m/s] $\times 10^{-3}$
S^s_S	MS1994	1.962	1.434	8.776	7.459	1.130	1.409
	LONG	1.271	1.299	6.907	6.082	0.978	1.097
	TINERT	0.334	0.502	1.217	1.324	0.381	0.407
S^m_S	MS1994	0.264	0.330	3.541	2.226	0.417	0.726
	LONG	0.248	0.211	0.921	1.020	0.195	0.220
	TINERT	0.189	0.218	0.533	0.972	0.115	0.150
S^l_S	MS1994	0.140	0.136	1.163	0.996	0.206	0.333
	LONG	0.162	0.156	1.175	0.671	0.184	0.221
S^s_M	MS1994	1.764	1.508	10.098	8.239	1.573	1.917
	LONG	1.322	0.617	3.002	2.546	0.592	0.663
	TINERT	0.496	0.459	0.989	1.288	0.281	0.347
S^m_M	MS1994	0.171	0.258	1.340	1.198	0.241	0.242
	LONG	0.142	0.191	0.427	0.658	0.159	0.206
	TINERT	0.155	0.204	0.348	0.713	0.152	0.215
S^l_M	MS1994	0.229	0.140	0.965	0.903	0.233	0.463
	LONG	0.147	0.115	0.608	0.608	0.142	0.177

S^s grid. Consequently, to properly evaluate results from the small grid the interval TINERT appears to be the least affected by the above mentioned problems, and thus the most suitable.

Concerning S^m and S^l results, it can be seen in Tabs. 4.6 and 4.7 and Fig. 4.30 that the scatter of all variables and parameters of S^m_S for MS1994 interval is generally twice as large as the one of S^l_S. Interestingly, S^m_M results for that interval feature a lower scatter which is almost of the same order as the scatter of the fine grid S^l results from both SGS models. The picture is changed for the LONG interval as the scatter difference for both the grid configurations and the SGS model is small, albeit slightly higher for the S^m grid (see Figs. 4.35 and 4.36 that show the detail of the scatter of the various grids for the LONG interval). There is thus a noticeable reduction of the scatter for most of the quantities evaluated between MS1994 and LONG for S^m results, while S^l also show a decrease of the scatter between those two intervals but only in the higher order moments and most significantly in the lower part of the ABL.

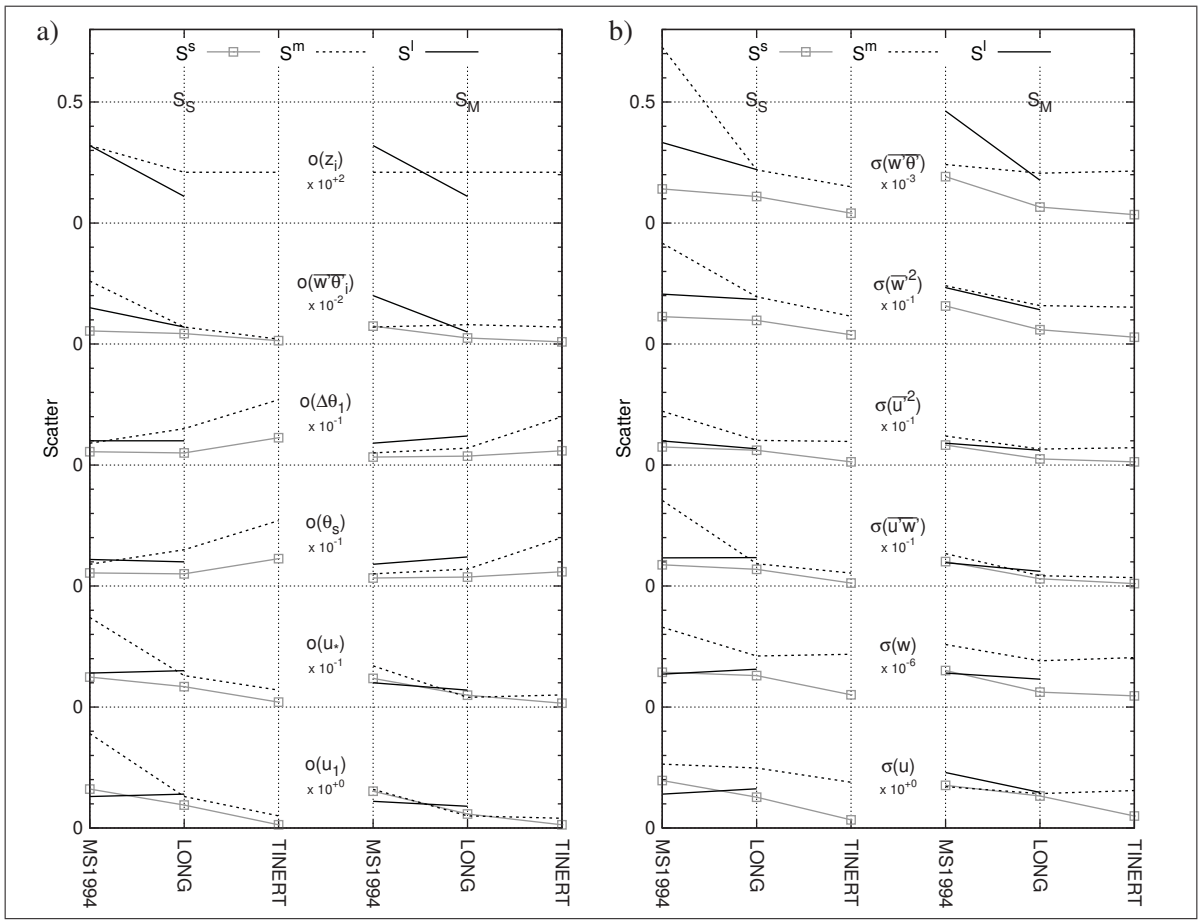

Figure 4.30 Evolution of the scatter as a function of time interval: a) scatter of the result parameters shown in Tab. 4.6; b) RMS of scatter from 0 to $1.2\ z_i$ as shown in Tab. 4.7. Variables names and scaling factors are shown in the centre of the graphs. Scatter from S^s is divided by 10, and it is not shown for z_i as it is too large

Finally, concerning TINERT interval, the scatter of the S^m results further decrease slightly (except for θ_s and $\Delta\theta_1$) to become equal or lower to the scatter of S^l for LONG interval. From Figs. 4.28 and 4.29, the scatter below $0.2\ z/z_i$ of S^m_S is clearly reduce for some variables going from LONG to TINERT interval, while, in the mixed layer, both LONG and TINERT results have a similar scatter. As a result, the decrease of scatter is not significant considering that TINERT interval is three time longer than LONG.

As a conclusion, it thus clearly appears that the longer the time interval, the less scatter there are. In addition, the coarser the mesh, the more scatter there are, and the more noticeable

the scatter reduction is when the time interval is lengthen. It was shown that results from S^s grid may not be representative before $0.5\,T_{inert}$ due to spurious phenomena. This is discarding results based on that grid for MS1994 and LONG intervals. Concerning S^m, while scatter is relatively high for MS1994, it is close to S^l results for the LONG interval, notably in the middle of the ABL. The TINERT interval further shows a small reduction of the scatter of S^m results but mostly in the near-surface region. Scatter of this last result is similar to S^l for the LONG interval. Finally, S^l result also shows a reduction of the scatter going from MS1994 to LONG. The latter is more noticeable for the higher order variables in the near-surface region.

As a consequence, MS1994 time interval appears to be at the edge of suitability even for the finer grid S^l. LONG interval leads to acceptable scatter for S^m and S^l grids, while the TINERT interval is required to use S^s results and for S^m scatter to be as low as S^l (during LONG interval) at all heights in the ABL. Considering the increase of computational time, the improvements going from LONG to TINERT are not significant with regards to the scatter.

4.3.1.2 Convective case

In the context of a buoyancy driven ABL where a constant heat flux is imposed at the ground surface, energy is permanently brought in the ABL (and in the whole computational domain) causing both the temperature in the whole ABL and its height to rise constantly. As a result, no permanent regime is expected for the convective case, but a quasi-steady state with a constantly increasing ABL temperature.

Furthermore, in such conditions the height of the top boundary may restrain the duration of computations. An approach similar to Mason and Brown (1999) would be required to prevent the inversion to rise (temperature above a given height is kept constant thanks to the addition of another source term in the temperature equation). In the present case, the upper inversion reaches the upper quarter of the domain after $0.49\,T_{inert}$. Considering a ten layers sponge is applied at the top boundary (roughly 400 m deep), results in the ABL after $0.49\,T_{inert}$ may be affected. This explains the sudden increase of C_{TKE} after $0.5\,T_{inert}$ in Fig. 4.31 d).

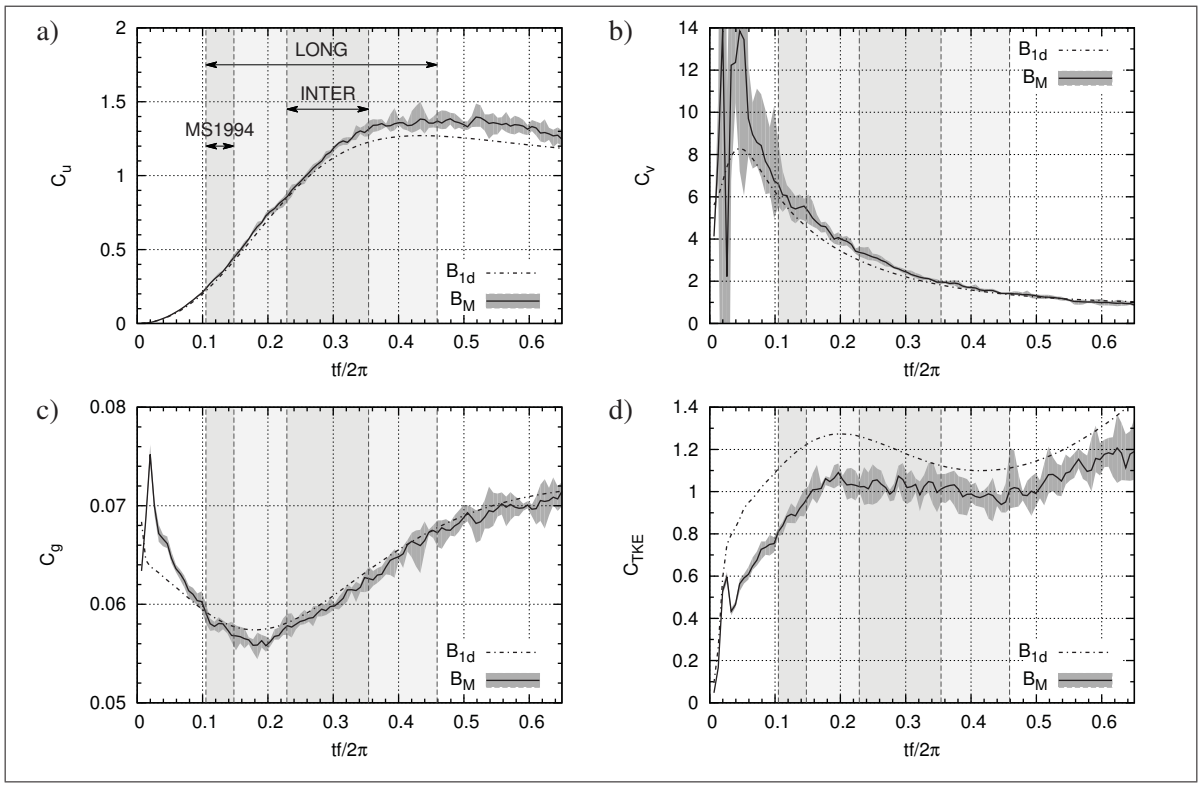

Figure 4.31 Same as Fig. 4.26 but for the convective case

Considering the above mentioned characteristics of the B case, the following three time intervals are elected here (shown in background light grey shaded area in Fig. 4.31 and that differ from their counterparts in the S case) to compute the flow statistics and their scatter:

MS1994: from $0.105\,T_{inert}$ to $0.148\,T_{inert}$, *i.e.* from 6400 s to 9000 s.

INTER: from $0.229\,T_{inert}$ to $0.354\,T_{inert}$, *i.e.* from 14000 s to 21600 s.

LONG: from $0.105\,T_{inert}$ to $0.459\,T_{inert}$, *i.e.* from 6400 s to 28000 s.

The interval MS1994 is the same as in Sec. 4.2 (Moeng and Sullivan, 1994)[9]. The interval LONG starts at the same location as MS1994 but it ends just before the inversion starts to interact with top boundary. It is nine times longer than MS1994. While the use of such a long interval is not recommended (Mason and Brown, 1999; Sorbjan, 2005a), it is meant to

[9] Note that MS1994, which refers to the time interval used by Moeng and Sullivan (1994), is different from the acronym MS94 used in the previous section, which refers to Moeng and Sullivan (1994) study.

Table 4.8 Result parameters from the convective case for model setups shown in Tab. 4.4 and the three time intervals

Name	Interval	u_* [m/s]	w_* [m/s]	z_i [m]	L_{MO} [m]	θ_s [K]	$\overline{w'\theta'}_i$ [K m/s]	U_1 [m/s]	$\Delta\theta_1$ [K]
B_{1d}	MS1994	0.590	1.963	989	-39.2	307.31	-0.017	5.65	4.93
	INTER	0.606	2.011	1074	-43.7	309.92	-0.025	5.22	4.75
	LONG	0.611	1.999	1053	-44.2	309.55	-0.012	5.43	4.75
B_S	MS1994	0.573	1.956	981	-27.3	307.90	-0.023	5.35	5.11
	INTER	0.586	2.044	1128	-29.5	310.49	-0.025	5.09	5.07
	LONG	0.593	2.034	1112	-30.3	310.26	-0.016	5.23	5.04
B_M	MS1994	0.579	1.962	989	-28.8	307.79	-0.028	5.29	4.99
	INTER	0.599	2.039	1120	-32.5	310.26	-0.024	5.01	4.81
	LONG	0.605	2.029	1103	-32.8	310.06	-0.015	5.18	4.81

better evaluate the scatter of the results. The last interval, INTER, is locate in an intermediate region (almost centred at the same time as LONG) starting after the peak of TKE and finishing well before the top boundary could have an impact on the solution. The coefficient C_{TKE} is almost constant during the whole INTER interval, advocating that a fully developed quasi-steady turbulent regime is well established. INTER is three times longer than MS1994.

4.3.1.2.1 Steadiness of the solution

Concerning the time evolution of B, Fig. 4.31 shows the evolution of integral coefficients, Eq. (4.4). Based on MS1994, INTER and LONG intervals, Tab. 4.8 summarize the various key parameters, Figs. 4.32 and 4.33 present the vertical profiles of the dimensional first order moment and non-dimensional first, second and third order moments, and finally Fig. 4.34 shows the streamwise and vertical velocity longitudinal spectra at various height agl in the ABL.

From Fig. 4.31 and Tab. 4.8, convective case results follow the same general trends as the shear case. However, inertial oscillation amplitude and time advancement slightly differ, and, since convection (originating from the heated surface) is the driving process of B, a clear increase of the ABL height z_i, and the temperature across the ABL is to note between MS1994 and the other two intervals. From Tab. 4.8, z_i is increased by roughly 10 % and θ_s by 2.5 K between MS1994 and INTER/LONG which cause L_{MO} to increase by more than 5 %.

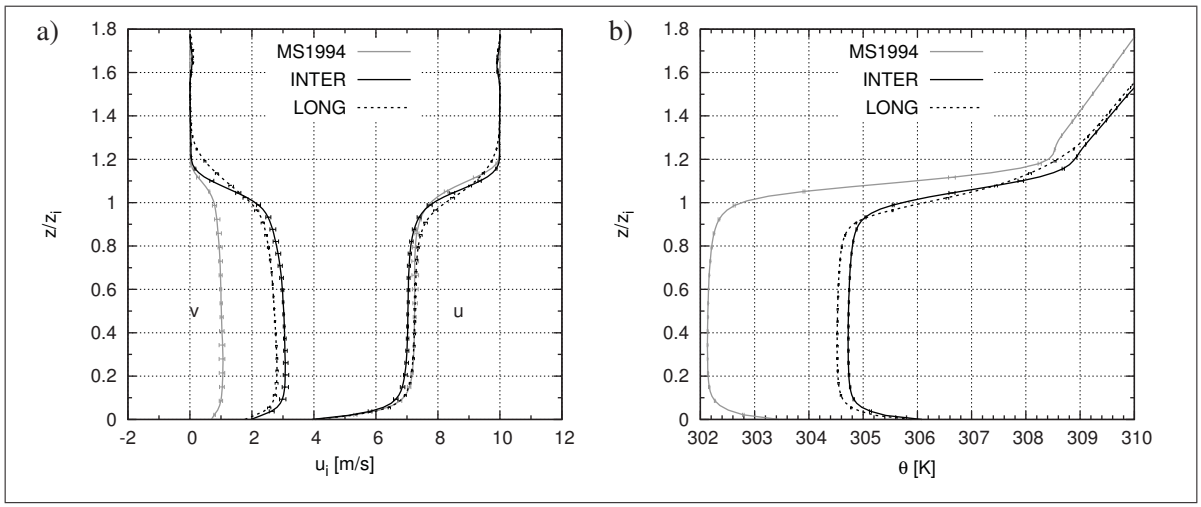

Figure 4.32 Dimensional profiles from B_S along with the scatter for the three time intervals: a) horizontal velocity components; b) potential temperature

Interestingly, as seen in Tab. 4.8 and Figs. 4.32, 4.33 and 4.34, results (even dimensional) from INTER and LONG intervals are very close (below 1 % of difference), which is explained by the fact that the two time intervals are centred at almost the same location. Only few of the upper ABL properties present a differences, such as $\overline{w'\theta'}_i$ that is reduced by more than 20 % for LONG in comparison of MS1994/INTER. This is a consequence of the reduction with time of temperature slope and gap at the inversion (notably after $0.35\,T_{inert}$ as seen in Fig. 4.32 b)) causing a less powerful entrainment rate and a smoother shape of the countergradient flux.

Concerning dimensional profiles, Fig. 4.32, all three (*i.e.* u, v and θ) exhibit well-mixed profiles. Furthermore, while u is almost unchanged for the three intervals, v is nearly multiplied by three. Both velocity components retains an almost vertical profile (notably for the u component) all along the simulations due the intense vertical mixing. The potential temperature profile, Fig. 4.32 b), also keeps an almost vertical profile in the mixed layer all along the computation. Changes at the inversion put aside, profiles from INTER and LONG intervals are very similar, and the increase of temperature in the mixed layer is of the same order as the one at the surface, namely ~ 2.5 K. This increase of the temperature is consistent with the value obtained by considering the integral mixed layer, *i.e.* $\left(\overline{w'\theta'}_s + \overline{w'\theta'}_i\right) \Delta t / z_i$.

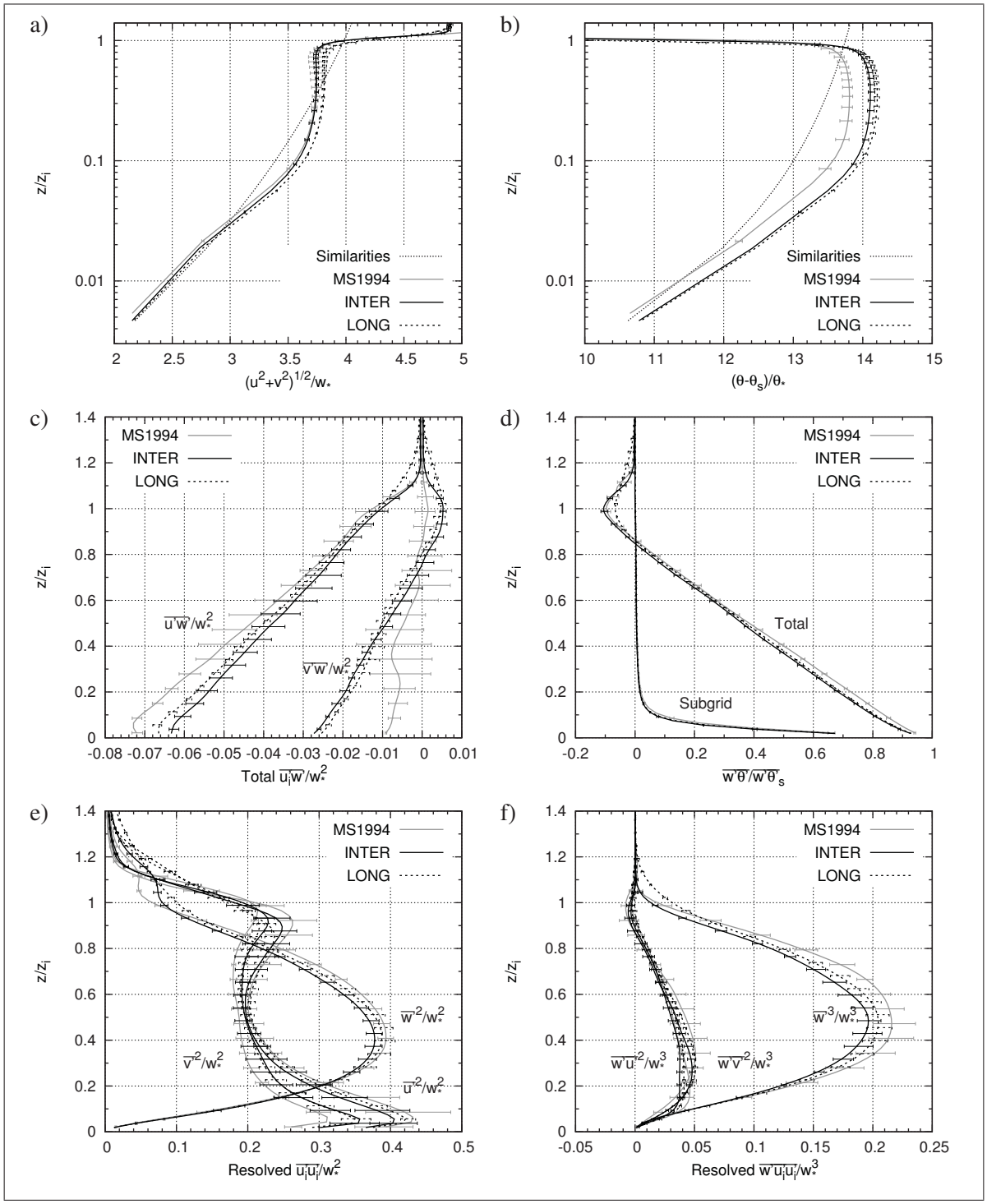

Figure 4.33 Profiles from B_S along with the scatter for the three time intervals: a) velocity modulus; b) potential temperature (both using a log scale in ordinate); c) total momentum fluxes; d) total and subgrid sensible heat flux; e) resolved velocity variances; f) resolved vertical flux of velocity variances

Dimensionless profiles, Fig. 4.33, show a good agreement between the three time intervals since results are almost always within the scatter. The only clear exception are the first order moments that show an offset for MS1994, and profiles at the inversion of some variables for LONG interval. Vertical momentum flux components, Fig. 4.33 c), also show notable differences between MS1994 and INTER/LONG. However, the vertical momentum flux magnitude almost superpose for the three intervals (not shown here). As a result, it can be concluded that the turbulent regime is fully developed and well established even for MS1994 time interval.

The evolution of the vertical momentum flux components as well as the slight changes in the horizontal velocity variances and their vertical fluxes are due to the spanwise velocity component increase with time in the mixed layer. It results in an increase of v vertical gradient across the inversion and at the surface, which causes a larger absolute $\overline{v'w'}$ and $\overline{v'^2}$ in those regions. Furthermore, $\overline{u'^2}$ and $\overline{v'^2}$ are getting closer throughout the whole ABL while $\overline{w'^2}$ is almost unchanged and $\overline{w'u'^2}$ and $\overline{w'v'^2}$ superpose above $0.6\,z_i$. However, due to the fading out of the inversion, the location of the peak of $\overline{u'^2}$ and $\overline{v'^2}$ at the inversion is lowered by $0.1\,z_i$, and $\overline{w'^2}$ is increased by more than 50 % just above the inversion between MS1994 and LONG.

Finally concerning the longitudinal spectra of u and w, Fig. 4.34, besides the obvious horizontal offset between MS1994 and INTER/LONG intervals due to the increase of z_i, the same remarks as above can be done: spectra from the three intervals are very close at all heights, notably concerning INTER and LONG, and almost always within the scatter of the results.

The biggest changes in Fig. 4.34 (when taking into account z_i time evolution) are between MS1994 and INTER/LONG and they are located in the lowest wave numbers notably at the level $z = 958$ m. In the near-surface region for the lowest wave numbers of MS1994, the slope of E_u differs from the mixed layer and a merge of the spectra appears when plot against zk_x (not shown here), as predicted by Drobinski *et al.* (2004) (albeit for the neutral ABL). E_w also feature slightly more energy in that region of the spectra. At the top of the ABL, E_w feature a drastic change with an large increase of the energy in the lowest wave numbers. This change is to be correlated with the fact that, while z_i increases, the spectra at a fixed height is shown (not

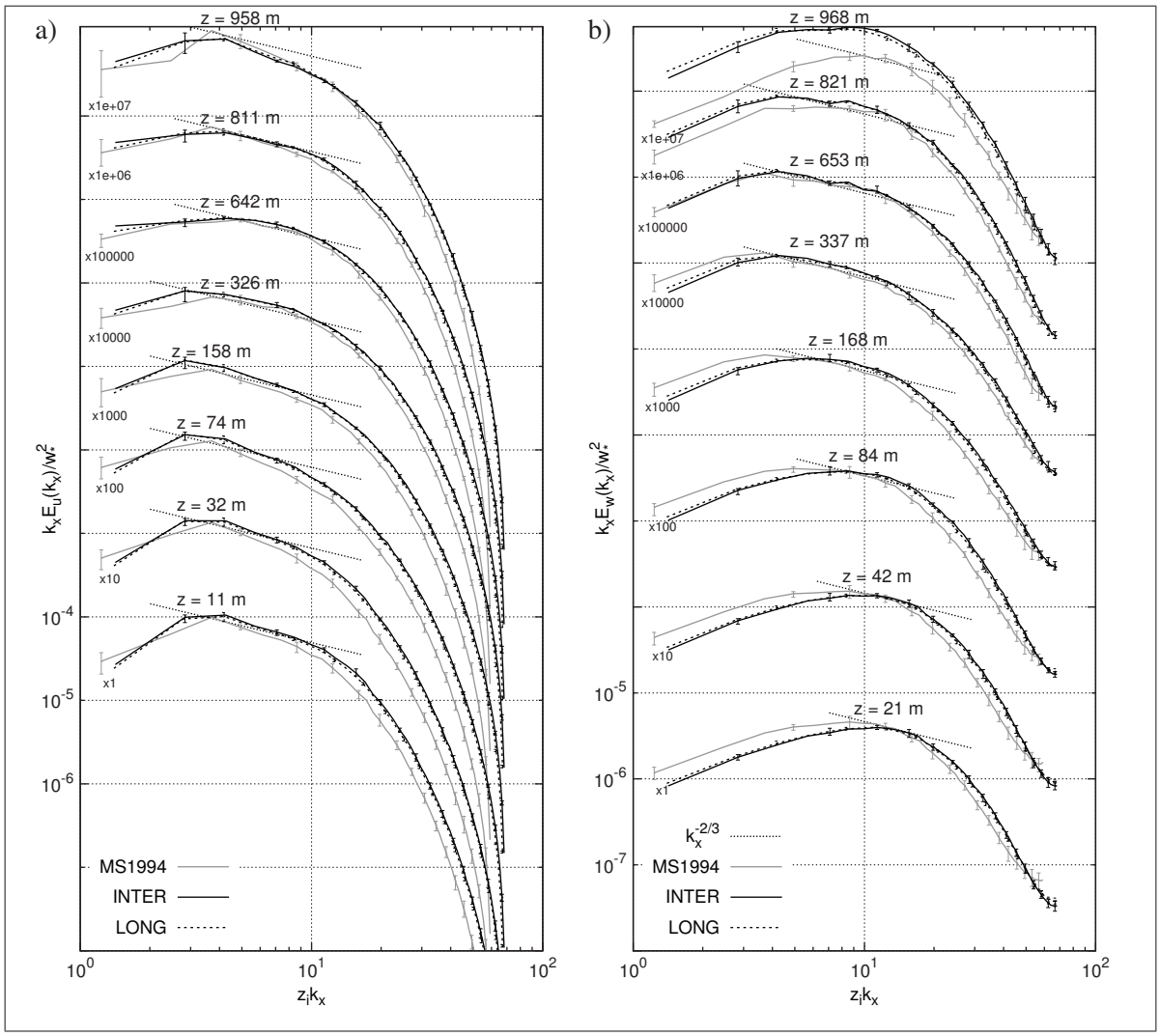

Figure 4.34 Longitudinal velocity spectra from B_S along with the scatter for the three time intervals: a) streamwise component; b) vertical component

at a constant z/z_i). For MS1994, $z = 958$ m almost correspond to the ABL height. The flow is thus clearly affected by the inversion and there is less energy in the velocity fluctuations than in the mixed layer. At the opposite this level is well below the inversion for INTER and LONG (see Tab. 4.8 for numerical values).

To summarize the time evolution of the convective case, it can be say that a representative quasi-steady convective ABL is already well established after $0.1\,T_{inert}$, *i.e.* during MS1994 interval. After $0.5\,T_{inert}$, the top of the ABL starts to interact with the top boundary condition

of the model. Better and more converged statistics appear to be obtained with the use of a interval longer than MS1994. However, a too long interval was proven to affect statistics (notably at the top of the ABL). The interval INTER of roughly $15\,\tau_*$ leads to optimum results.

4.3.1.2.2 Scatter of the results

Scatter of the result of the convective case was sometimes found to be large in Sec. 4.2. It was displayed for MS1994, INTER and LONG time intervals in Figs. 4.32, 4.33 and 4.34. Tab. 4.9 further shows the scatter of the result parameters and Tab. 4.10 present the root mean square of the scatter of selected variables from 0 to $1.2\,z_i$.

Table 4.9 Scatter of the result parameters from Tab. 4.8, Eq. (4.9), for the convective case and for the three time intervals

Name	Interval	$o\,(u_*)$ [m/s]	$o\,(w_*)$ [m/s]	$o\,(z_i)$ [m]	$o\,(L_{MO})$ [m]	$o\,(\theta_s)$ [K]	$o\left(\overline{w'\theta'}_i\right)$ [K m/s]	$o\,(U_1)$ [m/s]	$o\,(\Delta\theta_1)$ [K]
B_S	MS1994	0.008	0.014	21	1.81	0.045	0.008	0.10	-0.015
	INTER	0.004	0.013	21	1.51	0.060	0.006	0.11	-0.018
	LONG	0.004	0.039	63	1.68	0.024	0.003	0.06	-0.001
B_M	MS1994	0.007	0.000	0	1.43	0.052	0.005	0.09	-0.032
	INTER	0.005	0.013	21	1.58	0.025	0.006	0.07	-0.008
	LONG	0.004	0.013	21	0.84	0.019	0.003	0.05	-0.012

The scatter of second and third order moments from the convective case was of most concern in Sec. 4.2. As an example, $\overline{v'w'}$ in the mixed layer based on MS1994 interval features a scatter larger than its mean value, Fig. 4.8 b). The use of a longer the time interval such as INTER and LONG avoid this short coming as shown in Fig. 4.33 c). Similarly, vertical fluxes of velocity variances feature a scatter that is divided by two across the mixed layer.

More generally, from the Figs. 4.32, 4.33 and 4.34, there is a significant decrease of the scatter for all the variables displayed between MS1994 and INTER/LONG intervals. The scatter reduction for the first order moment, Figs. 4.32 and 4.33 a) and b), is less significant than for the second and third order moments shown in Fig. 4.33 c) to f). Those remarks can readily be confirmed in Tabs. 4.9 and 4.10. Between MS1994 and INTER, the scatter is generally

reduced and notably more homogeneous across the ABL for INTER. The locally high scatter values (close to the surface for u and v related quantities, and in the middle of the ABL for w related quantities) are thus absent of the results based on INTER. Differences between INTER and LONG are less notable, and while the scatter is reduced, it is far from being avoided.

Table 4.10 Root mean square of the dimensional scatter from 0 to $1.2\,z_i$, Eq. (4.10), of selected variables (shown in Figs. 4.32, 4.33 and 4.34) for the convective case and for the three time intervals

Name	Interval	$\sigma(u)$ [m/s] $\times 10^0$	$\sigma(w)$ [m/s] $\times 10^{-6}$	$\sigma(\theta)$ [K] $\times 10^0$	$\sigma(\overline{u'w'})$ [m^2/s^2] $\times 10^{-2}$	$\sigma(\overline{u'^2})$ [m^2/s^2] $\times 10^{-1}$	$\sigma(\overline{w'^2})$ [m^2/s^2] $\times 10^{-1}$	$\sigma(\overline{w'\theta'})$ [K m/s] $\times 10^{-3}$
B_S	MS1994	0.130	5.009	0.037	2.754	0.697	0.621	3.045
	INTER	0.111	3.246	0.041	2.500	1.436	0.696	1.972
	LONG	0.076	1.828	0.028	0.827	1.031	0.560	1.133
B_M	MS1994	0.087	3.469	0.037	3.756	1.054	0.880	3.967
	INTER	0.067	2.551	0.032	2.108	1.854	0.524	2.273
	LONG	0.059	1.449	0.017	1.233	0.886	0.303	1.398

To conclude concerning the scatter of the convective case, it is to say that while the turbulent regime is fully developed during MS1994 interval, a longer interval is required to reduce the scatter to an acceptable level. The INTER interval, which is three times as long as MS1994, presents a reduced and much more homogeneous scatter. All variables can be clearly evaluated using INTER. Further increasing the time interval reduce the mean scatter but to a least extent as shown with the LONG interval that is roughly three times longer than INTER. Considering the results from the previous section, the medium size interval, *i.e.* INTER, thus appears to be the best suited for the convective case reproduced here.

4.3.2 Horizontal grid

In order to evaluate the sensitivity of the LES results with regards to the horizontal properties of the grid, *i.e.* horizontal resolution and size of the domain, computations based on three different horizontal meshes, as shown in Tab. 4.4, are discussed here. As a reminder of the three grid discussed in the present section are fully uniform and feature the same properties in the vertical

with 96 uniformly distributed meshes in a $L_z = 1$ km deep domain leading to $\Delta z = 10.4$ m. Their horizontal properties can be summarize as:

Small grid, S^s: $N_i = N_j = 50$ with $L_{x_i} = 2$ km, thus, $\Delta x = \Delta y = 40$ m.
Medium grid, S^m: $N_i = N_j = 64$ with $L_{x_i} = 2$ km, thus, $\Delta x = \Delta y = 31.25$ m.
Large grid, S^l: $N_i = N_j = 96$ with $L_{x_i} = 3$ km, thus, $\Delta x = \Delta y = 31.25$ m.

The large grid S^l is the usual mesh that was used to obtain all the results from Sec. 4.2. This domain is roughly $2\pi z_i$ wide, thus allowing for the largest eddies (of the size of the ABL) to achieve two full turnover. This is a commonly used rule of thumb to define the horizontal size of the domain (Mason and Thomson, 1987; Porté-Agel *et al.*, 2000). The small S^s and medium S^m grids feature the same width, and the latter have the same resolution as S^l while the former is coarser. As a result, based on S^l, S^m and S^s, both impacts of a coarser grid and a smaller domain can be evaluated. Those grids were also used successfully in the literature to reproduce the very same case, *i.e.* by Sullivan *et al.* (1994) for the 64×64 grid and by Ding *et al.* (2001a) for the 50×50 grid, an other similar cases (Porté-Agel *et al.*, 2000; Chow *et al.*, 2005).

In this section, S^m and S^l results are compared in Fig. 4.35 and 4.36 for LONG interval, which allows to appreciate the impact of reducing the domain size while retaining the same resolution. Then, S^s and S^m grid results are compared in Fig. 4.37 and 4.38 for TINERT interval which allows to evaluate the impact of lowering the resolution while keeping the same domain size.

Results based on S^s, S^m and S^l were already introduced in the previous section and some of the outcomes of the grid comparison were already discussed by evaluating the time evolution and the scatter of the shear case (see the various tables and figures of Sec. 4.3.1.1). Indeed, from Fig. 4.26 and Tabs. 4.5, 4.6 and 4.7, it was found that integral coefficients evolution are very similar regardless of the grid used; the coarse grid results have larger scatter than the fine resolution results. However, the horizontal size of the domain does not seem to affect noticeably the scatter (of the integral coefficients).

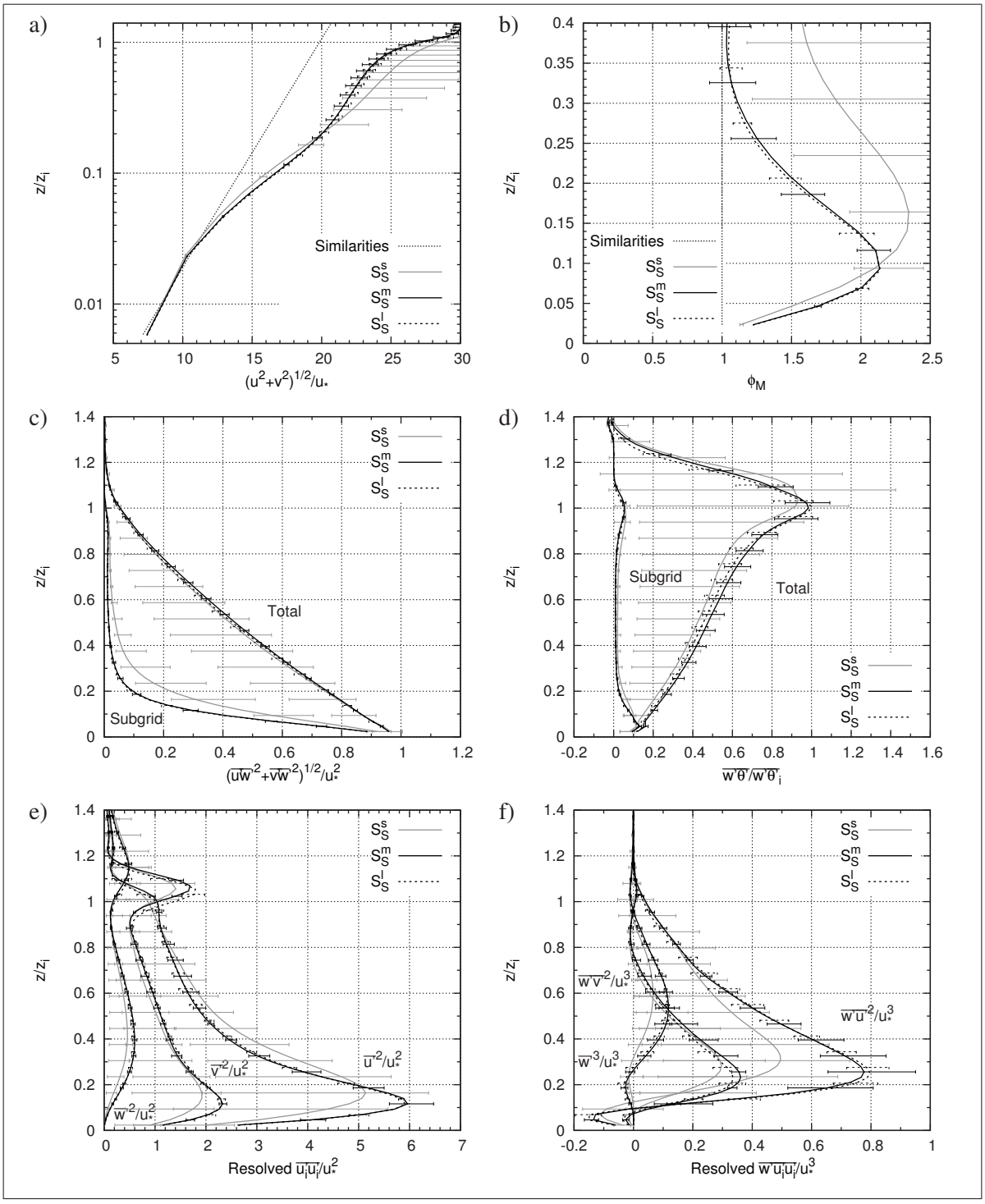

Figure 4.35 Profiles of first, second and third order moments for the small, medium and large grids and based on LONG time interval

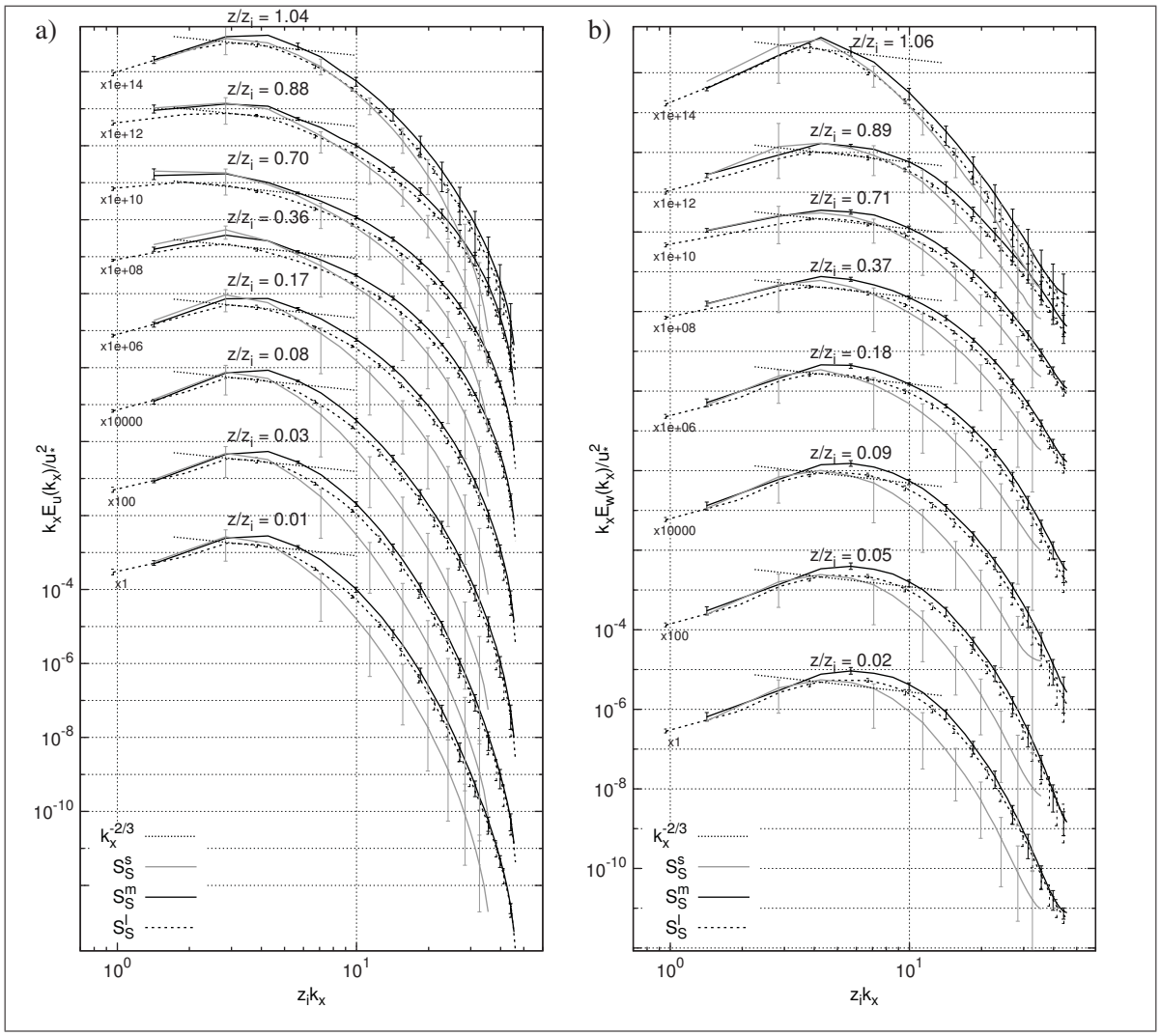

Figure 4.36 Longitudinal spectra of streamwise and vertical velocities from the small, medium and large grids and based on LONG time interval

More importantly, it was noted in Sec. 4.3.1.1.2 that for the 40 m resolution grid, *i.e.* S^s, the on-set of the turbulent regime is sometimes delayed, and few sporadic extinction of turbulence during the first half of computations are observed in few of the results based on S^s. This happens regardless of the SGS model used. Indeed, the mesh starts to be too coarse to allow resolving enough the flow close to the surface and let the shear instabilities develop for the turbulence to be self-sustained. As a result, the smallest mesh (50×50) is found to be at the edge of suitability for use with the present LES model and the shear case. Only TINERT time

interval, *i.e.* from 0.5 to $1\,T_{inert}$, allows to overcome troubles related to the on-set of turbulence. This data is shown in Fig. 4.37. It is also displayed for LONG interval in Fig. 4.35 to better appreciate the impact on statistics of the turbulence ignition delay caused by a too coarse grid.

From the comparison of the medium and large grid results, S^m and S^l in Fig. 4.35 and Tab. 4.5, it is to say that going from a 3 km to a 2 km side mesh does not change ensemble averaged results when using the same resolution (and all the other parameters). Indeed, results nearly always perfectly superpose and result parameter values are very close if not equal. In fact, the only notable (but small) difference between the two ensemble averaged results is in the vertical flux of velocity variances Fig. 4.35 f). The scatter of the results, as previously discussed, is slightly increased by reducing the domain size for the LONG interval. However, in Figs. 4.35 and 4.37 this increase is only notable on $\overline{u'^2}$ and $\overline{w'u'^2}$ profiles below $0.4\,z_i$.

From Fig. 4.36, velocity spectra of the medium grid results, S^m, appear to have more energy notably in the medium wave numbers (in the region where the spectra reach the $-5/3$ slope) for both velocity components. In the highest wave numbers, medium grid results also tend to have slightly more energy, notably in the mixed layer for the vertical velocity. These differences, while small, are higher than the scatter of the result. They can hardly be explained. At the lowest wave number, spectra slope are similar and the level of energy is generally the same in the surface layer (albeit spectra from 2 km side grids consistently starts at a higher wave number). Above, S^m results feature more energy. It is finally interesting to note (not shown here) that the -1 slope in the low wave numbers is slightly better represented for S^l results (*i.e.* a merge of the spectra is exhibit at a lower height).

Figs. 4.37 and 4.38 show comparisons between S^s and S^m based on TINERT interval. Differences in the results are all in line with what observed in the literature when a coarser mesh is used in conjunction with a Smagorinsky SGS model (Mason, 1994; Sullivan *et al.*, 1994; Ding *et al.*, 2001a; Brasseur and Wei, 2010). As illustrated in Fig. 4.37 c), while the total momentum flux is almost unchanged, the subgrid part is increased for S^s indicating that the flow is less resolved close to the surface than with S^m. Similarly the total heat flux is also unchanged,

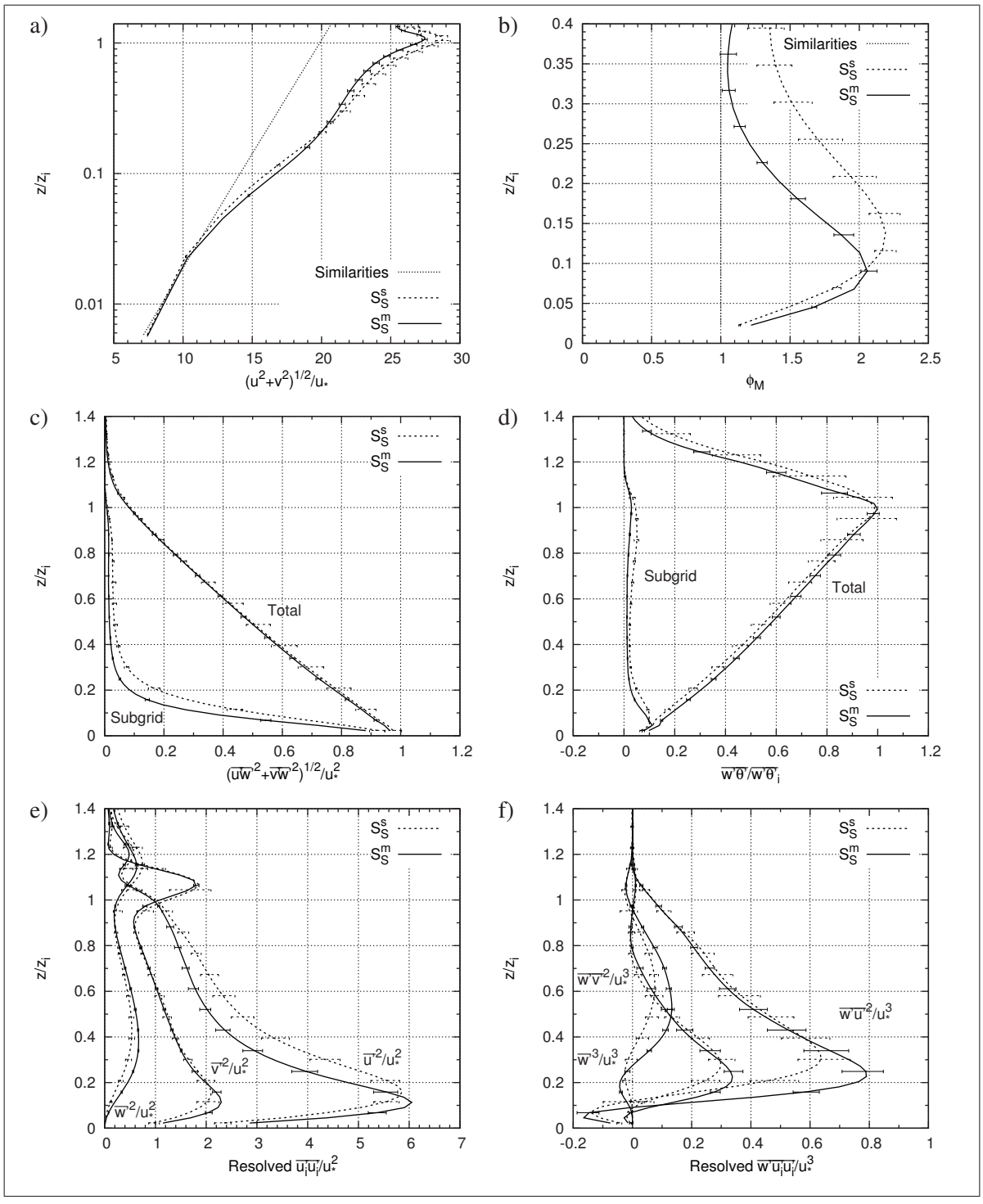

Figure 4.37 Profiles of first, second and third order moments for the small and medium grids and based on TINERT time interval

however, the subgrid heat flux increase is much less notable than for momentum. As a consequence and due to the over dissipative nature of the Smagorinsky SGS model (Porté-Agel *et al.*, 2000), the near-surface velocity shear is increased for S^s, Fig. 4.37 a) and b), which translates in a lower u_*, Tab. 4.5, and a larger departure from the similarity, Fig. 4.37 b). As illustrated by Sullivan *et al.* (1994), and recently theoretically justified by Brasseur and Wei (2010), the amplitude of deviation with Monin-Obukhov theory change slightly, while its height varies more notably depending on the horizontal resolution (getting higher with a coarser mesh). In parallel, the resolved $\overline{u'^2}$ and $\overline{v'^2}$ surface peak, Fig. 4.37 e), is higher in height and less intense for S^s, which is in agreement with a more resolved surface layer (Mason and Thomson, 1992; Sullivan *et al.*, 1994; Porté-Agel *et al.*, 2000). Finally, changes in the vertical flux of velocity variances, Fig. 4.37 f), are consistent with the above remarks. At the opposite, the heat flux is not sensitive to the mesh resolution.

Finally, the velocity spectra from S^s and S^m results are shown in Fig. 4.38, where it can be seen that at all heights, the E_u and E_w from the two results start at the same location and superpose for the two lowest wave numbers. Then, S^s results falloff more rapidly and they feature a notably lower energy level in the medium and high wave numbers. Indeed, due to it coarser resolution, the cut-off wave number of S^s (*i.e.* π/Δ) is roughly $10\, z_i k_x$ lower than for S^m, and this difference holds from the middle to the highest wave numbers, notably in the surface layer. As a consequence, spectra from the coarse grid hardly reaches the inertial subrange $-5/3$ slope, which is particularly true in the surface layer. They falloff very rapidly thus illustrating why S^s grid is at the edge of what can be used with the present model. As a result of the above, and when further considering that the scatter of coarse resolution results S^s is notably higher (often twice the scatter of S^m), results based on higher resolution grid thus prove to be better, notably in the near-surface region.

As a summary from the evaluation of the three grids, it is to conclude that going from a 2 km to a 3 km horizontal grid while keeping the same horizontal resolution does not change ensemble averaged results, which also appears to be the case in the studies of Moeng and Sullivan (1994) and Sullivan *et al.* (1994). Results perfectly superpose and only the scatter of $\overline{u'^2}$ and $\overline{w'u'^2}$

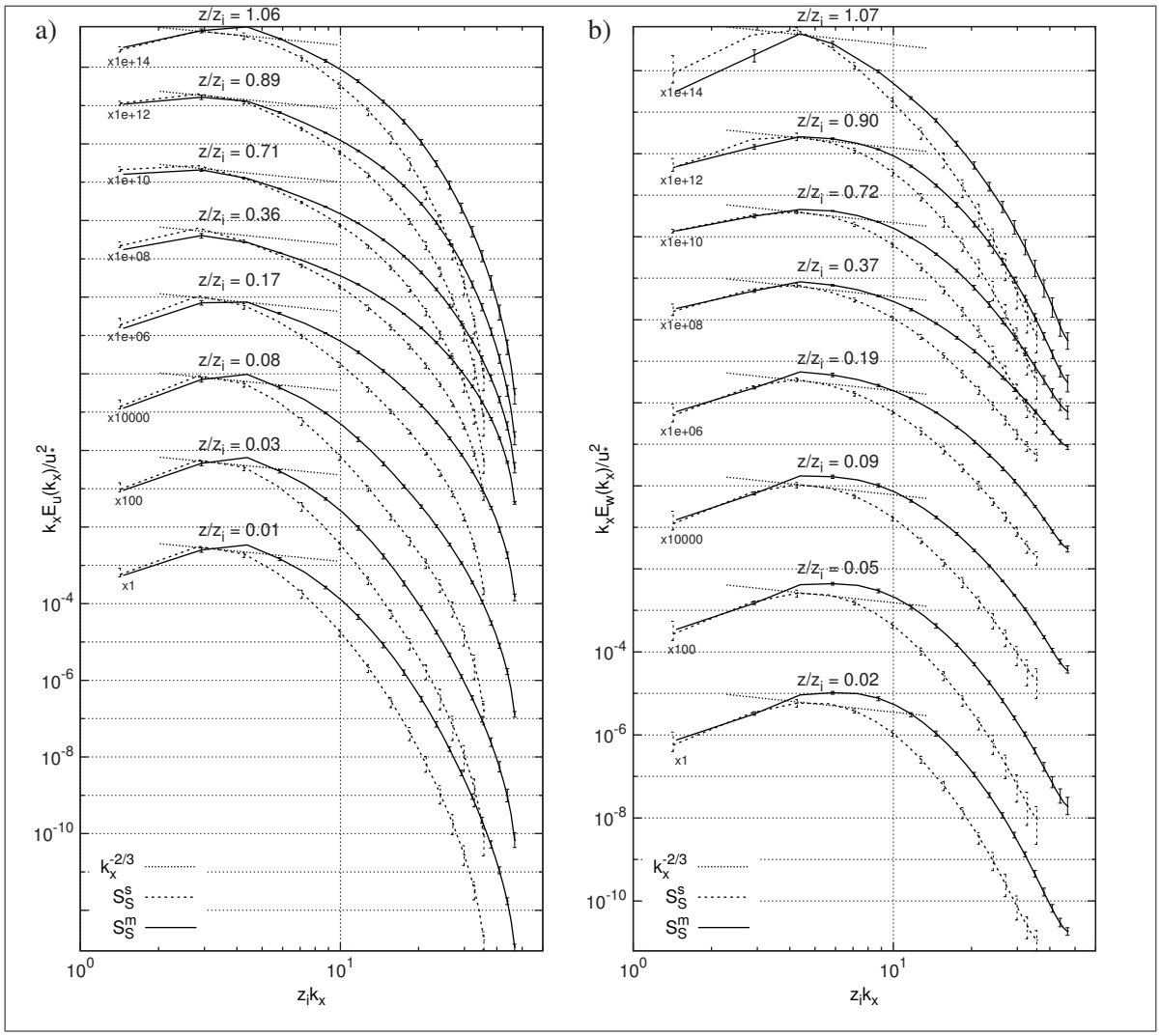

Figure 4.38 Longitudinal spectra of streamwise and vertical velocities from the small and medium grids and based on TINERT time interval

below $0.4\,z/z_i$ is increased in the 2 km side grid results for LONG interval. Furthermore, going from a 31.25 m to a 40 m horizontal resolution while retaining the same domain size, gives results in line with what obtained in the literature (Sullivan *et al.*, 1994; Mason, 1994; Brasseur and Wei, 2010). Flow close to the surface is notably less resolved and the departure from the similarity is increased with a maximum higher in height. However, the coarse mesh S^s, based on a 40 m resolution and 2 km side, prove to be at the edge of suitability to reproduce the shear case of Moeng and Sullivan (1994) with the current methods. Based on that grid, the

on-set of turbulence is sometimes delayed preventing the use of the results based on the LONG interval. Furthermore, the scatter of the results from that grid is very high, even for the TINERT interval. A better resolution grid must be used to allow an advance analysis of the results.

In the literature, similar or coarser grids than S^s have been used successfully in conjunction with the classical Smagorinsky SGS model to reproduce similar shear driven ABL (Andren *et al.*, 1994; Brown *et al.*, 2000; Porté-Agel *et al.*, 2000; Ding *et al.*, 2001a; Chow *et al.*, 2005). The present approach thus appears less suited for coarse meshes, which is perfectly in agreement with the findings of the spectral analysis of Sec. 4.2 (where the current model was found to over dissipate the fine structures in comparison to results from Brown *et al.* (2000) and Porté-Agel *et al.* (2000) due to more dissipative numerics). As a result of the above remarks, the medium grid appears to be as suited as the large grid to reproduce Moeng and Sullivan (1994) shear case, while the small grid, being at the edge of suitability, should be avoided.

4.3.3 Vertical grid

Since the beginning of the study, the shear and convective cases were reproduced based on a vertical grid with 96 uniformly distributed nodes in a 1 km and 3 km deep domain as in MS94. However, this notably departs from a classical configuration of the MC2 where its upper boundary is commonly located above 10 km, vertical grid is monotonically stretched upward, and the width/height ratio of the near-surface cells is commonly higher than 100. In addition, as described in Sec. 3.2.3, a multi-layer sponge is applied at the top of the domain to absorb waves and avoid their spurious reflexion in the computational domain. This sponge layer is based on the ten uppermost levels here, *i.e.* roughly ~ 100 m depth for S based on the uniform grid. When the roof of the model is lowered drastically, as in the present case, care must be taken for the upper boundary condition not to interact with the results.

Concerning the hybrid TKE and UKMO Smagorinsky SGS model used to reproduce all the cases in this section, it is noteworthy that following Brown *et al.* (1994) and Mason and Brown (1999), the filter width equals Δ_H, while it is set to $(\Delta x \Delta y x \Delta z)^{1/2}$ when $\Delta z > \Delta_H$ for the Smagorinsky SGS model (see Sec. 2.2.3.1 and Sec. 2.2.3.3). Thus, for S^m/S^l and B grids (that

have an aspect ratio of $\Delta_H/\Delta z = 3$ and 2.5 respectively), the vertical resolution is not included in the definition of the filter of both SGS models and $\Delta = \Delta_H$. As a consequence, changing the vertical mesh does not directly affect the filter width, and changes in the results may thus primarily be associated to the resolved scales.

As the consequence of the above, many aspects of the vertical grid impact on the results need to be studied. Furthermore, in the longer term, the current LES model might be used as a last level of nesting (of a mesoscale model) for real cases. A vertical uniform grid is very restrictive and the use of a non-uniform vertical grid would be desirable. Mainly, it would allow to raise top boundary while retaining a sufficient resolution in the whole ABL. In this section, the impact of the vertical grid on the results is evaluated by reproducing the shear case based on various non-uniform vertical grids. The sensitivity of the results to the vertical mesh (at various heights) is studied though the following aspects: increase of the top boundary height, refinement of the grid in the surface layer, reduction of the resolution in the mixed layer and at the inversion. These various cases also serve to complete the validation of the 3D turbulent diffusion implementation with regards to non-uniform vertical mesh. Indeed, vertical terms of the turbulent diffusion were already evaluated in Sec. 4.1.

The following three non-uniform vertical grids (obtained as described in Sec. 3.2.2.4), in addition to the usual uniform mesh, are used here to study the impact of the vertical grid:

Grid A: $n_k = 96$, $z_{top} = 1000$ m, uniform (same grid as Moeng and Sullivan (1994)).
Grid B: $n_k = 60$, $z_{top} = 1500$ m, $\alpha = 2$, $\sigma = 6$ and $z_{ref} = 500$ m.
Grid C: $n_k = 60$, $z_{top} = 1500$ m, $\alpha = 4$, $\sigma = 9$ and $z_{ref} = 550$ m.
Grid D: $n_k = 96$, $z_{top} = 3000$ m, $\alpha = 6$, $\sigma = 15$ and $z_{ref} = 600$ m.

Tab. 4.11 shows k indices along with corresponding height and resolution for key locations in the computational domain: “Surface” stands for the first level above the surface, “Mixed layer max.” for the level with the maximum Δz within the mixed layer, “Inversion min.” for the level with the minimum Δz at the inversion, “Inversion top” for the first level above the inversion with $\Delta z > 30$ m, and finally “Sponge” for the first level in the sponge layer.

Table 4.11 Details of the vertical grid properties at various key locations in the computational domain

Grid	Surface			Mixed layer max.			Inversion min.			Inversion top			Sponge		
	k	z [m]	Δz [m]	k	z [m]	Δz [m]	k	z [m]	Δz [m]	k	z [m]	Δz [m]	k	z [m]	Δz [m]
A	1	10.4	10.4			10.4			10.4			10.4	86	895.8	10.4
B	1	8.3	8.3	24	329.1	18.4	34	482.1	12.4	44	691.0	32.4	50	937.3	46.4
C	1	5.9	5.9	24	293.5	16.9	35	460.4	13.6	46	684.8	31.6	50	845.6	45.5
D	1	3.7	3.7	32	282.6	12.5	49	473.0	9.9	67	778.9	30.3	86	1906.6	88.7

From Tab. 4.11, resolution at the surface of non-uniform grids is always better than the uniform grid: it is divided by three going from grid A to grid D. At the opposite in the mixed layer, resolution of the uniform grids is always better than non-uniform grids: grid B is the worst case with $\Delta z = 18.4$ m at that height (which is almost twice as large as grid A) while grid D has almost the same resolution as A. At the inversion, resolutions are very similar for all grids: grid C is the worst case with 13.6 m followed by grid B with 12.4 m. Finally, there are 200 m for grid B and C and 300 m for grid D above the inversion before the resolution get higher than 30 m (*i.e.* roughly the horizontal resolution of S^m and S^l). Below that height, and thus in the entire ABL, Δz of all grids is much smaller than the horizontal resolution. Hence, and due the definition of the filter width used here, results should not be significantly impacted by the change of vertical resolution. The resolved part of the flow is expected not to decrease.

Result parameters from the column model, the Smagorinsky SGS model and the hybrid TKE SGS model are summarized in Tab. 4.12 for all the vertical grid configurations and the previously explored horizontal grids and time intervals. It is important to note that U_1 and $\Delta\theta_1$ are values at the first grid level, they are thus directly a function of the grid.

Results from the column model are nearly unchanged and all vertical grids lead to the same parameters as seen in Tab. 4.12. In fact, the vertical profiles of the various variables of interest (not shown here) are also almost unaffected by the vertical grid. This further confirms that the discretization of vertical terms in the turbulent diffusion (as well as the other parts of the model), is correctly implemented with regards to a non-uniform vertical grid.

Table 4.12 Result parameters from the shear case for the vertical grids evaluated in Sec. 4.3.3 and based on model setups detailed in Tab. 4.4 and two time intervals

Name	Interval	Grid	Realizations	u_* [m/s]	z_i [m]	θ_s [K]	$\overline{w'\theta'}_i$ [K m/s]	U_1 [m/s]	$\Delta\theta_1$ [K]
S_{1d}	LONG	A	1	0.547	516	300.76	-0.0311	4.50	-0.0023
		B	1	0.536	509	300.67	-0.0324	4.26	-0.0010
		C	1	0.548	511	300.77	-0.0313	3.91	-0.0000
		D	1	0.546	521	300.75	-0.0313	3.37	-0.0000
	TINERT	A	1	0.639	589	302.38	-0.0226	5.58	-0.0016
		B	1	0.636	597	302.33	-0.0241	5.22	-0.0006
		C	1	0.637	604	302.41	-0.0236	4.82	0.0003
		D	1	0.637	598	302.38	-0.0233	4.20	0.0001
S_S^s	TINERT	A	10	0.566	454	300.63	-0.0058	4.95	-0.0008
		B	10	0.571	485	300.50	-0.0063	4.63	0.0003
S_S^m	LONG	A	5	0.499	453	300.38	-0.0036	4.29	-0.0008
		B	1	0.494	498	300.34	-0.0028	3.99	0.0005
		C	1	0.500	450	300.37	-0.0038	3.68	0.0012
		D	1	0.496	463	300.37	-0.0050	3.14	0.0007
	TINERT	A	5	0.587	465	300.67	-0.0062	5.17	-0.0011
		B	1	0.583	429	300.53	-0.0053	4.83	0.0004
		C	1	0.584	434	300.62	-0.0074	4.36	0.0011
		D	1	0.570	463	300.61	-0.0078	3.65	0.0007
S_S^l	LONG	A	5	0.499	459	300.38	-0.0037	4.29	-0.0009
		B	5	0.498	455	300.35	-0.0041	3.96	0.0004
S_M^s	TINERT	A	10	0.579	459	300.75	-0.0071	4.89	-0.0010
		B	10	0.574	480	300.60	-0.0072	4.54	0.0002
S_M^m	LONG	A	5	0.512	461	300.40	-0.0048	4.17	-0.0010
		B	1	0.509	498	300.36	-0.0053	3.94	0.0004
		C	1	0.509	450	300.38	-0.0045	3.64	0.0012
		D	1	0.510	452	300.40	-0.0050	3.17	0.0007
	TINERT	A	5	0.601	465	300.77	-0.0076	5.06	-0.0012
		B	1	0.592	412	300.61	-0.0069	4.69	0.0003
		C	1	0.593	403	300.69	-0.0066	4.30	0.0010
		D	1	0.585	475	300.72	-0.0086	3.69	0.0006
S_M^l	LONG	A	5	0.515	465	300.40	-0.0047	4.20	-0.0010
		B	5	0.511	455	300.38	-0.0054	3.91	0.0003

Concerning the LES models, from in Tab. 4.12, changes in u_* and θ_s between the results from the four grids are generally lower than 1 %, except for the grid D that feature a value of u_* that is slightly lower (2.5 % lower than grid A results in the worst case for both S_S and S_M results). It is also interesting to note that $\Delta\theta_1$ changes sign between grid A and others vertical grids. The

absolute value of $\Delta\theta_1$ is however very small. Similarly, the minimum sensible heat flux at the inversion $\overline{w'\theta'}_i$ appears to be very sensitive to the vertical mesh used. However, this quantity is also very small and generally presents a relatively high scatter as discussed previously.

Finally at the opposite, the height of the ABL z_i features notable changes between the various results in Tab. 4.12. Indeed, grids B and C lead to a lower ABL than grid A and D. This is particularly clear for TINERT interval were this difference is roughly 10 %. This may indicate, together with the differences in the countergradient heat flux at the inversion, that processes in that region are sensitive to the vertical grid: a lower resolution than grid A at the inversion and above appears to impact the results, while a higher domain does not. As a result, and in order to isolate those changes, all the figures presented in this section use the reference height of 460 m to scale the results instead of the computed ABL height.

To further explore the impact of the vertical grid, Fig. 4.39 compares the results based on A and B grids for the large domain S^l and LONG interval. Fig. 4.40 also shows the results for those two vertical grids but for the small domain S^s and TINERT interval. Finally, Fig. 4.41 shows the results for the four vertical grids based on the medium grid S^m and TINERT interval.

Close to the surface, it can be seen from Figs. 4.39, 4.40 and 4.41 that the results are almost independent of the vertical grids. In fact, the non-dimensional shear and the third order moments differences are always lower than the scatter. The only noticeable difference (that is higher than the scatter and which is clearly seen on the three figures) is the reduction with the increase of the resolution of the small spurious negative heat flux in surface layer. From Fig. 4.41 d), the latter, which has no effect on the results (as discussed previously), is almost divided by two going from the uniform grid to grid D, which tends to indicate that it is caused by a discretization error. It can thus be concluded that the increase of the vertical grid resolution close to the surface has no impact on the results (when using S^s, S^m and S^l horizontal grids).

In the mixed layer, it can also be said from Figs. 4.39, 4.40 and 4.41 that changes related to the vertical grid are very small if not absent. The most clear but small difference is in the vertical flux of momentum that is always smaller in the upper part of the ABL for B, C and D grids,

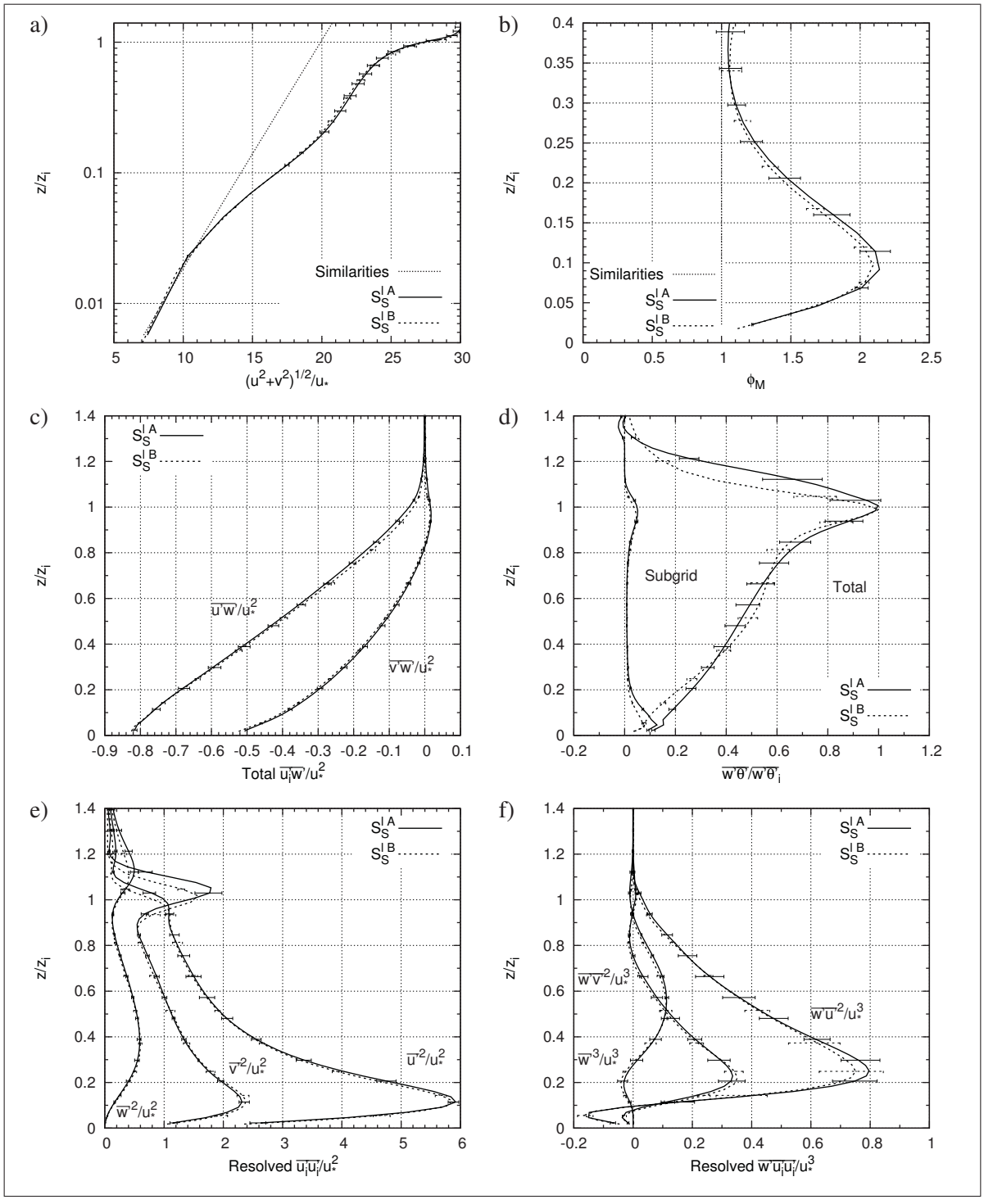

Figure 4.39 Profiles of first, second and third order moments for A and B vertical grids based on S_S^l and LONG time interval

see Figs. 4.41 c), 4.40 c) and 4.41 c). Furthermore, $\overline{u'w'}$ from all non-uniform grids almost perfectly superpose in the upper part of the ABL, as seen in Fig. 4.41 c). Those differences are thus neither due to the scatter nor to the changes in vertical resolution in the mixed layer, but they are most likely to be related with changes at the inversion.

In view of those results, it can be assume that at the surface and in the mixed layer, the increase of vertical resolution (as well as a stretched vertical grid) does not affect the results. The resolved part of the flow is not increase (which is also confirmed by the longitudinal velocity spectra, not shown here). Furthermore, due to the filter width definition used in the Smagorinsky and hybrid TKE SGS models, subgrid scales are also unchanged. Finally and since the results are not a function of the vertical grid, it is also to conclude that the discretization of the various terms with regards to a non-uniform vertical grids is correctly implemented.

The picture is changed at the inversion and neighbouring region, as the minimum heat flux as well as the local maximum in velocity variances presents some notable differences. Others variables are less affected, but they are all fading out to zero above the inversion (preventing a clearly appreciation of their differences).

For the large domain S^l with the LONG interval, Fig. 4.39, grid A and B flow features in that region are largely similar, notably when also considering that the scatter of the results is high. The local maximum in velocity variances show a slightly lower height and amplitude, while minimum heat flux is identical and only its return to zero shape above the inversion is different between the two grids. Grid B features a smoother transition and the positive heat flux region above the inversion is not anymore present. However, the scatter is this region is high.

When further considering S^s and S^m results for the TINERT interval as shown in Tab. 4.4, Figs. 4.40 and 4.41, it becomes clear that the resolved heat flux at the inversion (and velocities variances to a least extent) is sensitive to the vertical grid resolution, but not the height of the top boundary. In Figs. 4.40 d) and 4.41 d), grid B heat flux presents a spurious zigzag (which is also present for the LONG interval, not shown here). Resolved heat flux from grid C also shows a discontinuity above the inversion. These unusual shapes are confirmed by the notably

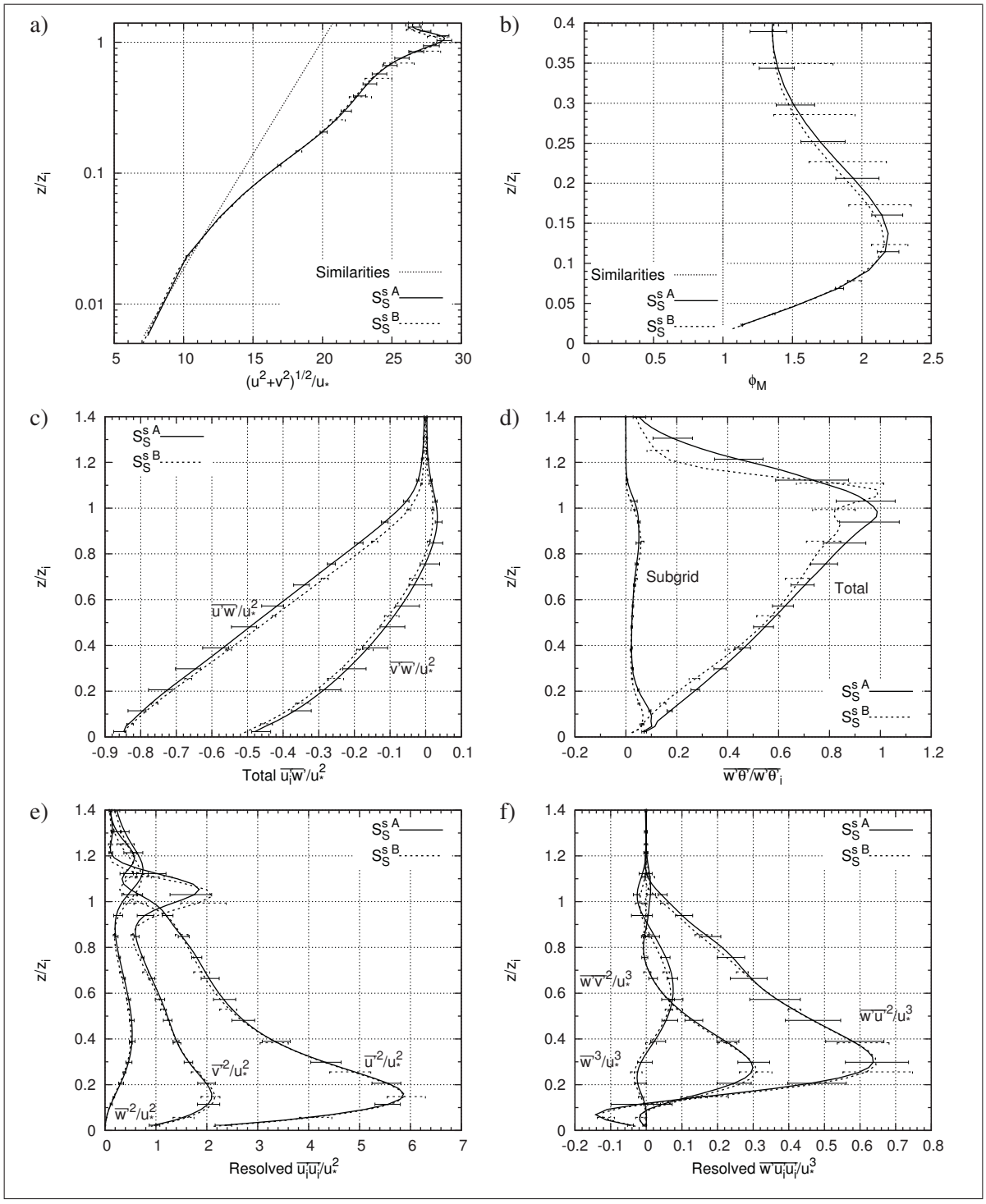

Figure 4.40 Profiles of first, second and third order moments for A and B vertical grid based on S_S^s and TINERT time interval

different z_i value for those cases. Those remarks tend to indicate that grid B and C are too coarse at the inversion causing the solver to struggle. However, with respectively $\Delta z = 12.4$ m and $\Delta z = 13.6$ m at the inversion, the resolution is indeed coarser but it is not far from the uniform grid resolution. In fact, and maybe more importantly, the stretching of the grid above the inversion is high for those grids, and there are only 200 m before $\Delta z > 30$ m for grids B and C. This height is of the same order as the depth required for the resolved heat flux to return to zero above the inversion. In comparison, grid D show 300 m before $\Delta z > 30$ m, and none of the above observed problems are present for that grid in Fig. 4.41. This latter grid is three times taller than grid A (see Tab. 4.11). However at the inversion, both results feature very similar shape (heat flux profiles superpose for the LONG interval, not shown here). Adding this to the good agreement in predicted z_i for both grids, it can be concluded that grid A is sufficiently tall and that the results are not impacted by the top boundary condition of the model.

As a result, heat flux at the inversion is very sensitive to the vertical grid resolution at that height and above in comparison to the other variables. A too high stretching above the inversion may impact the resolved heat fluxes of the whole inversion and in turn affect z_i. At the opposite, increasing the height of the top boundary does not appears to affect the results. However, and to mitigate those thoughts, the heat flux of the shear case is very small and not considered as a dominant variable. Furthermore, the differences noted above the inversion are not affecting the flow in the lowest two third of the ABL. It is thus somewhat confusing that a variable computed based on a negligible quantity is used to scale the results.

Finally, concerning the scatter of the results, Figs. 4.39 and Fig. 4.40, some of the profiles present a reduced scatter, while it is increased in other regardless of the vertical grid (*i.e.* the second versus the third order moments in Figs. 4.39). As a consequence, no clear tendency can be concluded. However, it is to note that small domain results S^s based on grid B are less affected by the turbulence ignition delay problems (which is clear ŵhen considering at statistics of S_s based on LONG interval - not shown here). For the TINERT interval however, the reduction of the scatter between grid A and B is not clear.

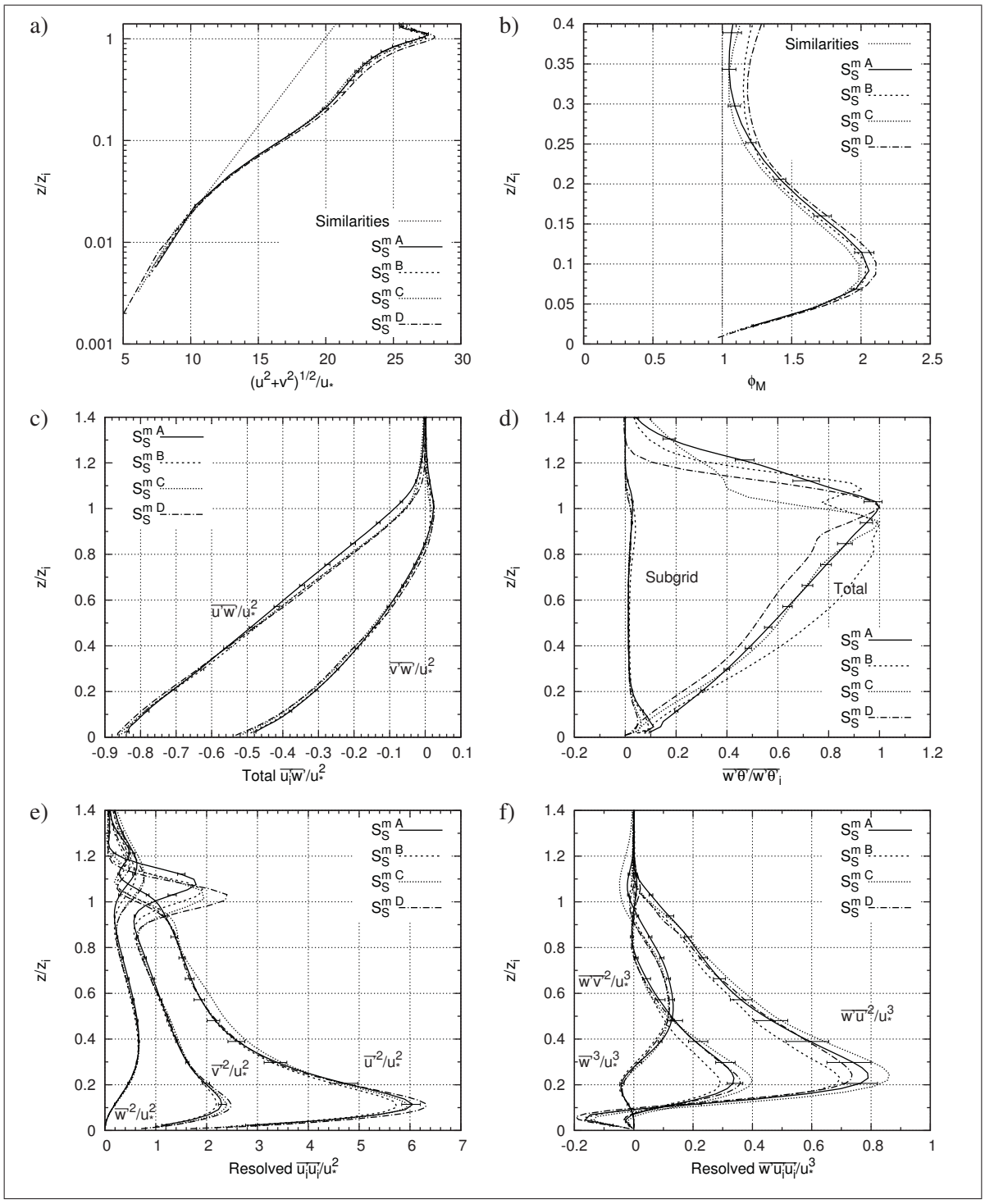

Figure 4.41 Profiles of first, second and third order moments for A, B, C and D vertical grids based on S_S^m and TINERT time interval. Only $S_S^{m\,A}$ is based on the ensemble average of five results

As a conclusion and from the four grid used here, the use of a finer vertical mesh close to the surface, as well as a coarser vertical grid in the mixed layer does not change the results. Both resolved and subgrid part of turbulent quantities are almost unaffected at these heights (and only the very small spurious surface heat flux is reduced by increasing the resolution). This shows that increasing the resolution anisotropically does not increase the resolved part of the flow, and subgrid scale quantities are also unaffected thanks to the filter width definition. As a consequence, non-uniform meshes have no impact on the results which confirms the proper discretization of the various terms. Similarly, increasing the height of the domain does not appears to affect the results. Thus, grid A seems to be perfectly suited even if a sponge is used as top boundary on the ten uppermost level of the domain. At the opposite, heat flux at the inversion is very sensitive to the vertical grid resolution (while other variables seem unaffected). Depending of the mesh at the inversion and above, heat flux shape differs and a spurious zigzag can develops. The mesh needs to be sufficiently fine not only in the upper part of the ABL, but also up to the top of the temperature inversion, in order to properly reproduce the heat flux minimum at the inversion. The computation based the large domain are generally less sensitive to the changes in vertical resolution at the inversion. As a result, the use of the minimum heat flux as the definition of the height of the boundary layer for shear case is very demanding for the model, and a good prediction of z_i may also imply that the processes at the inversion and above are correctly reproduced.

4.3.4 Time step

The last numerical parameter tested was the time step. As illustrated in the model description, Sec. 3.2.1, the current model is based on a Semi-Implicit Semi-Lagrangian (SISL) time stepping/advection scheme. This allows for the use of a rather large time step in comparison to Eulerian approaches (Girard *et al.*, 2005; Steppeler *et al.*, 2003), at least in the NWP context. Indeed, the commonly accepted maximum value of the CFL number that can be used with a SISL approach equals unity[10], while a value of roughly 0.25 is generally accepted for explicit Eulerian methods (Girard *et al.*, 2005; Steppeler *et al.*, 2003).

[10] Note however that the SL scheme is known to be stable for CFL higher than unity (Randall, 2011, Sec. 5.12).

Considering the geostrophic wind velocity $\boldsymbol{v}_g = (u_g, v_g) = (\text{const.}, 0)$, which is also the free atmosphere velocity vector modulus, a reference CFL can be defined such as

$$C_{\text{CFL}} = \frac{u_g \Delta t}{\Delta x}. \tag{4.11}$$

Based on numerical parameters from Tab. 4.4, $C_{\text{CFL}} = 0.75$ for S^s ($\Delta t = 2$ s, $\Delta x = 40$ m, $u_g = 15$ m/s), $C_{\text{CFL}} = 0.72$ for S^l and S^m ($\Delta t = 1.5$ s, $\Delta x = 31.25$ m, $u_g = 15$ m/s), and $C_{\text{CFL}} = 0.77$ for B ($\Delta t = 4$ s, $\Delta x = 52.03$ m, $u_g = 10$ m/s). These values are conservative in comparison to the generally accepted maximum CFL of the SISL scheme but still relatively high. As an example, it is higher than for all models used in Andren *et al.* (1994).

In this section, the impact of the time step is explored for the shear and convective cases. Concerning the shear case, results based on $C_{\text{CFL}} = 0.48$ and $C_{\text{CFL}} = 0.96$, in addition to $C_{\text{CFL}} = 0.72$, are discussed. For the convective case, given the conclusions from the shear case, only $C_{CFL} = 0.38$, in addition to $C_{\text{CFL}} = 0.77$, is studied.

4.3.4.1 Shear case

Wind speed in the free atmosphere is the fastest of the domain during the first part of the integrations of the shear case. Then, the velocity profile overshoot u_g at the top of the ABL after $0.5\,T_{inert}$ as seen in Figs. 4.26 b) and 4.27 a). As a result, the effective maximum CFL increases getting closer to the generally accepted limit of the SISL.

Based on these considerations, the three following values of C_{CFL} are evaluated here using the medium domain[11] S^m and the usual uniform vertical grid, Tab. 4.4:

$\boldsymbol{C_{\text{CFL}} = 0.48}$**:** $\Delta t = 1.0$ s for S^m. A priori conservative with regards to the SISL.
$\boldsymbol{C_{\text{CFL}} = 0.72}$**:** $\Delta t = 1.5$ s for S^m. A priori slightly conservative.
$\boldsymbol{C_{\text{CFL}} = 0.96}$**:** $\Delta t = 2.0$ s for S^m. Almost equal to the SISL generally accepted limit.

[11] Note that cases with $C_{CFL} = 0.96$ was also reproduced with the large grid, S^l, leading to the very same conclusions. These latter results are thus not shown here.

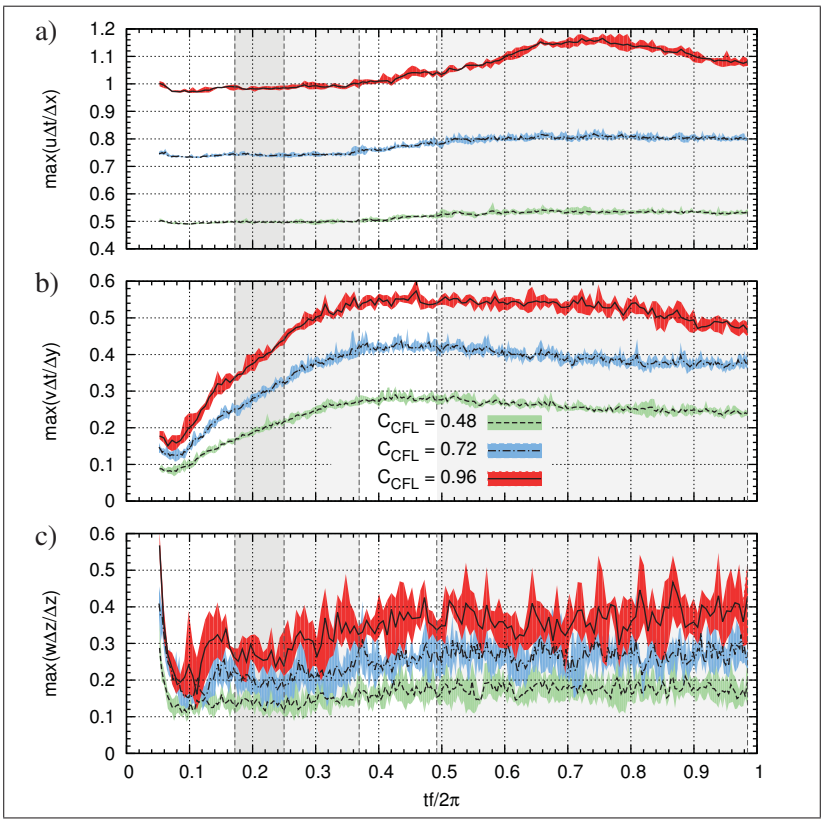

Figure 4.42 Maximum instantaneous local CFL, *i.e.* $C_{\mathrm{CFL}}^{\max}$, for the three directions based on S_S^m with C_{CFL} equal to 0.48, 0.72 and 0.96. Coloured overlaid regions show the scatter of the results. Grey overlaid background areas show post-processing time intervals

To better appreciate the effective maximum local instantaneous CFL of the shear case, *i.e.* $C_{\mathrm{CFL}}^{\max}$, Fig. 4.42 shows its evolution in the streamwise, spanwise and vertical directions. It can be seen that $C_{\mathrm{CFL}}^{\max} > 1$ in the streamwise direction after $0.4\,T_{inert}$ for $C_{\mathrm{CFL}} = 0.96$. The trends are however almost similar for all computations, and in fact, all curves scale perfectly when divided by their respective C_{CFL} (which returns $\max(u_i)/u_g$). Only computations based on $C_{\mathrm{CFL}} = 0.96$ departs from the others for $tf/2\pi > 0.55T_{inert}$ in the streamwise direction, Fig. 4.42 a), and less significantly in the spanwise direction, Fig. 4.42 b) (see also the differences between LONG and TINERT intervals in Tab. 4.13 and Figs. 4.43 and 4.44). It thus tend to indicate that computations using $C_{\mathrm{CFL}} = 0.96$ are biased after $tf/2\pi > 0.55T_{inert}$, while results based on $C_{\mathrm{CFL}} = 0.48$ and $C_{\mathrm{CFL}} = 0.72$ appear always valid.

Table 4.13 Result parameters from the shear case for the three C_{CFL} evaluated in Sec. 4.3.4.1 and based on model setups from Tab. 4.4 and two time intervals

Name	Interval	C_{CFL}	$C_{\mathrm{CFL}}^{\langle\overline{u}\rangle}$	$C_{\mathrm{CFL}}^{\max}$	u_* [m/s]	z_i [m]	θ_s [K]	$\overline{w'\theta'}_i$ [K m/s]	U_1 [m/s]	$\Delta\theta_1$ [K]
S_S^m	LONG	0.48	0.48	0.51	0.496	451	300.38	-0.0041	4.26	-0.0008
		0.72	0.72	0.76	0.499	453	300.38	-0.0036	4.29	-0.0008
		0.96	0.96	1.00	0.502	429	300.46	-0.0047	4.28	-0.0011
	TINERT	0.48	0.50	0.54	0.576	446	300.70	-0.0062	5.10	-0.0010
		0.72	0.76	0.82	0.587	465	300.67	-0.0062	5.17	-0.0011
		0.96	1.06	1.17	0.586	421	300.87	-0.0086	5.12	-0.0014
S_S^l	LONG	0.72	0.72	0.76	0.499	459	300.38	-0.0037	4.29	-0.0009
		0.96	0.96	1.01	0.498	438	300.46	-0.0049	4.25	-0.0011
S_M^m	LONG	0.48	0.48	0.51	0.508	463	300.40	-0.0056	4.13	-0.0009
		0.72	0.72	0.75	0.512	461	300.40	-0.0048	4.17	-0.0010
		0.96	0.96	1.00	0.513	429	300.49	-0.0054	4.14	-0.0012
	TINERT	0.48	0.50	0.54	0.590	467	300.82	-0.0078	4.99	-0.0021
		0.72	0.76	0.81	0.601	465	300.77	-0.0076	5.06	-0.0012
		0.96	1.06	1.15	0.599	425	300.97	-0.0092	5.00	-0.0015
S_M^l	LONG	0.72	0.72	0.76	0.515	465	300.40	-0.0047	4.20	-0.0010
		0.96	0.96	1.01	0.516	455	300.49	-0.0055	4.17	-0.0012

Tab. 4.13 shows the key parameters of results based on the three C_{CFL}. On that table, two others CFL are displayed: $C_{\mathrm{CFL}}^{\langle\overline{u}\rangle} = \max(u(z))\Delta t/\Delta x$ is based on the maximum averaged velocity shown in Fig. 4.27 (horizontal and time average during LONG and TINERT intervals), and $C_{\mathrm{CFL}}^{\max} = \max(u(x,y,z,t))\Delta t/\Delta x$ is based on the maximum instantaneous local velocity during LONG and TINERT intervals (as shown in Fig. 4.42). The latter quantity thus represent the worst situation. If $C_{\mathrm{CFL}}^{\max} < 1$, one is certain that the condition $\mathrm{CFL} < 1$ is never violated.

As a summary of Tab. 4.13, $C_{\mathrm{CFL}}^{\langle\overline{u}\rangle}$ is only different from C_{CFL} for TINERT time interval where is is at least 5 % higher. It thus reflects the overshooting of u_g by the averaged velocity profile illustrated in Fig. 4.27 a). For its part, $C_{\mathrm{CFL}}^{\max}$ is always higher than C_{CFL} (reaching unity for $C_{\mathrm{CFL}} = 0.96$ for LONG interval), and an increase is also to note going from LONG to TINERT time intervals. The increase of both $C_{\mathrm{CFL}}^{\max}$ and $C_{\mathrm{CFL}}^{\langle\overline{u}\rangle}$ between LONG and TINERT interval is notably higher for $C_{\mathrm{CFL}} = 0.96$ than for the cases with lower value of C_{CFL}. It thus tend to confirm the spurious behaviour of $C_{\mathrm{CFL}} = 0.96$ results during TINERT interval.

The other result parameters in Tab. 4.13 are almost unchanged by going from $C_{\mathrm{CFL}} = 0.48$ to 0.96 (with differences lower than 2 %). Only parameters sensitive to the inversion processes, *i.e.* $\overline{w'\theta'}_i$ and z_i, show noticeable differences for $C_{\mathrm{CFL}} = 0.96$. In fact, z_i is generally lower by ~ 7 % during both LONG and TINERT intervals for $C_{\mathrm{CFL}} = 0.96$. This latter case also shows a higher $\overline{w'\theta'}_i$ but only during TINERT interval (which is the reason of a higher θ_s).

As a consequence, surface parameters can be considered independent of C_{CFL} (in the range 0.48 to 0.96), while the inversion properties seems to be affected when C_{CFL} is close to its generally accepted limit, even if, on the one hand, averaged velocity profile is not clearly overshooting u_g (*i.e.* $C_{\mathrm{CFL}}^{\langle\overline{u}\rangle} = C_{\mathrm{CFL}}$), and on the other hand, $C_{\mathrm{CFL}}^{\max} \leq 1$. As a result, and in order for the spurious changes in z_i not to affect the whole profiles, all the figures presented in this section are based on the reference height of 460 m (instead of the computed z_i).

The shear case results obtained with the three C_{CFL} values are further studied through the comparison of their profile of first, second and third order moments, and longitudinal velocity spectra as shown respectively in Figs. 4.43 and 4.45 for S_S^m during LONG interval, and in Figs. 4.44 and 4.46 for S_S^m during TINERT interval.

4.3.4.1.1 Time step impact in the lower half of the ABL

Concerning the lower half of the ABL, it can be seen in Figs. 4.43 and 4.44 that all profiles for $C_{\mathrm{CFL}} = 0.48$ and $C_{\mathrm{CFL}} = 0.72$ almost perfectly superpose. Only $\overline{u'w'}$ and $\overline{u'^2}$ appears slightly higher for $C_{\mathrm{CFL}} = 0.48$ in the mixed layer, and $\overline{w'u'^2}$ surface layer maximum is higher for that same case but this difference is on par with the scatter. This confirm that results in the lower half of the ABL are mostly unchanged by lowering C_{CFL} below 0.72.

For their part, results based on $C_{\mathrm{CFL}} = 0.96$ are also similar to the ones with lower C_{CFL}, but with some exceptions. Momentum and momentum fluxes show almost no differences for both intervals, albeit the departure of ϕ_M from the similarity is always slightly lower for $C_{\mathrm{CFL}} = 0.96$ (not shown here). The potential temperature is higher in the whole ABL for $C_{\mathrm{CFL}} = 0.96$ due to the increased negative heat flux at the inversion (see Tab. 4.13) that bring more energy

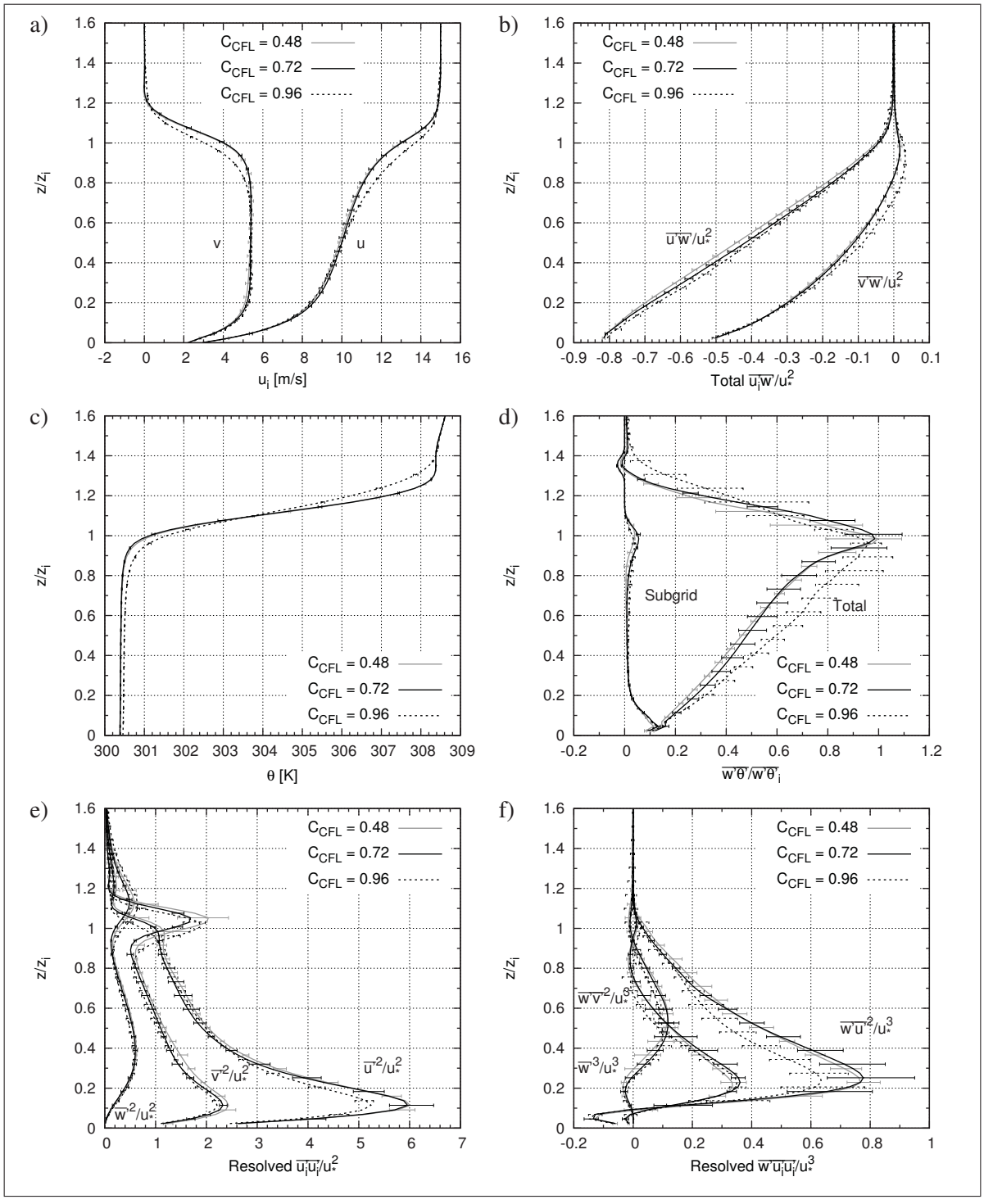

Figure 4.43 Profiles of first, second and third order moments for C_{CFL} equal to 0.48, 0.72 and 0.96 based on S_S^m and LONG time interval

in the ABL, which clearly appears for TINERT interval. Finally, profiles of $\overline{u'^2}$ and $\overline{w'u'^2}$ for $C_{\mathrm{CFL}} = 0.96$, Figs. 4.43 e) and f) and 4.44 e) and f), show a noticeably lower maximum in the surface layer while there are similar in the mixed layer. These latter differences are higher when based on LONG interval. At this point, while the changes in ϕ_M, $\overline{u'^2}$ and $\overline{w'u'^2}$ tend to indicate that the computation using $C_{\mathrm{CFL}} = 0.96$ is less dissipative in the lower half of the ABL, evidences are not strong enough for to draw conclusions.

When considering the streamwise and vertical velocity longitudinal spectra in the lower half of the ABL shown in Fig. 4.45 and 4.46, the differences become clearer. Indeed, while for $z_i k_x < 6$, no changes are to note at all heights in the ABL, the differences between results increase with wave numbers after $z_i k_x > 6$ (reaching their maximum at the highest wave number): the spectra falloff in the surface layer is faster when C_{CFL} it lower.

During LONG interval, Fig. 4.45, spectra from $C_{\mathrm{CFL}} = 0.48$ and $C_{\mathrm{CFL}} = 0.72$ results are similar very close to the surface. At the opposite, $C_{\mathrm{CFL}} = 0.96$ results clearly show more energy in the middle and high wave numbers. Above, results based on $C_{\mathrm{CFL}} = 0.72$ show a clear increase the with height of the little eddies energy, while $C_{\mathrm{CFL}} = 0.96$ results show a decrease: at the top of the surface layer, *i.e.* $z/z_i \sim 0.2$, the energy level of the former case is in between $C_{\mathrm{CFL}} = 0.48$ and $C_{\mathrm{CFL}} = 0.96$. Then, it reaches $C_{\mathrm{CFL}} = 0.96$ spectra in the mixed layer. Thus, surface layer velocity spectra from $C_{\mathrm{CFL}} = 0.96$ always have more energy in the middle and high wave numbers. Remarks for TINERT interval are similar when considering the lowest half of the ABL, as $C_{\mathrm{CFL}} = 0.96$ results always have the highest level of energy in the middle and high wave numbers, and $C_{\mathrm{CFL}} = 0.48$ results always have the lowest level.

The velocity spectra comparisons above show that in the lowest half of the ABL, the higher the time step, the more there are energy in the small structures. This might be caused by a higher numerical dissipation of the advection scheme of the method, *i.e.* the SL scheme, that is less suited for CFL below 0.5 (Girard *et al.*, 2005). Note however that both the lower wave numbers and almost all profiles from Figs. 4.43 and 4.44 are not affected by C_{CFL}, notably above the surface layer. This thus supports the conclusion of Brown *et al.* (2000) that found that in

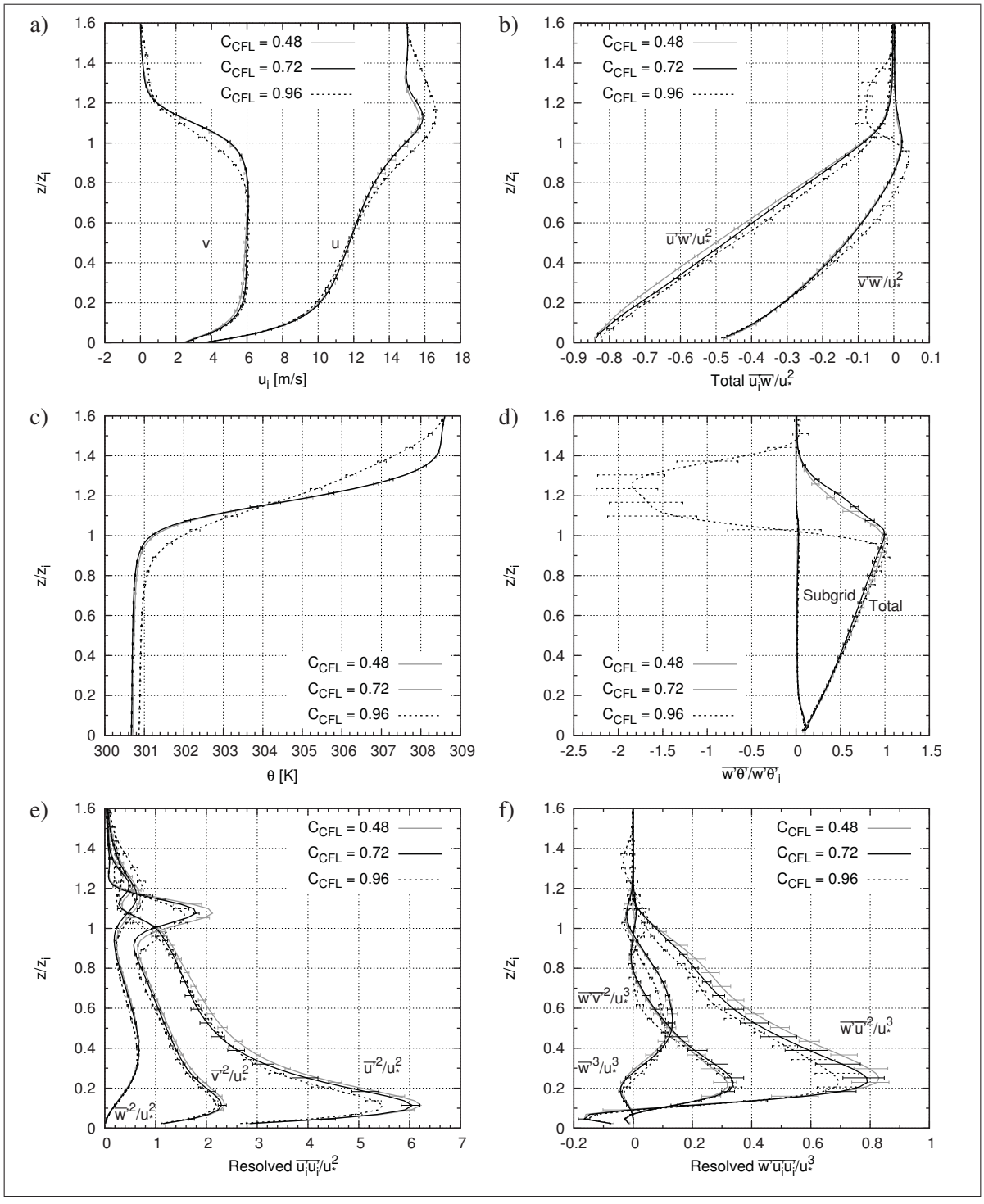

Figure 4.44 Profiles of first, second and third order moments for C_{CFL} equal to 0.48, 0.72 and 0.96 based on S_S^m and TINERT time interval

the mixed layer, LES results are not affected by an advection scheme that is more dissipative as long as the filter is located in the inertial subrange. At the opposite, since LES is clearly under-resolved in the surface layer, the advection scheme dissipation has a higher impact on the solution. The increased energy of the middle and high wave numbers for $C_{\mathrm{CFL}} = 0.96$ indicates that the flow is more resolved in the surface layer which helps to better reproduce the inertial subrange at lower height (as confirmed by plotting the spectra of that case based on similar scaling as in Fig. 4.25 - not shown here). Those remarks, thus explain the slightly better results obtained with $C_{\mathrm{CFL}} = 0.96$ in the surface layer in Figs. 4.43 and 4.44.

4.3.4.1.2 Time step impact in the upper half of the ABL and the inversion

Clear differences are to underline in the upper half of the ABL and at the inversion, but only for $C_{\mathrm{CFL}} = 0.96$. Results based on $C_{\mathrm{CFL}} = 0.48$ and $C_{\mathrm{CFL}} = 0.72$ are identical and only $\overline{v'^2}$ for $C_{\mathrm{CFL}} = 0.48$ always feature a slightly higher peak at the inversion. Profiles for $C_{\mathrm{CFL}} = 0.96$ for the LONG interval, Fig. 4.43, are similar to cases with a lower C_{CFL}, however: velocity and temperature gradient at the inversion are smoother; peaks of $\overline{v'^2}$ and more notably $\overline{w'^2}$ above the inversion are increased while $\overline{u'^2}$ slightly decrease; $\overline{v'w'}$ is also higher just below the inversion; and the neutral (slightly unstable) region above the inversion is always absent for $C_{\mathrm{CFL}} = 0.96$, causing the heat flux to smoothly return to zero above the inversion (no negative subgrid heat flux layer). All those remark tend to indicate that the mixing at the ABL top and across the inversion is increased when the effective CFL is close to one. It would explain the lower inversion height and higher heat flux at the inversion for $C_{\mathrm{CFL}} = 0.96$.

Concerning the spectra for the LONG interval in the upper half of the ABL, Fig. 4.45, high wave numbers energy level decreases with height for $C_{\mathrm{CFL}} = 0.96$ without affecting the mean profiles. In the low wave numbers, spectra are identical below the inversion for all cases. Above the inversion, spanwise and vertical velocity spectra have more energy for $C_{\mathrm{CFL}} = 0.96$ while streamwise velocity spectra tend to have less energy. Considering changes in the variances at the inversion for that case, there appears to be a redistribution of the large scale velocity fluctuations from the x to y and z directions explaining the increased diffusion.

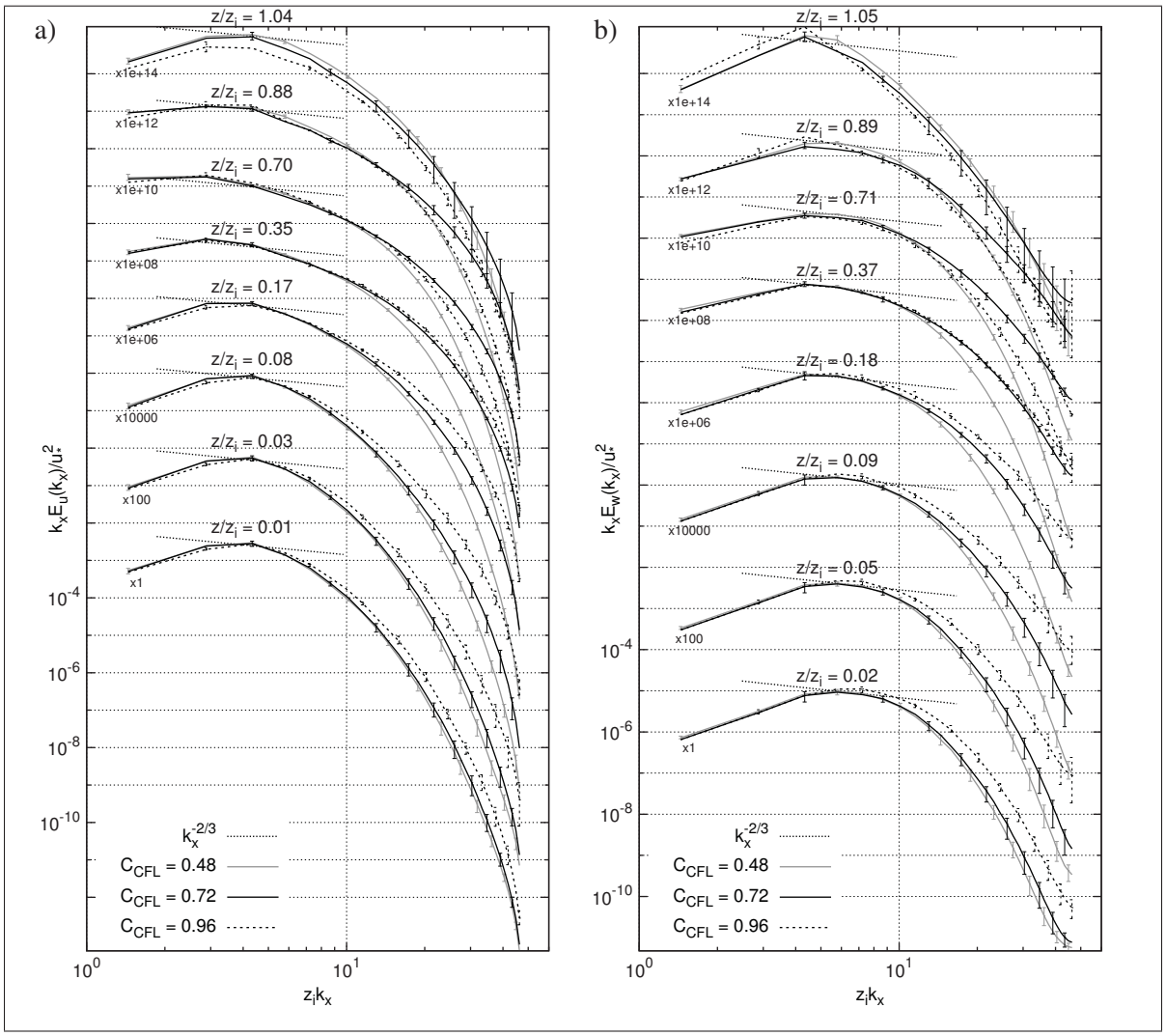

Figure 4.45 Longitudinal spectra of streamwise and vertical velocities for C_{CFL} equal to 0.48, 0.72 and 0.96 based on S_S^m and LONG time interval

Finally, concerning the results in the upper ABL and at the inversion for TINERT time interval, Figs. 4.44 and 4.46, it is to underline a clear departure from the usual profiles for $C_{\mathrm{CFL}} = 0.96$. Indeed, velocity, vertical momentum flux as well as vertical heat flux show a spurious departure for $C_{\mathrm{CFL}} = 0.96$ while both $C_{\mathrm{CFL}} = 0.48$ and 0.72 results are in agreement. Furthermore, velocity spectra for $C_{\mathrm{CFL}} = 0.96$ just below and above the inversion feature a spurious build-up of energy in the little structures. Those erroneous regions for $C_{\mathrm{CFL}} = 0.96$ during TINERT, perfectly correspond to locations where the velocity is higher than u_g as seen in Fig. 4.44 a).

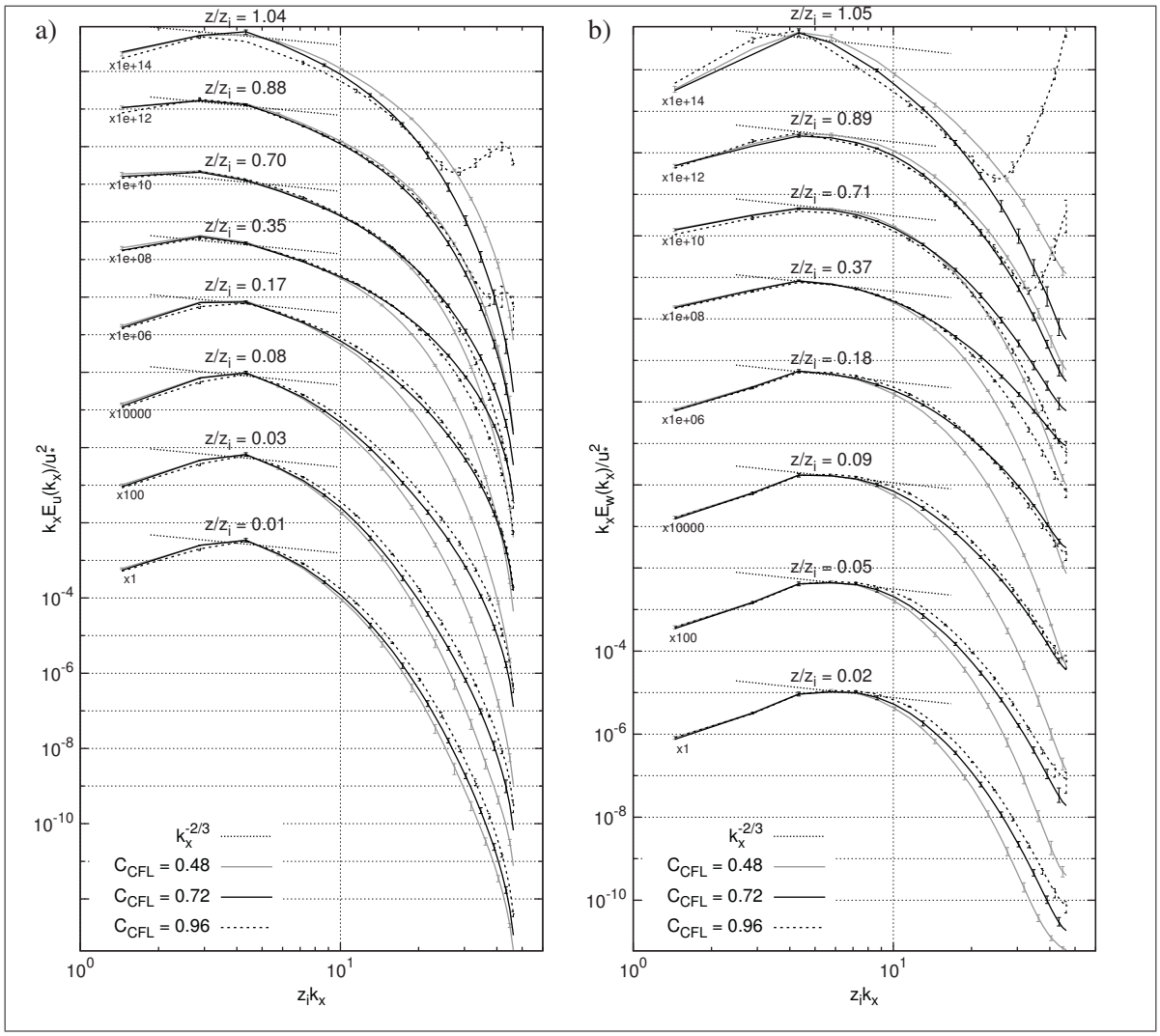

Figure 4.46 Longitudinal spectra of streamwise and vertical velocities for C_{CFL} equal to 0.48, 0.72 and 0.96 based on S_S^m and TINERT time interval

As a result, and without going any further, it can be concluded that $C_{\mathrm{CFL}}^{\max} > 1$ in the streamwise direction is not suitable for MC2. This is perfectly in agreement with its generally accepted limit of the SISL scheme. As a consequence, because the velocity overshoots u_g at the inversion after $tf/2\pi > 0.55T_{inert}$, results for $C_{\mathrm{CFL}} = 0.96$ are invalid at that height and during TINERT interval. At the opposite, $C_{\mathrm{CFL}} = 0.48$ and $C_{\mathrm{CFL}} = 0.72$ both lead to equivalent results that appears to be valid and unaffected by the increase of the effective CFL.

To conclude the evaluation of the impact of the times step on the shear case, it is to say that the SISL scheme generally accepted limit of $\mathrm{CFL} < 1$ prove to be real. A notable degradation of the results is observed where this condition is violated, such as at the inversion for $C_{\mathrm{CFL}} = 0.96$ during TINERT interval. Processes at the inversion are also affect, but still valid, when the effective CFL equals the theoretical limits. At the opposite, lowering the time step (or the effective CFL) below this critical limit does not appear to impact the results significantly. As a consequence, the degradation of the results at the inversion for $C_{\mathrm{CFL}} = 0.96$ does not impact surface flow. Finally, it was observed that the spectra falloff in the surface layer is always faster when C_{CFL} it lower. Thus, the shorter time step may also slightly increase the numerical dissipation inherent to the SL advection. This translate in slightly better surface results and a lower departure from the similarity for the case with the longest time step, *i.e.* $C_{\mathrm{CFL}} = 0.96$.

4.3.4.2 Convective case

In convective condition, the vertical mixing is largely increased across the whole atmosphere due to buoyant structures that go from the surface to the top of the ABL. As a results, horizontal velocity and temperature profiles are almost vertical, and as opposed to the shear case, the velocity never overshoot u_g, which indicates that the maximum CFL may be equal to C_{CFL}, at least in the horizontal direction.

However, as it was seen during the discussion of the flow structure, Sec. 4.2.4, the hot air is rising in narrow columns featuring large vertical velocities. As an example, for the instantaneous horizontal slices shown in Fig. 4.16, the maximum vertical velocity found is around 5.25 m/s leading to a CFL of 1.008 in the vertical direction which is slightly above the theoretical limit. Those large vertical velocity fluctuation are confirmed by $\overline{w'^2}$ profile Fig. 4.33 e), which further indicates that they are reaching their maximum at roughly $0.4\, z_i$ on average. Thus, when considering the consequences of having an effective maximum CFL larger than unity for the shear case, it is of interest to further evaluate the convective case with a smaller time step proceeding similarly as previously.

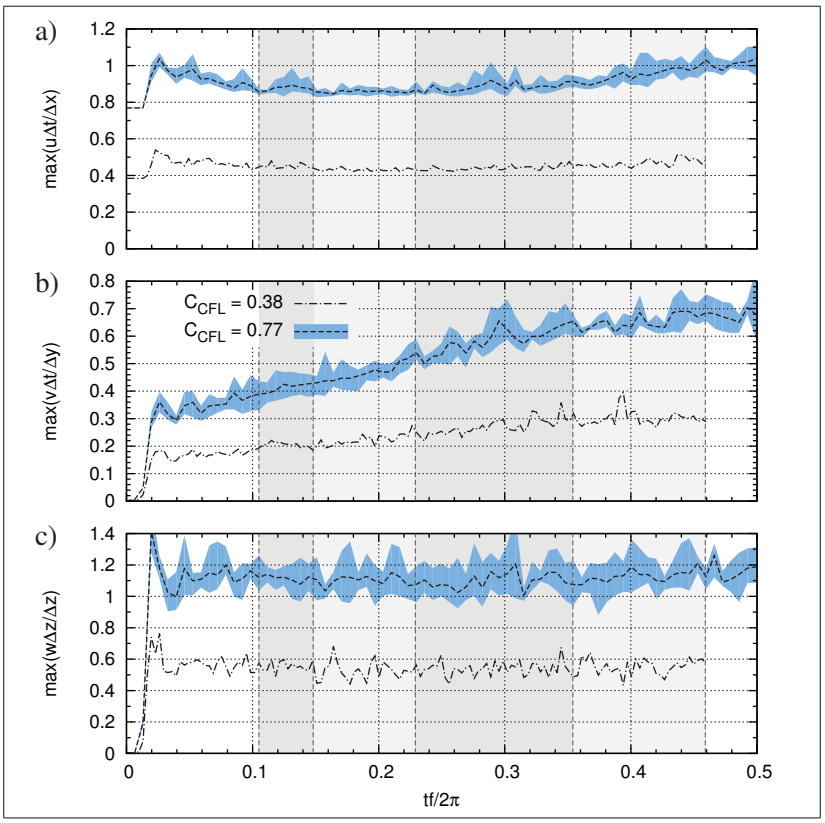

Figure 4.47 Maximum instantaneous local CFL, *i.e.* $C_{\mathrm{CFL}}^{\max}$, for the three directions based on B_S with C_{CFL} equal to 0.38, and 0.77. Coloured overlaid region show the scatter of the results. Grey overlaid background areas show post-processing time intervals

Based on these considerations, the two following values of C_{CFL} are evaluated here using the fully uniform domain B as described in Tab. 4.4:

$\boldsymbol{C_{\mathrm{CFL}} = 0.38}$**:** $\Delta t = 2$ s for B. A priori conservative with regards to the SISL.

$\boldsymbol{C_{\mathrm{CFL}} = 0.77}$**:** $\Delta t = 4$ s for B. A priori slightly conservative.

To better appreciate the effective maximum instantaneous local CFL of the convective case, *i.e.* $C_{\mathrm{CFL}}^{\max}$, Fig. 4.47 shows its evolution in the streamwise, spanwise and vertical directions. As introduced above, the highest $C_{\mathrm{CFL}}^{\max}$ are found for the vertical direction, with a value oscillating between 1 and 1.4 for $C_{\mathrm{CFL}} = 0.77$. For that same case, the streamwise direction

$C_{\mathrm{CFL}}^{\max}$ is notably higher than C_{CFL} and also close to unity at the beginning and the end of the integration. This higher instantaneous local CFL in the streamwise direction is caused by the large fluctuations taking place at the inversion, as seen on horizontal velocity variances profiles, Fig. 4.33 e) (vertical velocity of the rising plume transform in horizontal velocity fluctuations due to the mass conservation when overshooting the inversion) (Moeng and Sullivan, 1994).

Table 4.14 Result parameters from the convective case for the two C_{CFL} evaluated in Sec. 4.3.4.2 and based on model setups from Tab. 4.4 and two time intervals

Name	Interval	C_{CFL}	$C_{\mathrm{CFL}}^{\langle\overline{u}\rangle}$	$C_{\mathrm{CFL}}^{\max}$	u_* [m/s]	w_* [m/s]	z_i [m]	L_{MO} [m]	θ_s [K]	$\overline{w'\theta'}_i$ [K m/s]	U_1 [m/s]	$\Delta\theta_1$ [K]
B_S	INTER	0.38	0.38	0.67	0.576	2.041	1116	-27.1	310.50	-0.027	5.02	5.11
		0.77	0.77	1.21	0.586	2.044	1128	-29.5	310.49	-0.025	5.09	5.07
	LONG	0.38	0.38	0.68	0.588	2.041	1116	-29.6	310.27	-0.018	5.25	5.06
		0.77	0.77	1.21	0.593	2.034	1112	-30.3	310.26	-0.016	5.23	5.04
B_M	INTER	0.38	0.38	0.60	0.589	2.054	1137	-29.1	310.26	-0.030	5.00	4.86
		0.77	0.77	1.17	0.599	2.039	1120	-32.5	310.26	-0.024	5.01	4.81
	LONG	0.38	0.38	0.66	0.599	2.029	1095	-31.6	310.07	-0.018	5.19	4.84
		0.77	0.77	1.27	0.605	2.029	1103	-32.8	310.06	-0.015	5.18	4.81

However, trends in Fig. 4.47 are similar for the two computations, and as opposed to the shear case, all curves always scale perfectly when divided by their respective C_{CFL}. As a result, both case appears to be valid and an instantaneous CFL in the vertical direction locally larger than unity does not seem to affect results. Indeed, the same order of magnitude is obtained for the maximum velocity in the three direction for $C_{\mathrm{CFL}} = 0.38$ and $C_{\mathrm{CFL}} = 0.77$.

Tab. 4.13 shows key parameters of the convective case based on the two C_{CFL} for INTER and LONG intervals. On that table, $C_{\mathrm{CFL}}^{\langle\overline{u}\rangle}$ equals C_{CFL} for both intervals which confirms that averaged horizontal velocity never overshoot u_g. At the opposite, $C_{\mathrm{CFL}}^{\max}$ is generally higher by more than 50 %. This increase is caused by the large vertical velocity as shown in Fig. 4.47. The other result parameters does not show clear differences. Only u_* is generally slightly higher for $C_{\mathrm{CFL}} = 0.77$ regardless of the time interval, which in turn, causes L_{MO} to be higher. However, those two changes are very small. As a result, it can be said from Tab. 4.13 that all result parameters are largely independent of C_{CFL} (in the range 0.38 to 0.77).

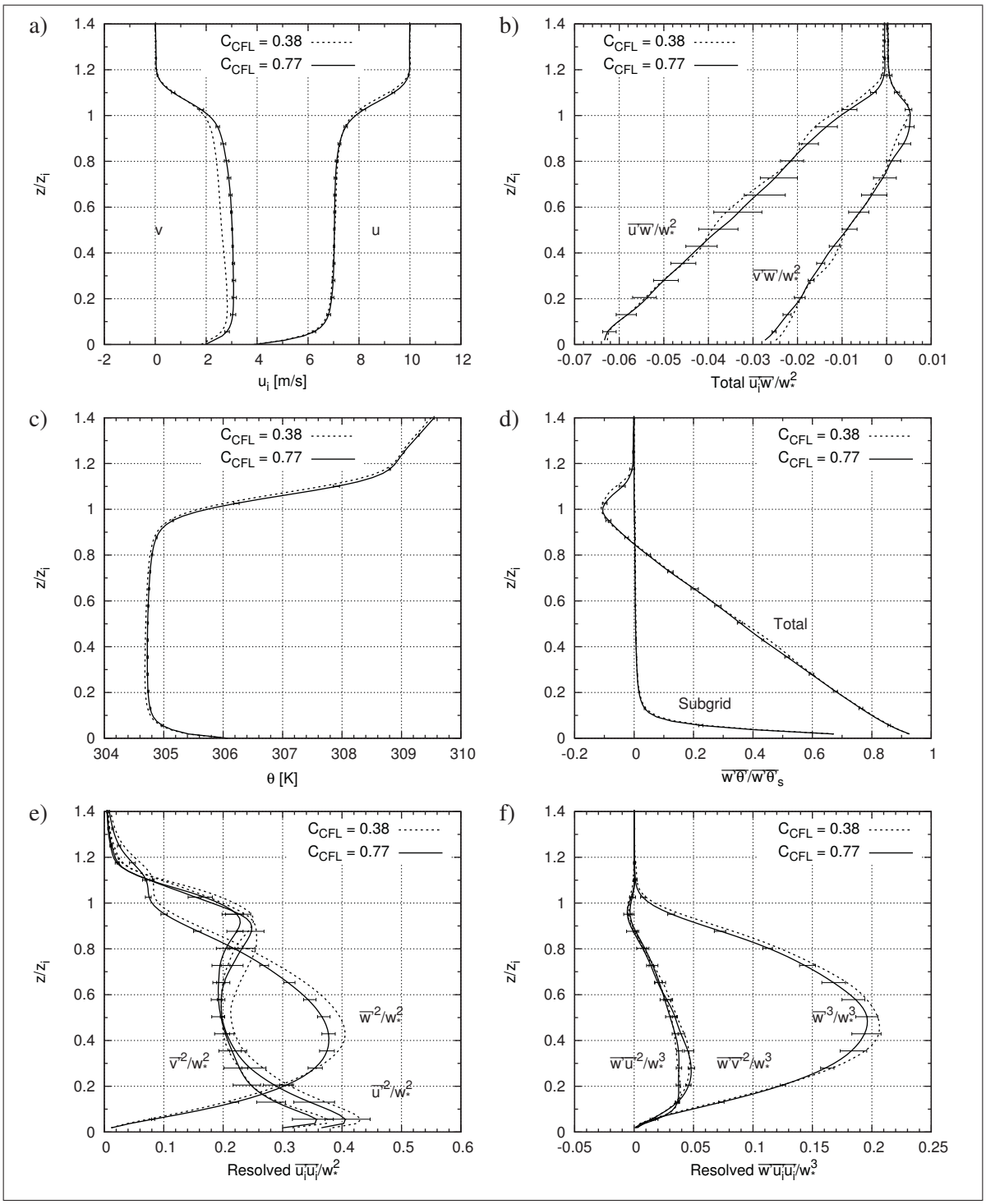

Figure 4.48 Profiles of first, second and third order moments for C_{CFL} equal to 0.38 and 0.77 based on B_S and INTER time interval. Only $C_{\mathrm{CFL}} = 0.77$ is based on the ensemble average of five results

In order to further explore differences between $C_{\mathrm{CFL}} = 0.38$ and 0.77 for the convective case, Fig. 4.48 shown first, second and third order moment profiles for INTER time interval. On that figure, differences between the two cases are generally within the scatter of $C_{\mathrm{CFL}} = 0.77$ results, and only v and the velocity variances present differences above the scatter. However, after further investigation (mainly by reproducing the same case with other SGS model as seen later), it was found that differences in the variances are most likely caused by the scatter. In fact, while the variances peaks in the middle of the ABL for $\overline{w'^2}$ and at the top of the ABL for $\overline{u'^2}$ and $\overline{v'^2}$ might indeed be very slightly increased by reducing C_{CFL}, differences observed in Fig. 4.48 e) are larger in comparison to the other cases studied (not shown here). Thus, the vertical velocity and its fluctuations does not appears to be a function of the CFL, albeit $C_{\mathrm{CFL}} = 0.77$ seems to be at the edge of what can be used in both the streamwise and the vertical direction. At the opposite, the spanwise velocity difference, Fig. 4.48 a), are not caused by the scatter, since similar difference was observed in all the cases studied (not shown here).

Finally, concerning the longitudinal velocity spectra shown in Fig. 4.49, differences between $C_{\mathrm{CFL}} = 0.38$ and 0.77 results are very similar to the ones observed in the shear case for $C_{\mathrm{CFL}} = 0.48$ and 0.96 during LONG interval: there is clear reduction of the energy of the higher wave numbers in the surface layer for $C_{\mathrm{CFL}} = 0.38$ starting at $z_i k_x > 1$, while in the low wave numbers, the largest changes are always lower than the scatter (allowing to conclude that lowering the CFL have no impact on the lowest wave numbers). Such a reduction of the small eddy energy is particularly visible for the vertical velocity longitudinal spectra where spectra falloff at all heights is much faster for $C_{\mathrm{CFL}} = 0.38$. However, when considering that there are almost no changes in all the profiles from Fig. 4.48, it appears that results are unaffected by the increased dissipation of the small structures. This it thus in good agreement with Brown *et al.* (2000) indicating that the filter is correctly located in the inertial subrange. Finally in Fig. 4.49, no spurious build up of the energy is observe at high wave number, as opposed to the shear case for $C_{\mathrm{CFL}} = 0.96$ during TINERT interval. It thus confirm that the model still operates properly with $C_{\mathrm{CFL}} = 0.77$ while the generally accepted limit for the CFL is clearly exceeded in the vertical direction and is very close in the streamwise direction.

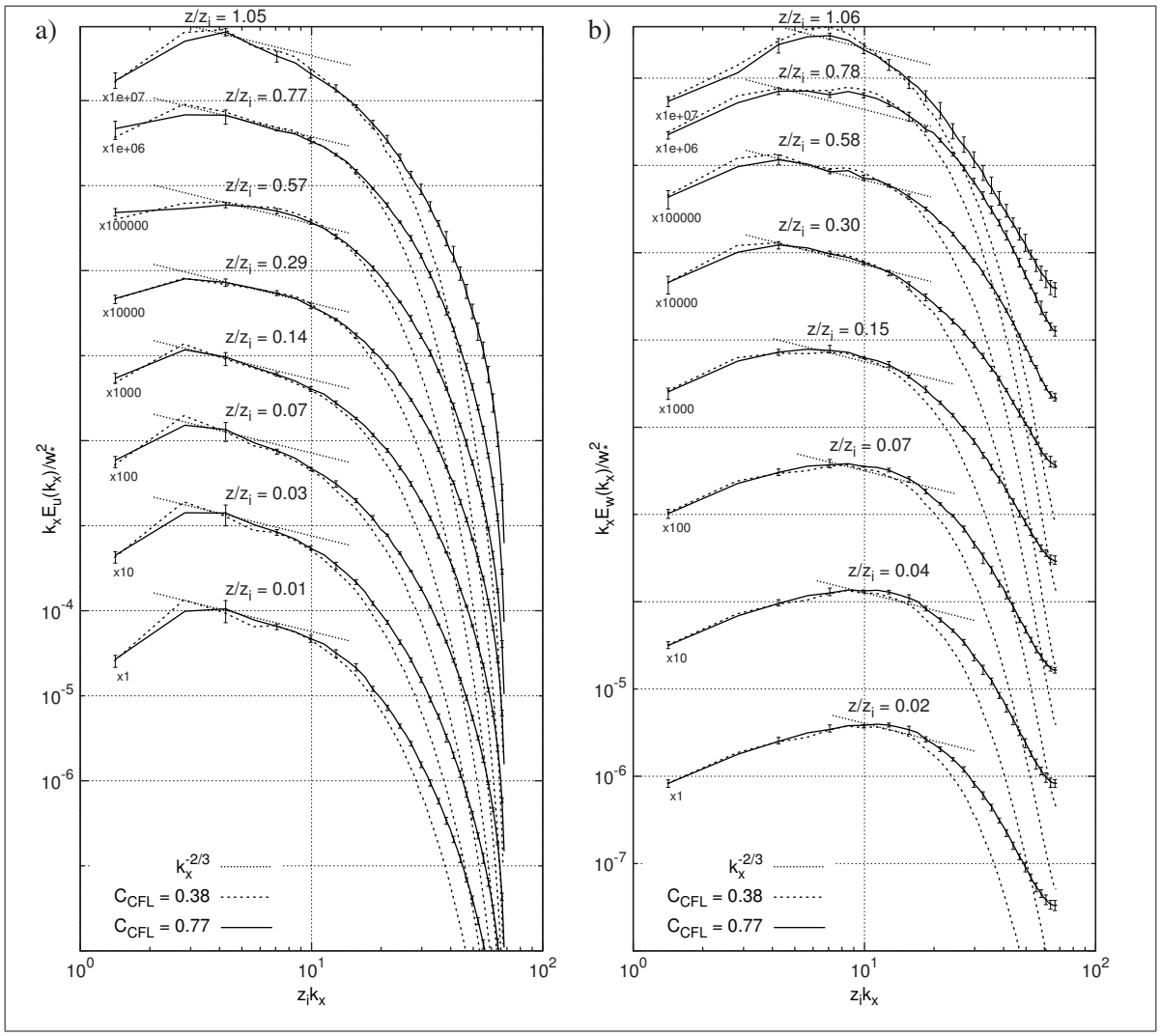

Figure 4.49 Longitudinal spectra of streamwise and vertical velocities for C_{CFL} equal to 0.38 and 0.77 based on B_S and INTER time interval. Only $C_{\mathrm{CFL}} = 0.77$ is based on the ensemble average of five results

To conclude this evaluation of the impact of the time step on the convective case, it is to note that for such a case, the vertical direction feature the highest effective CFL. The vertical profile of relevant quantities are almost identical for both $C_{\mathrm{CFL}} = 0.38$ and $C_{\mathrm{CFL}} = 0.77$, and only v was slightly lowered by reducing of the time step. At the spectral level, similar conclusion as for the shear case can be done: lowering the CFL decrease the energy of the smallest structures, however, since profiles of turbulent quantities are not affected (even close to the surface), it can be concluded that the filter is correctly located in the inertial subrange (Brown *et al.*, 2000).

Finally, it is to underline that, while valid, the results with $C_{\mathrm{CFL}} = 0.77$ appears to be at the edge of suitability of the model: the instantaneous local maximum CFL of w and u (at the beginning and the end of the integration) are equal or above than the theoretical limit. In fact, further increasing the C_{CFL} to 0.96 proved to crash the model.

4.3.5 Conclusion of the numerical parameters evaluation

In this section, the influence of the main numerical parameters on the results have been evaluated considering the shear and convective cases from Moeng and Sullivan (1994) and Sullivan *et al.* (1994). Here, a summary of the outcome of this section is presented.

First, and due to the large scatter of the results when using a similar time interval as Moeng and Sullivan (1994) for both the shear and the convective case, the impact of the post-processing parameters were evaluated by considering two longer time intervals. It allowed to assess the steadiness of the flow and the uncertainty of the results. For the shear case, the turbulence is already fully developed during MS1994 interval and an almost permanent state of the first order moments is reached after $0.5\,T_{inert}$. Furthermore, the longer the time interval, the less scatter there is. However, the latter never disappears. Concerning the convective case, a representative quasi-steady buoyancy driven ABL is already well established after $0.1\,T_{inert}$, *i.e.* during MS1994 interval, but the scatter is very high during this interval. As a result, a longer time interval must be used to obtain better and more converged statistics. However, a too long interval was proven to affect statistics (notably at the top of the ABL). After $0.5\,T_{inert}$, the top of the ABL starts to interact with top boundary condition. An interval of roughly $15\,\tau_*$ was found to lead to optimal results. As a consequence, MS1994 time interval appears to be limited for both cases, and a longer interval is required to reduce the scatter to an acceptable level allowing a better analysis of the results.

Concerning the horizontal grid and domain of the shear case, going from a 2 km to a 3 km horizontal grid while retaining the same resolution does not change ensemble averaged results. Furthermore, going from a 31.25 m to a 40 m horizontal resolution grid while retaining the same domain size, gives results in line with what obtained in the literature (Sullivan *et al.*,

1994; Mason, 1994). However, the coarser the mesh, the more scatter there are, and the more noticeable the scatter reduction is when the time interval is lengthen. In addition, the coarse mesh based on a 40 m resolution and 2 km side, prove to be at the edge of suitability to reproduce the shear case with the current methods. Based on that grid, the on-set of turbulence is sometimes delayed preventing the use of the results at the beginning of the integration. Furthermore with that grid, the scatter of the results is very high even for the longest interval. Given that similar or coarser grids have been used successfully in conjunction with classical Smagorinsky SGS models to reproduce similar shear driven ABL (Andren *et al.*, 1994; Brown *et al.*, 2000; Porté-Agel *et al.*, 2000; Ding *et al.*, 2001a; Chow *et al.*, 2005), the present approach thus appears less suited for coarse meshes, which is perfectly in line with the fact that the current approach is more dissipative as found in the spectral analysis, Sec. 4.2.

In the vertical, the use of a finer vertical mesh close to the surface, as well as a coarser vertical grid in the mixed layer does not change the results of the shear case, and both resolved and subgrid part of turbulent quantities are almost unaffected in the lowest half of the ABL. This is due to the fact that, unless $\Delta z > \Delta_H = (\Delta x \Delta y)^{1/2}$, the filter width is only defined by Δ_H in the UKMO Smagorinsky model. Thus, the non-uniform mesh has no impact on the results which also demonstrates that the discretization is well implemented. In the upper part of the ABL, and most notably at the inversion, some quantities, such as the heat flux, are very sensitive to the vertical mesh (while other variables seems unaffected) and small changes of the mesh at the inversion and above can prevent its proper reproduction. It was found that the mesh needs to be sufficiently fine up to the top of the temperature inversion, in order to properly reproduce the heat flux minimum at the inversion, *i.e.* entrainment process, and a good prediction of z_i also implies that the processes from above the inversion are correctly reproduced by the model.

Finally, concerning the times step, the SISL scheme generally accepted limit of $\mathrm{CFL} = 1$ prove to be true, but only in the horizontal. For the shear case, a notable degradation of the results is observed in places where this condition is violated. Processes are also affected, but still valid, when the effective CFL equals unity. For the convective case, the vertical direction features the highest instantaneous local CFL. However, maximum CFL above unity in the

vertical direction does not appear to affect the results. Finally, lowering the time step, or the effective CFL, does not appear to impact the results significantly. However, a shorter time step also slightly increases the numerical dissipation inherent to the SL advection scheme especially close to the surface, and the lower C_{CFL}, the faster the spectral falloff is. But, since profiles of turbulent quantities are not affected above the surface layer, it confirms that the filter is correctly located in the inertial subrange (Mason and Brown, 1999; Brown *et al.*, 2000).

4.4 LES of the full ABL: enhancements and new components

In the process of using MC2 for LES, some aspects of the method were refined in addition to the implementation of all the required components as described in Chap. 2 and Chap. 3. All results presented previously were based on the most advanced version of MC2 using both the UKMO Smagorinsky model, and the hybrid TKE SGS model (in addition to the column model). However, others SGS models as well as a new treatment of turbulent processes were also implemented. It is thus of interest to further explore the enhancement brought by these refinements and evaluate the new components.

In this section, the various SGS model implemented in MC2 and presented in Sec. 2.2.3 and Sec. 3.3.5 are first evaluated and compared. Then, the impact of the new vertical discretization of the physics introduced in Sec. 3.3.1.2 will be illustrated and discussed. Finally, a new version of the model where all turbulent processes and their boundary conditions are implemented directly within the dynamics, *i.e.* the standalone model (not relying anymore on the physics library) as presented in Sec. 3.2.5.2.1 and Sec. 3.2.5.5 is evaluated.

4.4.1 New SGS models

All results shown and discussed previously in this thesis were either based on the UKMO Smagorinsky SGS model (Brown *et al.*, 1994), or the hybrid TKE SGS model primarily developed at EC (Pelletier *et al.*, 2005) and refined during this study. Both approaches gave very similar results. Taking advantage of the TKE prognostic equation already implemented in MC2, the Deardorff (1980), the linear Kosović (1997) and the Redelsperger *et al.* (2001) SGS

models have also been implemented as described in Sec. 2.2.3 and Sec. 3.3.5. The inclusion of a prognostic equation for TKE theoretically allows to better take into account non-local flow features thanks to the advection of TKE. It rises the order of the SGS model to 1.5. However, and as opposed to the RANS for which an increase of the order of the model from first to one-and-a-half clearly enhances the results and the general abilities of approach, there is a general agreement that no clear improvement is obtained for LES of homogeneous dry cases (Andren *et al.*, 1994; Mason, 1994; Lesieur *et al.*, 2005) due to the more local nature of the SGS stresses computation in LES. In fact, the inclusion of the TKE proves to be useful when applying the LES model to more complex cases where surface is not anymore homogeneous (Chow and Street, 2009) or for cloud resolving LES models (Redelsperger and Sommeria, 1981; Cuxart *et al.*, 2000). It is nevertheless of interest to first evaluate and validate these additional SGS models in the context of an homogeneous surface full ABL, before being able to apply those approaches to more complex cases.

In the present section, based on the shear and convective cases thoroughly explored during the two previous section, results obtained with the five SGS models are compared and discussed.

4.4.1.1 Shear case

In order to evaluate the five SGS models for the shear case, it was decided, based on the evaluation of the Sec. 4.3.1, to use the medium grid S^m with the usual uniform vertical mesh and numerical parameters described in Tab. 4.4.

Result parameters obtained for the shear case with the five SGS models are shown in Tab. 4.15. In that table, S_S stands for the UKMO Smagorinsky SGS model (Mason and Brown, 1999), S_M for the hybrid TKE SGS model (Pelletier *et al.*, 2005), S_D for the Deardorff SGS model (Deardorff, 1980), S_R for the Redelsperger SGS model (Redelsperger *et al.*, 2001), and S_K for the linear Kosović SGS model (Kosović, 1997). Note that S_S and S_M results are based on the ensemble average of five computations, while the others results are based only on one computation. The scatter of the two former results thus serves as reference. Note also that S_K results are discussed separately.

Table 4.15 Result parameters from the shear case for the five SGS models and based on S^m setup from Tab. 4.4 and two time intervals. Only S_S and S_M are based on the ensemble average of five results

Interval	Name	Reali-zations	u_* [m/s]	z_i [m]	θ_s [K]	$\overline{w'\theta'}_i$ [K m/s]	U_1 [m/s]	$\Delta\theta_1$ [K]	$\phi_m^{\max}$
LONG	S_S	5	0.499	453	300.38	-0.0036	4.29	-0.0008	2.14
	S_M	5	0.512	461	300.40	-0.0048	4.17	-0.0010	2.08
	S_D	1	0.513	474	300.40	-0.0048	4.27	-0.0003	2.07
	S_R	1	0.528	442	300.41	-0.0045	4.21	-0.0002	1.97
	S_K	1	0.461	463	300.58	-0.0089	3.56	-0.0006	2.85
TINERT	S_S	5	0.587	465	300.67	-0.0062	5.17	-0.0011	2.06
	S_M	5	0.601	465	300.77	-0.0076	5.06	-0.0012	2.00
	S_D	1	0.600	463	300.75	-0.0070	5.10	-0.0004	2.08
	S_R	1	0.627	474	300.81	-0.0084	5.11	-0.0003	1.87
	S_K	1	0.455	495	300.94	-0.0058	3.61	-0.0005	5.61

In Tab. 4.15, friction velocity u_* is slightly lower for S_S than for S_M and S_D which have an identical value. At the opposite, u_* of S_R is 5 % higher than S_D. This latter difference may be associated with the improved representation of the surface layer by Redelsperger *et al.* (2001) SGS model. Indeed, and while velocity at the first level also appears almost unchanged for all the SGS models (except for S_S where it is 1 % higher), S_R always feature the lowest departure from the similarity as illustrated by the maximum of dimensionless vertical shear $\phi_M^{\max}$. During TINERT, the peak of ϕ_M from S_R is reduced by more than 10 % compared to S_D, which is solely due to the improved surface treatment of Redelsperger *et al.* (2001). Finally, $\Delta\theta_1$ is three time higher for S_S and S_M than for the others SGS models, but, this quantities is very small and it correspond to a temperature gradient of 10^{-4} K/m in the worst case.

Quantities related with the inversion, *i.e.* z_i and $\overline{w'\theta'}_i$, does not show any particular trends at the exception of the slightly lower (higher) $\overline{w'\theta'}_i$ for S_S (S_R) during TINERT that may be the explanation of the lower (higher) θ_s. However, the difference in $\overline{w'\theta'}_i$ between S_R and S_D can be hardly explained as those two models are identical above the surface layer. It can thus be attributed to the scatter of the results. As a result, except for S_R surface parameters that appear to be closer to the similarity, all the other parameters are largely unaffected by the SGS model which is in agreement with the conclusions of Andren *et al.* (1994).

Concerning S_K results, u_* as well as U_1 are always notably lower than other results, while ϕ_M is notably higher. In fact, after initial perturbations are damped, turbulence never develop with Kosović SGS model. Shear instabilities located in the surface layer are not triggered but damped. The SGS model thus appears too dissipative which is in agreement with its rather large value of $C_{S_{eqv}}$. The exact reason of this phenomena is however not clear. In fact, the same kind of results are obtained by using a van Driest like damping approach with the Deardorff SGS model, *i.e.* by clipping the filter Δ with κz (which is considered to be controversial by Redelsperger *et al.* (2001), but often used Sullivan *et al.* (1994)). It thus appears to be related to the definition of the effective filter width close to the surface. However, no solution were identified, and it was decided to focus on the others SGS model. Furthermore, this SGS model normally includes backscatter terms which increase fluctuations, notably in the surface layer and stably stratified regions (Kosović, 1997; Kosović and Curry, 2000). As a consequence, the results from the linear Kosović SGS model, S_K, are shown in Fig. 4.50 for illustration purpose but they will not be further considered in this section.

In Fig. 4.50 are shown profiles of first, second and third order moments for the results based on the five SGS models. On that figure, it can be seen that Redelsperger SGS model results, S_R, present some clear differences while the other SGS model give very similar results. Indeed, this approach features a lower deviation from the similarity in the surface layer, and in comparison to the other SGS models: the amplitude of ϕ_M nose is lower, Fig. 4.50 b), indicating that the surface velocity shear is lower which propagates in the whole ABL velocity profile that is closer to the similarity as shown in Fig. 4.50 a). Furthermore, surface maximum of resolved $\overline{u'^2}$ (and $\overline{v'^2}$ to a less extent), Fig. 4.50 e), is lower for S_R leading to a much shorter nose in total $\overline{u'^2}$ (and in the TKE) than all other results (which is also in line with better taking into account the surface (Mason and Thomson, 1992; Andren *et al.*, 1994; Sullivan *et al.*, 1994; Porté-Agel *et al.*, 2000)). However, the improvement in the surface layer using Redelsperger SGS model are not as clear as observed in the literature (Redelsperger *et al.*, 2001; Drobinski *et al.*, 2004). As a side note, the subgrid part of variances is almost unchanged between S_D and S_R above $0.15\, z/z_i$, but it is slightly higher for S_R below that height due to the surface

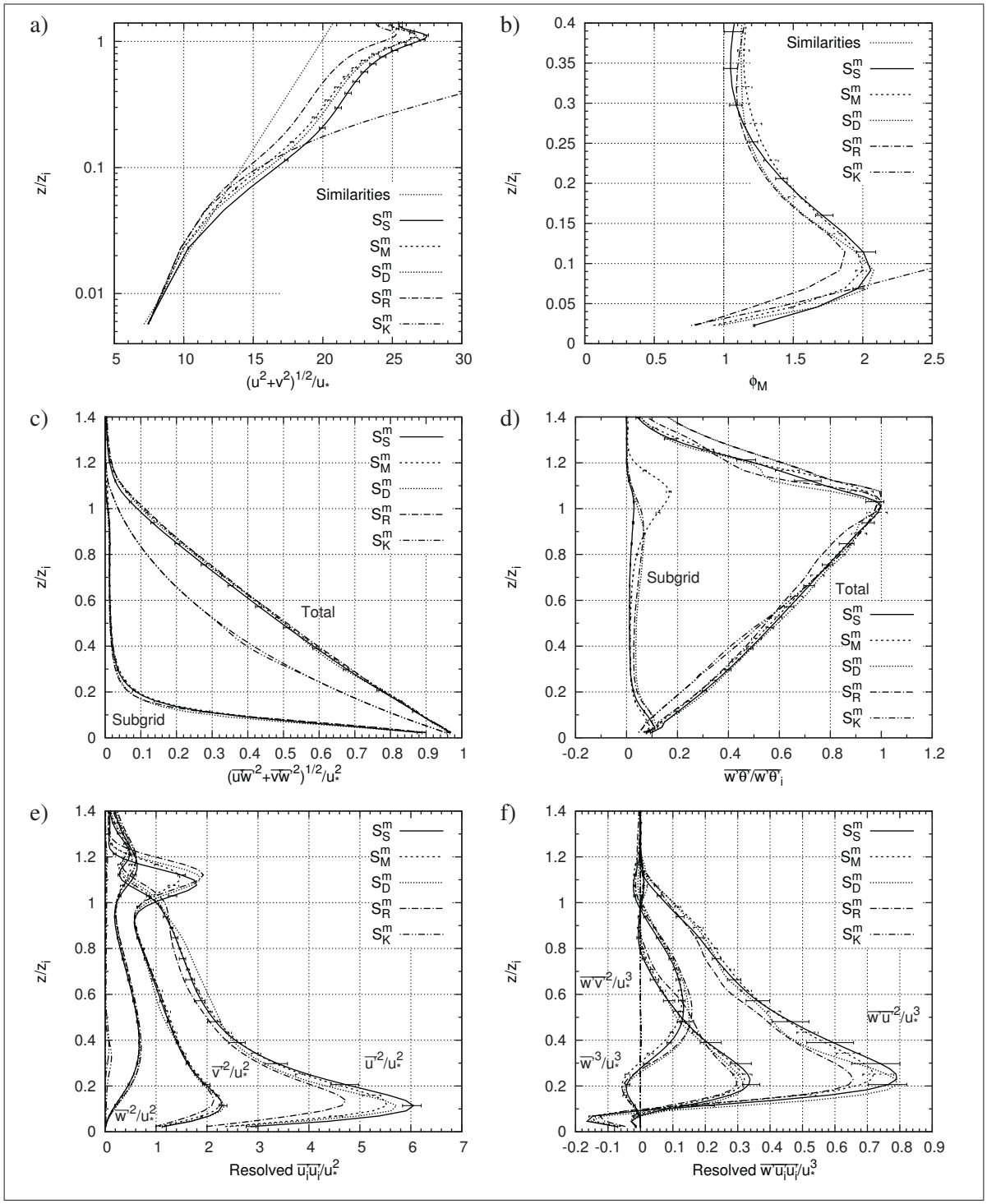

Figure 4.50 Profiles of first, second and third order moments from the five SGS models for the shear case relying on S^m setup from Tab. 4.4 and TINERT time interval. Only S_S and S_M are based on the ensemble average of five results

matching approach. As a result, the flow very close to the surface is less resolved with S_R than with S_D which was also described by Redelsperger *et al.* (2001). Finally, the above surface layer maximum in $\overline{w'u'^2}$ seems also to be lower for S_R however, the scatter for this quantity is as large as the differences between results.

Concerning S_S, S_M and S_D profiles shown in Fig. 4.50, differences are small, and they are most of the time below the scatter in the mixed layer. The only clear differences are seen for S_S horizontal velocity profile and non-dimensional gradient at the surface, and for S_M subgrid heat flux at the inversion. It is also of interest to underline that in the mixed layer, two groups are formed concerning the subgrid parts of the fluxes and variances: S_S/S_M and S_D/S_R. This is due to the differences in the filter definition, *i.e.* Δ_H in the former versus Δ_{3d} in the latter, causing a larger mixing length for S_S and S_M (and thus a larger value of $C_{S\,3d}$, *i.e.* $C_{S\,3d} = 0.216$ for S_S/S_M and $C_{S\,3d} = 0.181$ for S_D/S_R). As a result, S_S and S_M SGS model are more dissipative which increases the unresolved part of the flow. At the opposite, the total heat flux is also similar for all approaches but its subgrid part is slightly higher for S_R and S_D across the ABL due to the different Pr_t used ($1/3$ for S_R and S_D, 0.7 for S_D and 0.85 for S_M).

Velocity profiles of the hybrid TKE and Deardorff SGS models are very similar, while the deviation from the similarity of the Smagorinsky model is higher, Fig. 4.50 a). This is associated with the differences in ϕ_M very close to the surface, Fig. 4.50 b). Those changes are caused by the aggregated effect of the differences in the filter definition, the Smagorinsky constant and the surface matching of the length scales. Indeed, the flow is slightly less resolved in S_S and S_M due to the filter definition causing theoretically a larger departure from the similarity than for S_D. However, a surface matching of the length scales is used in S_S and S_M which helps to reproduce the surface layer (at different degree depending of the approach), while at the opposite, there are no special treatment in S_D. Differences of the same type were also found by Porté-Agel *et al.* (2000, Fig. 2 a)) and Sullivan *et al.* (1994, Fig. 6).

Concerning the notable increase of subgrid heat flux of S_M at the inversion (while the total heat flux is unchanged), Fig. 4.50 d), it is most probably caused by the stability function used

to take into account the stratification in the hybrid TKE SGS model. The stability functions of the column model are applied similarly as in the UKMO Smagorinsky SGS model. However, They do not include a critical Ri which is less appropriated for LES as discussed by Delage and Girard (1992) and Brown *et al.* (1994). Indeed, the stratification of the inversion produces $\mathrm{Ri} > \mathrm{Ri}_c = 0.25$, thus killing all subgrid fluxes in S_S. At the opposite, mixing coefficient from S_M reach progressively zero at the inversion allowing more subgrid mixing.

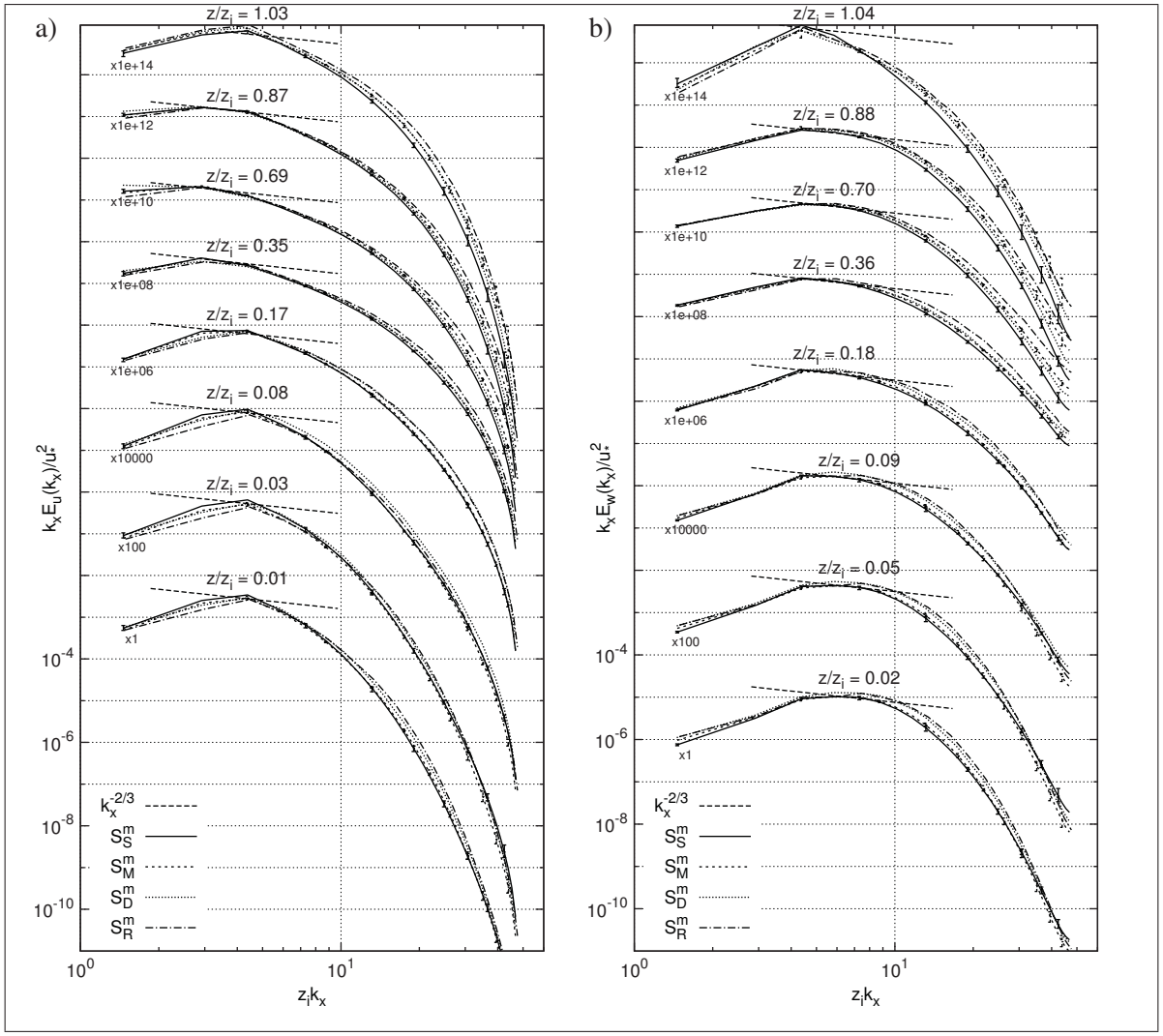

Figure 4.51 Longitudinal spectra of streamwise and vertical velocities from the four SGS models for the shear case relying on S^m setup from Tab. 4.4 and TINERT time interval. Only S_S and S_M are based on the ensemble average of five results

In Fig. 4.50, horizontal and vertical velocity longitudinal spectra are shown for the results based on the four SGS models. In the low wave numbers, spectra are not a function of the SGS model, except for S_R that have slightly less energy in E_u in the surface layer. In the medium and high wave numbers, there are generally two families of spectra featuring similar properties: S_D/S_R and S_S/S_M. This difference is most likely caused by the definition of the filter width (see Sec. 2.2.3): S_D and S_R effective filter width is smaller than in S_S and S_M causing an increase of the energy in the medium and higher wave numbers (which becomes clearly apparent in the surface layer). Spectra from S_S and S_M are very similar in the surface layer while S_M shows more energy in the upper ABL. Concerning S_R and S_D, following Redelsperger *et al.* (2001), E_u and E_w from S_R in the surface layer should feature more energy than S_D in the medium and high wave numbers. This can be observed, but it is marginal. In fact, it would be better observed on dimensional spectra as u_* from S_R is higher by 5 %. In the mixed layer and above, S_D tends to have a similar energy level as S_M while S_R has more energy. However, since S_R and S_D are identical far from the surface, this differences can not be explained.

As a summary of the comparison of the five simple SGS models, Redelsperger *et al.* (2001) SGS model clearly outperform the other SGS models when considering the lower part of the ABL. However, improvements are not as clear as shown in the studies from Redelsperger *et al.* (2001) and Drobinski *et al.* (2004). The others SGS model generally show similar results. However, differences in the filter definition (and thus the effective equivalent Smagorinsky constant $C_{S\,3d}$) have a clear impact on the results (which is clearly seen close to the surface): the use of $\Delta = \Delta_H$ in S_S/S_M (versus $\Delta = \Delta_{3d}$ in S_D/S_R) lead to a higher $C_{S\,3d}$ when relying on S^m grid causing slightly larger subgrid fluxes and lower energy level in the resolved medium and high wave numbers. At the opposite, the surface matching function from S_S and S_M only cause very little changes. Similarly, in the upper ABL and at the inversion, no clear differences are to underline (except the increase of S_M subgrid heat flux caused by the absence of a critical Ri). Finally, the linear Kosović (1997) SGS model, S_K, fail to reproduce the shear case. This appears to be related to the large value of C_S for that model and the definition of the filter width in the surface layer. However, those problems were not further investigated.

4.4.1.2 Convective case

The convective case is reproduced here using the five SGS model in a similar way as done for the shear case. However, considering that the flow is much more resolved in convective conditions, the SGS model is expected to have a lower impact on the results than for the shear case. Furthermore, as underlined in Sec. 4.3.1.2, the scatter of some of the higher order quantities such as momentum flux, variances and vertical flux of variances, is higher than for the shear case. This increases the uncertainty of the results (notably when no ensemble average of several realizations of the same case is done) and may prevent a very fine comparison of the SGS models for the convective case. However, it is of interest to assess the behaviour of the current model using various SGS models when buoyant instabilities are the dominant process producing turbulent mixing.

Tab. 4.16 shows result parameters for the five SGS models: B_S is the UKMO Smagorinsky SGS model (Mason and Brown, 1999), B_M the hybrid TKE SGS model (Pelletier *et al.*, 2005), B_D the Deardorff SGS model (Deardorff, 1980), B_R the Redelsperger SGS model (Redelsperger *et al.*, 2001), and B_K the linear Kosović SGS model (Kosović, 1997).

Table 4.16 Result parameters from the convective case for the five SGS models and based on model setup detailed in Tab. 4.4 and two time intervals. Only B_S and B_M are based on the ensemble average of five results

Interval	Name	Realizations	u_* [m/s]	w_* [m/s]	z_i [m]	L_{MO} [m]	θ_s [K]	$\overline{w'\theta'}_i$ [K m/s]	U_1 [m/s]	$\Delta\theta_1$ [K]
INTER	B_S	5	0.586	2.044	1128	-29.5	310.49	-0.025	5.09	5.07
	B_M	5	0.599	2.039	1120	-32.5	310.26	-0.024	5.01	4.81
	B_D	1	0.584	2.041	1116	-28.1	310.36	-0.029	5.06	4.93
	B_R	1	0.591	2.054	1137	-30.9	310.16	-0.028	5.04	4.79
	B_K	1	0.590	2.091	1200	-29.7	310.44	-0.044	5.09	4.79
LONG	B_S	5	0.593	2.034	1112	-30.3	310.26	-0.016	5.23	5.04
	B_M	5	0.605	2.029	1103	-32.8	310.06	-0.015	5.18	4.81
	B_D	1	0.590	2.029	1095	-29.6	310.14	-0.018	5.20	4.90
	B_R	1	0.599	2.042	1116	-32.2	309.93	-0.019	5.20	4.75
	B_K	1	0.595	2.042	1116	-31.1	310.19	-0.028	5.24	4.76

In Tab. 4.16, differences are generally small, and most of the time of the same order as the scatter as shown in Tab. 4.9. However, the order of magnitude for each parameters, except z_i, is the same regardless the time interval which thus tend to show that the trends in the small differences are not only caused by the scatter, but also by the SGS model. In fact, the only most notable difference is seen in the heat flux at the inversion for B_K that is always at least 30 % lower than the others results. However, as opposed to the shear case no clear departure of B_K from the other SGS models can be observed in the others parameters. Further than that, u_* of B_M and $\Delta\theta_1$ of B_S are generally slightly higher than the other results.

To further explore the results of the five SGS models for the convective case, Fig. 4.52 shows the profiles of interest of first, second and third order moments. It can be seen that at the exception of the potential temperature, the heat flux and the velocity at the inversion for B_K, all results are close and most of the time within the scatter.

Interestingly, results from the linear Kosović SGS model are in good agreement with the others models, which comes as a surprise since results of the shear case were fully biased. In fact, in the convective case the major instabilities originate from the heating surface. The latter heats the air in the near-surface region which then rises by convection up to the inversion following well known patterns. This process, which is mostly resolved, would take place even without SGS model as it is shown by Brown *et al.* (2000). As a result, since the production of turbulence due to buoyancy is dominant for the case B, a SGS model not properly triggering shear instabilities close to the surface would not kill all the turbulence (as opposed to in the shear case). It thus explains why B_K provide good results.

Nevertheless, linear Kosović SGS model results shows some non-negligible differences. As a reminder of Sec. 2.2.3, its dissipation length scales, λ_ε, in stable and neutral regions is relying on both ratios $k^{1/2}/N$ and $k^{1/2}/S$ (Kosović and Curry, 2000). In addition, it was found that, the linear Kosović model has an equivalent $C_S = 0.3$ which is notably higher than the other models. As a consequence, the subgrid TKE of B_K is roughly five times higher than for B_D, Fig. 4.52 e), which causes larger mixing coefficients and thus a stronger subgrid turbulent

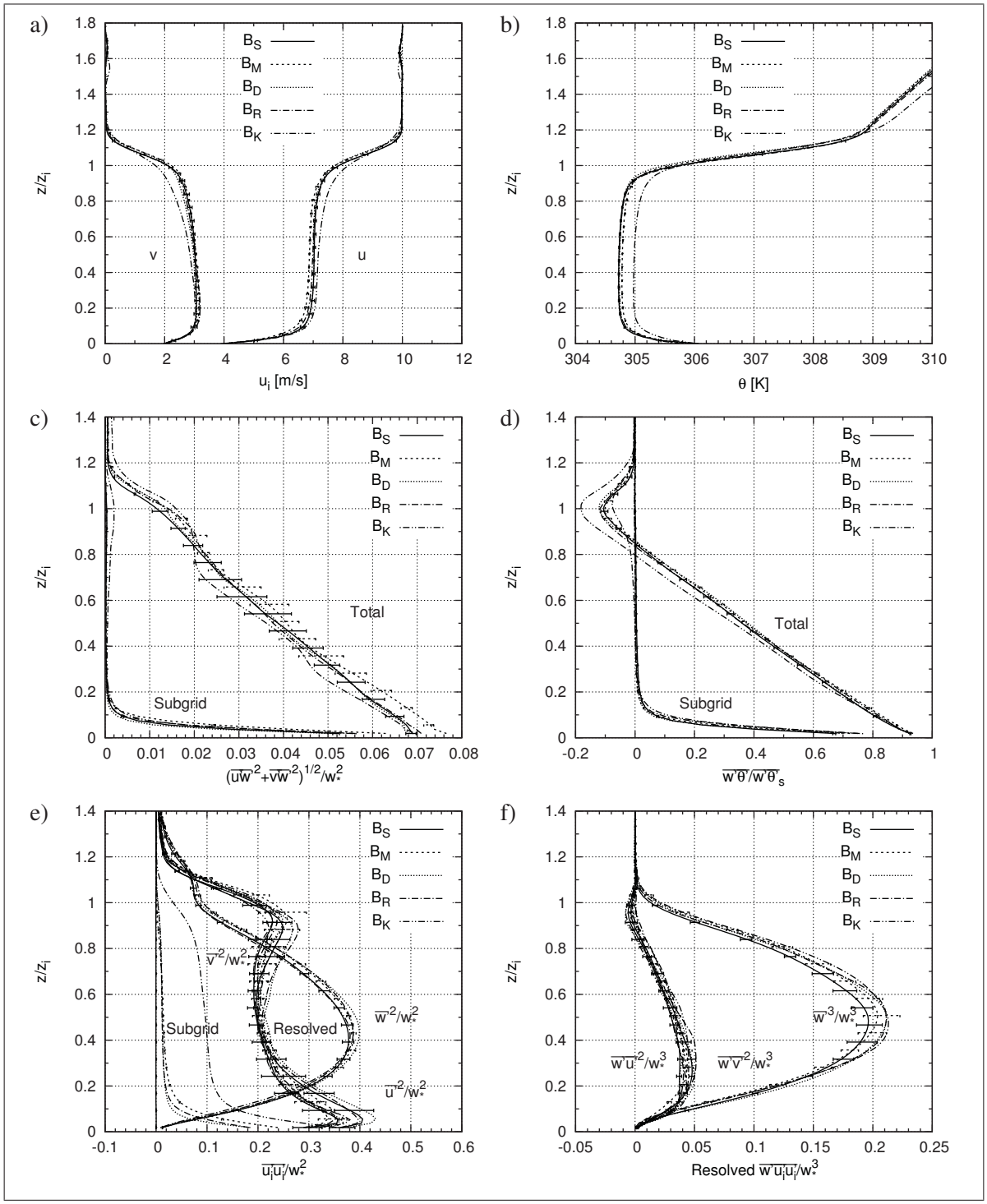

Figure 4.52 Profiles of first, second and third order moments from the five SGS models for the convective case and INTER time interval. Only B_S and B_M are based on the ensemble average of five results

diffusion, and a larger dissipation. Resolved fields may thus feature less small structures than the other SGS models. This does not appear clearly in the surface region of the fluxes since it is unstable, but it become clear in the mixed layer and the above regions. Finally, in Fig. 4.52 c) and d), since subgrid fluxes are very small within the mixed layer, such an increase of the SGS part of the fluxes is only noticeable at the inversion on these figures.

The consequences of the increased subgrid diffusion in B_K are clearly seen in the velocity and temperature profiles, Fig. 4.52 a) and b) (featuring a smoother transition at the inversion for B_K). Furthermore, since the counter-gradient heat flux is larger (due to it subgrid part), more energy is brought in the ABL which further explains its higher temperature of B_K. As a conclusion, the linear Kosović SGS model is clearly more diffusive than the others tested here in convective conditions. However, the obtained large value of subgrid TKE is somewhat suspect notably when considering that the resolved variances are almost unchanged for that model. Further validation is thus clearly needed to assess Kosović SGS model.

Concerning the others SGS models, no major differences are to underline, except for the slightly larger value of the non-dimensional momentum flux close to the surface for B_M. The latter correspond to a higher u_* which confirms that the velocity profile is closer to the similarity very close to the surface (as seen on the non-dimensional shear profile - not shown here). In fact, the hybrid TKE SGS model is also the one which feature the least resolved flow close to the surface. It is more relying on the SGS model, which includes the same stability function as the ones used at the boundary condition to compute surface momentum and heat fluxes. The flow very close to the surface thus tends to less depart from the similarity for B_M, albeit the improvement are just larger than the scatter. Finally, B_R results are similar to the others SGS models. It thus clearly show that the use of a similar matching function as in the neutral conditions neither affect the abilities of the model, nor improve significantly the results over Deardorff SGS model as opposed to the shear case.

Concerning the vertical and streamwise velocity longitudinal spectra shown in Fig. 4.53, it clearly appears that B_K feature less energy in the medium and high wave numbers across the

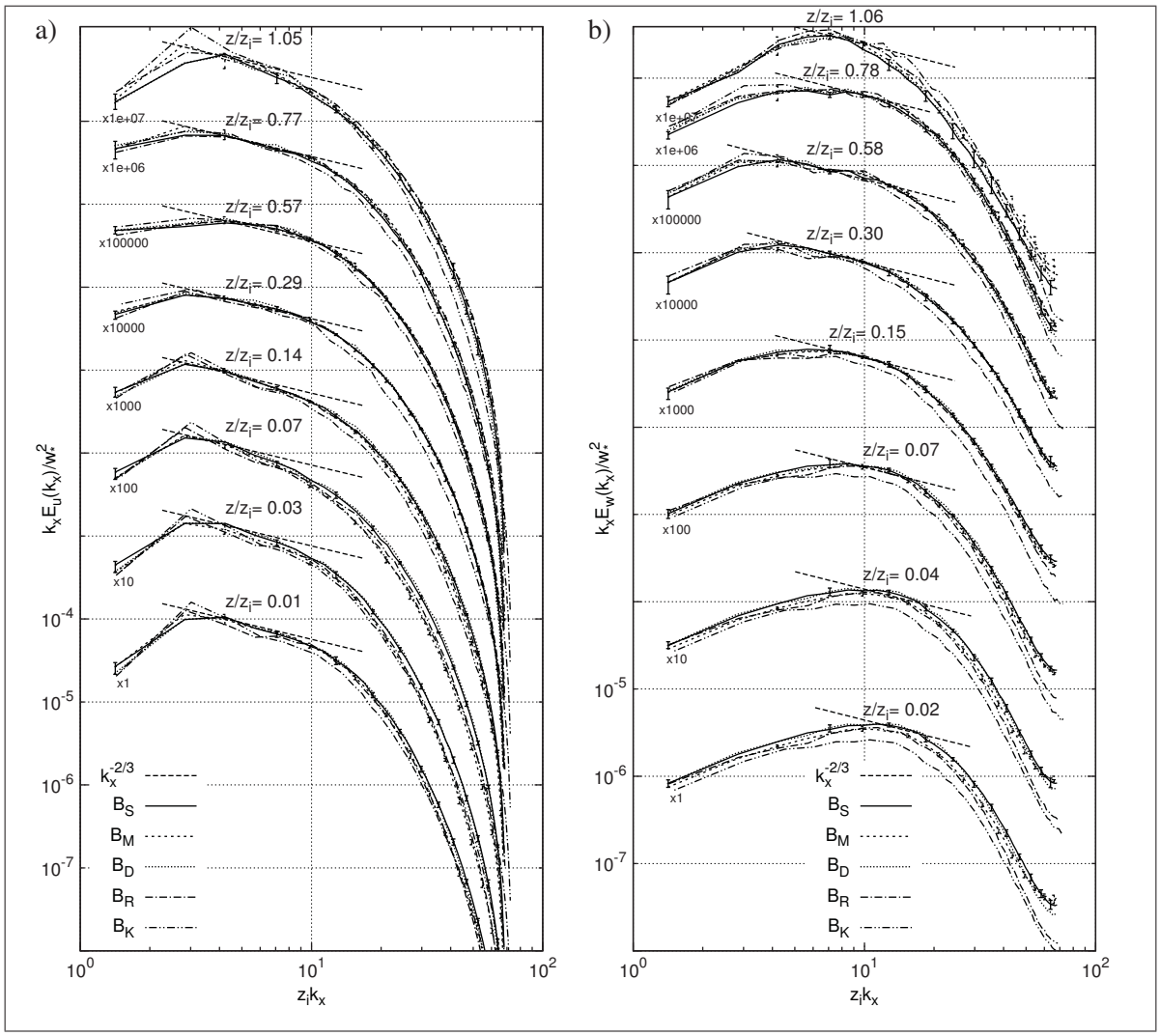

Figure 4.53 Longitudinal spectra of streamwise and vertical velocities from the five SGS models for the convective case and INTER time interval. Only B_S and B_M are based on the ensemble average of five results

whole domain confirming that there are less small structures. It is perfectly in line with the higher equivalent C_S of that model. The others SGS models present differences only for the smallest eddies in the surface layer. Concerning the streamwise velocity spectra, B_D and B_S have slightly more energy than the other results, while for the vertical velocity spectra, this difference is smaller than the scatter, and only B_R departs from the other models very close to the surface to reach B_K at the spectra tail.

As a conclusion, results from the convective case are almost independent of the SGS model. Only, the linear Kosović SGS model showed difference due to an increased subgrid mixing and dissipation. This model seemed to operate properly for the convective case, as opposed to the shear case, but subgrid flux (notably at the inversion) are larger than with the other SGS models. Further investigation and refinement are needed for that SGS model. All the others SGS models performed properly leading to very similar results that are almost always within the scatter, which is in agreement with the remarks from Nieuwstadt *et al.* (1992).

4.4.2 Vertical discretization of the physics

An important aspect not yet evaluated in the context of LES is the changes in the vertical discretization of the physics library of MC2, *i.e.* of all the parametrized processes not taken into account through the solving of the Euler equations of motion above a free slip wall.

As described in Sec. 3.3.1.2, the momentum and heat turbulent diffusion is staggered in MC2, however, as summarized hereafter, the original and the new version of the physics library feature notable differences:

Original physics library: as described in Sec. 3.3.1.2.1, u_i and T are located on the same level and K_M, K_T and the TKE are obtained on intermediate levels (momentum levels of the dynamics). As a result, T and w never change height while at every time steps u and v are interpolated vertically (and extrapolated at the surface) to the temperature z_t levels prior to the physical processes modelling (including turbulence diffusion). Then, horizontal velocity component tendencies from the physics are interpolated back on momentum level. As illustrated in Sec. 4.1 based on a simple Ekman theoretical case, this approach introduces a strong numerical mode in the near-surface region whose amplitude increases as the vertical mesh is refined. This original version of the physics library is sometimes called "unstaggered", but it is somewhat a misnomer as the turbulent diffusion is fully staggered (Mailhot and Benoit, 1982). We will thus call it "original" version and labelled with a "z" exponent hereafter.

New physics library: as described in Sec. 3.3.1.2.2, all variables have the same vertical location and staggering as in the dynamics, and TKE as well as mixing coefficients are computed on the vertical velocity z_w levels. As a result, the turbulent diffusion of the momentum is straightforward as all quantities are at the proper height for discretizing the differential operators, while for heat, K_T is interpolated on momentum levels prior to achieve the turbulent diffusion so that T never changes level. This version of the physics is referred to as "new" or "staggered", and it proved to totally remove the numerical mode in u and v for the simple Ekman case as seen in Figs. 4.2.

All the LES and column model results presented to date are based on the new version of the physics, and the impact of this change have not yet been evaluated in the context of a full ABL. In the present section based on the shear case and the medium domain S^m, the original and new version of the physics are compared and differences are discussed for the column model and the LES models based on both the Smagorinsky and the hybrid TKE SGS schemes.

Table 4.17 Result parameters from the shear case for the original (*i.e.* with a "z" exponent) and the new discretization of the physics. LES results are based on S^m setup from Tab. 4.4. Only S_S is based on the ensemble average of five results

Interval	Name	Realizations	u_* [m/s]	z_i [m]	θ_s [K]	$\overline{w'\theta'}_i$ [K m/s]	U_1 [m/s]	$\Delta\theta_1$ [K]
LONG	S_{1d}	1	0.547	516	300.76	-0.0311	4.50	-0.0023
	S^z_{1d}	1	0.549	463	300.78	-0.0352	4.52	-0.0024
	S_S	5	0.499	453	300.38	-0.0036	4.29	-0.0008
	S^z_S	1	0.490	474	300.36	-0.0037	4.42	-0.0011
	S_M	5	0.512	461	300.40	-0.0048	4.17	-0.0010
	S^z_M	1	0.517	463	300.40	-0.0058	4.19	-0.0012
TINERT	S_{1d}	1	0.639	589	302.38	-0.0226	5.58	-0.0016
	S^z_{1d}	1	0.638	832	302.46	-0.0536	5.57	-0.0017
	S_S	5	0.587	465	300.67	-0.0062	5.17	-0.0011
	S^z_S	1	0.571	453	300.61	-0.0058	5.25	-0.0014
	S_M	5	0.601	465	300.77	-0.0076	5.06	-0.0012
	S^z_M	1	0.595	474	300.75	-0.0075	4.98	-0.0014

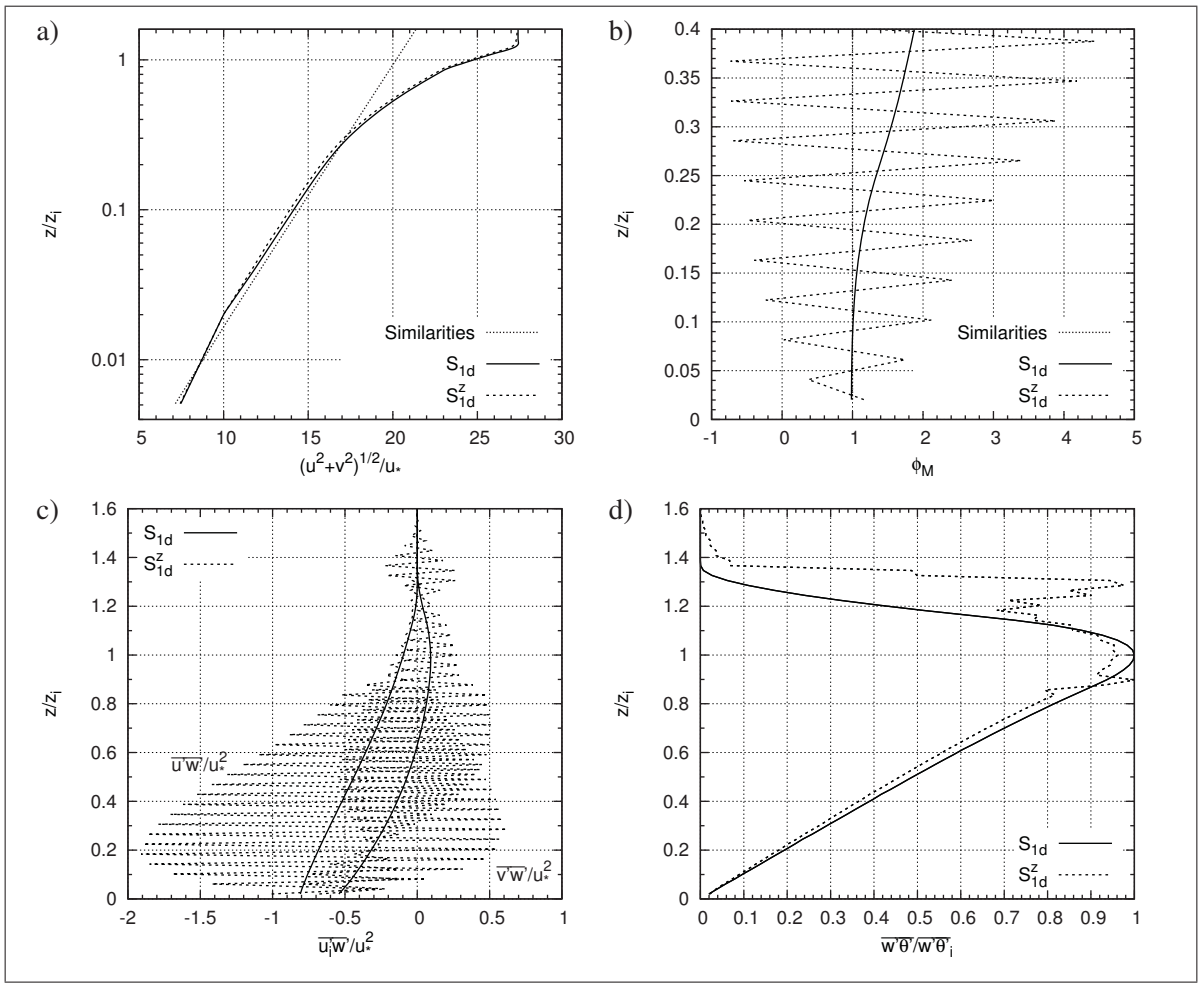

Figure 4.54 Profiles from the original and the new staggered physics for the column model and LONG time interval: a) horizontal velocity modulus; b) horizontal velocity shear; c) momentum fluxes; d) heat flux

Tab. 4.17 summarizes result parameters obtained with the original and the new version of the physics for the shear case and with both the column and LES models. At the exception of z_i from the column model, all parameters are almost unaffected by the changes in discretization. Concerning 1D results, as noted in Sec. 4.3.1.1.1, both version of this model features the highest increase of z_i and θ_s due to the largest value of $\overline{w'\theta'}_i$ (ten times larger than LES). S_{1d} and S^z_{1d} results are very similar during LONG interval, but this is not anymore the case for TINERT interval as S^z_{1d} presents unrealistic high z_i and $\overline{w'\theta'}_i$ which appears spurious in comparison to the results of the column model based on the new version of the physics.

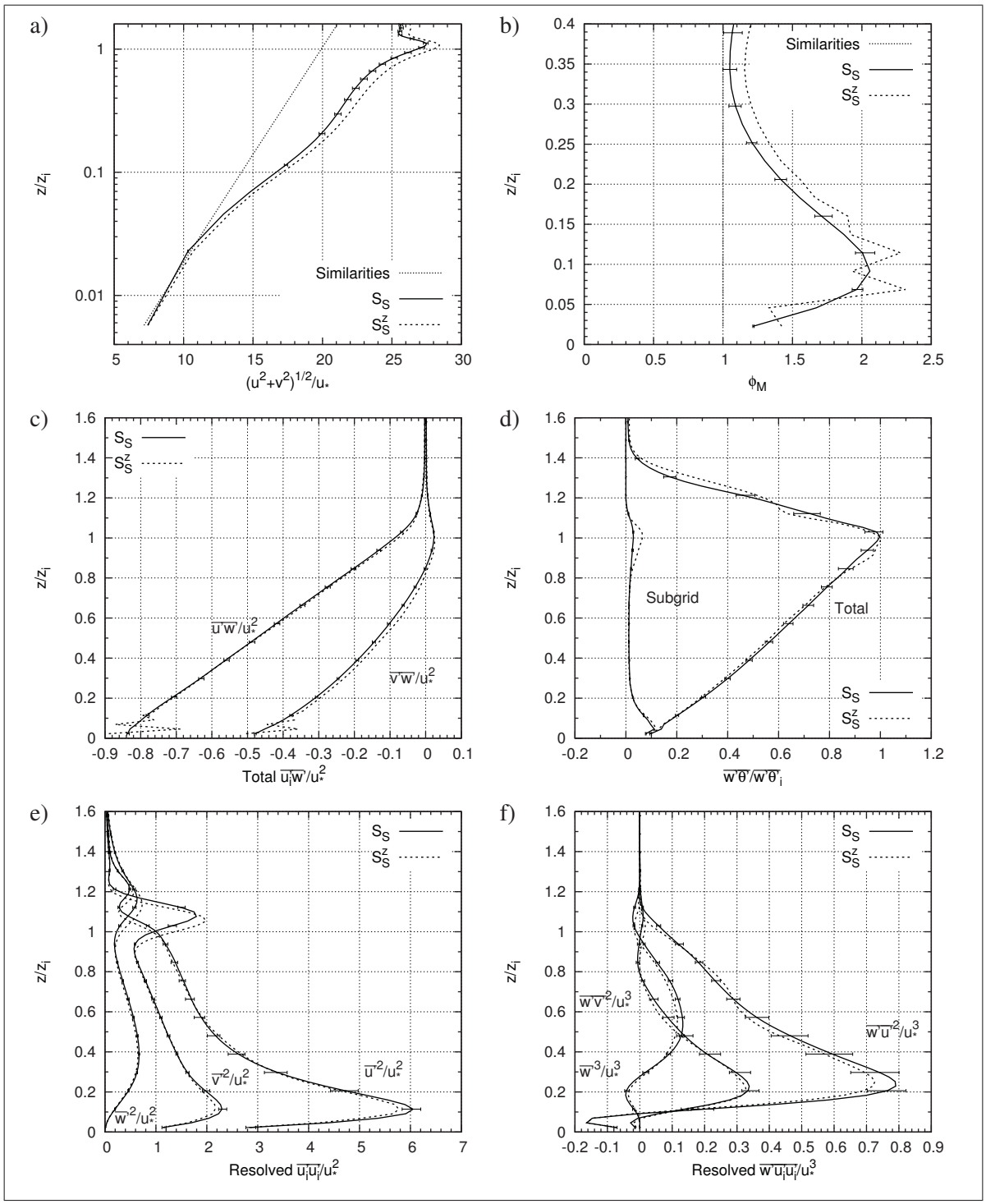

Figure 4.55 Profiles of first, second and third order moments from the original and the new staggered physics relying on S^m setup from Tab. 4.4 and TINERT time interval. Only S_S is based on the ensemble average of five results

In Fig. 4.54, column model results are illustrated though non-dimensional profiles of velocity, gradient function and momentum and heat fluxes. On that figure, new discretization impacts are well illustrated: the numerical mode already present for the simple Ekman case is also clearly observed when the column model is used to reproduce the shear case. Indeed, while the velocity profile is almost unaffected, Fig. 4.54 a), other variables show a large zigzag. Furthermore, there is a grid point offset of the zigzag between $\overline{u'w'}$ and $\overline{v'w'}$ leading to an unusual profile for the modulus of the vertical momentum flux (not shown here). However, the zigzag appears not to affect the mean transfer of energy across the ABL as result parameters are almost unchanged and results from S_{1d} seem to be the average profile of S^z_{1d} (while it is effectively two computations based on new and original version of the physics library).

Nevertheless, the zigzag in the momentum flux, which is at first only present in the ABL, increases with time and propagates above the inversion. This is most probably the cause of a numerical instabilities that develop just above the inversion in $\overline{w'\theta'}$ as seen in Fig. 4.54 d). In fact, this spurious peak also appears to increase with time up to a point where the whole solution is affected (notably in the inversion region). As a consequence, results based on TINERT interval for S^z_{1d} are biased and it was preferred to rely on LONG interval to compare column model results. A reference ABL height of 516 m was used to scale the results in Fig. 4.54. As a result of the above, it can be assumed that the new discretization of all the terms directly related to the vertical turbulence diffusion is correctly implemented. Furthermore, results are clearly improved with the new version of the model thanks to the removal of a numerical mode.

Concerning the LES results, parameters in Tab. 4.17 do not show clear differences between the original and the new version of the physics. To go further, Fig. 4.55 shows the usual profiles of interest, while Fig. 4.56 presents the longitudinal velocity spectra. LES results are notably less affected by the numerical mode than column model results, yet a zigzag can be clearly observed in the surface layer for ϕ_M and the vertical momentum fluxes. In fact, the numerical mode is caused by a vertical interpolation of u and v done before modelling the turbulent diffusion in the original version of the physics. As a result, only the subgrid part (modelled) of the various quantities is directly impacted by the numerical mode in S^z_S, while resolved quantities

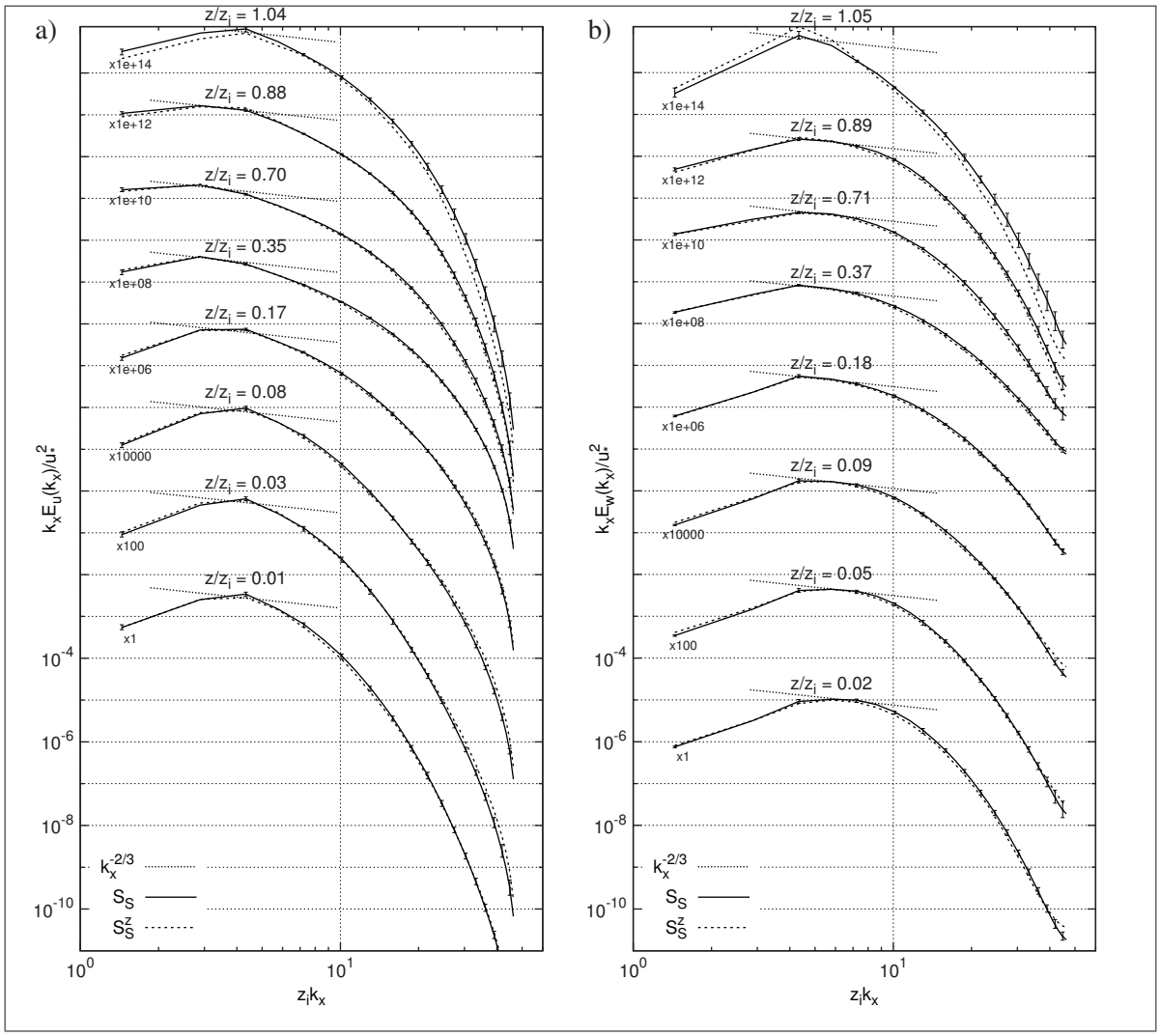

Figure 4.56 Longitudinal spectra of streamwise and vertical velocities from the original and the new staggered physics relying on S^m setup from Tab. 4.4 and TINERT time interval. Only S_S is based on the ensemble average of five results

are unaffected. Indeed, subgrid part of turbulent fluxes is only significant in the surface layer in LES, the numerical mode is thus less of concern and its signature is only seen close to the surface for ϕ_M, $\overline{u'w'}$ and $\overline{v'w'}$. Further than that, results are always within the scatter of S_S, and only a slight increase of the subgrid heat flux at the inversion can be observed in S_S^z. The subgrid and resolved part of $\overline{u'v'}$ also superpose (not shown here) which further confirm that horizontal terms of the turbulent diffusion, which computation is offset by half a level in the new model, are correctly implemented.

Differences in the velocity spectra, Fig. 4.56, are even smaller. Indeed, no particular pattern is found, and velocity spectra of both results always superpose clearly showings that resolved quantities are unaffected. Only, S_S show very slightly more energy in the middle and high wave numbers in the surface layer, while S_S^z have more energy in the low wave numbers, but these differences are of the same order of the scatter which is very small for TINERT interval.

As a conclusion, it can be said that the new discretization of the physics improve the results, notably for the 1D column model. Indeed, concerning the latter model, a large numerical mode polluting the profile of variable such as ϕ_M, $\overline{u'w'}$ and $\overline{v'w'}$, but with no effect on the averaged exchanges of energy with the surface, is removed when using the version of the model properly staggered. Furthermore, column model is stable during the whole run for the new version while numerical instabilities develop above the inversion for very long run for the original version. Concerning LES results, the same variables are improved by the new physics but only subgrid scale fluxes in the surface layer were found to be affected by the numerical mode. Improvements are thus less significant. Finally, since result parameters and averaged profiles are very similar between the two versions of the model, it can thus be assumed that the changes in the new version of the model are correctly implemented.

4.4.3 Standalone turbulence model

In order to further validate the standard 3D turbulence modelling approach implemented in MC2, and particularly the interface between the physics and the dynamics, and the splitting of horizontal (explicit in time) and vertical turbulent diffusion terms (implicit in time), all the turbulent modelling was implemented at the same location directly within the dynamics, meaning in effect that the physics library is not anymore used. The model is thus somewhat simplified and more importantly, limitations related to the physics library and its grid-to-grid interface are avoided. As a result, turbulence modelling can be achieved seamlessly at one location without splitting its horizontal and vertical terms. Furthermore, the model is more flexible as implementing and testing new components is much more straightforward. However, some of the mesoscale abilities of MC2 are lost in that version.

This new version of the LES-capable MC2 model is also referred to as standalone (since the dynamics can be used as a standalone LES model without the physics library). The two following version of the model are evaluated in this section:

Standard: standard version of the LES-capable MC2 (new version of the physics library)[12].
Standalone: standalone version of the LES-capable MC2 (physics library not involved).

As a summary, the standalone 3D turbulence diffusion described in Sec. 3.2.5.2.1 is fully explicit in time and achieved directly in height coordinates; its surface and top boundary conditions presented in Sec. 3.2.5.2.2 are similar to the standard model, *i.e.* fluxes are imposed at the surface and set to zero at the top; surface boundary terms are computed iteratively as illustrated in Sec. 3.3.7; and finally mixing coefficients are computed based on the UKMO Smagorinsky SGS model as described in Sec. 3.2.5.5 and Sec. 3.2.5.4. In the standalone model, main variables and their turbulent diffusion tendencies are not anymore interpolated in neither vertical (as required in the old version of the physics, see Sec. 4.4.2) nor horizontal directions (as always required when the physics library is involved, see Sec. 4.4.2) before and after turbulence modelling. Considering the findings of the previous section, this may also improve the results.

In this section, the standalone turbulence model is evaluated against the standard version using the shear and convective cases as benchmark. Both profiles of relevant quantities and longitudinal velocity spectra are compared as previously done.

Table 4.18 Numerical parameters of the shear and convective cases discussed in Sec. 4.4.3

Name	Model	$N_x \times N_y \times N_z$	L_{x_i} [km]	L_z [km]	Δt [s]	Iteration max.	Realizations
S_S	Standard	$64 \times 64 \times 96$	2	1	1.	60000	5
S_S^{nophy}	Standalone	$64 \times 64 \times 96$	2	1	1.	60000	1
B_S	Standard	$96 \times 96 \times 96$	5	2	2.	20000	1
B_S^{nophy}	Standalone	$96 \times 96 \times 96$	5	2	2.	20000	1

[12] All the column model and LES results previously discussed (except in Sec. 4.4.2) are based on the standard version of the model.

As a reminder, in the standard version of the turbulence modelling in MC2, the vertical turbulent diffusion is implicit in time and its horizontal components are explicit in time. Indeed, as discussed in Sec. 3.1, the implicit solver of Euler equations allows a rather large time steps (Girard *et al.*, 2005), and to take advantage of such a feature an implicit treatment of the vertical diffusion is required. This is particularly true in the mesoscale context where meshes close to the surface are highly deformated. In the LES context, while meshes are generally almost isotropic, the largest gradients of velocity and temperature are still found in the vertical direction. As a result, the explicit treatment of horizontal diffusion terms appears to be appropriate (while retaining the same implicit treatment in the vertical and the SISL CFL criteria discussed in Sec. 4.3.4).This approach was used to obtain the results from the previous sections.

Table 4.19 Result parameters using the standard and the standalone LES models (*i.e.* with a $^{\text{nophy}}$ exponent) for model setups shown in Tab. 4.18 and two time intervals. Only S_S is based on the ensemble average of five results

Interval	Name	u_* [m/s]	w_* [m/s]	z_i [m]	L_{MO} [m]	θ_s [K]	$\overline{w'\theta'}_i$ [K m/s]	U_1 [m/s]	$\Delta\theta_1$ [K]
LONG	S_S	0.496	0.0	451	∞	300.38	-0.0041	4.26	-0.0008
	S_S^{nophy}	0.499	0.0	442	∞	300.37	-0.0044	4.28	-0.0008
TINERT	S_S	0.576	0.0	446	∞	300.70	-0.0062	5.10	-0.0010
	S_S^{nophy}	0.579	0.0	463	∞	300.68	-0.0065	5.12	-0.0010
INTER	B_S	0.576	2.041	1116	-27.1	310.50	-0.027	5.02	5.11
	B_S^{nophy}	0.578	2.038	1116	-27.3	310.48	-0.024	5.07	5.10
LONG	B_S	0.588	2.041	1116	-29.6	310.27	-0.018	5.25	5.06
	B_S^{nophy}	0.587	2.025	1095	-28.5	310.26	-0.016	5.23	5.07

In the standalone model, both vertical and horizontal turbulent diffusion are explicit in time. As a result, a smaller time step may be required to satisfy the stability criteria of the new explicit numerical scheme of vertical turbulent diffusion (the constraint is however lower in the LES context than in the mesoscale context). Indeed, computations based on a $C_{\text{CFL}} = 0.72$ quickly diverged after initialization with that model, and it was found that computations based on $C_{\text{CFL}} = 0.48$ properly performed. Similarly, $C_{\text{CFL}} = 0.38$ was found appropriate for the convective case. No further evaluation of the time step impact on the standalone model is

discussed here. However, when considering the impact of the time step on the results of the standard model, *i.e.* Sec. 4.3.4 for both the shear and the convective cases, it was decided to compare results from the standard and the standalone model that are based on the same CFL so that all numerical parameters are identical and the solver of the equation of motion presents the same behaviour. As a summary, Tab. 4.18 present the numerical parameters of the shear and convective cases which are compared in this section.

In Tab. 4.19 are presented result parameter from the standard and the standalone version of the model for both the shear and the convective cases. On that table, results from both models are almost identical regardless of the interval and for both neutral and convective conditions. In fact, the differences are generally two order of magnitude lower than the parameter except for z_i where differences are slightly higher but they are still lower than the scatter. This is very promising as it demonstrates that, on the one hand, standalone model appears to be valid, and on the other hand, the large differences in the implementation of turbulent processes between the standard and the standalone models have no impact on result parameters.

From Fig. 4.57, it can also be seen that both version of the model are in very good agreement across the whole vertical domain for first and second order moments. Here only the main variables are shown, however, it is noteworthy that even the more sensitive variables such as the heat flux $\overline{w'\theta'}$, and third order moments $\overline{w'u_i'^2}$ from the shear case, as well as the momentum flux from the convective case are almost identical (not shown here). The biggest difference is seen in the variances of the convective case. However, it is to underline that no ensemble average was achieved for the convective case and only one simulation is used for both B_S and B_S^{nophy}. However, as shown in Fig. 4.33 f), the scatter of these quantities is very high. As a result, the differences observed are very likely to be less than the scatter of the results.

Finally, concerning the longitudinal velocity spectra, Fig. 4.58, results are also almost identical for the standard and the standalone approaches. Only the lowest wave numbers present some differences for the convective case. However, they are likely to be within the scatter.

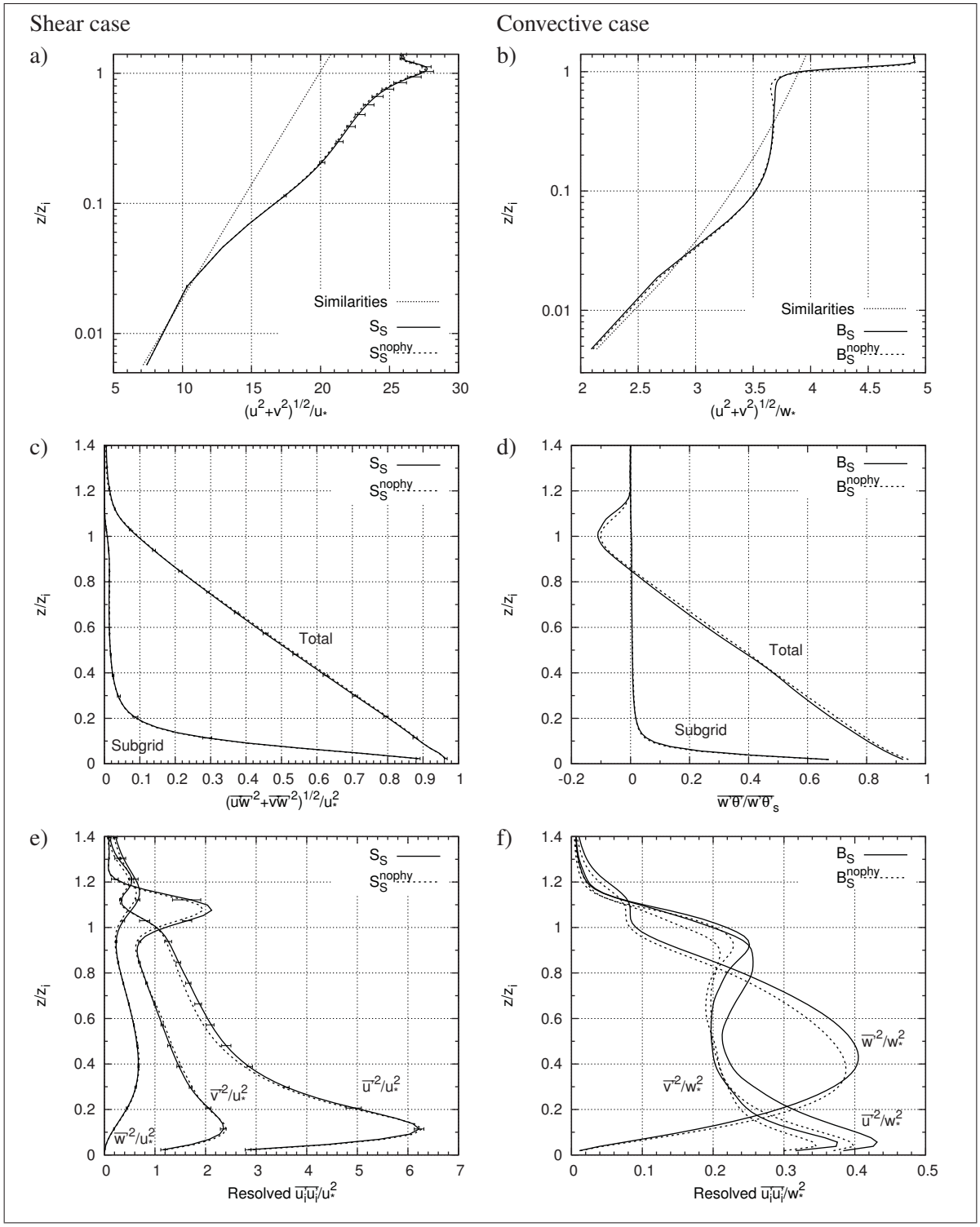

Figure 4.57 Profiles of first and second order moments from the standard and the standalone models and setups shown in Tab. 4.18: a), c) and e) shear case; b), d) and f) convective case. TINERT and INTER time intervals are used for the shear and convective case respectively. Only S_S is based on the ensemble average of five results

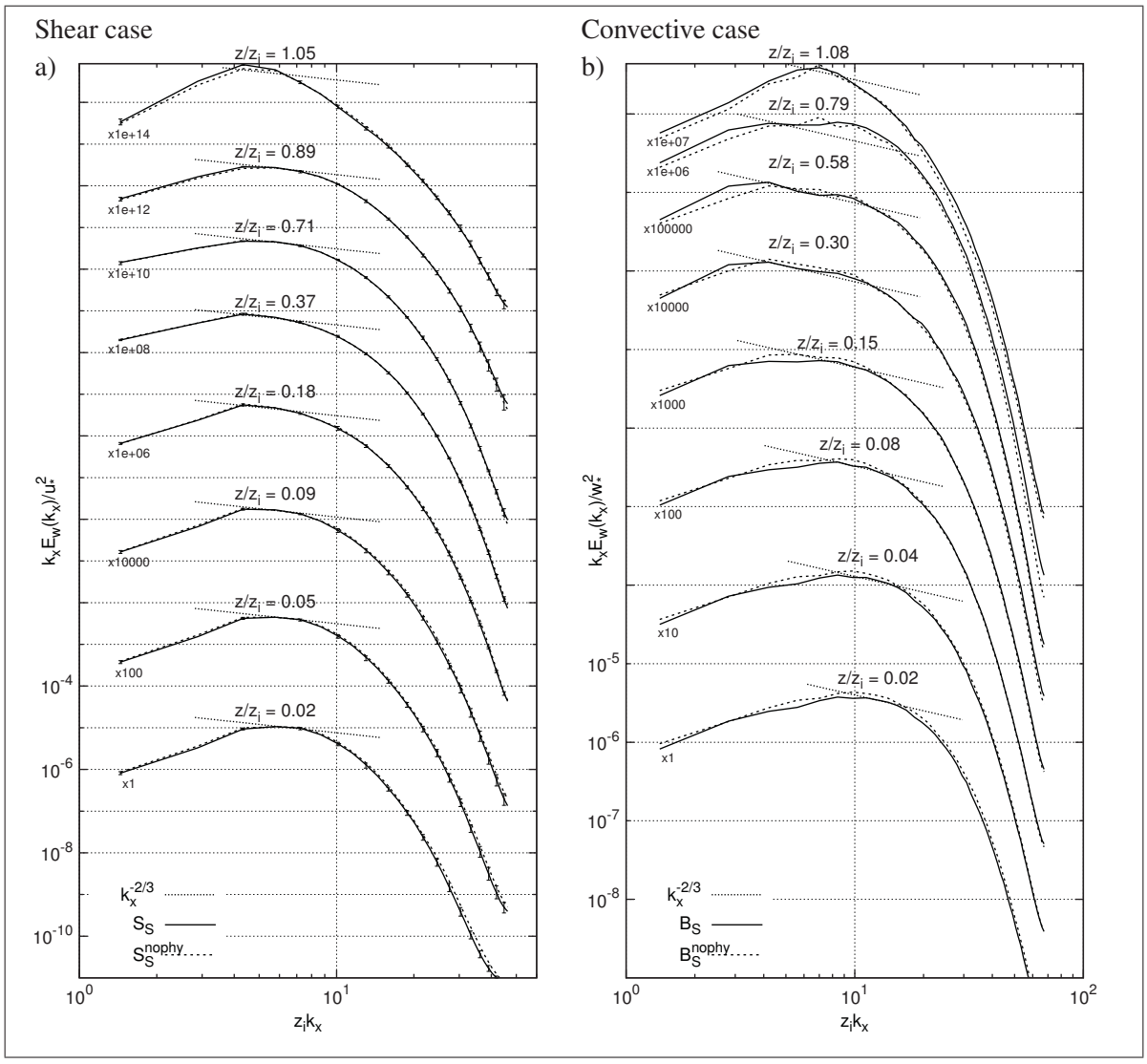

Figure 4.58 Longitudinal spectra of vertical velocity from the standard and the standalone models: a) shear case; b) convective case. TINERT and INTER time interval are used for the shear and convective case. Only S_S is based on the ensemble average of five results

As a conclusion, besides totally different implementations of the turbulent processes, the standard and standalone version of the LES-capable MC2 are in very good agreement and almost no differences can be observed in the various aspects of the solution. The outcomes are twofold: first, it proved that the standalone model is valid and that a proper time step was used with respect to the explicit turbulent diffusion. Second, it also showed that in the standard version of the model: the implicit-explicit approach (where horizontal and vertical turbulence diffusion

terms are split) allows a longer time step with no effect on the results; and the physics-dynamics interface (with the associated interpolations and transformation of the data) has no impact on the results. However as a closing remark, it is to underline as discussed in Sec. 3.5, that horizontal velocity components are interpolated linearly to the centre of the mesh prior to write MC2 output data (in both the standard and the standalone version of the model). This interpolation may filter the smallest structure of the resolved velocity fields. A similar horizontal interpolation is used at the interface between the physics and the dynamics in the standard version of the model, while it was avoided in the standalone version of the model. As a result, keeping u and v at their proper location to achieve the post-processing may be advantageous for the standalone model, and it would be interesting the evaluate the gains (notably in the velocity spectra at high wave number) that would be obtained by avoiding it.

4.5 Summary of the validation

During the present chapter, many aspects and new components of both the column model and the LES-capable MC2 were evaluated in comparison with results from the literature. Here, we come back on the main aspects discuss in this chapter along with the associated outcomes.

Ekman Boundary layer

In a first section, a simple Ekman theoretical case where the geostrophic wind can evolve with height and for which analytical solutions are known (Berger and Grisogono, 1998) was used to validate some fundamental aspects of the method. At first, this case was selected to assess the periodicity of lateral boundary conditions in the presence of a large scale pressure gradient and a Coriolis factor, but it further allowed to diagnose a problem in the vertical discretization of the model causing a large numerical mode (with a maximum amplitude at the surface) in the horizontal velocity components. This numerical mode was of concern in the context of using the approach at high resolution for LES. A new version of the model, labelled New and full based on a common vertical positioning of the main dynamical variables (*i.e.* where the dynamics and the physics are now based on the same vertical discretization) was introduced and it proved to fully solve the problem. Furthermore, based on that version, results were found

to be insensitive to both the resolution and stretching of the vertical mesh (as opposed to the original version of the model). Finally, the simple Ekman case also allowed to partially validate another version of the model (for the horizontally homogeneous cases), labelled Standalone, where all turbulence modelling is implemented directly in the dynamics of the model, and the physics library is not needed anymore (thus simplifying the method). This version of the model alleviates the need for interpolating main variables at the interface between the dynamics and the physics. It led to results almost identical to the new version of the method showing that the vertical components of the new turbulent diffusion were correctly implemented. All results obtained in this first section were promising and in addition to validate the required components for the LES of the full ABL, it allowed to improve the method.

LES of the full ABL: Shear and convective benchmark cases (Moeng and Sullivan, 1994)

In a second section, the shear and convective cases introduced by Moeng and Sullivan (1994) and Sullivan *et al.* (1994) were reproduced. These two cases were selected because they include all the features of a real full ABL while sufficiently simplified to be easily reproduced by LES. Furthermore, these studies are very detailed and many aspects of the solution from the surface to the inversion are evaluated by Moeng and Sullivan (1994) and Sullivan *et al.* (1994). In addition, the LES model used in those studies was thoroughly evaluated against other approaches (Nieuwstadt *et al.*, 1992; Andren *et al.*, 1994), and it is a reference in the domain of LES of the ABL. Finally, many subsequent studies found in the literature, focused on very similar cases allowing deeper comparisons and discussions.

This was the first evaluation of the introduced approach in the context of LES, as a result, it was decided to follow the guidelines provided by Moeng and Sullivan (1994) and Sullivan *et al.* (1994) and use identical numerical and post-processing parameters, in order to allow a full comparison of the results (not only non-dimensional quantities). Furthermore, all computations were achieved based on two different SGS model (the UKMO Smagorinsky and the hybrid TKE SGS models) in order to be able to compare these two scheme and increase our level of confidence. Obtained results were very satisfactory since first, second and third order

moments, as well as the velocity spectra of all velocity components were in good agreement with the comparison data and reference studies in the literature based on similar SGS models. On the one hand, in the mixed layer and at the top of the ABL, results compared very well with Moeng and Sullivan (1994) for both the shear and the convective cases. On the other hand, in the near-surface region, the current approach led to an error similar to other LES results based on dissipative only SGS models (*i.e.* Smagorinsky/Deardorff): streamwise velocity vertical gradient was clearly over-predicted in the surface layer in comparison to experimental data (due to the over-dissipative nature of the Smagorinsky model) (Porté-Agel *et al.*, 2000). However, this departure from the similarity appeared to be higher than in Moeng and Sullivan (1994) results. In fact, thanks to a spectral analysis, it was found that time stepping and advection numerical scheme of the LES-capable MC2, *i.e.* the SISL scheme, tends to dissipate more the smallest resolved eddies in comparison to the results found in the literature (Moeng and Wyngaard, 1988; Mason and Brown, 1999; Brown *et al.*, 2000; Porté-Agel *et al.*, 2000). Therefore, the small structures have less energy, and the flow is less resolved which is worsening the limitation of the Smagorinsky SGS model notably in the near-surface region.

Another outcome of the second section regarded the shear and convective cases post-processing parameters used in Moeng and Sullivan (1994) and Sullivan *et al.* (1994) studies. First, concerning the time interval used by Moeng and Sullivan for the post-processing, it was clearly shown that both cases are not in a steady state, partly due to the inertial oscillation, and even though a fully developed turbulent regime is well established during the whole interval. Furthermore and more importantly, non negligible differences were observed between computations based on the exact same model but for which only initial random velocity perturbations were changed. These differences, also called scatter here, were sometimes high (larger than the averaged variable itself) and an ensemble average of five computations based on the same model was necessary to reduce the uncertainty in the results. As a consequence of the above facts, and in order to be able to use those two cases to further evaluate various aspects of the current model, the shear and convective case clearly needed to be further explored in order to define the best suited post-processing parameters.

LES of the full ABL: numerical parameters

The third section of the chapter was dedicated to the study of the main numerical parameters, *i.e.* the horizontal resolution and domain size, the vertical resolution and domain size and the time step. However, and considering the outcomes of the previous section, the time evolution and scatter of both the shear and the convective cases were thoroughly explored in order to define the optimum post-processing parameters, *i.e.* length and location of the time interval used to compute flow statistics.

For the shear case, it was confirmed that the turbulence is already fully developed during the interval used by Moeng and Sullivan (1994) and that an almost permanent state of the first order moments is reached after $0.5\,T_{inert}$. Furthermore, the longer the time interval, the less scatter there are. However, the latter never disappeared totally even when using very long intervals. Concerning the convective case, it was also confirmed that a representative quasi-steady convective ABL is already well established after $0.1\,T_{inert}$, *i.e.* during Moeng and Sullivan (1994) interval. However, due to the constantly heating surface, this case never reaches a steady state. As for the shear case, the longer the interval, the less scatter there are, but, the scatter was always present regardless of the interval. Furthermore, a too long interval, was proven to affect statistics (notably at the top of the ABL), and, after $0.5\,T_{inert}$ the top of the ABL starts to interact with the top boundary of the model (the sponge layer), limiting the length of the integration. As a result, considering the evolution of the scatter as a function of the time interval, it became clear that the time interval used by Moeng and Sullivan (1994) was too short for both cases to obtain converged statistics of the flow and a longer interval was required to reduce the scatter to an acceptable level allowing a better analysis of the results.

Concerning the horizontal grid and domain size of the shear case, going from a 2 km to a 3 km horizontal grid while retaining the same resolution did not change ensemble averaged results. Furthermore, going from a 31.25 m to a 40 m horizontal resolution grid while retaining the same domain size, gave results in line with the literature (Sullivan *et al.*, 1994; Mason, 1994). However, the coarser the mesh, the more scatter there is, and the more noticeable the scatter

reduction is when the time interval is lengthened. In addition, the coarse mesh based on a 40 m resolution and 2 km sides, proved to be at the edge of suitability to reproduce the shear case of Moeng and Sullivan (1994) with the current version of the LES-capable MC2. Based on that grid, the ignition of turbulence was sometimes delayed preventing the use of the results based on that grid at the beginning of the integration (for Moeng and Sullivan (1994) time interval). Such a grid has been used successfully in many studies found in the literature for similar cases, which thus confirmed the finding of the spectra analysis that the introduced approach is more dissipative due to its Semi-Lagrangian advection scheme.

In the vertical, the use of a finer vertical mesh close to the surface, as well as a coarser vertical grid in the mixed layer did not changed the results of the shear case, and both resolved and subgrid part of turbulent quantities were almost unaffected in the lowest half of the ABL. This is due to the filter width definition of the UKMO Smagorinsky SGS model, but it showed that the resolved part of the flow is not increased by using anisotropic grids. Furthermore, it demonstrated that the discretization is well implemented with regards to no-uniform grids since the latter had no impact on the results. In the upper part of the ABL, and most notably at the inversion, it was found that the mesh needs to be sufficiently fine up to the top of the temperature inversion in order to properly reproduce the heat flux minimum at the inversion. A good prediction of z_i may also implies that the processes from above the inversion are correctly reproduced by the model. However, the heat flux minimum is very small with a high scatter in the context of the shear case which render its accurate prediction more challenging.

Finally, concerning the time step, the SISL scheme generally accepted $\mathrm{CFL} = 1$ limit was observed, but only in the horizontal. For the shear case, a notable degradation of the results is observed in places where $\mathrm{CFL} > 1$. Processes are also affected, but still valid, when the effective maximum CFL equals one. For the convective case, maximum CFL above one were found in the vertical direction, but they did not appear to impact the results. On the other hand, reducing the time step or the effective CFL, did not impact the results of both cases significantly. However, the numerical dissipation inherent to the SL advection scheme is slightly increased by a shorter time step, especially close to the surface. The spectra falloff in the sur-

face layer is always faster when C_{CFL} is lower. But, since profiles of turbulent quantities are not affected in the bulk of the ABL, it confirmed that the filter is correctly located in the inertial subrange (Brown *et al.*, 2000) for both the shear and the convective cases.

LES of the full ABL: enhancements and new components

The last section of the chapter was dedicated to the evaluation of the main enhancement and new components of the model. First, five classical SGS models were compared and it was seen that, at the exception of the Redelsperger *et al.* (2001) and the linear Kosović (1997) SGS model, the other SGS models, *i.e.* the UKMO Smagorinsky (Mason and Brown, 1999), hybrid TKE and Deardorff (1980) SGS models, showed very similar results for both the shear and the convective cases (where differences are most of the time within the scatter). Yet, due to the filter width definition that differs between Deardorff/Redelsperger and UKMO Smagorinsky/hybrid TKE SGS models, small but clear differences were observed. For S^m and S^l grids (that have an aspect ratio of 3), using $\Delta = (\Delta x \Delta y)^{1/2}$ with $C_S = 0.15$ is equivalent to using $\Delta = (\Delta x \Delta y \Delta z)^{1/3}$ with $C_S = 0.216$. As a result, since Deardorff and Redelsperger SGS models have an equivalent $C_S = 0.181$, they led to slightly lower subgrid fluxes and to a higher level of energy in the medium and high wave number eddies which was clearly seen close to the surface for the shear case. The surface matching of length scale in UKMO Smagorinsky and hybrid TKE SGS models only caused very little changes. Similarly, in the upper ABL and at the inversion, no clear differences were observed, except the increased subgrid heat flux for the hybrid TKE SGS model for the shear case most likely caused by the lack of a critical Ri. Concerning the Redelsperger *et al.* (2001) SGS model, thanks to the near-surface refinements it adds to the Deardorff model, this approach clearly outperformed all the other SGS models when considering the surface layer. No adaptation of this approach was done for convective condition (although it would be required for consistency with surface boundary), but results were not affected in comparison to the other SGS models. Improvements obtained in neutral condition were however not as significant as shown in Redelsperger *et al.* (2001) and Drobinski *et al.* (2004). Finally, the linear Kosović (1997) SGS model (without backscatter) clearly failed to reproduce the shear case. This appeared to be related to the large value of equivalent C_S for

that model and the definition of the filter width in the surface layer. At the opposite, and due the buoyant production of turbulence, this model seemed to perform properly for the convective case. However, and in agreement with the larger C_S, resolved part of the flow was unchanged while subgrid fluxes higher than for the other models. Further investigation and refinement are needed to better evaluate Kosović SGS model.

The second aspect evaluated in that last section was the new vertical discretization of the physics (where the main variables remains at the same levels as in the dynamics). This enhancement was included in all the results presented in the previous sections, but this section permitted to show that the LES and most notably the column model results are improved by such a modification. Indeed, concerning the latter, a large numerical mode polluting the profile of momentum related variables such as ϕ_M, $\overline{u'w'}$ and $\overline{v'w'}$, but with no effect on the averaged exchanges of energy with the surface, was removed when using the model version properly staggered. Furthermore, column model was more stable during the whole time interval. Concerning LES results, the same variables were improved but only subgrid scale fluxes in the surface layer were found to be affected by that spurious numerical mode. Improvements were thus less significant but still profitable. Finally, result parameters and averaged profiles were very similar between the original and the new versions of the physics, it can thus be assumed that the changes in the new version of the model were consistently implemented.

A last section was dedicated to the evaluation of a new version of the LES-capable MC2 (labelled standalone) where all turbulent modelling is achieve directly in the dynamics in height coordinates, avoiding the need of the physics library and its pressure coordinate, thus simplifying the approach. A very good agreement was obtained for the various aspects of the solution between the standard and the standalone version of the LES model. It thus proved that the standalone model is valid, and that the physics-dynamics interface (with the associated interpolations and transformation of the variables) as well as splitting horizontal and vertical turbulent diffusion terms had no impact on the results. However, a shorter time step was required due to the fully explicit turbulent diffusion implemented the standalone model. As a

result, it also showed that the implicit-explicit approach used for the turbulent diffusion in the standard model allows a longer the time step with no effect on the results.

As a conclusion of this chapter, although no new cutting edge features were introduced, the first thorough evaluation of a LES method based on the MC2 mesoscale model was achieved. Shear and convective full ABL cases from the literature were satisfactorily reproduced and the sensitivity to the various numerical parameters was evaluated. This model is based on a SISL advection scheme that allowed a rather large time step but which was found more dissipative than the approaches used in the literature. However, this increased dissipation only slightly affected the results in the near-surface region. A strong foundation was thus built for more advanced studied such as LES over complex terrain or diurnal cycles.

CONCLUSION

The main objectives of this thesis were to select, implement and evaluate an approach allowing for the modelling of the microscale and mesoscale ABL flows considering the various requirements and challenges of modern wind energy applications: complex environment in which wind turbine operate; multiscale nature of ABL flows and wind energy production facilities; increasing size of wind turbines and farms.

An extended literature review of ABL flow modelling ranging from microscales to mesoscales was first achieved keeping in mind the challenges faced by the modern wind energy industry. It allowed to provide a clear view of the specificities and abilities of the existing methods, and more importantly, to identify a suitable approach. The combined mesoscale/large eddy simulation (LES) modelling turned out to be the most promising approach. The Compressible Community Mesoscale Model (MC2) was elected as a basis in which the components required for LES had to be included. This effort began prior to the present thesis at Environment Canada (EC) (Pelletier *et al.*, 2005), however it was never completed and the LES-capable MC2 model had never been thoroughly validated.

A detailed description of the mathematical model and the numerical method of the LES-capable MC2 were then presented in order to have a complete view of the approach and to better appreciate the specificities of its implementation. Fundamental aspects of the proposed approach were finally evaluated based on both theoretical 1D Ekman boundary layer (Berger and Grisogono, 1998) and representative shear and buoyancy driven homogeneous surface full dry ABL cases (Moeng and Sullivan, 1994). It allowed to complete the proper implementation of new components required for LES in MC2 as well as to finely adapt and refine the mesoscale model. In the end, the obtained LES-capable mesoscale model was shown to perform on par with other similar LES models found in the literature, and it was thus demonstrated that MC2 was suitable for both microscales and mesoscales.

In this general conclusion, the contributions and achievements of the thesis are summarized, and recommendations for further work are briefly outlined.

Contributions

The main contributions of this thesis reside in the development and the evaluation of a LES model dedicated to the full ABL based on MC2. Several configurations of the LES-capable MC2 were evaluated, *i.e.* the standard model based on the original or new physics, and the standalone model. These allowed to show that:

- volumetric (diagonal) and deviatoric (non-diagonal) Reynolds tensor terms must to be split in the context of LES based on a compressible solver with the former requiring to be explicitly computed and added to the pressure;
- vertical interpolation (and extrapolation at the surface) of momentum related variables before and after achieving the vertical turbulent diffusion, *i.e.* at the interface between the dynamics and the physics, generates a spurious numerical mode in the vertical profiles with a maximum amplitude at the surface. Column model and LES results are affected and the extrapolation of momentum at the surface is particularly critical. The solution to this imperfection of the original version of the model is to use a contiguous vertical discretization in all the components of the model (as in the standard LES model based on the new physics and the standalone LES model - which perform similarly);
- horizontal and vertical turbulent diffusion splitting (explicit/implicit in time and in separate parts of the code as done in the standard model based on the original or new physics) has no impact on the LES results. A larger time step can however be used when the splitting is involved thanks to the implicit treatment of vertical turbulent diffusion;
- scatter of LES results, *i.e.* from simulations based on the exact same model but for which only initial random velocity perturbations are changed, is always present but it is influenced by numerical and post-processing parameters. The larger the domain or the longer the integration period, the lower the scatter is;
- the LES-capable MC2 appears to be more dissipative than reference models in the literature due to its SISL scheme.

Furthermore, by evaluating the sensitivity of the LES-capable MC2 to the main numerical parameters, it was found that:

- medium and large computational domain (with the same resolution) lead to similar results, while a coarser grid (with the same size as the medium computational domain) is at the edge of suitability for the shear case. Scatter of the results is a function of the resolution and the horizontal computational domain size;
- uniform and stretched vertical grids lead to the same results in the lower half of the ABL (for the column model, the UKMO Smagorinsky and hybrid TKE SGS models). Only a spurious but negligible heat flux at the surface of the shear case is reduced as the vertical resolution increases. In the upper ABL, a sufficiently refined mesh up to the top of the temperature inversion is required to properly reproduce the entrainment process;
- horizontal CFL must be lower than unity while this limit is less well defined in the vertical direction. In addition, numerical dissipation of the model increases when lowering the CFL which is clearly observed on the spectra notably close to the surface but not on the turbulence quantity profiles advocating that the filter is correctly located in the inertial subrange for the case reproduced (except in the near-surface region).

The last contribution concerning the LES-capable MC2 is the validation of five SGS models dedicated to the full ABL in neutral and convective conditions: the UKMO Smagorinsky, the hybrid TKE and the Deardorff SGS models are found to perform similarly while the Redelsperger SGS model performs best for the shear case in the near-surface region. The shear case is not correctly reproduced using the linear Kosovìc model. Definition of the filter width, *i.e.* Δ_H versus Δ_{3d}, has little impact on the profile of the first, second and third order moments, while small but clear differences are observed in velocity spectra.

Along the validation of the LES-capable MC2 approach, a detailed evaluation of Moeng and Sullivan (1994) shear and convective cases was also undertaken showing that both cases are in a quasi-steady state during the post-processing interval used by Moeng and Sullivan (1994). More precisely, concerning the shear case, a quasi-steady state is reached after $0.15\,T_{inert}$ fol-

lowed by a roughly statistically permanent state after $0.5\,T_{inert}$ with an ABL height almost constant along the integration but with a velocity profile that features an overshoot at the top of the ABL (which adds constraints on numerical parameters such as the time step). For its part, the convective case is in a quasi-steady state after $0.1\,T_{inert}$ and for the rest of the integration with an ABL height (and a mixed layer temperature) that steadily increases (restricting the integration duration). The scatter of the results based on Moeng and Sullivan (1994) post-processing parameters is however far from been negligible. As a result, a two times longer post-processing time interval than Moeng and Sullivan (1994) is required to obtain stable statistics for both the neutral and convective cases.

Achievements

The above contributions were possible thanks to many achievements that can be sorted into theoretical and practical realizations. The former mostly refer to the three first chapters of this thesis where a review of the ABL modelling from microscales to mesoscales was first achieved (Linear, RANS, Mesoscale, LES). Then, the formal development of the LES-capable MC2 mathematical model was presented in terms of Favre averaging to isolate non-linear turbulence terms which allowed to properly express the turbulent diffusion and closure. Finally, the numerical methods involved in the dynamic kernel and physics library of the LES-capable MC2 were thoroughly described, illustrating, among others things, all the specificities of the implementation of the model.

For their part, the practical achievements consist in the various adaptations and new components added to MC2 to obtain a LES-capable mesoscale model. This includes the adaptation of the operating mode of MC2 with the addition of: large scale geostrophic forcing; a surface boundary condition allowing the surface heat flux to be imposed instead of the surface temperature; a sounding like initialization of thermodynamic variables based on an arbitrary potential temperature and a geostrophic wind profiles; and an initialization of momentum based on truly random velocity perturbations (which seeds are different in every simulation). In addition, theoretical cases, *i.e.* sandbox to operate MC2 in special configurations, allowing to have ac-

cess to the physics library (Ekman, surface homogeneous periodic full ABL cases) and parallel processing were also implemented - both not possible before.

Many other refinements were brought to the model to allow for LES of the ABL. The most important are: the inclusion of the volumetric part of Reynolds tensor (full variances) with the pressure prior to solve the Euler equations of motion; the replacement of the original physics library by a new one featuring an improved staggering which required interfacing MC2 dynamic kernel with a new physics, and an adaptation of all the existing 3D turbulence modelling. Furthermore, several new components were also implemented in and around MC2 such as: a standalone LES model in the dynamics (not relying on the physics) based on a non-split fully explicit turbulent diffusion and a UKMO Smagorinsky SGS model; two new TKE based SGS models in the physics: Deardorff, Redelsperger SGS models; and a fully independent post-processing outside of MC2 (based on Octave and GNUPlot) to compute the first, second and third order moments, as well as longitudinal velocity spectra, and other quantities of interest.

Finally, it is also to underline that, in order to achieve the various developments and computations of the thesis, a Linux cluster had to be installed (by ourselves) along with the MC2 model and associated libraries and post-processing tools. A working environment to operate MC2 as a LES model was also developed.

Future work

During this study, a strong foundation was built allowing for more advanced studies based on the LES-capable MC2. Several features are still needed before considering the use of LES-capable MC2 for real cases and for wind energy applications.

A first improvement that would be required is the implementation of an improved SGS model that would allow to correct the usual bias of classical SGS models in the near-surface region as well as to improve their dissipative only behaviour in the flow interior. The choice of the approach is to be determined in a latter study, however in view of the literature review, an hybrid RANS/LES approach based on a $k - \omega$ RANS model that alleviates the needs for wall

functions and a dynamics Smagorinsky SGS model appears to be the most promising in the long term. The inclusion of a reconstruction model would also be to consider.

Another aspect yet to be completed is the inclusion of the metric factors related to the topography. These terms have already been implemented for the volumetric part of the Reynolds tensor which is processed in the dynamic kernel. However, they are still missing from all the horizontal components of the turbulent diffusion. It would allow the evaluation of the approach in the context of complex terrain, and permit the reproduction of real cases.

Last but not least, it would be interesting to take into account wind turbines directly within MC2. At first, this could be achieved based on the actuator disk approach. Such an addition would allow to study the impact on the flow of wind turbine and wind farms and evaluate their impact on the full ABL which is finely reproduced by means of LES.

Along these new features, it would also be interesting to evaluate the LES-capable MC2 based on an ideal isotropic homogeneous decaying turbulence case. For such a case, periodical boundary conditions need also to be implemented at the bottom and top boundaries (which present some complications as no halo exist for these boundaries). This would allow to properly evaluate the numerical dissipation of the SISL. Similarly, it would also be of interest to evaluate the model based on the purely adiabatic Ekman case of Andren *et al.* (1994). While such a case could be already reproduced with the actual version of the model (setting a perfectly neutral temperature profile across the vertical), it would be of interest to consider the flow as strictly adiabatic and incompressible, namely where temperature is not anymore a variable of importance. This could be achieved by manually setting the heat capacity at constant pressure c_p to a very large value, so that pressure and temperature become uncorrelated and temperature has no more an impact on the solution. This would further allow to strictly appreciate the impact of a compressible solver in the adiabatic incompressible context.

APPENDIX I

IMPLEMENTING LARGE-EDDY SIMULATION CAPABILITY IN A COMPRESSIBLE MESOSCALE MODEL

Nicolas Gasset, Robert Benoit, and Christian Masson
Research Laboratory on the Nordic Environment Aerodynamics of Wind Turbines,
École de technologie supérieure, Montréal (QC), Canada

Paper published in Monthly Weather Review, vol. 142, n° 8, p. 2733–2750, August 2014
URL: http://journals.ametsoc.org/doi/abs/10.1175/MWR-D-13-00257.1
(Initial submission: August 8, 2013; Accepted: February 12, 2014)

Abstract

The large size of modern wind turbines and wind farms triggers processes above the surface layer, which extend to the junction between microscales and mesoscales, and pushes the limits of existing approaches to predict the wind. The main objectives of this study are thus to introduce and evaluate an approach which will better account for physical processes within the Atmospheric Boundary Layer (ABL), and allow for both microscale and mesoscale modelling. The proposed method, which mathematical model and main numerical aspects are presented, combines a mesoscale approach with a Large-Eddy Simulation (LES) model based on the Compressible Community Mesoscale Model (MC2). It is evaluated relying on a shear-driven ABL case allowing to assess the model behaviour at very high resolution as well as more specific numerical aspects such as the vertical discretization and time and space splitting of turbulence related-terms. The proposed LES-capable mesoscale model is shown to perform on par with other similar reference LES models, while being slightly more dissipative. A new vertical discretization of the turbulent processes eliminates a spurious numerical mode in the solution. Finally, the splitting of horizontal and vertical turbulence-related terms is shown to have no impact on the results of the test cases. It is thus demonstrated that the revised MC2 is suitable at both microscales and mesoscales setting a strong foundation for future work.

APPENDIX II

TURBULENCE MODELLING BACKGROUND

The origin of turbulence modelling comes from the end of the nineteenth century with Boussinesq (1877), who first achieve the analogy with molecular viscosity for the non-linear advection (convection) term in Navier-Stokes equations. He introduced the eddy viscosity concept (exchanged fluid particles bring their own momentum that change the total momentum of the fluid parcel). Reynolds (1895) followed by introducing the now famous time averaging method, also called Reynolds averaging. Based on this latter averaging technique the Reynolds averaged Navier-Stokes (RANS) equation were born. Later, Boussinesq (1903), introduced the idea of shallow convection approximation *i.e.* neglect the density variation where it is not multiplied by the gravity, while conserving its product by the gravity in the calculations. That allowed to simplify Navier-Stokes equations for problems involving convection due to heat.

In the meantime, Prandtl (1904), had the idea of a mixing length (once again based on the molecular analogy: the mean-free path of a gas *i.e.* the average distance covered by a particle between successive impacts). This mixing length was the basis of a model for the eddy viscosity. This was the first algebraic model (zero equation model). Later, Prandtl (1945) also derived a model of the eddy viscosity based on the turbulent kinetic energy (TKE). This was the first one equation approach. Including an equation representing the evolution (prognostic equation) of the TKE allowed to consider the history of the flow. However, this kind of model had an important drawback, *i.e.* the mixing length needed to be known/guessed in advance to be able to compute the turbulent viscosity. As a result, this type of model are also referred to as "incomplete" since flow properties were needed to be known in an a priori manner.

Kolmogorov (1942) developed the first complete (two equation) approach with a prognostic equation for the TKE and an other for the so called specific dissipation, ω, defined as "the rate of dissipation of energy per unit of volume and time". This virtually permitted to compute the mean turbulent properties by only prescribing the initial flow state and the boundary conditions.

In the meantime, Kolmogorov also proposed hypothesis on the structure of the small scale turbulent characteristic and motion at high Reynolds numbers. This contributions to the theory of turbulence was very important since they describe the universal character of the small scales that allowed a better modelling. During the same period, Rotta (1951) derived a model that was not anymore based on the Boussinesq eddy viscosity approximation, but that had equation for the evolution of the various components of the Reynolds stress tensor (six in total). This model integrated in a natural manner the non-local and history effects (Wilcox, 1994) pushing approximation and closure hypothesis a step further. This model is know today as the Reynolds stress model or second order closure.

Interestingly, those various studies set the ground of the modern turbulence modelling even before the computer age started. Some of those models where more qualitative than quantitative, but the specificities of the various main family of RANS approaches was set. However, the lack of computational power at that time prevented those methods from being directly applicable during at least the ten following years.

Lilly (1962) and Smagorinsky (1963) were the first to propose and implement an approach that was based on a subgrid scale (SGS) model. The idea was to simulate the biggest scales/eddies and to model the smallest ones (smaller than the grid size). The filtering of the equations was thus spatial or spectral and not anymore in time. In that sense, Smagorinsky and Lilly are the fathers of all the LES approaches. In the SGS model they used, the turbulent viscosity was supposed to take into account subgrid scale dissipation through a Kolmogorov $k^{-5/3}$ cascade. It was express as the product of a squared characteristic length scale and the modulus of the strain of rate tensor. As a result, it can be seen as the adaptation of Prandtl's mixing-length theory to subgrid scale modelling. Production and dissipation of TKE were assumed equal. Lilly (1962) computed the model constants based on the Kolmogorov hypothesis (spectra model) and also proposed a second order SGS model with a prognostic equation for each of the Reynolds tensor components and for the TKE (Lilly, 1966). He also tried to include the effect of buoyancy in the SGS through a Richardson number dependency.

With the advent of computers, turbulence modelling became more realistic although being still very theoretical. This explains why the seventies have seen the explosion of the available CFD methods and applications.

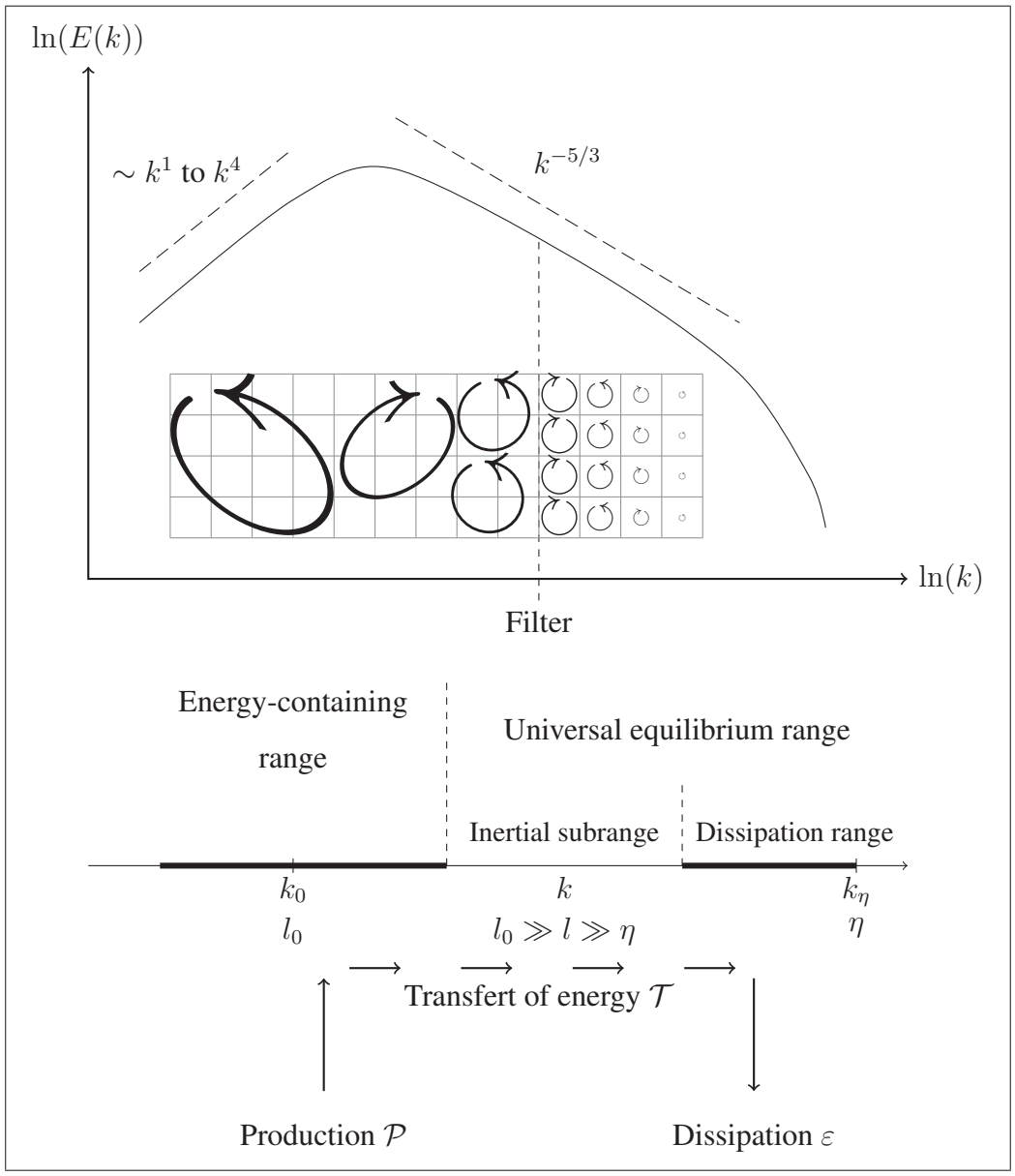

Figure-A II-1 Schematic view of the energy spectra of a turbulent flow. The diagram below is associated to the spectra and it indicates the range in wavenumber of the various regions of interest at very high Reynolds number. The axis have a logarithmic scale

1 Energy cascade and turbulent scales

As described by Richardson (1922), in a turbulent flow, big eddies (small wave numbers, $k = 2\pi/l$), break-up in smaller eddies that fed from the momentum of the former and so on to viscosity (in the molecular sense). This process is called the energy cascade. Large eddies produce and contain the main part of the turbulent energy (energy-containing range) while smaller once (universal equilibrium range) transfer this energy (inertial subrange) and finally dissipate it (dissipation range). In the inertial subrange, motion is mostly dominated by inertial effect while in the dissipative range both viscous and inertial effect can be important. The rate of dissipation ε is determined by the transfer of energy from the large scales $\mathcal{T}$. A schematic illustration is given in Fig. II-1 which is partly inspired by Pope (2000). When looked from the spectral angle, as seen on the upper part of Fig. II-1, this cascade exhibit a typical energy spectra shape where a maximum is found in the low wave numbers (large scale motion) then the spectra only decrease, first linearly and then faster in an exponential manner to reach its minimum at the highest wave numbers (small scale motion).

Bigger eddies can be characterized by the length scale l_0 (which is of the order of the flow scale) and by the speed u_0 (of the order of turbulent intensity $u' \equiv (2/3E)^{1/2}$) (Pope, 2000). Therefore, the energy contained by such an eddy is of the order of u_0^2 and its timescale is $\tau_0 = l_0/u_0$. This lead to a transfer of energy $\mathcal{T}$, and thus a rate of dissipation ε that scales with u_0^3/l_0. Finally, it is also of interest to introduce η, the characteristic length scale of the smallest eddies *i.e.* the one that are destroyed by viscous dissipation (dissipative scales).

Kolmogorov (1941) (*i.e.* Kolmogorov (1991) for a translation) elaborated a theory for flows with a sufficiently high Reynolds number in which are stated the following three hypothesis:

Local isotropy hypothesis: small scale eddies, $l \ll l_0$ (*i.e.* in the universal equilibrium range), are statistically isotropic.

First similarity hypothesis: statistics of motion of scales in the range $l \ll l_0$ (*i.e.* in the universal equilibrium range), have an universal character that is determined by both the dissipation rate ε and the molecular viscosity ν.

Second similarity hypothesis: statistics of motion of scales in the range $\eta \ll l \ll l_0$ (*i.e.* in the inertial subrange) have an universal character that is uniquely determined by the dissipation rate ε, and not the molecular viscosity, ν.

Given the two parameters ε and ν, the smallest eddy scale also called Kolmogorov dissipative scales are defined as

$$\eta = \left(\frac{\nu^3}{\varepsilon}\right)^{1/4}, \tag{A II-1}$$

$$u_\eta = (\varepsilon\nu)^{1/4}, \tag{A II-2}$$

$$\tau_\eta = \left(\frac{\nu}{\varepsilon}\right)^{1/2}. \tag{A II-3}$$

Interestingly, the Reynolds number computed based on these definition, $\mathrm{Re}_\eta = u_\eta\eta/\nu$, equals one. In addition, the ratio between Kolmogorov scales and the bigger eddy can be expressed in terms of large eddies Reynolds number, *i.e.*

$$\frac{l_0}{\eta} \sim \left(\frac{l_0 u_0}{\nu}\right)^{3/4} = \mathrm{Re}^{3/4}, \tag{A II-4}$$

$$\frac{u_0}{u_\eta} \sim \mathrm{Re}^{1/4}, \tag{A II-5}$$

$$\frac{\tau_0}{\tau_\eta} \sim \mathrm{Re}^{1/2}. \tag{A II-6}$$

The higher the Reynolds number of big eddies, the bigger the ratio between large and small scales. It implies that to be able to fully resolve all eddies such as it is done in Direct Numerical Simulation (DNS), we would require a domain of at least l_0 size, with a mesh of η resolution leading to a problem that have $\sim \mathrm{Re}^{9/4}$ meshes. As an example of typical values in the ABL, $l_0 = 1000$ m, $u_0 = 1.5$ m/s and $\nu = 1.5e^{-5}$ m^2/s, we have $\mathrm{Re} = 10^8$ and thus $\eta \sim 10^{-4}$ m. To fully resolve this problem, we would require a grid with $\sim 10^{17}$ nodes. However, while it would be also needed to account of the requirement in terms of time steps, this size of problem is already unrealistic. Instead of the l_0 and ν, we could also have used the integral length scale and the Taylor microscale which would have led to very similar result (Lesieur *et al.*, 2005).

Small scale having an universal character, they can be modelled, which reduces significantly the computational requirement. Indeed, by applying a spatial or spectral filter to the Navier-Stokes equations, small scales can be treated separately (in a subfilter scale manner). Usually the filter is located in the inertial subrange so that smaller scale motion statistics is uniquely determined by the dissipation rate. As a result, one of the main implication of the energy cascade and Kolmogorov hypothesis with regards to numerical modelling of turbulent flows is that the filter width need to be small enough (the mesh resolution in our case) to be located in region where turbulent motion is isotropic *i.e.* within the inertial subrange (region of validity of SGS model) while the domain need to be large enough to capture the energy containing eddies (for the flow to be self-sustained).

2 Filtering

The purpose of filtering a turbulent field, $f(\boldsymbol{x},t)$ is to decompose the latter in a mean part (large scale) $\overline{f}(\boldsymbol{x},t)$ and a fluctuating part (small scale) $f'(\boldsymbol{x},t)$ so that it can be written

$$f(\boldsymbol{x},t) = \overline{f}(\boldsymbol{x},t) + f'(\boldsymbol{x},t). \tag{A II-7}$$

In the case of a compressible flow, it is convenient to define an operator that also take into account the density fluctuations. It is called the Favre filtering

$$\widetilde{f} = \frac{\overline{\rho f}}{\overline{\rho}} \tag{A II-8}$$

and the decomposition can be written

$$f = \widetilde{f} + f' \tag{A II-9}$$

In this section, we will introduce the various common approaches to achieving this filtering and discuss the properties that are associated to them.

2.1 Statistical average

The first way to achieve this decomposition may be through the use of a statistical averages (also known under the name of ensemble average). Indeed, with this approach, the mean field $\langle f(\boldsymbol{x},t)\rangle$ of the turbulent field, $f(\boldsymbol{x},t)$ is computed based on the average of n random and independent realizations of the phenomenon. It thus comes that

$$\langle f(\boldsymbol{x},t)\rangle = \lim_{n\leftarrow\infty}\frac{1}{n}\sum_{i=1}^{n} f(\boldsymbol{x},t). \tag{A II-10}$$

The Taylor hypothesis also know as the ergodicity principle states that for a random steady function in time, it is equivalent to compute the average from an infinite number of independent realizations and the average from one realization that is infinitely long. It thus comes that the time average of $f(\boldsymbol{x},t)$, also called Reynolds average, is expressed as

$$\langle f(\boldsymbol{x})\rangle = \overline{f}(\boldsymbol{x}) = \lim_{T\leftarrow\infty}\frac{1}{T}\int_0^T f(\boldsymbol{x},t')dt'. \tag{A II-11}$$

When considering two random function f and g, the properties of such a statistical averaging approach are the following

$$\langle f+g\rangle = \langle f\rangle + \langle g\rangle\,, \tag{A II-12a}$$

$$\langle af\rangle = a\,\langle f\rangle \quad \text{with} \quad a=\text{const.}, \tag{A II-12b}$$

$$\langle\langle f\rangle\, g\rangle = \langle f\rangle\,\langle g\rangle \quad \text{which imply} \quad \langle\langle f\rangle\rangle = \langle f\rangle \text{ and } \langle f'\rangle = 0, \tag{A II-12c}$$

$$\left\langle\frac{\partial f}{\partial\xi}\right\rangle = \frac{\partial\,\langle f\rangle}{\partial\xi} \quad \text{with} \quad \xi=\boldsymbol{x},t, \tag{A II-12d}$$

$$\left\langle\iiiint f\,d\boldsymbol{x}dt\right\rangle = \iiiint \langle f\rangle\,d\boldsymbol{x}dt. \tag{A II-12e}$$

Those properties are respectively called linearity, conservation of constant, idempotency, and commutation of operator for the two last ones. Any operator that verifies these properties is called a Reynolds operator.

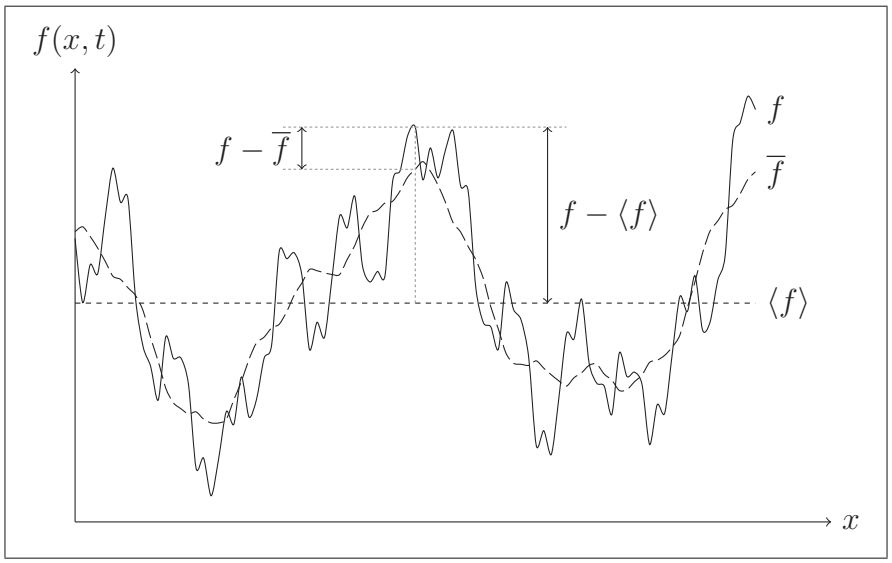

Figure-A II-2 Illustration of the decomposition of a turbulent signal, f, using both a convolution product based on a top-hat filter, $\overline{f}$, and a classical Reynolds operator, $\langle f\rangle$. The local character of the convolution filtering can be observed

2.2 Spatial filters

Removing the small scale structures (that have a bigger wave number than k_{sg}) from a fluctuating field, $f(\boldsymbol{x},t)$, can also be done throw the use of a filtering operator that is expressed mathematically for the physical space as a convolution product between the signal $f(\boldsymbol{x},t)$ and a function $G(\boldsymbol{x},t)$ which is associated to the characteristic filter size, Δ.

The filtered or resolved field $\overline{f}(\boldsymbol{x},t)$ is obtained by the relation

$$\overline{f}(\boldsymbol{x},t)=\iiiint_{-\infty}^{+\infty} f(\boldsymbol{x'},t')G(\boldsymbol{x}-\boldsymbol{x'};\Delta)d\boldsymbol{x'}dt', \tag{A II-13}$$

that can be written symbolically as

$$\overline{f}(\boldsymbol{x},t)=f(\boldsymbol{x},t)\star G(\boldsymbol{x};\Delta). \tag{A II-14}$$

In the Fourier space, the convolution operator is directly express as a classical product such as

$$\overline{\widehat{f}}(\boldsymbol{k},\omega) = \widehat{f}(\boldsymbol{k},\omega)\widehat{G}(\boldsymbol{k};k_{sg}), \tag{A II-15}$$

where k_{sg} is a cut-off wave number associated to the filter Δ (usually $k_{sg} = \pi/\Delta$), $\boldsymbol{k}$ is the wave vector associate to $\boldsymbol{x}$, ω is the frequency associated to t, and $\widehat{f}$ and $\widehat{G}$ are the Fourier transforms of f and G.

The filter introduced above have to have the following properties in order to allow the proper filtering of the prognostic equations: the linearity, the conservation of constants, idempotency and also the commutation with derivation. To be fully satisfied, the latter property implies that care has to be taken close to the boundaries in the case of non-periodical boundary conditions. Those properties are shared by the Reynolds operator presented earlier. However, it is to note that Reynolds operator filters are a restricted ensemble included in the filters verifying the three properties, in other words

$$\overline{\overline{f}\overline{g}} \neq \overline{f}\overline{g} \quad , \quad \overline{f'} \neq 0 \quad \text{and} \quad \overline{\overline{f}} \neq \overline{f}. \tag{A II-16}$$

As illustrated in Fig. II-2, the decomposition based on the convolution filter, $f - \overline{f}$, has a local character as opposed to the fluctuation related to the Reynolds operator, $f - \langle f \rangle$ for which the reference value $\langle f \rangle$ never changes. This imply that every location has its proper $\overline{f}$ value. This have great implications on the expression and thus the modelling of Navier-Stokes equations non-linear terms.

2.2.1 Leonard decomposition

As a result of the above, the general convolution filter applied to the product of $f = \overline{f} + f'$ by $g = \overline{g} + g'$ can be written as (Leonard, 1974)

$$\overline{fg} = \overline{\overline{f}\overline{g}} + \underbrace{\overline{\overline{f}g'} + \overline{f'\overline{g}}}_{C} + \underbrace{\overline{f'g'}}_{R}, \tag{A II-17}$$

where C is the cross term which take into account the coupling between resolved and subgrid scales fluctuation, and R the product of filtered fluctuations (known as the Reynolds tensor).

By introducing L such as

$$L = \overline{\overline{f}\overline{g}} - \overline{f}\overline{g}, \tag{A II-18}$$

one can write

$$\overline{fg} - \overline{f}\overline{g} = L + C + R, \tag{A II-19}$$

where L is fully defined by filtered quantities while the information on fluctuation is required to compute C and R. This expression is known as the Leonard decomposition (Leonard, 1974).

2.2.2 Classical filters

Because of their features, three filters are mainly used for LES. They are relatively simple, symmetric and fulfil the required properties eqs. (A II-12). There are illustrated in Fig. II-3.

Box or top-hat filter: it consists in the local averaging of the signal. In the Fourier space this filter show oscillation, which can have the effect of incorporating non-local frequencies

$$G(x;\Delta) = \begin{cases} 1/\Delta, & \text{if} \quad |x| \leq \Delta/2 \\ 0, & \text{otherwise} \end{cases}, \tag{A II-20}$$

$$\widehat{G}(k;k_{sg}) = \frac{\sin(k\Delta/2)}{k\Delta/2}. \tag{A II-21}$$

Gaussian filter: it also correspond to a local averaging of the signal but for which a weighting with distance is applied. It has the advantage of having the same shape in the physical

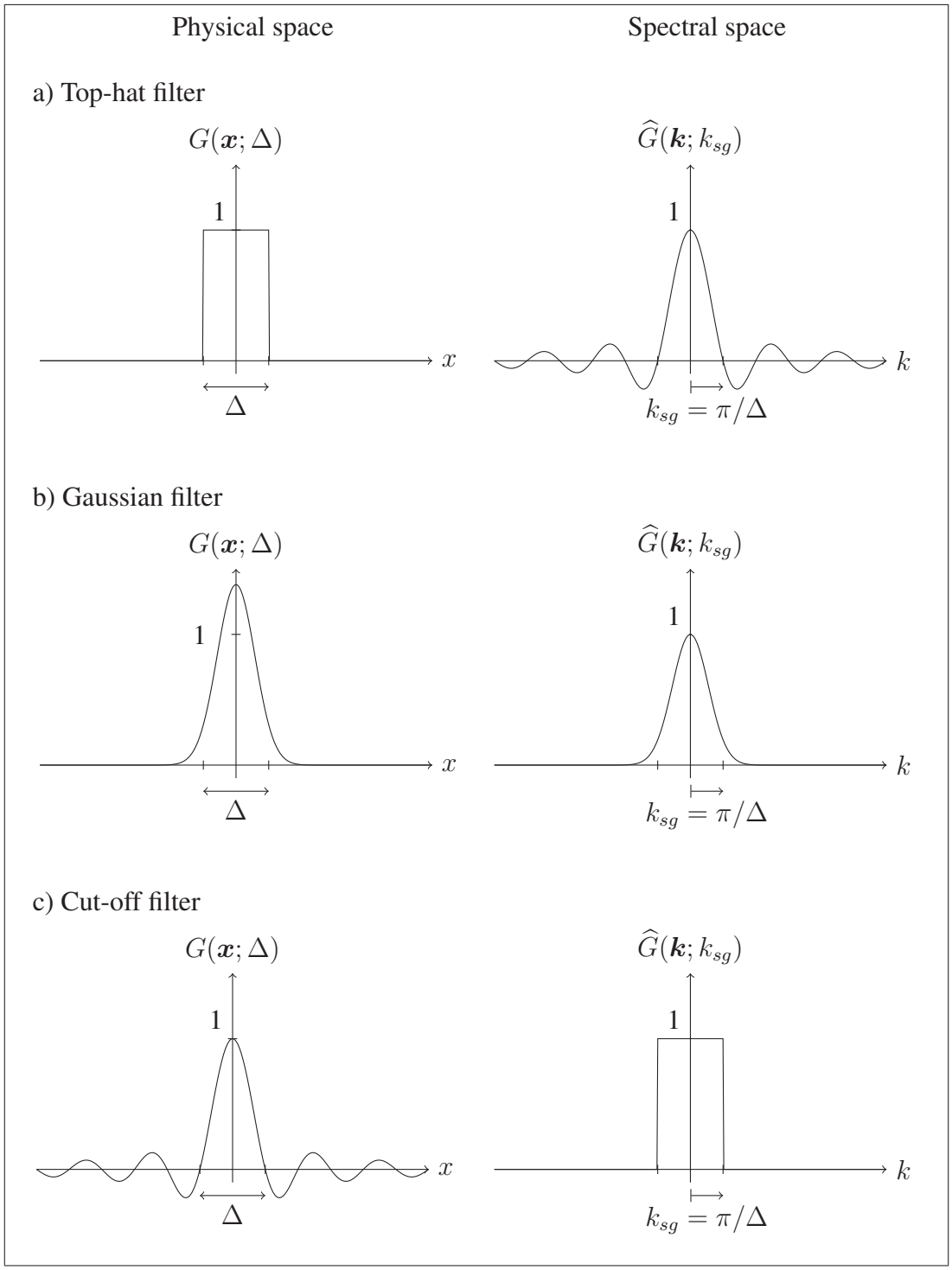

Figure-A II-3 Illustration of the filter shapes commonly used in LES. $G(\boldsymbol{x};\Delta)$ of the top-hat and Gaussian filters are normalized by Δ. The shape of the filters are shown in the physical space on the left column, and in the Fourier space on the right

and spectra domain, without oscillation (as opposed to the two other filters)

$$G(x;\Delta) = \sqrt{\frac{6}{\pi\Delta}^{\,2}}\, e^{\dfrac{-6x^2}{24}}, \tag{A II-22}$$

$$\widehat{G}(k;k_{sg}) = \exp\left(\frac{-\Delta^2 k^2}{24}\right). \tag{A II-23}$$

Sharp or cut-off filter: generally used in the spectra space, it removes any fluctuation above a given wave number k_{sg}, *i.e.* a cut-off wave number associated to the filter Δ. When the cut-off filter is used, there are no interaction between the large and small scale as opposed to the two previous filter

$$G(x;\Delta) = \frac{\sin(k_{sg}x)}{k_{sg}x} \quad \text{with} \quad k_{sg} = \frac{\pi}{\Delta}, \tag{A II-24}$$

$$\widehat{G}(k;k_{sg}) = \begin{cases} 1, & \text{if} \quad |k| \leq k_{sg} = \pi/\Delta \\ 0, & \text{otherwise} \end{cases}. \tag{A II-25}$$

Fig. II-4 shows the effect on the energy spectra of the three filters presented above. The unfiltered filter is based on a refined Kolmogorov spectra model that intent to include the large scale and dissipative scale behaviours (see Pope (2000, p. 232-234)). The cut-off wave number used with all the filters is roughly located in the central part of inertial subrange. It is interesting to remark that the top-hat and the Gaussian filtered spectra quickly deviate from the constant slope of the inertial subrange *i.e.* -5/3. This is important to be considered when dealing with spectra coming from model outputs (and us that are already filtered).

2.2.3 Differential filters

An alternative family of filters are differential filters (Sagaut, 2006). Although their present interesting abilities, they have been less used in practice than the filters presented earlier. They

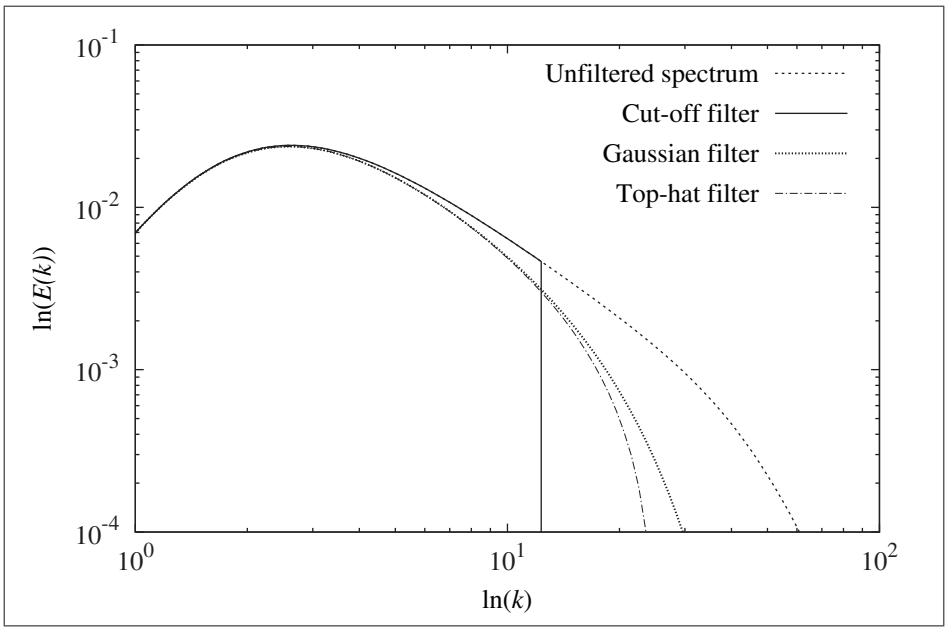

Figure-A II-4 Energy spectrum unfiltered and filtered based on the three filters presented in Fig. II-3. The same cutoff wave number, $k_{sg} = 12.56$ m^{-1}, is used with every filter. The unfiltered filter in based on a Kolmogorov simple model

can be defined such as

$$f = \overline{f} + \tau \frac{\partial \overline{f}}{\partial t} + \Delta_i \frac{\partial \overline{f}}{\partial x_i} + \Delta_{ij} \frac{\partial^2 \overline{f}}{\partial x_i \partial x_j} + ... \qquad \text{(A II-26)}$$

Berselli *et al.* (2006) affirm that differential filters are a correct extension of filtering by convolution to bounded domains.

2.2.4 Grid filter

A particular approach to filter fluctuating field is to use control volumes. First used by Deardorff (1970), it is equivalent to the finite volume method which cut a domain in control volumes. Based on those volumes, the conservation equations can then be solved.

A special case is to use the grid cells as control volume. That way, the filtering is implicit and directly dependent on the grid of the computational domain. Mathematically, these cell

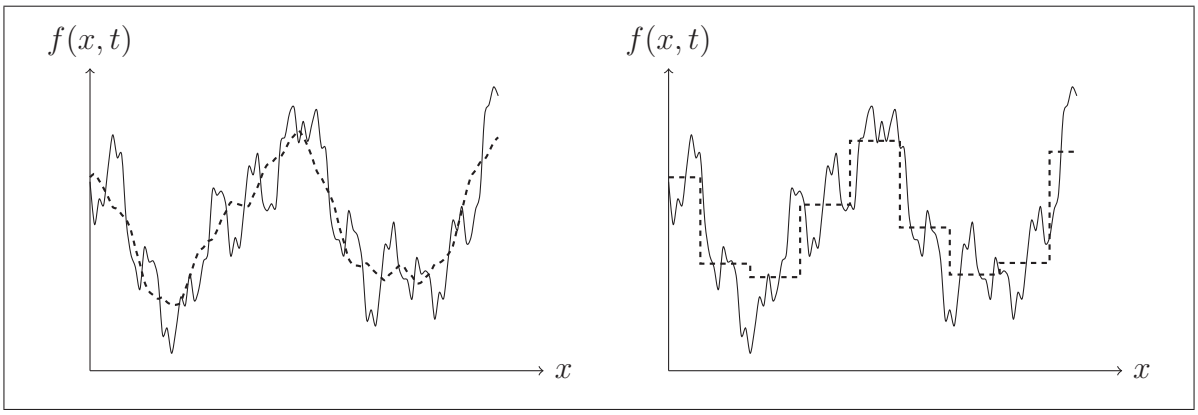

Figure-A II-5 Effect on a turbulent signal of a classical convolution filtering (left) and a filtering based on control volumes (right)

averages are equivalent to the top-hat convolution filtering with a filter characteristic length being equal to the mesh resolution. However, this filtering operator is slightly more general than the convolution product since it conveniently have the same properties as the Reynolds operators, and we thus have again

$$\overline{\overline{f}\overline{g}} = \overline{f}\overline{g} \quad , \quad \overline{f'} = 0 \quad \text{and} \quad \overline{\overline{f}} = \overline{f}. \tag{A II-27}$$

Due to the straightforward application of this kind of filter and the great simplification it brings (in comparison to explicit convolution filtering), this approach have been historically heavily used. Fig. II-5 shows an illustration of the effect of such a filter on of fluctuating function. However, such a filtering approach have to important shortcomings. Filtered fields are constant within the control volume and a discontinuity is observed at the border. In addition, as opposed to the convolution filtering, no flexibility is possible concerning the choice of filter for both the shape and the characteristic size (that directly depends on the grid).

APPENDIX III

SOLUTION OF VERTICAL DIFFUSION EQUATION

Derived from the Benoit *et al.* (1989, Appendix C) and Mailhot *et al.* (1998, Appendix 2).

1 Transformation to σ coordinates

We want to solve the general vertical diffusion equation

$$\begin{aligned}\frac{\partial \psi}{\partial t} &= -\frac{1}{\rho}\frac{\partial}{\partial z}\left(\rho\overline{w'\psi'}\right) \\ &= \frac{1}{\rho}\frac{\partial}{\partial z}\left[\rho K_\psi\left(\frac{\partial \psi}{\partial z}-\gamma_\psi\right)\right],\end{aligned} \tag{A III-1}$$

for $\psi = u$, v, θ, q or E.

At the top of the domain, a no-flux condition is imposed (Neumann)

$$K_\psi\left(\frac{\partial \psi}{\partial z}-\gamma_\psi\right) = 0, \tag{A III-2}$$

while at the base of the domain, also taken to be the anemometer level, the condition is continuity of the flux for $\psi \neq E$ (Cauchy)

$$\rho K_\psi\left(\frac{\partial \psi}{\partial z}-\gamma_\psi\right)\Big|_a = C_\psi C_M V_a\left(\psi_a-\psi_s\right), \tag{A III-3}$$

and an imposed surface layer expression for $\psi = E$ (Dirichlet)

$$\psi|_a = E_a. \tag{A III-4}$$

Before processing, eq. (A III-1)-(A III-4) are transformed for the sigma coordinate

$$\frac{\partial \psi}{\partial t} = \frac{\partial}{\partial \sigma}\left[\tilde{K}_\psi\left(\frac{\partial \psi}{\partial \sigma}+\tilde{\gamma}_\psi\right)\right], \tag{A III-5}$$

with at the top and bottom boundaries

$$\tilde{K}_\psi \left(\frac{\partial \psi}{\partial \sigma} + \tilde{\gamma}_\psi \right) \Big|_{\sigma_1} = 0, \tag{A III-6}$$

$$\tilde{K}_\psi \left(\frac{\partial \psi}{\partial \sigma} + \tilde{\gamma}_\psi \right) \Big|_{\sigma=1} = -AC_\psi C_M V_a \left(\psi_a - \psi_s \right), \tag{A III-7}$$

and where

$$A = \frac{g\sigma}{RT}, \tag{A III-8}$$

$$\tilde{K}_\psi = A^2 K_\psi, \tag{A III-9}$$

$$\tilde{\gamma}_\psi = A^{-1} \gamma_\psi. \tag{A III-10}$$

2 Time discretization

The time discretization is implicit, with the time step $\Delta t'$, being either $2\Delta t$ for $\psi \neq E$ or Δt, for $\psi = E$. The initial value (at time $n-1$ or n) is denoted by ψ^*

$$\frac{\psi^{n+1} - \psi^*}{\Delta t'} = \frac{\partial}{\partial \sigma} \left[\tilde{K}^*_\psi \left(\frac{\partial \psi^{n+1}}{\partial \sigma} + \tilde{\gamma}_\psi \right) \right], \tag{A III-11}$$

subject to

$$\tilde{K}^*_\psi \left(\frac{\partial \psi^{n+1}}{\partial \sigma} + \tilde{\gamma}_\psi \right) \Big|_{\sigma_1} = 0, \tag{A III-12}$$

$$(\psi \neq E): \qquad \tilde{K}^*_\psi \left(\frac{\partial \psi^{n+1}}{\partial \sigma} + \tilde{\gamma}_\psi \right) \Big|_{\sigma=1} = -A \left(C_\psi C_M V_a \right)^{n-1} \left(\psi^{n+1} - \psi^{n+1}_s \right), \tag{A III-13}$$

$$(\psi = E): \qquad \psi^{n+1} \big|_{\sigma=1} = E^n_a. \tag{A III-14}$$

For $\psi = E$, $\tilde{K}^*_\psi$ is computed from E^n (not E^*), while for $\psi \neq E$, $\tilde{K}^*_\psi$ is computed from E^{n+1}.

3 Vertical discretization

In terms of centred finite differences on a vertical grid, assuming that $\tilde{K}_\psi$ and $\tilde{\gamma}_\psi$ are located on staggered levels σ^K with respect to main variable ψ, the vertical diffusion equation eq. (A III-11) can be expressed as (within the domain)

$$\frac{\psi_k^{n+1}-\psi_k^*}{\Delta t'} = \frac{1}{\sigma_{k-1}^K-\sigma_k^K}\left[\underbrace{\tilde{K}^*_{\psi,k-1}\left(\frac{\psi_{k-1}^{n+1}-\psi_k^{n+1}}{\sigma_{k-1}-\sigma_k}+\tilde{\gamma}_{\psi,k-1}\right)}_{\text{(I)}} - \underbrace{\tilde{K}^*_{\psi,k}\left(\frac{\psi_k^{n+1}-\psi_{k+1}^{n+1}}{\sigma_k-\sigma_{k+1}}+\tilde{\gamma}_{\psi,k}\right)}_{\text{(II)}}\right]. \tag{A III-15}$$

At the top of the domain ($\sigma=\sigma_T$), term (I) is replaced using eq. (A III-12), while at the bottom ($\sigma=\sigma_B=1$), term (II) is replaced using eq. (A III-13) ($\psi\neq E$). If $\psi=E$ the boundary values for ψ^{n+1} is directly used (this case is not treated in what follows).

Going further in the development of eq. (A III-15) by first letting

$$d_{k-1}^K = \frac{\tilde{K}^*_{\psi,k-1}}{(\sigma_{k-1}-\sigma_k)}\frac{\Delta t'}{\left(\sigma_{k-1}^K-\sigma_k^K\right)}, \tag{A III-16a}$$

$$d_{k+1}^K = \frac{\tilde{K}^*_{\psi,k}}{(\sigma_k-\sigma_{k+1})}\frac{\Delta t'}{\left(\sigma_{k-1}^K-\sigma_k^K\right)}, \tag{A III-16b}$$

$$\Gamma_k^K = \left(\tilde{K}^*_{\psi,k-1}\,\tilde{\gamma}_{k-1}-\tilde{K}^*_{\psi,k}\,\tilde{\gamma}_k\right)\frac{\Delta t'}{\left(\sigma_{k-1}^K-\sigma_k^K\right)}, \tag{A III-16c}$$

and rearranging terms, one can get

$$\psi_k^{n+1}-\psi_k^* = d_{k-1}^K\,\psi_{k-1}^{n+1}-\left(d_{k-1}^K d_{k+1}^K\right)\psi_k^{n+1}+d_{k+1}^K\,\psi_{k+1}^{n+1}+\Gamma_k^K, \tag{A III-17}$$

which can be written as the matrix problem:

$$\left(\boldsymbol{I}-\boldsymbol{D}^K\right)\Delta\boldsymbol{\psi} = \boldsymbol{D}^K\boldsymbol{\psi}^*+\boldsymbol{\Gamma}^K, \tag{A III-18}$$

and finally, adding the boundary conditions eqs. (A III-12) and (A III-13), the full problem can be written

$$\left(\boldsymbol{I} - \boldsymbol{D}^K - \boldsymbol{B}\right) \Delta\boldsymbol{\psi} = \boldsymbol{D}^K \boldsymbol{\psi}^* + \boldsymbol{\Gamma}^K + \boldsymbol{A} + \boldsymbol{B}\boldsymbol{\psi}^*, \tag{A III-19}$$

where $\boldsymbol{I}$ is the identity matrix, $\boldsymbol{D}^K$ is the tridiagonal diffusion matrix with the non-zero elements

$$D^K_{k,k-1} = \frac{\tilde{K}^*_{\psi,k-1}}{(\sigma_{k-1} - \sigma_k)} \frac{\Delta t'}{\left(\sigma^K_{k-1} - \sigma^K_k\right)}, \tag{A III-20a}$$

$$D^K_{k,k+1} = \frac{\tilde{K}^*_{\psi,k}}{(\sigma_k - \sigma_{k+1})} \frac{\Delta t'}{\left(\sigma^K_{k-1} - \sigma^K_k\right)}, \tag{A III-20b}$$

$$D^K_{k,k} = -D^K_{k,k-1} - D^K_{k,k+1}, \tag{A III-20c}$$

with

$$D^K_{1,0} = -D^K_{N-1,N} = 0, \tag{A III-20d}$$

and finally

$$\Delta\psi_k = \psi^{n+1}_k - \psi^*_k, \tag{A III-20e}$$

$$A_k = -\delta_{k,N-1} \ \left(C_\psi C_M V_a\right)^{n-1} \psi^{n+1}_s \frac{\Delta t'}{\sigma^K_{k-1} - \sigma^K_k}, \tag{A III-20f}$$

$$B_{i,k} = \delta_{i,N-1} \, \delta_{k,N-1} \ \left(C_\psi C_M V_a\right)^{n-1} \frac{\Delta t'}{\sigma^K_{k-1} - \sigma^K_k}, \tag{A III-20g}$$

$$\Gamma^K_k = \left(\tilde{K}^*_{\psi,k-1} \, \tilde{\gamma}_{k-1} - \tilde{K}^*_{\psi,k} \, \tilde{\gamma}_k\right) \frac{\Delta t'}{\sigma^K_{k-1} - \sigma^K_k}. \tag{A III-20h}$$

Equation eq. (A III-19) is solved for $\Delta\psi$. Note that the equation is not solved at $k = N$. Note also that the discretized equation eq. (A III-19) ($k = 1, N-1$) conserve the net boundary flux, as does the continuous form eq. (A III-11).

REFERENCES

Benoit, Robert, Jean Côté, and Jocelyn Mailhot. 1989. "Inclusion of a TKE Boundary Layer Parameterization in the Canadian Regional Finite-Element Model". *Monthly Weather Review*, vol. 117, n° 8, p. 1726–1750.

Berselli, L. C., T. Iliescu, and W. J. Layton, 2006. *Mathematics of large eddy simulation of turbulent flows*. Springer Verlag, 348 p.

Deardorff, James W. April 1970. "A numerical study of three-dimensional turbulent channel flow at large Reynolds numbers". *Journal of Fluid Mechanics*, vol. 41, n° 02, p. 453–480.

Kolmogorov, A. N. July 1991. "The Local Structure of Turbulence in Incompressible Viscous Fluid for Very Large Reynolds Numbers". *Proceedings of the Royal Society A: Mathematical, Physical and Engineering Sciences*, vol. 434, n° 1890, p. 9–13.

Leonard, A. 1974. "Energy Cascade in Large-Eddy Simulations of Turbulent Fluid Flows". *Advances in Geophysics*, vol. 18, p. 237.

Lesieur, Marcel, Olivier Métais, and Pierre Comte, 2005. *Large-Eddy Simulations of Turbulence*, volume 20. New York : Cambridge University Press, 233 p.

Lilly, Douglas K. May 1962. "On the numerical simulation of buoyant convection". *Tellus*, vol. 14, n° 2, p. 148–172.

Lilly, Douglas K. 1966. *The representation of small-scale turbulence in numerical simulation experiments*. NCAR Manuscript No. 281. Boulder, Colorado : National Center for Atmospheric Research, 23 p.

Mailhot, Jocelyn, Stéphane Bélair, Robert Benoit, Bernard Bilodeau, Yves Delage, Luc Fillion, Louis Garand, Claude Girard, and André Tremblay. 1998. *Scientific Description of RPN Physics Library - Version 3.6 -*. Technical report. Dorval, Québec, Canada : Recherche en Prévision Numérique, Atmospheric Environment Service, 197 p.

Pope, Stephen B., 2000. *Turbulent Flows*. Cambridge ; New York : Cambrige University Press, 771 p.

Sagaut, Pierre, 2006. *Large eddy simulation for incompressible flows: an introduction*. ed. 3rd. Berlin : Springer Verlag, 556 p.

Smagorinsky, Joseph. 1963. "General circulation experiments with the primitive equations: 1. The basic experiment". *Monthly Weather Review*, vol. 91, n° 3, p. 99–164.

Wilcox, David C, 1994. *Turbulence Modeling for CFD*. La Cañada ; California : DCW Industries, Inc., 477 p.

BIBLIOGRAPHY

Alinot, Cedric and Christian Masson. 2005. "k-ϵ model for the atmospheric boundary layer under various thermal stratifications". *Journal of Solar Energy Engineering, Transactions of the ASME*, vol. 127, n° 4, p. 438–443.

André, J. C., G. de Moor, P. Lacarrère, and R. du Vachat. October 1978. "Modeling the 24-Hour Evolution of the Mean and Turbulent Structures of the Planetary Boundary Layer". *Journal of the Atmospheric Sciences*, vol. 35, n° 10, p. 1861–1883.

Andren, A., Andy R. Brown, Paul J. Mason, J. Graf, Ulrich Schumann, Chin-Hoh Moeng, and Frans T. M. Nieuwstadt. October 1994. "Large-eddy simulation of a neutrally stratified boundary layer: A comparison of four computer codes". *Quarterly Journal of the Royal Meteorological Society*, vol. 120, n° 520, p. 1457–1484.

Asselin, Richard. June 1972. "Frequency Filter for Time Integrations". *Monthly Weather Review*, vol. 100, n° 6, p. 487–490.

Ayotte, Keith W. 2008. "Computational modelling for wind energy assessment". *Journal of Wind Engineering and Industrial Aerodynamics*, vol. 96, n° 10-11, p. 1571–1590.

Bardina, J., Joel H. Ferziger, and W. C. Reynolds. 1980. "Improved subgrid-scale models for large eddy simulation". In *13th AIAA Fluid and Plasma Dynamics Conference*. (Snowmass, CO 1980), p. 10. American Institute of Aeronautics and Astronautics.

Bartello, Peter and Stephen J. Thomas. 1996. "The Cost-Effectiveness of Semi-Lagrangian Advection". *Monthly Weather Review*, vol. 124, n° 12, p. 2883–2897.

Beare, Robert J., Malcolm K. Macvean, Albert A. M. Holtslag, Joan Cuxart, Igor Esau, Jean-Christophe Golaz, Maria Antònia Jimenez, Marat Khairoutdinov, Branko Kosović, David C. Lewellen, Thomas S. Lund, Julie K. Lundquist, Anne Mccabe, Arnold F. Moene, Yign Noh, Siegfried Raasch, and Peter P. Sullivan. May 2006. "An Intercomparison of Large-Eddy Simulations of the Stable Boundary Layer". *Boundary-Layer Meteorology*, vol. 118, n° 2, p. 247–272.

Bechmann, Andreas. 2006. "Large-Eddy Simulation of Atmospheric Flow over Complex Terrain". Ph.D., Risø National Laboratory, Roskilde, Denmark, 93 p.

Bechmann, Andreas and Niels N. Sørensen. January 2010. "Hybrid RANS/LES method for wind flow over complex terrain". *Wind Energy*, vol. 13, n° 1, p. 36–50.

Bechmann, Andreas, Jacob Berg Jørgensen, Jakob Mann, Niels N. Sørensen, and Pierre-Elouan Réthoré. 2010. "The Bolund Project". <http://windenergyresearch.org/2010/09/the-bolund-project/>.

Bélair, Stéphane, Jocelyn Mailhot, J. Walter Strapp, and J. Ian MacPherson. 1999. "An Examination of Local versus Nonlocal Aspects of a TKE-Based Boundary Layer Scheme in Clear Convective Conditions". *Journal of Applied Meteorology*, vol. 38, n° 10, p. 1499–1518.

Benoit, Robert. 1977. "On the Integral of the Surface Layer Profile-Gradient Functions.". *Journal of Applied Meteorology*, vol. 16, n° 8, p. 859–860.

Benoit, Robert, Jean Côté, and Jocelyn Mailhot. 1989. "Inclusion of a TKE Boundary Layer Parameterization in the Canadian Regional Finite-Element Model". *Monthly Weather Review*, vol. 117, n° 8, p. 1726–1750.

Benoit, Robert, Michel Desgagné, Pierre Pellerin, Simon Pellerin, Yves Chartier, and Serge Desjardins. 1997. "The Canadian MC2: A Semi-Lagrangian, Semi-Implicit Wideband Atmospheric Model Suited for Finescale Process Studies and Simulation". *Monthly Weather Review*, vol. 125, n° 10, p. 2382–2415.

Benoit, Robert, Christoph Schär, P. Binder, S. Chamberland, H. C. Davies, Michel Desgagné, Claude Girard, C. Keil, N. Kouwen, Daniel Lüthi, D. Maric, E. Müller, Pierre Pellerin, J. Schmidli, F. Schubiger, C. Schwierz, M. Sprenger, A. Walser, S. Willemse, Wei Yu, and E. Zala. 2002. "The Real-Time Ultrafinescale Forecast Support during the Special Observing Period of the MAP". *Bulletin of the American Meteorological Society*, vol. 83, n° 1, p. 85.

Berger, Bradford W. and Branko Grisogono. 1998. "The Baroclinic, Variable Eddy Viscosity Ekman Layer". *Boundary-Layer Meteorology*, vol. 87, n° 3, p. 363–380.

Bergeron, Guy, René Laprise, Daniel Caya, André Robert, Michel Giguère, Robert Benoit, and Yves Chartier. 1994. *Formulation of the Mesoscale Compressible Community (MC2) model*. Technical report. Centre coopératif pour la recherche en mésométéorologie.

Bergström, Hans and Nikolaus Juuso. 2006. "A study of valley winds using the MIUU mesoscale model". *Wind Energy*, vol. 9, n° 1-2, p. 109–129.

Bitsuamlak, G. T., Ted Stathopoulos, and Claude Bedard. 2004. "Numerical evaluation of wind flow over complex terrain: Review". *Journal of Aerospace Engineering*, vol. 17, n° 4, p. 135–145.

Blackadar, Alfred K. 1962. "The Vertical Distribution of Wind and Turbulent Exchange in a Neutral Atmosphere". *Journal of Geophysical Research*, vol. 67, n° 8, p. 3095–3102.

Bonaventura, Luca. 2000. "A Semi-implicit Semi-Lagrangian Scheme Using the Height Coordinate for a Nonhydrostatic and Fully Elastic Model of Atmospheric Flows". *Journal of Computational Physics*, vol. 158, n° 2, p. 186–213.

Bosveld, Fred C., Evert I. F. de Bruijn, and Albert A. M. Holtslag. 2008. "Intercomparison of Single-column Models for GABLS3 preliminary Results". In *18th Symposium on Boundary Layers and Turbulence*. (Stockholm, Sweden 2008), p. 4.

Bosveld, Fred C., Peter Baas, and Albert A. M. Holtslag. 2010. "The Third GABLS SCM Intercomparison and Evaluation Case". In *19th Symposium on Boundary Layers and Turbulence*. (Keystone, Colorado, USA 2010), p. 8.

Bougeault, Philippe and P. Lacarrère. 1989. "Parameterization of Orography-Induced Turbulence in a Mesobeta–Scale Model". *Monthly Weather Review*, vol. 117, n° 8, p. 1872.

Brasseur, James G. and Tie Wei. 2010. "Designing large-eddy simulation of the turbulent boundary layer to capture law-of-the-wall scaling". *Physics of Fluids*, vol. 22, n° 2, p. 021303.

Brodeur, Philippe and Christian Masson. 2008. "Numerical Site Calibration Over Complex Terrain". *Journal of Solar Energy Engineering*, vol. 130, n° 3, p. 31020.

Brown, Andy R. January 1999. "The sensitivity of large-eddy simulations of shallow cumulus convection to resolution and subgrid model". *Quarterly Journal of the Royal Meteorological Society*, vol. 125, n° 554, p. 469–482.

Brown, Andy R., S. H. Derbyshire, and Paul J. Mason. 1994. "Large-eddy simulation of stable atmospheric boundary layers with a revised stochastic subgrid model". *Quarterly Journal of the Royal Meteorological Society*, vol. 120, n° 520, p. 1485–1512.

Brown, Andy R., Malcolm K. MacVean, and Paul J. Mason. 2000. "The Effects of Numerical Dissipation in Large Eddy Simulations". *Journal of the Atmospheric Sciences*, vol. 57, n° 19, p. 3337–3348.

Brown, Andy R., J. M. Hobson, and Nigel Wood. 2001. "Large-Eddy Simulation Of Neutral Turbulent Flow Over Rough Sinusoidal Ridges". *Boundary-Layer Meteorology*, vol. 98, n° 3, p. 411–441.

Busch, N. E. and Hans A. Panofsky. 1968. "Recent spectra of atmospheric turbulence". *Quarterly Journal of the Royal Meteorological Society*, vol. 94, n° 400, p. 132–148.

Businger, Joost A., John C. Wyngaard, Y. Izumi, and E. F. Bradley. March 1971. "Flux-Profile Relationships in the Atmospheric Surface Layer". *Journal of the Atmospheric Sciences*, vol. 28, n° 2, p. 181–189.

Castelli, SilviaTrini, Enrico Ferrero, and Dominico Anfossi. 2001. "Turbulence Closures In Neutral Boundary Layer Over Complex Terrain". *Boundary-Layer Meteorology*, vol. 100, n° 3, p. 405–419–419.

Castelli, SilviaTrini, Enrico Ferrero, Dominico Anfossi, and R. Ohba. 2005. "Turbulence closure models and their application in RAMS". *Environmental Fluid Mechanics*, vol. 5, n° 1, p. 169–192–192.

Castro, F. A., J. M. L. M. Palma, and A. Silva Lopes. June 2003. "Simulation of the Askervein Flow. Part 1: Reynolds Averaged Navier-Stokes Equations (k - ϵ Turbulence Model)". *Boundary-Layer Meteorology*, vol. 107, n° 3, p. 501–530.

Chow, Fotini Katopodes and Robert L. Street. May 2009. "Evaluation of Turbulence Closure Models for Large-Eddy Simulation over Complex Terrain: Flow over Askervein Hill". *Journal of Applied Meteorology and Climatology*, vol. 48, n° 5, p. 1050–1065.

Chow, Fotini Katopodes, Robert L. Street, Ming Xue, and Joel H. Ferziger. July 2005. "Explicit Filtering and Reconstruction Turbulence Modeling for Large-Eddy Simulation of Neutral Boundary Layer Flow". *Journal of the Atmospheric Sciences*, vol. 62, n° 7, p. 2058–2077.

Churchfield, M. J., G. Vijayakumar, James G. Brasseur, and P. J. Moriarty. 2010. "Wind Energy-Related Atmospheric Boundary Layer Large-Eddy Simulation Using OpenFOAM: Preprint". In *19th Symposium on Boundary Layers and Turbulence*. (Keystone, Colorado, USA 2010), p. 26.

Clark, Terry L. June 1977. "A small-scale dynamic model using a terrain-following coordinate transformation". *Journal of Computational Physics*, vol. 24, n° 2, p. 186–215.

Clark, Terry L. and W. R. Peltier. November 1977. "On the evolution and stability of finite-amplitude mountain waves". *Journal of the Atmospheric Sciences*, vol. 34, n° 11, p. 1715–1730.

Crosman, Erik T. and John D. Horel. June 2010. "Sea and Lake Breezes: A Review of Numerical Studies". *Boundary-Layer Meteorology*, p. 1–29.

Cuxart, Joan, Philippe Bougeault, and Jean-Luc Redelsperger. 2000. "A turbulence scheme allowing for mesoscale and large-eddy simulations". *Quarterly Journal of the Royal Meteorological Society*, vol. 126, n° 562, p. 1–30.

Cuxart, Joan, Albert A. M. Holtslag, Robert J. Beare, E. Bazile, Anton Beljaars, A. Cheng, L. Conangla, M. Ek, F. Freedman, R. Hamdi, A. Kerstein, H. Kitagawa, G. Lenderink, David C. Lewellen, Jocelyn Mailhot, T. Mauritsen, V. Perov, G. Schayes, Gert-Jan Steeneveld, Gunilla Svensson, Peter A. Taylor, Wensong Weng, S. Wunsch, and K.-M. Xu. 2006. "Single-Column Model Intercomparison for a Stably Stratified Atmospheric Boundary Layer". *Boundary-Layer Meteorology*, vol. 118, n° 2, p. 273–303.

Dalpé, Benoit and Christian Masson. September 2008. "Numerical study of fully developed turbulent flow within and above a dense forest". *Wind Energy*, vol. 11, n° 5, p. 503–515.

Deardorff, James W. 1972. "Numerical Investigation of Neutral and Unstable Planetary Boundary Layers". *Journal of the Atmospheric Sciences*, vol. 29, n° 1, p. 91–115.

Deardorff, James W. 1973. Three-Dimensional Numerical Modeling of the Planetary Boundary Layer. Haugen, D. A., editor, *Workshop on Micrometeorology*, chapter 7, p. 271–311. American Meteorologic Society.

Deardorff, James W. 1974. "Three-dimensional numerical study of turbulence in an entraining mixed layer". *Boundary-Layer Meteorology*, vol. 7, n° 2, p. 199–226.

Deardorff, James W. 1980. "Stratocumulus-capped mixed layers derived from a three-dimensional model". *Boundary-Layer Meteorology*, vol. 18, n° 4, p. 495–527.

Delage, Yves. July 1974. "A numerical study of the nocturnal atmospheric boundary layer". *Quarterly Journal of the Royal Meteorological Society*, vol. 100, n° 425, p. 351–364.

Delage, Yves. 1988. "A parameterization of the stable atmospheric boundary layer". *Boundary-Layer Meteorology*, vol. 43, n° 4, p. 365–381.

Delage, Yves. 1997. "Parameterising sub-grid scale vertical transport in atmospheric models under statically stable conditions". *Boundary-Layer Meteorology*, vol. 82, n° 1, p. 23–48.

Delage, Yves and Claude Girard. 1992. "Stability functions correct at the free convection limit and consistent for for both the surface and Ekman layers". *Boundary-Layer Meteorology*, vol. 58, n° 1, p. 19–31.

Delaunay, Didier, Aurélien Chantelot, T. Guyader, and P. Alexandre. 2004. "Meteodyn WT: A software for wind resource assessment in complex terrain". In *Proceedings of the European Wind Energy Conference & Exhibition EWEC 2004*. (London, UK 2004).

Detering, H. W. and D. Etling. October 1985. "Application of the E – ϵ turbulence model to the atmospheric boundary layer". *Boundary-Layer Meteorology*, vol. 33, n° 2, p. 113–133.

Ding, Feng, Pal S. Arya, and Yuh-Lang Lin. 2001a. "Large-Eddy Simulations of the Atmospheric Boundary Layer Using a New Subgrid-Scale Model – I. Slightly unstable and neutral cases". *Environmental Fluid Mechanics*, vol. 1, n° 1, p. 29–47.

Ding, Feng, Pal S. Arya, and Yuh-Lang Lin. March 2001b. "Large-Eddy Simulations of the Atmospheric Boundary Layer Using a New Subgrid-Scale Model – II. Weakly and moderately stable cases". *Environmental Fluid Mechanics*, vol. 1, n° 1, p. 49–69.

Drobinski, Philippe, Pierre Carlotti, Rob K. Newsom, Robert M. Banta, Ralph C. Foster, and Jean-Luc Redelsperger. March 2004. "The Structure of the Near-Neutral Atmospheric Surface Layer". *Journal of the Atmospheric Sciences*, vol. 61, n° 6, p. 699–714.

Drobinski, Philippe, Pierre Carlotti, Jean-Luc Redelsperger, Robert M. Banta, Valery Masson, and Rob K. Newsom. 2007. "Numerical and Experimental Investigation of the Neutral Atmospheric Surface Layer". *Journal of the Atmospheric Sciences*, vol. 64, n° 1, p. 137–156.

Duynkerke, P. G. March 1988. "Application of the E – ϵ Turbulence Closure Model to the Neutral and Stable Atmospheric Boundary Layer". *Journal of the Atmospheric Sciences*, vol. 45, n° 5, p. 865–880.

Dyer, A. J. 1974. "A review of flux-profile relationships". *Boundary-Layer Meteorology*, vol. 7, n° 3, p. 363–372.

Easom, Gary. 2000. “ Improved turbulence models for computational wind engineering ”. Ph.D., University of Nottingham. <http://etheses.nottingham.ac.uk/113/>, 220 p.

Eidsvik, Karl J. 2005. “ A system for wind power estimation in mountainous terrain. Prediction of Askervein hill data ”. *Wind Energy*, vol. 8, n° 2, p. 237–249.

Eidsvik, Karl J., A. Holstad, I. Lie, and T. Utnes. 2004. “ A Prediction System for Local Wind Variations in Mountainous Terrain ”. *Boundary-Layer Meteorology*, vol. 112, n° 3, p. 557–586.

Environment Canada. 2004. “ Canadian Wind Energy Atlas ”. <www.windatlas.ca>.

Finardi, S., G. Brusasca, M. G. Morselli, F. Trombetti, and F. Tampieri. March 1993. “ Boundary-layer flow over analytical two-dimensional hills: A systematic comparison of different models with wind tunnel data ”. *Boundary-Layer Meteorology*, vol. 63, n° 3, p. 259–291.

Finardi, S., F. Trombetti, F. Tampieri, and G. Brusasca. 1995. “ An assessment of mixing-length closure schemes for models of turbulent boundary layers over complex terrain ”. *Boundary-Layer Meteorology*, vol. 73, n° 4, p. 343–356.

Foken, Thomas. 2006. “ 50 Years of the Monin-Obukhov Similarity Theory ”. *Boundary-Layer Meteorology*, vol. 119, n° 3, p. 431–447.

Frank, Helmut P. and Lars Landberg. 1997. “ Modelling the wind climate of Ireland ”. *Boundary-Layer Meteorology*, vol. 85, n° 3, p. 359–378.

Frank, Helmut P., Erik Lundtang Petersen, Reijo Hyvönen, and Bengt Tammelin. 1999. “ Calculation on the Wind Climate in Northern Finland: The Importance of Inversion and Roughness Variations during the Seasons ”. *Wind Energy*, vol. 2, n° 2, p. 113–123.

Gal-Chen, T. and R. C. J. Somerville. 1975. “ On the use of a coordinate transformation for the solution of the Navier-Stokes equations ”. *Journal of Computational Physics*, vol. 17, n° 2, p. 209–228.

Garratt, J. R., 1992. *The Atmospheric Boundary Layer*. Cambridge : Cambridge University Press, 336 p.

Garratt, J. R., G. D. Hess, W. L. Physick, and P. Bougeault. 1996. “ The atmospheric boundary layer – advances in knowledge and application ”. *Boundary-Layer Meteorology*, vol. 78, n° 1, p. 9–37.

Gasset, Nicolas, Gérard J. Poitras, Yves Gagnon, and Carl Brothers. 2005. “ Study of atmospheric boundary layer flows over a coastal cliff ”. *Wind Engineering*, vol. 29, n° 1, p. 3–24.

Georgelin, Marc, Philippe Bougeault, Thomas Black, Nedjlejka Brzovic, Andrea Buzzi, Javier Calvo, Vincent Casse, Michel Desgagné, Ryad El-Khatib, Jean-Francois Geleyn, Teddy Holt, Song-You Hong, Teruyuki Kato, Jack Katzfey, Kazuo Kurihara, Bruno Lacroix, Francois Lalaurette, Yvon Lemaitre, Jocelyn Mailhot, Detlev Majewski, Pietro Malguzzi, Valery Masson, John McGregor, Enrico Minguzzi, Tiziana Paccagnella, and Clive Wilson. 2000. " The second COMPARE exercise: A model intercomparison using a case of a typical mesoscale orographic flow, the PYREX IOP3 ". *Quarterly Journal of the Royal Meteorological Society*, vol. 126, p. 991–1029.

Germano, Massimo, Ugo Piomelli, Parviz Moin, and William H. Cabot. 1991. " A dynamic subgrid-scale eddy viscosity model ". *Physics of Fluids A: Fluid Dynamics*, vol. 3, n° 7, p. 1760.

Giebel, Gregor, Lars Landberg, Georges N. Kariniotakis, and Richard A. Brownsword. 2003. " State-of-the-Art on Methods and Software Tools for Short-Term Prediction of Wind Energy Production ". In *Proceedings of the European Wind Energy Conference & Exhibition EWEC 2003*. (Madrid, Spain 2003).

Girard, Claude and Yves Delage. 1990. " Stable Schemes for Nonlinear Vertical Diffusion in Atmospheric Circulation Models ". *Monthly Weather Review*, vol. 118, n° 3, p. 737–745.

Girard, Claude, Robert Benoit, and Michel Desgagné. 2005. " Finescale Topography and the MC2 Dynamics Kernel ". *Monthly Weather Review*, vol. 133, n° 6, p. 1463–1477.

Global Wind Energy Council (GWEC). 2011. *Global Wind Report 2011 - Annual market update*. Annual report. Global Wind Energy Council (GWEC), 65 p.

Gray, M. E. B., J. Petch, S. H. Derbyshire, Andy R. Brown, Adrian P. Lock, H. A. Swann, and P. R. A. Brown. 2001. *Version 2.3 Of The Met Office Large Eddy Model: Part II. Scientific Documentation*. APR Turbulence and Diffusion Report 276. FitzRoy Road, Exeter EX1 3PB, UK : UK Met Office, 48 p.

Grubišić, Vanda, James D. Doyle, Joachim Kuettner, Richard Dirks, Stephen A. Cohn, Laura L. Pan, Stephen Mobbs, Ronald B. Smith, David C. Whiteman, Stanley Czyzyk, Simon Vosper, Martin Weissmann, Samuel Haimov, Stephan F. J. de Wekker, and Fotini Katopodes Chow. October 2008. " The Terrain-Induced Rotor Experiment ". *Bulletin of the American Meteorological Society*, vol. 89, n° 10, p. 1513–1533.

Haltiner, George J. and Roger T. Williams, 1980. *Numerical Prediction and Dynamic Meteorology*. ed. 2nd. New York ; New York : John Wiley and Sons, 477 p.

Hargreaves, D. M. and Nigel G. Wright. May 2007. " On the use of the k–ϵ model in commercial CFD software to model the neutral atmospheric boundary layer ". *Journal of Wind Engineering and Industrial Aerodynamics*, vol. 95, n° 5, p. 355–369.

Hobson, J. M., Nigel Wood, and Andy R. Brown. 1999. " Large-eddy simulations of neutrally stratified flow over surfaces with spatially varying roughness length ". *Quarterly Journal of the Royal Meteorological Society*, vol. 125, n° 558, p. 1937–1958.

Holton, James R., 2004. *An introduction to dynamic meteorology*, volume 88 of *International geophysics series*. ed. 4th. Amsterdam ; Boston ; London : Elsevier Academic Press, 535 p.

Holtslag, Albert A. M. and Frans T. M. Nieuwstadt. July 1986. " Scaling the atmospheric boundary layer ". *Boundary-Layer Meteorology*, vol. 36, n° 1-2, p. 201–209.

Hoxey, R. P., P. J. Richards, and J. L. Short. 2002. " A 6m cube in an atmospheric boundary layer flow. Part I. Full-scale and wind-tunnel results ". *Wind and Structures, An International Journal*, vol. 5, n° 2-4, p. 165–176.

Hunt, J. C. R. and Pierre Carlotti. 2001. " Statistical Structure at the Wall of the High Reynolds Number Turbulent Boundary Layer ". *Flow, Turbulence and Combustion*, vol. 66, n° 4, p. 453–475.

Hurley, Peter J. 1997. " An evaluation of several turbulence schemes for the prediction of mean and turbulent fields in complex terrain ". *Boundary-Layer Meteorology*, vol. 83, n° 1, p. 43–73.

Iizuka, S. and H. Kondo. 2004. " Performance of various sub-grid scale models in large-eddy simulations of turbulent flow over complex terrain ". *Atmospheric Environment*, vol. 38, n° 40, p. 7083–7091.

Ishihara, Takeshi, Yozo Fujino, and Kazuki Hibi. 2001. " A wind tunnel study of separated flow over a two-dimensional ridge and a circular hill ". *Journal of Wind Engineering*, vol. 89, n° The Fifth Asia-Pacific Conference on Wind Engineering. Koyto, p. 573–576.

Jackson, P. S. and J. C. R. Hunt. 1975. " Turbulent wind flow over a low hill ". *Quarterly Journal of the Royal Meteorological Society*, vol. 101, n° 430, p. 929–955.

Kariniotakis, Georges N., Ignacio Martí, D. Casas, Pierre Pinson, Torben Skov Nielsen, Henrik Madsen, Gregor Giebel, J. Usaola, Ismael Sanchez, A. M. Palomares, Richard A. Brownsword, Jens Tambke, Ulrich Focken, Matthias Lange, P. Louka, G. Kallos, C. Lac, G. Sideratos, and Gael Descombes. 2004. " What Performance Can Be Expected by Short-term Wind Power Prediction Models Depending on Site Characteristics? ". In *Proceedings of the European Wind Energy Conference EWEC 2004*. (London, UK 2004).

Khurshudyan, Leon H., William H. Snyder, and Igor V. Nekrasov. 1982. *Flow and Dispersion of Pollutants Over Two-Dimensional Hills : Summary Report on Joint Soviet-American Study*. EPA-600/4-81-067. Environmental Sciences Research Laboratory, US Environmental Protection Agency, 130 p.

Khurshudyan, Leon H., William H. Snyder, Igor V. Nekrasov, R. E. Lawson, R. S. Thompson, and Schiermeier F. A. 1990. *Flow and Dispersion of Pollutants Within Two-Dimensional Valleys: Summary Report on Joint Soviet-American Study*. EPA/600/S3-90/025. Atmospheric Research and Exposure Assessment Laboratory, US Environmental Protection Agency, 9 p.

Kim, H. G. and V. C. Patel. 2000. “ Test of turbulence models for wind flow over terrain with separation and recirculation ”. *Boundary-Layer Meteorology*, vol. 94, n° 1, p. 5–21.

Klemp, Joseph B. and William C. Skamarock. 2004. Model numerics for convective-storm simulation. Fedorovich, E., Richard Rotunno, and Bjorn Stevens, editors, *Atmospheric Turbulence and Mesoscale Meteorology: Scientific Research Inspired by Doug Lilly*, chapter 6, p. 117–137. Cambridge University Press, Cambridge, ed. 1. ISBN 9780521835886.

Knopp, T., B. Eisfeld, and Javier Calvo. February 2009. “ A new extension for k–ω turbulence models to account for wall roughness ”. *International Journal of Heat and Fluid Flow*, vol. 30, n° 1, p. 54–65.

Kosović, Branko. 1997. “ Subgrid-scale modelling for the large-eddy simulation of high-Reynolds-number boundary layers ”. *Journal of Fluid Mechanics*, vol. 336, p. 151–182.

Kosović, Branko and Judith A. Curry. 2000. “ A Large Eddy Simulation Study of a Quasi-Steady, Stably Stratified Atmospheric Boundary Layer ”. *Journal of the Atmospheric Sciences*, vol. 57, n° 8, p. 1052–1068.

Landberg, Lars, Gregor Giebel, Henrik Aalborg Nielsen, Torben Skov Nielsen, and Henrik Madsen. 2003a. “ Short-term Prediction – An Overview ”. *Wind Energy*, vol. 6, n° 3, p. 273–280.

Landberg, Lars, Lisbeth Myllerup, Ole Rathmann, Erik Lundtang Petersen, Bo Hoffmann Jørgensen, Jake Badger, and Niels Gylling Mortensen. 2003b. “ Wind Resource Estimation – An Overview ”. *Wind Energy*, vol. 6, n° 3, p. 261–271.

Lapointe-Thériault, David. 2012. “ Vers une résolution numérique de la couche limite atmosphérique à micro-échelle avec la méthode de simulation des grandes échelles (LES) sous OpenFOAM ”. M.Sc., École de technologie superieure, 173 p.

Laprise, René, Daniel Caya, Guy Bergeron, and Michel Giguère. 1997. “ The Formulation of the André Robert MC2 (Mesoscale Compressible Community) Model ”. *Atmosphere-Ocean*, vol. 35, n° 1, p. 195–220.

Launder, B. E. and D. B. Spalding, 1972. *Mathematical models of turbulence*. Academic Press.

Launder, B. E. and D. B. Spalding. 1974. “ The numerical computation of turbulent flows ”. *Science*, vol. 3, n° 2, p. 269–289.

Lenderink, G. and Albert A. M. Holtslag. 2004. “ An updated length-scale formulation for turbulent mixing in clear and cloudy boundary layers ”. *Quarterly Journal of the Royal Meteorological Society*, vol. 130, n° 604, p. 3405–3427.

Leonard, A. 1974. “ Energy Cascade in Large-Eddy Simulations of Turbulent Fluid Flows ”. *Advances in Geophysics*, vol. 18, p. 237.

Lesieur, Marcel, Olivier Métais, and Pierre Comte, 2005. *Large-Eddy Simulations of Turbulence*, volume 20. New York : Cambridge University Press, 233 p.

Levitan, Marc L., Kishor C. Mehta, Chee V. Chok, and Daniel L. Millsaps. January 1990. " An overview of Texas Tech's wind engineering field research laboratory ". *Journal of Wind Engineering and Industrial Aerodynamics*, vol. 36, p. 1037–1046.

Lilly, Douglas K. May 1962. " On the numerical simulation of buoyant convection ". *Tellus*, vol. 14, n° 2, p. 148–172.

Lilly, Douglas K. 1966. *The representation of small-scale turbulence in numerical simulation experiments*. NCAR Manuscript No. 281. Boulder, Colorado : National Center for Atmospheric Research, 23 p.

Lilly, Douglas K. 1992. " A proposed modification of the Germano subgrid-scale closure method ". *Physics of Fluids A: Fluid Dynamics*, vol. 4, n° 3, p. 633.

Lun, Yu Fat, Akashi Mochida, Shuzo Murakami, Hiroshi Yoshino, and Taichi Shirasawa. 2003. " Numerical simulation of flow over topographic features by revised k-ϵ models ". *Journal of Wind Engineering and Industrial Aerodynamics*, vol. 91, n° 1-2, p. 231–245.

Mailhot, Jocelyn and Robert Benoit. 1982. " A Finite-Element Model of the Atmospheric Boundary Layer Suitable for Use with Numerical Weather Prediction Models ". *Journal of the Atmospheric Sciences*, vol. 39, n° 10, p. 2249–2266.

Mailhot, Jocelyn, Stéphane Bélair, Robert Benoit, Bernard Bilodeau, Yves Delage, Luc Fillion, Louis Garand, Claude Girard, and André Tremblay. 1998. *Scientific Description of RPN Physics Library - Version 3.6 -*. Technical report. Dorval, Québec, Canada : Recherche en Prévision Numérique, Atmospheric Environment Service, 197 p.

Manwell, J. F., J. G. McGowan, and Anthony L. Rogers, 2002. *Wind energy explained theory, design and application*. Chichester ; New York : John Wiley & Sons, 577 p.

Marusic, I., G. J. Kunkel, and Fernando Porté-Agel. 2001. " Experimental study of wall boundary conditions for large-eddy simulation ". *Journal of Fluid Mechanics*, vol. 446, p. 309–320.

Mason, Paul J. 1989. " Large-Eddy Simulation of the Convective Atmospheric Boundary Layer ". *Journal of the Atmospheric Sciences*, vol. 46, n° 11, p. 1492–1516.

Mason, Paul J. 1994. " Large-eddy simulation: A critical review of the technique ". *Quarterly Journal of the Royal Meteorological Society*, vol. 120, n° 515, p. 1–26.

Mason, Paul J. and Andy R. Brown. 1999. " On Subgrid Models and Filter Operations in Large Eddy Simulations ". *Journal of the Atmospheric Sciences*, vol. 56, n° 13, p. 2101–2114.

Mason, Paul J. and D. J. Thomson. 1987. "Large-Eddy simulations of the neutral-static-stability planetary boundary layer". *Quarterly Journal of the Royal Meteorological Society*, vol. 113, n° 476, p. 413–443.

Mason, Paul J. and D. J. Thomson. 1992. "Stochastic backscatter in large-eddy simulations of boundary layers". *Journal of Fluid Mechanics*, vol. 242, p. 51–78.

Mellor, George L. and Tetsuji Yamada. October 1974. "A Hierarchy of Turbulence Closure Models for Planetary Boundary Layers". *Journal of the Atmospheric Sciences*, vol. 31, n° 7, p. 1791–1806.

Mellor, George L. and Tetsuji Yamada. 1982. "Development of a turbulence closure model for geophysical fluid problems". *Reviews of Geophysics*, vol. 20, n° 4, p. 851.

Meneveau, Charles, Thomas S. Lund, and William H. Cabot. April 1996. "A Lagrangian dynamic subgrid-scale model of turbulence". *Journal of Fluid Mechanics*, vol. 319, p. 353.

Miranda, P. M. A. and I. N. James. October 1992. "Non-Linear Three-Dimensional Effects On Gravity-Wave Drag: Splitting Flow and Breaking Waves". *Quarterly Journal of the Royal Meteorological Society*, vol. 118, n° 508, p. 1057–1081.

Moeng, Chin-Hoh. 1984. "A Large-Eddy-Simulation Model for the Study of Planetary Boundary-Layer Turbulence". *Journal of the Atmospheric Sciences*, vol. 41, n° 13, p. 2052–2062.

Moeng, Chin-Hoh and Peter P. Sullivan. 1994. "A Comparison of Shear- and Buoyancy-Driven Planetary Boundary Layer Flows". *Journal of the Atmospheric Sciences*, vol. 51, n° 7, p. 999–1022.

Moeng, Chin-Hoh and John C. Wyngaard. December 1988. "Spectral Analysis of Large-Eddy Simulations of the Convective Boundary Layer". *Journal of the Atmospheric Sciences*, vol. 45, n° 23, p. 3573–3587.

Moeng, Chin-Hoh and John C. Wyngaard. July 1989. "Evaluation of Turbulent Transport and Dissipation Closures in Second-Order Modeling". *Journal of the Atmospheric Sciences*, vol. 46, n° 14, p. 2311–2330.

Moss, W. D. and S. Baker. 1980. "Recirculating flows associated with two-dimensional steps". *Aeronautical Quarterly*, vol. 31, n° 3, p. 151–172.

Murakami, Shuzo. June 1997. "Current status and future trends in computational wind engineering". *Journal of Wind Engineering and Industrial Aerodynamics*, vol. 67-68, p. 3–34.

Murakami, Shuzo. 1998. "Overview of turbulence models applied in CWE–1997". *Journal of Wind Engineering and Industrial Aerodynamics*, vol. 74-76, n° 1-2, p. 1–24.

Nieuwstadt, Frans T. M. July 1984. “ The Turbulent Structure of the Stable, Nocturnal Boundary Layer ”. *Journal of the Atmospheric Sciences*, vol. 41, n° 14, p. 2202–2216.

Nieuwstadt, Frans T. M., Paul J. Mason, Chin-Hoh Moeng, and Ulrich Schumann. 1992. “ Large-Eddy Simulation of the Convective Boundary Layer: A Comparison of Four Computer Codes ”. In *8th Symposium on Turbulent Shear Flows*. p. 343–367. Springer, Berlin.

Panton, Ronald L., 1996. *Incompressible Flow*. ed. 3rd. New York ; New York : Wiley-Interscience, 840 p.

Patel, V. C. September 1998. “ Perspective: Flow at High Reynolds Number and Over Rough Surfaces–Achilles Heel of CFD ”. *Journal of Fluids Engineering*, vol. 120, n° 3, p. 434–444.

Pelletier, Claude, Jocelyn Mailhot, Adrian P. Lock, and Claude Girard. November 2005. *Three-Dimensional Turbulent Diffusion in MC2*. Working Notes. Recherche en Prévision Numérique (RPN), Environnement Canada (EC), 48 p.

Petersen, Erik Lundtang, Niels Gylling Mortensen, Lars Landberg, Jørgen Højstrup, and Helmut P. Frank. 1998. “ Wind Power Meteorology. Part I: Climate and Turbulence ”. *Wind Energy*, vol. 1, n° 1, p. 2–22.

Pielke, Roger A. and Melville E. Nicholls. June 1997. “ Use of meteorological models in computational wind engineering ”. *Journal of Wind Engineering and Industrial Aerodynamics*, vol. 67-68, p. 363–372.

Pinard, Jean-Paul, Robert Benoit, and Wei Yu. September 2005. “ A WEST Wind Climate Simulation of the Mountainous Yukon ”. *Atmosphere-Ocean*, vol. 43, n° 3, p. 259–282.

Pinson, Pierre and Georges N. Kariniotakis. 2004. “ On-line assessment of prediction risk for wind power production forecasts ”. *Wind Energy*, vol. 7, n° 2, p. 119–132.

Pinty, Jean-Pierre, Robert Benoit, Evelyne Richard, and René Laprise. 1995. “ Simple Tests of a Semi-Implicit Semi-Lagrangian Model on 2D Mountain Wave Problems ”. *Monthly Weather Review*, vol. 23, n° 10, p. 3042–3058.

Piomelli, Ugo. May 1999. “ Large-eddy simulation: achievements and challenges ”. *Progress in Aerospace Sciences*, vol. 35, n° 4, p. 335–362.

Piomelli, Ugo. 2008. “ Wall-layer models for large-eddy simulations ”. *Progress in Aerospace Sciences*, vol. 44, n° 6, p. 437–446.

Pope, Stephen B., 2000. *Turbulent Flows*. Cambridge ; New York : Cambrige University Press, 771 p.

Porté-Agel, Fernando, Charles Meneveau, and Marc B. Parlange. 2000. “ A scale-dependent dynamic model for large-eddy simulation: application to a neutral atmospheric boundary layer ”. *Journal of Fluid Mechanics*, vol. 415, p. 261–284.

Poulos, Gregory S., William Blumen, David C. Fritts, Julie K. Lundquist, Jielun Sun, Sean P. Burns, Carmen Nappo, Robert Banta, Rob K. Newsom, Joan Cuxart, Enric Terradellas, Ben Balsley, and Michael Jensen. 2002. “ CASES-99: A Comprehensive Investigation of the Stable Nocturnal Boundary Layer ”. *Bulletin of the American Meteorological Society*, vol. 83, n° 4, p. 555–581.

Quinn, A. D. and P. J. Richards. March 2002. “ A 6m cube in an atmospheric boundary layer flow Part 2: Computational solutions ”. *Wind and Structures, An International Journal*, vol. 5, n° 2-4, p. 177–192.

Randall, David A. 2010. The Anelastic and Boussinesq Approximations. *Quick Studies in Atmospheric Science*, p. 19. Department of Atmospheric Science, Colorado State University. <http://kiwi.atmos.colostate.edu/group/dave/pdf/AneBous.pdf>.

Randall, David A. 2011. Riding along the air. *An Introduction to Numerical Modeling of the Atmosphere*, chapter 5, p. 73. Department of Atmospheric Science, Colorado State University. <http://kiwi.atmos.colostate.edu/group/dave/at604.html>.

Redelsperger, Jean-Luc and Gilles Sommeria. 1981. “ Méthode de représentation de la turbulence d’échelle inférieure à la maille pour un modèle tri-dimensionnel de convection nuageuse ”. *Boundary-Layer Meteorology*, vol. 21, n° 4, p. 509–530.

Redelsperger, Jean-Luc and Gilles Sommeria. 1986. “ Three-dimensional simulation of a convective storm: sensitivity studies on subgrid parameterization and spatial resolution ”. *Journal of the atmospheric sciences*, vol. 43, n° 22, p. 2619–2635.

Redelsperger, Jean-Luc, F. Mahe, and Pierre Carlotti. 2001. “ A simple and general subgrid model suitable both for surface layer and free-stream turbulence ”. *Boundary-Layer Meteorology*, vol. 101, n° 3, p. 375–408.

Richards, P. J. and R. P. Hoxey. 1993. “ Appropriate Boundary-Conditions for Computational Wind Engineering Models Using the k-ϵ Turbulence Model ”. *Journal of Wind Engineering and Industrial Aerodynamics*, vol. 46–47, p. 145–153.

Robert, André, Tai Loy Yee, and Harold Ritchie. July 1985. “ A Semi-Lagrangian and Semi-Implicit Numerical Integration Scheme for Multilevel Atmospheric Models ”. *Monthly Weather Review*, vol. 113, n° 3, p. 388–394.

Ross, A. N., S. Arnold, S. B. Vosper, S. D. Mobbs, N. Dixon, and A. G. Robins. December 2004. “ A comparison of wind-tunnel experiments and numerical simulations of neutral and stratified flow over a hill ”. *Boundary-Layer Meteorology*, vol. 113, n° 3, p. 427–459.

Rossby, Carl-Gustaf. 1932. “ A generalization of the theory of the mixing length with applications to atmospheric and oceanic turbulence ”. *MIT Meteorological papers*, vol. I, n° 4, p. 1–36.

Russo, Joseph M. and John W. Zack. January 1997. “ Downscaling GCM Output with a Mesoscale Model ”. *Journal of Environmental Management*, vol. 49, n° 1, p. 19–29.

Sagaut, Pierre, 2006. *Large eddy simulation for incompressible flows: an introduction*. ed. 3rd. Berlin : Springer Verlag, 556 p.

Schlichting, H., 1979. *Boundary-layer theory*. ed. 1st. McGraw-Hill, 817 p.

Schmidt, Helmut and Ulrich Schumann. March 1989. “ Coherent structure of the convective boundary layer derived from large-eddy simulations ”. *Journal of Fluid Mechanics*, vol. 200, p. 511–562.

Schumann, Ulrich. 1975. “ Subgrid scale model for finite difference simulations of turbulent flows in plane channels and annuli ”. *Journal of Computational Physics*, vol. 18, n° 4, p. 376–404.

Senocak, Inanc, Andrew S. Ackerman, Michael P. Kirkpatrick, David E. Stevens, and Nagi N. Mansour. 2007. “ Study of near-surface models for large-eddy simulations of a neutrally stratified atmospheric boundary layer ”. *Boundary-Layer Meteorology*, vol. 124, n° 3, p. 405–424.

Shaw, William J., Julie K. Lundquist, and Scott J. Schreck. 2009. “ Research Needs For Wind Resource Characterization ”. *Bulletin of the American Meteorological Society*, vol. 90, n° 4, p. 535–538.

Shuman, Frederick G. 1957. “ Numerical Methods in Weather Prediction: II. Smoothing and Filtering ”. *Monthly Weather Review*, vol. 85, n° 11, p. 357.

Silva Lopes, A., J. M. L. M. Palma, and F. A. Castro. 2007. “ Simulation of the Askervein flow. Part 2: Large-eddy simulations ”. *Boundary-Layer Meteorology*, vol. 125, n° 1, p. 85–108.

Skamarock, William C., Joseph B. Klemp, Jimy Dudhia, David O. Gill, Dale M. Barker, Michael G. Duda, Xiang-Yu Huang, Wei Wang, and Jordan G. Powers. 2008. *A description of the Advanced Research WRF Version 3*. NCAR Technical Note June. Boulder, Colorado, USA : Mesoscale and Microscale Meteorology Division , National Center for Atmospheric Research, 113 p.

Smagorinsky, Joseph. 1963. “ General circulation experiments with the primitive equations: 1. The basic experiment ”. *Monthly Weather Review*, vol. 91, n° 3, p. 99–164.

Sommeria, Gilles. 1976. “ Three-Dimensional Simulation of Turbulent Processes in an Undisturbed Trade Wind Boundary Layer ”. *Journal of the Atmospheric Sciences*, vol. 33, n° 2, p. 216–241.

Sorbjan, Zbigniew. 2003. Air-Pollution Meteorology. Zannetti, P., editor, *Air Quality Modeling: Theories, Methodologies, Computational Techniques, and Available Databases and Software. Vol. I – Fundamentals*, chapter 4, p. 63. The EnviroComp Institute and the Air & Waste Management Association.

Sorbjan, Zbigniew. 2005a. Large-eddy simulations of the atmospheric boundary layer. Zannetti, P., editor, *Air Quality Modeling: Theories, Methodologies, Computational Techniques, and Available Databases and Software. Vol. II – Advanced Topics*, chapter 5B, p. 71. The EnviroComp Institute and the Air & Waste Management Association. <http://academic.mu.edu/sorbjanz/Sorbjan.pdf>.

Sorbjan, Zbigniew. September 2005b. " Statistics of Scalar Fields in the Atmospheric Boundary Layer Based on Large-eddy Simulations. Part 1: Free Convection ". *Boundary-Layer Meteorology*, vol. 116, n° 3, p. 467–486.

Spera, David A., 1994. *Wind Turbine Technologies*. ed. 1st. New York : American Society of Mechanical Engineers Press, 638 p.

Stangroom, Paul. 2004. " CFD Modelling of Wind Flow Over Terrain ". Ph.D., University of Nottingham. <http://etheses.nottingham.ac.uk/112/>, 298 p.

Stathopoulos, Theodore. June 1997. " Computational wind engineering: Past achievements and future challenges ". *Journal of Wind Engineering and Industrial Aerodynamics*, vol. 67-68, p. 509–532.

Stathopoulos, Theodore. 2002. " The numerical wind tunnel for industrial aerodynamics: Real or virtual in the new millennium? ". *Wind and Structures, An International Journal*, vol. 5, n° 2-4, p. 193–208.

Steppeler, J., R. Hess, U. Schättler, and Luca Bonaventura. 2003. " Review of numerical methods for nonhydrostatic weather prediction models ". *Meteorology and Atmospheric Physics*, vol. 82, n° 1–4, p. 287–301.

Stoll, Rob and Fernando Porté-Agel. January 2006. " Effect of Roughness on Surface Boundary Conditions for Large-Eddy Simulation ". *Boundary-Layer Meteorology*, vol. 118, n° 1, p. 169–187.

Stull, Roland B., 1988. *An introduction to boundary layer meteorology*. Dordrecht ; Boston : Kluwer Academic Publishers, 666 p.

Sullivan, Peter P., James C. McWilliams, and Chin-Hoh Moeng. 1994. " A subgrid-scale model for large-eddy simulation of planetary boundary-layer flows ". *Boundary-Layer Meteorology*, vol. 71, n° 3, p. 247–276.

Sumner, Jonathon and Christian Masson. 2010. " k - ϵ Simulations of the Neutral ABL: Achieving Horizontal Homogeneity on Practical Grids ". In *48th AIAA Aeroscpace Sciences Meeting*. (Orlando, Florida 2010), p. 1–12. American Institute of Aeronautics and Astronautics.

Sumner, Jonathon, Christophe Sibuet Watters, and Christian Masson. May 2010. "CFD in Wind Energy: The Virtual, Multiscale Wind Tunnel". *Energies*, vol. 3, n° 5, p. 989–1013.

Svensson, Gunilla and Albert A. M. Holtslag. 2006. "Single column modeling of the diurnal cycle based on CASES99 data - GABLS second intercomparison project". In *17th Symposium on Boundary Layers and Turbulence*. (San Diego, CA, USA 2006), p. 22–25.

Svensson, Gunilla and Albert A. M. Holtslag. 2007. "The diurnal cycle - GABLS second intercomparison project". *GEWEX News*, vol. 17, n° 1, p. 9–10.

Takemi, Tetsuya and Richard Rotunno. January 2005. "CORRIGENDUM". *Monthly Weather Review*, vol. 133, n° 1, p. 339–341.

Tanguay, Monique, André Robert, and René Laprise. 1990. "A Semi-implicit Send-Lagrangian Fully Compressible Regional Forecast Model". *Monthly Weather Review*, vol. 118, n° 10, p. 1970.

Taylor, Peter A. and Yves Delage. 1971. "A note on finite-difference schemes for the surface and planetary boundary layers". *Boundary-Layer Meteorology*, vol. 2, n° 1, p. 108–121.

Taylor, Peter A., John L. Walmsley, and James R. Salmon. 1983. "A simple model of neutrally stratified boundary-layer flow over real terrain incorporating wavenumber-dependent scaling". *Boundary-Layer Meteorology*, vol. 26, n° 2, p. 169–189.

Taylor, Peter A., Paul J. Mason, and E. F. Bradley. 1987. "Boundary-layer flow over low hills". *Boundary-Layer Meteorology*, vol. 39, n° 1-2, p. 107–132.

Teixeira, Joao, B. Stevens, C. S. Bretherton, R. T. Cederwall, James D. Doyle, Jean-Christophe Golaz, Albert A. M. Holtslag, S. A. Klein, Julie K. Lundquist, David A. Randall, A. Pier Siebesma, and Pedro M. M. Soares. 2008. "Parameterization of the Atmospheric Boundary Layer: A View from Just Above the Inversion". *Bulletin of the American Meteorological Society*, vol. 89, n° 4, p. 453.

Tennekes, H. and J. L. Lumley, 1972. *A First Course in Turbulence*. Cambridge : The MIT press, 300 p.

Thomas, Stephen J., Claude Girard, Robert Benoit, and Pierre Pellerin. 1998. "A New Adiabatic Kernel for the MC2 Model". *Atmosphere-Ocean*, vol. 36, p. 241–270.

Tritton, D. J., 1988. *Physical Fluid Dynamics*. ed. 2nd. Oxford : Oxford University Press, 519 p.

Troen, Ib and Erik Lundtang Petersen, 1989. *European Wind Atlas*. Roskilde : Risø National Laboratory, 656 p.

Uchida, T. and Y. Ohya. 2003. “Large-eddy simulation of turbulent airflow over complex terrain”. *Journal of Wind Engineering and Industrial Aerodynamics*, vol. 91, n° 1-2, p. 219–229.

Undheim, O., H. I. Andersson, and E. Berge. 2006. “Non-Linear, Microscale Modelling of the Flow Over Askervein Hill”. *Boundary-Layer Meteorology*, vol. 120, n° 3, p. 477–495.

van Dop, Han, Albert A. M. Holtslag, and Jordi Vilà. 2008. “Les Houches Summer School”. <http://www.phys.uu.nl/~dop/summerschool/lectures.html>.

van Driest, ER. 1956. “On turbulent flow near a wall”. *Journal of the Aeronautical Science*, vol. 23, n° 11, p. 1007–1011.

Walmsley, John L. and Peter A. Taylor. 1996. “Boundary-layer flow over topography: Impacts of the Askervein study”. *Boundary-Layer Meteorology*, vol. 78, n° 3-4, p. 291–320.

Weng, Wensong and Peter A. Taylor. 2003. “On Modelling the One-Dimensional Atmospheric Boundary Layer”. *Boundary-Layer Meteorology*, vol. 107, n° 2, p. 371–400–400.

Wilcox, David C, 1994. *Turbulence Modeling for CFD*. La Cañada ; California : DCW Industries, Inc., 477 p.

Wright, Nigel G. and Gary Easom. December 2003. “Non-linear k–ϵ turbulence model results for flow over a building at full-scale”. *Applied Mathematical Modelling*, vol. 27, n° 12, p. 1013–1033.

Wyngaard, John C. 1975. “Modeling the planetary boundary layer – Extension to the stable case”. *Boundary-Layer Meteorology*, vol. 9, n° 4, p. 441–460.

Wyngaard, John C. 2004. “Toward Numerical Modeling in the "Terra Incognita" ”. *Journal of the Atmospheric Sciences*, vol. 61, n° 14, p. 1816.

Wyngaard, John C. and O. R. Coté. 1974. “The evolution of a convective planetary boundary layer – A higher-order-closure model study”. *Boundary-Layer Meteorology*, vol. 7, n° 3, p. 289–308.

Yu, Wei, Robert Benoit, Claude Girard, Anna Glazer, David Lemarquis, James R. Salmon, and Jean-Paul Pinard. 2006. “Wind Energy Simulation Toolkit (WEST): A Wind Mapping System for Use by the WindEnergy Industry”. *Wind Engineering*, vol. 30, n° 1, p. 15–33.

Zhang, C. X. 1994. “Numerical predictions of turbulent recirculating flows with a k–ϵ model”. *Journal of Wind Engineering and Industrial Aerodynamics*, vol. 51, n° 2, p. 177–201.